



***In silico* explorations of gold–biomolecule  
interactions for the engineering of  
biomedical gold nanomaterials**

A thesis submitted in fulfilment of the requirements for the degree of  
Doctor of Philosophy

**Patrick Raymond Charchar**

B. App. Sci. (Hons. 1st Class), RMIT University, 2012

B. App. Sci. (Physics) with Distinct, RMIT University, 2011

B. App. Sci. (Nanotechnology) with Distinct, RMIT University, 2011

School of Engineering  
College of Science, Engineering and Health  
RMIT University

March 2018

Primary Supervisor:  
Secondary Supervisors:

Professor Irene Yarovsky  
Dr Nevena Todorova  
Dr Andrew J. Christofferson

# Declaration of Candidature

---

I certify that except where due acknowledgement has been made, the work is that of the author alone; the work has not been submitted previously, in whole or in part, to qualify for any other academic award; the content of the choose an item is the result of work which has been carried out since the official commencement date of the approved research program; any editorial work, paid or unpaid, carried out by a third party is acknowledged; and, ethics procedures and guidelines have been followed.

I also acknowledge the support I have received for my research through the provision of an Australian Government Research Training Program Scholarship.

Patrick Raymond Charchar

March 2018

# Acknowledgements

---

As I sit and reflect on whom to thank, two phrases immediately come to mind: “standing on the shoulders of giants” and “it takes a village to raise a child”. In this case, the *village* is big and it’s full of *giants* whose shoulders I have stood on to be where I am today.

The first to thank are the educators: the teachers who nurtured my inquisitiveness, the lecturers who humbled me with their wealth of knowledge, and the supervisors who mentored and bestowed on me their first-hand wisdoms. Without the educators my mind would have never been cultivated. There are the supporters: the family that *still* refer to me as Prof. Pat (much to my annoyance), the friends who relentlessly pestered “are you a doctor yet?”, and the countless others who simply sat and listened to me broadcast about “gold nanoparticles this” and “molecular modelling that”. It is the supporters’ undying faith in me that kept me interested in my work and gave me the capacity to keep going. Then, there are my colleagues: the people I spent every day with during this mammoth endeavour, always happy to share their skills and always available for chats, lunch, coffee, and the occasional sneaky beer or wine. Without these fantastic people, the journey wouldn’t have been anywhere near as enjoyable as it was!

When it comes to thanking individuals, my primary supervisor Professor Irene Yarovsky is easily at the top of the list. Not because of formality, but rather because of the genuine respect, admiration and gratitude I have for her. Her guest lecture in *Nanotechnology Practice* during my undergraduate studies first introduced me to the world of molecular modelling and captured my imagination. Since then, she has consistently provided me with invaluable opportunities, leadership, insight, understanding, and encouragement that I am forever indebted to.

My secondary supervisors, Dr Nevena Todorova and Dr Andrew J. Christofferson, have also left their footprints across the pages of this thesis through the direction, support and friendship they have afforded me. To Nev, a huge thank you goes out for her continuous advice, persistence, loyalty, kindness, and reassurance throughout my PhD. Additionally, for always finding me when I got lost... like at Kings Cross. Andy I thank for his willingness and enthusiasm to guide, help, discuss, and teach me any impulsive thing I have requested. I sincerely value the many and extensive conversations we have shared over the years, be it intellectual or personal.

I have been extremely lucky to be part of a wonderfully stimulating, fun and professional group. Dr George Yiapanis, Dr Matthew Penna, Dr M. Harunur Rashid, and Dr Tu Le I thank

for providing such exceptional role models for me to aspire towards. Dr Kester W. J. Wong, Dr Adam Makarucha, Enxi (Jacky) Peng, Alan Bentvelzen, Lachlan Shaw, Wenxuan Li, and Kamron Ley specifically, I cheers for being such great mates. What an absolute pleasure it's been to share this adventure from the inception with Kam and his reliably clever wit!

I convey my deepest appreciations to Prof. Molly M. Stevens and her brilliant biomaterials team (past and present) including Dr Yiyang Lin, Dr Heiko Andresen, Dr Ciro Chippani, Dr Coline Jumeaux, Dr Karla-Luise Herpoldt, Amanda Diez Fernandez and the many others I have had the privilege of meeting, knowing and working with. I especially express my gratitude to Dr Lin for his tireless work, generosity, and genuine nature.

I also extend my thanks to Prof. Stefano Corni, Prof. Mike Finnis, and Prof. Jeffery Reimers for the very useful discussions and directions they have provided.

This work has been funded through the Australian Research Council under the Discovery Project schemes DP0984565, DP140101888, and DP170100511 and I acknowledge the financial support I have received: the Australian Government for the receipt of an Australian Postgraduate Award; the Australian Nanotechnology Network, Victorian Life Sciences Computational Initiative (VLSCI), RMIT University's School of Graduate Research, the University of Cambridge, and the Thomas Young Center (UK) for the provision of travel grants and fellowships. I likewise acknowledge the generous allocation of computational resources from the Australian National Computational Infrastructure (NCI), the Victorian Partnership for Advanced Computing (VPAC) and Melbourne Bioinformatics (previously VLSCI).

On a personal note, I thank all my close friends and family for their sympathy and tolerance over the past few years as this certainly hasn't been an easy feat and I'm sure it's taken a toll on them. My dearest siblings are three of the most amazing people I know, each a formidable character who has triumphed in the face of adversity but never forgotten to always look out for me. I thank them for being my unspoken pillars of support, helping me to trust my own judgement and follow my own path. My parents I thank for appreciating the hard work I put in, encouraging me to learn, and teaching me independence. Teta and Jido I thank for listening and pretending to know what I'm talking about... and of course, the elbows! To the Tites, thanks for being such resilient, kind-hearted, awesome people and for all the Fridays!

Finally, I dedicate this thesis to my most beautiful fiancée Marcy who is the reason I get up in the morning (literally). Without her there is no way I could have achieved this and words cannot express how grateful I am for her continued support, patience, and honesty. I love her more than I can describe and her charisma, uniqueness, nerve, and talent simply cannot be rivalled.

# Publications List

---

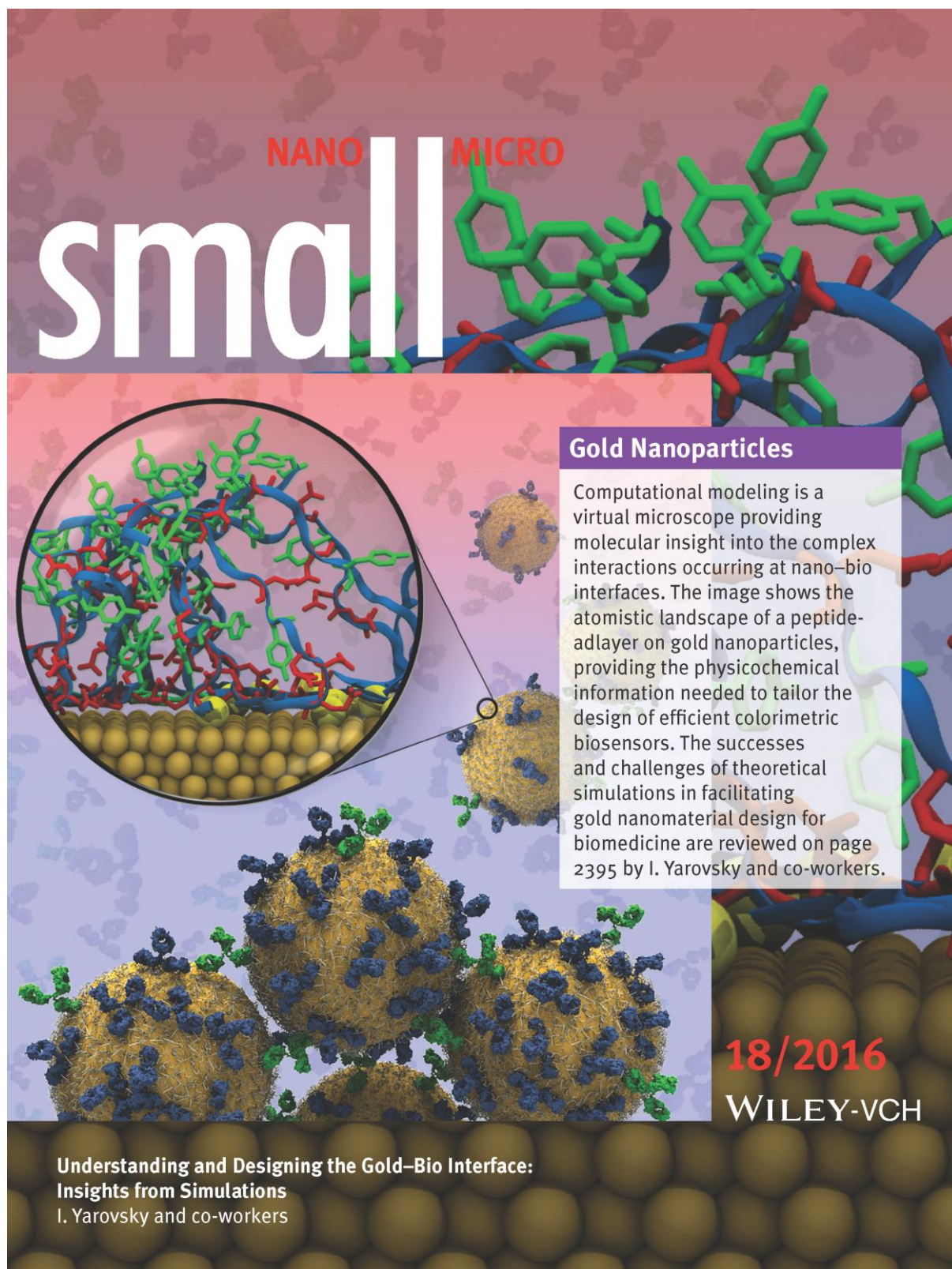
## Peer-Reviewed Publications

1. Y. LIN,\* **P. CHARCHAR**,\* A. J. CHRISTOFFERSON, M. R. THOMAS, N. TODOROVA, M. MAZO, J. DOUTCH, R. RICHARDSON, I. YAROVSKY, and M. M. STEVENS. Surface Ligand Effects on the Structure and Fluorescence of Peptide-Protected Gold Nanoclusters, In preparation. **\*Equally contributing authors**
2. **P. CHARCHAR**, A. J. CHRISTOFFERSON, N. TODOROVA, and I. YAROVSKY. Understanding and designing the gold-bio interface: Insights from simulations, *Small*, **12**: 2395-2418, 2016. DOI: [10.1002/smll.201503585](https://doi.org/10.1002/smll.201503585)
3. H. ANDRESEN, M. MAGER, M. GRIEBNER, **P. CHARCHAR**, N. TODOROVA, N. BELL, G. THEOCHARIDIS, S. BERTAZZO, I. YAROVSKY, and M. M. STEVENS. Single-step homogeneous immunoassays utilizing epitope-tagged gold nanoparticles: On the mechanism, feasibility, and limitations, *Chem. Mater.*, **26**: 4696-4704, 2014. DOI: [10.1021/cm500535p](https://doi.org/10.1021/cm500535p)

## Conference/Workshop Presentations

1. **P. CHARCHAR**, N. TODOROVA, A. CHRISTOFFERSON, Y. LIN, H. ANDRESEN, M. M. STEVENS AND I. YAROVSKY. Correlating Simulations of Peptide-Coated Gold Nanoparticles to Experiments. *AIMECS*, Melbourne, Australia, Jul 2017. **(Contributed Talk)**
2. **P. CHARCHAR**, N. TODOROVA, A. J. CHRISTOFFERSON AND I. YAROVSKY. Molecular dynamics investigations into peptide-coated gold nanoclusters for biomedical applications. *ACEMD*, Sydney, Australia, Jul 2016. **(Contributed Talk)**
3. **P. CHARCHAR**, N. TODOROVA, A. J. CHRISTOFFERSON AND I. YAROVSKY. Computational modelling of peptide-gold nanoclusters for biomedical applications. *7<sup>th</sup> International Nanomedicine Conference*, Sydney, Australia, Jun 2016. **(Contributed Talk)**
4. **P. CHARCHAR**, N. TODOROVA, A. J. CHRISTOFFERSON AND I. YAROVSKY. Investigating peptide-coated gold nanoclusters with ONETEP. *6<sup>th</sup> ONETEP Masterclass*, Cambridge, United Kingdom, Sep 2015. **(Contributed Talk)**
5. **P. CHARCHAR**, N. TODOROVA, A. J. CHRISTOFFERSON, Y. LIN, M. M. STEVENS AND I. YAROVSKY. Fluorescent peptide-coated gold nanoclusters: Multiscale modelling method to understand pH-sensitivity. *Nanotechnology & Medicines for Tomorrow*, Melbourne, Australia, Nov 2014. **(Poster)**
6. **P. CHARCHAR**, N. TODOROVA, A. J. CHRISTOFFERSON, Y. LIN, M. M. STEVENS AND I. YAROVSKY. Multiscale approach to model pH-responsive fluorescent peptide-Au<sub>25</sub> nanoclusters. *Ian Snook Conference on Chemical Physics*, Melbourne, Australia, Nov 2014. **(Poster)**
7. **P. CHARCHAR**, N. TODOROVA, A. J. CHRISTOFFERSON, Y. LIN, M. M. STEVENS AND I. YAROVSKY. Investigating the pH-responsiveness of fluorescent peptide-functionalised Au<sub>25</sub> nanoclusters through a multiscale simulation methodology. *5<sup>th</sup> COMBINE Australia Student Symposium*, Melbourne, Australia, Nov 2014. **(Poster)**

8. **P. CHARCHAR**, N. TODOROVA, A. J. CHRISTOFFERSON AND I. YAROVSKY. Molecular design of nano-sensors for biomedical applications: Exploring the bio-nano interface through simulation. *Borland Forum*, Melbourne, Australia, Oct 2014. (**Contributed Talk, Presentation Award**)
9. **P. CHARCHAR**, N. TODOROVA, A. J. CHRISTOFFERSON AND I. YAROVSKY. *In silico* engineering of gold nanomaterial biosensors: Exploring interactions with biomolecules. *RMIT HDR Student Conference*, Melbourne, Australia, Oct 2014. (**Contributed Talk**)
10. **P. CHARCHAR**, N. TODOROVA, A. J. CHRISTOFFERSON AND I. YAROVSKY. Biomolecule passivated gold nanomaterials for biomedical applications: Atomistic understanding through simulations. *RMIT HIRi Annual Research Day*, Melbourne, Australia, Sep 2014. (**Contributed Talk**)
11. **P. CHARCHAR**, N. TODOROVA, H. ANDRESEN, M. M. STEVENS AND I. YAROVSKY. Multiscale simulations of gold nanoparticles for biological applications: Opportunities and challenges. *ICONN*, Adelaide, Australia, Feb 2014. (**Contributed Talk**)
12. **P. CHARCHAR**, N. TODOROVA, H. ANDRESEN, M. M. STEVENS AND I. YAROVSKY. Peptide interactions with gold surfaces: A computational study. *ICFPAM*, Auckland, New Zealand, Dec 2013. (**Poster**)
13. **P. CHARCHAR**, N. TODOROVA, H. ANDRESEN, M. M. STEVENS AND I. YAROVSKY. Peptide functionalised gold nanoparticles for efficient biosensing: Insights from simulations. *4<sup>th</sup> Asia-Pacific Symposium on Nanobionics*, Melbourne, Australia, Nov 2013. (**Contributed Talk**)
14. **P. CHARCHAR**, N. TODOROVA, H. ANDRESEN, M. M. STEVENS AND I. YAROVSKY. Biosensing utilising epitope-tagged gold nanoparticles: Computational investigations into the peptide-gold interface. *ASB*, Melbourne, Australia, Nov 2013. (**Poster**)
15. **P. CHARCHAR**, N. TODOROVA, H. ANDRESEN, M. M. STEVENS AND I. YAROVSKY. Peptide decorated gold nanoparticles for biosensing: In silico insights. *Cytochrome P450: Modelling Toxicity*, Guildford, United Kingdom, Sep 2013. (**Contributed Talk**)
16. **P. CHARCHAR**, N. TODOROVA, Y. LIN, M. M. STEVENS AND I. YAROVSKY. Fluorescent peptide-protected gold nanoclusters. *5<sup>th</sup> ONETEP Masterclass*, Cambridge, United Kingdom, Aug 2013. (**Contributed Talk**)
17. **P. CHARCHAR** CASE STUDY 2: BIO-NANO-GOLD INTERACTIONS. *4<sup>th</sup> Workshop on Computational Modelling of Proteins & Membranes*, Melbourne, Australia, Jul 2013. (**Contributed Talk**)
18. **P. CHARCHAR**, N. TODOROVA, H. ANDRESEN, Y. LIN, M. M. STEVENS AND I. YAROVSKY. Interactions of bioactive peptides with nanogold: Insights from theoretical simulations. *12<sup>th</sup> MPG Student Symposium*, Melbourne, Australia, Jul 2013. (**Poster**)



**NANO** | **MICRO**

# small

## Gold Nanoparticles

Computational modeling is a virtual microscope providing molecular insight into the complex interactions occurring at nano–bio interfaces. The image shows the atomistic landscape of a peptide–adlayer on gold nanoparticles, providing the physicochemical information needed to tailor the design of efficient colorimetric biosensors. The successes and challenges of theoretical simulations in facilitating gold nanomaterial design for biomedicine are reviewed on page 2395 by I. Yarovsky and co-workers.

**18/2016**  
WILEY-VCH

**Understanding and Designing the Gold–Bio Interface:  
Insights from Simulations**  
I. Yarovsky and co-workers

DOI: [10.1002/smll.201670092](https://doi.org/10.1002/smll.201670092)



# Table of Contents

---

<b>Declaration of Candidature</b>	<b>iii</b>
<b>Acknowledgements</b>	<b>iv</b>
<b>Publications List</b>	<b>vi</b>
<b>List of Figures</b>	<b>xii</b>
<b>List of Tables</b>	<b>xvi</b>
<b>List of Equations</b>	<b>xvii</b>
<b>Abstract</b>	<b>1</b>
<b>Chapter 1: Introduction</b>	<b>3</b>
1.1 Overview .....	3
1.1.1 Scope of the Thesis .....	3
1.2 Nanotechnology and Nanomaterials .....	4
1.3 Gold Nanoparticles.....	6
1.3.1 The Origin of Gold Nanoparticles .....	6
1.3.2 Size-Dependent Morphology.....	8
1.3.3 Optical Properties.....	9
1.3.4 Functionalisation.....	11
1.4 Gold Nanomaterials for Biomedicine .....	13
1.4.1 Diagnostics, Therapeutics and Theranostics.....	13
1.4.2 Design Principles and the Biomolecular Corona.....	14
1.5 Conclusion .....	16
<b>Chapter 2: Computational Studies of Au-Bio Systems</b>	<b>17</b>
2.1 Introduction .....	17
2.2 Electronic Structure Calculations .....	20
2.2.1 Structure Determination and Mechanics of Nanoparticle Formation .....	20
2.2.2 Optical and Electronic Properties.....	22
2.2.3 Gold Interactions with Biomolecules .....	23
2.3 Force Field Approaches .....	24
2.3.1 Nanoparticle Synthesis and Design.....	24
2.3.2 Targeted Applications: Biomedical Materials and Devices.....	29
2.3.3 Benign-by-Design: Nanotoxicology.....	32
2.4 Conclusions and Context of the Thesis .....	35
<b>Chapter 3: Computational Methodologies</b>	<b>37</b>
3.1 Introduction .....	37
3.2 Quantum Mechanical Methods .....	37
3.2.1 Basics of Quantum Theory.....	38
3.2.2 Common Approximations .....	39
3.2.3 The Hartree-Fock Procedure.....	41

---

3.2.4	Density Functional Theory .....	42
3.3	Classical Molecular Mechanics .....	44
3.3.1	The Potential Energy Function .....	44
3.3.2	Polarisability .....	46
3.3.3	Gold–Biomolecular Force Fields .....	48
3.3.4	Periodic Boundary Conditions.....	52
3.3.5	Treatment of Non-Bonded Interactions .....	52
3.3.6	Energy Minimisation .....	54
3.4	Classical Molecular Dynamics.....	55
3.4.1	Equations of Motion.....	55
3.4.2	Thermodynamic Ensembles .....	57
3.4.3	Temperature and Pressure Coupling.....	58
3.4.4	Bond Constraints .....	59
3.4.5	Enhanced Sampling Techniques .....	61
3.5	Simulation Procedure Employed in the Thesis .....	61
<b>Chapter 4: Peptide-Coated Plasmonic Gold Nanoparticles</b>		<b>62</b>
4.1	Introduction .....	62
4.1.1	Experimental Project Design and Computational Aims .....	65
4.2	Computational Details.....	68
4.3	Results.....	69
4.3.1	Peptide-Monolayer Characterisation .....	69
4.3.2	Immuno-Dominant Residues .....	73
4.3.3	Solvent Effects .....	75
4.4	Discussion and Conclusions .....	76
<b>Chapter 5: Peptide-Coated Fluorescent Au<sub>25</sub> Nanoclusters</b>		<b>80</b>
5.1	Introduction .....	80
5.1.1	Experimental Project Design and Computational Aims .....	83
5.2	Computational details .....	86
5.2.1	Molecular Dynamics .....	86
5.2.2	Quantum Mechanics.....	89
5.3	Results.....	91
5.3.1	General Au <sub>25</sub> (SP) <sub>18</sub> Size, Shape and Peptide Flexibility .....	91
5.3.2	Effect of N-terminal Acetylation .....	93
5.3.3	Increasing Peptide Hydrophobicity/Aromaticity .....	100
5.3.4	Influence of Histidine Protonation.....	101
5.3.5	Hypothesis for Aspartic Acid PL Quenching.....	102
5.4	Discussion and Conclusions .....	105
<b>Chapter 6: Alkanethiol-Functionalised Au<sub>25</sub> Nanoclusters</b>		<b>108</b>
6.1	Introduction .....	108
6.1.1	Experimental Project Design and Computational Aims .....	109
6.2	Computational details .....	111
6.3	Results.....	112
6.3.1	Effect of Solvent on AuNC properties .....	112
6.4	Discussion and Conclusions .....	116

---

<b>Chapter 7: Conclusions and Perspectives</b>	<b>119</b>
7.1 Research Summary, Limitations, Future Work .....	119
7.2 Perspective on the Current State of the Au–Bio Simulation Field .....	123
<b>Bibliography</b>	<b>124</b>
<b>Appendices</b>	<b>155</b>
<b>Appendix A: Force Field Parameterisations</b>	<b>156</b>
A.1 Parameters for Au–S–C–C Dihedral .....	156
A.2 Partial Atomic Charges on SC <sub>8</sub> H <sub>17</sub> .....	160
A.3 General Amber Force Field Parameterisation of Doxorubicin .....	161
<b>Appendix B: Non-standard Analysis Techniques</b>	<b>163</b>
B.1 Moment of inertia to determine AuNC size/shape.....	163
B.2 Electrostatic Potential Acting on Subset of Molecular System .....	167
<b>Appendix C: Supplementary Results (Chapter 4)</b>	<b>171</b>
C.1 Progressively Loaded Peptides on Au(111) .....	171
C.2 Equilibration of Sterically-Saturated Systems.....	173
C.3 Peptide Root-Mean-Square Fluctuations .....	174
C.4 Single Immobilised Epitopes on Au (111) .....	175
C.5 Density Distribution of Immuno-Dominant HA Residues .....	176
C.6 Radial Distributions of Solvent Atoms .....	177
<b>Appendix D: Supplementary Results (Chapter 5)</b>	<b>179</b>
D.1 Experimental Characterisations for Au <sub>25</sub> (SP) <sub>18</sub> .....	179
D.1.1 Absorbance, Emission and Light Scattering Properties.....	180
D.1.2 Small Angle X-Ray Scattering.....	182
D.2 Equilibration of MD Models.....	182
D.2.1 Root-Mean-Square Deviations (RMSD).....	183
D.2.2 Radius of Gyration (R <sub>g</sub> ) .....	186
D.3 Overall Au <sub>25</sub> (SP) <sub>18</sub> Structure and Peptide Flexibility.....	189
D.3.1 Hydrodynamic Diameter (D <sub>h</sub> ) .....	189
D.3.2 Ligand Radius of Gyration (R <sub>g</sub> ).....	192
D.3.3 Atomic Root-Mean-Square Fluctuations (RMSF) .....	193
D.4 Location of Specific Residues and Peptide Configurational Entropy.....	196
D.4.1 Residue Minimum Distances to the Gold Core.....	196
D.4.2 Peptide Backbone Angle vs. C-terminal–Au <sub>25</sub> S <sub>18</sub> Distances .....	200
D.5 Water Structuring.....	203
D.5.1 Radial Distribution Functions.....	203
D.5.2 Hydrogen Bonding .....	206
D.5.3 Water Mobility.....	210
D.6 Suggestion for Aspartate Electron Transfer to Au and PL Quenching .....	214
D.6.1 Classical Electrostatic Potential Energy .....	214
D.6.2 Quantum Mechanical (ONETEP) Results.....	216

# List of Figures

---

<b>Figure 1.1</b>	Relative sizes of molecules, biological entities and macroscopic materials compared to representative examples of nanomaterials. ....	6
<b>Figure 1.2</b>	The 4 <sup>th</sup> century Roman Lycurgus cup. ....	7
<b>Figure 1.3</b>	Transition from molecule-like to bulk-like electronic properties as a function of the number of gold atoms. ....	9
<b>Figure 1.4</b>	Mechanisms and examples of the size-dependent optical properties of gold nanomaterials. ....	11
<b>Figure 1.5</b>	Selection of common gold-binding ligand molecules. ....	12
<b>Figure 1.6</b>	Biomolecular coronas formed around nanoparticles in various different biological environments. ....	15
<b>Figure 2.1</b>	Molecular models and simulation approaches used to capture physicochemical interactions at the interface between gold nanomaterials and biological matter. ....	19
<b>Figure 2.2</b>	Optimised $[\text{Au}_{25}(\text{SR})_{18}]^-$ (where $\text{R} = \text{CH}_3$ ) structural isomers with the corresponding X-ray diffraction patterns compared to experiment. ....	20
<b>Figure 2.3</b>	TDDFT obtained absorbance spectrum of $[\text{Au}_{25}(\text{SH})_{17}\text{Py}(\text{NH}_2)_2\text{S}]^-$ (where $\text{Py} = \text{pyrene} = \text{C}_{16}\text{H}_{10}$ ). ....	22
<b>Figure 2.4</b>	Integrated approach using experimental measurements and molecular simulations to establish design principles for specific interactions-driven peptide binding sequences to gold surfaces. ....	25
<b>Figure 2.5</b>	Docking example showing different protein binding conformations dictated by AuNP size and curvature. ....	26
<b>Figure 2.6</b>	Examples from the literature showing the strong dependence of Au(111) citrate adlayer structuring on the overall charge of the gold surface. ....	28
<b>Figure 2.7</b>	One of the largest all-atom models of protein-gold nanoparticle systems to date showing $\alpha$ -synuclein interacting with 12 nm AuNP. ....	29
<b>Figure 2.8</b>	Exemplar <i>in silico</i> all-atom models where AuNPs feature as non-functional substrate carriers. ....	30
<b>Figure 2.9</b>	Computational studies investigating how an amyloid fibril forming protein responds in the presence gold nanomaterials. ....	33
<b>Figure 2.10</b>	Coarse-grained simulation study to study an insulin protein corona formation on 5 nm AuNP. ....	34
<b>Figure 3.1</b>	Schematics illustrating induced polarisation and the rigid-rod model. ....	47
<b>Figure 3.2</b>	Preferred conformations of biomolecular species adsorbed to gold surfaces as obtained from calculations employing the GoIP-CHARMM FF. ....	51
<b>Figure 3.3</b>	A three-dimensional visualisation of periodic boundary conditions. ....	53
<b>Figure 3.4</b>	Graphical representation of a complex one-dimensional potential energy function and an energy minimisation process. ....	55

---

<b>Figure 3.5</b>	Visual representation of the leap-frog algorithm.....	57
<b>Figure 3.6</b>	Visual representation of the LINCS algorithm. ....	60
<b>Figure 4.1</b>	Cartoon illustration showing the in vivo role of antibodies in cell destruction, and the main features involved in antibody–antigen binding. ....	63
<b>Figure 4.2</b>	Linear representation of the engineered peptides used in this work.....	65
<b>Figure 4.3</b>	Schematic depiction of an epitope-tagged AuNP solution undergoing a colourimetric response after antibody-induced AuNP aggregation.....	66
<b>Figure 4.4</b>	Empirically measured immunoassay response curves for the HA and HSV epitope-coated AuNPs. ....	67
<b>Figure 4.5</b>	Computational setup depicting the approach taken to thermally equilibrate the dense peptide monolayers on Au(111). ....	69
<b>Figure 4.6</b>	Normalised peptide-monolayer number density as a function of height above the Au(111) surface. ....	70
<b>Figure 4.7</b>	Typical equilibrium monolayer structures and distribution of immunodominant residues observed from the simulated epitope–gold systems. ....	72
<b>Figure 4.8</b>	Solvent structuring in the HSV-NT monolayer.....	76
<b>Figure 4.9</b>	Representative antibody fragment with an epitope–Au surface.....	78
<b>Figure 5.1</b>	Effect of N-terminal acetyl capping on AuNC PL. ....	84
<b>Figure 5.2</b>	Correlation of peptide hydrophobicity to increased PL intensity.....	85
<b>Figure 5.3</b>	Experimental PL of peptide-protected AuNCs as a function of solution pH. ....	85
<b>Figure 5.4</b>	Example of the Au <sub>25</sub> (SP) <sub>18</sub> and peptide structures used for MD, with ligands extended. ....	87
<b>Figure 5.5</b>	Average MD obtained Au <sub>25</sub> (SP) <sub>18</sub> size and shape. ....	91
<b>Figure 5.6</b>	Peptide-ligand structuring/flexibility for an exemplar Au <sub>25</sub> (SP) <sub>18</sub> system.....	92
<b>Figure 5.7</b>	Effect of acetyl on the minimum distance distributions between gold and amino acids that are capable of electron charge transfer or donation of delocalised electron density. ....	93
<b>Figure 5.8</b>	Comparing Au <sub>25</sub> (SP) <sub>18</sub> conformations with and without acetyl.....	95
<b>Figure 5.9</b>	MD obtained water structuring around Au <sub>25</sub> (SP) <sub>18</sub> . ....	96
<b>Figure 5.10</b>	Average weighted number of H-bonds proximate water molecules form. ....	97
<b>Figure 5.11</b>	Average <i>minimum</i> distance distributions of <i>proximate</i> water atoms relative to AuS <sub>nearest</sub> . ....	98
<b>Figure 5.12</b>	The pH dependent (de)protonation of histidine residues in solution.....	101
<b>Figure 5.13</b>	Classical electrostatic potential cost for removal of an aspartate carboxylate electron, as a function of ASP–Au <sub>25</sub> S <sub>18</sub> distance.....	103
<b>Figure 5.14</b>	Selected frontier orbitals on different conformers of Au <sub>25</sub> (SP) <sub>18</sub> (where P = CH <sup>+</sup> YGDD) calculated using the ONETEP program. ....	105
<b>Figure 5.15</b>	Peptide–Au <sub>25</sub> S <sub>18</sub> interactions that alter photoluminescence. ....	107
<b>Figure 6.1</b>	Schematic depiction of the multimodal “quantum rattles” illustrating the constituent components in the constructs.....	109

<b>Figure 6.2</b>	Hydrophobic drug loading and release profiles comparing nanostructures with and without gold constituents. ....	110
<b>Figure 6.3</b>	Initial structures used to perform molecular dynamics on the hydrophobic clusters. ....	111
<b>Figure 6.4</b>	Time evolved average root-mean-square deviations for $\text{Au}_{25}(\text{SC}_8\text{H}_{17})_{18}$ . ....	112
<b>Figure 6.5</b>	Effect of solvent on $\text{Au}_{25}(\text{SC}_8\text{H}_{17})_{18}$ conformations. ....	113
<b>Figure 6.6</b>	Octanethiol–solvent and octanethiol–octanethiol distribution functions. ....	115
<b>Figure 6.6</b>	Average carbon and sulphur atomic root-mean-square fluctuations. ....	115
<b>Figure 6.8</b>	Schematic illustration of proposed nanocluster ‘fit’ in silica pores. ....	116
<b>Figure 6.9</b>	Size comparison of a doxorubicin molecule and $\text{Au}_{25}(\text{SC}_8\text{H}_{17})_{18}$ . ....	118
<b>Figure A.1</b>	Au–S–C–C dihedral examined in dihedral scanning. ....	157
<b>Figure A.2</b>	Comparison of the quantum mechanical potential energy scan and the derived molecular modelling parameters. ....	157
<b>Figure A.3</b>	Larger fragment for dihedral scan. ....	159
<b>Figure A.4</b>	Dihedral scan of larger fragment with smaller fragment for comparison. ....	159
<b>Figure A.5</b>	$\text{H}_{17}\text{C}_8\text{S}-\text{SC}_8\text{H}_{17}$ geometries before and after geometry optimisation. ....	160
<b>Figure A.6</b>	Final $\text{SC}_8\text{H}_{17}$ partial charges used in molecular dynamics simulations. ....	160
<b>Figure A.7</b>	Chemical schematic of doxorubicin at physiological pH. ....	161
<b>Figure A.8</b>	Before (left) and after (right) correcting doxorubicin bonds. ....	161
<b>Figure A.9</b>	Final doxorubicin structure and partial charges. ....	162
<b>Figure B.1</b>	Example ellipsoid of the whole complex. ....	165
<b>Figure B.2</b>	Accurate ellipsoid representation of dynamic nanocluster size. ....	165
<b>Figure B.3</b>	Schematic example of the inertial reference frames for inertia and diagonalised tensors. ....	166
<b>Figure C.1</b>	Setup of progressively loaded peptide-gold systems. ....	172
<b>Figure C.2</b>	Time evolution of peptide monolayer root-mean-square deviations and system potential energy. ....	173
<b>Figure C.3</b>	Root-mean-square fluctuations of peptide-monolayer amino acids. ....	174
<b>Figure C.4</b>	Au(111) adsorbed HA-CT peptide highlighting the epitaxial matching of tyrosine phenol rings and hexagonal packing of gold atoms. ....	175
<b>Figure C.5</b>	Side views of HSV peptides adsorbed onto Au(111). ....	176
<b>Figure C.6</b>	Normalised atomic number density of HA immuno-dominant residues as a function of height above the Au(111) surface. ....	176
<b>Figure C.7</b>	Radial distribution of solvent atoms relative to peptide IDS. ....	178
<b>Figure D.1</b>	Experimental characterisation of an exemplar peptide-protected AuNC (where the coating peptides are CHYGDD). ....	180
<b>Figure D.2</b>	UV–Vis absorbance and photoluminescence spectra of peptide-protected Au clusters. ....	181

---

<b>Figure D.3</b>	Findings from small angle X-ray scattering. ....	182
<b>Figure D.4</b>	Time evolved average root-mean-square deviations for each Au <sub>25</sub> (SP) <sub>18</sub> . ....	185
<b>Figure D.5</b>	Time-evolution of the radius of gyration for each Au <sub>25</sub> (SP) <sub>18</sub> . ....	188
<b>Figure D.6</b>	Hydrodynamic diameter calculated from the equilibrated trajectories. ....	191
<b>Figure D.7</b>	Density map comparing average ligand radius of gyration against standard deviation. ....	192
<b>Figure D.8</b>	Average C $\alpha$ root-mean-square fluctuations for each residue. ....	195
<b>Figure D.9</b>	Average minimum distance distributions between residues and Au <sub>25</sub> S <sub>18</sub> . ....	199
<b>Figure D.10</b>	Density maps of peptide backbone angle as a function of C-terminal to AuS <sub>nearest</sub> distance. ....	202
<b>Figure D.11</b>	Average radial distributions of selected atomic components relative to the central Au <sub>25</sub> (SP) <sub>18</sub> gold atom (Au <sub>centre</sub> ). ....	205
<b>Figure D.12</b>	Decay of water out of dynamic water selections. ....	212
<b>Figure D.13</b>	Comparison of water decay for acetylated and non-acetylated systems. ....	213
<b>Figure D.14</b>	Aspartate classical electrostatic potential energy versus Au <sub>25</sub> S <sub>18</sub> distance. ...	215
<b>Figure D.15</b>	Density of states for Au <sub>25</sub> (SP) <sub>18</sub> conformers, where P = CH <sup>+</sup> YGDD. ....	216

# List of Tables

---

<b>Table 1.1</b>	Properties of AuNPs used to generate a biosensing signals. ....	14
<b>Table 4.1</b>	Percentage peptide–Au adsorption and peptide-monolayer thickness. ....	71
<b>Table 4.2</b>	Monolayer solvent accessible surface areas. ....	74
<b>Table 5.1</b>	Engineered sequences used to prepare peptide-protected AuNCs. ....	83
<b>Table 5.2</b>	Investigated peptide sequences with varied residue hydrophobicities. ....	85
<b>Table 5.3</b>	QM derived summed partial atomic charges on selected components of Au <sub>25</sub> Cys <sub>18</sub> (with acetylated or protonated amine N-termini). ....	99
<b>Table 6.1</b>	Average Au <sub>25</sub> (SC <sub>8</sub> H <sub>17</sub> ) <sub>18</sub> dimensions determined by an ellipsoid model. ....	114
<b>Table 6.2</b>	Criteria and evaluated likelihood for AuNC confinement in silica pores. ....	118
<b>Table A.1</b>	Final parameters for the Au–S–C–C dihedral. ....	158
<b>Table C.1</b>	Orientation information of H <sub>2</sub> O atoms relative to the peptides IDS. ....	177
<b>Table D.1</b>	Number of residues within 0.5 nm to any Au <sub>25</sub> S <sub>18</sub> atom. ....	196
<b>Table D.2</b>	Hydrogen bonds involving water within 0.4 nm of Au <sub>25</sub> S <sub>18</sub> . ....	206
<b>Table D.3</b>	Electrostatic energy difference before electron removal and after. ....	216
<b>Table D.4</b>	Mulliken atomic partial charges. ....	216
<b>Table D.5</b>	Kohn–Sham orbitals of Au <sub>25</sub> (SP) <sub>18</sub> (conformer I). ....	217
<b>Table D.6</b>	Kohn–Sham orbitals of Au <sub>25</sub> (SP) <sub>18</sub> (conformer II). ....	218
<b>Table D.7</b>	Kohn–Sham orbitals of Au <sub>25</sub> (SP) <sub>18</sub> (conformer III). ....	220
<b>Table D.8</b>	Kohn–Sham orbitals of Au <sub>25</sub> (SP) <sub>18</sub> (conformer III'). ....	221



# List of Equations

---

<b>Equation 3.1</b>	The multi-body wavefunction. ....	38
<b>Equation 3.2</b>	The time-independent Schrödinger equation. ....	38
<b>Equation 3.3</b>	The quantum mechanical Hamiltonian operator. ....	38
<b>Equation 3.4</b>	$N$ -electron Hamiltonian operator. ....	39
<b>Equation 3.5</b>	The $N$ -electron wavefunction as a Slater determinant. ....	40
<b>Equation 3.6</b>	Linear combination of atomic orbitals. ....	40
<b>Equation 3.7</b>	The Hartree–Fock equation. ....	41
<b>Equation 3.8</b>	Force field functional form. ....	45
<b>Equation 3.9</b>	Polarisability determined from the rigid-rod model. ....	47
<b>Equation 3.10</b>	Non-bonded cut-off radius imposed by the <i>minimum image convention</i> . ....	53
<b>Equation 3.11</b>	Total Coulomb energy using the Ewald summation method. ....	54
<b>Equation 3.12</b>	Newton’s Second Law of motion. ....	56
<b>Equation 3.13</b>	Conservative force as a function of potential energy. ....	56
<b>Equation 3.14</b>	Taylor series expansion of atomic position. ....	56
<b>Equation 3.15</b>	Taylor series expansion of atomic velocity. ....	56
<b>Equation 3.16</b>	Taylor series expansion of atomic acceleration. ....	56
<b>Equation 3.17</b>	Updated atomic positions using the Verlet algorithm. ....	56
<b>Equation 3.18</b>	Calculating current atomic velocities using the Verlet algorithm. ....	57
<b>Equation 3.19</b>	Updating atomic velocities using the leap-frog algorithm. ....	57
<b>Equation 3.20</b>	Updating atomic positions using the leap-frog algorithm. ....	57
<b>Equation 3.21</b>	The Berendsen thermostat algorithm. ....	58
<b>Equation 3.22</b>	The equation of motion redefined by the Nosé–Hoover thermostat. ....	58
<b>Equation 3.23</b>	Definition of the Nosé–Hoover <i>friction coefficient</i> . ....	59
<b>Equation 3.24</b>	The equation of motion for the Nosé–Hoover <i>friction coefficient</i> . ....	59
<b>Equation 3.25</b>	The Berendsen barostat algorithm. ....	59
<b>Equation 3.26</b>	The equation of motion redefined by the Parrinello–Rahman barostat. ....	59



# Abstract

---

This thesis employs computational molecular modelling techniques to explore the physicochemical interactions occurring at the interface between gold nanomaterials and their biological coatings in order to better understand, predict, and ultimately design the properties of novel biomedical devices. In direct collaboration with experimental research, atomistic classical molecular dynamics (MD) simulations are used to investigate ligand conformational behaviour, reveal structure–property relationships, and guide the effective engineering of three distinct functionalised gold nanomaterial systems.

A general introduction is given in Chapter 1 to provide a background into the appeal of gold nanomaterials for biological applications, including an outline of the unique size-dependent properties these fascinating materials possess and examples of how nanogold-based devices are revolutionising diagnostic methods and the treatment of disease. In the subsequent Chapter 2, the current successes and challenges associated with multiscale computational strategies for simulating Au–bio systems, from electronic structure calculations to force field methods, are given to illustrate links between different approaches and their relationship to experiment and applications. In Chapter 3, a methodological overview of physics-based computational techniques is presented, focusing on gold interfacial all-atom classical MD due to its application in this thesis.

Chapter 4 utilises MD to clarify the conformations adopted by different peptide-monolayers on Au(111) surfaces and explores how these relate to the experimental efficacy of an *in vitro* diagnostic approach, which identifies and quantifies the presence of disease marking antibody molecules in solution. The peptide-monolayers formed on Au(111) are found to be intimately related to the inclusion and location of particular amino acids in individual peptide chains of the monolayers, with certain residues strongly influencing the conformational landscapes exhibited. The complex gold–peptide-topographies and solvent exposure of antibody-specific residues correlate well with empirical performance and provide non-intuitive characterisations of the assemblies unattainable through experiments.

To study how peptide-ligand conformations affect the photoluminescence (PL) properties of Au<sub>25</sub> nanoclusters that are capable of *in vivo* bioimaging, MD is used in conjunction with quantum mechanical calculations in Chapter 5. Following the systematic MD modelling of different Au<sub>25</sub>(SP)<sub>18</sub> nanoclusters (where P = hexapeptide), properties such as peptide

arrangement, hydrodynamic radii, distribution of chemical groups around the gold core, water structuring, and hydrogen bond networking are each correlated with experimentally measured AuNC PL. Key findings from this chapter present design principles to optimise the PL of these systems and postulate potential mechanisms for PL quenching.

Next, Chapter 6 employs MD to examine octanethiol-protected Au<sub>25</sub> nanoclusters, which are inherently hydrophobic and form an integral component in a composite gold–silica theranostic material. Simulations in explicit water and ethanol solvents reveal significant structural differences in the alkanethiol ligand layers on Au<sub>25</sub>(SC<sub>8</sub>H<sub>17</sub>)<sub>18</sub> and these differences are then used to hypothesise a steric–kinetic mechanism to explain performance issues that these materials face in their drug delivery applications.

The outcomes of this thesis contribute to the overall understanding of organic–inorganic materials in targeted applications through exploring the intricate interactions that occur on the nanoscale. This work also highlights how the synergistic union of theoretical and experimental approaches can be used to produce translational research, improve insight, and facilitate the development of biocompatible gold nanomaterials for applications in the fields of bioimaging, biosensing, drug delivery, and biomedicine in general.

# Chapter 1:

## Introduction

---

### 1.1 Overview

Gold nanomaterials show enormous potential to provide significant biomedical advancements in biosensing,<sup>4,5</sup> bioimaging,<sup>6-8</sup> drug delivery,<sup>9</sup> magnetic and photothermal therapies,<sup>10</sup> antimicrobial devices<sup>11</sup> as well as many other innovative diagnostic<sup>12</sup> and therapeutic technologies.<sup>10,13</sup> The widespread applicability of gold nanoparticles (AuNPs) within these diverse contexts is largely owed to the unique size-dependent chemical, physical and optical properties they exhibit, along with the ease in which they can be synthesised and functionalised by biologically relevant chemistries.<sup>14</sup> State-of-the-art engineering of efficient and safe gold nanomaterials for *in vitro* and *in vivo* applications involves multiple levels of design challenges.<sup>4,14-19</sup> These include the careful selection of metallic core size and functional layer (peptides, antibodies, DNA, organic and other ligands); the solvent/buffer composition; effects of external forces such as mechanical stresses, electric and magnetic fields; and even the choice of the biological environment itself (plasma/lipid membranes). Despite significant recent advancements in experimental synthesis and characterisation,<sup>20</sup> a comprehensive multiscale understanding of the structure and dynamics of the Au–bio interface relevant to biomolecular and physiological responses is still lacking. *In silico* methods are widely accepted as a means to complement, clarify and predict experimental findings at time and length resolutions technologically unattainable in the laboratory. In light of this, this thesis aims to develop and apply computational strategies to practical Au–bio interfacial systems, providing specific insights to aid in the rational design and optimisation of AuNPs for biomedical applications.

#### 1.1.1 Scope of the Thesis

This thesis explores the physicochemical interactions occurring at the functional interface of biologically coated AuNPs through the use of molecular modelling approaches. The overall aim of this work is to complement and rationalise empirical data in order to predict AuNP behaviour, develop structure–property relationships, and guide the effective engineering of novel biomedical devices.

The first three chapters of this thesis are devoted to providing a background into the biological appeal of AuNPs, and give an overview of how computational approaches produce

physicochemical information that can facilitate the design of efficient biomedical devices. Chapter 1 introduces what nanomaterials are, gives a synopsis of the history and properties of AuNPs, and provides representative examples of how AuNPs can revolutionise diagnostic methods and the treatment of diseases. Chapter 2 delivers a perspective into the multiscale computational strategies available to simulate the Au–bio interface and presents exemplar studies of their application. Following this, the technical details of the computational methodologies used in this thesis are outlined in Chapter 3.

In Chapters 4 to 6, molecular modelling results are presented from studies performed concurrently, and in collaboration, with the innovative biomaterials engineering Stevens' group at Imperial College London (<http://www.stevensgroup.org/>). Chapter 4 focuses on molecular dynamics simulations of anti-viral peptide monolayers on Au(111) surfaces and illustrates the effect that amino acid sequence has on the complex peptide-layer topographies formed on AuNPs. The results presented demonstrate why particular peptide-functionalised AuNPs display superior experimental performance as plasmonic antibody biosensors.<sup>3</sup> Chapter 5 explores the relationships between peptide ligands and the photoluminescence of peptide-functionalised Au<sub>25</sub> nanoclusters via the systematic modelling of different amino acid substitutions. Properties such as hydrodynamic radius, embedded water content, and the distribution of chemical groups around the gold core are shown to collectively affect the measured fluorescence of the peptide-AuNC materials.<sup>1</sup> Next, Chapter 6 investigates the structure and dynamics of octanethiol-functionalised Au<sub>25</sub> in explicit water and ethanol solutions. The AuNCs form part of a composite theranostic material<sup>21</sup> and significant structural differences observed in the different solvents help explain performance issues for these materials in their drug delivery applications.

Finally, Chapter 7 outlines the key outcomes of this work and presents future perspectives. The outlook of this thesis is towards a promising approach to synergy between experiments and simulations in providing molecular insight into the Au–nano–bio interface.

## 1.2 Nanotechnology and Nanomaterials

Nanotechnology, by definition, involves the manipulation of matter at dimensions of roughly one billionth of a meter with the aim of understanding, controlling and utilising the new properties of the materials that emerge at the sub-microscopic scale. No longer described as an emerging field, nanotechnology is attributed to many major advances in technology and medicine. For example, nanotechnology has contributed to impressive developments in: computing, electronics, energy generation and storage;<sup>22</sup> medicine and healthcare;<sup>23</sup> automotive, nautical and aerospace materials;<sup>24</sup> agriculture and food production;<sup>25</sup> as well

as everyday consumer products such as textiles<sup>26</sup> and cosmetics.<sup>27</sup> Despite the science-fiction portrayal of nanotechnology in popular culture (consider Star Trek, Red Dwarf, Doctor Who, Terminator and GI Joe to name a few), the field itself is not an entirely new one. In Nobel laureate Richard P. Feynman's famous 1959 lecture "There's Plenty of Room at the Bottom" to the American Physics Society,<sup>28</sup> it was foretold about nanotechnology that "in the year 2000, when they look back at this age, they will wonder why it was not until the year 1960 that anybody began seriously to move in this direction". In his seminal speech Feynman described the possibility of synthesising materials via the direct manipulation of atoms. After many years of scientific research, nanotechnologies are only now starting to gain commercial use, with inventories reporting there are over 3,000 consumer products containing nanomaterials currently available for purchase on the European market.<sup>29</sup>

The unique, and often superior, properties that make nanomaterials appealing for so many applications can predominantly be attributed to their large surface-to-volume ratio. While atoms in the core of a nanomaterial determine intrinsic properties such as hardness and conductivity, under-coordinated surface atoms define a particle's solution characteristics and chemical reactivity. Moreover, as the size of a nanostructure decreases below ~10 nm, quantum confinement affects the electronic and optical properties. This leads to an enlarged band gap that makes NPs electronically akin to molecular species, i.e. randomly moving electrons become confined to discrete energy levels instead of continuous bands.

As depicted in Figure 1.1, nanomaterials can be broadly classified into three categories based on their composition (organic, inorganic or hybrid). Organic nanomaterials, such as self-assembling lipid- and biopolymer-based NPs, are generally simple to prepare, biodegradable, biocompatible, bioselective and have good stability in biological fluids.<sup>30</sup> The second group, inorganic nanostructures, are perhaps the best known for their industrial uses<sup>31,32</sup> and include: carbon-based derivatives (e.g. nanotubes, fullerene particles and graphitic sheets), silicon and other metallic NPs, mesoporous silica and many metal oxide species. These materials possess exceptional electrical, chemical, thermal and optical properties that are beneficial for accurate biosensors, enhanced diagnostic tools and therapeutic devices.<sup>33</sup> The third category of nanomaterials are termed *hybrid* since they are composed of a combination of organic and inorganic elements, such as metal-organic frameworks and bio-functionalised (metal or semi-conductor) NPs. Hybrid assemblies exhibit attributes of both aforementioned nanomaterial classes and arguably offer the most tunability and customisation for specific properties and applications.<sup>34</sup> Regardless of the type however, all nanomaterials have sizes comparable to biological molecules and typical cellular components (Figure 1.1), which provides a unique opportunity to exploit their

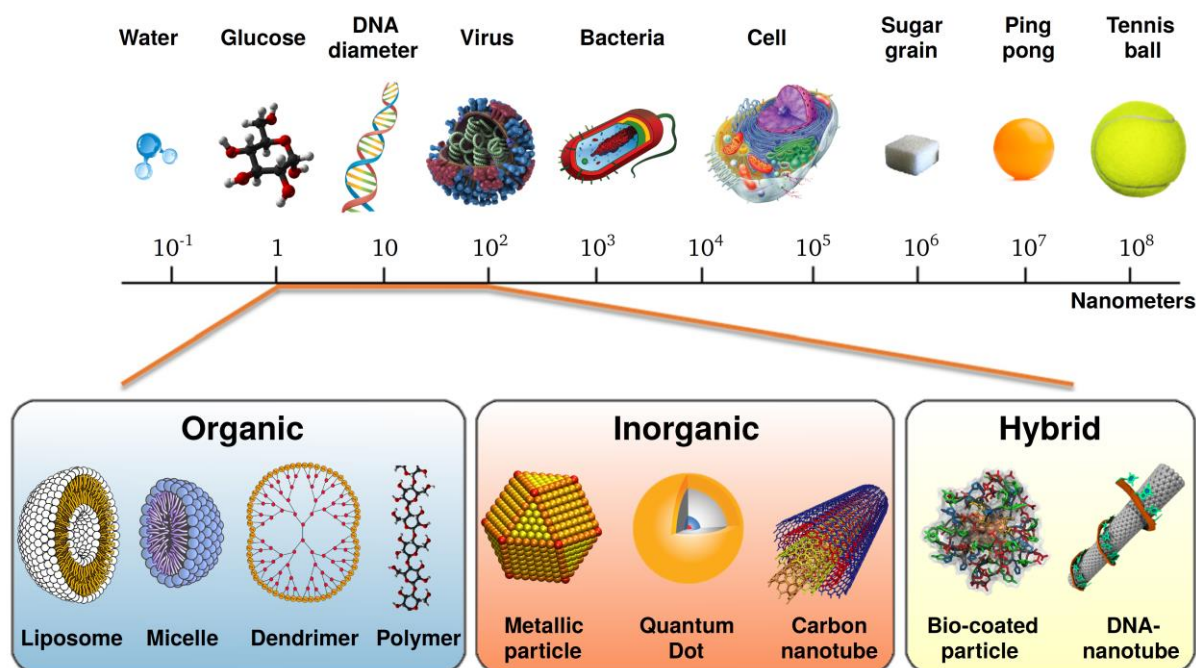


**Figure 1.1 | Relative sizes of molecules, biological entities and macroscopic materials compared to representative examples of nanomaterials.** Main figure adapted with permission.<sup>35</sup> Copyright 2016, Elsevier Ltd. DNA-nanotube adapted with permission.<sup>36</sup> Copyright 2008, American Chemical Society.

properties for medicine via manipulation of fundamental biological phenomena occurring at the nanoscale. Gold nanomaterials, especially those functionalised with biologically-compatible molecules, display a perfect blend of properties to achieve this.<sup>13</sup>

### 1.3 Gold Nanoparticles

Gold, as a precious metal, has been used in jewellery, coinage and decoration since ancient times and has well-known physical and chemical characteristics. In its purest, bulk form, gold is yellow in colour, shiny, soft, malleable and ductile. Metallic gold has a melting point of  $1,064.18^{\circ}\text{C}$ , a face-centred cubic (FCC) crystal structure with a precise lattice parameter of  $0.40782\text{ nm}$ , is a good conductor of heat and electricity, reflects infrared radiation, and is virtually chemically inert.<sup>37</sup> However, when gold is miniaturised to nanoscale dimensions, these distinct properties drastically change. For example, AuNPs with radii less than  $10\text{ nm}$  melt at significantly reduced temperatures (due to high surface energy)<sup>38</sup> and are known to catalyse a variety of chemical reactions,<sup>39</sup> while colloidal AuNP suspensions are renowned for producing vibrantly coloured solutions that optically depend on constituent NP sizes.

#### 1.3.1 The Origin of Gold Nanoparticles

Historically, the first use of AuNPs involved exploiting their unique optical properties to create red-coloured glass and ceramics, even though their existence (and role in the process) was unknown at the time. Perhaps the most famous and earliest example of this is



the Roman Lycurgus cup (Figure 1.2), which is dated back to the 4<sup>th</sup> century.<sup>40</sup> Due to trace amounts of 50–100 nm gold and silver NPs<sup>41</sup> being incorporated into the glass during its fabrication, in reflected light the Lycurgus Cup appears jade green while in transmitted light it glows a deep ruby red. This dichroic effect results from the NPs scattering light when the glass is illuminated from the outside and absorbing light when illuminated from the inside/behind.<sup>42</sup> Although a stunning specimen of ancient nanotechnology, the colouring of glass using precious metals was not routine for the time period and the Romans were unable to control the process, preventing the technology from developing any further.

At the end of the 17<sup>th</sup> century (1,300 years later), the production of red-coloured glass using gold was finally revisited. This was sparked by the discovery of *Purple of Cassius* (a gold preparation obtained via the reduction of a gold chloride aqueous solution) and the innovation that it could be added as a colourant to melted glass.<sup>43</sup> Over a century later, in 1857, Michael Faraday made the first suggestion of the existence of NPs in his Bakerian Lecture to the Royal Society.<sup>44</sup> Faraday postulated the composition of “*Purple of Cassius* to be essentially a finely-divided gold, associated with more or less oxide of tin” and attempted “to induce the belief that finely-divided metallic gold is the source of the ruby colour” in stained glass. In 1905, Viennese chemist Richard Adolf Zsigmondy conclusively showed, thanks to a light-scattering based microscope he co-developed, that *Purple of Cassius* is indeed composed of “very finely divided gold with colloidal stannic acid” (and subsequently he was awarded the 1925 Nobel Prize in Chemistry for this work).<sup>45</sup>



**Figure 1.2 | The 4<sup>th</sup> century Roman Lycurgus cup.** The dichroic optical effect the glass is due to the presence of AuNPs; it appears green (left) unless illuminated from the inside/behind, in which case it glows red (right). Reproduced from the British Museum free image service.<sup>40</sup>

Shortly after, in 1908, Gustav Mie proposed a theoretical basis for the optical properties of homogenous spherical particles that provided the first rationalisation as to why AuNPs create coloured solutions.<sup>46</sup> Essentially, Mie used Maxwell's electromagnetic theory to explain that the colour of gold colloids comes from the absorption/scattering of light however the physical nature of these processes remained unclear until the 1950–60s and the electronic band theory of metals was established. It is now known that incident light on a AuNP induces a collective excitation of the metal's conduction electrons and these oscillating electrons absorb and scatter light. This process is called Localised Surface Plasmon Resonance (LSPR) and will be expanded on in Section 1.3.2.

Starting in the 1940s, the advent of transmission electron microscopy allowed researchers to physically 'see' NPs and precisely measure their size and morphology.<sup>47</sup> Around the same period, solution-phase synthesis of low polydispersity AuNPs was accomplished by using trisodium citrate ( $\text{Na}_3\text{C}_6\text{H}_5\text{O}_7$ ) to reduce gold salt (tetrachloroauric acid,  $\text{HAuCl}_4$ ). Conceived in 1940 by Hauser and Lynn,<sup>48</sup> the approach was made famous in 1951 by Turkevich and co-workers in their landmark description of the nucleation/growth process of AuNPs,<sup>49</sup> then later refined by Frens in 1973.<sup>50</sup> Although still commonly used,<sup>51,52</sup> citrate-stabilised AuNPs aggregate irreversibly upon being dried and can therefore only exist in solution.

In the late 1980s, a scientific interest in self-assembled monolayers of thiols on planar gold surfaces began<sup>53,54</sup> that led to an important advancement in the fabrication of stable AuNPs. In 1994 and 1995, Brust *et al.* pioneered a simple method for the room temperature preparation of thiol-functionalised AuNPs that could be dehydrated and re-dissolved without irreversible aggregation or decomposition.<sup>55,56</sup> Small adaptations of the Brust–Schiffrin method have since emerged to produce 'gram-scale' quantities of AuNPs with tailored gold core dimensions and a wide range of biomolecular ligand functionalities.<sup>54,57,58</sup>

### 1.3.2 Size-Dependent Morphology

Today, AuNPs are perhaps one of the most extensively studied and attractive nanomaterials due to their fascinating properties, which are heavily influenced by particle size and morphology.<sup>59</sup> The structure of monolayer-protected AuNPs, such as those synthesised using the Turkevich and Brust–Schiffrin methods, consists of three parts:

1. **Core/central atoms:** a close-packed symmetric metallic interior that determines crystallinity and overall shape.
2. **Surface atoms:** high-energy, exposed metal atoms which lie on a NP's outer surface facets or at their edges and vertices. These sites govern catalytic activity.<sup>60</sup>

3. **Ligand layer:** the passivating outer layer of molecules that are anchored to the surface metal atoms, stabilise the AuNPs against irreversible aggregation and/or provide surface functionality that influences the particles' solution properties.

Although these fundamental structural features are universal, AuNPs can be separated into two broad subclasses based on their size and size-dependent properties. Particles of 10–300 nm diameter exist in a variety of shapes (e.g. rods, stars, polyhedrons, and wires<sup>59</sup>) and are characterised by isotropic FCC gold lattices that feature various fractions of (111), (100) and (110) Miller index surface facets.<sup>61</sup> These larger AuNPs display electronic band structures (i.e. valence and conduction bands) typical of bulk-like semiconductor/insulator materials.<sup>62</sup> Particles < 10 nm in diameter consist of a countable number (tens to hundreds) of atoms and are commonly referred to as gold *nanoclusters* (AuNCs). In this size regime there is a transition from FCC crystal structuring to non-FCC geometric core morphologies (e.g. icosahedral) around 2–3 nm 'effective diameter' (Figure 1.3).<sup>63</sup> Moreover, as NC size decreases there is an increase in the density of under-coordinated gold atoms (edges and corners) which leads to enhanced catalytic activity,<sup>64</sup> and molecular-like electronic structure emerges. Further discussion about AuNCs morphology is given in Section 2.2.1.

### 1.3.3 Optical Properties

Of the many useful characteristics nanoscale gold materials exhibit, their remarkable size-dependent optical properties are particularly beneficial for biosensing and cellular imaging applications.<sup>5</sup> As consequence of their different morphologies and electronic structuring, large AuNPs and small AuNCs have different optical responses when irradiated with light. For AuNPs of diameter  $d \ll \lambda$  but  $> 5\text{--}10$  nm (where  $\lambda$  is the wavelength of the incident light), absorbed photons cause the quasi-free conduction band electrons on the gold surface

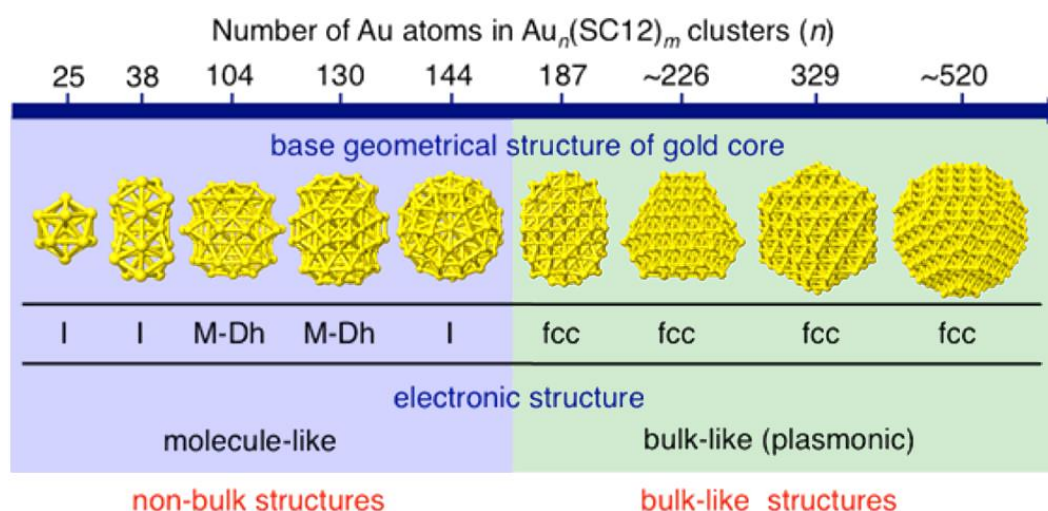


**Figure 1.3 | Transition from molecule-like to bulk-like electronic properties as a function of the number of gold atoms.** Reproduced with permission.<sup>63</sup> Copyright 2015, American Chemical Society.

to undergo collective coherent oscillations in a process called LSPR (Localised Surface Plasmon Resonance, Figure 1.4a). These surface plasmon oscillations then typically decay by either radiating energy through light scattering or by converting the absorbed light to heat.

For AuNPs, this LSPR absorption predominately occurs in the visible region of the electromagnetic spectrum and results in intensely coloured colloidal solutions.<sup>65-68</sup> In general, there is a complementary relationship between the apparent colour of an object (or solution in this case) and the wavelength of light the material absorbs, for example if green light is absorbed, red is perceived. Consequently, the colour of AuNP solutions is dependent on the wavelength of light absorbed which in turn strongly depends on the size and shape of the AuNPs as these affect the frequency at which LSPR occurs. The larger the NPs, the more red-shifted the absorption maximum and subsequently the more 'blue' the colloidal solution appears (Figure 1.4b). Interestingly, when NPs coalesce or are in close proximity to each other, the change in interparticle spacing is also accompanied by a significant Stokes shift in the absorbed LSPR wavelength.<sup>69</sup> Therefore, the aggregation of AuNPs in solution (or re-dispersion of AuNP aggregates) results in a visible colour change to be observed at nano-molar concentrations and provides a basis for very sensitive plasmonic biosensors.<sup>70,71</sup>

On the other hand, AuNCs (< 3 nm in diameter) have electronic structuring analogous to molecular species. In this smaller size regime the continuous band structuring that bulk-like materials exhibit breaks up into discrete electron energy levels (see Section 2.2.2). Hence, when AuNCs are exposed to light of an appropriate frequency they display vibrant *fluorescence*.<sup>7,8,72,73</sup> As shown representatively in the Jablonski diagram of Figure 1.4c, this photoluminescence occurs as a result of valence electrons from the AuNCs absorbing incident photons and becoming excited to higher energy states, thereafter they lose some energy through non-radiative pathways (e.g. vibrational energy). When the electrons relax back down to the ground state, a photon of lower energy is released than the photon initially absorbed. This is typical of (non-resonant) fluorescence, meaning excitation and emission occur at different wavelengths, i.e. the absorbed radiation can be in UV region while emission occurs in the visible light spectrum (Figure 1.4d).

For both small AuNCs and larger AuNPs, the frequency, intensity and quenching of absorbed/emitted light is heavily influenced by the size, shape, solvent, and environment in the vicinity of the particles. To exploit and tune these optical properties for biological settings, it is necessary to carefully design gold particles with attached functional molecules that can act as a bridge between the inorganic and organic systems.

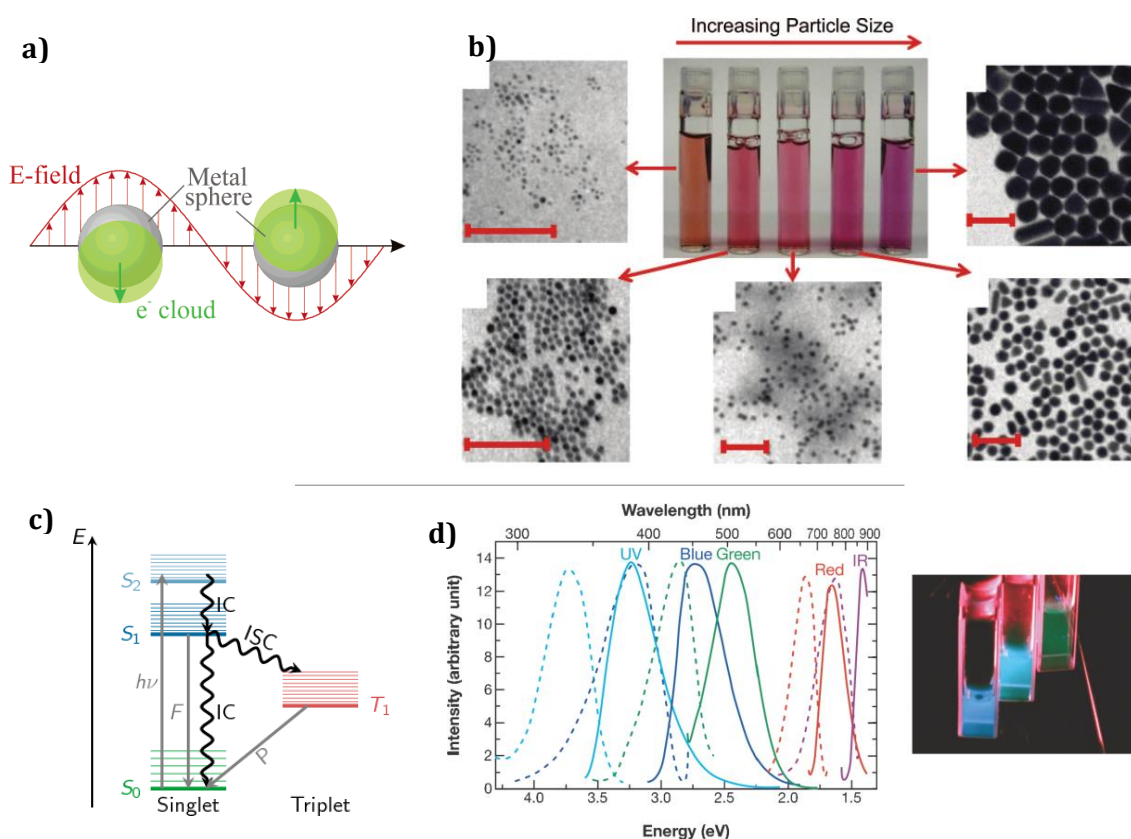


**Figure 1.4 | Mechanisms and examples of the size-dependent optical properties of gold nanomaterials.** (a) Schematic of plasmon oscillations of a metal sphere, showing the displacement of the conduction electron charge cloud relative to the nuclei in response to an incident electric field. Adapted with permission.<sup>66</sup> Copyright 2003 American Chemical Society. (b) Aqueous solutions of AuNPs whose colour depends on particle size. Adapted with permission.<sup>74</sup> Copyright 2008, American Chemical Society. (c) Jablonski diagram showing photophysical processes for AuNCs. Radiative processes: absorption ( $h\nu$ ), fluorescence (F), and phosphorescence (P); Non-radiative processes: internal conversion (IC) and intersystem crossing (ISC). (d) Excitation (dashed), emission (solid) spectra and images of AuNCs under UV irradiation (366 nm). Adapted with permission.<sup>75</sup> Copyright 2004, the American Physical Society.

### 1.3.4 Functionalisation

Gold nanomaterials are rarely used as bare materials (especially in biology) as they coalesce in aqueous solutions.<sup>76,77</sup> Instead, they are typically coated with synthetic or biologically inspired molecules that improve colloidal stability and impart specific functionality onto the particles. To do this, ligand molecules are anchored to gold via chemical (chemisorption) or physical (electrostatic or hydrophobic) interactions, frequently through self-assembly processes.<sup>78</sup> Examples of molecular species that have been shown to bind to AuNP surfaces can be found in <sup>65,67,79-81</sup> and references therein and include: amines, phosphines, thiols, dendrimers, polymers (e.g. PEG, PMMA), biomolecules (e.g. DNA/RNA, proteins) as well as many others (e.g. porphyrins, salts etc.). Figure 1.5 shows a small selection of common hydrophobic and hydrophilic gold-binding ligand molecules.

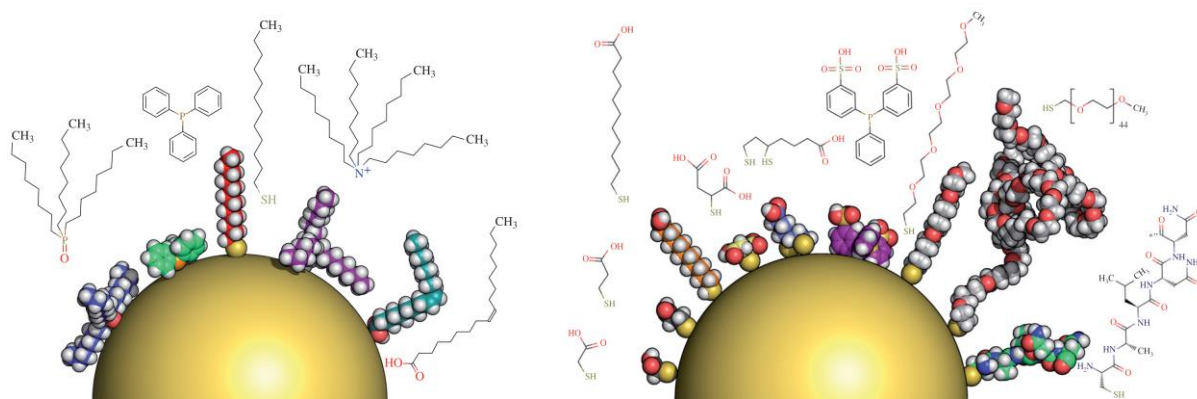


**Figure 1.5 | Selection of common gold-binding ligand molecules.** Representative images are drawn to scale showing 5 nm diameter AuNPs with different hydrophobic (left) and hydrophilic (right) ligand molecules. Adapted with permission.<sup>82</sup> Copyright 2010, the Royal Society.

Of the many chemical groups that possess affinity to gold surfaces, thiols are the most commonly used for AuNP passivation. This is due to the robustness and strength ( $\sim 200 \text{ kJ mol}^{-1}$ ) of the Au-S bond,<sup>54</sup> as well as the simple and modifiable Brust-Schiffrin synthesis approach<sup>55,56</sup> to obtain functional thiol-stabilised AuNPs.<sup>54,57</sup> While Au-S interactions are often described as purely covalent, the exact nature of this bonding has been a topic of extensive debate,<sup>83-86</sup> with recent evidence suggesting there are significantly large contributions to the bond character from van der Waals (vdW) dispersion forces.<sup>87</sup>

In the context of small thiol-protected gold clusters ( $\text{Au}_n(\text{SR})_m$ ), by selecting appropriate R-groups one can manipulate many innate characteristics of the underlying AuNCs.<sup>32</sup> These include stability,<sup>88,89</sup> photoluminescence,<sup>90,91</sup> optical activity,<sup>92</sup> magnetism,<sup>93</sup> redox behaviour,<sup>94</sup> and even induce SPR absorbance in much smaller than expected AuNCs.<sup>95,96</sup> Furthermore, ligand characteristics such as hydrophobicity and charge can be tailored to influence responsiveness to external stimuli,<sup>97</sup> solubility and molecular recognition.<sup>98</sup>

For biological applications, peptides are particularly appealing ligands (normally anchored via cysteine residues) as they seamlessly integrate with biological components, are water soluble, and they display a range of properties that are readily controlled by varying their length and composition.<sup>99,100</sup> With appropriate design of their amino acid sequence, peptides can act as recognition elements for the specific detection of a variety of biomolecular targets such as disease markers, proteases/enzymes, antibodies and other biologically relevant proteins.<sup>5,99</sup> Ultimately, this allows for the properties of both the gold core *and* the peptide functional layer to be accurately controlled via their respective synthesis methods, enabling the fabrication of highly specialised biomedical devices.

## 1.4 Gold Nanomaterials for Biomedicine

Gold nanomaterials are able to transform the conventional ways that we diagnose and treat diseases. For example, they can: dynamically interact with and respond to their environment creating ultra-sensitive biosensors,<sup>71</sup> be loaded with molecules to deliver drugs into targeted locations<sup>101</sup> or be selectively heated to destroy cancer cells when injected into tumour sites.<sup>102</sup> Due to the diversity of research on biomedical AuNPs and AuNCs, and the scope of this thesis, this section is not intended to be an exhaustive overview but rather serves as a general introduction to ways in which gold can be used for biomedical applications. Readers are referred to detailed reviews in each relevant section.

### 1.4.1 Diagnostics, Therapeutics and Theranostics

There are two kinds of clinical diagnostic tests that need to be considered, *in vitro* assays and *in vivo* imaging. The former of these tests are performed on biological samples that have been taken from a living body (e.g. blood, urine, tissue) and typically aim to either: determine/confirm the presence of a disease in an individual; or to measure the quantity of a particular constituent in the sample (e.g. blood sugar). Alternatively, *in vivo* diagnostic tests are conducted within living organisms, such as laboratory animals or the human body, and are often used to track and visualise specific abnormalities within the body in a time-resolved manner, such as the size, shape and location of a tumour. The modes in which AuNPs can be used for both *in vitro* and *in vivo* diagnostics are discussed below.

Gold-based diagnostic biosensors, like all sensors, are composed of two parts: a recognition element (functional coating) to selectively bind a target of interest and a transduction component (metallic core) to signal the binding event. As discussed in Section 1.3.4, AuNP surfaces can facilitate diverse ligand chemistries that allow for the specific detection of a variety of biochemical molecules. Binding between a ligand molecule and a target analyte then generates a detectable signal by either inducing structural changes in the assay, or by altering the physicochemical properties of the underlying gold material (Table 1.1).

There is a huge multitude of AuNP- and AuNC-based *in vitro* tests that have been developed to detect an assortment of different species including: small organic molecules, nucleic acids, proteins, pathogens, and even cells.<sup>12</sup> In addition, by exploiting the optical properties of AuNPs and AuNCs, sensitive *in vivo* imaging devices have also been created.<sup>103</sup> For further examples please see <sup>4,5,104,105</sup> and references therein.

Gold-based technologies are also practical for the *in vivo* treatment of diseases, primarily through drug delivery and photothermal therapies. For the former, pharmaceutical molecules are conjugated onto carrier AuNPs and transported to desired regions in the body

**Table 1.1 | Properties of AuNPs used to generate a biosensing signals.**

Property	Detectable signal
LSPR (AuNP > 3.5 nm)	Colourimetric, LSPR absorption
Photoluminescence (fluorophore: AuNC or ligands)	Stokes shift, quantum yield
Redox (AuNP-films, -wires or -supported electrodes)	Electrical conductivity/current
Surface-enhanced Raman scattering (AuNP > 3.5 nm)	Raman intensity

where they are selectively delivered to kill malignant cells. In the latter, AuNPs are embedded into tumour sites and externally applied electromagnetic radiation stimulates LSPR to make the NPs a point source of heat (via the release of vibrational energy) and cause cell hyperthermia/death. In addition, AuNPs can enhance radiotherapy,<sup>100,106</sup> induce cell apoptosis through photochemical generation of free radical oxygen,<sup>107</sup> and block cancerous pathways.<sup>108</sup> Further therapeutic applications of gold can be found here [10,13,59](#).

As discussed above, gold nanomaterials are inherently multifunctional. They can serve as optical probes and contrast agents for diagnostic imaging, kill cells through photothermal effects, and they can release drugs in response to external stimuli. Moreover, these functions can be combined into a single *theranostic* material that provides both targeted therapy and diagnosis. This is especially valuable for cancer treatment since AuNPs are able to both identify and hamper the growth of cancer *in vivo*.<sup>109</sup> Supplementing the previously mentioned reviews, references [33,110](#) detail theranostic research surrounding AuNPs.

#### 1.4.2 Design Principles and the Biomolecular Corona

For engineered gold nanomaterials to be effective for their intended biomedical applications (especially *in vivo*) there are several requirements to be considered.<sup>111</sup> These are as follows:

**Stealth:** It is vital that *in vivo* AuNPs do not trigger an immune response and reach their target undetected, avoiding unwanted adsorption from other entities.

**Targeting:** To be successful, AuNPs must specifically and selectively recognise their target while discouraging non-specific interactions.

**Aggregation:** Irreversible NP aggregation can significantly affect colloidal stability, cellular uptake, biodistribution and toxicity.<sup>15</sup> While *in situ* aggregate formation is usually undesirable, some biosensors exploit this to generate a signal (e.g. Chapter 4).

**Elimination:** Upon completing their objective, AuNPs need to be eliminated from the body but it is important to control the rate of elimination. If cleared too quickly, the probability of reaching their therapeutic/diagnostic target is reduced however prolonged tissue retention presents serious concerns for toxicity.<sup>112</sup>



Of course while the engineering of surface coating molecules is critical to meeting these conditions, to effectively translate AuNP-biomaterials from the bench-top to the clinic it is necessary to characterise NPs in an environment that is as close to their intended environment as possible. Therefore, it is worth noting that the physicochemical properties and behaviours of nanomaterials characterised under idealised conditions (as is often the case for *proof-of-concept* studies) are not the same as in the complex physiological environment.<sup>113</sup> As NPs progress through *in vivo* pathways, or experience biological fluids (e.g. blood, plasma, interstitial fluid, cell cytoplasm) during *in vitro* applications, they encounter a diverse mixture of biomolecules that adsorb to their surface with varying affinities forming what is known as a protein/biomolecular ‘corona’ (Figure 1.6). This corona, whose constituents are suggested to be constantly and dynamically in exchange with other molecules, is what primarily interacts with biological systems and thereby constitutes a major element of the particles’ biological identity and hence its fate.<sup>16,114,115</sup>

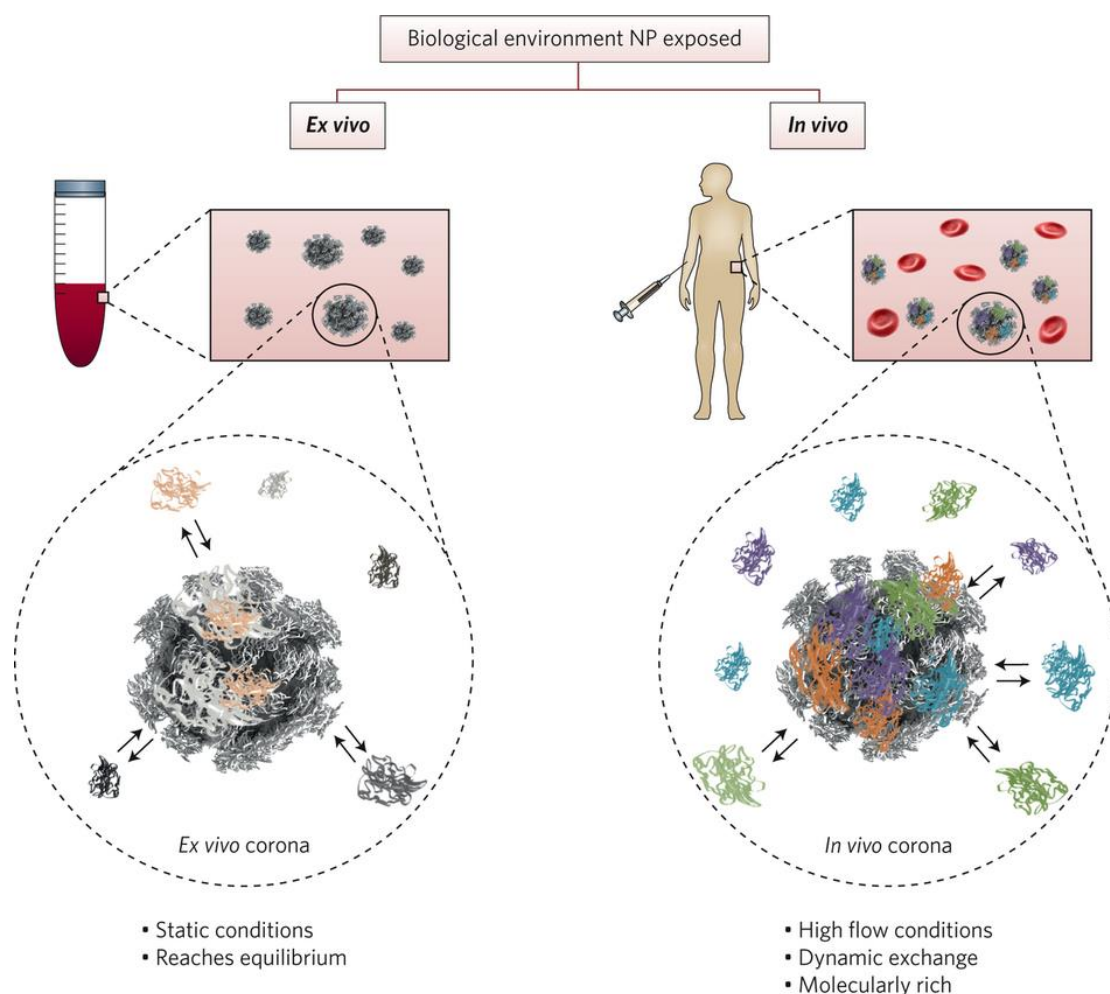


**Figure 1.6 | Biomolecular coronas formed around nanoparticles in various different biological environments.** In *ex vivo* environments biomolecules rapidly adsorb onto NPs until the corona is in equilibrium. In *in vivo*, a molecularly richer corona is formed that is in dynamic exchange with other molecules as it evolves over time. Reproduced with permission.<sup>117</sup> Copyright 2017, Nature Publishing.

Consequently, it is typical to aim at maximising specific interactions for molecular targeting and recognition while discouraging non-specific interactions that lead to unwanted corona formation and potential adverse effects, such as loss of NP functionality and selectivity. Alternatively, there are efforts to exploit the biomolecular corona by designing NPs to adsorb particular plasma proteins as a means to target certain cells and promote internalisation.<sup>116</sup> In either case, to successfully engineer new bio-nanomaterials it is paramount to understand the structure and dynamics of the AuNP–bio interface before, during, and after corona formation. Computational and theoretical methods can accelerate this insight and are a widely accepted approach to enhance, elucidate and predict empirical findings at multiple time scales, length scales and levels of detail (Chapter 2).

## 1.5 Conclusion

This chapter has delivered an overview of the unique and exciting properties exhibited by nano-sized gold materials, which form the basis of a considerable number of diagnostic and therapeutic biomedical technologies. Our ability to rationally design AuNP-based biomedical devices requires intimate knowledge about how AuNPs and their properties adjust in biological media (e.g. plasma, cell membranes and, various intra and extracellular environments) as well as how the components of biological milieu (e.g. water, proteins, lipid bilayers, and DNA) respond to the presence of AuNPs. While advances in empirical approaches<sup>20</sup> have improved the synthesis and characterisation of AuNPs, experimental techniques are deficient in comprehensively probing the atomic and sub-atomic length and time scales needed to interpret the fundamental interactions occurring at the nano–bio interface. In the following chapter recent computational works that bring complementary and critical insights to the structure and dynamics of Au–bio interfaces are discussed.

## Chapter 2:

# Computational Studies of Au–Bio Systems

A perspective of the current successes and challenges associated with the multiscale computational treatment of Au–bio interfacial systems, from electronic structure calculations to force field methods, is provided to illustrate the links between different approaches and their relationship to experiment and applications. Content from this chapter has been published in the journal *Small* and is reproduced in part with permission.<sup>2</sup> Copyright 2016, Wiley-VCH Verlag GmbH & Co. While I am solely responsible for all adaptations to the original text that are included in this thesis and I personally collected, examined and interpreted all literature outlined here, I would like to explicitly acknowledge the contributions each co-author made to the publication.<sup>2</sup> Specifically, sections in the paper were primarily written by the following: **P.C.** (1.) *Introduction*, (3.) *All-Atom Molecular Mechanics and Dynamics (Force Field Methods)*, (4.) *Coarse-Grained and Simplified Approaches*, and (5.) *Enhanced Sampling Techniques*; **A.J.C.** (2.) *Electronic Structure Calculations*; **N.T.** (6.) *Applications*; and **I.Y.** (1.) *Introduction*, and (7.) *Conclusions*. Methodological details of the computational techniques discussed in this thesis chapter are further described in the subsequent Chapter 3.

---

## 2.1 Introduction

Theoretical and computational approaches provide an opportunity to systematically probe and visualise the interface between gold nanoparticles (AuNPs) and biological matter at resolutions unavailable to experiments. These techniques offer enormous promise in providing an in-depth appreciation of the structure and dynamics of gold–bio systems, which is essential information needed to design and optimise gold nanoparticles (AuNPs) for incorporation and efficiency within biomedical devices and *in vivo*. The gold–bio interface is inherently complex and contains phenomena simultaneously occurring across multiple time and length scales. For example, charge transfer reactions<sup>118</sup> take place at femtosecond time scales and angstrom resolutions; while ligand exchanges,<sup>119</sup> biomolecular conformational changes,<sup>120</sup> AuNP reconstructions<sup>79,121</sup> progress over milliseconds to hours and can span tens of nanometres (see Heinz *et al.*<sup>122</sup> for a description of the relevance of each time/length scale to the physics/chemistry of nano–bio interfaces). It is therefore necessary to employ a computational technique that is commensurate to the physicochemical phenomena of interest (Figure 2.1).

Methodologies based on quantum mechanics (QM, Section 3.2) perform calculations with electrons explicitly represented and therefore can derive properties of materials that depend on electronic distribution, including the modelling of chemical reactions where bonds are broken and formed. In the context of Au nanomaterials, QM calculations are primarily used for AuNP structure determination, analysis of optical properties, chemical functionalisation characteristics, and force field (FF) parameterisation for classical simulations (see Figure 2.1a–f and several literature reviews that discuss the role of QM calculations in describing structural, morphological and optical properties of Au surfaces and particles<sup>85,123-125</sup> – especially Ma *et al.*<sup>126</sup>). While QM calculations provide accurate and precise molecular information, they are also very time-consuming as well as CPU and memory intensive. Unfortunately, the complexity and size of Au–bio systems, which can contain inorganic, biomolecular, ionic and aqueous species, quickly renders even the most efficient QM techniques computationally intractable. Furthermore, the common workaround to increase QM system size by neglecting solvent effects is less than ideal since these effects are well known to play an active role in biological processes.<sup>127</sup>

Force field methods (also known as molecular mechanics, MM) ignore electronic motions and calculate the energy of a system as a function of the nuclear positions only. Simulations of this nature are based on the laws of classical mechanics, thermodynamics and statistical physics (see Section 3.3). Although MM approaches cannot provide properties that depend on electronic distribution, they complement enthalpically driven QM calculations with a description of the system’s free energy that includes both the enthalpic *and* entropic contributions. Classical simulations are therefore able to investigate thermodynamic properties of larger gold–bio systems (Figure 2.1g–n) in physiological environments and at an appreciable level of accuracy without compromising computational efficiency.

In this chapter, recent studies employing QM and classical MM approaches to provide electronic and molecular insight into complex bio–gold systems are summarised. The reviewed literature not only illustrates how computational approaches are being used to investigate Au–nano–bio systems, it also highlights capabilities and challenges associated with their application. In Section 2.2, QM studies are described that examine Au–bio interactions to advance knowledge in the physical, chemical and optical properties of AuNP systems. These range from revolutionary discoveries that have transformed our understanding of gold nanocluster (AuNC) morphologies, to approaches that are aimed at providing accurate parameters for MM FF development. Section 2.3 presents research that utilises classical MM techniques, in synergy with experimental data, to explain and design biologically active gold nanomaterials. Examples are given of how MM simulations are

helping engineer AuNPs for: amyloid fibril inhibition, improved cellular penetration (for drug delivery), and facet selective peptide adsorption. Finally, Section 2.4 gives some brief conclusions and outlines the research questions this thesis intends to resolve. Please note that technical details of methodologies discussed in this chapter, especially those that are directly relevant to results presented in this thesis, are described in Chapter 3.

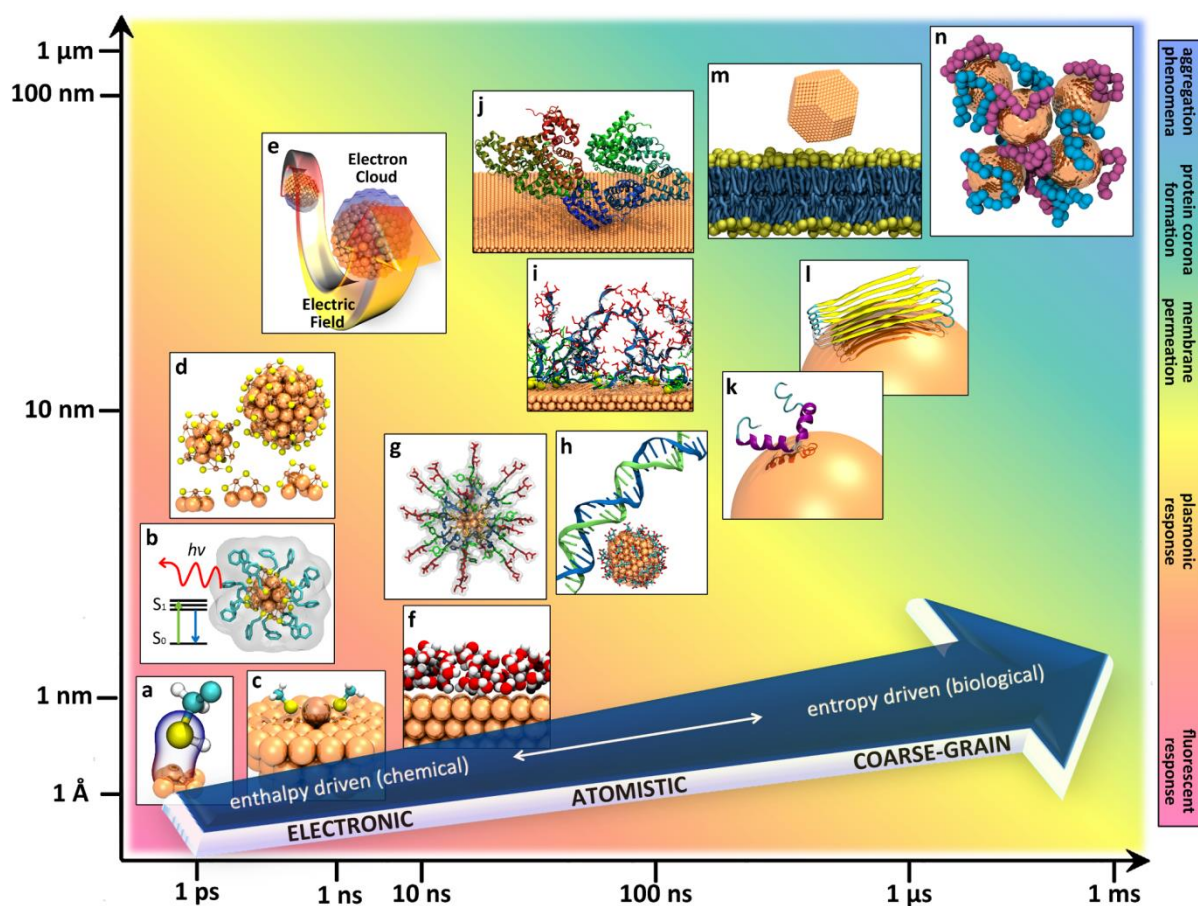


**Figure 2.1 | Molecular models and simulation approaches used to capture physicochemical interactions at the interface between gold nanomaterials and biological matter.** (a) Au surface functionalisation reactions; (b) AuNC electronic excitation and fluorescence, (c) AuNP growth; (d) AuNP structure/morphology; (e) AuNP surface plasmon resonance; (f) Au–solvent interactions and polarisation; (g–l) biomolecular interactions and adsorption on Au surfaces and NPs, including (in the order of appearance) grafted functional chains/peptides, DNA, self-assembled monolayers, protein complexes, individual proteins, and fibrillar protein aggregates; (m) AuNP–lipid membrane interactions and internalisation mechanisms; and (n) AuNP aggregation. The background colour indicates the relevance of each model/method to biomedical applications. The temporal and spatial resolutions shown reflect the scale of the AuNP properties (a–n) and the blue arrow is indicative of the (current) modelling approaches capable to treat each respective phenomena; however, as high performance computing capabilities increase it is expected that the time and length scales of each method will also increase. Images (a–n) were created using the VMD 1.9.2 program<sup>128</sup> with some components and structures adopted from protein data bank entries (PDB ID: 4F5S, 4S05, 2L86), published models<sup>129</sup> and X-ray crystal structures.<sup>130,131</sup> Reproduced with permission.<sup>2</sup> Copyright 2016, Wiley-VCH Verlag GmbH & Co.

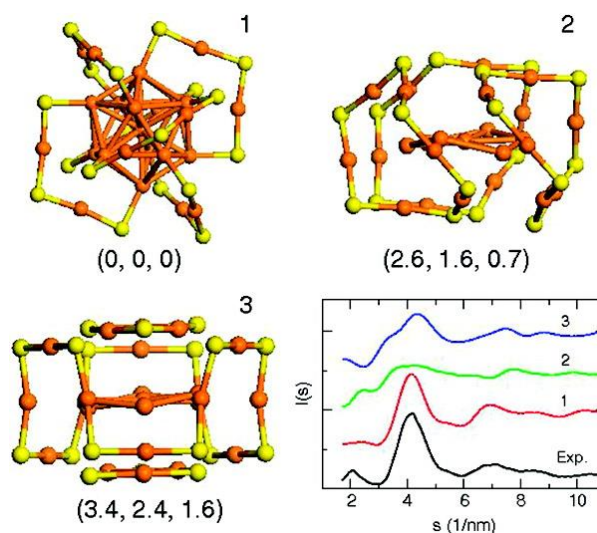


**Figure 2.2 | Optimised  $[\text{Au}_{25}(\text{SR})_{18}]^-$  (where  $\text{R} = \text{CH}_3$ ) structural isomers with the corresponding X-ray diffraction patterns compared to experiment.** Gold (orange) and sulphur (yellow) are shown but methyl groups are omitted. Reproduced with permission.<sup>133</sup> Copyright 2008, American Chemical Society.

## 2.2 Electronic Structure Calculations

### 2.2.1 Structure Determination and Mechanics of Nanoparticle Formation

Structure determination (i.e. exact atomic arrangement) is critical for understanding the physical and chemical properties of molecules and materials.<sup>132</sup> One of the most significant early successes for AuNC characterisation is the structure determination of  $\text{Au}_{25}$  by Akola *et al.* in 2008.<sup>133</sup> In this pioneering work, three  $\text{Au}_{25}(\text{SR})_{18}$  isomers were geometry optimised with DFT and their theoretical X-ray diffraction patterns and optical absorption spectra were calculated (in agreement with experimental data, Figure 2.2). Properties such as electron affinities and ionisation potentials were also assessed and collectively this information was used to predict the ground state structure of  $\text{Au}_{25}(\text{SR})_{18}$  (labelled **1** in Figure 2.2), which was later confirmed by X-ray crystallography.<sup>131,134</sup> Similarly, in 2010 DFT was successfully used to determine the structure of  $\text{Au}_{38}(\text{SR})_{24}$ <sup>135</sup> just prior to the resolution of the X-ray crystal structure.<sup>136</sup>

The revolutionary discovery established from these early studies (and the experimental crystallisation of  $\text{Au}_{25}$ ,<sup>131,134</sup>  $\text{Au}_{38}$ <sup>136</sup> and  $\text{Au}_{102}$ <sup>137</sup>) is that thiolated AuNC assemblies exhibit highly symmetric gold cores that are surrounded by adatom gold “staples” (**1** of Figure 2.2). This view of AuNC morphology is quite contrasting to previous models that proposed thiolates simply form a protective layer on NC surfaces.<sup>85</sup> The “staple” motif has since been shown to consistently appear in various experimentally and computationally determined structures, including:  $\text{Au}_{22}(\text{SR})_{18}$ ,<sup>138,139</sup>  $\text{Au}_{67}(\text{SR})_{35}$ ,<sup>140</sup>  $\text{Au}_{144}(\text{SR})_{60}$ ,<sup>141</sup>  $\text{Au}_{147}(\text{SR})_n$  (where  $n = 0, 12, 24, 50, 72$ ),<sup>142</sup>  $\text{Au}_{187}(\text{SR})_{68}$ ,<sup>143</sup> and  $\text{Au}_{333}(\text{SR})_{79}$ ,<sup>144</sup> as well as on planar Au surfaces.<sup>145</sup>

Several other works have been focused on elucidating the formation of these Au–sulphur staples.<sup>146-148</sup> While it should be noted that the empirical compositions of many of these exceptionally stable “magic number” AuNCs are associated with closed-electron shell valence counts,<sup>125</sup> this is not a strict requirement for AuNC formation<sup>149</sup> as geometric features and symmetry are also known to play a role in AuNC stability.<sup>150</sup>

DFT structure prediction is particularly useful in the absence of X-ray crystal data (since not all AuNPs diffract to atomic resolution), however it is sensitive to input parameters<sup>151</sup> (Section 3.2.4) and the calculated lowest-energy model is not always the one found in nature. For example, in 2012 Pei *et al.* proposed an interlocked catenane-like arrangement for Au<sub>24</sub>(SR)<sub>20</sub> based on DFT,<sup>152</sup> but in 2014 Das *et al.* resolved the crystal structure<sup>153</sup> and it did not match the lowest-energy model. Instead, Das’ structure correlated to the third-lowest energy model (**Iso3** in Pei *et al.*). Furthermore, for atomic configurations with limited experimental data, semi-empirical methods such as density functional tight-binding<sup>154-156</sup> and approaches employing empirical potentials<sup>157-159</sup> are often used as a first step in geometry optimisation where first-principles calculations are prohibitively expensive.

In addition to static structure determination, QM methods are beneficial for investigating the dynamics of AuNP formation, including aspects such as: self-assembly/aggregation,<sup>160-162</sup> doping,<sup>163-165</sup> metal oxidation,<sup>166</sup> ligand exchange,<sup>89,130,167-170</sup> and the binding of small molecules to gold surfaces<sup>171-173</sup> and AuNCs.<sup>174-176</sup> Using DFT to study alkanethiol self-assembled monolayer formation on AuNPs, Barnard showed that the most favourable adsorption sites are the (111) facets adjacent to (111)|(111) edges and that alkanethiol concentration and chain length guide the growth of AuNPs into different morphologies.<sup>177</sup> DFT calculations have also provided insight in the effects of collocation of different adsorbents on nano-gold,<sup>178</sup> atomic substitutions,<sup>179</sup> chiral transfer,<sup>180</sup> and adsorption-induced gold reconstructions.<sup>181</sup> Despite these accomplishments, probing the precise mechanics of AuNP formation, specifically on the gold core itself, is a challenge for *ab initio* methods. Recent works have made great strides in this direction by considering the nucleation and growth process of small AuNCs at the QM level,<sup>182,183</sup> and by examining growth as a function of colloidal stability.<sup>182</sup>

First-principles methods are an invaluable tool to determine AuNC structures and to reveal how nanoparticles form. As morphological information becomes more comprehensive, the capability to predict experimentally valid structures will enable us to better understand the intrinsic size-dependent physical and chemical properties of nano-gold and this will undoubtedly assist in the development of novel biologically relevant gold-based materials.

## 2.2.2 Optical and Electronic Properties

As one of the key biomedical applications for nano-gold is biosensing,<sup>33</sup> an extensive understanding of AuNPs' (and AuNCs') optical and electronic properties is essential. Time-dependent density functional theory (TDDFT) is an extremely advantageous method for calculating electronic excited states, and can provide insight into the origin and nature of a systems' optical properties.<sup>184</sup> Several examples in the literature employ TDDFT to investigate gold assemblies. Tlahuice-Flores *et al.* showed that Au<sub>25</sub> geometry distortions reduce the energy difference between the highest occupied and lowest unoccupied molecular orbitals (HOMO and LUMO, respectively);<sup>185</sup> Antonello *et al.* found that oxidation state affects the triple degeneracy of the Au<sub>25</sub> HOMO;<sup>186</sup> and for the recently crystallised Au<sub>18</sub>(SR)<sub>14</sub>,<sup>187,188</sup> TDDFT revealed that the HOMO extends over the staple with the LUMO on the core kernel, in contrast to other nanoclusters. In a series of papers by Fihey *et al.*, a combined MM and QM approach was used to systematically modify the ligand on Au<sub>25</sub> until excited-state charge transfer was enabled (Figure 2.3)<sup>189</sup> and a molecular switch could be formed.<sup>190</sup> For larger AuNPs (> 200 atoms), Fihey *et al.* employed TDDFT in combination with a discrete interaction model to simulate surface plasmon resonance.<sup>191,192</sup>

Although TDDFT is an exceptional method for examining the optical behaviour of AuNCs, other QM-based methods can also be used to predict optical spectra (and validate theoretically proposed structures – see Section 2.2.1) or explore electron transfer processes. For example, Tlahuice-Flores *et al.* used standard DFT methods to produce IR and low-frequency Raman spectra of AuNCs, which is useful to “fingerprint” clusters based on size,

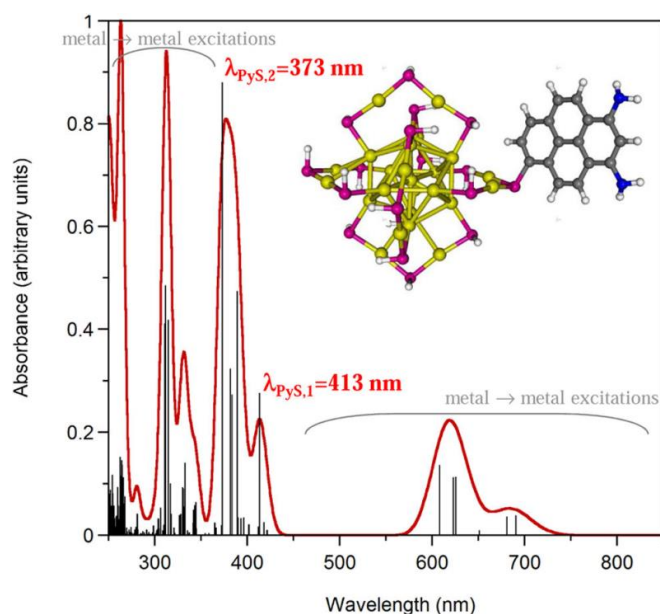


**Figure 2.3 | TDDFT obtained absorbance spectrum of [Au<sub>25</sub>(SH)<sub>17</sub>Py(NH<sub>2</sub>)<sub>2</sub>S]<sup>-</sup> (where Py = pyrene = C<sub>16</sub>H<sub>10</sub>). Reproduced with permission.<sup>189</sup> Copyright 2014, American Chemical Society.**



composition and structure;<sup>193</sup> and Corni *et al.* showed that dye–metal charge transfer interactions can adequately be modelled by having AuNPs represented as a polarisable continuum and only treating dye molecules explicitly at the QM level of theory.<sup>194</sup>

Several factors need to be carefully considered when interpreting calculated absorption spectra and other optical properties of nanoparticles and clusters. In addition to the choice of DFT parameters,<sup>195</sup> obtained results are well-known to be very sensitive to: size, shape, “magic number”;<sup>196</sup> atomic substitutions;<sup>197-202</sup> and the truncation of ligands (e.g. shortening aliphatic chains to CH<sub>3</sub> or H for the sake of computational efficiency).<sup>203,204</sup> Moreover, the optimisation of excited states, which is required for fluorescence emission spectra, is extremely computationally intensive and can only currently be achieved for small molecules.<sup>205</sup> While these limitations are not fundamental flaws of DFT, they technologically inhibit the calculation of emission spectra for most ligand-protected AuNCs due to size restrictions and the need to explicitly include all ligand atoms.<sup>204</sup>

### 2.2.3 Gold Interactions with Biomolecules

In addition to structure determination and optical characterisation, QM calculations can study the adsorption of biomolecules to AuNP surfaces through both physisorption and chemisorption mechanisms. Physisorption, i.e. the accumulation of molecules onto a surface without chemical binding, is generally non-specific (apart from hydrogen bonding and  $\pi$ – $\pi$  stacking), reversible, and dominated by van der Waals (vdW) forces with binding energies in the 2–10 kcal mol<sup>-1</sup> range per functional group. Chemisorption processes on the other hand, such as the thiolate functionalisation of gold, involve a direct molecule-to-surface chemical reaction which leads to binding energies that can be a hundred times stronger.<sup>206</sup> Regardless of the type of adsorption, the proper treatment of weak dispersion interactions is critical.<sup>207-211</sup> This is especially true when considering water–gold interactions, as several studies have shown that dispersion is essential to properly model adsorption energy, binding orientation, and diffusion.<sup>212-214</sup>

Adsorption studies and improving our understanding of water–gold interactions are also very important when parameterising MM FFs for nano–bio systems<sup>215,216</sup> (discussed in Section 3.3.3). For example, in the parameterisation of the GolP FF,<sup>215</sup> Hoefling *et al.* found substantial differences between the DFT-derived orientations of gold-adsorbed amino acid building blocks and the geometries obtained from molecular dynamics (MD) simulations with explicit solvent.<sup>217</sup> In vacuum, the molecular orientations are driven by attractive dispersion interactions and the repulsive exchange term of the DFT functional, while in explicit solvent MD simulations the charged groups reorient for maximum exposure to

water. To extend the GolP FF to the GolP-CHARMM FF,<sup>216</sup> Wright *et al.* utilised Plane Wave DFT (with the vdW-DF<sup>218,219</sup> and revPBE<sup>220</sup> functionals to treat dispersion) in order to examine the binding of both water and amino acid functional groups to Au(111) and Au(100) surfaces. From their *in vacuo* calculations they found that Au(100) binding affinity and selectivity was greatest for molecules containing sulphur or nitrogen, which weakly chemisorb to gold surfaces. In addition, their water adsorption calculations showed that water molecules preferentially orient their oxygen atoms directly above gold atoms and closer to the Au interface than their hydrogen atoms (see Figure 3.2). Nadler *et al.* also observed this in similar DFT investigations,<sup>212</sup> suggesting that gold-interfacial water molecules tend to act as hydrogen bond donors.

Apart from gold surfaces, QM has been useful to derive FF parameters for organically-coated AuNCs,<sup>221,222</sup> and to examine the interactions between a small number of gold atoms and amino acids such as cysteine<sup>223</sup> and glycine.<sup>224</sup> For individual amino acids interacting with small AuNCs, Pakiari *et al.* found that anionic amino acids were favoured.<sup>225</sup> Similar results were found for the tripeptide glutathione,<sup>226</sup> which is an alternative capping ligand to alkanethiolates (references given in Section 6.1) for AuNC nano–bio applications.

In addition to amino acids, the interactions of nucleobases with gold surfaces<sup>227</sup> and small clusters<sup>228</sup> have also been investigated. A recent DFT study found that the energy barrier for the interaction of nucleobases with small AuNCs follows the order  $G > A > C > T > U$ .<sup>229</sup> Moreover, Rai *et al.* observed that AuNCs can also alter the properties of DNA base pairs.<sup>230</sup>

## 2.3 Force Field Approaches

Recent FF and methodological developments of classical simulation approaches (Section 3.3.3) provide a platform to improve our understanding of the different interactions occurring at the Au–bio interface (Figure 2.1g–l), and help us gain insight into large scale phenomena such as AuNP aggregation and membrane permeation (Figure 2.1m–n). This has already afforded a novel route to the generation of nanoparticle assemblies with predictable architectures<sup>217,231–233</sup> targeting specific applications.

### 2.3.1 Nanoparticle Synthesis and Design

The design of peptide sequences that can discriminate between gold facets under aqueous conditions offer a promising route to control the growth and organisation of biomimetically-synthesised AuNPs. As such, computational modelling has secured an important role in emerging fields such as bionanocombinatorics and biomaterials engineering where specifically designed/encoded biomolecules and nanostructures are used to create materials and devices with unique properties and functions.

Over the years, several gold-adsorbing peptides have been identified (summarised in Tang *et al.*<sup>234</sup>), some of which have shown binding affinities similar to those of thiols on gold. Due to the small molecular weights of these ligands, they have become favourable models for molecular simulations and have been investigated in varying conditions using different techniques.<sup>234-240</sup> Initial studies describing peptide–nanogold mechanisms of interactions focused on the enthalpic contributions to binding, by describing the probable number, distribution, and type of residue–surface contacts.<sup>236,241-243</sup> Also, classical “brute-force” MD simulations have provided insights into the entropic factors of binding. For instance, Vila Verde *et al.* explored the influence of peptide flexibility and conformational movement on peptide binding,<sup>238,244</sup> and Heinz *et al.* estimated the configurational entropic changes of strong binding peptides adsorbing to gold.<sup>235</sup> Although both studies had limitations in their MD approaches, such as the lack of structural data for comparison, the period of time over which the binding behaviour was monitored, and the nature of the peptide–gold interactions (i.e. the surface only interacts with the peptide via dispersive interactions), their results correlated well with experimental observations. While the assumption that the gold surface does not reconstruct in response to peptide/solvent interactions may be reasonable, neglecting polarisation of the gold surface (Section 3.3.2) is potentially more serious.<sup>245</sup> Tang *et al.* employed experimental methods in conjunction with MD simulations using the polarisable GōLP-CHARMM FF and enhanced sampling techniques (see Section 3.4.5) to study the binding of various peptide sequences to a Au(111) surface (Figure 2.4).<sup>234</sup> Their work quantitatively demonstrated the importance of entropically motivated adsorption and established design principles for creating both entropically and enthalpically driven nanomaterial-binding peptide sequences. Furthermore, the interplay between sequence, conformation(s) and binding propensity were noted to significantly impact the affinity of peptides to gold.

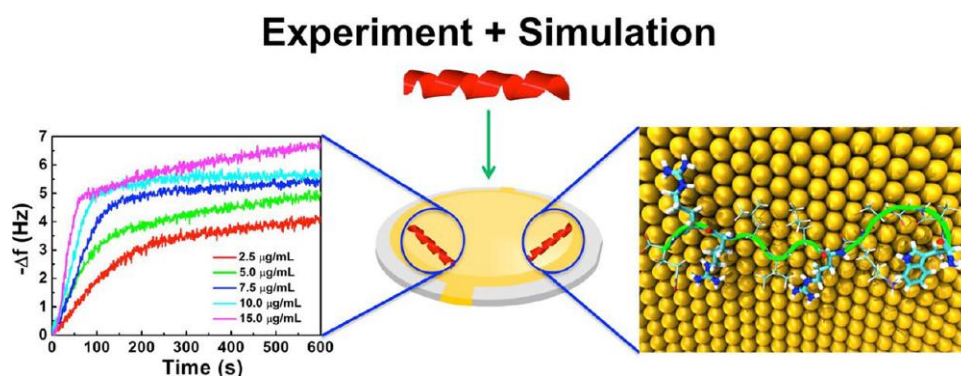


**Figure 2.4 | Integrated approach using experimental measurements and molecular simulations to establish design principles for specific interactions-driven peptide binding sequences to gold surfaces.** Reproduced with permission.<sup>234</sup> Copyright 2013, American Chemical Society.

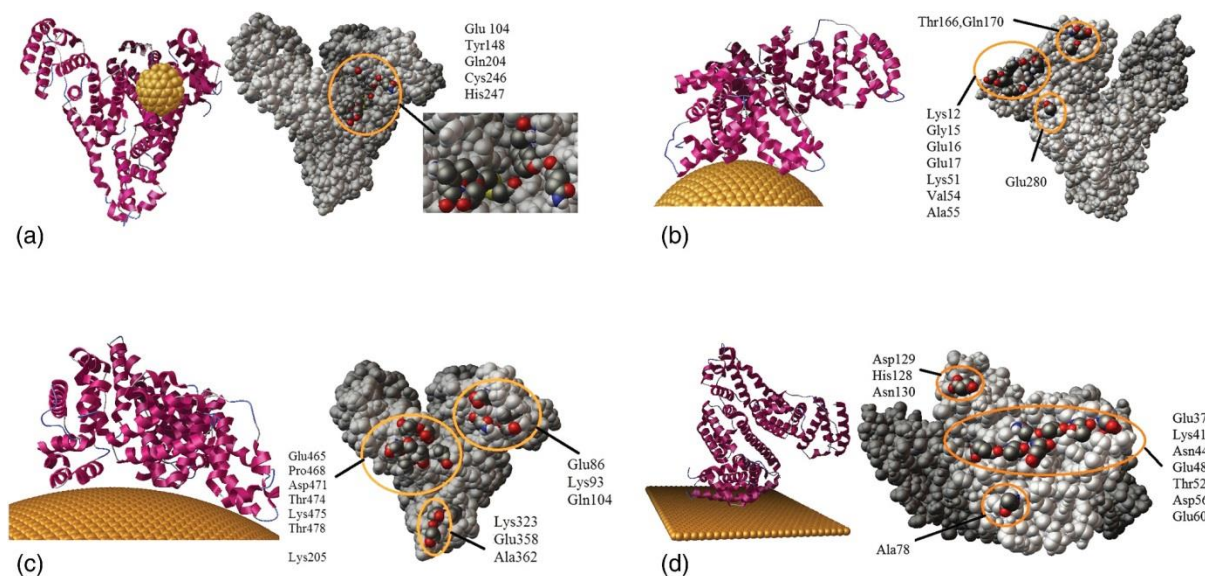


**Figure 2.5 | Docking example showing different protein binding conformations dictated by AuNP size and curvature.** The circled regions in the space filling models show the contact amino acids for the human serum albumin protein on the different sized AuNPs: **(a)** 1–3 nm, **(b)** 4–10 nm, **(c)** 11–20 nm, and **(d)** > 20 nm. Reproduced with permission.<sup>249</sup> Copyright 2014, AIP Publishing LLC.

Several MD simulation studies have provided the structural connections between a given peptide sequence and its binding affinity to the commonly-featured Au(111) and Au(100) facets,<sup>89,123,235,237,246</sup> which is information not easily obtained by experiment. In a recent work, Wright *et al.* used the combination of enhanced sampling techniques with the GoIP-CHARMM FF to predict the adsorption free energy of a gold-binding peptide, AUBP1, at the aqueous Au(111), Au(100)(1 × 1) and Au(100)(5 × 1) interfaces.<sup>240</sup> Their results showed that the peptide adsorption to the Au(111) surface is stronger than to Au(100), irrespective of the reconstruction status of the latter. The surface hydration of gold was identified as the key determining factor in peptide–surface recognition, further highlighting the importance of explicit solvent treatment in classical FF simulations. Subsequent works from the same group have similarly focused on peptide adsorption and interactions on gold surfaces to reveal residue-specific binding preferences.<sup>247,248</sup>

Protein–gold adsorption can also be investigated using molecular docking approaches, where rigid body transformations and rotations explore different binding orientations. For example, Khan *et al.* used molecular docking to investigate the adsorption of human serum albumin (a major protein component in human serum) onto AuNPs that cover a span of different sizes (1–200 nm).<sup>249</sup> Although water molecules, ions and the citrate-coating of the AuNPs were not physically considered, their findings revealed that curvature and particle size substantially affect stable protein–gold binding conformations (Figure 2.5).

While the interactions of proteins with bare Au surfaces have been investigated in detail, albeit with differences in methodological approaches and techniques used, the study of proteins interacting with functionalised Au surfaces is still in its infancy. In reality, bare NPs are unstable and prone to aggregation in solution. To combat this problem, NPs are often synthesised with various functional capping agents (surfactants) conjugated to their surface, such as citrate, alkanethiol, or peptide ligands, which aid the colloidal stability and solubility of the AuNPs. However, translating this into a computational model requires an accurate description of any covalent, semi-covalent and/or van der Waals interactions between relevant gold facets and the ligated molecules. The recent development of citrate parameters for gold has enabled a more realistic representation of the functionalised gold interface in full atomic detail.<sup>232,250</sup> Despite recent experimental efforts,<sup>251</sup> structural information about citrate anions adsorbed onto Au surfaces is still limited. From a modelling perspective, the net negative ( $-3e$ ) charge of each gold-adhered citrate molecule contributes to the electrostatic forces present at the gold interface and therefore it is important to carefully consider the structure and arrangement of the adlayer. Computational studies that have looked into this differ in their treatment of the underlying gold core's surface charge. For example, Wright *et al.* assumed a neutral gold surface to investigate a range of citrate densities adsorbed at the aqueous Au(111) interface using MD simulations.<sup>252</sup> Their work showed that citrate overlayers are disordered, and many of their key characteristics, such as the formation of 3D rather than 2D morphologies, are invariant with surface density (Figure 2.6a). Generally, the anions closest to the Au surface oriented with their carboxylate groups pointing away from the surface. The authors postulate that from their findings they expect small biomolecules interacting with citrate-coated AuNPs to coadsorb at the Au–citrate interface, rather than (or as well as) displace the adsorbed citrates. In contrast, Brancolini *et al.* studied the interaction between  $\beta_2$ -microglobulin ( $\beta_2m$ ) and a citrate-coated 5 nm AuNP, using a positively charged gold core (corresponding to electrochemistry experiments).<sup>253</sup> Their simulations showed rigid structuring of the citrate layer without any displacement from the surface (Figure 2.6b). Repeating their simulations using charge neutral gold led to qualitatively similar results for the mechanisms of interactions between protein and citrate-capped gold; however, the positively charged gold core resulted in better agreement with the NMR data for  $\beta_2m$ .<sup>253</sup>

Utilising Brancolini's approach,<sup>253</sup> Wang *et al.* performed explicit solvent MD simulations of amylin (hIAPP) interacting with both neutral and charged citrate-coated Au(111) and Au(100) surfaces.<sup>254</sup> Their simulations showed different protein behaviour on the charged and neutral surfaces; however, irrespective of the gold facet and surface charge, the N-

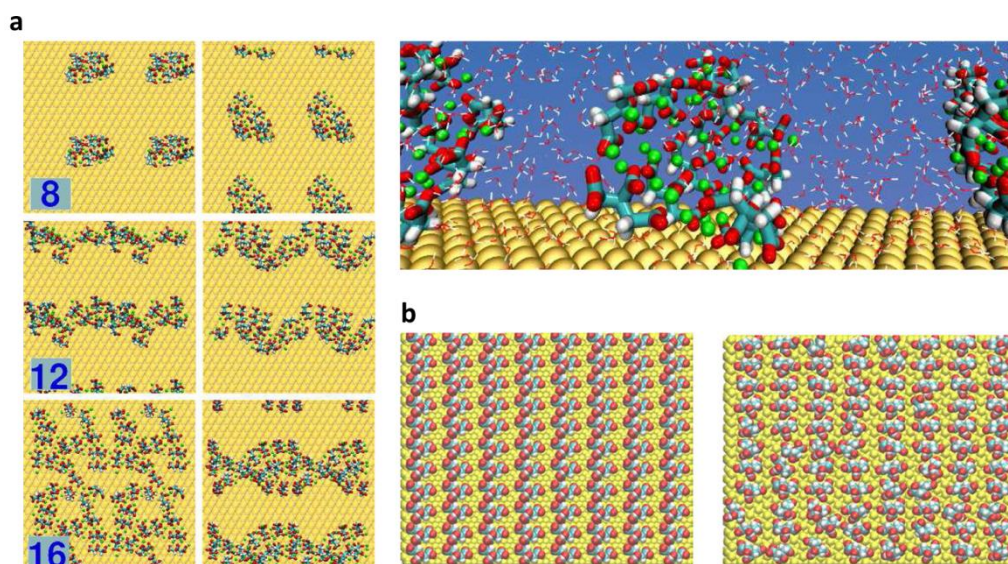


**Figure 2.6 | Examples from the literature showing the strong dependence of Au(111) citrate adlayer structuring on the overall charge of the gold surface. (a)** Citrate assemblies of varying surface densities on a neutral Au(111) surface. Adapted and reproduced with permission.<sup>252</sup> Copyright 2014, American Chemical Society. **(b)** Initial (left) and final (right) citrate distribution on a positively charged Au(111) surface. Reproduced with permission.<sup>253</sup> Copyright 2015, American Chemical Society.

terminal region of amylin consistently displayed preferential binding to the citrate-capped gold surface. This example highlights that a careful consideration of the surface and functional layer treatment in computer simulations of Au surfaces in solution is required. In a different study, the binding orientation of  $\alpha$ -synuclein to a 12 nm AuNPs coated with anionic citrate and cationic (16 mercaptohexadecyl) trimethylammonium bromide (MTAB) was investigated using NMR spectroscopy and MD simulations,<sup>255</sup> where the interactions between the gold and the rest of the system were represented by van der Waals interactions only (Figure 2.7). Similar to Wang *et al.*,<sup>254</sup> their results showed that the N-terminal region of  $\alpha$ -synuclein interacted favourably with the negatively charged citrate-protected NP, while the C-terminal region was strongly attracted to the MTAB coated NP. Despite the lack of treatment of polarisation effects or crowding effects of neighbouring proteins, the simulations were in agreement with the NMR results that suggested a reversal of protein binding orientation upon changing the AuNP surface charge.

A well-established technique to conjugate molecules to AuNPs and AuNCs in order to introduce new functionalities is a reaction known as ligand exchange.<sup>256</sup> In an interesting QM/MM study by Rojas-Cervellera *et al.*, the mechanism for ligand exchange of a glutathione molecule in  $[\text{Au}_{25}(\text{SG})_{18}]^-$  (where G = glutathione) to a protein fragment of an anti-influenza antibody was studied.<sup>257</sup> The findings of their work showed which glutathione peptide ligand will be preferentially substituted and that it occurred through a mechanism which involved a proton transfer. Classical MD simulations have also been useful in characterising

the binding mechanisms of peptide functionalised-AuNCs with various proteins.<sup>258-260</sup> Others have provided insight into the mechanisms of direct electron transfer between redox proteins and electrode surfaces, which play an important role in bioelectrocatalysis, enzymatic biofuel cells and biochips.<sup>261-264</sup>

### 2.3.2 Targeted Applications: Biomedical Materials and Devices

Self-assembled monolayers (SAMs) impart functionality to underlying gold nanostructures that can be tailored for specific applications. Much work has been done both experimentally and computationally to characterise SAMs on AuNPs.<sup>78</sup> In many cases the NP simply acts as a carrier vehicle and it is really the structure and properties of the functional layer and/or corona formation that are of interest for applications. Depending on the AuNP surface coverage density, and the length and type of the conjugates, the solvent-exposed outer functional layer of a SAM may be minimally affected by the Au surface due to relatively long separations from the NP surface itself. Although not ideal, this means an explicit representation of the AuNP interactions with the environment may not be necessary and as such specific Au surface–bio parameters can be completely omitted from some simulation models to reduce computational cost. Several studies have employed this approach and their results were well correlated to experiments.

For example, experimental protein assays and MD simulations were used to investigate the adsorption of cytochrome C (Cyt C)<sup>265</sup> and lysozyme (Lyz)<sup>266</sup> onto SAM-protected AuNPs with only the monolayer being represented explicitly. In these studies, the SAMs had regular nanoscale variations of hydrophobic octanethiol and hydrophilic mercaptohexanol ligands (Figure 2.8a), and the simulations revealed that amphipathic, amine-containing, amino acids

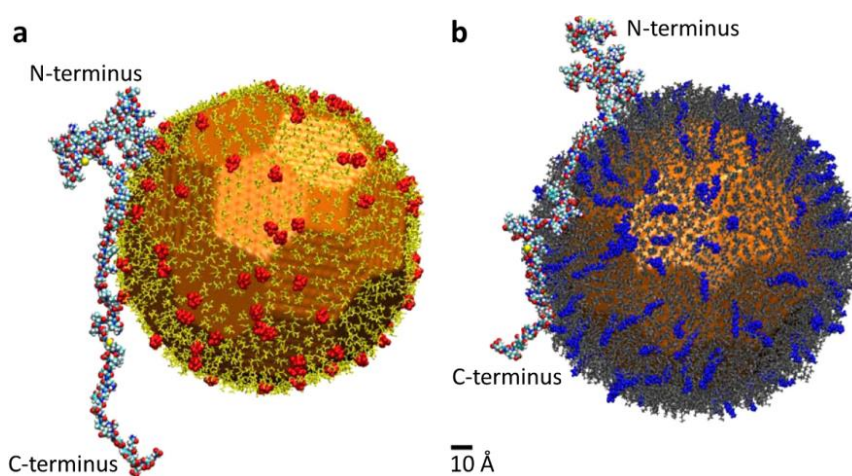


**Figure 2.7 | One of the largest all-atom models of protein–gold nanoparticle systems to date showing  $\alpha$ -synuclein interacting with 12 nm AuNP.** The functionalisation of the AuNP is (a) citrate (negative) ligands, and (b) MTAB (positive) conjugates. Reproduced with permission.<sup>255</sup> Copyright 2015, American Chemical Society

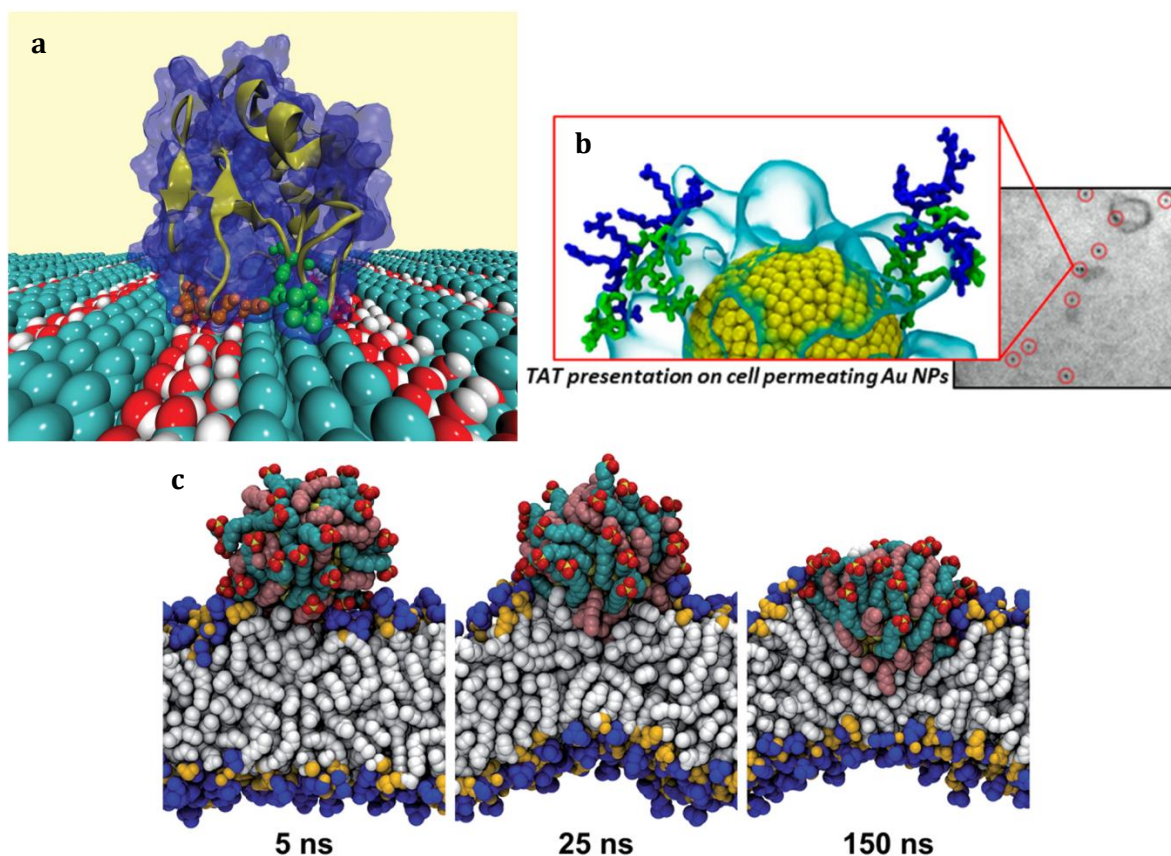


**Figure 2.8 | Exemplar *in silico* all-atom models where AuNPs feature as non-functional substrate carriers. (a)** Nanopatterned surface selectively interacting with proteins. Reproduced with permission.<sup>266</sup> Copyright 2013, The Royal Society of Chemistry. **(b)** Peptide-functionalised nanoparticle used as cell-permeating agent. Reproduced with permission.<sup>268</sup> Copyright 2013, American Chemical Society. **(c)** Mixed alkanethiol-coated AuNP embedding into a lipid bilayer. Reproduced with permission.<sup>269</sup> Copyright 2015, Royal Society of Chemistry.

facilitated direct protein adsorption to the nanostructured surfaces. Specifically, lysine played a significant role in the selective adsorption of Cyt C onto the nanostructured surfaces,<sup>265</sup> while for Lyz, it was the amphipathic character of arginine that enabled the protein to form close contacts with both polar and non-polar surface ligands simultaneously.<sup>266</sup> In a separate study using the same AuNPs, it was shown that nanoscale structuring had an appreciable effect on the local organisation, structure and energetics of the interfacial solvent.<sup>267</sup> Collectively, these findings suggested that nanopatterned surfaces are able to be designed with interfacial hydrophobicity that can selectively interact with different proteins, and in particular amphipathic amino acids can be used to engineer synthetic proteins for selective adsorption on nanopatterned surfaces.

Nanoparticle functionalisation with cell-penetrating peptides, such as the transcription transactivation TAT peptide from the human HIV-1 virus, has proven to be a good strategy in the development of drug delivery vehicles, albeit with variable performance.<sup>270-272</sup> In a conjoined experimental/computational study that also features AuNPs as non-functional



substrate carriers, the effects of TAT peptide concentration and distribution on small pentapeptide-functionalised (CALNN) AuNPs was investigated.<sup>268</sup> Here the NP was modelled as a neutral sphere commensurate in size to a 3 nm AuNP, and the interactions between the CALNN–TAT peptide layer and the solvent were the primary focus of the simulations. The results provided evidence that the TAT concentration and distribution on the NP surface distinctly influenced the properties of the peptide layer in solution and this directly correlated with the AuNPs' experimentally determined cell internalisation capacity (Figure 2.8b). This study demonstrated the need to control the structure and dynamics of functional peptides in solution in order to achieve the desired membrane-permeating activity of peptide-functionalised NPs for efficient drug delivery.

To study the spontaneous fusion and membrane permeation characteristics of monolayer-protected AuNPs, many have used all-atom as well as simplified modelling approaches.<sup>273-276</sup> A recent coarse-grained (CG) study by Quan *et al.* showed that the asymmetry of lipid membranes and the surface chemistry of AuNPs have an important role in how the two species interact.<sup>277</sup> In this work, the AuNP anionic/cationic nature was found to control whether the particles adhered to the membrane surface or penetrated to the membrane core, and the asymmetric distribution of charged lipids in membranes helped facilitate NP permeation. Pioneering research by Van Lehn *et al.* utilising CG<sup>278</sup> and atomistic simulations<sup>269,274,279-283</sup> also predicted the unbiased behaviour of ligand-functionalised nanoparticles interacting with cell membranes (Figure 2.8c), for drug delivery and biosensing applications. Their investigations showed that the interaction with solvent-exposed lipid tail protrusions is the transition step for AuNP insertion into defected and pristine bilayers. They also identified several methodological issues of importance in studying NP-bilayer interactions:<sup>269</sup> (1) in free energy calculations of NP insertion, while the NP–bilayer distance may be the more-widely used (and logical) reaction coordinate, considering only the distance can result in missing the subtle interplay of lipid and ligand fluctuations;<sup>163,174</sup> (2) there is a necessity for free boundary conditions to accommodate the asymmetric insertion of NPs via the hydrophobic effect, which generates bilayer curvature; and (3) accurate atomistic models capable of representing ligand flexibility and electrostatics interactions are required in order to resolve bilayer interior to aqueous solution dielectric constant differences, and the corresponding free energy cost for exposing charges to a low dielectric environment.

Experiments have also shown that functionalised AuNPs can be used for DNA sensing applications.<sup>284</sup> In particular, Mirkin and co-workers exploited DNA–AuNPs to develop a highly selective colourimetric diagnostic method for DNA detection.<sup>285</sup> Other applications

are similarly expected to arise as a result of advances in the preparation of crystalline materials based on DNA-linked particles and computational insight. Even though these are challenging materials to describe due to their complexity, size, and the polyelectrolyte character of DNA, important progress has been made using all-atom and CG MD simulations, as demonstrated in a perspective by Lee *et al.*<sup>286</sup> For example, MD simulations have been used to characterise the conformation DNA adopts when linking AuNPs to form nanoparticle superlattice crystals.<sup>287,288</sup> Lee *et al.* showed that double-stranded DNA molecules transition from A-form to B-form when connected between two Au(111) surfaces irrespective of salt-concentration or mechanical constraints imposed by the separation distance between the surfaces.<sup>287</sup> Using much larger, million-atom MD simulations, Ngo *et al.* studied different supercrystals of DNA-functionalised 3 nm faceted AuNPs in water.<sup>288</sup> Their work demonstrated noticeable differences in the linking DNA structure from that of B-form DNA due to DNA contraction, deviation in base-base stacking and hydrogen bond breaking.

### 2.3.3 Benign-by-Design: Nanotoxicology

Understanding possible adverse effects of inorganic particles on the normal structure and dynamics of biomolecules is crucial for any medical application. Nanoparticles and clusters can affect the structure of proteins and ultimately their function.<sup>289,290</sup> Furthermore, due to the large surface-to-volume ratio of NPs, they can promote a locally increased concentration of proteins and facilitate the formation of insoluble amyloid aggregates.<sup>291</sup> These amyloid fibrils are associated with many debilitating diseases<sup>292</sup> and recent studies suggest that depending on their size, shape and chemistry, nanoparticles may either facilitate formation of these toxic species<sup>291,293</sup> or ultimately be used as therapeutic agents for the treatment of amyloid-type conditions.<sup>33,65,110,294</sup> In either situation, any biomedical application requires a detailed understanding of the complex interactions at the bio-nano interface. One of the initial computational studies of amyloid peptide interactions with AuNPs is that of Hoefling *et al.* where the GolP FF was used to study the adsorption mechanism of amino acids and  $\beta$ -sheet forming polypeptides on an Au(111) surface.<sup>233,295</sup> Their results showed that amino acids with an intrinsic propensity to form  $\beta$ -sheets were “predisposed” to interact with gold surfaces. The latter work revealed that the adsorption of  $\beta$ -stranded peptides occurred in a stepwise mechanism on the polarised Au(111) surface, where the positively charged amino acid arginine facilitated the initial contact formation between the protein and gold surface. The observation of a very fast and strong adsorption indicated that in a biological matrix no bare gold surfaces will be present, instead the biomolecular corona and bioactivity of AuNPs will critically depend on the history of particle administration and the proteins present during initial contact between gold and biological material.

More recently, Brancolini *et al.* presented comprehensive studies based on experiment and multiple levels of theory, including: docking by Brownian dynamics; Poisson–Boltzmann electrostatics calculations; and enhanced atomistic MD molecular simulations; to study the  $\beta_2\text{m}$  protein in the presence of charged (citrate-capped) AuNPs<sup>253</sup> and hydrophobic (thiol-protected) AuNCs<sup>222</sup> (Figure 2.9). Their simulations showed that the interaction of  $\beta_2\text{m}$  with the charged surface of citrate-capped AuNPs did not disrupt the structure of the protein and did not form any unfolded amyloidogenic intermediates. Moreover, the MD results suggested that in a low pH environment the effects of certain protonated residues (HIS<sub>31</sub> in particular), which are known to destabilise the protein toward amyloidogenic intermediates, are enhanced by the interaction with the negative citrate surface. Similar to their previous findings on hydrophobic AuNCs,<sup>222</sup> this work highlighted that AuNP surfaces may provide either stabilising or destabilising effects with respect to amyloidogenic proteins and to control the outcome, a proper balance of electrostatic and hydrophobic interactions between the NP surface and protein is essential.

Since the ground breaking publication by Dawson *et al.*,<sup>115</sup> it is well recognised that in complex biological milieu NPs adsorb a biomolecular corona which changes their physicochemical properties and confers upon them a new (and changing) bio-identity, different from their properties when in pristine form (Figure 1.6). Recent experimental research shows that corona-coated AuNPs significantly reduced the amyloid inhibitory effects of the same bare NPs,<sup>296</sup> while other corona-coated NPs, such as graphene oxide,<sup>297</sup> silica, polystyrene and multi-walled carbon nanotubes,<sup>298</sup> showed higher inhibitory effects on amyloid- $\beta$  fibrillation compared to the bare particles. These studies suggest that in order to obtain a more accurate insight into the therapeutic or toxic effects of NPs, it is necessary

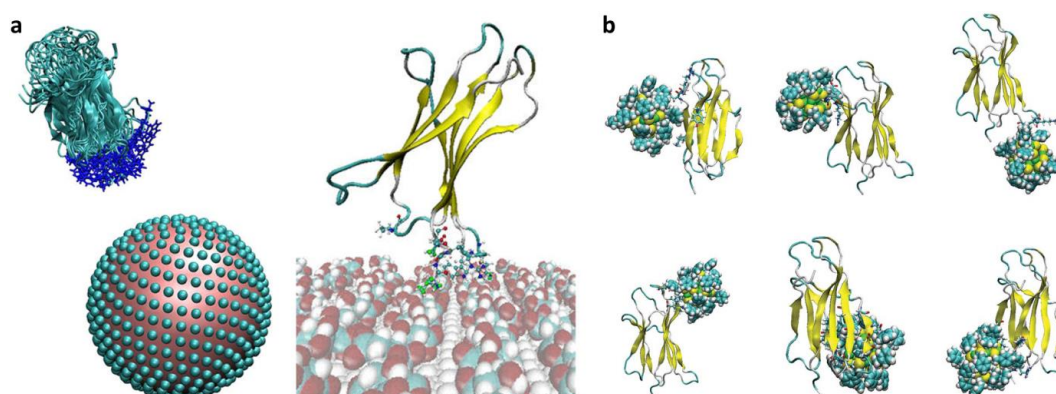


**Figure 2.9 | Computational studies investigating how an amyloid fibril forming protein responds in the presence gold nanomaterials. (a)**  $\beta_2$ -microglobulin ( $\beta_2\text{m}$ ) interacting with a citrate-coated nanoparticle modelled as a dielectric sphere and in all-atom detail. Reproduced with permission.<sup>253</sup> Copyright 2015, American Chemical Society. **(b)**  $\beta_2\text{m}$  interacting in six favourable ways with all-atom  $[\text{Au}_{25}(\text{S}(\text{CH}_2)_2\text{Ph})_{18}]^-$  (where Ph = phenyl =  $\text{C}_6\text{H}_5$ ) AuNCs. Adapted and reproduced with permission.<sup>222</sup> Copyright 2014, Royal Society of Chemistry.

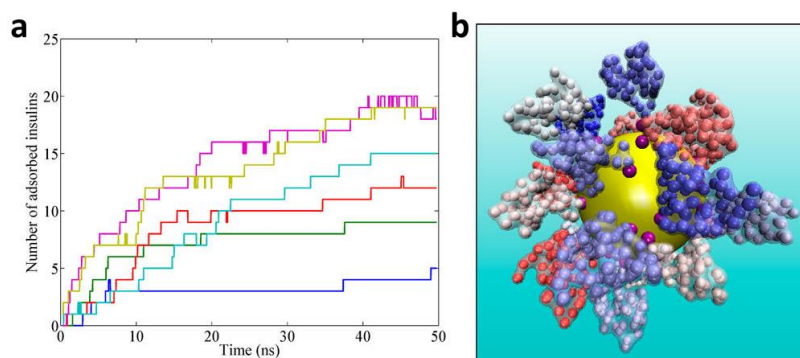


**Figure 2.10 | Coarse-grained simulation study to study an insulin protein corona formation on 5 nm AuNP. a)** The number of insulin proteins bound to the citrate-coated AuNP during the simulations at different protein concentrations: 10 (blue), 20 (green), 34 (red), 50 (cyan), 70 (purple), and 100 (brown). **b)** Snapshot of the protein corona (20 insulin molecules) formed on the citrate-coated AuNP. Reproduced with permission.<sup>301</sup> Copyright 2015, American Chemical Society.

to investigate the biological effects of the protein corona—NP complex. Mahmoudi and co-workers suggested that appropriate handling of the physicochemical properties of NPs is a promising strategy to tune the protein corona decoration, and consequently, its effect on the fibrillation process.<sup>298</sup> The mechanisms of corona formation are complex and depend on many parameters, such as: physicochemical properties of the NP (size, shape, composition, surface decoration, and surface charges); the nature of the physiological environment (blood, cell cytoplasm, etc.); and the duration of exposure. For computational modelling, the temporal and spatial resolutions of all-atom simulations are unable to provide insight into all parameters at the same time,<sup>299</sup> while CG simulation methods can accommodate a few parameters with reasonable computational expense at the cost of atomistic detail.<sup>236,300</sup> Tavanti *et al.* employed CG simulations to study protein corona formation on multiple citrate-coated AuNPs by two of the most abundant plasma proteins, insulin and fibrinogen (Figure 2.10).<sup>301</sup> Their simulations included 10–100 insulin and 1–8 fibrinogen proteins in the presence of 5 nm AuNPs. Using this simplistic approach they were able to explore the protein concentration effects on NP adsorption, the competitive binding process of the two proteins on the NPs, and the dual NP binding to fibrinogen in comparison with experiment. In a similar work, CG simulations were used to study ubiquitin corona formation on AuNPs of different sizes (10, 16, 20 and 24 nm diameters) in bare and citrate-coated form.<sup>302</sup>

It is evident that advances in simulation algorithms and “petascale” computing capabilities are moving the atomic resolution models of biological systems into the million-to-billion atom regime, providing insight into the structure and real time evolution of supramolecular complexes. A recent review highlights the progress driven by large-scale MD simulations in applications ranging from cell biology and health sciences to biofuel production,<sup>303</sup> re-emphasising the ever-increasing role of simulations as a ‘computational microscope’<sup>304</sup>

complementary to experiments. These and other examples highlight the ability of theoretical simulations to help derive the understanding necessary for designing Au nanomaterials for precise targeting in biological medium while avoiding undesirable non-specific adsorption processes. The growth in successful applications of computational studies in conjunction with experiments will enable the “benign-by-design” concept for nanomedicine to become a reality sooner rather than later.

## 2.4 Conclusions and Context of the Thesis

Through a multiscale molecular modelling approach, electronic, atomistic, and coarse-grained levels of treatment can offer a multidimensional view of the complex bio–nano–gold interface. Indeed, while the number of computational works targeting the Au–bio interface at varying levels of theory has drastically increased in recent years, an all-encompassing comprehensive knowledge of these systems has not yet been realised. This is largely due to serious challenges associated with the computational approaches themselves as well as the huge variability in possible Au nanostructures and even greater variety of their biomedical applications. Nevertheless, DFT and *ab initio* based methods (Section 2.2) have been hugely beneficial for investigating the optical (e.g. fluorescent and plasmonic), chemical (e.g. thiol functionalisation and “staple” formation) and physical (e.g. morphological) properties of engineered AuNPs and AuNCs which inherently involve electronic effects. On the other hand, classical mechanics approaches (Section 2.3) have revealed imperative information into the packing of ligands onto NP surfaces, as well as the conformational responses of proteins and lipid bilayers to the presence of the AuNPs, which are largely governed by physical interactions (e.g. electrostatic and van der Waals forces). Coarse-grained simulations have also been tremendously helpful when the packing and self-assembly of ligands, or the AuNPs themselves, become the point of main interest, even though there is a sacrifice of chemical detail. Despite all current approximations and limitations, multiscale molecular modelling has been able to provide non-intuitive insights in the nano–bio interface structure and properties at the electronic and all-atom levels that were not achievable through any other techniques, and will therefore remain an indispensable tool for obtaining fundamental knowledge of gold (and other) nano–bio systems.

In general, there is still a substantial gap in the scientific knowledge relating to the underlying principles and molecular mechanisms that govern:

1. How biomolecules (especially peptides) interact with gold nanomaterials?
2. How specific Au-biomolecule interactions affect the particles’ optical properties?

Therefore, the aim of this thesis is to apply a systematic approach using classical molecular dynamics techniques (Chapter 3) to investigate the structural, dynamic and thermodynamic

properties of Au–bio interfacial systems and contribute to the overall understanding of these organic-inorganic materials in targeted applications. This is achieved through the exploration of three distinct functionalised gold nanomaterial systems, including: plasmonic peptide-coated AuNPs useful for the colorimetric sensing and diagnosis of diseases (Chapter 4); fluorescent peptide-coated AuNCs with potential for biosensing and cellular imaging (Chapter 5); and alkanethiol-protected fluorescent AuNCs for targeted drug delivery and cellular imaging (Chapter 6). The outcomes of this thesis describe the intricate interactions that occur on the nanoscale and offer interesting atomistic insights that aid the development and design of new gold nanomaterials within biological settings.

## Chapter 3:

# Computational Methodologies

A methodological overview of physics-based computational procedures used for investigating Au–bio systems under various conditions is presented. Focus is given to all-atom classical molecular mechanics and molecular dynamics techniques due to their application in the studies presented in this thesis (Chapters 4–6). Sections 3.3.1–3.3.3 are published in the journal *Small* and reproduced in part with permission.<sup>2</sup> Copyright 2016, Wiley-VCH Verlag GmbH & Co. Details identifying the individual contributions each co-author made to the *Understanding and Designing the Gold–Bio Interface: Insights from Simulations* publication<sup>2</sup> are given in the opening outline for Chapter 2.

---

### 3.1 Introduction

Molecular modelling is an umbrella term that embodies all theoretical computational methods that mimic the behaviour of electrons, atoms, and molecules to describe (sometimes very complex) chemical systems. These approaches are a powerful tool (ideally in complement with experimental data) to understand, explain, and provide perspectives that yield new information at temporal and spatial resolutions, and well controlled environmental conditions, that are unachievable with any other technique. As described in Chapter 2, and perfectly encapsulated in Figure 2.1, different levels of theory are able to probe distinct gold–biomolecular phenomena and mechanisms. This chapter gives an informative summary of these methodologies.

First a brief synopsis of the various types of quantum mechanical (QM) techniques available to perform molecular modelling is delivered. Then, in Section 3.3, a detailed discussion of classical molecular mechanics (MM), its underlying methodologies and general concepts is presented. Following this, in Section 3.4, emphasis is placed on the algorithms that govern, modulate, and maintain the physics of a classical molecular dynamics (MD) simulation, a method that is applied extensively throughout this thesis. Finally, a succinct generalised procedure outlining the steps used to construct molecular models and perform MD is given.

### 3.2 Quantum Mechanical Methods

The concepts of QM are non-trivial to understand and this section was written with the aid of many references.<sup>305-309</sup> Unfamiliar readers are encouraged to consult them.

### 3.2.1 Basics of Quantum Theory

All matter is described at a fundamental level by quantum mechanics and underpinning all QM is the multi-body *wavefunction*:

$$\Psi(\mathbf{r}_1, \mathbf{r}_2, \dots, t) \quad (3.1)$$

Here,  $\mathbf{r}_1, \mathbf{r}_2, \dots$  etc. are the  $(x, y, z)$  positions vectors of all fundamental particles in the system (electrons, protons, neutrons) and the wavefunction evolves in time,  $t$ . In other words, a wavefunction is a mathematical function that describes the quantum state of a system. Through the wavefunction all information about the system (e.g. particle positions, momentums, and/or spins) can be determined, albeit in a probabilistic sense. The *physical* significance of the wavefunction is that its square,  $\Psi^2$ , provides a *probability distribution* for finding particle one at  $\mathbf{r}_1$ , particle two at  $\mathbf{r}_2$ , etc. for a given time. Note that a wavefunction describing an electron (or pair of electrons) in an atom is often called an *atomic orbital* whereas a wavefunction describing an electron in a molecule is called a *molecular orbital*.

Most QM calculations are focused on determining an approximate, time-*independent* form of a system's wavefunction by solving the time-independent Schrödinger equation:

$$\hat{H} \Psi(\mathbf{r}) = E \Psi(\mathbf{r}) \quad (3.2)$$

where  $\hat{H}$  is the *Hamiltonian operator* acting on the system's wavefunction  $\Psi$  that depends only on particle positions,  $\mathbf{r}$ , and  $E$  is the total energy of the system. An "operator" is simply the mapping of one function to another function and in QM, all observables (like energy, momentum, velocity etc.) are formulated as operators. In Equation 3.2, the Hamiltonian operator (known as the total energy operator) is itself is a sum of two other operators, the kinetic ( $\hat{T}$ ) and the potential ( $\hat{V}$ ) energy operators:

$$\hat{H} = \hat{T} + \hat{V} = \frac{-\hbar^2}{2m} \frac{\partial^2}{\partial \mathbf{r}^2} + V(\mathbf{r}) \quad (3.3)$$

where  $\hbar$  is Planck's constant,  $m$  is particle mass and  $V$  is potential energy.

There are many eigenfunctions (wavefunctions) with corresponding eigenvalues (energies) that satisfy Equation 3.2 for a particle confined in a potential (e.g. an electron in an atom). Each  $\psi$  and  $E$  solution gives a stationary (equilibrium) state of the quantum system and this importantly implicates that there is a different wavefunction ( $\psi_1, \psi_2, \psi_3, \dots$ ) for each *allowed energy* ( $E_1, E_2, E_3, \dots$ ) in a system, meaning electron energies are *quantised* not *continuous*. In most cases we would like to solve the Schrödinger equation for the *ground-state* of a system, i.e. we want to find the wavefunction ( $\psi_1$ ) that has the lowest associated energy ( $E_1$ ).



### 3.2.2 Common Approximations

To solve Equation 3.2 and obtain properties for a system of interest, it is first necessary to make several simplifications to the form of the wavefunction and Hamiltonian. The types and degrees of simplifications made give rise to different classes of QM techniques. There are *theoretical* approximations that, in principle, limit the accuracy of the methods that use them and there are *computational* approximations that reduce the cost of computational resources at the expense of numerical accuracy. Equation 3.2, already implies the neglect of relativistic effects and the separation of time and position variables to produce a time-independent relation, however, a few more QM approximations are still needed.

The *Born–Oppenheimer approximation*<sup>310</sup> is a theoretical simplification that assumes nuclei are infinitely heavier than electrons and allows for the Schrödinger equation to be solved assuming that nuclear positions are fixed, i.e. nuclei have no kinetic energy. In other words, electrons can be described as moving in a static electric field of stationary nuclei. Wavefunctions of a system will therefore only be functions of electronic coordinates and the molecular Hamiltonian operator will only contain terms for: electron kinetic energies, electron–nucleus attractions, electron–electron repulsions, and nucleus–nucleus repulsions.

While the Schrödinger equation can be exactly solved for the hydrogen atom, in multi-electron systems the motion of electrons cannot be decoupled from each other and consequently there is no analytical solution to Equation 3.2 for polyelectronic systems. This is mainly due to the electron–electron Coulomb repulsion in the Hamiltonian but other complexities (e.g. *spin* and *antisymmetry* of electrons) also factor in.

Because non-interacting systems *can* be solved analytically, many QM techniques start by assuming electrons do not directly interact with each other and then introduce corrections to help offset this assumption. For non-interacting electrons, the Hamiltonian for  $N$  electrons can be rewritten as a sum of one-electron Hamiltonians ( $\hat{h}$ ):

$$\hat{H} = \sum_i^N \hat{h}_i = \sum_i^N \left( \frac{-\hbar^2}{2m_i} \frac{\partial^2}{\partial \mathbf{r}^2} + V_i(\mathbf{r}) \right) \quad (3.4)$$

An appropriate form (as we will see below) for a  $N$ -electron wavefunction is then a  $N \times N$  determinant composed of single-electron wavefunctions (called a *Slater determinant*<sup>311</sup>):

$$\Psi(\mathbf{x}_1, \mathbf{x}_2, \dots, \mathbf{x}_N) = \frac{1}{\sqrt{N!}} \begin{vmatrix} \phi_1(\mathbf{x}_1) & \phi_2(\mathbf{x}_1) & \dots & \phi_N(\mathbf{x}_1) \\ \phi_1(\mathbf{x}_2) & \phi_2(\mathbf{x}_2) & \dots & \phi_N(\mathbf{x}_2) \\ \vdots & \vdots & \ddots & \vdots \\ \phi_1(\mathbf{x}_N) & \phi_2(\mathbf{x}_N) & \dots & \phi_N(\mathbf{x}_N) \end{vmatrix} \quad (3.5)$$

Here, the total electronic wavefunction  $\Psi$  is now made-up of a linear combination of “spin orbitals”  $\phi_i$  that are functions of space-spin coordinates  $\mathbf{x} = \{\mathbf{r}, \omega\}$ . Each of these spin orbitals are a one-electron wavefunction that is the product of a spatial orbital  $\psi(\mathbf{r})$  and a spin function ( $\omega$ ), which can be spin up ( $\alpha$ ) or down ( $\beta$ ). For example,  $\phi_N(\mathbf{x}_1)$  indicates a function that depends on the space-spin coordinates of the electron labelled “1”.

Representing the electronic wavefunction as a *single* Slater determinant is called the *Hartree–Fock (HF)* or *mean-field approximation* and it is particularly convenient. Interchange of any two rows or columns of the determinant physically corresponds to electron exchange, and these results in wavefunction sign reversal (satisfying the *antisymmetry property*, without this *exchange interaction* is missing). If any two rows or columns are identical, the wavefunction collapses ( $\Psi = 0$ ), i.e. occupation of a spin orbital by more than one electron is forbidden (satisfying the *Pauli exclusion principle*). Finally, the factor in front of Equation 3.5 ensures the wavefunction is normalised.

When  $\Psi$  describes molecules, the one-electron functions that go into a Slater determinant are often approximated as a finite *linear combination of atomic orbitals* (LCAO):

$$\phi_i = \psi_i \omega_i = \left[ \sum_{v=1}^K c_{vi} \varphi_{vi} \right] \omega_i \quad (3.6)$$

where  $\phi$  is the spin orbital of electron  $i$  with spin  $\omega$ ,  $c_v$  are coefficients, and  $\varphi_v$  are so called *basis functions* or *atomic orbitals* (since they are typically atom-centered). The complete set of  $K$  one-particle basis functions that build the spatial orbitals ( $\psi$ ) of an atom are called a *basis set*. The smallest possible basis set for an atom is referred to as a *minimal basis set*, and usually it contains one basis function per electronic orbital of the atom it is describing (including unoccupied orbitals), e.g. a minimal basis set for carbon has 5 basis functions (1s, 2s, 2p<sub>x</sub>, 2p<sub>y</sub>, and 2p<sub>z</sub>). If there are *two* basis functions per electron, this is called a *double zeta basis set*, e.g. 10 functions for carbon, and likewise for *triple zeta*. There are many types of basis sets that vary in the number and functional forms of the basis functions. Two common examples of basis function types are *Slater-type orbitals (STO)* and *Gaussian type orbitals (GTO)*. The former are *inspired* by exact atomic orbital solutions to the Schrödinger equation for the hydrogen atom, while the latter are mathematical Gaussian functions. It is important to mention that molecular orbitals that go into or come out of a QM calculation (apart from hydrogen) are not *true* molecular orbitals. They are guesses to what orbitals “might look like” since they are solutions to *approximate* Schrödinger equations.

One last mention before moving onto the next section is the *variational principle/theorem*. The variational principle says for any time-independent Hamiltonian operator, any *wavefunction* that is not the *ground-state wavefunction* will have an associated energy that is greater than or equal to the true ground-state energy for the given Hamiltonian. This provides a method for finding the ground-state wavefunction of a system, the *variational method*. Basically after guessing a “trial” wavefunction for the problem, which consists of some adjustable parameters, these parameters are continually adjusted until the energy of the trial wavefunction is minimised. The resulting trial wavefunction is then assumed to be a sufficient estimate of the true ground-state wavefunction of the system and the energy of the trial wavefunction is an upper bound to the exact ground-state energy.

With the groundwork laid, there are now two main approaches to take to find the ground-state wavefunction of a system and both are self-consistent, i.e. the variables in the equations to be solved depend on themselves so they must be solved in an iterative manner. The first is termed *wavefunction methods* (the simplest of which is the *HF procedure* or often just called *HF*), and the other is density functional theory.

### 3.2.3 The Hartree–Fock Procedure

In the HF procedure, because we are using a *single* Slater determinant to represent  $\Psi$ , it is necessary to reformulate the molecular Hamiltonian and this leads to a new *approximate* single-electron Schrödinger equation called the *Hartree–Fock equation*<sup>312,313</sup>:

$$\hat{F}[\{\phi_j\}]\phi_i = \varepsilon_i\phi_i \quad (3.7)$$

Here,  $\hat{F}$  is a new operator called the *Fock operator* that is generated by a set of orbitals  $\{\phi_j\}$  and applied to a single one-electron orbital  $\phi_i$  to obtain its energy  $\varepsilon$ . In other words  $\hat{F}$  is a *functional* (note the square brackets) of the  $j$  orbitals used to generate it, where a *functional* simply means a function that depends on another function. Since the Fock operator depends on the orbitals used to generate it, Equation 3.7 actually means that the eigenfunctions ( $\phi_i$ ) of a Fock operator are new orbitals, with new  $c_{vi}$  (Equation 3.6), that in-turn can be used to construct a new Fock operator. So, after a basis set is chosen and an *initial* guess is made for the linear  $c_{vi}$  parameters, a Fock operator is constructed and Equation 3.7 is solved. The new set of orbitals  $\phi$  (with new  $c_{vi}$  and energies  $\varepsilon$ ) are then used to construct a new  $\hat{F}$  and this continues until  $c_{vi}$  no longer change. In practice this is done by matrices. At this point, the system’s total energy has converged and a self-consistent set of one-electron orbitals has been constructed through the *variational method*. Ultimately, the accuracy of  $\Psi$  described by these orbitals only depends on the chosen basis set.

At the end of a ground-state QM calculation (HF or otherwise) we get the following: the electronic energy (one point on the potential energy surface); the electronic wavefunction (can be used to get dipole moments, polarisability, electrostatic potential, etc.); orbital locations (which can give insight into bonding); and orbital energies/occupancy (i.e. the amount of energy required to remove/put an electron from/in that orbit).

The HF approach, or more accurately Equation 3.6 with 3.7, describes a system of  $N$  non-interacting “electron-like” particles (that have zero charge and physical dimensions), each moving in an effective potential created by the other  $N-1$  particles. In other words, each electron is independent of all others except that it feels the Coulomb repulsion due to the *average* positions of all other electrons. This introduces an *error* in  $\Psi$  and its energy. Given a large basis set this energy error (called the total *electron correlation energy*,  $E_c$ ) only represents about  $\sim 1\%$  of *true* ground-state energy however this energy difference has significant ramifications for studying chemical properties such as dispersive effects, which are crucial for intermolecular interactions. There are several techniques available that attempt to recover  $E_c$  such as: using *multiple* Slater determinates to represent  $\Psi$  (called configuration interaction),<sup>314</sup> Møller–Plesset perturbation theory,<sup>315</sup> and coupled cluster methods,<sup>316</sup> but these will not be discussed here.

### 3.2.4 Density Functional Theory

The electron density ( $\rho(\mathbf{r})$ ) of a system, i.e. the probability of finding  $N$  electrons within a volume element, is one of the most important properties we can examine from an electronic structure calculation. Not only can other properties be obtained from it such as dipoles and electrostatic potentials,  $\rho(\mathbf{r})$  is also something that can be measured experimentally, e.g. by X-ray diffraction. In 1964, Hohenberg and Kohn discovered two more very important features of  $\rho(\mathbf{r})$ .<sup>317</sup> The first is that the total energy of an electron gas (including exchange *and* correlation) is a unique functional of  $\rho(\mathbf{r})$ , i.e.  $E[\rho(\mathbf{r})]$ . The second is that the ground-state electron density and energy can be obtained variationally via minimisation of  $E[\rho(\mathbf{r})]$ , or in other words, any *density* that is not the *ground-state density*, will have an energy higher than the true ground-state energy. Density functional theory (DFT) is built on these.

Modern DFT, or Kohn–Sham DFT,<sup>318</sup> bears a lot of similarities to the HF procedure described in Section 3.2.3. The system is still treated as a fictitious system  $N$  of non-interacting electrons that is represented by a *single* Slater determinate constructed from a set of *fictitious* orbitals, in this case called Kohn–Sham (KS) orbitals. KS orbitals are still found by solving one-electron equations similar to Equation 3.7, except that the Fock operator is replaced by the Kohn–Sham operator, which is slightly more complicated and contains an

exchange–correlation term (more below). In a DFT calculation, a self-consistent approach is used to take an initial guess of the system’s total electron density, which produces a set of single-electron wavefunctions that in turn are used to improve the value of the density. The cycle of density updates and wavefunction generation continues iteratively until convergence of the density (and electronic energy) is finally achieved.

Before we can solve for the electron density of a system, we need to first make a *guess* at what it looks like. Practically speaking, the accuracy and quality of DFT calculations strongly rely on the choice of an appropriate *functional* to describe the electron density of the system. These DFT functionals can be divided into different groups based on the approximations used for the exchange–correlation terms in them: local density approximations (LDA, functional depends *only* on the local density at a given point), general gradient approximation (GGA, functional depends on local density *and* its gradient), hybrid functionals (mixes in Hartree–Fock exchange), and others. These will not be discussed here; the only note that will be made is that while HF *only* considers electron exchange, DFT explicitly considers both exchange and correlation through these functionals.

For large nanoparticle systems (thousands of atoms), where conventional DFT becomes prohibitively computationally expensive, simplified QM approaches such as tight-binding<sup>319</sup> and other semi-empirical methods<sup>320,321</sup> play a valued role. These methods use empirical parameters within a QM framework to improve computational performance, albeit with many approximations such as: only explicitly calculating valence electron interactions, or completely neglecting two-electron interactions.

### Linear-Scaling DFT

Over the last few decades, the development of linear-scaling  $O(N)$  methods such as ONETEP<sup>322,323</sup> and SIESTA<sup>324</sup> have become significant tools for studying large (biomolecular) systems at the electronic level (see the comprehensive review by Cole *et al.*<sup>325</sup>). The key feature of these methods is their computational efficiency obtained by exploiting the inherent locality or “near-sightedness” of the single-particle density matrix, while retaining accuracy akin to traditional plane-wave basis set codes. Such efficiency opens up the possibility of performing accurate DFT calculations on systems with tens of thousands of atoms, including nanomaterials,<sup>326</sup> proteins,<sup>327</sup> and more complex systems such as nanoparticles interfaced with complete proteins<sup>328</sup> and gold/thiolate molecular junctions.<sup>329</sup>

QM techniques can also be combined with MM methods to investigate large complex systems, where the electronic properties of a selected region are described at the QM level and the surrounding environment described at the MM level.<sup>330,331</sup> A challenge of this

method is the uncertainty in how to define these two (or more) regions, which will ultimately affect the accuracy of the results, especially if the QM region is not large enough or the interface between the QM and MM regions is not modelled accurately.

While each of these QM strategies are slightly different in methodology, they can all produce highly accurate results to determine the total energy, predict molecular structures and derive properties that depend on electronic distribution (see Section 2.2). These properties often cannot be determined by other methods and include: electric multipole moments (i.e. dipole, quadrupole etc.); electron density distributions; atomic charge distributions (on each nucleus of the system); bond orders (i.e. number of chemical bonds between pairs of atoms); bond formation and breakage; electrostatic potentials (useful for rationalising interactions between molecules); thermodynamic values (e.g. enthalpy driven heat of formation); electron transfer; polarisation effects; and the development of parameters to be used in classical modelling methods.

Ultimately, the application of QM to large Au–bio systems (such as interfacial systems in solvent) is limited both by computational capacity and the range of approximations currently involved in the methodologies themselves. While linear-scaling DFT methods show the most promise, they still need significant developments to become a routine tool for modelling the dynamic evolution of biologically relevant nano–bio systems. Instead, classical approaches offer an attractive alternative to model large Au–bio systems.

### 3.3 Classical Molecular Mechanics

Although not as accurate or robust as QM techniques, MM methods enable the investigation of much larger systems in realistic atomic detail to better understand and predict the macroscopic (often physical) properties of inorganic and biological materials. This scale up is achieved by applying the *Born–Oppenheimer* approximation to assume that electronic motion is negligible and that the Hamiltonian of a system depends only on nuclear variables (i.e. only on atomic positions). Consequently, this means that MM approaches cannot investigate electronic properties however they can provide accurate calculations of physical phenomena in a fraction of the computer time.

#### 3.3.1 The Potential Energy Function

Underlying all MM methods is an analytical expression called a force field (FF) that describes the interactions between particles/atoms. Used to calculate the total potential energy ( $V^{tot}$ ) of a molecular system, a common functional form of a FF is given below.

$$\begin{aligned}
V^{tot} = & \sum_{bond} K_b(b - b_0)^2 + \sum_{angle} K_\theta(\theta - \theta_0)^2 + \sum_{torsion} K_\varphi[1 + \cos(n\varphi - \delta)] \\
& + \sum_{LJ} 4\varepsilon_{ij} \left[ \left( \frac{\sigma_{ij}}{r_{ij}} \right)^{12} - \left( \frac{\sigma_{ij}}{r_{ij}} \right)^6 \right] + \sum_{Coulomb} \frac{q_i q_j}{4\pi\varepsilon_0 r_{ij}} + \sum V^{other}
\end{aligned} \tag{3.8}$$

Each term of Equation 3.8 is composed of two distinct components which collectively describe the energetic contributions associated with a specific type of inter-atomic interaction, namely: a function used to generate the potential energy of that interaction; and the corresponding equilibrium parameters for the function (empirically and/or theoretically determined). The first two terms of Equation 3.8 describe covalent bond stretching and angle bending using harmonic functions (Hooke's Law) with force constants  $K_b$  and  $K_\theta$  defining the strength of the energetic penalties imposed for deviations of the bond length ( $b$ ) and angle ( $\theta$ ) from defined minimum energy positions ( $b_0$  and  $\theta_0$ , respectively). The torsion term uses a periodic function to model how varying the dihedral angle ( $\varphi$ ) between atoms separated by three covalent bonds affects the energy with respect to the potential barrier to rotation ( $K_\varphi$ ), periodicity ( $n$ ), and phase ( $\delta$ ). Non-bonded atom pair interactions are described as functions of the separation distance  $r$  between the centres of particles  $i$  and  $j$ . Close-range repulsion and van der Waals (vdW) dispersion interactions are represented by a Lennard-Jones (LJ) 12-6 potential where  $\sigma_{ij}$  and  $\varepsilon_{ij}$  are the finite distance at which the inter-atomic LJ potential is zero and the potential well depth, respectively. Electrostatic interactions are treated via Coulomb's law where  $\varepsilon_0$  is the permittivity of free space and  $q_i$  is the partial charge assigned to each atom. Finally, the last term of Equation 3.8 encompasses all other *FF specific* interactions that may feature, such as term coupling, out-of-plane bending, induced polarisation (Section 3.3.2), external applied forces, etc.

Since most FFs employ an almost identical (or at least very similar) functional form, it is primarily the availability and quality of a FF's parameters that reflect how accurately inter-atomic interactions (and subsequently physical phenomena) are emulated *in silico*. Well-established biological FFs (e.g. AMBER,<sup>332</sup> CHARMM,<sup>333</sup> GROMOS,<sup>334</sup> and OPLS/AA<sup>335</sup>) have been developed and validated over several decades to reproduce basic biomolecular properties, however they lack parameters for investigating biomolecule behaviour in gold-containing systems. Due to gold's innate chemical inertness, most species (excluding thiols) primarily physisorb to gold, therefore extending conventional biological FFs to capture this interaction *mainly* requires reliable gold-organic vdW parameters and atomic charges (see Appendix A for examples generating custom atomic charges from this thesis).

Many FFs handle vdW interactions through a LJ potential, commonly in the 12–6 form (Equation 3.8). By incorporating tailored gold-specific LJ parameters (i.e.  $\sigma_{ij}$ ,  $\epsilon_{ij}$  where  $i = j = \text{Au}$ ) for various Au surface facets and cluster geometries into an existing FF's functional form, the interaction energy between gold and other atom types can be estimated (Section 3.3.3). This is done through assuming the validity of standard mixing/combination rules, such as  $\sigma_{ij} = (\sigma_i + \sigma_j)/2$  and  $\epsilon_{ij} = (\epsilon_i \times \epsilon_j)^{1/2}$  which are already established approximations within biological FFs. Yet as highlighted by Latour,<sup>336</sup> parameters derived to represent biomolecule–solution interactions should not automatically be assumed to be directly transferable to biointerfacial systems. With this in mind, the only viable approach to modelling AuNP–bio interfacial systems is through developing parameters (in a consistent way) to be both specific for particular Au nanostructures or surface facets *and* compatible with extensively tested bio-organic FFs. Ideally, further developments and refinements of gold–bio FFs will be done in conjunction with experimental data however at this moment, there is little (if any) useable data available for this purpose. While some metal–molecule adsorption experiments have been specifically designed and used for validating non-bond interaction potentials,<sup>234</sup> QM calculations are currently filling the parameterisation gap.

### 3.3.2 Polarisability

Before discussing the different types of gold–biomolecule FFs available (Section 3.3.3), it is worth mentioning the importance of polarisation, also known as image charge effects. This is a phenomenon that occurs when (charged) molecules come in proximity to metal-like materials. Essentially, the delocalised *sea-of-electrons* of gold (surfaces) becomes polarised, i.e. dipoles are induced, by the intrinsic electron-cloud electric field of a nearby molecule (Figure 3.1). Image effects not only create an attractive interaction between charges and metals, they can also affect mutual interactions between charges in adsorbed molecules.

Although not all classical FFs for metal–molecule interactions explicitly include polarisation terms in their functional form, some effects might still be implicitly included in the remaining two-body metal–molecule parameters, depending on the parameterisation approach (e.g. QM approaches where polarisation is intrinsic). Nevertheless, since many biomolecules invariably feature charged domains, polarisation effects are generally not negligible. Therefore, the incorporation of explicit, on-the-fly, polarisability for gold atoms in classical simulations is ideal. A few dynamic models currently implemented for this purpose include the rigid-rod approach of Iori and Corni,<sup>337</sup> and more recently the capacitance-polarisability interaction model which also allows an atomistic description of charge migration within a particle.<sup>338,339</sup> Other *a posteriori* methods to quantitatively measure facet-dependent polarisation effects have also been published in the literature,<sup>246</sup>



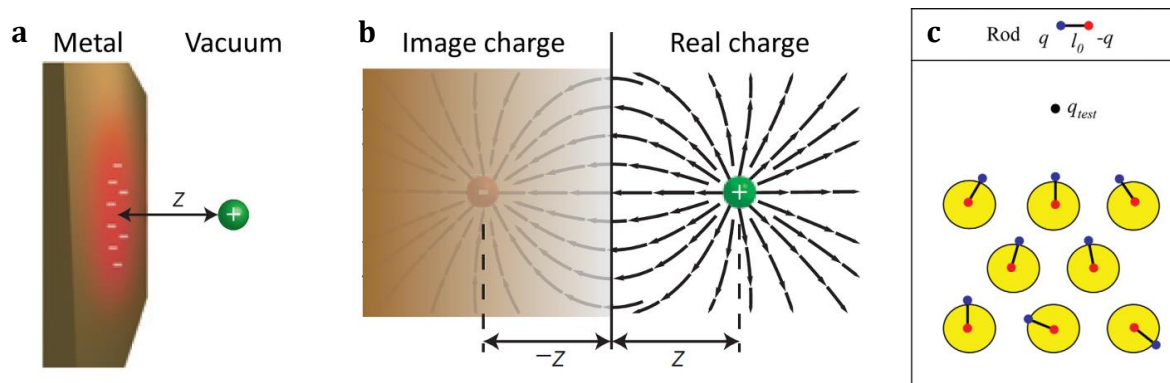


**Figure 3.1 | Schematics illustrating induced polarisation and the rigid-rod model. (a)** A charged particle at close proximity to a metal induces a net charge at the surface. **(b)** Electric field produced by the external point charge (field lines shown by arrows). Reproduced and adapted with permission.<sup>341</sup> Copyright 2013, Nature Publishing Group. **(c)** A two-dimensional depiction of the rigid-rod model used to dynamically polarise atoms (circles). Adapted with permission.<sup>337</sup> Copyright 2008, Wiley Periodicals, Inc.

however these carry the limitation that the atomic positions cannot respond to the image potential (see discussion given in Jha *et al.*<sup>340</sup>).

In the rigid-rod approach<sup>337</sup> (which underpins the FF utilised in Chapter 4), polarisability is emulated through the addition of a virtual interaction site on each gold atom. The virtual site has mass  $m$ , charge  $q$  and is forced to remain at a fixed radial distance  $l_0$ , but otherwise rotationally unrestrained, from the original gold atom's centre (which has an opposite charge of  $-q$  assigned to it, Figure 3.1c). This site has no vdW parameters therefore it can only interact with other atoms via electrostatic interactions, and interactions between the virtual site and its respective gold atom do not contribute to the energy and force calculations of a simulation. When an external charge comes in proximity to a given gold atom (i.e. the partial atomic charge on a nearby biomolecule atom), the rod freely rotates to find the most energetically favourable position. Since the rod always has a finite dipole moment given by,  $\mu = ql_0$ , the orientationally averaged dipole moment only yields physically meaningful results for temperatures  $T$  greater than zero. The polarisability  $\alpha$  is therefore given by Equation 3.9 (where  $k_b$  is the Boltzmann constant).

$$\alpha = \frac{\mu^2}{3k_b T} = \frac{q^2 l_0^2}{3k_b T} \quad (3.9)$$

While it is noted that this method to treat polarisation is: qualitative; empirical in nature, i.e. sacrifices the realism of a quantum description; and does not allow for charge accumulation to develop on the metal, the rigid-rod method has been very successfully incorporated into several FFs to describe induced polarisation on gold surfaces<sup>215,216,342,343</sup> (as further discussed in Section 3.3.3), as well as for carbonaceous nanomaterials.<sup>344</sup>

### 3.3.3 Gold–Biomolecular Force Fields

When FFs are developed they are usually designed with a specific application in mind, and aim to explicitly reproduce some characteristic of a particular atomic system as a validation step. This focus may be ensuring that the crystal structure of a small AuNCs is maintained, or verifying that the experimental interaction energies and adsorption geometries of molecules onto different gold surface facets are adequately reproduced. Although there is no one-size-fits-all FF capable of replicating all complex physicochemical phenomena at the gold–bio interface, currently there are two conceptually different mainstream approaches commonly taken when constructing gold–biomolecular FFs. One approach is targeted at general and transferable interfacial gold-specific parameters capable of modelling any shaped gold material as well as reconstruction of the substrate within a single comprehensive framework. The alternative approach introduces a number of tailored parameters aimed at differentiating the interactions between particular biomolecular species and different crystallographic facets and shapes of gold, while keeping the geometry of the gold substrate/centre rigidly intact. For detailed descriptions of both methods, including validation data, please refer to discussions given the literature,<sup>343,345</sup> and references therein. Presented herein is a general account of both approaches, as well as others, used in developing custom FFs able to represent the interactions occurring between gold (surfaces and clusters) and biomolecules (e.g. water, ligands, proteins, and DNA). As with all simulation work, there is no single *best* method to model gold, rather the best approach for a system is one that most accurately reproduces the properties of interest.

#### Lennard–Jones Gold Particles

Possibly the most “transferable” and hence popular gold LJ parameters are those of the METAL/INTERFACE FF of Heinz et al.<sup>122,346</sup> which were developed to reproduce the experimentally measured bulk density and surface tension of homoatomic face-centred face-centred cubic (FCC) metals. Available as 12–6 and 9–6 LJ parameter sets,  $\sigma_{\text{Au,Au}}$  and  $\epsilon_{\text{Au,Au}}$  are claimed to be compatible with a wide-range of organic FFs such as AMBER,<sup>332</sup> CHARMM,<sup>333</sup> OPLS/AA,<sup>335</sup> COMPASS,<sup>347</sup> and CVFF.<sup>348</sup> The applicability with so many organic FFs is reasoned to be a result of parameter validation only involving properties of pure gold and non-bonded interactions. The LJ description of gold in the METAL/INTERFACE FF allows for the classical Hamiltonian energy expression to reproduce the FCC structure and surface energy of gold which leads to agreement of the calculated metallic thermal and mechanical properties with experimental values.<sup>122</sup> Furthermore, the authors assert that these metallic properties dictate all interactions with other components (e.g. biomolecules) and this enhances the LJ parameters’ applicability to interfacial systems.

While the gold atoms in this FF are charge-neutral, they are not geometrically restricted, allowing for the exploration of molecules interacting with different crystallographic surfaces,<sup>349</sup> faceted and spherical AuNPs,<sup>350,351</sup> as well as other shaped gold constructs.<sup>237,352</sup> Polarisation is not described explicitly, but polarisation effects were quantitatively tested *a posteriori* and found to contribute up to ~20% of the binding energy for highly charged biopolymers on the Au(111) surface, while for other surfaces such as the Au(100) the contribution from polarisation is even more significant or even dominant.<sup>246</sup> Peptide/protein binding to Au(111) using the METAL FF is described as a “soft epitaxy” type mechanism, with adsorption via the surface’s hollow sites,<sup>241</sup> which is (albeit indirectly) supported by experimental studies showing near perfect epitaxial ordering of alkanes and some amino acids at monolayer coverage on Cu(111) and Pt(111) surfaces. Alternative hypotheses suggest that interfacial water structuring rather than epitaxy is what plays a critical role in influencing peptide–gold binding.<sup>240</sup> It should also be mentioned that as a result of solely relying on LJ terms to maintain gold atoms in the desired FCC morphology, the depth of the LJ potential well is relatively large (12–6:  $\epsilon_{\text{Au,Au}} = 19.1 \text{ kJ mol}^{-1}$ ) since it represents strong cohesion. Although this raises concerns about overestimating the strength of vdW interactions between mixed species, computed water and peptide adsorption energies using the METAL FF are in agreement with experiment,<sup>235</sup> and recently published thiolated AuNC FFs also features similar magnitude  $\epsilon$  values for gold atoms.<sup>353</sup>

Besides the METAL FF, several other sets of LJ parameters have been used to model bio–gold systems while relying on cross-terms to govern gold’s interactions with organic and biomolecular components.<sup>354–360</sup> These include: the hydrophilic parameters of Vila Verde;<sup>244</sup> parameters borrowed and modified from the generic Dreiding<sup>361</sup> and Universal<sup>362</sup> FFs, parameters adapted from experimental data,<sup>363</sup> and those taken from self-assembled organic monolayers on gold substrates.<sup>364</sup> It is worth noting that due to the ubiquitous nature of thiolates in AuNP–bio systems, it is often necessary to accurately and explicitly represent the Au–S bond (e.g. found between deprotonated cysteine and Au) within the simulation protocol. There have been many examples in the literature where harmonic potentials,<sup>365,366</sup> Morse potentials<sup>355,367</sup> and various strong short-range potentials<sup>354,368,369</sup> have been used to reproduce this bond for specific applications. However, as adhesion of many biomolecules (such as proteins) to gold is known to be largely dominated by secondary interactions, standard mixing rules may fail to accurately describe the varying physicochemical strength of interaction different atom types have with gold. This issue has been a strong motivator behind the also popular GOLF family of FFs.<sup>215,216,222,342,343,370</sup>

### Peptides and Proteins on Crystallographic Gold Facets

The Gold-Protein (GolP) FF, as the name suggests, was designed to examine how proteins interact with gold surfaces. It was parameterised against both QM and experimental data to reproduce adsorption geometries and interaction strengths of natural amino acids on the (111) facet initially.<sup>215</sup> Although interactions between gold and other atomic species are still governed by 12-6 LJ potentials, GolP additionally introduces explicit “Au-X” LJ terms to ensure weakly chemisorbed sulphur- and nitrogen-containing molecules (imidazole, NH<sub>3</sub>, CH<sub>3</sub>SH and CH<sub>3</sub>SCH<sub>3</sub>) and  $\pi$ -conjugated species are correctly described. Furthermore, two unique features of the GolP FF are the inclusion of LJ virtual sites to constructively direct the geometry of biomolecule adsorption (as obtained from DFT calculations), and the use of the rigid-rod dipole method<sup>337</sup> to dynamically and efficiently describe gold polarisation. The inclusion of polarisation effects is not only beneficial for the reasons discussed in Section 3.3.2, but also because this potentially enables the transferability of gas-phase derived parameters to the condensed phase, as demonstrated by the polarisable AMOEBA FF.<sup>371</sup>

The GolP Au(111) surface is represented as a 5-layer periodic slab in two dimensions with gold atoms holding no partial atomic charge and no intra-surface (i.e. gold-gold) parameters. As a result, gold atoms must be kept rigid in their equilibrium position, which disables gold lattice deformations and removes the ability of the FF to describe nanocrystal growth or compute metallic properties. However, for studying gold surface-biomolecular interfaces this is an acceptable approximation, considering the much stronger cohesion of gold relative to soft OPLS/AA<sup>372</sup> (henceforth be referred to as GolP-OPLS).

To address the facet-selectivity of peptide adsorption, Wright et al. reparameterised GolP-OPLS with the CHARMM FF<sup>333,373,374</sup> and extended it to describe biomolecule interactions with the Au(111) and Au(100) surface facets (Figure 3.2), which are the most common facets of AuNPs larger than 3 nm.<sup>61</sup> Termed GolP-CHARMM,<sup>216</sup> the FF analogously features virtual sites and dynamic polarisation while additionally introducing explicit LJ terms to reproduce the energetics and structuring of water at gold surfaces (Figure 3.2), an important aspect for biological applications. In a further extension, the GolP-CHARMM FF was expanded to describe reconstructed Au(100)-*hex* surfaces, approximated as (1 × 5).<sup>343</sup> Although experimental evidence shows that both Au(111) and Au(100) are present in their reconstructed forms in biologically relevant conditions,<sup>375</sup> only Au(100)-*hex* shows significant morphological differences from its unreconstructed counterpart Au(100)(1 × 1). Through MD with GolP-CHARMM, the authors highlight that this surface reconstruction cannot be ignored as differences in water structuring at the native and reconstructed Au(100) interfaces leads to significant discrepancies in peptide binding affinities.<sup>240,343</sup>

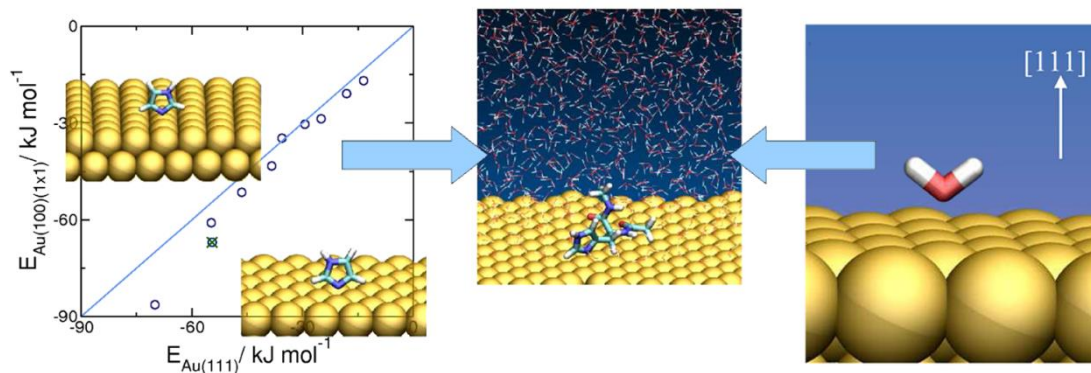


**Figure 3.2 | Preferred conformations of biomolecular species adsorbed to gold surfaces as obtained from calculations employing the GoIP-CHARMM FF.** The left panel shows a plot of the facet specific adsorption energies for different small molecules (insets show example of imidazole adsorption). The right panel depicts a single water molecule adsorbed to Au(111) which reproduces the general structuring obtained from DFT calculations. The central panel displays a capped histidine amino acid in a fully solvated system. Adapted with permission.<sup>216</sup> Copyright 2013, American Chemical Society.

### *Small Thiolated Gold Nanoclusters*

Unlike gold surfaces and faceted NPs, small thiol-protected AuNCs exhibit a very different atomic arrangement<sup>149</sup> from that of the well-recognised FCC lattice (see Figure 1.3). Instead, these small AuNCs (approx. < 3 nm) exhibit X-ray crystal structures that contain highly symmetric gold cores, surrounded by adatom “staples” (see models in Figures 2.2 and 2.3). Within this small size regime, capturing the quantum chemical nature (no longer bulk metal band structuring) and vastly different morphology of AuNCs, presents a significant FF design challenge for classical all-atom molecular simulation. The limited availability of experimental data and the newness of the chemical characterisation of AuNCs has hindered the development of AuNC FFs, which is reflected by the fact that only very few all-atom (staple motif containing) thiolate-AuNC FFs have appeared, namely for:  $\text{Au}_{25}(\text{SR})_{18}$ ,<sup>221,222,290,376,377</sup>  $\text{Au}_{38}(\text{SR})_{24}$ ,<sup>221,378</sup>  $\text{Au}_{144}(\text{SR})_{60}$ ,<sup>379,380</sup> and very recently  $\text{Au}_m(\text{SR})_n$ <sup>353,381</sup> Within these FFs, gold can be designated different atom types depending on the coordination to metallic and/or ligand atoms (i.e. Au–Au–Au, Au–Au–S or S–Au–S).<sup>221,222</sup> This allows for interaction parameters to be optimised for each gold type much like different atom types are treated in biological FFs. Similar to many atomistic surface FFs, gold atoms may be neutral<sup>376</sup> or have assigned charges,<sup>379</sup> and either be forced to occupy their equilibrium positions (restricting intra-gold interactions and removing the need for Au–Au parameters)<sup>376</sup> or allowed to evolve under a fully parameterised Au–Au FF.<sup>222</sup> While a primary parameterisation goal for these FFs is to maintain the internal AuNC morphology of an experimental crystal structure, this only applies to the Au and S atoms, and exploration of the ligand-conformational energy landscape is of prime importance.<sup>377</sup>

Recently, GolP-OPLS compatible parameters for  $[\text{Au}_{25}(\text{S}(\text{CH}_2)_2\text{Ph})_{18}]^-$  were developed to investigate how small hydrophobic AuNCs interact with proteins.<sup>222</sup> Bond parameters (and corresponding angles) for Au–Au, Au–S and S–C atom pairs were established based on extensive *ab initio* calculations and validated against the experimental  $[\text{Au}_{25}(\text{SR})_{18}]^-$  crystal structure. Charges for gold and organic atoms were also derived in addition to LJ parameters fitted to replicate the QM interaction of (an OPLS) methane molecule with the AuNC, but unlike its predecessor the FF does not contain dynamic polarisation.

### 3.3.4 Periodic Boundary Conditions

To overcome the computational prohibition associated with modelling very large (sometimes infinite) systems, approximations can be applied to the boundaries/borders of a simulation so that a much smaller subset of the original model can be used. Periodic boundary conditions minimise edge effects in a finite system while still allowing for molecules to interact with each other and solvent as if they were in a bulk fluid. Essentially atoms of a system are placed into a space-filling box (called a unit cell) that is replicated so that each atom is surrounded by translated copies (or images) of itself (Figure 3.3). In three dimensions this results in a unit cell having 26 nearest neighbouring image cells. During a simulation the number of particles in the unit cell remains constant since a particle leaving the central box is replaced by an image particle from an opposite side. Consequently, only the properties of the original simulation box need to be recorded and propagated.

### 3.3.5 Treatment of Non-Bonded Interactions

Non-bonded interactions are the most computationally intensive and expensive calculations in classical MM since the number of non-bonded pairs grows exponentially with system size. While reducing the cost of this task (as much as practical), some important concerns also get addressed. The first is that a particle must only interact with another particle/molecule once (i.e. not multiple times across periodic boundaries, and never with its own images), and the second is related to the accurate treatment of long-range electrostatics effects.

To deal with the former, it is necessary to apply the *minimum image convention* which ensures that only the nearest image of each particle is considered when calculating short-range non-bonded interactions. As shown in Equation 3.10, this is achieved by imposing a cut-off radius ( $R_c$ ) that truncates all non-bonded interactions that exceed a distance more than half the length of the shortest periodic box vector (**a**, **b** or **c**).

$$R_c < \frac{1}{2} \min(\|\mathbf{a}\|, \|\mathbf{b}\|, \|\mathbf{c}\|) \quad (3.10)$$

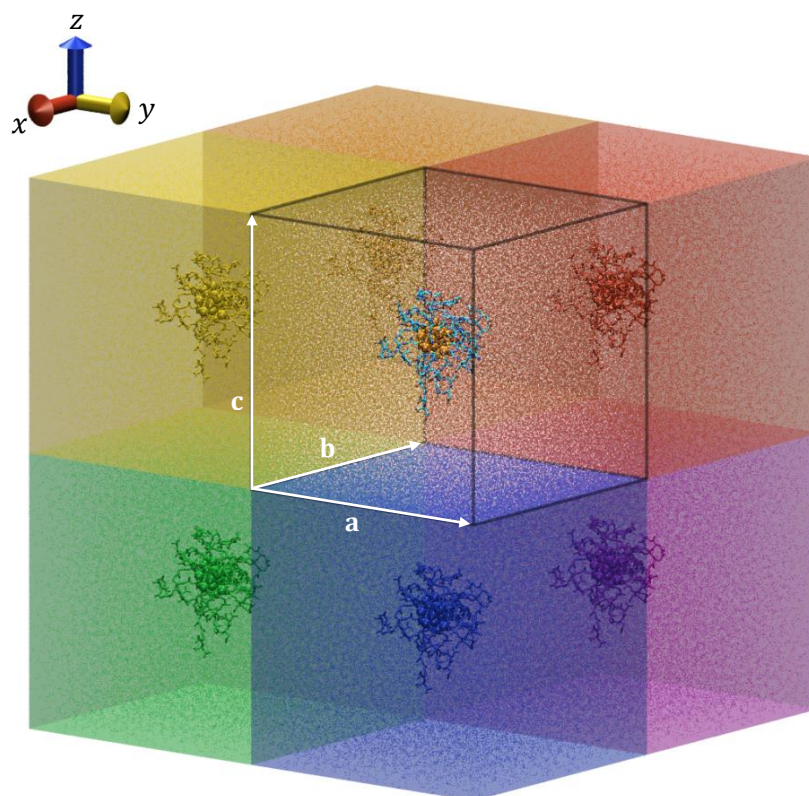


**Figure 3.3 | A three-dimensional visualisation of periodic boundary conditions.** The unit cell containing a fully solvated peptide-coated AuNC model is outlined in black, box vectors **a**, **b** and **c** are drawn in white, and 6 (out of a total 26) nearest neighbouring image cells are shown.

When investigating large solutes in explicit solvent (such as the functionalised-AuNC shown in Figure 3.3), to properly satisfy the *minimum image convention* the length of each box vector must be greater than the length of the solute in the direction of the vector *plus* the cut-off radius. This guarantees that no molecule will interact with both sides of a solute.

Cut-off treatments are generally quite adequate when describing vdW interactions since the LJ potential for a given pair of particles rapidly decays to a negligible value at relatively short distances ( $> 1.5$  nm). This, however, is not the case for the Coulomb potential that decays with the inverse of  $r_{ij}$  (see Equation 3.8) and cannot simply be truncated without loss of accuracy to the system's potential energy. Also, these long-range interactions need to extend into adjacent image cells and this poses the risk of self-interaction artefacts.

Some of these issues have been resolved with the Ewald summation method,<sup>382</sup> which removes the need to directly solve the Coulomb potential in Equation 3.8 (for  $N$  particles and their periodic images). Instead, each point charge is replaced by a smeared Gaussian to estimate the electrostatic potential *field*. Each charge interacts with the resulting field to yield the potential energy. As shown in Equation 3.11, this allows the total electrostatic

interaction energy ( $V^{es}$ ) to be broken up into: a short-range term ( $V_{sr}$ , for  $r_{ij} < R_c$ ); a long-range term ( $V_{lr}$ , for  $r_{ij} > R_c$ ); and a constant term ( $V_c$ ) to correct for self-interactions.

$$V^{es}(r_{ij}) = V_{sr}(r_{ij}) + V_{lr}(r_{ij}) - V_c \quad (3.11)$$

This representation of the electrostatic potential allows the slow converging sum in Equation 3.8 to effectively be replaced by two quickly-converging terms: one solved directly in real space ( $V_{sr}$ ), and one solved using Fourier Transforms in reciprocal space ( $V_{lr}$ ). To extend this technique to large systems where the Ewald method becomes computationally unaffordable, the smooth Particle Mesh Ewald (PME)<sup>383</sup> approach maps charges onto a three-dimensional grid then calculates  $V_{lr}$  in reciprocal space. This method gives the *exact* result for the electrostatic energy of a periodic system containing an infinitely replicated *neutral* box of charged particles (i.e. counter-ions need to be incorporated into the system to ensure overall charge neutrality). The PME method has been used throughout this thesis as it is a computationally efficient approach for the treatment of long-range electrostatics.<sup>384,385</sup>

### 3.3.6 Energy Minimisation

The potential energy of a molecular system is a rugged, complex and multi-dimensional landscape (Figure 3.4). The troughs (*local minima*) in the energy landscape are associated with metastable structures that molecules adopt, the ridges represent free energy barriers between these states, and the single deepest point is the *global minimum*. Knowledge of all stationary points on a potential energy surface gives a complete description of all free energies, structural conformations, and transitions for a given system. Unfortunately, it is near impossible to comprehensively sample the entirety of this configurational space, even for relatively small systems sizes, in a practical amount of time (Section 3.4.5 discusses approaches that improve our endeavour). However, there are methods to find the nearest *local minimum* and these are termed energy minimisation (EM) techniques.

Given an atomic configuration, EM changes the geometry of a system in a step-wise fashion until the inter-atomic forces on each atom are acceptably close to zero, and the net energy of the system reaches the nearest *local minimum* described by the potential energy function of a FF (Figure 3.4). At each EM step, an algorithm differentiates the potential energy function to produce an *energy gradient* with respect to atomic coordinates. The magnitude of this gradient is also the net force acting on the system (see Equation 3.13 in Section 3.4.1) and the sign of the gradient provides information about which direction on the potential energy landscape the nearest *local minimum* is. The *steepest descent* method, which is utilised in this thesis, iteratively takes steps in the direction of the negative gradient until the local energy minimum is achieved (as specified by an energy convergence criterion).



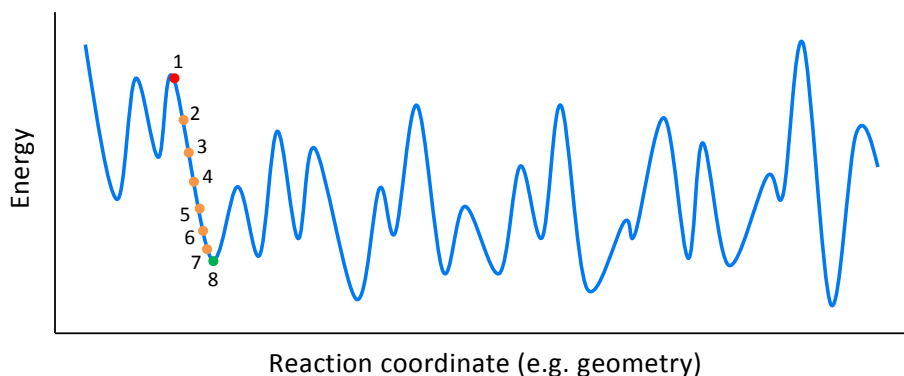


**Figure 3.4 | Graphical representation of a complex one-dimensional potential energy function and an energy minimisation process.** Starting from an initial atomic structure (point 1), most energy minimisation methods determine the energy and slope of the potential energy function then use numerical methods to adjust the atomic coordinates to reduce the potential energy. This process is then repeated iteratively (points 2–7) until the nearest *local minimum* structure (point 8) is obtained.

The process of EM removes a system’s kinetic energy, reduces the forces on all particles, and eliminates steric clashes between atoms. This is especially important when manually building a molecular model, a procedure which is often done without the help of *a priori* knowledge of a molecules’ three-dimensional structure. For these reasons, EM is often a required step in preparing a system for MD since it ensures the initial configuration is not too far from an energetic equilibrium. If a configuration is very far from equilibrium, performing MD on that configuration will result in very large atomic forces and energy differences that may cause the simulation to fail.

### 3.4 Classical Molecular Dynamics

Molecular dynamics is a numerical approach to study the structural time-evolution of a many-particle system. First applied to physical systems in the late 50s and early 60s,<sup>386-388</sup> MD is now a widely used method to investigate nanoscale phenomena. Unlike EM where the goal is to minimise the potential energy, MD samples many regions across the potential energy surface to generate a Boltzmann weighted ensemble of thermodynamic equilibrium structures. Analysis of the molecular trajectories produced from MD provides valuable and insightful structural, dynamic, and thermodynamic information (see Chapter 2).

#### 3.4.1 Equations of Motion

Classical MD is based on solving the differential form of Newton’s equations of motion for a system of  $N$  interacting particles:

$$\mathbf{F}_i = m_i \mathbf{a}_i = m_i \frac{d^2 \mathbf{r}_i}{dt^2}, \quad i = 1 \dots N \quad (3.12)$$

Equation 3.12, Newton's second law, states that the force ( $\mathbf{F}_i$ ) acting on any atom ( $i$ ) in a system is the product of its mass ( $m_i$ ) and acceleration ( $\mathbf{a}_i$ ), which can be expressed as the second order differential of atomic position ( $\mathbf{r}_i$ ) with respect to time ( $t$ ). If the force acting on a particle is conservative, i.e. a function of position only, then it can be derived from the system's potential energy function ( $V$ ), which itself is defined by the FF (see Equation 3.8):

$$\mathbf{F}_i = -\frac{dV}{d\mathbf{r}_i} \quad (3.13)$$

By combining Equations 3.12 and 3.13, the derivative of the potential energy is related to changes in position as a function of time. Because the motion of atoms is coupled to all other atomic motions, the potential energy is a complicated function of  $3N$  atomic coordinates and there is no analytical solution to the equations of motion. Instead numerical methods (MD integrators) such as the Verlet,<sup>389</sup> leap-frog,<sup>390</sup> Beeman's<sup>391</sup> and velocity Verlet<sup>392</sup> algorithms are used. By using a finite time-step ( $\delta t$ ), changes to the force on a particle due to its own motion can be neglected and therefore atomic positions ( $\mathbf{r}$ ), velocities ( $\mathbf{v}$ ), and accelerations ( $\mathbf{a}$ ) can be approximated by Taylor series expansions:

$$\mathbf{r}(t + \delta t) = \mathbf{r}(t) + \delta t\mathbf{v}(t) + \frac{1}{2}\delta t^2\mathbf{a}(t) + \frac{1}{6}\delta t^3\mathbf{b}(t) \dots \quad (3.14)$$

$$\mathbf{v}(t + \delta t) = \mathbf{v}(t) + \delta t\mathbf{a}(t) + \frac{1}{2}\delta t^2\mathbf{b}(t) \dots \quad (3.15)$$

$$\mathbf{a}(t + \delta t) = \mathbf{a}(t) + \delta t\mathbf{b}(t) \dots \quad (3.16)$$

where  $\mathbf{b}(t)$  is the time derivative of acceleration.

The Verlet integrator,<sup>389</sup> as shown in Equation 3.17, uses current atomic coordinates and accelerations,  $\mathbf{r}(t)$  and  $\mathbf{a}(t)$  respectively, as well as previous atomic coordinates,  $\mathbf{r}(t - \delta t)$ , to determine new positions at the next time-step,  $\mathbf{r}(t + \delta t)$ .

$$\mathbf{r}(t + \delta t) = 2\mathbf{r}(t) - \mathbf{r}(t - \delta t) + \mathbf{a}(t)\delta t^2 \quad (3.17)$$

While this method is straightforward, there are caveats in Equation 3.17: (1) the term  $(t)t^2$  takes on very small values compared to the other two terms and this may result in numerical problems; (2) velocities are inaccurate since they do not explicitly feature in the algorithm and must be estimated after positions have been calculated for the next time-step:

$$\mathbf{v}(t) = \frac{\mathbf{r}(t + \delta t) - \mathbf{r}(t - \delta t)}{2\delta t} \quad (3.18)$$

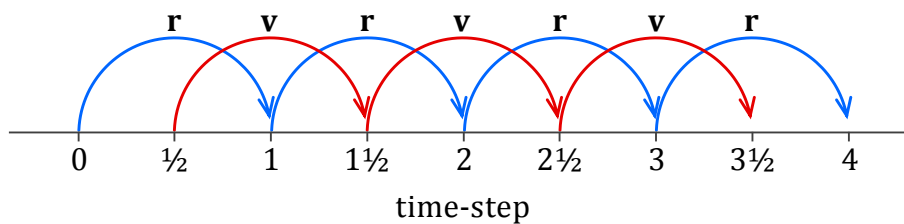


**Figure 3.5 | Visual representation of the leap-frog algorithm.** The velocities ( $\mathbf{v}$ ) and positions ( $\mathbf{r}$ ) are calculated half time-steps apart so that the two quantities appear to *leap-frog* over each other.

An alternative to this is the leap-frog algorithm<sup>390</sup> (employed in this thesis) which calculates/uses velocities at half time-step intervals,  $\mathbf{v}(t \pm \frac{1}{2}\delta t)$ , to determine positions at full time-steps,  $\mathbf{r}(t + \delta t)$ . This is done using the following two relations:

$$\mathbf{v}(t + \frac{1}{2}\delta t) = \mathbf{v}(t - \frac{1}{2}\delta t) + \mathbf{a}(t)\delta t \quad (3.19)$$

$$\mathbf{r}(t + \delta t) = \mathbf{r}(t) + \mathbf{v}(t - \frac{1}{2}\delta t)\delta t \quad (3.20)$$

The algorithm's name is reflective of the fact that velocities and positions *leap* over each other like *frogs* leaping over one another (see Figure 3.5). Velocities in this method are explicitly calculated, albeit not at the same time as the positions, yet this integrator is fast and accurate for most MD applications.

The classical equations of motion used in MD are deterministic, i.e. once initial coordinates and velocities (often randomly assigned) are known, a time-dependent trajectory that describes positions, velocities and accelerations at a later time can be calculated. In practice, Equations 3.14–3.20 are also modified for temperature and pressure coupling (Section 3.4.3), and extended to include the conservation of constraints (Section 3.4.4).

### 3.4.2 Thermodynamic Ensembles

MD can be performed using various different thermodynamic ensembles including: microcanonical ( $NVE$ ), canonical ( $NVT$ ) and isothermal–isobaric ( $NPT$ ), depending on the requirements of the user. Each of these ensembles are in statistical equilibrium with respect to a set of macroscopic variables, denoted above by the three symbols in parentheses, namely: total number of particles ( $N$ ), total energy ( $E$ ), volume ( $V$ ), pressure ( $P$ ), and temperature ( $T$ ). While these quantities can fluctuate and influence the nature of a system's *microstates* (i.e. the system's configuration at a particular time-step), the average of these properties over a series (or *ensemble*) of Boltzmann distributed microstates remains constant. In other words, taking the  $NVT$  ensemble as an example, the number of particles, volume, and temperature are observable parameters of the system that are in statistical equilibrium and therefore remain fixed over the ensemble of the system's microstates.

It is often desirable to perform simulations in a thermally controlled setting with either constant volume (*NVT*) or constant pressure (*NPT*). The former is useful when simulating systems that require a fixed unit cell size, for instance an infinite surface that extends across periodic boundaries (see Chapter 4), while the latter is advantageous when directly comparing with experimental measurements that are regularly carried out in isothermal–isobaric environments (see Chapters 5 and 6).

### 3.4.3 Temperature and Pressure Coupling

To maintain temperature in a MD simulation, systems can be coupled to an external bath with the use of thermostat algorithms. To apply temperature coupling to a molecular system, two of the most widely used thermostats are the *weak-coupling* Berendsen<sup>393</sup> and *extended-ensemble* Nosé–Hoover<sup>394,395</sup> schemes (although there are others<sup>396,397</sup> available).

The Berendsen thermostat<sup>393</sup> utilises first-order kinetics to weakly couple a system to an external heat bath with a given temperature  $T_0$ . Using Equation 3.21, the Berendsen algorithm slowly modulates temperature deviations, via a time constant  $\tau$ , to exponentially decay the system temperature back to  $T_0$ .

$$\frac{dT}{dt} = \frac{T_0 - T}{\tau} \quad (3.21)$$

While coupling strength is easy to adjust (by changing  $\tau$ ) and the scheme is very efficient at relaxing a system to a target temperature, the Berendsen thermostat suppresses kinetic energy fluctuations leading to an improper Boltzmann distribution of states.<sup>398</sup>

An approach which remedies this to give a correct thermodynamic ensemble is the Nosé–Hoover temperature coupling algorithm.<sup>394,395</sup> In this method two additional degrees of freedom are added to a system’s Hamiltonian: a thermal reservoir and frictional term. The friction term takes the form of an additional force in Newton’s equations of motion that is proportional to the product of each particle’s velocity and a *friction coefficient* ( $\xi$ , sometimes also called a heat bath variable), effectively replacing Equation 3.12 by:

$$\frac{\mathbf{F}_i}{m_i} = \frac{d^2\mathbf{r}_i}{dt^2} + \xi \frac{d\mathbf{r}_i}{dt}, \quad i = 1 \dots N \quad (3.22)$$

This *friction coefficient* is an independent dynamic quantity that depends on the *position* of the imaginary heat reservoir to which the system is coupled ( $s$ , Equation 3.23) and comes with its own equation of motion (Equation 3.24).

$$\xi = \frac{d \ln(s)}{dt} \quad (3.23)$$

$$\frac{d\xi}{dt} = \frac{1}{Q}(T - T_0) \quad (3.24)$$

where  $T$  and  $T_0$  are the current instantaneous temperature and the desired reference temperature, respectively. The parameter  $Q$  has dimensions of energy  $\times$  (time)<sup>2</sup>, and can be considered as an “effective mass” associated with  $s$  that determines the strength of the coupling between the reservoir and the real system, therefore it influences the temperature fluctuations. The Nosé–Hoover thermostat is strongly coupled to the system and modulates temperature using oscillatory relaxations, which can make it slow to converge to  $T_0$ .

Analogous to the above *thermostats*, the Berendsen<sup>393</sup> and Parrinello–Rahman<sup>399,400</sup> *barostats* couple a system to a “pressure bath”. In these approaches, the external bath incrementally scales unit cell dimensions to regulate pressure to a given reference value.

For the Berendsen barostat,<sup>393</sup> the scaling of the system pressure ( $\mathbf{P}$ ) towards a reference pressure ( $\mathbf{P}_0$ ) is performed via first-order kinetics, with coupling constant  $\tau_p$ :

$$\frac{d\mathbf{P}}{dt} = \frac{\mathbf{P}_0 - \mathbf{P}}{\tau_p} \quad (3.25)$$

Again, while this *weak-coupling* scheme quickly converges, it fails to adequately sample fluctuations in pressure and volume needed to accurately generate a true thermodynamic ensemble, especially for small systems.<sup>398</sup>

Alternatively, the *extended-ensemble* Parrinello–Rahman<sup>399,400</sup> barostat can be combined with the Nosé–Hoover thermostat,<sup>394,395</sup> to (in principle) obtain a true *NPT* ensemble. In the Parrinello–Rahman method, the systems equations of motion include a matrix box vector term ( $\mathbf{M}$ , similar to the frictional term in Equation 3.22):

$$\frac{\mathbf{F}_i}{m_i} = \frac{d^2 \mathbf{r}_i}{dt^2} + \mathbf{M} \frac{d\mathbf{r}_i}{dt}, \quad i = 1 \dots N \quad (3.26)$$

A common approach used to equilibrate a MD simulation is to first use a *weak-coupling* scheme to quickly converge the temperature/pressure then switch to an *extended-ensemble* schemes to probe the correct thermodynamic ensemble (see Chapters 5 and 6).

#### 3.4.4 Bond Constraints

While a complete FF (see Equation 3.8), together with a topology, provides terms that satisfy bond lengths, bond and torsional angles, there are often times where it is desirable to

neglect motions along one (or multiple) degrees of freedom to increase computational efficiency. This is only beneficial if the neglected degrees of freedom do not influence the phenomena being studied, e.g. the vibration of atomic bonds when investigating large conformational changes of a biomolecule. *Bond constraint* algorithms such as SHAKE<sup>401</sup> or LINCS<sup>402</sup> can be incorporated into a simulation to remove bond vibrations, which can occur on time scales as short as 1 fs for hydrogen bonds. Constraints allow for integration time-steps (Section 3.4.1) to be increased, often from 1 fs to 2 fs, significantly reducing the computational demand needed to run a simulation.

In the SHAKE algorithm,<sup>401</sup> at each time-step bonds (and/or angles) are reset to their equilibrium/prescribed values by applying a constraint force to preserve the desired atom separations at the new positions (after an unconstrained update). Because the coordinates of the particles are not independent, and the equations of motion in each coordinate direction are connected, the SHAKE method considers and solves each constraint iteratively until all constraints are satisfied to within a user specified tolerance – usually within a few iterations. While this approach is simple and numerically stable, if displacements are large no solutions may be found due to the iterative nature of the algorithm, i.e. satisfying one constraint may cause another constraint to be violated.

The Linear Constraint Solver (LINCS) method<sup>402</sup> is a non-iterative process that always uses two steps, after an unconstrained update (Figure 3.6). In the first step the new bonds are projected onto the old directions of the bonds. Following this, the lengthening due to rotation is corrected, which results in bonds at time  $t$  having the same length ( $d$ ) as the bonds at time  $(t - \delta t)$ . Although the algorithm is based on matrices, no matrix multiplications are needed, making the method applicable to very large molecules. The LINCS algorithm is comparable in accuracy and more stable than the SHAKE approach, while being three to four times faster.<sup>402</sup>

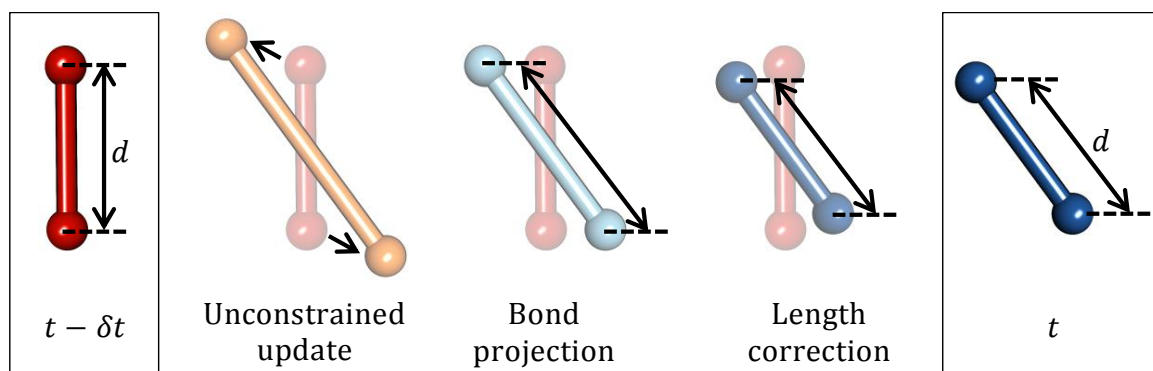


**Figure 3.6 | Visual representation of the LINCS algorithm.** The three position updates of a bond that the algorithm goes through are shown for a single time-step, from  $(t - \delta t)$  to  $t$ .

### 3.4.5 Enhanced Sampling Techniques

Extraction of realistic kinetic and thermodynamic quantities from gold–bio interface simulations requires a thorough and comprehensive sampling of the potential energy landscape. For complex systems this free-energy profile is characterised by multiple low energy metastable states separated by high energy barriers (Figure 3.4). Classical (brute-force) MD simulations can often fail to cross high energy barriers and sample rare events due to the inherent femtosecond integration time steps and limited simulation times. Therefore, as with other systems incorporating highly flexible molecules, it is necessary to employ techniques capable of robust sampling of the conformational space to obtain a statistically representative depiction of the system's behaviour. Some of these techniques include umbrella sampling,<sup>403</sup> metadynamics,<sup>404,405</sup> replica-exchange based techniques,<sup>406-411</sup> and approaches based on performing exhaustive multiple independent MD simulations starting from different initial orientations, structures and/or velocities (as has been done in this thesis). Several comprehensive reviews on the advancement and need of enhanced sampling techniques have recently appeared<sup>336,412-414</sup> (see especially Pietrucci *et al.*<sup>415</sup>). Through the development of advanced sampling simulations techniques, along with the increase in computational power, rigorous conformational sampling and more accurate determination of both the enthalpic and entropic contributions to the behaviour of biomolecules at the Au interface in solution can be achieved.

## 3.5 Simulation Procedure Employed in the Thesis

While specific details such as: particular FF and parameters, cut-offs, box dimensions, simulation times, etc. are described in the *Computational Details* of each results chapter (see Sections 4.2, 5.2, and 6.2), here the general approach used in this thesis to construct molecular models and run MD simulations is described below.

1. *Identify the problem/phenomena of interest to be studied.*

This is presented upfront in Sections 4.1.1, 5.1.1, and 6.1.1 after a succinct introduction and literature review relevant to the problem of interest.

2. *Select suitable tools to perform the simulations, i.e. software and FF.*
3. *Generate/obtain the initial coordinates for each molecular component of the system.*
4. *Generate a topology file for the system which contains all appropriate FF parameters.*
5. *Define the simulation box and solvate the system.*
6. *Energy minimise the system.*
7. *(Optional) Perform short restrained MD to equilibrate the solvent.*
8. *Run unrestrained MD to equilibrate the entire system and produce data for analysis.*
9. *Analyse and visualise the resulting trajectories and data files.*

## Chapter 4:

# Peptide-Coated Plasmonic Gold Nanoparticles

In this chapter, different monolayers of anti-viral peptides on Au(111) surfaces are investigated using molecular dynamics simulations. The relationship between the complex peptide-topographies displayed on gold surfaces and the experimental performance of recently synthesised plasmonic AuNP biosensors is explored. This work has been performed in collaboration with the biomaterials engineering team of Prof. Molly M. Stevens at Imperial College London to whom due acknowledgment is given, especially Dr Heiko Andresen, for all empirical results (Section 4.1.1) presented. Research from this chapter is published in the journal *Chemistry of Materials* where my contributions are recognised as first and primary computational author. Content has been adapted/reprinted in part with permission.<sup>3</sup> Copyright 2014, American Chemical Society.

---

## 4.1 Introduction

The identification and quantification of antibodies circulating in blood and other bodily fluids is a major discipline of clinical chemistry that has been particularly important for the medical diagnosis of infections, immune deficiencies, allergies, and autoimmune disorders for many decades.<sup>416-418</sup> Moreover, antibody detection forms the basis of many laboratory routines and immunoassays that competitively measure drug and small molecule content in biological samples.<sup>419</sup> Therefore it is highly desirable to develop antibody biosensors with improved sensitivity, cost efficiency, and simplicity compared to conventional methods. For *in vitro* diagnostic purposes, there is also a need for rapid and robust signal transduction upon antibody-analyte binding, which preferably occurs through a single-step electrical or optical readout mechanism. One way to realise this goal is to use the aggregation of gold nanoparticles (AuNPs) to generate an optical signal in response to chemical binding.<sup>12</sup>

Antibodies, otherwise known as immunoglobulin molecules, are large Y-shaped proteins that are produced *in vivo* when cells of the immune system encounter toxins or other foreign substances (e.g. pathogens). The role of antibodies in the body is to selectively recognise and bind to antigens (molecular tags) present on the surface of unwanted entities, then to trigger complex biochemical pathways intended to neutralise or destroy the invader (Figure 4.1). Each antibody has two identical sequences of amino acids located at the tips of its two “arms” that form the molecule’s antigen-binding sites (paratopes), which are very specific to



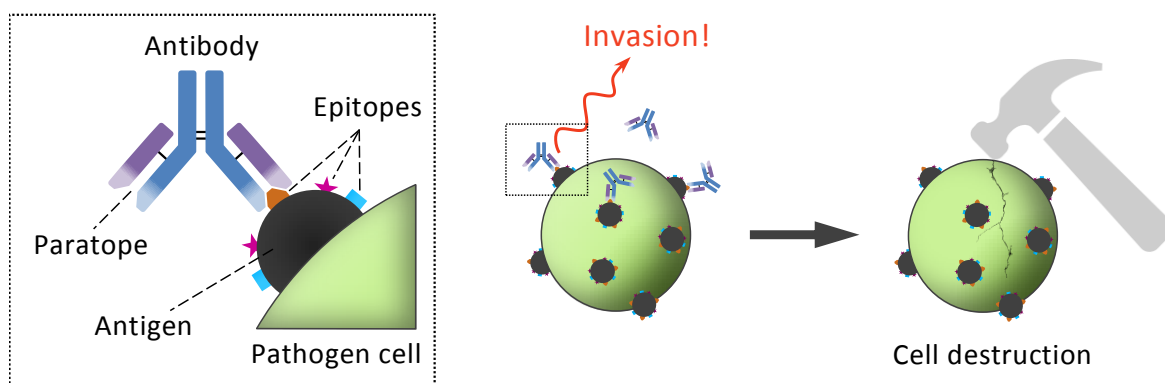


**Figure 4.1 | Cartoon illustration showing the *in vivo* role of antibodies in cell destruction, and the main features involved in antibody–antigen binding.** Upon binding to an antigen, antibodies generate a signal that initiates an immune response to destroy the foreign cell.

a particular epitope (antigenic determinant) present on an antigen. The binding between paratope and epitope is therefore analogous to a lock-and-key and since each antibody is bivalent, the cross-linking of antigens results in very stable antibody–antigen binding.

In principle, the bivalent and specific nature of immunoglobulin targets could be exploited to cross-link antigen-coated AuNPs and create single-step homogenous immunoassays. However, aggregated NPs generally require an interparticle spacing that is smaller than the constituent NPs' diameters to induce a distinct shift in surface plasmon resonance adsorption (Section 1.3.2); a prerequisite that is compromised when antibodies or full-length protein-antigens functionalise AuNPs due to the sheer size of these molecules.<sup>99</sup> Instead, short immuno-dominant peptide-epitope ligands minimise the interparticle spacing of NP aggregates to offer more conducive optical shifts, while still retaining capacity for lock-and-key specificity via antibody–antigen interactions.<sup>420</sup>

To successfully design biosensors that take advantage of this approach, the cross-linking mechanisms between coated AuNPs and antibodies needs to be optimised in order to direct NP aggregation in the desired setting. This typically requires precise *a priori* paratope–epitope binding information and although experimental characterisation of therapeutic immunoglobulins is improving,<sup>421</sup> many antibodies and their complexations with antigens are not yet crystallised. To exacerbate matters, even if information exists for *similar* antibody fragments that are known to specifically bind to an epitope, the primary sequence of these *similar* antibodies, as well as the shape of the immune complexes formed, might be completely different to the antibodies of interest. Alternatively, the characterisation of epitope–AuNP surfaces *prior to antibody exposure* (as is the focus of this present work) allows for structure–property relationships to infer favourable conditions that may encourage (or discourage) antibody cross-linking, without any explicit antibody structures.

Classical molecular modelling has proven to be an invaluable tool to provide atomistic detail into the nano-bio interface of bioactive AuNPs,<sup>2</sup> as summarised in Section 2.3.1. Although molecular dynamics (MD) investigations into peptide-gold adsorption are starting to gain traction,<sup>89,123,238,240,243,247,248,358,422-424</sup> only very few studies simulate experimentally dense peptide-monolayers on gold substrates.<sup>268,425-429</sup> In the separate works of Duchesne *et al.*<sup>425</sup> and Todorova *et al.*,<sup>268</sup> CALNN-coated AuNPs that feature additional functional peptide heterogeneities incorporated into their monolayer matrices are simulated using MD with approximate models. For the former study, the conformational space and volume explored by the functional peptides (CALNNGK GALVPRGSGKbiotinTAK) was assessed with CALNN-AuNPs being represented as only the monolayer's solvent exposed residues (i.e. asparagine) arranged to reproduce the curvature of a CALNN layer on a 10 nm AuNP.<sup>425</sup> On the other hand, Todorova *et al.* analysed how the monolayer concentration and distribution of HIV-1 TAT (GRKKRRQRRPPQ) on CALNN-AuNPs correlates with experimental membrane permeation efficacy by modelling peptides on NPs that are approximated as neutral 3 nm spheres.<sup>268</sup> Colangelo *et al.* recently used MD simulations of CALNN (and CFGAILSS) peptide-monolayers on fully atomistic spherical (5, 10 and 25 nm) AuNPs to show how peptide secondary structure depends on: AuNP size, peptide density, Au-S bond lateral freedom, and gold surface hydration.<sup>426</sup> The approaches used in these studies are convenient for modelling relatively small AuNPs (< 20–30 nm) however they become expensive and unsuitable for much bigger gold constructs.

When large AuNPs are the substrate of interest, local NP curvature becomes negligible in reference to the simulation cell dimensions and this allows for a planar description of gold. For example, White *et al.* used MD to investigate the spatial organisation of a homogeneous peptide-monolayer made up of inherently  $\alpha$ -helical synthetic peptides (each 30 residues long) on a planar gold surface and found that the monolayer displayed a repeating pattern of well-defined hydrophobic and hydrophilic regions.<sup>427</sup> Helical peptides also featured in the work of Nowinski *et al.*, where replica exchange MD simulations were used to investigate the secondary structure of 4 peptide-monolayers on a gold surface.<sup>429</sup> Bergamini *et al.* employed the polarisable GoIP FF<sup>215</sup> with a harmonic potential emulating strong Au-S bonding to evaluate the thickness of a hexapeptide (CLPFFA) monolayer on a Au(111) surface.<sup>428</sup> While studies such as these emphasise how peptide-gold MD simulations provide detailed physicochemical information that is inaccessible to experiments, much more nano-bio interfacial research is still needed to build a generic comprehensive knowledge into these systems to aid the design of novel nano-biotechnologies.

### 4.1.1 Experimental Project Design and Computational Aims

An *in vitro* diagnostic approach to identify and quantify the presence of disease marking anti-viral antibody molecules was recently developed using epitope-tagged AuNP biosensors that generate a colourimetric response upon antibody binding.<sup>3</sup> Explicitly, 60 nm AuNPs were synthesised and functionalised with short peptides decorating their surface, which correspond to linear viral epitopes such as those exhibited on pathogenic cells (Figure 4.1). These peptides are the *Haemophilus influenzae* hemeagglutinin epitope YPYDVPDYA (HA), herpes simplex virus glycoprotein D epitope TQPELAPEDPED (HSV), and the c-Myc protein epitope EEQKLISEEDLL (Myc), which each exclusively interact with the anti-viral antibodies for: human influenza virus, herpes simplex virus, and the Myc regulatory gene whose overexpression is associated with cancer, respectively. In addition, a cysteine residue and a glycine spacer, as well as Glu–Asp–Glu in the case of the HA-epitope, were flanked on either the C-terminus (CT) or the N-terminus (NT) of the peptides (Figure 4.2) to direct their anchoring to, and increase the colloidal stability of, the AuNPs.<sup>3</sup>

The generic concept of the immunoassays, as shown in Figure 4.3, is that initially the AuNP suspensions appear *red* in colour before being exposed to a solution (e.g. patient serum/blood) possibly containing the analogous anti-viral antibodies for the gold-passivating epitopes. If the antibodies are indeed present in the serum, their bivalent/multivalent nature is expected to cause cross-linking of the peptide-coated AuNPs, via antigen-specific interactions, resulting in an overall solution colour change to *blue*.

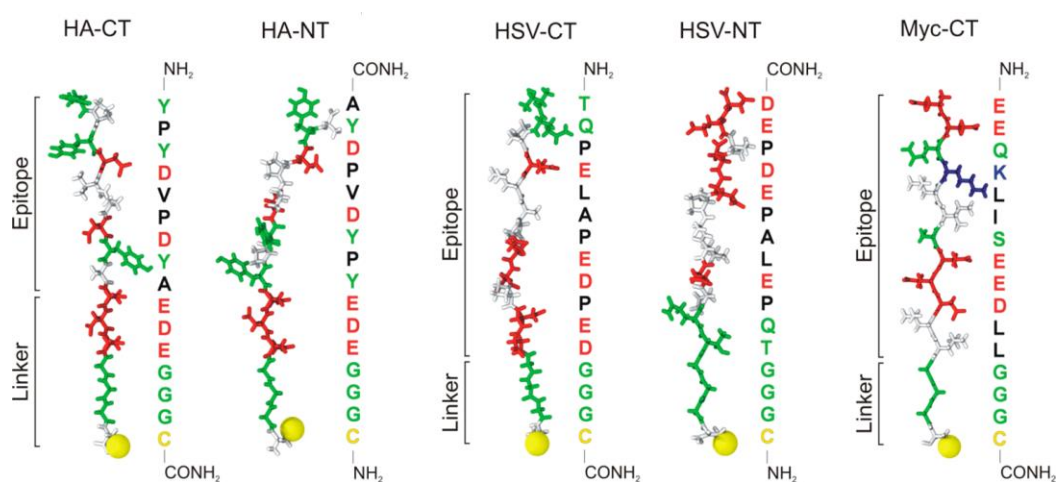


**Figure 4.2 | Linear representation of the engineered peptides used in this work.** HA, *Haemophilus influenzae* hemeagglutinin epitope; HSV, herpes simplex virus glycoprotein D epitope; Myc, c-Myc protein epitope. Each peptide is 16 amino acids in length and labelled to show the epitope fragment that is immuno-dominant, and the linker region used to direct binding to the AuNPs either via the C-terminus (CT) or the N-terminus (NT). Colouring is as follows: red, negatively charged residues; blue, positively charged residues; green, polar residues; white/black, nonpolar residues; yellow, terminal sulphur. Adapted with permission.<sup>3</sup> Copyright 2014, American Chemical Society.

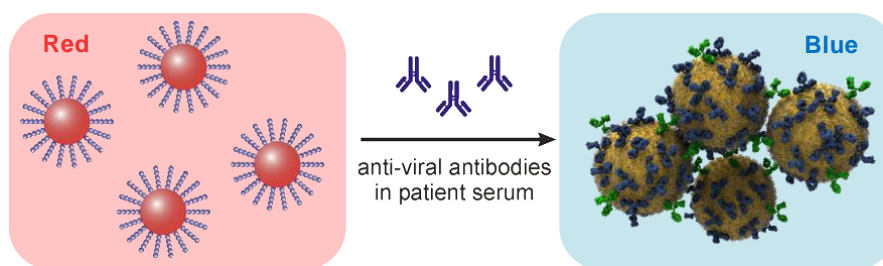


**Figure 4.3 | Schematic depiction of an epitope-tagged AuNP solution undergoing a colourimetric response after antibody-induced AuNP aggregation.** The focus of this chapter is to better understand, and improve, this scheme through characterising the epitope–AuNP surface (scenario on the left) using molecular dynamics simulations. The green immunoglobulin molecules shown in the right image are representative of antibodies that are tethered between two AuNPs. The image on the right is adapted with permission.<sup>3</sup> Copyright 2014, American Chemical Society.

However, in the absence of the specific anti-viral antibodies, no aggregation is anticipated and therefore the solution colour should remain unchanged. It is this distinct colourimetric response that presents a simple yet effective technique to quickly, cheaply and efficiently detect circulating antibodies *in vitro*.

In practice, each system's capacity to form cross-linked AuNP aggregates depends on a range of factors including, antibody concentration, individual epitope–antibody pairs, and the immobilisation direction of the peptides on the gold.<sup>3</sup> For example, after the epitope-tagged AuNPs were mixed with solutions containing their cognate antibodies (at a range of concentrations), a spectroscopic aggregated-versus-dispersed ratio (A/D) was measured to quantify the amount of AuNPs involved in cross-linking for each sample (Figure 4.4). The results revealed that even though the HA-CT and HSV-CT epitope systems exhibited very similar assay responses, their N-terminal counterparts lead to an enhancement (HSV-NT) or strong reduction (HA-NT) of the assay sensitivity. Moreover, neither the Myc-CT epitope nor the Myc-NT epitope led to detectable aggregation of AuNPs after the addition of anti-Myc antibody (data not shown). Therefore according their experimental A/D ratios, the peptide-AuNPs' likelihood to yield a positive assay response can be ranked as follows: HSV-NT (best-performer) > (HA-CT = HSV-CT) > HA-NT > (Myc-CT = Myc-NT) (non-performers).

These experimental findings immediately bring about two questions: (1) why do some antibody–epitope–gold assemblies have a higher propensity for selective aggregation compared to others? and (2) how does epitope–gold orientation, i.e. C-terminal or N-terminal immobilisation affect the cross-linking reaction? Since we know the atomic composition of the epitopes (Figure 4.3), interrogating the antibody structures would normally be the first approach when seeking answers to these questions. This requires knowledge of (at least) the primary sequence of the antibodies in question, knowledge that

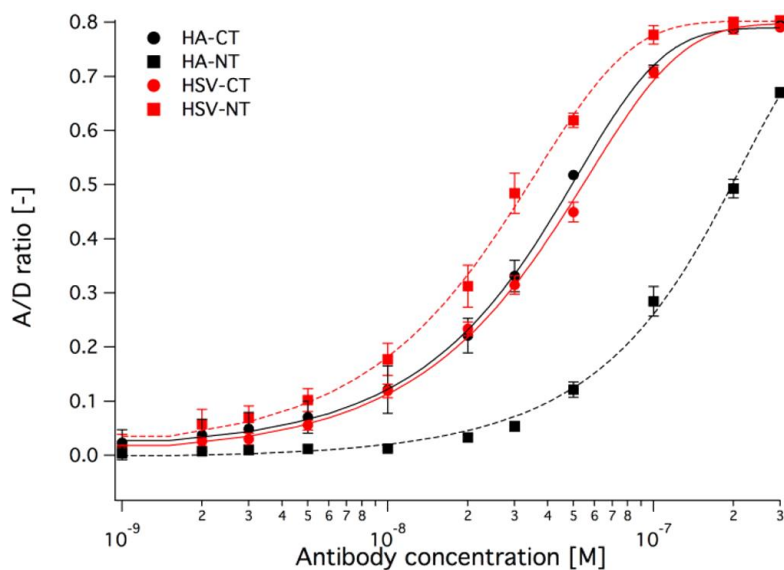


**Figure 4.4 | Empirically measured immunoassay response curves for the HA and HSV epitope-coated AuNPs.** N-terminal immobilisation of the HA epitope results in significant cross-linking impairment while for the HSV epitope, N-terminal anchoring to gold increased assay sensitivity. Note: A large A/D ratio indicates AuNP aggregation (stimulated by antibody-gold cross-linking). Adapted with permission.<sup>3</sup> Copyright 2014, American Chemical Society.

is currently unavailable due to challenges in experimental characterisation.<sup>421</sup> Arguably, the second best approach is to pursue a better understanding of the peptide-monolayer landscape presented on the surface of the AuNPs. This will provide topographic-type information that can be used to gauge what an antibody will “see”, and hence interact with, as it approaches a functionalised AuNP in solution. This also reduces the complexity of the antibody-epitope-gold system to one that only involves the AuNP and epitope-monolayer. While current experimental characterisation techniques are limited in their ability to probe this landscape, computational methodologies are not (see Section 4.1).

In this chapter, MD simulations are used to investigate peptide-monolayers formed on planar Au(111) surfaces in order to resolve the abovementioned questions. Following an outline of the computational details employed (Section 4.2), properties of the peptide-monolayers such as their overall thickness and average atomic mobility are presented (Section 4.3.1). Next, Section 4.3.2 focuses on exploring the solvent accessibility and geometric distribution of specific amino acid regions of the epitope-monolayers that are expected to be essential for paratope binding, and therefore antibody crosslinking. Finally, Section 4.3.3 determines the role solvent has in stabilising the various peptide-monolayer assemblies on gold. In the subsequent Section 4.4, these results are summarised and discussed in the context of the empirical findings, then concluding remarks are given.

## 4.2 Computational Details

Classical MD simulations were performed using the GROMACS (version 4.5.5) software package<sup>430</sup> in conjunction with the GolP FF,<sup>215</sup> which is parameterised for interactions between amino acids and gold (111) surfaces and includes dynamic polarisation for gold atoms. The approximation that 60 nm AuNPs are planar on a submicrometer resolution is supported by experimental and computational evidence that large AuNPs are truncated octahedral in morphology predominantly composed of Au(111) facets.<sup>61</sup> Switch cut-offs were employed to truncate the calculation of atom–atom Coulomb and van der Waals interactions at 1.0 nm, with long-range electrostatics treated using the particle mesh Ewald method<sup>383</sup> (grid spacing of 0.1 nm). MD was performed in the canonical *NVT* ensemble with the Nosé–Hoover thermostat<sup>394,395</sup> regulating temperature to 300 K. An integration time step of 2 fs was applied with all bond lengths constrained using the LINCS algorithm.<sup>402</sup>

Peptide-monolayer–gold systems for each of the HA-CT, HA-NT, HSV-CT, HSV-NT and Myc-CT epitope-peptides (shown in Figure 4.2) were constructed by placing 16 identical peptides, in extended initial conformations, equidistant apart and in close proximity above a five-layer Au(111) slab (Figure 4.5) using the PACKMOL<sup>431</sup> program. This peptide density was established via MD simulations progressively loading the gold surface from low density up to the steric limit (see Appendix Section C.1) and corresponds to approximately one peptide per 2.23 nm<sup>2</sup> gold surface area, which is ~1.5-fold lower than the experimentally measured 1.4 nm<sup>2</sup> per peptide.<sup>3</sup> Peptide–gold models were placed in a periodic simulation box of dimensions 6.09 × 5.86 × 8.50 nm<sup>3</sup>, and solvated with ~7,000 H<sub>2</sub>O molecules (water density of ~1 g cm<sup>-3</sup>) utilising the SPC water model.<sup>432</sup> To emulate an experimental NaCl salt concentration of 150 mM and to conserve overall charge neutrality, 107 Na<sup>+</sup> (or 91 Na<sup>+</sup> for Myc-CT) and 27 Cl<sup>-</sup> were also added. The *x*–*y* box dimensions of the unit cell were chosen to produce a perfectly periodic Au(111) surface, and the *z*-dimension was made sufficiently large to ensure the +*z* periodic image did not influence the peptide–water interface. Throughout MD, gold atoms were held frozen in their ideal bulk lattice positions and Au–S bonds were unrestrained, both conditions that are consistent with the parameterisation of the GolP FF.<sup>215</sup> The steepest decent algorithm was employed to energy minimise each system within a convergence criterion of 20 kJ mol<sup>-1</sup> nm<sup>-1</sup>, following which the systems were equilibrated over 200 ns of MD (Figure 4.5). Production data for statistical analysis was collected every 5 ps over the final 5 ns of the trajectories, which is determined to be the equilibrium simulation stage as verified by monitoring energy drifts and root-mean-square deviations of atomic positions (Appendix Section C.2).

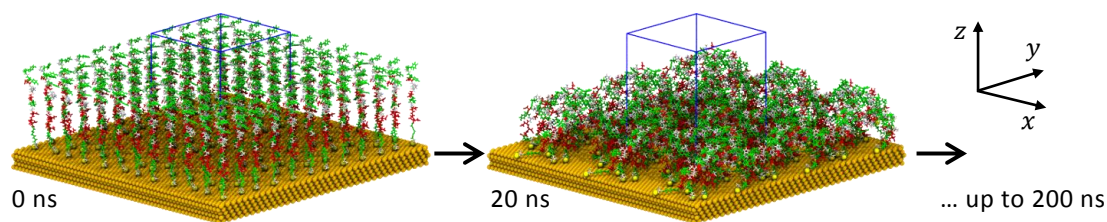


**Figure 4.5 | Computational setup depicting the approach taken to thermally equilibrate the dense peptide monolayers on Au(111).** The initially linear-extended peptide-epitopes (left) gradually relax into their preferred monolayer configurations on the gold surface (right) over 200 ns of MD. The Au(111) surface (gold), peptide atoms (coloured as per Figure 4.2) and unit cell (blue) are shown but for clarity, the solvent molecules are not displayed.

### Analysis Procedures

Unless otherwise stated, analysis was performed on the equilibrated stage of the MD simulations with GROMACS 4.5.5 analysis tools,<sup>430</sup> and visualisation was achieved with the VMD 1.9.1 package.<sup>128</sup> Specifically, root-mean-square deviations and potential energies (Appendix Figure C.2) were calculated using *g\_rmsd* and *g\_energy*, respectively. Root-mean-square atomic fluctuations (Appendix Figure C.3) were calculated with *g\_rmsf*. Normalised atomic distribution profiles to get monolayer thickness (Figure 4.6 and Table 4.1) and density of specific residues relative to gold (Figure 4.7 and Appendix Figure C.6) were obtained with *g\_dens* (also see description in first paragraph of Section 4.3.1). Monolayer solvent accessible surface area values (Table 4.2) were attained via *g\_sas*. Radial distributions for solvent atoms (Figure 4.8, Appendix Figure C.7 and Appendix Table C.1) were calculated with *g\_rdf*.

## 4.3 Results

### 4.3.1 Peptide-Monolayer Characterisation

To measure, characterise, and compare structural differences between the various peptide-monolayers formed on Au(111), atomic density plots with respect to the *z*-axis, i.e. the axis perpendicular to the gold surface (see Figure 4.5), are calculated. This is achieved by partitioning the simulation box into 85 *x*-*y* cross-sections (0.1 nm in depth), totalling the number of atoms in each volumetric slice, and dividing by the cross-sectional volume to give a number density ( $\rho$ ). Each volumetric number density is then time-averaged across the ensemble of equilibrated peptide-monolayer structures produced from MD and divided by the total number of peptide atoms in the respective monolayer. In this way, the outputted densities are normalised ( $\rho_{\text{norm}}$ ) with respect to differences in the total number of peptide atoms for each system (HA: 3,488 atoms, HSV: 3,296 atoms, and Myc: 3,728 atoms).

The normalised atomic distribution profiles are plotted in Figure 4.6. Initially,  $< 0.2$  nm from Au(111), repulsive interatomic forces prevent peptide atoms from approaching too

close to gold. At  $z$ -distances of 0.2–0.6 nm, “surface-bound” peptide atoms, such as the gold-anchoring sulphur atoms and other adsorbed amino acids, contribute to  $\rho_{\text{norm}}$ , therefore the area under the plots in this range indicates the percentage of each peptide-monolayer that is surface-bound (Table 4.1). Interestingly, approximately one fifth to one quarter of each peptide monolayer is surface-bound with subtle variations between HA-CT to HA-NT layers, but a  $\sim 6\%$  increase in peptide adsorption for HSV-NT compared to HSV-CT. While differences between systems are observed for  $\rho_{\text{norm}}$  at distances  $> 0.6$  nm (e.g. note the depression in the HSV-NT layer density between 1.1–1.9 nm versus HSV-CT), perhaps more useful is the interpretation of this data to estimate the thickness of the peptide-monolayers. This is approximated to be the height above the gold surface where the cumulative peptide density is 90 % (see inset of Figure 4.6 and Table 4.1). In this case, an opposite trend is observed to peptide–Au adsorption with HSV epitopes forming a peptide layer of equal thickness in both immobilisation directions whereas C-terminal immobilisation of HA results in a  $\sim 0.2$  nm more compact monolayer when measured against HA-NT.

To elaborate on these findings and obtain an impression of the flexibility of the peptide chains within each epitope-monolayer, ensemble-averaged root-mean-square fluctuations (RMSF) are calculated for each  $\alpha$ -carbon ( $C\alpha$ ) atom (Appendix Section C.3). This technique effectively measures how far a residue’s  $C\alpha$  atoms fluctuate about their average locations, which is beneficial to characterise local changes along the peptide chains. For all systems,

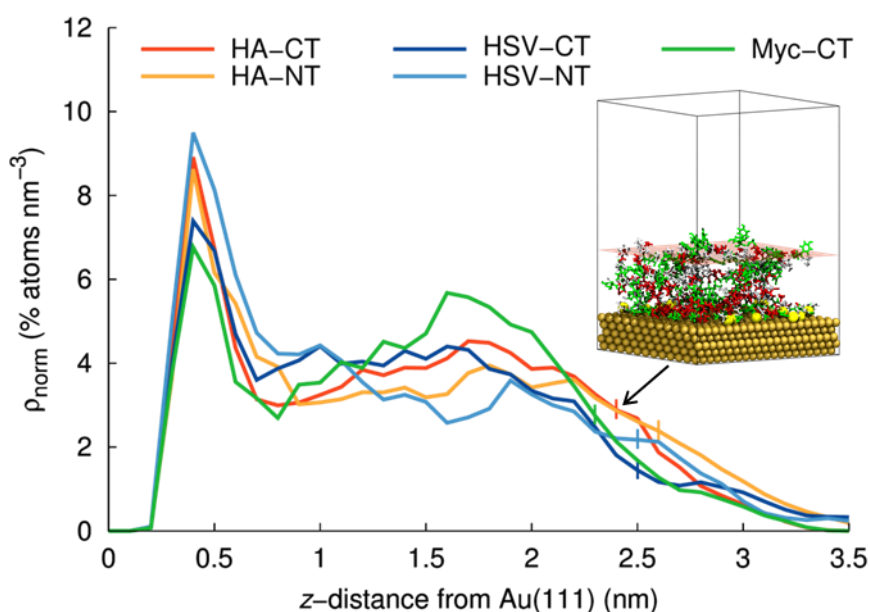


**Figure 4.6 | Normalised peptide-monolayer number density as a function of height above the Au(111) surface.** The inset shows a representation of the HA-CT peptide monolayer with the drawn  $x$ - $y$  cross-sectional plane illustrating the estimate of the peptide-monolayer thickness (indicated by a vertical line in the density plots). The criterion used to approximate this thickness is given in the text.



**Table 4.1 | Percentage peptide–Au adsorption and peptide-monolayer thickness.**

System	Surface bound atoms* (%)	Monolayer thickness† (nm)
HA-CT	24.5	2.4
HA-NT	24.0	2.6
HSV-CT	22.8	2.5
HSV-NT	28.8	2.5
Myc-CT	20.0	2.3

\*Cumulative peptide density < 0.6 nm.

†Height above Au(111) where peptide density ~90%.

the majority of the C $\alpha$  atoms show minimal RMSFs indicating that most peptide chains remain relatively rigid within the equilibration time. However, the epitope ends of the chains (especially for HA-NT) show more fluidity than the remainder of the layers.

Visual comparison of each system's ensemble of peptide conformations reveals unambiguous differences (Figure 4.7), especially when comparing between the N- and C-terminally gold-immobilised sequences. For example, although the monolayer thickness is similar (~2.5 nm) for HSV-NT and HSV-CT, the distribution of the individual peptide chains is not. In the HSV-NT monolayer, peptides are elongated and evenly dispersed as opposed to the C-terminally immobilised counterpart (HSV-CT), which assembles in more clustered structures and forms a compact peptide layer. Likewise for the HA epitope systems, HA-NT displays extended structures on Au(111) leading to a monolayer that is ~0.2 nm thicker, while for HA-CT, chain–chain interactions cause peptide agglomerates to accumulate within the layer. For the experimentally non-performing Myc-CT system, a compact yet evenly dispersed peptide coating is formed on the Au(111) surface. These noticeable differences are found to be directly related to the primary structure of the peptide-monolayers, i.e. sequence of the consistent amino acid subunits, with the inclusion and location of certain residues strongly influencing the conformational landscapes exhibited.

MD simulations of single peptides adsorbing onto Au(111) were conducted to investigate the influence gold has on amino acid and peptide conformations (Appendix Section C.4). Most prominent are the interactions of gold with aromatic and negatively charged residues. If aromatic residues are present in the peptide sequence (e.g. in the HA peptides), the chains remain flexible and dynamic until the aromatic rings are flush with the surface and thereafter the peptides become “locked” into surface-bound configurations (Appendix Figure C.4). Previous computational studies similarly observe epitaxial fitting of aromatic rings into the hexagonal packing of gold atoms on Au(111),<sup>235</sup> and show that tyrosine is a strong Au(111)-binding residue.<sup>89,233</sup> The single peptide simulations also reveal that all peptides manoeuvre their negatively charged amino acids away from the surface in order to

maximise charged residue solvent exposure. While it may appear counterintuitive since the gold surface has an overall neutral charge, this repulsive response seems to be an inherent feature of the GolP force field.<sup>233</sup> For the monolayer systems, these energetically favourable gold–amino acid binding preferences, together with peptide–peptide and peptide–solvent interactions (further discussed below), govern the conformations observed (Figure 4.7).

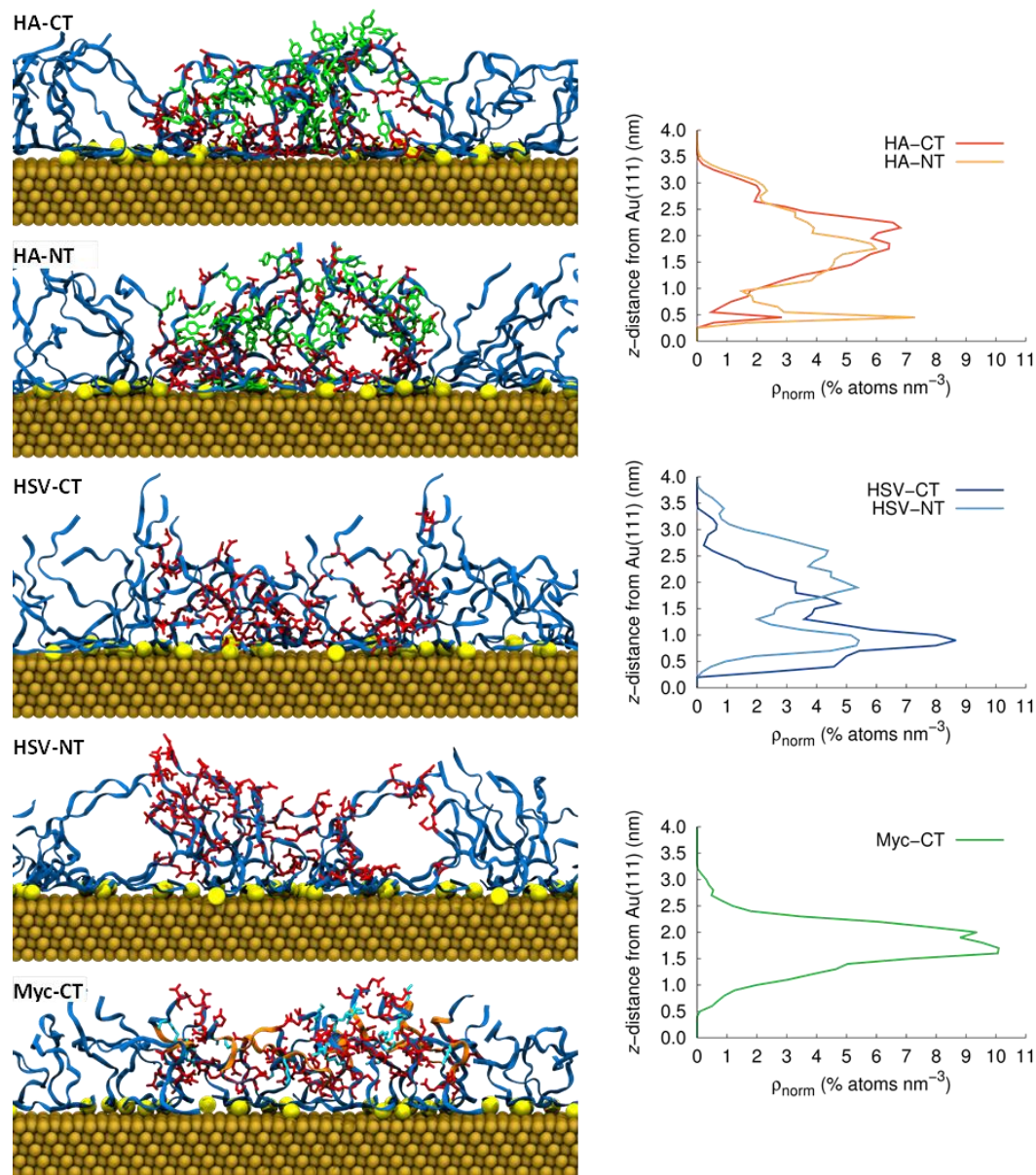


**Figure 4.7 | Typical equilibrium monolayer structures and distribution of immuno-dominant residues observed from the simulated epitope–gold systems. (Left)** Representative images highlighting differences in overall peptide–monolayer structuring. Peptide backbones are shown in ribbon representation with the terminal immobilisation sulphurs displayed as yellow spheres. Negatively charged Asp and Glu (red), positively charged Lys (cyan), and aromatic Tyr (green) residues are highlighted as liquorice representations in the central unit cell, and the core epitope motif LISE for Myc-CT is shown in orange. The Au(111) surface is displayed in gold and for clarity, water and salt molecules are not shown. **(Right)** Normalised atomic density plots as functions of height above the Au(111) surface for immuno-dominant residues in each system. HA: Y and D; HSV: D and E; Myc: LISE core motif.

### 4.3.2 Immuno-Dominant Residues

To associate the abovementioned peptide-monolayer assemblies to the experimental performance of the nanoparticle systems (Figure 4.4), there is a need to identify how likely it is that an incoming antibody will bind to epitopes within the monolayer (and result in AuNP cross-linking). The peptides used throughout this project are *linear* viral epitopes, i.e. the paratopes of their cognate anti-viral antibodies bind to the entire immuno-dominant sequence (IDS) which is labelled as *epitope* in Figure 4.2. Despite explicitly knowing the primary IDS, neither the HA or HSV antibody paratopes (nor their antigen binding mechanisms) have previously been characterised, so the exact immuno-dominant residues (IDRs) within the epitope IDS that are essential for complimentary antibody binding remain unknown. Since biophysical and structural studies show that charge–charge interactions (i.e. “salt bridges”) can make critical contributions to antibody–antigen binding,<sup>433</sup> it is assumed that the acidic residues (Asp and Glu) in the charged HA and HSV IDS will form strong electrostatic interactions with oppositely charged regions of the antibodies’ paratopes. In addition, a study of 53 non-redundant antigen–antibody complexes found that antibody paratopes feature tyrosine residues almost two-times more than any other residue.<sup>434</sup> For these reasons it is logical to consider charged and aromatic amino acids as IDRs, and assume that their distribution within the monolayer constructs (see density plots in Figure 4.7) can be used to gauge for advantageous antibody-binding configurations.

For the HA epitope–AuNP systems, peptide conformations are predominantly affected by the location of Tyr residues in the epitopes’ primary sequence (Figure 4.2). For HA-CT, hydrophobic Tyr residues are located near the free N-terminus of the peptide chains and encourage the chain-ends to fold into the layer to reduce their aqueous exposure. In turn this solvates negatively charged amino acids so that they occupy outer regions of the monolayer in two clustered sections at 1.7 nm and 2.3 nm above the Au(111) surface (Appendix Figure C.6a). In the N-terminally immobilised HA epitope system, aromatic residues are primarily consolidated around the middle of the IDS where they are intrinsically shielded from the solvent and this leads to more than two-times the amount of Au-bound Tyr residues compared to HA-CT (peak at 0.4 nm in Figure 4.7 and Appendix Figure C.6b). The distribution of negatively charged residues in the HA-NT layer is more evenly spread, however the density of residues close (< 1.3 nm) to the gold interface is higher than HA-CT and, due to the increased extension of peptide chains, the density also attenuates further from the gold surface (> 3.0 nm, Appendix Figure C.6a).

For the HSV systems, charged amino acids of HSV-NT are solvent exposed at the peptides’ free C-termini and contribute to peptide–peptide repulsions at the outermost sections of the

**Table 4.2 | Monolayer solvent accessible surface areas.\***

System	Total monolayer (nm <sup>2</sup> )	IDS <sup>†</sup> (nm <sup>2</sup> )	IDRs <sup>‡</sup> (nm <sup>2</sup> )
HA-CT	154.7 ± 2.1 (0.6 ± 0.1)	99.1 ± 1.4 (0.7 ± 0.1)	63.5 ± 1.2 (0.8 ± 0.1)
HA-NT	160.5 ± 2.4 (0.6 ± 0.2)	110.1 ± 2.4 (0.8 ± 0.2)	66.1 ± 1.7 (0.8 ± 0.2)
HSV-CT	155.2 ± 1.7 (0.6 ± 0.1)	138.3 ± 1.6 (0.7 ± 0.1)	65.9 ± 1.0 (0.8 ± 0.1)
HSV-NT	164.9 ± 2.2 (0.6 ± 0.1)	149.0 ± 1.9 (0.8 ± 0.1)	80.5 ± 1.4 (1.0 ± 0.1)
Myc-CT	152.9 ± 2.7 (0.6 ± 0.1)	136.5 ± 2.5 (0.7 ± 0.1)	43.3 ± 1.0 (0.7 ± 0.1)

\*SASA is given as mean ± standard deviation, and normalised per residue (in brackets).

†IDS labelled as *epitope* in Figure 4.2.

‡Specific IDRs important for antigen–antibody binding. HA: Y and D; HSV: D and E; Myc: LISE core motif.

monolayer. This allows for a more even distribution and elongation of ligand chains, both steric features that are postulated to be conducive in enabling antibody binding. In contrast, HSV-CT assembles in more clustered structures and forms a significantly more compact peptide layer with charged residues concealed in the peptide monolayer (Figure 4.7).

While there is little information available on the antibody–antigen binding mechanisms for HA and HSV, the X-ray crystal structure of the paratope–epitope complex for c-Myc has been previously resolved<sup>435</sup> and IDRs within the peptide–epitope have been reported.<sup>435,436</sup> The core epitope motif is made up of the linear sequence of residues L<sub>12</sub>I<sub>11</sub>S<sub>10</sub>E<sub>9</sub> (numbering from the C-terminus in Figure 4.2). As illustrated in Figure 4.7, MD simulations show that the Myc-CT forms a compact peptide assembly driven by ionic interactions between the basic Lys and the acidic Glu/Asp residues. Although Glu residues are exposed to the aqueous interface, the LISE segment is mainly buried in the bulk of the monolayer and this is anticipated to be a major factor in the experimental non-performance of Myc-CT.

To facilitate the binding between paratope and antigenic determinant, peptide-monolayers, and ideally their IDRs, should be as solvent accessible as possible to maximise the logistics of being reachable to the antigen-binding sites of the antibodies. This has been assessed through solvent accessible surface area (SASA) calculations of the monolayers, IDS, and IDRs that are expected to be essential for lock-and-key binding (Table 4.2). A probe radius of 1.4 nm was used to map the peptide–gold Connolly surface and the results show that although all monolayer and IDS are relatively evenly solvent accessible (0.6–0.8 nm<sup>2</sup> per residue), the immuno-dominant charged residues in HSV-NT are significantly more solvent exposed. This is postulated to beneficially aid the HSV-NT AuNP system establish salt-bridges with the anti-viral HSV antibody, which is correlated to HSV-NT's superior experimental performance (Figure 4.4). The IDRs of Myc-CT are appreciably less exposed than the other systems and this complements the non-performance of the assembly.

### 4.3.3 Solvent Effects

Intermolecular radial distribution functions (RDFs), otherwise known as pair correlation functions  $g(r)$ , are calculated to measure the average separation between solvent and peptide IDS atoms (Figure 4.8 and Appendix Figure C.7). In all systems, positively charged salt ions ( $\text{Na}^+$ ) accumulate in very close proximity to the epitopes' IDS (sharp navy blue  $g(r)$  peaks at  $\sim 0.25$  nm of Figure 4.8a and Appendix Figure C.7a) due to electrostatic interactions of  $\text{Na}^+$  with  $\text{Glu}^-$  and/or  $\text{Asp}^-$  residues. This structuring provides a dynamic shielding mechanism between like charges in adjacent peptide chains and ultimately lowers the systems' overall potential energy to promote more stable monolayer assemblies. Comparing amplitudes of the RDF maxima reveals that the amount of  $\text{Na}^+$  ions correlates with the trends observed for IDS solvent exposure (Table 4.2), i.e. more cations interact with HSV-NT epitopes than HSV-CT, and the same goes for HA-NT versus HA-CT. In contrast, there is negligible  $\text{Cl}^-$  ion organisation in all systems except for the HSV-NT coating where a small electrical double layer is apparent (green peak at  $\sim 0.35$  nm in Figure 4.8a).

In a similar fashion, water molecules also participate in the electrostatic buffering of peptide charges by embedding into, and structuring around, the monolayers. In Figure 4.8b and Appendix Figure C.7b, the discrete hydrogen (blue) and oxygen (red) RDF peaks at  $\sim 0.18$  nm and  $\sim 0.27$  nm suggest that at least two hydration shells form around the peptides' IDS. The approximate ratio of the hydrogen to oxygen RDF peak amplitudes at the first hydration shell (Appendix Table C.1) is used to estimate the orientation of water molecules at the IDS–water interface. For example, a ratio of 2 (hydrogens) to 1 (oxygen) indicates no preferential orientation of hydrogen or oxygen atoms to the peptides; a ratio of 2 to 2 implies that interactions between structured water's oxygen atoms and the peptide chains is a third more favourable than interactions with water's hydrogen atoms, i.e. 66.7% of water molecules are facing their oxygen atoms towards the IDS; and a ratio of 2 to 0.5 indicates the exact opposite, that 66.7% of water molecules in proximity of the IDS are oriented with their hydrogen atoms nearer to the peptides.

The MD simulations show that in all systems, aside from HA-CT, water molecules spontaneously and preferentially position their hydrogen atoms towards the IDS of the peptide chains, in particular the negatively charged amino acids (Figure 4.8c and d). Therefore the dipole moments of individual water atoms at the peptide–water interface are directed towards the monolayer allowing for water to donate positive charge to the epitopes. Although weaker than  $\text{Na}^+$  interactions with negative residues, water molecules help facilitate a denser packing of individual chains in the peptide monolayers by obstructing electrostatic repulsions between neighbouring  $\text{Glu}^-$  and  $\text{Asp}^-$  residues.

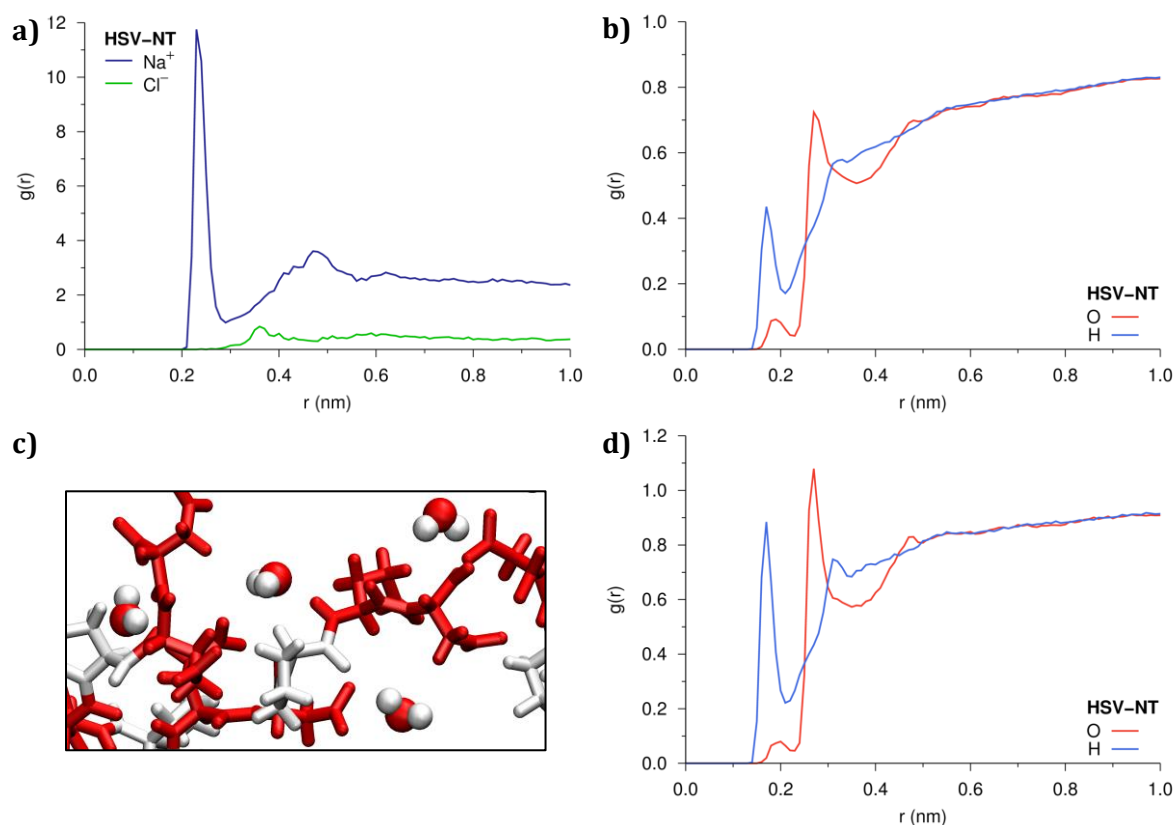


**Figure 4.8 | Solvent structuring in the HSV-NT monolayer.** (a) The radial distribution of  $\text{Na}^+$  (blue) and  $\text{Cl}^-$  (green) ions relative to the IDS of HSV-NT demonstrates that the cations strongly interact with the epitopes (large peak at  $\sim 0.25$  nm) and  $\text{Cl}^-$  ions form a small electrical double layer (peak at  $\sim 0.35$  nm). (b) The RDF of hydrogen (blue) and oxygen (red) atoms of water molecules around the IDS in the monolayers shows two prominent solvation shells and the suggestion of a third. (c) An illustrative snapshot from MD highlighting the preferential orientation of water molecules' (red and white van der Waals spheres) hydrogen atoms towards the negatively charged residues in the peptide chains (red liquorice representations). (d) The RDF of water molecules in relation to negatively charged aspartate and glutamate residues further highlights this structuring with a very large hydrogen maxima at  $\sim 0.18$  nm compared to oxygen.

#### 4.4 Discussion and Conclusions

Through analysing the structural landscapes exhibited on the surface of each epitope–gold complex, it is apparent that monolayer conformations are strongly influenced by peptide–peptide and peptide–gold interactions and therefore intimately related to amino acid composition and location within individual peptide sequences. For example, the HA epitope–AuNP systems contain three aromatic Tyr residues per peptide that endeavour to reduce their solvent exposure and epitaxially interact with the gold surface. For HA-CT, where two of the three hydrophobic amino acids are intrinsically located at the free N-terminus of the peptides, the drive to reduce hydration promotes a compact layer that causes negatively charged Asp residues to become solvent exposed in the process. When the epitopes functionalise the AuNPs via a mirror-inverted immobilisation direction, the Tyr

residues in HA-NT more readily interact with the gold surface, there is a higher concentration of Asp<sup>-</sup> amino acids inherently close to Au(111), individual peptide chains are more extended, and a thicker monolayer is produced. In the HSV and Myc systems, electrostatic (rather than hydrophobic) effects are deduced to be the main motivation for the monolayer configurations. For HSV-NT, four of the five negatively charged residues in the IDS are at the unbound C-terminus of the peptides and consequently, to minimise Asp<sup>-</sup>/Glu<sup>-</sup> electrostatic repulsions, the peptide chains remain elongated and well dispersed in the peptide layer. In the Myc-CT simulations on the other hand, it is the attraction between basic (lysine) and acidic (glutamate/aspartate) residues that prompts a compact layer to form where the paratope-binding LISE segment of the IDS is mainly buried in the bulk of the monolayer. For all systems, the stability of the assemblies is enhanced through peptide-solvent interactions that lower overall potential energy by balancing electrostatic interactions. The dynamic shielding of like charges in adjacent peptides also helps to support a denser packing of individual chains in the monolayers.

To correlate these properties to the empirical capacity each system has for forming AuNP aggregates in the desired conditions, it is first important to understand how different epitope conformations influence antibody binding. While this usually requires an explicit and prior knowledge of the unique paratope-epitope complexation specific for each antibody-antigen pair, this information is rarely available. Instead, immuno-dominant residues essential for complimentary antibody binding are predicted from the literature and general features that are expected to contribute to advantageous epitope-antibody binding are explored. Interestingly, the MD simulations reveal that the HSV-NT monolayer (also the best experimentally cross-linking system) displays superior elongation and dispersion of peptide chains, which is anticipated to sterically enable the coordination of antibodies around the peptides' IDS. Furthermore, the assumed IDR within the HSV-NT epitopes are found to be significantly more solvent exposed compared to the other systems and this is postulated to beneficially establish salt-bridges between the peptide monolayers and anti-viral HSV antibodies. On the contrary, the (experimentally non-performing) Myc-CT monolayer is compressed and has noticeably less solvent exposure of its immuno-dominant (LISE) residues when juxtaposed against the other monolayers. In relation to epitope immobilisation orientation on gold, the clear monolayer differences observed are very probable to influence antibody binding since the matching of epitopes to their cognate antibody paratopes is almost certain to be more effective in one orientation over another.

It would be ideal to simulate the MD obtained epitope-AuNP surfaces with antibodies to confirm how epitope conformation and immobilisation orientation influences binding

propensity. Unfortunately, there are still no available epitope-relevant antibody structures for the peptides/antibodies used experimentally in this study. Despite this, Figure 4.9 has been artificially constructed to provide a perspective on the scale of how big a *typical* antibody binding region is compared to the epitope–NP surfaces. The paratope region of the antibody fragment is likely to be a relatively small sequence of amino acids between the red and green protein chains. From this image it is easy to see how extended epitopes (blue) on the surface are expected to facilitate binding more readily than compact epitopes.

Following the justification provided, one might assume that longer spacers between the IDRs and the gold surface might lead to better steric binding with the antibodies. While this may well be true, antibody *binding* only constitutes a small part of these assays. Upon binding, antibodies also need to *cross-link* the NPs and furthermore, the *interparticle spacing* between the aggregated NPs needs to be as small as possible to obtain an “eye-readable” distinct shift in optical signal. Experimentally, the substitution of the glycine-triplet spacer HA and HSV epitopes (Figure 4.2) with a longer and more flexible polyethylene glycol spacer (11 ethylene oxide units) resulted in a slower assay response and a loss of assay sensitivity.<sup>3</sup>

Therefore, when interpreting the MD results in the context of antibody-induced AuNP cross-linking, several factors need to be carefully considered. Although the binding between an antibody and epitope monolayer may be optimal, there is a chance that an immunoglobulin molecule will bind with both valences to the same AuNP and this will effectively disable cross-linking. Additionally, the axial symmetry of immunoglobulin molecules or the

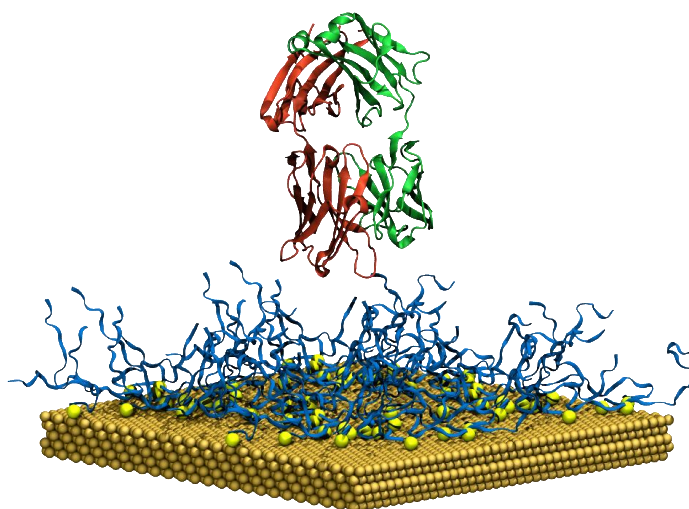


**Figure 4.9 | Representative antibody fragment with an epitope–Au surface.** This image highlights the size difference between a typical epitope-binding fragment of an antibody (shown in red and green) and the MD equilibrated HSV-NT functionalised Au(111) surface. It is easy to see how the linearly extended HSV-NT peptides (blue) in this system are likely to sterically encourage antibody binding. Please note that no MD has been conducted with this antibody fragment (PDB Code: 3W9E). Its orientation and positioning have been arbitrarily chosen for the image.



particular molecular structure of the antigen–antibody immune complex might be fundamentally impaired to bivalent cross-linking. Finally, the equilibrium monolayer structure may drastically change during and upon antibody interaction and therefore may not be the ideal representation to infer if multiple antibody binding events will occur or to establish the AuNP cross-linking propensity of a system. As antibody characterisation improves, it would be very interesting to check these scenarios via modelling the specific antibodies in this study interacting with the epitope–AuNP surfaces (Figure 4.9).

In addition, as force fields advance and computational resources increase, the complexity of atomistic simulations could also increase to give better insights into these fascinating multicomponent systems. Namely, larger and more realistic nanoparticle models could be used to study the effect of curvature on monolayer conformation, multiple nanoparticle aggregations could be modelled in solution, and complex physiological environments could be explored (inclusion of serum and blood proteins). Ultimately though, to generate generic design principles for antibody–epitope–AuNP colourimetric bioassays there first needs to be more experiments and simulations performed on protein epitopes that have *linear* amino acid sequences and the cognate antibodies that recognise them.

Despite the fact that a purely molecular-scale examination of the epitope–gold interface cannot completely explain the selective experimental aggregation performance of the various coated AuNPs, the presented study not only characterises the assemblies with a resolution that is empirically unavailable, it also provides non-intuitive insights. This work also highlights how the synergy between theoretical and experimental approaches can produce translational research that facilitates the development of novel bioassays.

## Chapter 5:

# Peptide-Coated Fluorescent Au<sub>25</sub> Nanoclusters

Correlations between peptide ligand conformations and the photoluminescent properties of Au<sub>25</sub> nanoclusters are explored in this chapter using classical molecular dynamics. Structure–property relationships are established that link differences in the particles' hydrodynamic radii, embedded water content and distribution of chemical groups around the gold core atoms to changes in the experimentally measured photoluminescence of the materials. This research has been performed concurrently, and in collaboration, with the biomaterials engineering team of Prof. Molly M. Stevens at Imperial College London to whom due acknowledgment is given, predominantly Dr Yiyang Lin, for all empirical results presented (Section 5.1.1 and Appendix Section D.1). Recognition is also given to Dr Andrew Christofferson (RMIT University) for parameterisation of the Au–S–C–C dihedral used in the classical force field (Appendix Section A.1), and the quantum mechanical results presented at the end of Section 5.3.2. Special acknowledgement is made to Prof. Stefano Corni (CNR Institute of Nanoscience, Italy) for useful discussions relating to the *a posteriori* electrostatic potential analysis presented in Section 5.3.5, and to Dr Matthew Penna (RMIT University) for his input and advice involving the analysis of water in the molecular dynamics systems. Gratitude is also expressed to the developer's group of the ONETEP program (<http://www.onetep.org/Main/People>) for their assistance, guidance, and recommendations, particularly during the 2013 and 2015 ONETEP masterclasses in the U.K. Research from this chapter is in the final stages of preparation for publication submission with joint first authorship.<sup>1</sup>

---

## 5.1 Introduction

Gold nanomaterials are attracting extensive research attention for applications within a wide range of biomedical fields<sup>437</sup> due to their rich and tuneable, size-dependent, physical, chemical, and photoluminescent properties (Section 1.4). Of particular interest are gold nanoclusters (AuNCs) whose sizes are comparable to the de Broglie wavelength of electrons near the Fermi energy of metallic gold (0.5 nm), since they experience molecule-like interactions with incident light to produce intense photoluminescence (PL, see Section 1.3.3). Compared to organic dyes, AuNCs exhibit broad excitation ranges, weak photobleaching, red/near-infrared (NIR) emission, and less toxicity, which makes them ideal for cellular and subcellular imaging.<sup>438</sup> To enable their application as biological probes,

much effort has been devoted to the design of biocompatible clusters using biomolecules.<sup>14</sup> For instance, some of the first highly luminescent AuNCs to be synthesised using “green chemistry” routes involved exploiting the reduction capacity of bovine serum albumin at basic pH.<sup>439</sup> Since then, a series of proteins including human serum albumin,<sup>440</sup> papain,<sup>441</sup> insulin,<sup>442</sup> bovine pancreatic ribonuclease A,<sup>443</sup> lysozyme,<sup>444</sup> and lactoferrin<sup>445</sup> have all been used to template AuNC nucleation, while the NIR emission properties of the AuNCs have enabled their application as novel contrast agents for the PL imaging of tumours *in vivo*.<sup>446</sup>

Over the past few decades many hypotheses have emerged regarding the nature of AuNC PL.<sup>19</sup> For example, solid-state models suggest that the red/NIR PL of Au<sub>25</sub>(SG)<sub>18</sub> (where SG = glutathione) arises from intraband (*sp-sp*) and interband (*d-s*) electronic transitions in the gold core.<sup>447,448</sup> Ligand exchange reactions of Au<sub>25</sub>(SG)<sub>18</sub> with functionalised-glutathione and 3-mercaptopropan-2-ol indicated that “emission is an inherent property of the core, and the same electronic transitions can be accessed for a variety of ligands”.<sup>449</sup> Likewise, very recent work has highlighted that despite the fact that structural isomers of Au<sub>38</sub>(S(CH<sub>2</sub>)<sub>2</sub>Ph)<sub>24</sub> (where Ph = phenyl = C<sub>6</sub>H<sub>5</sub>) display varied absorbance spectra and electronic relaxation pathways, core-to-core transitions are still the underlying source of Au<sub>38</sub>'s PL.<sup>450</sup> Contrasting theories propose that AuNC PL emission is independent of core-based electronic transitions and core size, but rather results from localised electronic surface states related to ligand atoms.<sup>451</sup> There have also been suggestions that AuNC PL is either: correlated to ligand-to-metal charge transfer (LMCT),<sup>91,452</sup> which strongly depends on the type of ligands;<sup>453</sup> or linked to ligand-to-metal-metal charge transfer (LMMCT) that is associated with the presence of aurophilic (Au–Au) interactions.<sup>454-456</sup> Moreover, the interplay between surface ligand and gold is reported to influence the emission *intensity* of PL AuNCs. The exchange of nonpolar ligands with more polar species has been shown to increase emission intensity with a linear dependence on the number of substituted polar ligands.<sup>457</sup> Additionally, it has been suggested that ligands containing electron-rich atoms (e.g. N, O) or groups (e.g. amides and carbonyls) are able to directly donate delocalised electron density to the gold core of Au<sub>25</sub> NCs via the Au–S bond, which can significantly enhance fluorescence quantum yield.<sup>91</sup>

In complement to experimental findings, theoretical approaches provide non-intuitive insight into the electronic, structural and dynamic behaviour of the Au–bio interface that is not achievable through any other technique (see Chapter 2). Work by Aikens in 2009 using time-dependent density functional theory (TDDFT) showed that aliphatic ligand chain length plays only a minor role on the excitation energy of [Au<sub>25</sub>(SR)<sub>18</sub>]<sup>–</sup> (where R = H, CH<sub>3</sub>, CH<sub>2</sub>CH<sub>3</sub>).<sup>458</sup> Instead, the geometric and electronic structure of the gold *core* primarily dictates the discrete optical absorption exhibited. In a follow up, TDDFT was used to

investigate [Au<sub>25</sub>(SR)<sub>18</sub>]<sup>-</sup> (where R = H, CH<sub>3</sub>, CH<sub>2</sub>CH<sub>3</sub>, CH<sub>2</sub>CH<sub>2</sub>CH<sub>3</sub>) in the gas phase before and after photoexcitation and revealed that indeed all excited states arise from Au<sub>13</sub> *core-based* orbitals.<sup>204</sup> The authors suggest that subtle differences in the AuNCs' PL are predominantly brought about by the ligands' interactions with the AuNC core, and not from "semi-ring" (or "staple" motif) states. Tlahuice-Flores *et al.* used DFT to systematically study the structure and electronic optical properties of [Au<sub>25</sub>(SR)<sub>18</sub>]<sup>-</sup> with 11 different ligands: low polarity substituents, where R = H, CH<sub>3</sub>, C<sub>6</sub>H<sub>13</sub>, and (CH<sub>2</sub>)<sub>2</sub>Ph; thiophenols, where R = PhX, and X = H, Cl, COOH, NO<sub>2</sub>; and chiral molecules, where R = N-acetylcysteine, H<sub>2</sub>C\*H(X)Ph, and X = NH<sub>2</sub>, CH<sub>3</sub>.<sup>185</sup> They found that distortions to the Au<sub>25</sub>S<sub>18</sub> framework, such as puckering, tilting and rotation effects, are strongly correlated to a reduction in the energy difference between the highest occupied and lowest unoccupied molecular orbitals, i.e. the HOMO-LUMO gap, and that these distortions are generally associated with electron-withdrawing ligands. Although the DFT and TDDFT methodologies are ideal for examining how ligands affect the electronic and optical properties of AuNCs (also see Section 2.2.2), the computational expense associated with these techniques restricts: the ligand (and gold core) sizes able to be investigated, the capacity to include explicit solvent effects, and the ability to dynamically explore and optimise structures in different local minima of the potential energy surface.

Combining DFT with quantum mechanics/molecular mechanics (QM/MM) approaches, Rojas-Cervellera *et al.* reported that the HOMO-LUMO gap of [Au<sub>25</sub>(SG)<sub>18</sub>]<sup>-</sup> and [Au<sub>25</sub>(SCH<sub>3</sub>)<sub>18</sub>]<sup>-</sup> depends sensitively on both ligands and solvent.<sup>331</sup> In a recent subsequent work, [Au<sub>25</sub>(SG)<sub>18</sub>]<sup>-</sup> structures were also investigated with molecular dynamics (MD) and QM/MM to determine the mechanisms for ligand exchange of glutathione to an antibody protein fragment,<sup>257</sup> and important reaction used to introduce functionality to AuNCs. For the QM/MM components of both computational studies, gold atoms and glutathione cysteine segments (-S-CH<sub>2</sub>-C-) were treated by DFT, while the remainder of the ligands and solvent were handled using classical MM, for a total simulation time of 7–7.5 ps. While simulations of this time scale are unable to adequately sample the effect of conformational changes, supplementing with classical MD simulations can help achieve equilibrated structures.<sup>257</sup>

Force field (FF) approaches that model biologically relevant AuNCs over longer periods of time are starting to appear and expected to increase since the advent of FFs that inherently consider structural Au-S staple motifs (see Section 3.3.3). For example, classical MD simulations have been useful to characterise interactions between: *proteins and AuNCs* that are densely functionalised with peptides<sup>258-260,459</sup> or thiophenols;<sup>222</sup> *pairs of AuNCs* coated with glutathione and other small molecules;<sup>380,460</sup> as well as, *single peptides and spherical*

gold particles (5 nm).<sup>461</sup> In addition, there is a number of MD works targeting AuNCs decorated with alkanethiol molecules and their derivatives (summarised in Section 6.1).

Despite considerable theoretical and experimental efforts, fundamental understanding into the PL origin of ligand-coated AuNCs remains incomplete. This is especially true for biocompatible ligands, such as peptides, due to the complex chemistries and conformational space that the biomolecules can explore, making it difficult to separate the effects of primary and secondary structure on the PL mechanisms of AuNCs. In this chapter, various hexapeptide-protected Au<sub>25</sub> NCs are simulated with both MD and QM to elucidate how the local chemical environment near the AuNC surface, and peptide conformations exhibited, correlate to the experimentally measured PL intensities of these materials.

### 5.1.1 Experimental Project Design and Computational Aims

A library of 24 different hexapeptides (Table 5.1) have recently been synthesised and used to produce bioactive PL AuNCs with potential for bioimaging and biosensing applications.<sup>1</sup> The synthetic peptides are intentionally designed to investigate the effect of peptide structure (e.g. primary sequence, N-terminal capping, electron-withdrawing capacity, and hydrophobic character) and solution pH on the PL properties of small AuNCs. Specifically, cysteine (C) residues at the peptides' N-termini are introduced to anchor the peptide-ligands to gold via covalent Au-S bonding, while aspartic acids (D) are appended to the C-termini to provide negative charges for enhanced solubility of the clusters. The amino acids between cysteine and aspartic acid are systematically varied to investigate their roles in influencing the PL performance of the AuNCs.

The rationale behind the chosen sequences can be illustrated by examining the CHYGDD peptide sequence, which contains histidine (H), tyrosine (Y), and glycine (G), as an example. Since tyrosine is known to display reducing<sup>462</sup> and antioxidant capabilities,<sup>463</sup> and histidine

**Table 5.1 | Engineered sequences used to prepare peptide-protected AuNCs.†**

<i>CXXGDD</i>			
CGGGDD* (39.4)	CQGGDD (189.1)	CGYGDD* (292.7)	CFGGDD (388.7)
CKGGDD (145.6)	CSGGDD (215.2)	CHYGDD* (303.3)	CYGGDD* (400.9)
CNGGDD (162.8)	CHGGDD* (251.1)	CVGGDD* (347.0)	CFFGDD (513.3)
CTGGDD (176.2)	CVVGDD* (253.9)	CYHGDD* (365.4)	CYYGDD* (875.3)
<i>Ac-CXXGDD</i>			
Ac-CGGGDD* (90.6)	Ac-CHGGDD* (732.5)	Ac-CHYGDD* (873.9)	Ac-CYHGDD* (877.7)
<i>Other</i>			
CDGGGD (102.0)	DGYCGD (516.1)	CYYGRR*‡	Ac-CYYGRR*‡

\*Au<sub>25</sub>(SP)<sub>18</sub> (where P = peptide) structures investigated with molecular modelling.

†Colours and values in brackets represent the maximum AuNC PL emission intensity measured experimentally at pH 7.5 using a spectrofluorometer (Appendix Figure D.2). Reported values are in *photon counts per second* × 10<sup>3</sup>.

‡PL of comparable magnitude to other sequences but measured independently so not reported here.

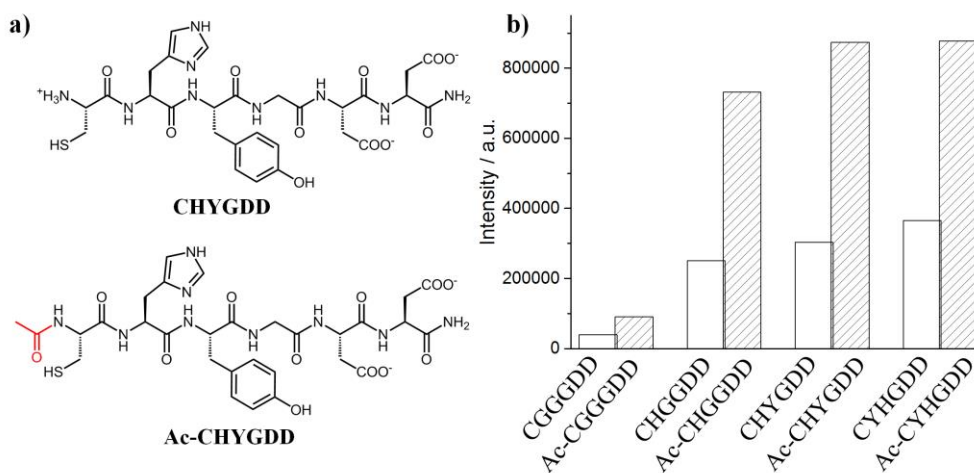


**Figure 5.1 | Effect of N-terminal acetyl capping on AuNC PL. (a)** Representative structures of CHYGDD and Ac-CHYGDD showing the subtle difference of peptide structure at the N-terminus. **(b)** Maximum emission intensity of AuNCs prepared from capped and uncapped peptides ( $E_x = 400$  nm).

is electron-rich with a high affinity towards metallic surfaces,<sup>464</sup> this sequence is expected to be a good candidate to promote *in situ* NC nucleation. Indeed, the resultant solution(s) from CHYGDD (and the other sequences) is found to contain intensely luminescent small metallic NCs that are determined to be approximately 25 gold atoms in size with a hydrodynamic diameter ( $D_h$ ) of  $\sim 3.1$  nm (Appendix Figure D.1).<sup>1</sup>

Cysteine acetylation is noted to affect AuNC PL through N-terminal amine groups. The PL intensity of AuNCs prepared from Ac-CGGGDD is measured to be  $\sim 2.3$  times higher than that of CGGGDD without acetyl capping (Figure 5.1). Similar phenomena are observed for peptide sequences CHGGDD/Ac-CHGGDD, CHYGDD/Ac-CHYGDD, and CYHGDD/Ac-CYHGDD which display PL enhancements of 2.9, 2.9 and 2.4-fold increases, signifying that the capping of N-terminal amine with  $-\text{COCH}_3$  positively impacts the PL intensity.

The effect of residue hydrophobicity/aromaticity on the PL of AuNCs prepared from 17 peptide sequences (Table 5.2) is also studied. Each peptide is assigned a hydrophobicity score by summing individual hydrophobicity indices<sup>465</sup> for the three amino acids adjacent to cysteine, i.e. residues 2–4 (numbering from the N-terminus). As shown in Figure 5.2a, an increase in peptide hydrophobicity is linearly correlated to stronger AuNC PL. Furthermore, electron-rich and donating tyrosine residues are found to efficiently promote PL, which is observed to depend on the number of aromatic residues and their proximity to cysteine in the primary sequence, e.g. CYYGDD > CYGGDD > CGYGGDD > CGGGDD (Figure 5.2b).

When the peptide-protected AuNCs are diluted into buffer solutions at pH 7.5 or pH 5.5, PL intensity is noted to be inversely proportional to pH for CGGGDD, CVGGDD, CVVGGDD, CHGGDD, CYGGDD and CHYGDD, but unresponsive for acetyl-capped sequences (Figure 5.3).

Since PL variations in this manner are expected to originate from peptide–Au interactions and not morphological changes of Au core structure, it is anticipated that protonation/deprotonation of titratable groups (i.e. carboxyl, imidazole and amine moieties) is important for AuNC PL, especially near the peptides' N-termini.

**Table 5.2 | Investigated peptide sequences with varied residue hydrophobicities.**

Sequence (Hydrophobicity*)			
CDGGDD (-1.25)	CTGGDD (-0.16)	CHYGDD (-0.03)	CYYGDD (1.87)
CKGGDD (-1.01)	CSGGDD (-0.15)	CYHGDD (-0.03)	CFFGDD (2.25)
CHGGDD (-0.98)	CVVGDD (-0.15)	CYGGDD (0.92)	
CQGGDD (-0.60)	CVGGDD (-0.09)	CGYGDD (0.92)	
CNGGDD (-0.44)	CGGGDD (-0.03)	CFGDD (1.11)	

\*Calculated as the sum of the hydrophobicity indices<sup>465</sup> for the three amino acids closest to cysteine.

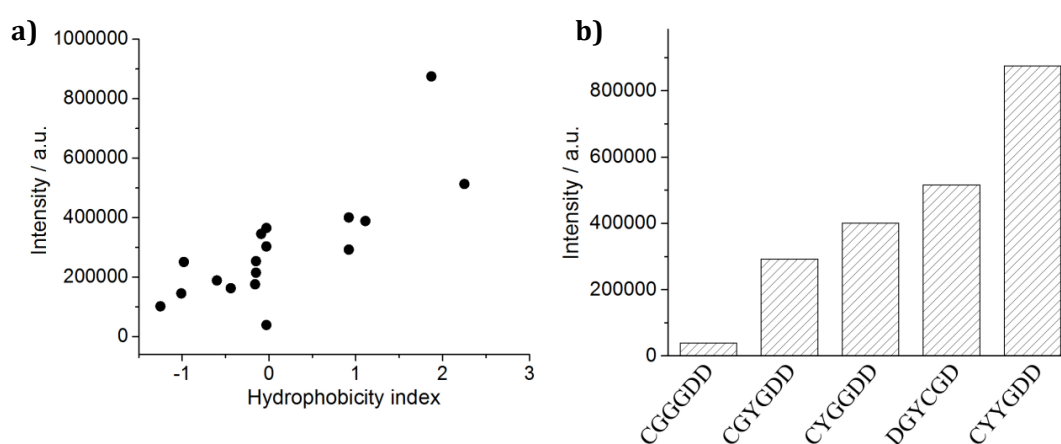


**Figure 5.2 | Correlation of peptide hydrophobicity to increased PL intensity. (a)** Relationship between peptide side-group hydrophobicity and AuNC PL. The hydrophobicity index was calculated as the sum of the individual hydrophobicity indices of the three amino acids close to cysteine.<sup>465</sup> **(b)** Effect of tyrosine and cysteine position on the PL response of the peptide-protected AuNCs.

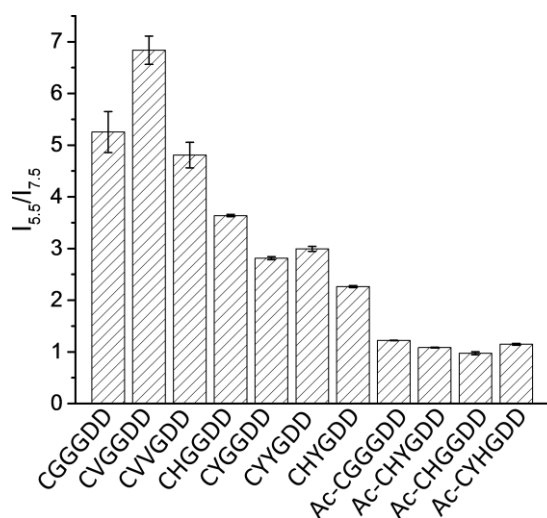


**Figure 5.3 | Experimental PL of peptide-protected AuNCs as a function of solution pH.** The ratio of the PL at pH 5.5 and pH 7.5 ( $I_{5.5}/I_{7.5}$ ) is used to elucidate PL pH responsiveness. A ratio  $\sim 1$  indicates a pH independent PL response while a ratio  $> 1$  signifies intensified PL in acidic solution.

To characterise and explore the structure, dynamics and interaction mechanisms of the Au<sub>25</sub>(SP)<sub>18</sub> (where P = peptide) and water, extensive all-atom MD simulations in explicit solvent are performed and reported in this chapter. The purpose of this study is to employ MD (and QM) to elucidate how the physicochemical properties of the functional AuNC-peptide interface varies with amino acids sequence and how these relative differences are correlated to the observed PL responses accounted above.

Following a description of the computational details employed in this work (Section 5.2), MD simulations are used to characterise general properties of the Au<sub>25</sub>(SP)<sub>18</sub> nanocluster systems, such as hydrodynamic radii, volumes, and overall peptide flexibilities (Section 5.3.1). Next, detailed investigations are undertaken to clarify how the presence of N-terminal acetyl caps on peptide ligands affect: the distribution of amino acids around the gold-sulphur NC cores; peptide conformation; structuring and dynamics of water molecules; as well as the formation of hydrogen bond networks (Section 5.3.2). This subsection concludes with results from QM calculations that clarify how acetyl affects partial charge distribution on the AuNC cores. In Section 5.3.3, results are presented to propose the role aromatic residues play in promoting increased empirical PL. Findings are then reported in Section 5.3.4 relating to MD simulations involving doubly protonated histidine residues, emulating the amino acids in a low pH environment. Finally, Section 5.3.5 elaborates on the role of aspartate in quenching PL and delivers the outcomes from linear-scaling DFT calculations of a Au<sub>25</sub>(SP)<sub>18</sub> system in explicit/implicit solvent. In the succeeding Section 5.4, the computational findings of this chapter are combined with the experimental evidence from above to generate principles for designing biocompatible AuNCs for broad applications in the field of bioimaging and biosensing, then concluding remarks are given.

## 5.2 Computational details

### 5.2.1 Molecular Dynamics

The AuNC structure used for MD contains 25 gold atoms (in agreement with experiment) and a morphology consistent with that of highly stable Au<sub>25</sub>(SR)<sub>18</sub> clusters, which can conceptually be divided into an icosahedral Au<sub>13</sub> core protected by six  $-\text{[SR-(Au-SR)}_2\text{]-}$  “staple” motifs.<sup>466</sup> The peptide-coated AuNCs modelled (indicated by asterisks in Table 5.1) were constructed by attaching, via the N-terminal cysteine, 18 extended peptide ligands equidistantly onto the X-ray crystal structure<sup>466</sup> of Au<sub>25</sub>(SR)<sub>18</sub> (Figure 5.4). All peptides have been NH<sub>2</sub> capped on the C-terminus and N-terminated with either a NH<sub>3</sub><sup>+</sup> moiety or a CH<sub>3</sub>CO acetyl group (denoted by an “Ac-” prefix). To emulate the protonation state of histidine (H) in neutral (pH 7.5) and acidic (pH 5.5) aqueous solution, two cognate models were built for



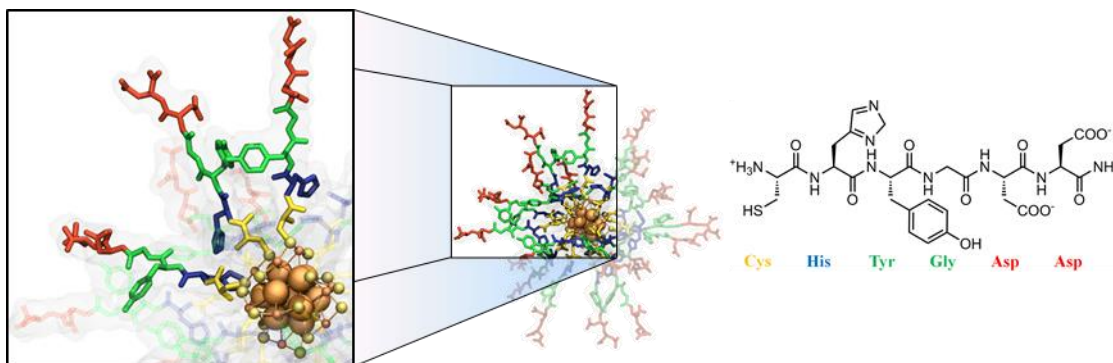


**Figure 5.4 | Example of the Au<sub>25</sub>(SP)<sub>18</sub> and peptide structures used for MD, with ligands extended. (Left)** Images highlighting the components that make up the Au<sub>25</sub>(SP)<sub>18</sub> models, i.e. the icosahedral Au<sub>13</sub> core, six [S-(Au-S)<sub>2</sub>]- “staple” motifs, and 18 peptide-ligands. **(Right)** Schematic showing the chemical structure of the exemplar capping-peptide (from N- to C-terminus: CHYGDD). The C-termini of all peptides used in this study are amide capped, whereas the N-termini are free amine. Peptide atoms (left) are coloured as indicated in the schematic, gold atoms are orange, and solvent is hidden for clarity.

peptides (Ac-)CHGGDD, (Ac-)CHYGDD and (Ac-)CYHGDD with all imidazole groups either singly-protonated or doubly-protonated (H<sup>+</sup>), respectively. In total, 19 different Au<sub>25</sub>(SP)<sub>18</sub> models were constructed with the following peptide sequences: CGGGDD as a control; CVGGDD, CHGGDD, CYGGDD, CGYGDD, CHYGDD, CYHGDD, CYYGDD, and CVVGDD to explore hydrophobicity and individual amino acid location; Ac-CGGGDD, Ac-CHGGDD, Ac-CHYGDD and Ac-CYHGDD to study N-terminal acetyl capping; and CH<sup>+</sup>GGDD, CH<sup>+</sup>YGDD, CYH<sup>+</sup>GDD, Ac-CH<sup>+</sup>GGDD, Ac-CH<sup>+</sup>YGDD, and Ac-CYH<sup>+</sup>GDD to examine histidine protonation. The chosen models represent diverse and distinct experimental systems with distributed PL intensities.

Explicit solvent MD simulations were conducted using the GROMACS 4.6.5 software.<sup>430</sup> Peptide interatomic interactions were modelled using the all-atom AMBER99SB-ILDN FF,<sup>467</sup> with CYX parameters used for charge neutral (unprotonated) cysteine residues. The TIP3P model was used for water.<sup>468</sup> Bonded parameters and Lennard-Jones potentials between Au and peptide atoms (S, C, and H) were adopted from a FF parameterised for similar monolayer-protected AuNCs assuming no explicit partial charges on gold atoms.<sup>221</sup> Additional parameters for the Au-S-C-C dihedral were obtained from a quantum mechanics dihedral scan at the B3LYP/6-31G\* level (with the LanL2DZ basis set for Au) in Gaussian09<sup>469</sup> (see Appendix A.1). For non-bonded interactions, long-range electrostatics were evaluated using the Particle Mesh Ewald method with a real space cutoff of 1 nm and a 0.12 nm fast Fourier transform grid spacing, while van der Waals (vdW) interactions were truncated at 1 nm. To preserve the core crystal structure<sup>466</sup> of Au<sub>25</sub>(SP)<sub>18</sub> during MD, distance restraints<sup>470</sup> of 1,000 kJ mol<sup>-1</sup> nm<sup>-2</sup> were applied between Au-Au atoms. Each Au<sub>25</sub>(SP)<sub>18</sub> was placed in a periodic cubic box of side length ~8.4 nm, solvated with ~19,000 water molecules (water density of ~1 g cm<sup>-3</sup>) and Na<sup>+</sup> or Cl<sup>-</sup> counter ions were added to

ensure a neutral simulation cell. Energy minimisation was carried out using the steepest descent algorithm to remove any steric clashes and 1 ns of position restrained MD was performed using the Berendsen<sup>393</sup> thermostat and barostat to equilibrate the solvent around the AuNCs at 300 K temperature and 1 atm pressure. Position restraints were then removed and 100 ns of *NPT* (constant pressure and temperature ensemble) MD was performed with the Nosé–Hoover thermostat<sup>395</sup> and Parrinello–Rahman barostat<sup>394</sup> to maintain temperature and pressure at 300 K and 1 atm. The LINCS algorithm<sup>399</sup> was applied to constrain all bonds to their equilibrium lengths, which enabled a time step of 2 fs to be used for each simulation, and frames were outputted to a trajectory file every 2 ps. To enhance conformational sampling, each system was simulated ten times starting from different initial atomic velocities, resulting in a total of 1  $\mu$ s of MD for each Au<sub>25</sub>(SP)<sub>18</sub>.

### Analysis Procedures

Properties and structures presented in this chapter are ensemble averaged over ten independent trajectories for each Au<sub>25</sub>(SP)<sub>18</sub> system and, unless stated otherwise, analysis has been performed on the thermally equilibrated stage of the simulations covering the final 20 ns of each trajectory (i.e. 200 ns of production data per system), as verified in Appendix Section D.2 by monitoring energy trends and convergence of the radius of gyration ( $R_g$ ) and root-mean-square deviation (RMSD). Statistical analysis was primarily performed using the GROMACS 4.6.5 suite analysis tools<sup>430</sup> and the VMD 1.9.2 package,<sup>128</sup> as detailed below.

GROMACS programs were used for the following analyses. Root-mean-square deviations (Appendix Figure D.4) were calculated with *g\_rmsd*. Ellipsoid volumes and shapes (Figure 5.5) were calculated with *g\_principal*, *g\_dist* and a custom python script for matrix algebra (see descriptions in Section 5.3.1 and Appendix B.1). Root-mean-square fluctuations of each residue's alpha carbon atoms (Figure 5.6a and Appendix Figure D.8) were obtained with *g\_rmsf*. To acquire the *radial minimum distance distributions* between residues and the gold core (Figure 5.7, Appendix Figure D.9, Appendix Table D.1 and Figure 5.11), i.e. at any given time there is X residues within a certain distance to the *nearest* gold or sulphur atom, *g\_rdf* was used with the *-rdf res\_com* and *-surf mol* flags, group 1 index being all Au<sub>25</sub>S<sub>18</sub> atoms and group 2 being heavy atoms of the residue of interest or water. To obtain the *absolute minimum distance distributions* between aspartate residues and the gold core (used in Figure 5.13), i.e. at any given time the closest ASP residue to gold is at distance X, *g\_mindist* with the *-resptime* flag was used. Calculation of the electrostatic potential energy part of Figure 5.13 has been described in Appendix Section B.2.

VMD was used for the following analyses and visualisation. Radius of gyration measurements for the nanoclusters (Appendix Figure D.5) and individual peptide chains (Figure 5.6b and Appendix Figure D.7) were obtained with *measure rgvr*. Peptide backbone angles and C-terminal to gold distances (Figure 5.8b and Appendix Figure D.10) were calculated using atomic center-of-masses as coordinate locations and distance vectors. Analyses done with *dynamic* water selections were particularly non-trivial. Radial distribution functions given in (Figure 5.9a and Appendix Figure D.11) were manually created. First selections were made for different types of atoms, e.g. gold, peptide, water within X nm of gold or sulphur etc., then the number of atoms present in each radial shell (0.5 Å thickness) from the central gold atom of the nanoclusters was calculated and outputted every 10 ps. These atom counts from *dynamic selections* were then post-processed via the formula given in the caption of Appendix Figure D.11 to give a radial distribution (and standard deviation) value at each distance. The atom density of bulk water, i.e. the water density far from the nanoclusters, was used to normalise the plots. The same data was also used to make the water histogram plots in Figure 5.9b. Hydrogen bond analysis (Figure 5.10 and Appendix Table D.2) was done with *package hbonds* and dynamic water selections again (see description given in Section 5.3.2 for weighting). Water decay profiles (Appendix Section D.5.3) also employed dynamic water selections and a description of how these were generated can be found in the caption of Appendix Figure Figure D.12.

Hydrodynamic diameter estimates (Appendix Section D.3.1) were obtained for  $2 \times 10^4$  configurations per system (i.e. 1 frame every 10 ps) using the path-integration program ZENO<sup>471</sup> with  $1.5 \times 10^5$  random paths at each configuration to achieve low uncertainty in  $D_h$ .

### 5.2.2 Quantum Mechanics

The QM calculations presented at the end of Section 5.3.2 were performed in a consistent approach to Fihey *et al.*<sup>189</sup> Initial geometries of the Au<sub>25</sub>Cys<sub>18</sub> AuNCs, with acetylated (259 atoms) or protonated amine N-termini (331 atoms), were taken from equilibrated MD simulation snapshots. Geometry optimisation of the cysteine ligands was performed by keeping the gold core frozen in the crystal structure geometry<sup>466</sup> and using the Amsterdam Density Functional (ADF) program<sup>472</sup> with the BP86 DFT exchange correlation functional and triple- $\zeta$  polarised (TZP) basis set with a frozen core approximation for Au orbitals up to 4f. Relativistic effects were accounted for using the zero-order regular approximation (ZORA),<sup>473</sup> and solvent effects were treated using the conductor-like screening model (COSMO).<sup>474</sup> This choice of QM package and theory was used because it was found that geometry optimisation in this way produces better ground-state structures.<sup>189</sup> Electrostatic potential (ESP) atomic partial charge calculations of the optimised structures were

performed using Gaussian09,<sup>469</sup> with the PBE DFT functional<sup>475</sup> and the relativistic double- $\zeta$  LANL2DZ basis set and effective core potential (ECP) for Au atoms, and the 6-31G(d) basis set for other atoms. Solvent effects were treated using the Polarizable Continuum Model (PCM).<sup>476</sup> The change in methodology to Gaussian and a smaller basis set was done to emulate the approach of Fihey *et al.*<sup>189</sup>

Single-point energy calculations are also performed in Section 5.3.5 using the linear-scaling DFT code ONETEP,<sup>477</sup> which employs a set of strictly localised non-orthogonal generalised Wannier functions (NGWFs)<sup>478</sup> to achieve accuracy that is comparable to traditional plane-wave DFT codes. The ONETEP program self-consistently minimises the total energy of a system with respect to both density kernel and NGWFs. The NGWFs are expanded in a basis set of periodic sinc (psinc) functions<sup>479</sup> and optimised *in situ* until converged to a kinetic energy cut-off. The reasons for changing to this *linear-scaling* methodology are entirely based on computational efficiency. In this section of the study, ground-state energy calculations are performed on structures containing 1816 and 3658 atoms. Without linear-scaling, even single-point calculations on systems of these sizes are extremely computationally demanding with QM codes like Gaussian and ADF.

In Section 5.3.5 three MD obtained snapshots (conformers) of Au<sub>25</sub>(SP)<sub>18</sub> (where P = CH+YGDD) with all *proximate* and *embedded* water (selections defined in Section 5.3.2) were used to conduct implicit solvent calculations, which are performed in two steps. First, open boundary conditions are used to determine the isosurface of the ground state density *in vacuo* to define a ‘solute cavity’ where implicit solvent will subsequently *not* be applied; then, the calculations are restarted applying a relative dielectric permittivity of 78.54 around the ‘solute’ that smoothly tapers to 1 at the cavity boundaries. Explicit internalised water is maintained in the structures containing a total of 1816 atoms because these molecules are deemed structural and removing them would disrupt the electrostatics. Also, from a physical and practical perspective, a dielectric cannot be locally applied in the regions where structural water is removed, i.e. within the cavity. To explore if water in the first hydration layer around the nanoclusters does more than just screen electrostatics, an implicit solvent calculation was also performed on a system where the ‘solute’ explicit contains all *hydration*, *embedded*, and *proximate water* (3658 atoms in total).

The PBE generalised-gradient approximation was used to describe exchange and correlation,<sup>475</sup> and norm-conserving pseudopotentials were employed to describe the interactions between electrons and nuclei. The Elstner damping function<sup>480</sup> was utilised to correct for dispersion interactions, however, no dispersion parameters are available for Au

in this approach therefore dispersion interactions involving gold were neglected. The Au<sub>25</sub>(SP)<sub>18</sub> (+ water) systems are centred in each supercell, and sufficient padding (20 bohr) is added the box dimensions to ensure electron density propagating out from the NGWF spheres does not interfere with the open boundaries. In all cases, NGWF radii of 9 Bohr were used for all atoms, truncation of the density kernel was applied at 1,000 Bohr, and the kinetic energy cut-off for the psinc basis was 880 eV.

## 5.3 Results

### 5.3.1 General Au<sub>25</sub>(SP)<sub>18</sub> Size, Shape and Peptide Flexibility

The ensemble of atomistic Au<sub>25</sub>(SP)<sub>18</sub> structures predicted from MD show an average  $R_g$  between 1.2–1.5 nm (Appendix Figure D.5) and a corresponding  $D_h$  of 3.2–3.9 nm (Appendix Figure D.6) in good agreement with both dynamic light scattering (Appendix Figure D.1) and small angle X-ray scattering experiments (Appendix Figure D.3). To characterise the size and shape of each ligated-AuNC system, the moment of inertia tensor for Au<sub>25</sub>(SP)<sub>18</sub> is calculated and diagonalised at every simulation frame to find the principal axes of the peptide-coated AuNCs. These principal moments of inertia are then used to represent Au<sub>25</sub>(SP)<sub>18</sub> as a “best fitting” inertia ellipsoid with an easily measurable volume and sphericity that is comparable between each system (see Appendix B.1). Average values of Au<sub>25</sub>(SP)<sub>18</sub> volume presented in Figure 5.5a highlight the emergence of a correlation between NC volume and PL intensity. With the exception of CHYGDD and CYGGDD, inflated Au<sub>25</sub>(SP)<sub>18</sub> volumes (where P = CXXGDD) are observed to complement the experimentally

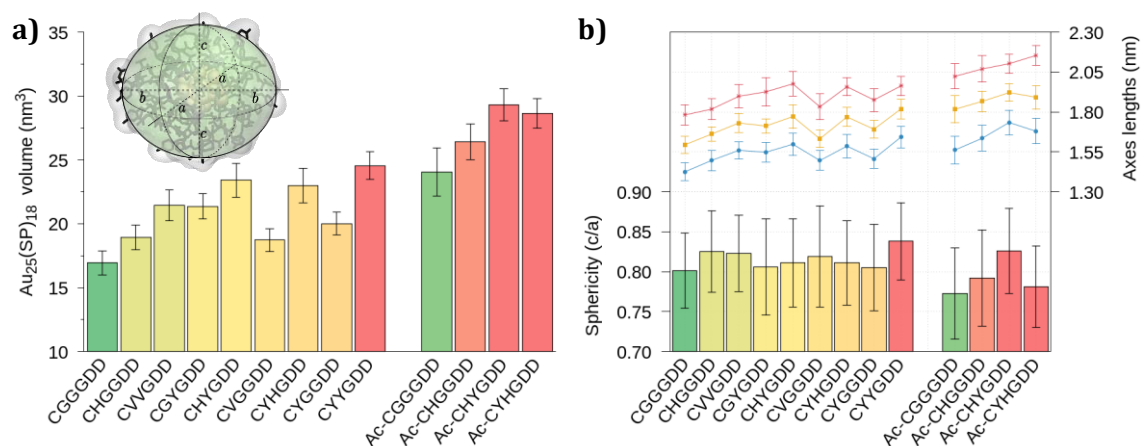


**Figure 5.5 | Average MD obtained Au<sub>25</sub>(SP)<sub>18</sub> size and shape. (a)** Au<sub>25</sub>(SP)<sub>18</sub> volumes and inset illustrating a snapshot of the CHYGDD system with the “best fitting” inertia ellipsoid superimposed. The inset suggests that AuNC size and shape is adequately described using an ellipsoid with semi-principal axes  $a$  (major),  $c$  (minor) and  $b$  (orthogonal to  $a-c$ ). **(b)** Au<sub>25</sub>(SP)<sub>18</sub> semi-axis lengths  $a$  (red),  $b$  (yellow) and  $c$  (blue) and calculated sphericity ratio ( $c/a$ ). A ratio of 1 indicates a perfect sphere and a value of 0.5 is an oblate/prolate ellipsoid, i.e. twice as long as it is wide. In both (a) and (b), error bars represent standard deviations and histogram colours reflect experimental PL intensity (see Table 4.2).

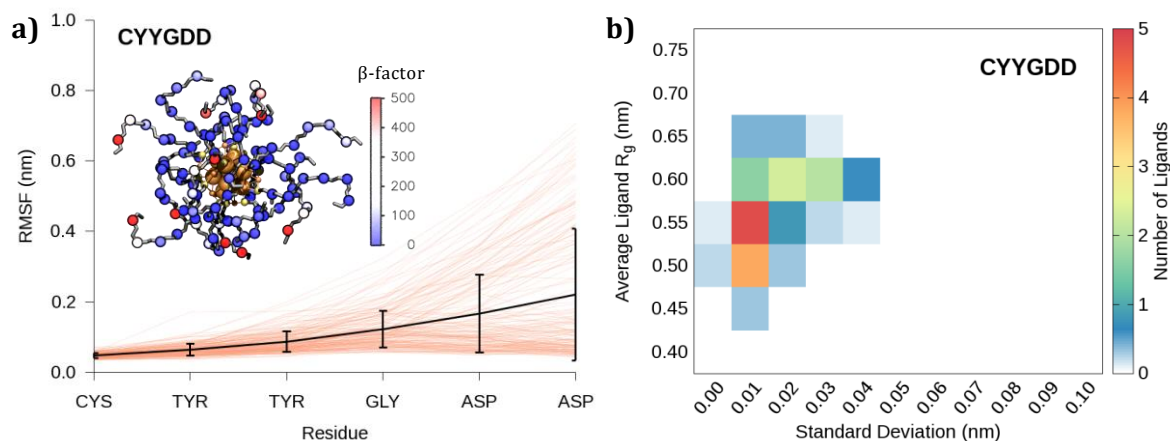


**Figure 5.6 | Peptide-ligand structuring/flexibility for an exemplar Au<sub>25</sub>(SP)<sub>18</sub> system.** (a) C $\alpha$  RMSF for each residue. The black line is the ensemble averaged RMSF with standard deviation error bars, whereas coloured lines are the RMSFs for single ligands (18 ligands per system  $\times$  10 simulations). The inset is a representative structure showing Au (orange), S (yellow), N and C backbone atoms (grey), and C $\alpha$  atoms (coloured by  $\beta$ -factor, where:  $\beta = 8\pi^2/3 \times \text{RMSF}^2$  and RMSF is in  $\text{\AA}$ ). (b) Population of average ligand  $R_g$  (y-axis) against standard deviation in that value (x-axis). Summing a given row's populations provides an average count of compact/extended peptide-chains (note the fully extended peptides have a  $R_g$  of 0.67–0.86 nm), whereas the columns reveal the flexibility of conformations.

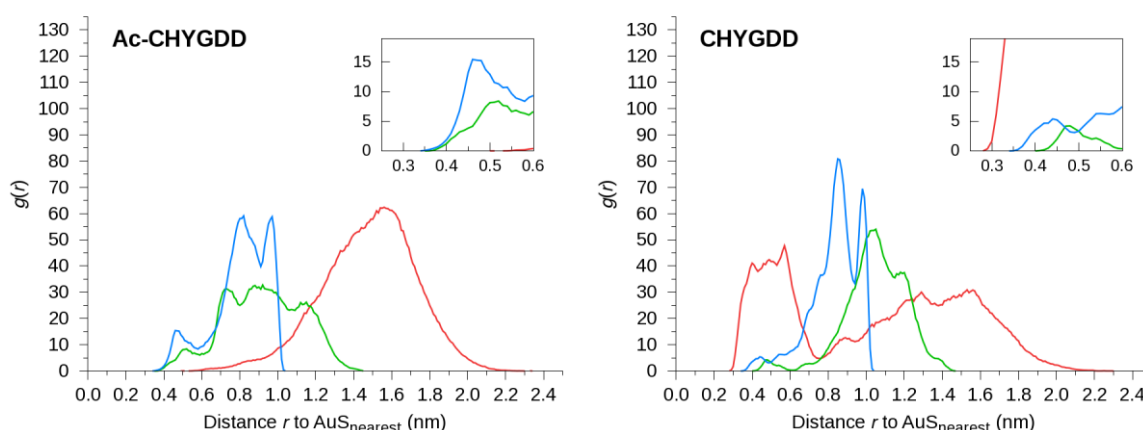
determined AuNC fluorescence performance. This volume to PL intensity relationship is also noted when comparing NCs coated with peptides that have different N-terminal caps but are otherwise identical in primary sequence. Acetyl capping of peptides (i.e. Ac-CGGGDD, Ac-CHGGDD, Ac-CHYGDD, and Ac-CYHGDD) is found to result in an overall Au<sub>25</sub>(SP)<sub>18</sub> volume increase of 24–42% (versus CGGGDD, CHGGDD, CHYGDD, and CYHGDD). No conclusive trends are observed between AuNC shape and PL, as the degree of sphericity is similar for all systems studied (Figure 5.5b).

Relative Au<sub>25</sub>(SP)<sub>18</sub> volume enlargement is associated with steric hindrance near the gold-interface, i.e. the inclusion of two bulky aromatic residues adjacent to cysteine (e.g. CHYGDD, CYHGDD and CYYGDD) or the acetylation of cysteine. These steric effects cause an increase in extended peptide chain conformations, which can be quantitatively estimated via the average  $R_g$  of individual peptide-ligands (Figure 5.6a and Appendix Figure D.7). The majority of Au<sub>25</sub>(SP)<sub>18</sub> peptides in double aromatic and acetyl-containing systems have a mean  $R_g$  larger than 0.58 nm, which is comparable in magnitude to the  $R_g$  for the fully extended peptide-ligands on Au (0.67–0.86 nm) and therefore suggests peptide elongation. In addition, the standard deviation of the average ligand  $R_g$  increases (especially when acetyl is present), implying that peptide conformations are more fluid for these systems. Similar findings regarding peptide backbone flexibility are also obtained from the average root-mean-square fluctuations (RMSF) of each residue's alpha carbon (C $\alpha$ ) atoms. While unsurprisingly the solvent exposed (and untethered) C-terminals residues show the

greatest structural variability (Figure 5.6b and Appendix Figure D.8), acetylation not only results in approximately two to six times more flexible C-terminals, it considerably increases RMSFs along the entire peptide chains (compared to uncapped peptide systems).

### 5.3.2 Effect of N-terminal Acetylation

To examine how these geometric features affect PL, it is useful to understand the distribution of different chemical groups around gold for the various systems. Since it is expected that the electronic properties of Au<sub>25</sub> are primarily dictated by the interactions between ligand atoms and the AuNC core,<sup>204</sup> specific focus is given to amino acids with chemistries that are capable of partial charge donation (TYR) or electron transfer (ASP, HIS) to the Au<sub>25</sub>S<sub>18</sub> nanocluster core as these interactions are likely to influence PL in this context.<sup>91</sup> The average distributions of *minimum* distances between the centres-of-mass of side-chain heavy-atoms (TYR: phenol, ASP: carboxylate oxygen atoms, and HIS: imidazole) relative to the nearest AuNC core atom (either gold or sulphur, AuS<sub>nearest</sub>) are presented in Figure 5.7 (and Appendix Figure D.9). For peptide sequences CGGGDD, CHGGDD, CHYGDD and CYHGDD, an average of 6–7 negatively charged ASP residues are consistently situated in close proximity ( $r < 0.5$  nm) to Au<sub>25</sub>S<sub>18</sub>, whereas for the acetyl-containing counterparts there are effectively none (Appendix Table D.1). It is postulated that the correlation between experimental fluorescence enhancement and the distancing of the C-terminal ASP residues from Au<sub>25</sub>S<sub>18</sub> suggests an unfavourable direct electron transfer from the carboxylate groups on ASP to the Au core may be quenching PL in the uncapped systems (as further discussed in Section 5.3.5). In the acetyl-capped Au<sub>25</sub>(SP)<sub>18</sub> systems, the closest registered ASP residue is an average of 0.7–1.0 nm away from the Au<sub>25</sub>S<sub>18</sub> core (Appendix



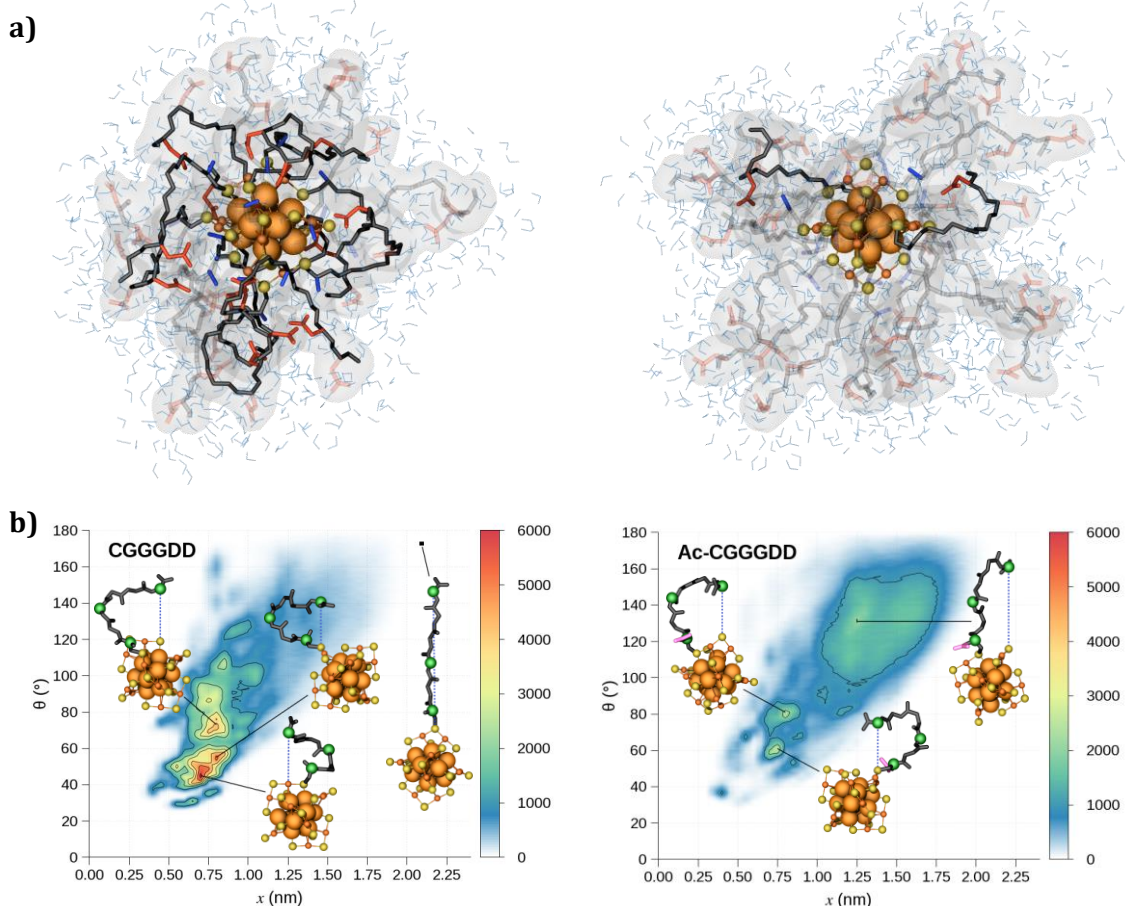
**Figure 5.7 | Effect of acetyl on the minimum distance distributions between gold and amino acids that are capable of electron charge transfer or donation of delocalised electron density.** Pairwise distribution functions,  $g(r)$ , show the minimum distances from ASP (red), TYR (green), and HIS (blue) residues to the closest Au<sub>25</sub>S<sub>18</sub> atom for CHYGDD (left) and Ac-CHYGDD (right) systems. The insets are enlarged regions to illustrate the probability of residues being within close proximity to the gold core.

Table D.1), outside of the 0.5 nm range typical for electron transfer interactions.<sup>481,482</sup> In contrast, while all systems show only minimal populations of TYR and HIS residues in Au<sub>25</sub>S<sub>18</sub> contact range, the presence of acetyl subtly encourages the locality of aromatic groups to Au<sub>25</sub>S<sub>18</sub> (see figure insets), which is believed to bolster PL (Section 5.3.3).

The dramatic increase in ASP proximity to Au<sub>25</sub>S<sub>18</sub> for peptide sequences CGGGDD, CHGGDD, CHYGDD and CYHGDD (and other non-acetyl capped peptides) results from the electrostatic attraction between positively charged NH<sub>3</sub><sup>+</sup> groups on N-terminal CYS residues and negatively charged COO<sup>-</sup> groups on C-terminal ASP residues. The strong interactions between these groups drive the C-terminal region of the peptide chains to embed close to the Au<sub>25</sub>S<sub>18</sub> core (Figure 5.8a) and leads to more compressed ligand layers, smaller Au<sub>25</sub>(SP)<sub>18</sub> volumes, and a decrease in peptide configurational entropy. For sequences CGGGDD, CHGGDD, CHYGDD and CYHGDD, a large proportion of peptides have small C-terminal to gold distances (0.5–1.0 nm) and acute backbone angles (40–60°) denoting turn-like peptide conformations, whereas for Ac-CGGGDD, Ac-CHGGDD, Ac-CHYGDD and Ac-CYHGDD, individual peptide chains assume more diverse and elongated structures (Figure 5.8b and Appendix Figure D.10).

Despite all Au<sub>25</sub>(SP)<sub>18</sub> with uncapped sequences having a smaller overall volume compared to acetyl capped systems (Figure 5.5a), water has a greater propensity to penetrate into the AuNCs' peptide layers in the absence of acetyl (see Figure 5.9a and Appendix Figure D.11). To further explore solvent structuring in the MD simulations, water molecules are categorised into 4 mutually exclusive groups: *bulk water* (outside of the 1<sup>st</sup> hydration layer), *hydration water* (present at the peptide hydration layer interface), *embedded water* (contained inside the peptide layer) and *proximate water* (within 0.4 nm of any Au<sub>25</sub>S<sub>18</sub> atom). In Figure 5.9b and c, the time-averaged distribution and number of *proximate*, *embedded*, and *hydration water* are respectively presented for the (Ac-)CYHGDD system. From both  $g(r)$  and the average number of H<sub>2</sub>O, it is clear that acetyl capping influences the amount of water present within the peptide layer, with significantly less *proximate water* in capped systems assumed to encourage AuNC PL performance (further discussed below).





**Figure 5.8 | Comparing Au<sub>25</sub>(SP)<sub>18</sub> conformations with and without acetyl.** (a) Representative structures of Au<sub>25</sub>(SP)<sub>18</sub> where P = CGGGDD (left) and Ac-CGGGDD (right) showing how the presence of N-terminal NH<sub>3</sub><sup>+</sup> groups (dark blue) encourage more compact peptide structures due to the electrostatic attraction with C-terminal COO<sup>-</sup> groups (red). (b) Density maps of peptide backbone angles as a function of C-terminal to AuS<sub>nearest</sub> distances. Inset figures are representative Au<sub>25</sub>(SP)<sub>18</sub> structures from populated “hot-spots” showing only the peptide of interest and Au<sub>25</sub>S<sub>18</sub> for clarity. Angle  $\theta$  is measured between backbone C $\alpha_1$ -C $\alpha_3$ -C $\alpha_6$  atoms (shown as green spheres and numbered from the N-terminus) and  $x$ -distances are measured from C $\alpha_6$ -AuS<sub>nearest</sub> (blue dotted lines). Contour lines are drawn around density regions in increments of 1,000 frequency and acetyl groups are shown in pink. For both (a) and (b), gold, sulphur and peptide backbones are coloured orange, yellow and black, respectively.

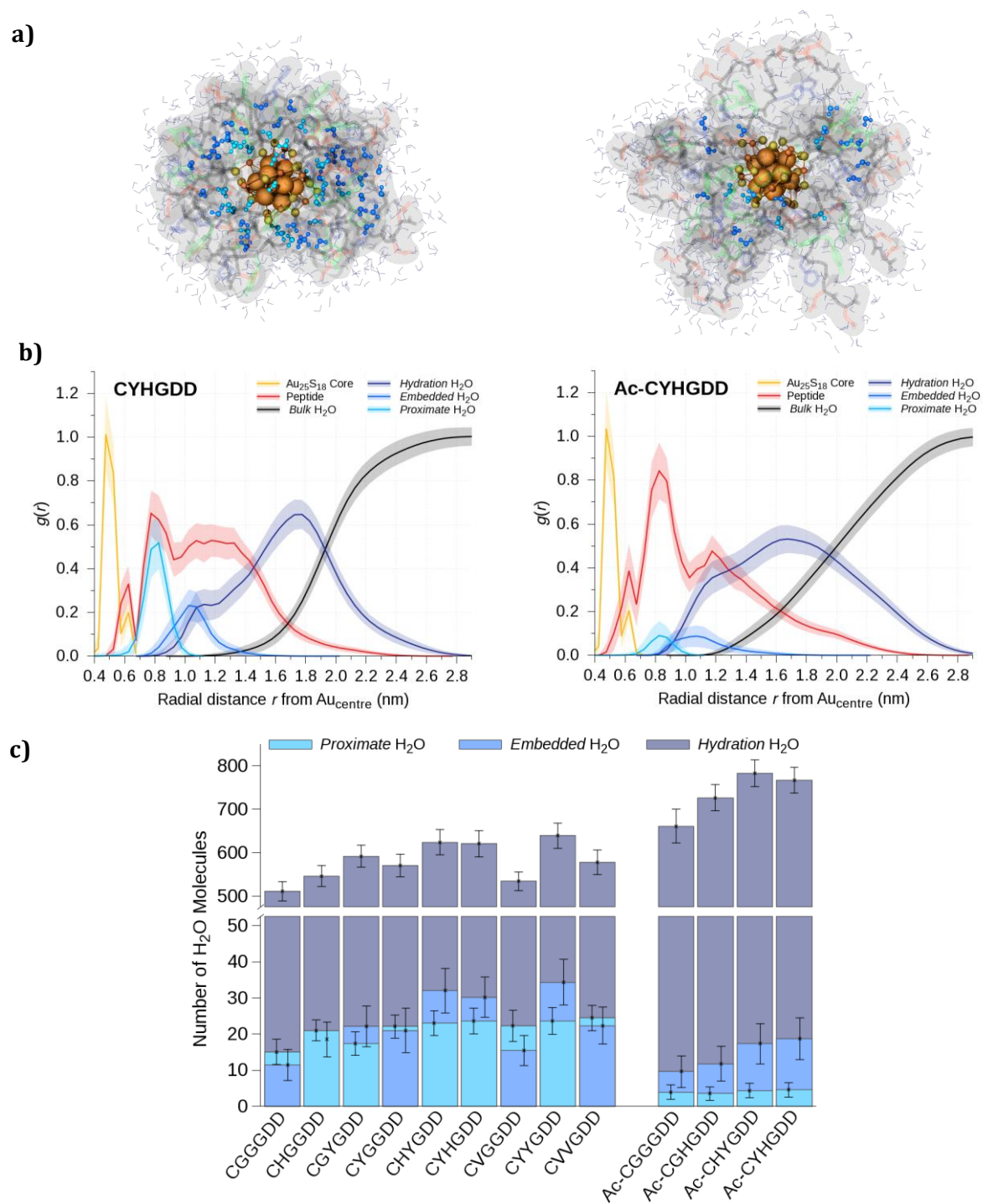


**Figure 5.9 | MD obtained water structuring around Au<sub>25</sub>(SP)<sub>18</sub>.** **(a)** Representative images of Au<sub>25</sub>(SP)<sub>18</sub> for P = CHYGGDD and P = Ac-CHYGGDD respectively. H<sub>2</sub>O molecules are coloured as defined in the legends of (b) and (c), the gold-passivating peptide vdW surface and individual chains are drawn transparently to show peptide backbones (black) as well as histidine (blue), tyrosine (green) and aspartate (red) side-chain atoms. *Bulk* water molecules and counter ions are not shown for clarity. **(b)** Radial distributions of selected atomic components relative to the central Au<sub>25</sub>(SP)<sub>18</sub> gold atom (Au<sub>centre</sub>). Plots are normalised by both radial shell volume ( $dr = 0.05$  nm) and by *bulk* water density far from the AuNCs ( $\rho_{\text{bulk-water}} = 0.100573$ ). **(c)** The average number of *proximate*, *embedded* and *hydration* H<sub>2</sub>O for each simulated system. Please note the broken *y*-axis and that error bars represent standard deviation.

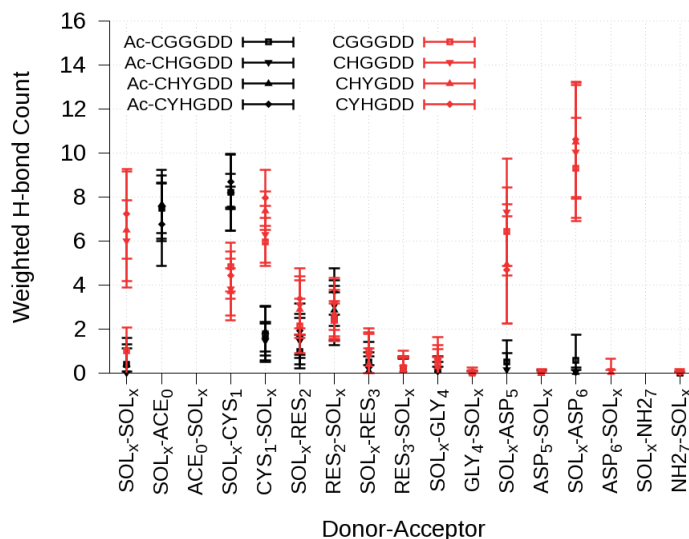


**Figure 5.10 | Average weighted number of H-bonds proximate water molecules form.** Weighted H-bonds for acetyl-capped (black) and uncapped (red) systems show differences in *proximate* water molecules' H-bond preferences. Error bars represent standard deviations and only H-bonds that appear in the MD trajectories with an occupancy > 20% are considered for the plot.

Hydrogen bond (H-bond) analysis of *proximate* water is presented in Figure 5.10 to show the ensemble-averaged, weighted hydrogen bonds that form between *proximate* H<sub>2</sub>O and other moieties over the equilibrated MD trajectories. The weighting is such that H-bonds are multiplied by their occupancy, i.e.  $2 \times 20\%$  H-bonds and  $1 \times 40\%$  H-bond both contribute 0.4 to the weighted H-bond count (y-axis). Only significant H-bonds with an occupancy > 20% are assumed contribute to the H-bond count (see Appendix Table D.2 for average weighted H-bond counts per system that have a weighting – standard deviation > 0.1). In this way the weighted H-bond populations in Figure 5.10 reflect both the *number* and *occupancy* of significant H-bonds between donor and acceptor groups.

In uncapped systems, *proximate* water molecules make a total of  $34.4 \pm 18.0$  weighted H-bonds with other species throughout the equilibrated MD simulations and of those  $\sim 40\% \pm 8\%$  are between water (donor) and aspartate carboxylate oxygen atoms (acceptor). H-bonds to cysteine molecules make up another  $\sim 32\% \pm 3\%$  ( $\sim 12\% \pm 2\%$  with water donating H-bonds to a backbone cysteine oxygen atom and  $\sim 20\% \pm 2\%$  with water acting as an acceptor from NH<sub>3</sub><sup>+</sup>), and  $\sim 13\% \pm 8\%$  are from water molecules establishing a solvent-solvent network near the gold core. In contrast, for Au<sub>25</sub>(SP)<sub>18</sub> where P = Ac-CGGGDD, Ac-CHGGDD, Ac-CHYGDD and Ac-CYHGDD, the reduction in internalised water (Figure 5.9c) leads to two-times less *proximate* H-bonds ( $17.1 \pm 8.7$ ). H-bonds between solvent and cysteine make up  $\sim 45\% \pm 4\%$  (H<sub>2</sub>O donor =  $38\% \pm 2\%$  and H<sub>2</sub>O acceptor =  $7\% \pm 4\%$ ), another  $\sim 34\% \pm 4\%$  are from interactions with carbonyl oxygen atoms on acetyl, and both solvent-aspartate and solvent-solvent H-bonds are negligible.

These differences in H-bond formation (especially the donor/acceptor predisposition of water) impact on the orientation of H<sub>2</sub>O molecules around Au<sub>25</sub>S<sub>18</sub>. In N-terminally acetyl capped system, water is primarily a H-bond donor to both cysteine and acetyl oxygen atoms and therefore the dipole moments (and hydrogen atoms) of H<sub>2</sub>O molecules are predominantly pointing towards Au<sub>25</sub>S<sub>18</sub>. For uncapped systems, dipole moments are directed away from Au<sub>25</sub>S<sub>18</sub> since water molecules accept H-bonds from cysteine (by pointing their oxygen atoms towards Au<sub>25</sub>S<sub>18</sub>), and donate H-bonds to aspartate (by directing their hydrogen atoms to the peptide–bulk water interface and consequently point their oxygen atoms to the gold core). This finding is substantiated by average *minimum* distance distributions of *proximate* water atoms relative to AuS<sub>nearest</sub> (Figure 5.11) that reveal significant water structuring with oxygen atoms favourably pointed towards Au<sub>25</sub>S<sub>18</sub> in uncapped systems. This is also apparent through careful inspection of Figure 5.9a. It should be emphasised however that the FF used in these simulations assumes no partial charge on the gold atoms and a  $-0.098$  charge on sulphur, in contrast to the positively charged gold and more negatively charged sulphur determined from QM calculations (discussed below). While there structuring of water is expected to be driven by peptide–water interactions, currently water only interfaces with Au<sub>25</sub> through vdW interactions and therefore electrostatic interactions with Au<sub>25</sub> are neglected.

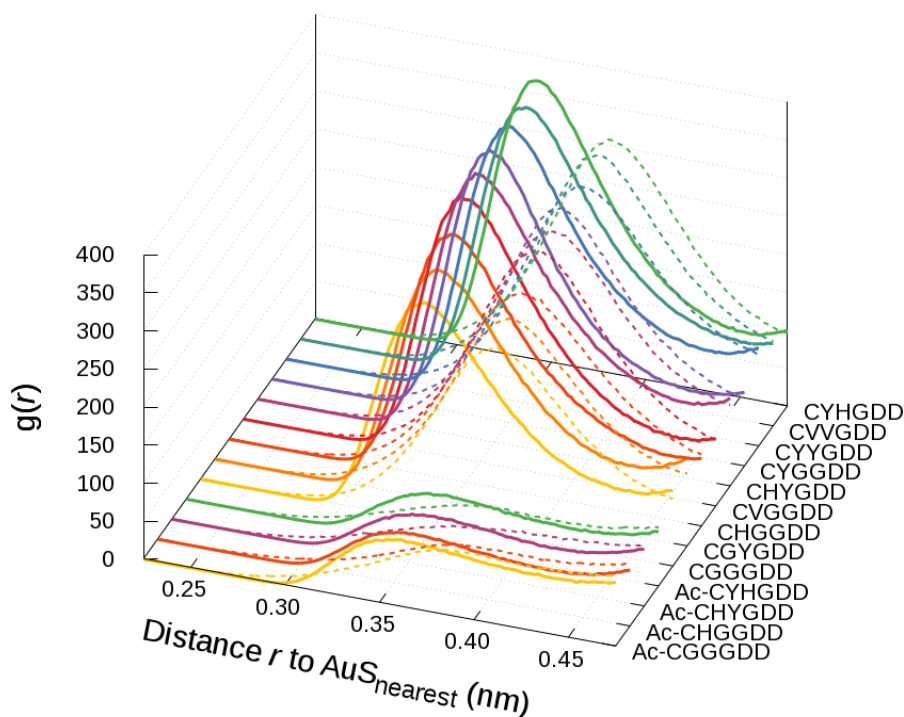


**Figure 5.11 | Average *minimum* distance distributions of *proximate* water atoms relative to AuS<sub>nearest</sub>.** Solid and dashed lines show the minimum distances of H<sub>2</sub>O oxygen and hydrogen atoms to AuS<sub>nearest</sub>, respectively. For uncapped systems, the oxygen peak at  $\sim 0.34$  nm and the hydrogen peak at  $\sim 0.38$  nm indicate that water molecules preferentially orient the oxygen atoms towards Au<sub>25</sub>S<sub>18</sub>.

**Table 5.3 | QM derived summed partial atomic charges on selected components of Au<sub>25</sub>Cys<sub>18</sub> (with acetylated or protonated amine N-termini).**

N-terminus	Au <sub>25</sub> S <sub>18</sub>	Au <sub>25</sub>	S <sub>18</sub>	Au <sub>13</sub> core	[S-(Au-S) <sub>2</sub> ] <sub>6</sub> staples
Protonated amine	-1.59	3.38	-4.97	2.35	-3.94
Acetyl	-2.50	2.84	-5.33	2.22	-4.72

Both *proximate* and *embedded* water are likely to influence the electronic density distribution around Au<sub>25</sub>S<sub>18</sub> and it is suggested that a lower presence of internalised water in acetyl systems may be directly related to enhanced fluorescence. For example, studies have shown that the electronic (and optical) properties of quantum dot fluorophores are strongly influenced by surface-adsorbed water molecules.<sup>483</sup> In uncapped systems, the lone pair of electrons on H<sub>2</sub>O oxygen atoms are facing gold and potentially able to donate partial charge to Au<sub>25</sub>S<sub>18</sub>, however at a distance of ~0.34 nm to the gold core this partial charge donation is only marginally expected to enhance fluorescence (if at all). In either case, more detailed studies are needed to test these hypotheses and explore solvent effects on Au<sub>25</sub>S<sub>18</sub>.

In addition to differences in the distribution of water molecules around Au<sub>25</sub>S<sub>18</sub>, the dynamic movement of water internalised within the Au<sub>25</sub>(SP)<sub>18</sub> NCs is also affected by the presence of acetyl (Appendix Section D.5.3). N-terminal acetylation does not drastically alter movement of *embedded* water (except perhaps in double aromatic systems, further discussed in Section 5.3.3), however, it does consistently impact on *proximate* water molecules' migration away from Au<sub>25</sub>S<sub>18</sub> (see Appendix Figure D.13). In acetyl-containing systems, the number of water molecules in the *proximate* selection quickly decays as water molecules exchange between *embedded* and *proximate* groups due to the decreased solvent H-bonding observed in these systems. This faster diffusion implies that individual water molecules in acetyl systems are less likely to significantly disrupt the electronic properties of the Au core as opposed to uncapped systems where the H<sub>2</sub>O molecule are more tightly bound.

Partial charge donation from electron-rich N-terminal acetyl groups to the gold core may be another mechanism affecting the electronic properties of the nanoclusters. Single-point QM calculations of Au<sub>25</sub>(SP)<sub>18</sub>, where P = cysteine with N-termini either uncapped (-NH<sub>3</sub><sup>+</sup>) or acetylated (-NCOCH<sub>3</sub>), reveal that electron charge distributes within the systems so that partial charges on Au<sub>25</sub>S<sub>18</sub> atoms are collectively almost a full integer more negative ( $\Delta q = -0.91$ ) when cysteine is acetyl capped versus amine terminated (Table 5.3). This is in line with the experimental findings of Wu *et al.* that suggest the donation of partial charge from ligands to core should increase fluorescence.<sup>91</sup> Approximately 60% of the charge difference is due to a reduction in the positive partial charge on the gold atoms ( $\Delta q = -0.54$ ), with ~15% from the Au<sub>13</sub> core ( $\Delta q = -0.13$ ). Analysis of atomic contributions to molecular

orbitals shows that the HOMO is mostly on the central Au atom of Au<sub>13</sub>, while the LUMO is primarily distributed across the remaining Au<sub>13</sub> atoms. This nicely correlates with previous DFT/TDDFT studies establishing that orbitals of the Au<sub>13</sub> core are responsible for all photoexcited states (and therefore optical properties) of Au<sub>25</sub>.<sup>204,458</sup> While the interplay between atomic coordinates, electron distribution, and PL intensity is complicated and difficult to unravel, these results suggest that the majority of electron density increase on the Au<sub>25</sub>S<sub>18</sub> atoms of the acetyl-capped systems (relative to the primary amine systems) occurs on the Au-S-Au “staple” atoms (~85% or  $\Delta q = -0.78$ ) and this affects the PL arising from excitations involving molecular orbitals centred on the Au<sub>13</sub> core.

### 5.3.3 Increasing Peptide Hydrophobicity/Aromaticity

The hydrophobicity/aromaticity of the peptide sequences empirically impacts on the AuNCs' PL (Figure 5.2). In the MD simulations, peptide sequences with aromatic residues promote enlarged AuNC volume (Figure 5.5a),  $R_g$  (Appendix Figure D.5) and  $D_h$  (Appendix Figure D.6) due to steric effects caused by increased numbers of bulky groups close to the gold core. For example, the  $D_h$  of AuNCs is calculated to be 3.21 nm, 3.48 nm, 3.60 nm, and 3.68 nm for CGGGDD, CVVGDD, CHYGDD and CYYGDD, where  $D_h$  increases as amino acid side groups become more hydrophobic and aromatic. This effect is also confirmed by small angle X-ray scattering (SAXS), with experimental  $R_g$  trends (Appendix Figure D.3) supporting the simulation results and indicating a more expanded nature for hydrophobic/aromatic peptide layers of CVVGDD (1.13 nm), CYHGDD (1.13 nm), and CYYGDD (1.10 nm) compared to that of CGGGDD (1.01 nm). While AuNC polydispersity and peptide-shell valency will likely influence the apparent empirical configurations, the expanded peptide structures on the Au surface generally indicate longer peptide C-terminal–Au<sub>25</sub>S<sub>18</sub> distances. This however does not necessarily mean aspartate residues (that potentially quench PL, see Section 5.3.5) are distanced from Au<sub>25</sub>S<sub>18</sub> as peptide hydrophobicity increases (Appendix Table D.1). Instead, it is believed that aromatic groups allow for a higher degree of delocalised electron density to be provided to the gold core, through the proximity of moieties such as imidazole and phenol (Appendix Figure D.9 and Appendix Table D.1), and this is what is expected to strengthen the fluorescence intensity, as has been previously proposed.<sup>91</sup>

While it is also observed that aromaticity/hydrophobicity slightly increases the number of *proximate* and *embedded* water molecules (Figure 5.9c), this does not seem to be directly related to AuNC PL however water may inadvertently be screening negatively charged residues from interacting with Au<sub>25</sub>S<sub>18</sub>. From Appendix Figure D.13 it is also noted that although the dynamic movement of *proximate* water in NH<sub>3</sub><sup>+</sup> N-terminated systems shows no obvious dependence on sequence (within the standard deviation of the decay plots),

there does appear to be an emergent trend that as hydrophobicity/aromaticity increases the movement of *embedded* water into and out of the peptide layers is hindered. This is an interesting observation that is potentially caused by trapping of water inside hydrophobic cages, or may be an artefact related to how the models were built. Curiously, acetyl capping of CHYGDD and CYHGDD seems to disrupt this reduced water mobility indicating that hydrogen bonding difference in these systems (Appendix Table D.2) may be playing a role in causing this. In any case, to properly elucidate the mechanisms for these phenomena and the potential consequences they have on AuNC PL further investigations are needed.

### 5.3.4 Influence of Histidine Protonation

It was initially thought that titratable histidine groups may be responsible for the pH responsive fluorescence the peptide-coated AuNCs exhibit. Since imidazole has a pKa ~6–7, a pH-induced change in HIS protonation state (Figure 5.12) will likely result in a pH responsive interaction with Au<sub>25</sub>S<sub>18</sub> that ultimately influences PL. In particular, it was hypothesised that at higher pH (> 7) de-protonated HIS may be involved in photoinduced electron transfer (PET) with the Au<sub>25</sub>S<sub>18</sub> fluorophore to weaken PL while at low pH (< 6), PET inhibition is caused by imidazole protonation and stronger fluorescence emerges. While this process is known to quench fluorescence,<sup>484</sup> the empirical evidence shows that pH responsive AuNC PL can be obtained with capping peptides that do not contain HIS (Figure 5.3). Although HIS PET may not be a primary PL influencer, the role of HIS protonation onto the properties of Au<sub>25</sub>(SP)<sub>18</sub> are still explored through MD.

The main physical difference between the protonated and deprotonated histidine systems is the introduction of an additional positive charge on each peptide ligand (i.e. a further +18 per system), which affects the properties of the systems in several ways. Supplementary electrostatic attractions serve to bring the negatively charged C-termini of the peptides closer to the gold core (Appendix Table D.1 and Appendix Figure D.9), resulting in more compact (Appendix Figure D.6), less mobile (Appendix Figure D.8) peptide layers. A large increase in the number of turn-like peptide conformations is observed in the ensemble of MD structures (Appendix Figure D.10) and the increase in charge–charge proximity draws

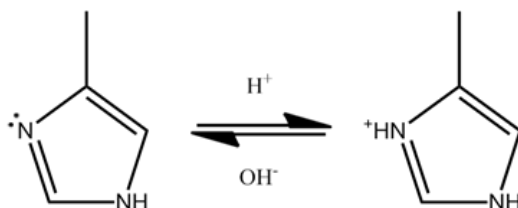


**Figure 5.12 | The pH dependent (de)protonation of histidine residues in solution.** The standard pKa for this process is ~6–7, therefore at pH 7.5 the majority of histidine residues will be deprotonated and at pH 5.5 almost all of the residues will be protonated.

more water to internalise close to Au<sub>25</sub>S<sub>18</sub>, especially when histidine is adjacent to cysteine. For example, compare the *proximate* water peaks (Ac-)CHGGDD and (Ac-)CHYGDD to their protonated counterparts in Appendix Figure D.11. In addition to these effects, the location of the histidine residues themselves become more distant from the gold core to minimise peptide–peptide electrostatic repulsions, particularly between NH<sub>3</sub><sup>+</sup> and HIS<sup>+</sup> moieties in non-acetylated systems (Appendix Table D.1).

While each of these findings can be postulated to decrease PL when histidine is protonated, the empirical evidence is on the contrary. This could imply that if HIS is involved in PET when the residues are deprotonated (pH 7.5), the hindrance of PET at low pH may have a greater outcome on enhancing the PL than the collective abovementioned effects. More detailed investigations are of course needed to confirm/dispute this speculation.

### 5.3.5 Hypothesis for Aspartic Acid PL Quenching

To rationalise the correlation between aspartate residue distance to Au<sub>25</sub>S<sub>18</sub> and the reduction of experimental fluorescence, investigations are pursued to elucidate motivators behind this effect. It is hypothesised that PET<sup>484</sup> between the carboxylate groups on aspartate residues and the AuNC core disrupts the PL of Au<sub>25</sub>S<sub>18</sub> (especially in systems that are not acetylated). Previous experimental and computational studies have shown that carboxylate groups are capable of photoinduced single-electron transfer to silver<sup>485,486</sup> and other materials.<sup>487-489</sup> As a first step to explore this hypothesis further, the energy required to extract single carboxylate electrons from aspartate residues is estimated using a classical *a posteriori* approach (see Appendix Section B.2).

The removal of an electron charge distributed equally on the two carboxylate oxygen atoms of an aspartate is considered to be energetically associated to the electrostatic potential acting on the given residue, which is caused by collective contributions from all other charges in the system. Although configurations are unable to respond to charge dissociation in this approach, the change in total potential energy after electron removal is useful to simply estimate how electrostatically and energetically favourable aspartate ionisation is. The smaller the energy difference (energetic penalty), the more likely it is assumed that an electron can be ejected/transferred. In addition, for charge transfer to occur it is generally required for the electron donor (ASP) and electron acceptor (Au<sub>25</sub>S<sub>18</sub>) to be in close contact range (< 0.5 nm).<sup>482</sup> Consequently, for an electron to migrate from aspartate to gold and encourage PL quenching, both energetic and geometric conditions must be met.

Density maps showing the classical electrostatic potential energy cost for electron removal, as a function of minimum carboxylate oxygen distance to Au<sub>25</sub>S<sub>18</sub>, are given in Appendix



Figure D.14. For analysed systems, i.e. Au<sub>25</sub>(SP)<sub>18</sub> where P = (Ac-)CGGGDD, (Ac-)CH(+)YGGD, CYH(+)GDD, CVVGDD, CYYGDD, aspartate residues are found to be  $\sim 650$  kJ·mol<sup>-1</sup> more stable before their carboxylate partial charges are perturbed (Appendix Table D.3). In other words, it costs  $\sim 650$  kJ·mol<sup>-1</sup> for an aspartate residue to forfeit an electron regardless of its geometric location in the peptide layer. From Figure 5.13 and Appendix Table D.3 it is noted that in non-acetyl systems a moderate amount ( $\sim 2$ – $3\%$ ) of aspartate residues are both within electron transfer proximity ( $< 0.5$  nm) of Au<sub>25</sub>S<sub>18</sub> and exhibit a lower energy requirement ( $< 600$  kJ·mol<sup>-1</sup>) to lose an electron. In contrast, there are no ASP residues in this range for acetyl systems, except for Ac-CGGGDD which has a relative population of  $\sim 0.3\%$ . These classical results indicate that the absence of acetyl increases the number of states where the local electrostatic environment around aspartate better facilitates electron dissociation and this may inadvertently promote electron transfer to the gold core.

Single-point, spin-polarised, explicit/implicit solvent QM calculations are performed to further test the hypothesis that aspartate may be disrupting fluorescence. The linear-scaling density function theory code ONETEP is used for this purpose with the aim of estimating the

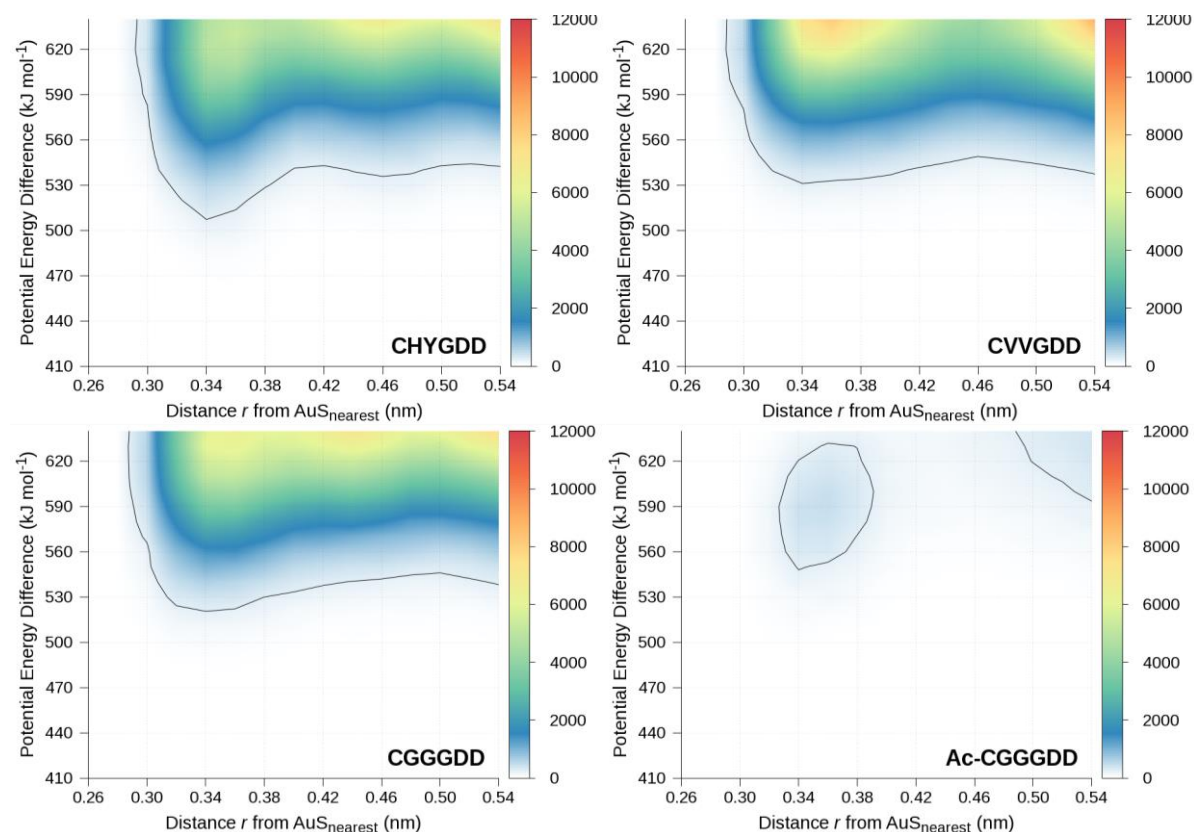


**Figure 5.13 | Classical electrostatic potential cost for removal of an aspartate carboxylate electron, as a function of ASP–Au<sub>25</sub>S<sub>18</sub> distance.** Selected plots are shown with ASP–Au<sub>25</sub>S<sub>18</sub> separations  $< 0.54$  nm and energetic penalties  $< 650$  kJ·mol<sup>-1</sup>. Contour lines are drawn around regions  $> 200$  in population and highlight that aspartate residues close to the gold core may forfeit an electron with a reduced energetic cost (compared to the average 650 kJ·mol<sup>-1</sup>).

locations of, and the energy gaps between, the frontier orbitals of the system to verify if electron transfer is theoretically viable. Atomistic structures inputted to these calculations are equilibrated MD configurations that explicitly contain gold (25 atoms), peptide (1,530 atoms), *embedded*, and *proximate* water (~261 atoms), and an implicit solvent continuum is also employed to represent *hydration* and *bulk* water.

Converged ONETEP simulations have currently been achieved for three conformers (labelled **I–III**) of Au<sub>25</sub>(SP)<sub>18</sub>, where P = CH<sup>+</sup>YGDD, and preliminary analysis of these results is promising. The findings suggest that the majority of HOMO/LUMO orbitals are localised on the Au<sub>25</sub>S<sub>18</sub> core (see Appendix D.6.2) in agreement with other theoretical studies<sup>490</sup> and the calculated density of states remains relatively unchanged between the three conformers (Appendix Figure D.15). The Mulliken partial charges on different atomic components of Au<sub>25</sub>S<sub>18</sub> (Appendix Table D.4) on the other hand are moderately sensitive to changes in peptide conformation and vary quite drastically from the atomic partial charges calculated for Au<sub>25</sub>Cys<sub>18</sub> in Table 5.3. This signifies that careful consideration is needed if deducing trends from partial charges derived from a single/few calculation(s) and more statistics are likely required to draw anything conclusive.

Given that the peptide-coated AuNCs in this project are designed to be completely water soluble and they are intended to undergo their desired biological tasks in an aqueous environment, it is necessary to incorporate as much explicit water in the QM calculations as feasible to ensure a correct physical description of the system is emulated. To establish if an increase in explicitly represented solvent atoms impacts the computed results and therefore the escalated computational expense is justified, a single point calculation of conformer **III** was also performed with all *hydration* water atoms included (denoted as conformer **III'**) leading to a total system size of 3,658 atoms. Comparing the results between **III** and **III'** reveals that more explicit water does not significantly alter the partial charge distribution on Au<sub>25</sub>S<sub>18</sub> (Appendix Table D.4), however, there is an obvious shift in the local density of states near the HOMO–LUMO gap (Appendix Figure D.15). This indicates that solvent molecules (and their interactions) are likely to be essential for the optical properties of the system and it is thus advisable to include the first hydration shell of water (at least) in the QM calculations to ensure solvent effects on the system are reasonably approximated.

While it is acknowledged that ground-state calculations cannot accurately predict optical emission and electron transfer characteristics that are inherently excited-state properties, ground-state orbital locations (and energies) may still prove useful to infer first-order approximations about these phenomena. For example, it can be assumed that

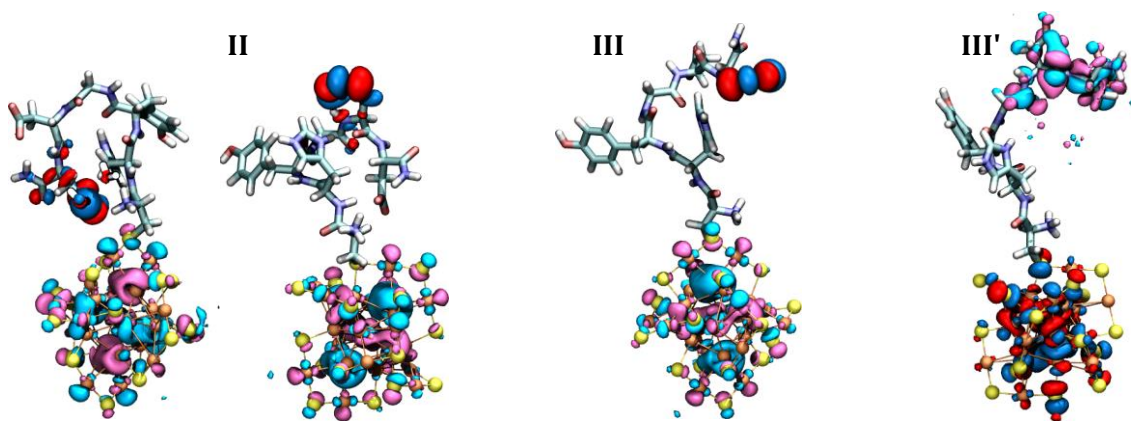


**Figure 5.14 | Selected frontier orbitals on different conformers of Au<sub>25</sub>(SP)<sub>18</sub> (where P = CH+YGDD) calculated using the ONETEP program.** The images suggest that the proposed quenching of PL by ASP–Au<sub>25</sub>S<sub>18</sub> electron transfer is conceivable since occupied (red/blue) and unoccupied (pink/cyan) orbitals separated by an appropriate energy difference ( $\sim 1.78$ – $1.89$  eV or  $\sim 655$ – $695$  nm) consistently appear on the groups of interest (other atoms hidden). Isosurfaces = 0.02.

photoexcitation of an electron will likely result in a transition from a HOMO to a LUMO, therefore knowing the original location of the ground-state orbitals (especially the HOMO that is to be excited) is assumed to be beneficial for deducing which atoms are involved in this photoinduced transition. Since Au<sub>25</sub> fluorescence is produced by Au–Au electron interactions,<sup>490</sup> processes (such as electron transfer) that disrupt these interactions are expected to reduce PL. If an orbital on Au<sub>25</sub>S<sub>18</sub> is at precisely the right energy separation to an opposite occupancy orbital not located on the gold core, photoexcitation may cause charge transfer to transpire between these two orbitals and lead to a non-radiative, fluorescence quenching transition. In particular, if this process competes in energy to the peak emission wavelength of the system (i.e.  $\sim 675$  nm, see Appendix Figure D.2), this could hypothetically contend with the natural electron transitions in Au<sub>25</sub>.

Molecular orbital analysis (Appendix Tables D.5–D.8) reveals that while most HOMO (and preceding orbitals, abbreviated as HOMO+X) and LUMO (and succeeding orbitals, abbreviated as LUMO–X) pairs with an energy difference corresponding to a wavelength of  $675 \pm 15$  nm are exclusively on the Au<sub>25</sub>S<sub>18</sub> core, there are some exceptions. Interestingly, these excepted orbitals are situated on aspartate residues and their corresponding orbitals are localised on the gold core (Figure 5.14). This demonstrates that aspartate quenching through electron transfer may indeed be viable, however further QM exploration (especially with different systems and higher levels of theory, e.g. TDDFT) is needed to verify this.

## 5.4 Discussion and Conclusions

The local chemical environment near the gold core is crucial for quenching or enhancing AuNC PL. Through the observed correlations between the PL performance of the peptide-

functionalised AuNCs and the structure of the peptide layers, enhancement of the AuNC fluorescence intensity in these systems is proposed to be achieved through one or more of the following approaches. (1) Acetyl capping of N-terminal amine groups synergistically enhances AuNC PL performance via a variety of mechanisms (Section 5.3.2) including: replacement of electron-withdrawing groups with partial electron density donating moieties in the vicinity of Au<sub>25</sub>S<sub>18</sub>; removal of the electrostatic attraction between the peptide termini, which increases the thickness of the coating layer and distances the negative peptide C-termini from gold; and reducing the propensity for water to penetrate into the peptide layers, while enabling its free movement to escape proximity of the Au<sub>25</sub>S<sub>18</sub>, where PL can be adversely affected. (2) Introduction of hydrophobic/aromatic residues in the peptide sequences (Section 5.3.3) provides delocalised electrons for partial charge donation from the ligands to the Au core. (3) Lowering solution pH appears to affect the protonation state of the N-terminal amine groups, however due to the scope of this work, this has not been computationally explored here.

In relation to point (3), deprotonated amine groups close to the gold surface are considered to be associated with weaker natural PL emission from the Au<sub>25</sub> clusters in light of the empirical evidence. Since HIS replacement does not affect the pH-induced difference in PL observed (Figure 5.3), it is suggested that pH sensitivity is due to a change in the protonation state of N-terminal amine groups, which have previously been shown to have pKa values as high as 9.1 or as low as 6.8, with an average value of  $\sim 7.7 \pm 0.5$ .<sup>491</sup> At pH 7.5,  $\sim 50\%$  of N-terminal amines are deprotonated and can transfer electrons to Au through the nitrogen lone pair, as has been shown between deprotonated amines and fullerenes.<sup>492</sup> When solution pH is decreased to 5.5, only  $\sim 1\%$  of amines remain deprotonated thus eliminating the possibility of NH<sub>2</sub> donating electrons to Au. In other words, at pH 7.5 (in the absence of acetyl), neutral N-terminal amines can quench PL through PET whereas at pH 5.5, although electron-withdrawing NH<sub>3</sub><sup>+</sup> groups close to Au are unfavorable for fluorescence,<sup>91</sup> the denial of PET quenching appears to outweigh this.

Capping with acetyl (at any pH) eliminates PET quenching, removes electron-withdrawing positive charges from close proximity to Au, and introduces electron density donating groups. The amide group on cysteine (instead of amine) from acetylation stabilises the lone pair on nitrogen through electron delocalisation to sufficiently disfavor electron transfer from nitrogen to gold. Instead, acetyl promotes partial charge donation through the carbonyl oxygen atoms, which is another proposed PL enhancing effect (Figure 5.15). This is in line with strategies reported in literature of intensifying Au<sub>25</sub> fluorescent yield through increasing the direct donation of delocalised electrons (or reducing the electron-

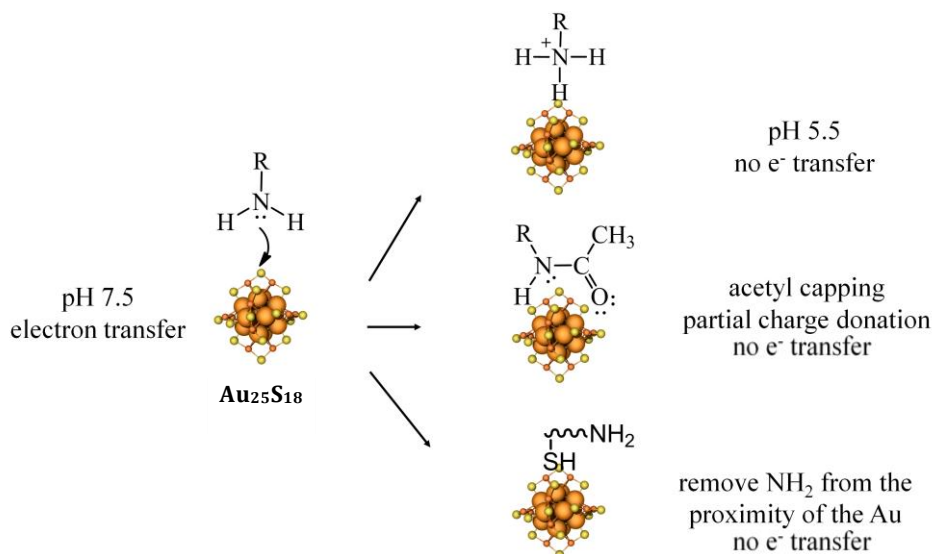


**Figure 5.15 | Peptide-Au<sub>25</sub>S<sub>18</sub> interactions that alter photoluminescence.** The proposed quenching mechanism (left) can be nullified to generate PL AuNCs via one or more of the strategies displayed on the right: (top) lowering solution pH to protonate amine at the N-terminus; (middle) replacing N-terminal amine via acetylation; (bottom) repositioning the free amine away from the Au surface by altering the Au-Cys location.

withdrawing capacity) from the ligands to the metal core.<sup>91</sup> In addition, PL enhancement of AuNCs can be achieved by “geographic” removal of free amine, i.e. removing it from the close proximity to the gold core by modifying the sequence order to change the Au-Cys bond location, e.g. DGYCGD (see Table 5.1 and Figure 5.2b). It must also be noted that interactions such as  $\pi$ - $\pi$ , cation- $\pi$ , and water mediated charge shielding may play a significant role in enhancing fluorescence and mitigating quenching.

In conclusion, this chapter has provided a multiscale theoretical insight into the functional physicochemical interface of different peptide coatings on AuNCs intended for cellular imaging applications. In conjunction with experiment, key design principles for the general enhancement of AuNC photoluminescence are proposed. First, groups that can directly electron transfer to the gold core such as carboxylates and deprotonated amines should be kept as far from the gold as possible. This can be accomplished by capping amine groups on the gold-anchoring cysteine residues with acetyl, by designing the ligand attachment point so that amine groups are inherently removed from proximity of the Au core, and/or by lowering solution pH to ensure complete protonation of N-terminal amines. Second, groups that can donate a *partial* electron density to the gold core, such as tyrosine and acetyl, should be kept as *close* to the gold as possible. The findings of this work contribute to the overall understanding of the molecular mechanisms of PL AuNCs and facilitate a rational approach to design biocompatible AuNCs for broad biomedical applications.

## Chapter 6:

# Alkanethiol-Functionalised Au<sub>25</sub> Nanoclusters

In this chapter, classical molecular dynamics is used to examine the properties of octanethiol-protected Au<sub>25</sub> nanoclusters. These small hydrophobic nanostructures form part of a novel gold-silica composite material called a “quantum rattle” that has theranostic potential.<sup>21</sup> The findings of this work reveal that the gold nanoclusters exhibit significant structural and dynamic differences in water and ethanol, which is information that assists in explaining performance issues these materials encounter when being used for drug delivery applications. This research is conducted in collaboration with the biomaterials engineering team of Prof. Molly M. Stevens at Imperial College London to whom due acknowledgment is given, especially Dr Mathew Hembury and Dr Ciro Chiappini, for all empirical results presented (Section 6.1.1).

---

## 6.1 Introduction

Composite nanoparticles are a relatively new class of material that combine multiple individual nanostructures into a single multimodal system. The properties of the separate constituent components in these assemblies integrate to form efficient, multifunctional, and often hierarchical materials that show great promise for theranostic applications.<sup>33,493,494</sup> Composite nanoparticles based on mesoporous silica<sup>495</sup> (MS) are extensively being studied since MS has a large surface area, tuneable size and porosity, low cytotoxicity, and is easy to functionalise through silane chemistry. These features are attractive for both the loading of water-insoluble biomedical agents, and their transport/delivery *in vivo*.<sup>496-500</sup> In addition, MS can be synthesised to host gold nanoparticles (AuNPs) and nanoclusters (AuNCs), depending on its porosity and internal cavities.<sup>501-503</sup> This imparts increased functionality to the constructs based on the properties of nano-gold, such as enabling photothermal therapy and imaging modalities (see Section 1.4), and it facilitates stimulus responsive releasing of drugs trapped inside MS pores by gold “gatekeepers”.<sup>504</sup> Furthermore, gold nanostructures coated with hydrophobic ligands, such as alkanethiols, enhance the drug-carrying capacity, loading efficiency, and prolonged/controlled release of drug payloads in these systems.<sup>505</sup>

Alkanethiol-gold nanomaterials, especially self-assembled monolayers (SAMs) on planar gold, have been a subject of intense experimental and theoretical research.<sup>54,79,506</sup> As such, there is a huge cohort of computational studies focusing on: the formation<sup>359,507-513</sup> and

characterisation<sup>173,211,514-518</sup> of alkanethiol-gold SAMs, including those with mixed-monolayers;<sup>279,519-522</sup> the mechanisms for alkanethiol-AuNPs to spontaneously interact/aggregate,<sup>356,380,523-533</sup> or to permeate between different mediums, e.g. from aqueous solution to lipid bilayer<sup>269,273,275,280-283,534-536</sup> or organic electrolyte;<sup>537</sup> the effect of radiation on alkanethiol-gold SAMs;<sup>245,538-540</sup> the interactions of biomolecules with alkanethiol-SAM-gold structures;<sup>263,265,266,368,541-550</sup> as well as, other fascinating alkanethiol-gold systems.<sup>551-554</sup> In the interest of brevity these will not be summarised here, however, computational research that is directly relevant to this chapter will be mentioned and discussed in the context of the presented results.

### 6.1.1 Experimental Project Design and Computational Aims

A novel *in vivo* and *in vitro* hybrid theranostic material has recently been realised by innovatively incorporating different sized gold nanostructures inside a hollow MS vessel (Figure 6.1). This gold-silica “quantum rattle” (QR) exploits the biocompatibility of MS to host bioactive molecules (e.g. the chemotherapy drug Doxorubicin, DOX) alongside fluorescent AuNCs (< 2 nm diameter) and photothermal AuNPs (~7.3 nm in diameter) in order to synergistically provide multimodal imaging and therapy for tumour treatment.<sup>21</sup> The gold nanomaterials are coated by 1-octanethiol (S(CH<sub>2</sub>)<sub>7</sub>CH<sub>3</sub> or SC<sub>8</sub>H<sub>17</sub>) and contained within the MS via an *in situ* synthesis protocol. It is proposed that the larger AuNPs form in the internal cavities whereas the smaller AuNCs nucleate inside the MS pores. The dimensions of the compartments within the ~150 nm (total diameter) QRs are well defined, with cylindrical-like MS pores being ~25 nm in length and ~2.5 nm in diameter, while the internal cavities are ~100 nm in diameter.

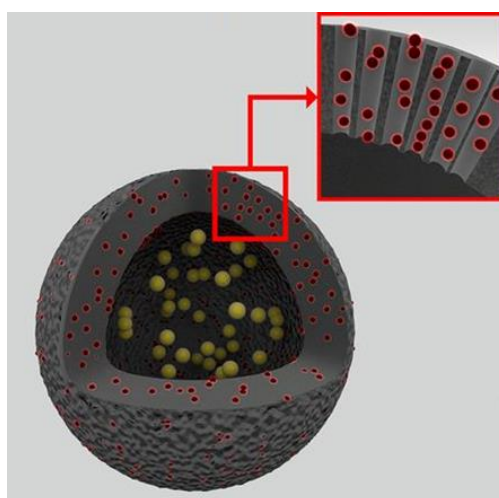


**Figure 6.1 | Schematic depiction of the multimodal “quantum rattles” illustrating the constituent components in the constructs.** The quantum rattles are composed of hollow mesoporous silica shells (grey) that host AuNCs (red) inside their mesopores and gold nanoparticles AuNPs (yellow) inside their macrocavity. Adapted with permission.<sup>21</sup> 2015, National Academy of Sciences.

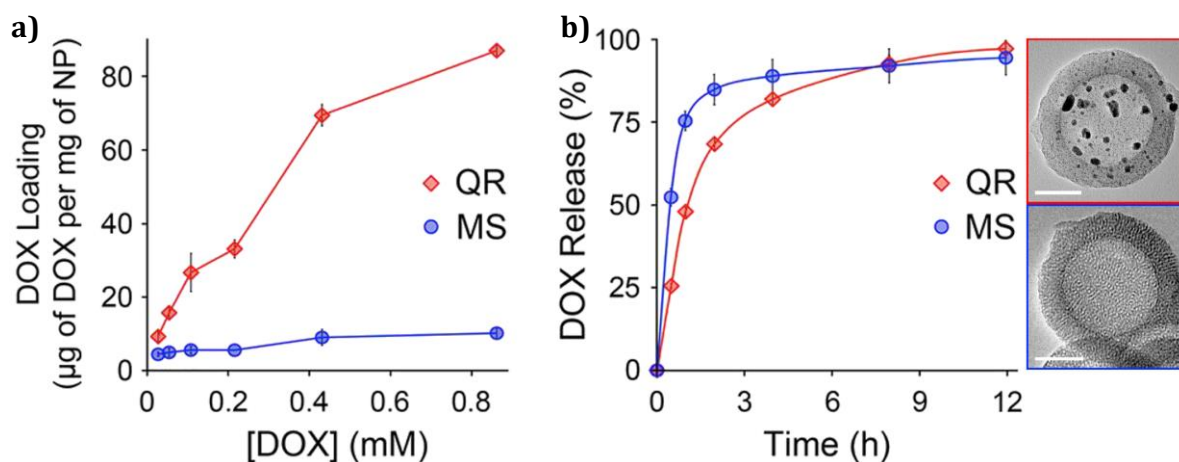


**Figure 6.2 | Hydrophobic drug loading and release profiles comparing nanostructures with and without gold constituents.** (a) The doxorubicin (DOX) loading efficiencies for the gold-containing quantum rattles (QR, red) is up to nine-fold larger compared to the gold-deficient mesoporous silica (MS, blue). The amount of DOX uptake (*y*-axis) is plotted against the DOX concentration in the aqueous loading solution (*x*-axis). (b) Drug release (in PBS) shows that the QRs modulate DOX release over a 12 hr period whereas for MS, the DOX release plateaus after ~4 hrs. (Inset) Transmission electron micrographs of QR and MS. Scale bars = 50 nm. Adapted with permission.<sup>21</sup> 2015, National Academy of Sciences.

Two interesting experimental observations emerge from these systems that require further clarification through molecular-level insight. (1) When the (drug-free) QRs are transferred to ethanol solvent, the AuNCs easily and readily evacuate from the silica pores, however, if the QRs are in an aqueous solution the escape of the AuNCs is considerably hindered. (2) There is a stark difference in the drug loading and release profiles of the QR and MS systems (Figure 6.2). The QRs show up to nine-fold increase in the concentration of loaded DOX compared to hollow MS (Figure 6.2a) signifying that AuNPs enhance hydrophobic DOX drug-carrying capacity. Then, when the DOX-loaded constructs are placed in PBS solution, the presence of AuNC “gatekeepers” in the QR pores, which are absent in the plain MS, modulate the diffusion of DOX and prolong the release of drug over time (Figure 6.2b).

This chapter is primarily concerned with using MD simulations to explore how different solvent environments affect the properties of Au<sub>25</sub>(SC<sub>8</sub>H<sub>17</sub>)<sub>18</sub>. Section 6.2 outlines the computational details employed in this study. The following Section 6.3 presents results that highlight the structural variability octanethiol-coated AuNCs exhibit when solvated in water and ethanol solutions. AuNC properties such as overall shape, structure, and bonding preferences are assessed. These results are then discussed in Section 6.4 to correlate pore occupation (abovementioned experimental observation 1) with a proposed steric-kinetic driving force. Comments are also made regarding future work, the molecular nature of DOX, and DOX–Au<sub>25</sub>(SC<sub>8</sub>H<sub>17</sub>)<sub>18</sub> interactions that are likely to control the drug’s loading and release kinetics (experimental observation 2). Finally, closing remarks are given.



## 6.2 Computational details

The computational approach taken is analogous to that described in Chapter 5. First, the octanethiolate–Au<sub>25</sub> clusters, Au<sub>25</sub>(SC<sub>8</sub>H<sub>17</sub>)<sub>18</sub>, were constructed in the Discovery Studio 3.5 Visualizer software<sup>555</sup> by attaching all ligands in extended conformations and equidistant on the crystal structure<sup>466</sup> model of Au<sub>25</sub>(SR)<sub>18</sub>. The nanoparticle complex was then placed in a periodic cubic box of lattice constant  $\sim 5.9$  nm and solvated with either 6693 water molecules (Figure 6.3a) or 1928 ethanol molecules (Figure 6.3b). Energy minimisation was carried out using the steepest decent algorithm then followed by 1 ns of position restrained MD to equilibrate the solvent around the gold–ligand nanoclusters at a temperature of 300 K and pressure of 1 atm. Upon removing position restraints,  $3 \times 100$  ns *NPT* simulations with different starting velocities were performed in both water and ethanol solvents.

The Nosé–Hoover<sup>394,395</sup> and Parrinello–Rahman<sup>399</sup> approaches were applied to control the temperature and pressure. A time step of 2 fs was used throughout the computations by utilising the LINCS algorithm<sup>402</sup> to convert all bonds to constraints, and frames were output to a trajectory file every 2 ps. The all-atom AMBER99SB-ILDN force field (FF)<sup>467</sup> was used to represent the organic thiolate ligands (SC<sub>8</sub>H<sub>17</sub>) with atomic partial charges for the ligands explicitly parameterised using Gaussian09<sup>469</sup> (see Appendix Section A.2). The TIP3P model was used for water<sup>468</sup> and general amber FF parameters for liquid ethanol.<sup>556,557</sup> The Au–organic Lennard Jones potentials employed are identical to those in Chapter 5 and were adopted from a FF<sup>221</sup> parameterised for similar monolayer-protected gold nanoclusters that assumes no explicit partial charges on the Au. The cutoff for Lennard–Jones interactions and the real-space part of the Particle Mesh Ewald electrostatic potential was set to 1 nm. Au–Au distance restraints were applied to maintain the Au<sub>25</sub>(SR)<sub>18</sub> crystal structure<sup>466</sup> during MD.

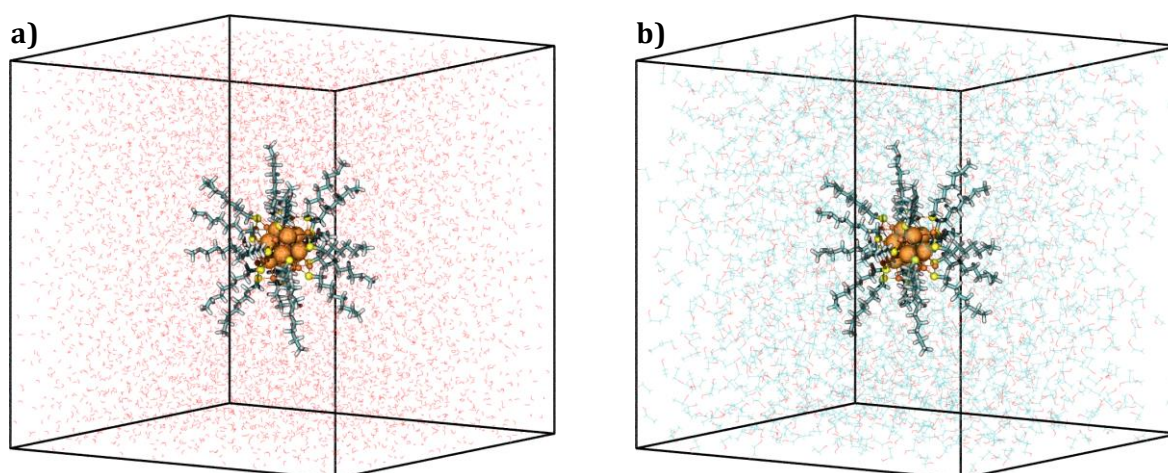


**Figure 6.3 | Initial structures used to perform molecular dynamics on the hydrophobic clusters.** The Au<sub>25</sub>(SC<sub>8</sub>H<sub>17</sub>)<sub>18</sub> NCs are simulated in both (a) water and (b) ethanol solvents. Gold (orange), sulphur (yellow), carbon (teal), hydrogen (white), and oxygen (red) atoms are shown in each unit cell (black).

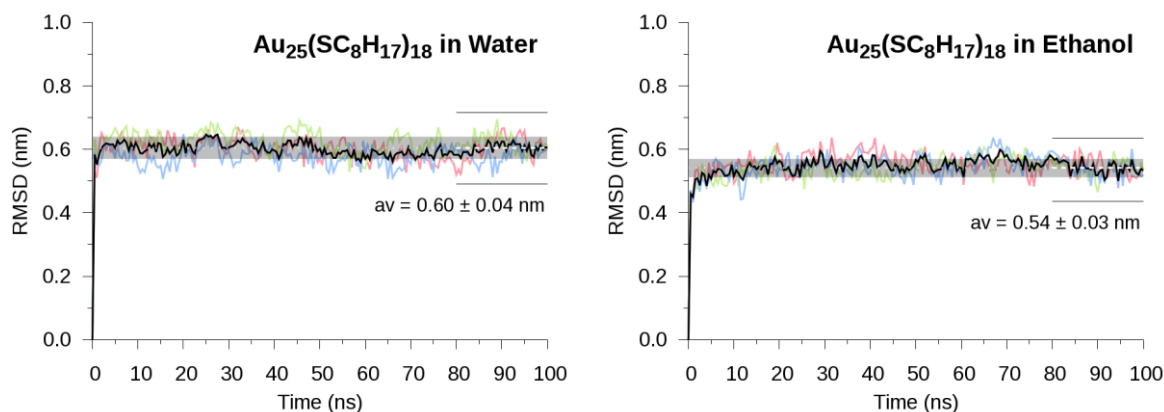


**Figure 6.4 | Time evolved average root-mean-square deviations for Au<sub>25</sub>(SC<sub>8</sub>H<sub>17</sub>)<sub>18</sub>.** Coloured lines represent 3 independent molecular dynamics simulations and the black lines are the average. The plateau after ~10ns indicates equilibration.

To clarify how the presence of AuNCs in the QR assemblies affects the loading and releasing of the chemotherapy drug DOX, several MD simulations are planned to be conducted (see Section 6.4). The ground work for these simulations has been prepared by parameterising the DOX molecule in a compatible approach to the AuNCs, i.e. the general amber FF<sup>558</sup> was used to assign bonded and van der Waals (vdW) parameters, and Gaussian09<sup>469</sup> was consulted to determine partial atomic charges (See Appendix A.3). MD simulations were conducted using the GROMACS 4.6.5 software.<sup>430</sup>

### Analysis Procedures

GROMACS was primarily used for statistical analysis presented in this chapter, which has been performed on structures that are thermally equilibrated. This is verified by monitoring root-mean-square deviations (RMSD) of the octanethiol chains over time (Figure 6.4, using *g\_rmsd*), and correspond to frames from the MD trajectories that evolved between simulation times 10–100 ns. Nanocluster volumes (Table 6.1) were calculated with *g\_principal*, *g\_dist* and a custom python script for matrix algebra (see Appendix B.1). Radial distributions (Figure 6.6) were calculated with *g\_rdf* and root-mean-square atomic fluctuations (Figure 6.7) were calculated with *g\_rmsf*. The VMD 1.9.1 package<sup>128</sup> was employed to calculate the angles and distances used to create the conformational plots in Figure 6.5, as well as for visualisation of all systems.

## 6.3 Results

### 6.3.1 Effect of Solvent on AuNC properties

The ensemble of atomistic Au<sub>25</sub>(SC<sub>8</sub>H<sub>17</sub>)<sub>18</sub> configurations obtained from MD show obvious structural differences when systems are simulated in different solvent environments. Density maps presented in Figure 6.5a and b highlight geometric conformations adopted by

the AuNCs' organic ligands when solvated in water and in ethanol, respectively. The angle ( $\theta$ ) formed between carbon atoms C<sub>1</sub>-C<sub>4</sub>-C<sub>8</sub> (numbered in an ascending order from sulphur) is used to assess if the octanethiol chains assume conformations that are linear ( $\theta > 160^\circ$ ), softly-curved ( $130^\circ < \theta < 160^\circ$ ), or sharply-curved ( $\theta < 130^\circ$ ), while the distance ( $x$ ) between the untethered chain ends (C<sub>8</sub>) and the nearest Au<sub>25</sub>S<sub>18</sub> atom provides a measure of ligand compactness against the AuNC surface. The highly populated region in the top-right of Figure 6.5b signifies that ethanol strongly promotes linear chains that are perpendicular to the Au<sub>25</sub>S<sub>18</sub> surface. In contrast, Figure 6.5a depicts a moderately more even density dispersion, but with an accumulation of ligand states where  $\theta=113$ - $124^\circ$  and  $x=0.45$ - $0.85$  nm implying the formation of curved and compact structures. These discrepancies are emphasised by the difference map of the two plots (Figure 6.5d), which shows that going from water to ethanol decreases (blue) compact conformations and increases (red) ligand extension. Representative snapshots also visually accentuate this (Figure 6.5c and e).

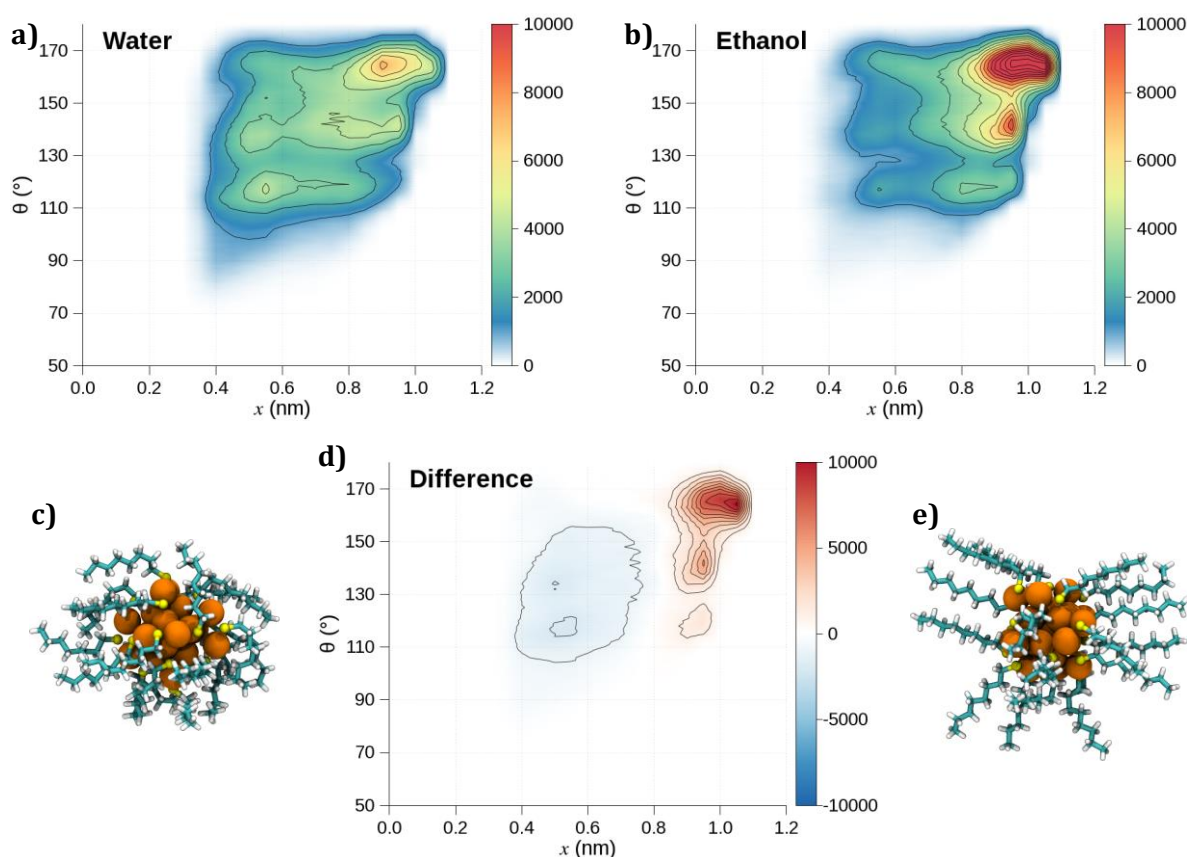


**Figure 6.5 | Effect of solvent on Au<sub>25</sub>(SC<sub>8</sub>H<sub>17</sub>)<sub>18</sub> conformations.** (a) and (b) are density maps of octanethiol backbone angles as a function of chain-end to AuS<sub>nearest</sub> distances, with (d) showing the difference map of the two plots. Contour lines are drawn at regions of 1,000 frequency and increments used for binning the data are:  $dx = 0.05$  nm (25 bins) and  $d\theta = 1^\circ$  (180 bins). Representative snapshots of the nanocluster complexes in water (c) and ethanol (e) taken from the MD simulations. Gold (orange), sulphur (yellow), carbon (teal), and hydrogen (white) atoms are shown while solvent is hidden for clarity.

**Table 6.1 | Average Au<sub>25</sub>(SC<sub>8</sub>H<sub>17</sub>)<sub>18</sub> dimensions determined by an ellipsoid model.**

Solvent	a (nm)	b (nm)	c (nm)	Volume (nm <sup>3</sup> )
Water	1.42 ± 0.09	1.05 ± 0.07	0.87 ± 0.05	5.35 ± 0.22
Ethanol	1.39 ± 0.07	1.17 ± 0.06	0.96 ± 0.07	6.56 ± 0.36

These observed conformations are found to be governed by different chain–solvent and chain–chain interaction propensities that vary based on the immersing solvent. When water surrounds the AuNCs, intermolecular pair correlation functions  $g(r)$  show minimal solvent structuring and only a single hydrophobic hydration shell emerges around the ligands (Figure 6.6a). On the other hand, the well-defined peaks at 0.38 nm, 0.41 nm, and 0.92 nm in Figure 6.6b (solid lines) signify that ligands readily interact with ethanol through C–C vdW interactions and at least 3 solvation shells form. The C<sub>8</sub> carbon on the octanethiol chains is solvated by ethanol primarily through interactions with the methyl groups on the ethanol solvent molecules, in a similar fashion to the previously reported solvation of *n*-octadecane by methanol.<sup>559</sup> Comparing the 1<sup>st</sup> solvation shells, terminal carbon atoms are coordinated by either ~11.4 water molecules or ~8.7 ethanol molecules (noting the size difference between the molecules). Furthermore, while intermolecular octanethiol interactions in both solvent systems yield very similar profiles (Figure 6.6c), the  $g(r)$  amplitude differences (e.g. compare the peak heights at ~0.5 nm) reveal that the ligands in water display a higher probability to network through C–C vdW interactions (compared to the aliphatic ligands in ethanol) in order to reduce their solvent exposure. The ‘bundling’ of ligands (as shown in Figure 6.5e) resulting from C–C interactions on adjacent ligands consistently appears in computational research involving small AuNCs.<sup>369,376,513</sup>

To approximate the overall size of the AuNCs, the principal moments of inertia for Au<sub>25</sub>(SC<sub>8</sub>H<sub>17</sub>)<sub>18</sub> are calculated at every simulation frame and used to fit the AuNCs to an ellipsoidal model<sup>376</sup> (as described in see Appendix B.1). On average, the gold–ligand complexes solvated in water exhibit ~20% smaller volumes compared to the structures in ethanol (see Table 6.1). This further supports the findings that ligands in water favour self-interactions by collapsing onto the cluster surface to maximise hydrophobic shielding, while in ethanol, octanethiol freely interacts with the solvent to adopt extended conformations. Although there is slightly larger standard deviation of the average volume in ethanol (Table 6.1), it is ascertained through the root-mean-square atomic fluctuations of sulphur and carbon atoms on each octanethiol chain that there is minimal difference in aliphatic chain flexibility on the gold surface as a consequence of solvent (see Figure 6.7).

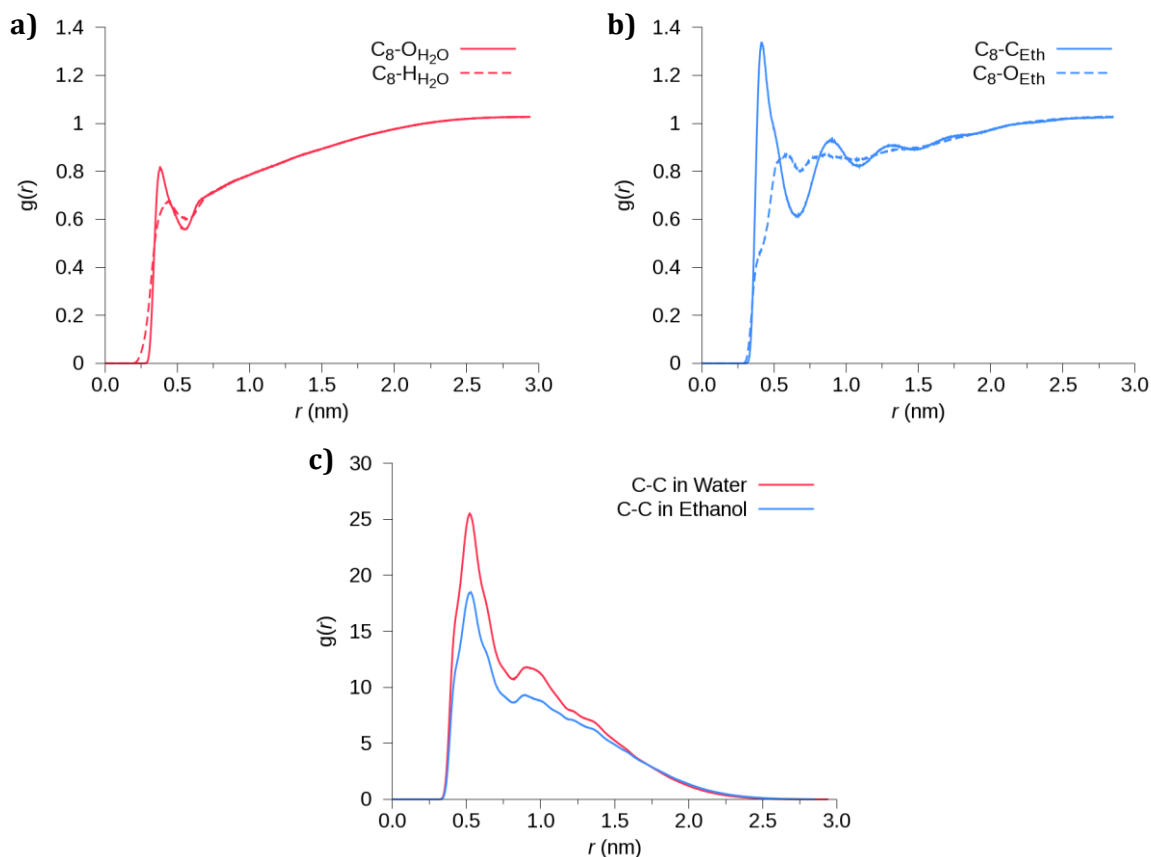


**Figure 6.6 | Octanethiol-solvent and octanethiol-octanethiol distribution functions.** The plots in (a) and (b) are the radial distributions of water (solid=oxygen, dashed=hydrogen) and ethanol solvents (solid=methyl carbon, dashed=oxygen) with respect to the terminal carbon atoms on the ligands ( $C_8$ ), respectively. The peaks indicate 1 hydrophobic hydration shell formed in water versus at least 3 solvation shells in ethanol. (c) Ligand-ligand distribution (all intermolecular carbon pairs).

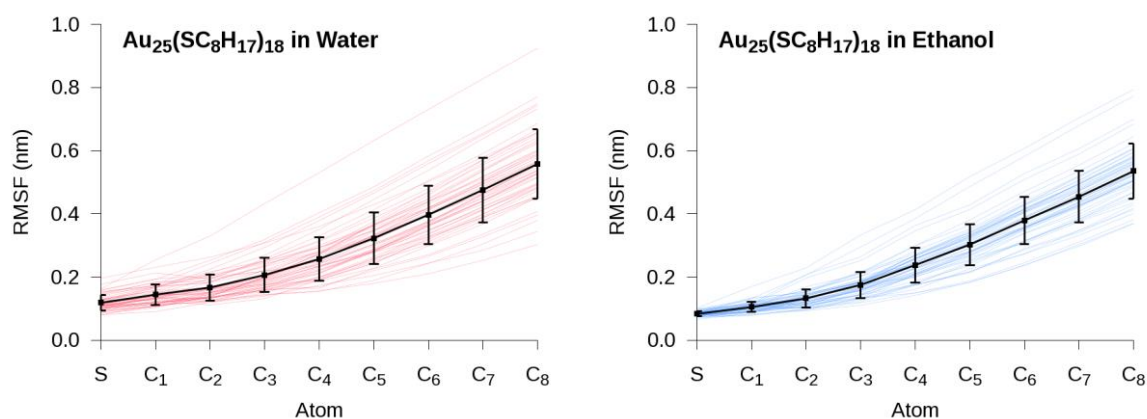


**Figure 6.7 | Average carbon and sulphur atomic root-mean-square fluctuations.** The black lines are ensemble averaged RMSFs (y-axes) with standard deviation error bars, whereas the coloured lines are the RMSFs for the 18 octanethiol ligands per system  $\times$  3 simulations.

## 6.4 Discussion and Conclusions

It is proposed from the MD results that the larger volume and conformational differences of the octanethiol ligand-layer in ethanol (compared to water) are what encourage the evacuation of the AuNCs from the small ( $\sim 2.5$  nm) MS pores in experiments where QRs are transferred from aqueous to ethanol solvent. From a strictly geometric perspective, there are two ways in which the AuNCs can be situated in the cylindrical pores; with their major semi-axis  $a$  parallel to the pore opening (Figure 6.8a) or perpendicular to it (Figure 6.8b). Therefore, if the Au<sub>25</sub>(SC<sub>8</sub>H<sub>17</sub>)<sub>18</sub> structures obtained from each MD frame are considered to be rigid ellipsoids that do not interact with silica, criteria can be established to approximate the likelihood of the AuNCs being an appropriate size to reside in the MS pores. Figure 6.8c and d provide two exemplar structures taken from MD to visually show these criteria. It is determined that the natural nanocluster sizes observed in ethanol are almost certainly too large to adequately fit inside the pores, whereas in aqueous hydration the MS is expected to be clogged with AuNCs (Table 6.2). It is therefore probable that a steric-kinetic driving force compels the Au<sub>25</sub>(SC<sub>8</sub>H<sub>17</sub>)<sub>18</sub> complexes to abandon the narrow confinement of the silica pores when the QRs are placed in an ethanol solution and the elongation of the octanethiol ligands is also likely to aid this migration process. It is also noted that the extension of alkanethiol chains in organic solvents has previously been reported for Au<sub>25</sub>(SC<sub>*n*</sub>H<sub>2*n*+1</sub>)<sub>18</sub> ligands in benzene<sup>376</sup> and *n*-octadecane molecules in methanol.<sup>559</sup>

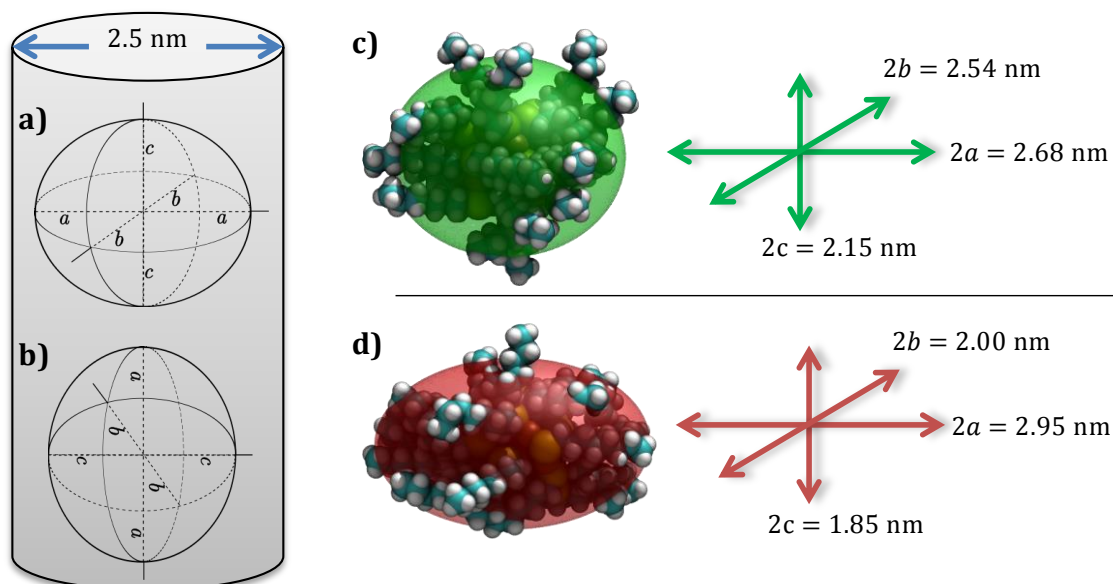


**Figure 6.8 | Schematic illustration of proposed nanocluster 'fit' in silica pores.** Cartoon showing an ellipsoid situated inside the cylindrical MS pore with its major semi-axis (a) parallel or (b) perpendicular to the pore opening. Example frames where the 'rigid' AuNC ellipsoid will not fit in the pore (c), or may fit in the pore (d) if oriented correctly.

To complement and substantiate these findings, future work includes MD of multiple AuNCs in ethanol and water solutions. Simulations of this kind will provide information on the tendency for these AuNCs to aggregate in the different solvents. Furthermore, modelling of an amorphous silica pore with single AuNCs and multiple AuNCs in each solvent is expected to be even more insightful. Both of these suggested directions are expected to pose significant challenges to ensure potentials between components in the systems are adequately and correctly represented to describe the molecular level interactions.

To elucidate how AuNCs in the QR assembly affects DOX drug loading and releasing profiles (Figure 6.2), several MD simulations are intended as future work. First, DOX is to be simulated free in aqueous and PBS solutions, i.e. in the absence of gold and silica, to explore the diffusion process of the drug during loading and delivery. Then, equilibrated structures from MD simulations of Au<sub>25</sub>(SC<sub>8</sub>H<sub>17</sub>)<sub>18</sub> in water will be used to investigate the spontaneous binding of single (and multiple) DOX molecules to the octanethiol-coated AuNCs. Finally, DOX–AuNC complexes will be placed in PBS solution to investigate if spontaneous desorption occurs during the drug-delivery phase of the experimental protocol.

While these simulations containing DOX constitute future work, comments can still be made regarding the expected molecular interactions and the implications these might have to clarify the empirical systems. The anthracycline doxorubicin molecule contains two main moieties that are likely to be important for its interactions with the AuNCs, AuNPs, and silica surfaces in the QR constructs. The first is the anthracene functional group (the three fused benzene rings) that presents a large hydrophobic surface area, and the second is the hexosamine sugar group that contains a protonated (positively charged) amine at physiological pH (pKa ~8.2). To gain an impression of the size of DOX, Figure 6.9 shows the drug molecule placed to scale next to an equilibrated AuNC structure (with water hidden). The increase in drug loading for gold-containing QRs is likely due to the anthracene group on DOX hydrophobically interacting with the octanethiol-coatings on the AuNCs/AuNPs, and the positively charged amine on DOX is expected to contribute to pointed electrostatic interactions with the silica surface and probably slow its release from the QRs. These hypotheses will be tested through the MD simulation protocols described.

In conclusion, this chapter has presented classical MD investigations that examine the properties of octanethiol-protected Au<sub>25</sub> nanoclusters to provide valuable molecular-level insight into experimentally relevant systems. Through simulations in different solvents, structural properties are obtained that help to explain empirical results and illustrate why AuNCs are present in MS pores when the QRs are solvated in water as opposed to ethanol.

**Table 6.2 | Criteria and evaluated likelihood for AuNC confinement in silica pores.\***

Likelihood of fitting in pore	Criteria <sup>†</sup>	Water <sup>‡</sup>	Ethanol <sup>‡</sup>
<b>Certain</b>	$(2b + 0.4 \text{ nm}) < (2a + 0.4 \text{ nm}) < 2.5 \text{ nm}$	0.00 %	0.00 %
<b>Possible</b>	$(2b + 0.4 \text{ nm}) < 2.5 \text{ nm} < (2a + 0.4 \text{ nm})$	53.53 %	3.31 %
<b>Impossible</b>	$2.5 \text{ nm} < (2b + 0.4 \text{ nm}) < (2a + 0.4 \text{ nm})$	46.47 %	96.69 %

\*2.5 nm silica pores.

<sup>†</sup>0.4 nm is added to account for vdW overlap, i.e. ~0.2 nm on each wall and ~0.2 nm on semi-axes length

<sup>‡</sup>Gathered from 270 ns of data (45,000 frames × 3 independent trajectories).

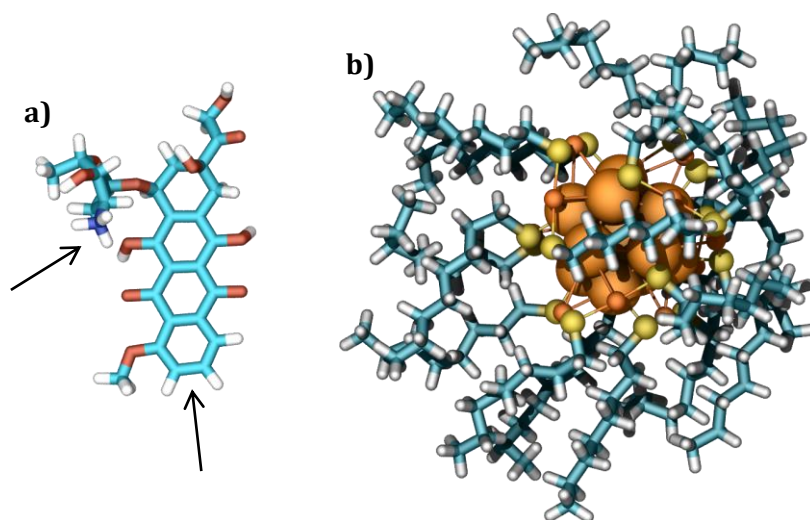


**Figure 6.9 | Size comparison of a doxorubicin molecule and Au<sub>25</sub>(SC<sub>8</sub>H<sub>17</sub>)<sub>18</sub>.** (a) The DOX molecule with arrows pointing to the hydrophobic anthracene group and the positively charged NH<sub>3</sub><sup>+</sup> moiety. (b) Representative equilibrated frame taken from the AuNC simulations in water. Gold (orange), sulphur (yellow), carbon (teal), nitrogen (blue), oxygen (red), and hydrogen (white) atoms are shown.



### 7.1 Research Summary, Limitations, Future Work

In this thesis, computational modelling techniques have been employed to investigate the physicochemical properties of gold nanomaterials interfaced with biological molecules. The work presented is motivated and performed in direct collaboration with experimental research that aims to develop innovative and superior *in vivo* and *in vitro* gold-based biomedical devices. These fascinating and advantageous materials constructively exploit the unique properties of gold nanomaterials integrated with biological functionalities (Chapter 1) to create biosensors and drug-delivery vehicles that are controllable, selective, and sensitive. However, to successfully design bio-nanomaterials for specific applications, it is helpful to accompany careful experimental parameter optimisation with theoretical modelling perspectives that are able to complement, clarify, and predict experimental findings at spatial and temporal resolutions technologically unattainable in the laboratory. Multiscale *in silico* strategies have been, and will continue to be, invaluable tools for exploring interactions at the bio-nano interface<sup>2</sup> in order to elucidate how materials and their properties adjust in biological media and how the components of biological milieu respond to the presence of gold nanomaterials (Chapter 2). This thesis has used molecular modelling approaches (Chapter 3) to investigate three distinct functionalised gold nanomaterial systems: Au(111) coated by various 16 amino-acid peptide-monolayers; Au<sub>25</sub>(SP)<sub>18</sub> nanoclusters (NCs, where P = hexapeptides); and octanethiol-coated Au<sub>25</sub> NCs.

In Chapter 4, classical molecular dynamics (MD) was used to establish the relationship between the complex peptide-topographies displayed on gold surfaces and the experimental performance of plasmonic gold nanoparticle (AuNP) biosensors, which generate a colourimetric signal upon antibody-induced AuNP aggregation. Through characterising the peptide-peptide, peptide-gold, and peptide-solvent interactions occurring in the systems, it was found that monolayer conformations are intimately related to amino acid composition and location within individual peptide sequences. Aromatic tyrosine residues endeavour to reduce their solvent exposure and epitaxially interact with the planar gold surface, whereas electrostatic effects between charged residues encourage the dispersion of peptide chains, and solvent molecules dynamically shield like charges in adjacent peptides. The competition of these interactions collectively produces different monolayer conformations and these are

then correlated to the empirical capacity each system has to form AuNP aggregates upon exposure to peptide-specific antibodies.

To examine how the epitope-peptide conformations are likely to influence AuNP binding with antibody molecules, immuno-dominant residues in each epitope-monolayer were predicted from previously published literature and general features that are expected to contribute to advantageous epitope-antibody interactions were explored. Two features assumed to promote antibody binding are: (1) the solvent exposure of immuno-dominant residues to form strong contacts with an antibody's paratopes; and (2) the elongation and dispersion of peptide chains within the monolayers to enable the steric coordination of antibodies around the immuno-dominant residues. While MD simulations reveal that the best and worst experimentally performing antibody-epitope-gold systems satisfy and fail these criteria respectively, in the context of antibody-induced AuNP cross-linking several other factors need to be considered. Although epitope-antibody binding may be presumed from the equilibrium monolayer structures, immunoglobulin molecules may bind with both valences to the same AuNP, they may radically alter the monolayer structure and cause a 'butterfly effect', or they may be fundamentally impaired to bivalent cross-linking.

Computational limitations also need to be identified, appreciated, and reflected upon. For example, improvements in conformational sampling may provide a better description of how the monolayers behave, a three-point water model may not be sufficient to describe complex water interactions, curvature of the nanoparticles is neglected, and idealised (frozen) crystallographic Au(111) facets dominant for the NPs of the size considered are employed while other less dominant facets, such as Au(100), are ignored. Even though each of these can influence the microstructure of the monolayers, the overall observed trends are expected to remain consistent. In addition, the empirical setup is designed to provide a *proof-of-concept* for this type of biosensing material and in reality conditions such as temperature, pressure, system size, and realistic physiological environment (e.g. the crowded macromolecular milieu of various bodily fluids) need to be better approximated from both an experimental and theoretical perspective to assess clinical applicability. Ideas for continuation of this research include modelling the monolayer-gold systems interacting with antibodies (as their experimental characterisation improves) to better understand AuNP cross-linking processes, and investigating the aggregation between multiple AuNPs.

Chapter 5 utilised MD in conjunction with quantum mechanical (QM) calculations to study how peptide-ligand conformations and the photoluminescence (PL) of Au<sub>25</sub> NCs are related. First, general properties of Au<sub>25</sub>(SP)<sub>18</sub> such as hydrodynamic radii and volumes are obtained

with MD and used to describe the overall size of the AuNC systems, in good agreement with experimental characterisations. Then, properties of  $\text{Au}_{25}(\text{SP})_{18}$  with different hexapeptide-ligands were systematically investigated to clarify how the distribution of amino acids around the gold-sulphur NC cores ( $\text{Au}_{25}\text{S}_{18}$ ), peptide conformation, structuring/dynamics of water molecules, and the formation of hydrogen bond networks each correlate with the experimentally observed AuNC PL. Geometry optimisation of  $\text{Au}_{25}(\text{Cys})_{18}$  (with and without acetyl caps) using QM shows that N-terminal acetylation redistributes electron charge within the systems so that partial atomic charges on  $\text{Au}_{25}\text{S}_{18}$  are collectively  $\sim 1e^-$  more negative. Moreover, the hypothesis that aspartate located close to the gold core may result in PL quenching is explored using an *a posteriori* classical approach to estimate the energetic cost for electron removal from aspartate, and four single-point QM calculations of  $\text{Au}_{25}(\text{SP})_{18}$  in explicit solvent (between  $\sim 1800$ – $3600$  atoms) are conducted. These analyses reveal to a first-order approximation that electron transfer between aspartate and gold may be a reasonable mechanism to rationalise quenching in  $\text{Au}_{25}(\text{SP})_{18}$  systems, with frontier orbitals found at an appropriate energy separation and geometric location to facilitate this.

Key findings from the chapter suggest that the local chemical environment near the gold core is crucial for quenching or enhancing AuNC PL. In particular, the enhancement of AuNC fluorescence intensity in these systems is proposed to be achievable through several mechanisms. (1) Replacement of electron-withdrawing groups (e.g.  $\text{NH}_3^+$ ) with partial electron density donating moieties (e.g.  $\text{C}=\ddot{\text{O}}$ : or aromatic groups) in the vicinity of  $\text{Au}_{25}\text{S}_{18}$ . (2) Removal of residues such as aspartate (and possibly histidine) that may be engaged in photoinduced electron transfer to gold. (3) Designing of ligands to reduce the propensity of water penetrating into the peptide layers where PL can be adversely affected. (4) Lowering solution pH to affect the protonation state of titratable groups (empirically suggested).

Several computational deficiencies are acknowledged with the approaches taken to accomplish this work, however the insight provided from these calculations is well correlated with experimental results, informative, and non-intuitive. Nonetheless, for the MD simulations there are recognised force field (FF) issues such as utilising a neutral partial atomic charge description of gold atoms, the inability for the AuNCs to reconstruct, neglect of polarisation effects, simplistic water models, and a potentially insufficient van der Waals description of Au-peptide interactions that are all expected to affect computational accuracy. Furthermore, polydispersity in the experimental samples, different gold models (e.g. charge states, shapes, and sizes), supplementary QM sampling with more diverse systems, and a better treatment of gold dispersion interactions (for ONETEP) are all essential improvements. With recent advances in computational hardware and high-level

density functional theory (DFT) methods, a better electronic structure understanding of biologically relevant nano-bio systems in realistic environments should become feasible, and in turn this will facilitate the improvement of FF models (including reactive FFs).

Besides some of the abovementioned suggestions, to expand the scope of this work simulations can be conducted with multiple nanoclusters in a single cell to look at effects of aggregation and a higher levels of QM theory (e.g. time-dependent DFT) should be consulted to properly investigate electronic excitation and optical properties. Additionally, there have been recent developments of specific FF for Au<sub>25</sub> and other sized clusters (Section 3.3.3) that would be ideal to employ for MD of these systems and will likely be a crucial advancement for other applications such as investigating AuNC-induced catalysis.

In the penultimate chapter of this thesis, Chapter 6, MD was used to examine the properties of octanethiol-protected Au<sub>25</sub> nanoclusters, which are intrinsically hydrophobic and form a constituent component of a gold-mesoporous silica (MS) composite material called a 'quantum rattle' (QR). Simulations in this chapter are conducted to explain why AuNCs situated inside the cylindrical mesopores of the QRs easily and readily evacuate from the silica pores when solvated in ethanol but not water. Results from this study highlight that an increase in volume and conformational elongation of the octanethiol ligand-layer in ethanol (compared to water) are likely to encourage the evacuation of the AuNCs from the small (~2.5 nm) MS pores. It is suggested that these differences lead to a steric-kinetic driving force that compels the Au<sub>25</sub>(SC<sub>8</sub>H<sub>17</sub>)<sub>18</sub> complexes to abandon the narrow confinement of the pores when the aqueously solvated QRs are transferred to an ethanol solution.

While the gold-passivating ligands in this chapter are shorter and less chemically intricate than the peptides used in Chapter 5, similar force field issues and model approximations are expected to influence the ability of the MD computations to accurately represent the empirical setup. Primarily, the inclusion of partial charges on gold atoms, better solvent models, and further simulations of the size, polydispersity, and morphology of the AuNCs will be beneficial to improving the quality of the computational findings. The natural progression of this project will be testing the hypotheses offered in Section 6.4 regarding molecular interactions occurring between Au<sub>25</sub>(SC<sub>8</sub>H<sub>17</sub>)<sub>18</sub> and the chemotherapy drug doxorubicin (DOX) and future considerations involve simulations with a combination of DOX, alkanethiol-AuNCs, and an amorphous silica pore (to represent MS).

In conclusion, Chapters 4-6 predict AuNP and AuNC behaviours, reveal structure-property relationships, and guide the effective engineering of innovative biomedical devices. The outcomes of this thesis contribute to the overall understanding of these organic-inorganic

materials in targeted applications through exploring the intricate interactions that occur on the nanoscale. The approaches used throughout this research are expected to prove broadly useful in the future design of novel bioassays. This work also highlights how the synergy between theoretical and experimental approaches produces translational research to facilitate the development of biocompatible gold nanomaterials for applications in the fields of bioimaging, biosensing, drug delivery, and biomedicine in general.

## 7.2 Perspective on the Current State of the Au–Bio Simulation Field

As described in several extensive reviews,<sup>2,126,336,345,560-563</sup> computational approaches are widely accepted, essential tools that provide in-depth characterisation, non-intuitive relationships, and fundamental understandings into nanoscale materials. In the context of atomistic modelling techniques, three main challenges are faced on the quest to produce accurate and significant Au–bio simulations that are directly relevant to experiment.

1. The careful development and validation of FFs that are appropriate for specific gold nanostructures (e.g. surfaces, AuNPs, and AuNCs) *and* contain interatomic potentials that reasonably capture the interactions gold substrates have with biomolecular species (e.g. amino acids, nucleic acids, lipids, water, etc.), including polarisation effects.
2. Associated to this, the availability of experimentally complex atomic-scale structures of the gold substrates and other constituent components in the system are needed. These should be physically realistic, well-resolved, and meaningful to the experimental conditions in order to build the initial coordinates/models of a simulation. This involves a full molecular topology of the system that includes atomic composition, general structural arrangement of the substrate (e.g. “staple” motifs in AuNCs), typical pairwise bond and angle distributions, protonation states of titratable groups appropriate to the solution pH, and any other potential interfacial solvent structuring affects.
3. Extensive and comprehensive conformational sampling of the system’s potential energy landscape is needed to generate statistically relevant structural ensembles that are useful for extracting realistic kinetic and thermodynamic quantities from gold–bio interfacial simulations. This not only requires an increase in computational power, it also necessitates more efficient algorithms and approaches that are able to spontaneously evolve a system to biologically relevant timescales.

Advancement of experimental technologies will also enable molecular simulation progress. Despite the hurdles and limitations faced, multiscale molecular modelling is able to probe the nano–bio interface in ways that are unachievable through any other techniques, and therefore these methods will remain indispensable and relevant for many years to come.

# Bibliography

---

1. Y. LIN\*, P. CHARCHAR\*, A. J. CHRISTOFFERSON, M. R. THOMAS, *et al.* Surface ligand effects on the structure and fluorescence of peptide-protected gold nanoclusters, In preparation. \*Equally contributing authors
2. P. CHARCHAR, A. J. CHRISTOFFERSON, N. TODOROVA, AND I. YAROVSKY. Understanding and designing the gold-bio interface: Insights from simulations, *Small*, **12**: 2395-2418, 2016. DOI: [10.1002/sml.201503585](https://doi.org/10.1002/sml.201503585)
3. H. ANDRESEN, M. MAGER, M. GRIEBNER, P. CHARCHAR, *et al.* Single-step homogeneous immunoassays utilizing epitope-tagged gold nanoparticles: On the mechanism, feasibility, and limitations, *Chem. Mater.*, **26**: 4696-4704, 2014. DOI: [10.1021/cm500535p](https://doi.org/10.1021/cm500535p)
4. P. D. HOWES, R. CHANDRAWATI, AND M. M. STEVENS. Colloidal nanoparticles as advanced biological sensors, *Science*, **346**: 1247390, 2014. DOI: [10.1126/science.1247390](https://doi.org/10.1126/science.1247390)
5. K. SAHA, S. S. AGASTI, C. KIM, X. LI, *et al.* Gold nanoparticles in chemical and biological sensing, *Chem. Rev.*, **112**: 2739-2779, 2012. DOI: [10.1021/cr2001178](https://doi.org/10.1021/cr2001178)
6. M. CUI, Y. ZHAO, AND Q. SONG. Synthesis, optical properties and applications of ultra-small luminescent gold nanoclusters, *Trend. Anal. Chem.*, **57**: 73-82, 2014. DOI: [10.1016/j.trac.2014.02.005](https://doi.org/10.1016/j.trac.2014.02.005)
7. V. K. A. SREENIVASAN, A. V. ZVYAGIN, AND E. M. GOLDYS. Luminescent nanoparticles and their applications in the life sciences, *J. Phys.: Condens. Matter*, **25**: 194101, 2013. DOI: [10.1088/0953-8984/25/19/194101](https://doi.org/10.1088/0953-8984/25/19/194101)
8. L.-Y. CHEN, C.-W. WANG, Z. YUAN, AND H.-T. CHANG. Fluorescent gold nanoclusters: Recent advances in sensing and imaging, *Anal. Chem.*, **87**: 216-229, 2015. DOI: [10.1021/ac503636j](https://doi.org/10.1021/ac503636j)
9. G. AJNAI, A. CHIU, T. KAN, C.-C. CHENG, *et al.* Trends of gold nanoparticle-based drug delivery system in cancer therapy, *J. Exp. Clin. Med.*, **6**: 172-178, 2014. DOI: [10.1016/j.jecm.2014.10.015](https://doi.org/10.1016/j.jecm.2014.10.015)
10. M. YAMADA, M. FOOTE, AND T. W. PROW. Therapeutic gold, silver, and platinum nanoparticles, *WIREs Nanomed. Nanobiotechnol.*, **7**: 428-445, 2015. DOI: [10.1002/wnan.1322](https://doi.org/10.1002/wnan.1322)
11. Y. ZHANG, T. P. SHAREENA DASARI, H. DENG, AND H. YU. Antimicrobial activity of gold nanoparticles and ionic gold, *J. Environ. Sci. Health Part C: Environ. Carcinog. Ecotoxicol. Rev.*, **33**: 286-327, 2015. DOI: [10.1080/10590501.2015.1055161](https://doi.org/10.1080/10590501.2015.1055161)
12. W. ZHOU, X. GAO, D. LIU, AND X. CHEN. Gold nanoparticles for in vitro diagnostics, *Chem. Rev.*, **115**: 10575-10636, 2015. DOI: [10.1021/acs.chemrev.5b00100](https://doi.org/10.1021/acs.chemrev.5b00100)
13. X. YANG, M. YANG, B. PANG, M. VARA, *et al.* Gold nanomaterials at work in biomedicine, *Chem. Rev.*, **115**: 10410-10488, 2015. DOI: [10.1021/acs.chemrev.5b00193](https://doi.org/10.1021/acs.chemrev.5b00193)
14. N. GOSWAMI, K. ZHENG, AND J. XIE. Bio-ncs – the marriage of ultrasmall metal nanoclusters with biomolecules, *Nanoscale*, **6**: 13328-13347, 2014. DOI: [10.1039/c4nr04561k](https://doi.org/10.1039/c4nr04561k)
15. T. L. MOORE, L. RODRIGUEZ-LORENZO, V. HIRSCH, S. BALOG, *et al.* Nanoparticle colloidal stability in cell culture media and impact on cellular interactions, *Chem. Soc. Rev.*, **44**: 6287-6305, 2015. DOI: [10.1039/c4cs00487f](https://doi.org/10.1039/c4cs00487f)
16. D. DOCTER, D. WESTMEIER, M. MARKIEWICZ, S. STOLTE, *et al.* The nanoparticle biomolecule corona: Lessons learned – challenge accepted?, *Chem. Soc. Rev.*, **44**: 6094-6121, 2015. DOI: [10.1039/c5cs00217f](https://doi.org/10.1039/c5cs00217f)

17. C. M. BEDDOES, C. P. CASE, AND W. H. BRISCOE. Understanding nanoparticle cellular entry: A physicochemical perspective, *Adv. Colloid Interface Sci.*, **218**: 48-68, 2015. DOI: [10.1016/j.cis.2015.01.007](https://doi.org/10.1016/j.cis.2015.01.007)
18. S.-T. YANG, Y. LIU, Y.-W. WANG, AND A. CAO. Biosafety and bioapplication of nanomaterials by designing protein-nanoparticle interactions, *Small*, **9**: 1635-1653, 2013. DOI: [10.1002/sml.201201492](https://doi.org/10.1002/sml.201201492)
19. J. ZHENG, C. ZHOU, M. YU, AND J. LIU. Different sized luminescent gold nanoparticles, *Nanoscale*, **4**: 4073-4083, 2012. DOI: [10.1039/c2nr31192e](https://doi.org/10.1039/c2nr31192e)
20. A. LEIFERT, Y. PAN-BARTNEK, U. SIMON, AND W. JAHNEN-DECHENT. Molecularly stabilised ultrasmall gold nanoparticles: Synthesis, characterization and bioactivity, *Nanoscale*, **5**: 6224-6242, 2013. DOI: [10.1039/c3nr00916e](https://doi.org/10.1039/c3nr00916e)
21. M. HEMBURY, C. CHIAPPINI, S. BERTAZZO, T. L. KALBER, *et al.* Gold-silica quantum rattles for multimodal imaging and therapy, *Proc. Natl. Acad. Sci. U. S. A.*, **112**: 1959-1964, 2015. DOI: [10.1073/pnas.1419622112](https://doi.org/10.1073/pnas.1419622112)
22. C. TAN, X. CAO, X.-J. WU, Q. HE, *et al.* Recent advances in ultrathin two-dimensional nanomaterials, *Chem. Rev.*, **117**: 6225-6331, 2017. DOI: [10.1021/acs.chemrev.6b00558](https://doi.org/10.1021/acs.chemrev.6b00558)
23. B. PELAZ, C. ALEXIOU, R. A. ALVAREZ-PUEBLA, F. ALVES, *et al.* Diverse applications of nanomedicine, *ACS Nano*, **11**: 2313-2381, 2017. DOI: [10.1021/acsnano.6b06040](https://doi.org/10.1021/acsnano.6b06040)
24. V. KOSTOPOULOS, A. MASOURAS, A. BALTOPOULOS, A. VAVOULIOTIS, *et al.* A critical review of nanotechnologies for composite aerospace structures, *CEAS Space Journal*, **9**: 35-57, 2016. DOI: [10.1007/s12567-016-0123-7](https://doi.org/10.1007/s12567-016-0123-7)
25. S. M. RODRIGUES, P. DEMOKRITOU, N. DOKOOZLIAN, C. O. HENDREN, *et al.* Nanotechnology for sustainable food production: Promising opportunities and scientific challenges, *Environ. Sci.: Nano*, **4**: 767-781, 2017. DOI: [10.1039/c6en00573j](https://doi.org/10.1039/c6en00573j)
26. A. K. YETISEN, H. QU, A. MANBACHI, H. BUTT, *et al.* Nanotechnology in textiles, *ACS Nano*, **10**: 3042-3068, 2016. DOI: [10.1021/acsnano.5b08176](https://doi.org/10.1021/acsnano.5b08176)
27. A. LOHANI, A. VERMA, H. JOSHI, N. YADAV, *et al.* Nanotechnology-based cosmeceuticals, *ISRN Dermatol*, **2014**: 843687, 2014. DOI: [10.1155/2014/843687](https://doi.org/10.1155/2014/843687)
28. R. P. FEYNMAN. There's plenty of room at the bottom, *Eng. Sci.*, **23**: 22-36, 1960.
29. DANISH CONSUMER COUNCIL. (Oct 11). *The nanodatabase*. Available: <http://nanodb.dk/>
30. S. LAL AND R. KUMAR. Synthesis of organic nanoparticles and their applications in drug delivery and food nanotechnology: A review, *J. Nanomater. Mol. Nanotechnol.*, **03**: 2014. DOI: [10.4172/2324-8777.1000150](https://doi.org/10.4172/2324-8777.1000150)
31. W. J. STARK, P. R. STOESEL, W. WOHLLEBEN, AND A. HAFNER. Industrial applications of nanoparticles, *Chem. Soc. Rev.*, **44**: 5793-5805, 2015. DOI: [10.1039/c4cs00362d](https://doi.org/10.1039/c4cs00362d)
32. W. KURASHIGE, Y. NIIHORI, S. SHARMA, AND Y. NEGISHI. Precise synthesis, functionalization and application of thiolate-protected gold clusters, *Coord. Chem. Rev.*, **320-321**: 238-250, 2016. DOI: [10.1016/j.ccr.2016.02.013](https://doi.org/10.1016/j.ccr.2016.02.013)
33. E.-K. LIM, T. KIM, S. PAIK, S. HAAM, *et al.* Nanomaterials for theranostics: Recent advances and future challenges, *Chem. Rev.*, **115**: 327-394, 2015. DOI: [10.1021/cr300213b](https://doi.org/10.1021/cr300213b)
34. S. PAROLA, B. JULIÁN-LÓPEZ, L. D. CARLOS, AND C. SANCHEZ. Optical properties of hybrid organic-inorganic materials and their applications, *Adv. Funct. Mater.*, **26**: 6506-6544, 2016. DOI: [10.1002/adfm.201602730](https://doi.org/10.1002/adfm.201602730)
35. J. K. L. WONG, R. MOHSENI, A. A. HAMIDIEH, R. E. MACLAREN, *et al.* Will nanotechnology bring new hope for gene delivery?, *Trends Biotechnol.*, **35**: 434-451, 2017. DOI: [10.1016/j.tibtech.2016.12.009](https://doi.org/10.1016/j.tibtech.2016.12.009)
36. R. R. JOHNSON, A. T. C. JOHNSON, AND M. L. KLEIN. Probing the structure of DNA-carbon nanotube hybrids with molecular dynamics, *Nano Lett.*, **8**: 69-75, 2008. DOI: [10.1021/nl071909j](https://doi.org/10.1021/nl071909j)
37. *Crc handbook of chemistry and physics, internet version*. Boca Raton, FL: CRC Press, 2005.

38. G. SCHMID AND B. CORAIN. Nanoparticulated gold: Syntheses, structures, electronics, and reactivities, *Eur. J. Inorg. Chem.*, **2003**: 3081-3098, 2003. DOI: [10.1002/ejic.200300187](https://doi.org/10.1002/ejic.200300187)
39. Y. CHEN, G. LI, H. QIAN, AND R. JIN, "Catalysis by atomically precise gold nanoclusters," in *Catalysis by materials with well-defined structures*, Z. Wu and S. H. Overbury, Eds., ed: Academic Press, 2015, pp. 239-262.
40. THE BRITISH MUSEUM. (23 Feb 2017). Available: <http://www.britishmuseum.org>
41. D. J. BARBER AND I. C. FREESTONE. An investigation of the origin of the colour of the lycurgus cup by analytical transmission electron microscopy, *Archaeometry*, **32**: 33-45, 1990. DOI: [10.1111/j.1475-4754.1990.tb01079.x](https://doi.org/10.1111/j.1475-4754.1990.tb01079.x)
42. G. L. HORNYAK, C. J. PATRISSI, E. B. OBERHAUSER, C. R. MARTIN, *et al.* Effective medium theory characterization of Au/Ag nanoalloy-porous alumina composites, *Nanostruct. Mater.*, **9**: 571-574, 1997. DOI: [10.1016/S0965-9773\(97\)00127-X](https://doi.org/10.1016/S0965-9773(97)00127-X)
43. L. B. HUNT. The true story of purple of cassius, *Gold Bull.*, **9**: 134-139, 1976. DOI: [10.1007/bf03215423](https://doi.org/10.1007/bf03215423)
44. M. FARADAY. Experimental relations of gold (and other metals) to light, *Philos. Trans. R. Soc. London*, **147**: 145-181, 1857. DOI: [10.1098/rstl.1857.0011](https://doi.org/10.1098/rstl.1857.0011)
45. J. CARBERT. Gold-based enamel colours, *Gold Bull.*, **13**: 144-150, 1980. DOI: [10.1007/bf03215460](https://doi.org/10.1007/bf03215460)
46. G. MIE. Beiträge zur optik trüber medien, speziell kolloidaler metallösungen, *Ann. Phys.*, **330**: 377-445, 1908. DOI: [10.1002/andp.19083300302](https://doi.org/10.1002/andp.19083300302)
47. J. TURKEVICH AND J. HILLIER. Electron microscopy of colloidal systems, *Anal. Chem.*, **21**: 475-485, 1949. DOI: [10.1021/ac60028a009](https://doi.org/10.1021/ac60028a009)
48. E. A. HAUSER AND J. E. LYNN, "Experiments in colloid chemistry," ed New York: McGraw-Hill, 1940, p. 18.
49. J. TURKEVICH, P. C. STEVENSON, AND J. HILLIER. A study of the nucleation and growth processes in the synthesis of colloidal gold, *Discuss. Faraday Soc.*, **11**: 55, 1951. DOI: [10.1039/df9511100055](https://doi.org/10.1039/df9511100055)
50. G. FRENS. Controlled nucleation for the regulation of the particle size in monodisperse gold suspensions, *Nat. Phys. Sci.*, **241**: 20-22, 1973. DOI: [10.1038/physci241020a0](https://doi.org/10.1038/physci241020a0)
51. J. KIMLING, M. MAIER, B. OKENVE, V. KOTAYDIS, *et al.* Turkevich method for gold nanoparticle synthesis revisited, *J. Phys. Chem. B*, **110**: 15700-15707, 2006. DOI: [10.1021/jp061667w](https://doi.org/10.1021/jp061667w)
52. M. WUITHSCHICK, A. BIRNBAUM, S. WITTE, M. SZTUCKI, *et al.* Turkevich in new robes: Key questions answered for the most common gold nanoparticle synthesis, *ACS Nano*, **9**: 7052-7071, 2015. DOI: [10.1021/acsnano.5b01579](https://doi.org/10.1021/acsnano.5b01579)
53. C. D. BAIN AND G. M. WHITESIDES. Modeling organic surfaces with self-assembled monolayers, *Angew. Chem. Int. Ed.*, **28**: 506-512, 1989. DOI: [10.1002/anie.198905061](https://doi.org/10.1002/anie.198905061)
54. J. C. LOVE, L. A. ESTROFF, J. K. KRIEBEL, R. G. NUZZO, *et al.* Self-assembled monolayers of thiolates on metals as a form of nanotechnology, *Chem. Rev.*, **105**: 1103-1169, 2005. DOI: [10.1021/cr0300789](https://doi.org/10.1021/cr0300789)
55. M. BRUST, M. WALKER, D. BETHELL, D. J. SCHIFFRIN, *et al.* Synthesis of thiol-derivatized gold nanoparticles in a 2-phase liquid-liquid system, *J. Chem. Soc. Chem. Commun.*, 801-802, 1994. DOI: [10.1039/c39940000801](https://doi.org/10.1039/c39940000801)
56. M. BRUST, J. FINK, D. BETHELL, D. J. SCHIFFRIN, *et al.* Synthesis and reactions of functionalised gold nanoparticles, *J. Chem. Soc. Chem. Commun.*, 1655-1656, 1995. DOI: [10.1039/c39950001655](https://doi.org/10.1039/c39950001655)
57. A. C. TEMPLETON, W. P. WUELFING, AND R. W. MURRAY. Monolayer-protected cluster molecules, *Acc. Chem. Res.*, **33**: 27-36, 2000. DOI: [10.1021/ar9602664](https://doi.org/10.1021/ar9602664)
58. N. R. JANA AND X. PENG. Single-phase and gram-scale routes toward nearly monodisperse Au and other noble metal nanocrystals, *J. Am. Chem. Soc.*, **125**: 14280-14281, 2003. DOI: [10.1021/ja038219b](https://doi.org/10.1021/ja038219b)



59. E. C. DREADEN, A. M. ALKILANY, X. HUANG, C. J. MURPHY, *et al.* The golden age: Gold nanoparticles for biomedicine, *Chem. Soc. Rev.*, **41**: 2740-2779, 2012. DOI: [10.1039/c1cs15237h](https://doi.org/10.1039/c1cs15237h)
60. D. R. ALFONSO, D. KAUFFMAN, AND C. MATRANGA. Active sites of ligand-protected Au<sub>25</sub> nanoparticle catalysts for CO<sub>2</sub> electroreduction to CO, *J. Chem. Phys.*, **144**: 184705, 2016. DOI: [10.1063/1.4948792](https://doi.org/10.1063/1.4948792)
61. A. S. BARNARD, X. M. LIN, AND L. A. CURTISS. Equilibrium morphology of face-centered cubic gold nanoparticles > 3 nm and the shape changes induced by temperature, *J. Phys. Chem. B*, **109**: 24465-24472, 2005. DOI: [10.1021/jp054279n](https://doi.org/10.1021/jp054279n)
62. E. RODUNER. Size matters: Why nanomaterials are different, *Chem. Soc. Rev.*, **35**: 583-592, 2006. DOI: [10.1039/b502142c](https://doi.org/10.1039/b502142c)
63. Y. NEGISHI, T. NAKAZAKI, S. MALOLA, S. TAKANO, *et al.* A critical size for emergence of nonbulk electronic and geometric structures in dodecanethiolate-protected Au clusters, *J. Am. Chem. Soc.*, **137**: 1206-1212, 2015. DOI: [10.1021/ja5109968](https://doi.org/10.1021/ja5109968)
64. M. PELOW. Catalysis: The accelerator, *Nature*, **495**: S10-11, 2013. DOI: [10.1038/495S10a](https://doi.org/10.1038/495S10a)
65. E. BOISSELIER AND D. ASTRUC. Gold nanoparticles in nanomedicine: Preparations, imaging, diagnostics, therapies and toxicity, *Chem. Soc. Rev.*, **38**: 1759-1782, 2009. DOI: [10.1039/b806051g](https://doi.org/10.1039/b806051g)
66. K. L. KELLY, E. CORONADO, L. L. ZHAO, AND G. C. SCHATZ. The optical properties of metal nanoparticles: The influence of size, shape, and dielectric environment, *J. Phys. Chem. B*, **107**: 668-677, 2003. DOI: [10.1021/jp026731y](https://doi.org/10.1021/jp026731y)
67. M.-C. DANIEL AND D. ASTRUC. Gold nanoparticles: Assembly, supramolecular chemistry, quantum-size-related properties, and applications toward biology, catalysis, and nanotechnology, *Chem. Rev.*, **104**: 293-346, 2004. DOI: [10.1021/cr030698+](https://doi.org/10.1021/cr030698+)
68. W. HAISS, N. T. K. THANH, J. AVEYARD, AND D. G. FERNIG. Determination of size and concentration of gold nanoparticles from UV-vis spectra, *Anal. Chem.*, **79**: 4215-4221, 2007. DOI: [10.1021/ac0702084](https://doi.org/10.1021/ac0702084)
69. E. NOURISAEID, A. MOUSAVI, AND A. ARPANAEI. Colorimetric DNA detection of transgenic plants using gold nanoparticles functionalized with I-shaped DNA probes, *Phys. E*, **75**: 188-195, 2016. DOI: [10.1016/j.physe.2015.09.018](https://doi.org/10.1016/j.physe.2015.09.018)
70. R. DE LA RICA AND M. M. STEVENS. Plasmonic elisa for the ultrasensitive detection of disease biomarkers with the naked eye, *Nat. Nanotechnol.*, **7**: 821-824, 2012. DOI: [10.1038/nnano.2012.186](https://doi.org/10.1038/nnano.2012.186)
71. L. RODRÍGUEZ-LORENZO, R. DE LA RICA, R. A. ÁLVAREZ-PUEBLA, L. M. LIZ-MARZÁN, *et al.* Plasmonic nanosensors with inverse sensitivity by means of enzyme-guided crystal growth, *Nat. Mater.*, **11**: 604-607, 2012. DOI: [10.1038/nmat3337](https://doi.org/10.1038/nmat3337)
72. S. PALMAL AND N. R. JANA. Gold nanoclusters with enhanced tunable fluorescence as bioimaging probes, *WIREs Nanomed. Nanobiotechnol.*, **6**: 102-110, 2014. DOI: [10.1002/wnan.1245](https://doi.org/10.1002/wnan.1245)
73. J. ZHENG, P. R. NICOVICH, AND R. M. DICKSON. Highly fluorescent noble-metal quantum dots, *Annu. Rev. Phys. Chem.*, **58**: 409-431, 2007. DOI: [10.1146/annurev.physchem.58.032806.104546](https://doi.org/10.1146/annurev.physchem.58.032806.104546)
74. C. J. MURPHY, A. M. GOLE, J. W. STONE, P. N. SISCO, *et al.* Gold nanoparticles in biology: Beyond toxicity to cellular imaging, *Acc. Chem. Res.*, **41**: 1721-1730, 2008. DOI: [10.1021/ar800035u](https://doi.org/10.1021/ar800035u)
75. J. ZHENG, C. ZHANG, AND R. M. DICKSON. Highly fluorescent, water-soluble, size-tunable gold quantum dots, *Phys. Rev. Lett.*, **93**: 077402, 2004. DOI: [10.1103/PhysRevLett.93.077402](https://doi.org/10.1103/PhysRevLett.93.077402)
76. R. PAMIES, J. G. H. CIFRE, V. F. ESPÍN, M. COLLADO-GONZÁLEZ, *et al.* Aggregation behaviour of gold nanoparticles in saline aqueous media, *J. Nanopart. Res.*, **16**: 2014. DOI: [10.1007/s11051-014-2376-4](https://doi.org/10.1007/s11051-014-2376-4)
77. B. INGHAM, T. H. LIM, C. J. DOTZLER, A. HENNING, *et al.* How nanoparticles coalesce: An in situ study of Au nanoparticle aggregation and grain growth, *Chem. Mater.*, **23**: 3312-3317, 2011. DOI: [10.1021/cm200354d](https://doi.org/10.1021/cm200354d)

78. E. COLANGELO, J. COMENGE, D. PARAMELLE, M. VOLK, *et al.* Characterizing self-assembled monolayers on gold nanoparticles, *Bioconjugate Chem.*, **28**: 11-22, 2017. DOI: [10.1021/acs.bioconjchem.6b00587](https://doi.org/10.1021/acs.bioconjchem.6b00587)
79. C. VERICAT, M. E. VELA, G. BENITEZ, P. CARRO, *et al.* Self-assembled monolayers of thiols and dithiols on gold: New challenges for a well-known system, *Chem. Soc. Rev.*, **39**: 1805-1834, 2010. DOI: [10.1039/b907301a](https://doi.org/10.1039/b907301a)
80. G. E. JOHNSON AND J. LASKIN. Understanding ligand effects in gold clusters using mass spectrometry, *Analyst*, **141**: 3573-3589, 2016. DOI: [10.1039/c6an00263c](https://doi.org/10.1039/c6an00263c)
81. T. MIZUHARA, D. F. MOYANO, AND V. M. ROTELLO. Using the power of organic synthesis for engineering the interactions of nanoparticles with biological systems, *Nano Today*, **11**: 31-40, 2016. DOI: [10.1016/j.nantod.2015.11.002](https://doi.org/10.1016/j.nantod.2015.11.002)
82. R. A. SPERLING AND W. J. PARAK. Surface modification, functionalization and bioconjugation of colloidal inorganic nanoparticles, *Philos. Trans. R. Soc. A*, **368**: 1333-1383, 2010. DOI: [10.1098/rsta.2009.0273](https://doi.org/10.1098/rsta.2009.0273)
83. J. R. REIMERS, M. J. FORD, A. HALDER, J. ULSTRUP, *et al.* Gold surfaces and nanoparticles are protected by Au(0)-thiyl species and are destroyed when Au(i)-thiolates form, *Proc. Natl. Acad. Sci. U. S. A.*, **113**: E1424-E1433, 2016. DOI: [10.1073/pnas.1600472113](https://doi.org/10.1073/pnas.1600472113)
84. T. BÜRGI. Properties of the gold-sulphur interface: From self-assembled monolayers to clusters, *Nanoscale*, **7**: 15553-15567, 2015. DOI: [10.1039/c5nr03497c](https://doi.org/10.1039/c5nr03497c)
85. H. HÄKKINEN. The gold-sulfur interface at the nanoscale, *Nat. Chem.*, **4**: 443-455, 2012. DOI: [10.1038/nchem.1352](https://doi.org/10.1038/nchem.1352)
86. S.-S. LEE, B. KIM, AND S. LEE. Structures and bonding properties of gold-arg-cys complexes: DFT study of simple peptide-coated metal, *J. Phys. Chem. C*, **118**: 20840-20847, 2014. DOI: [10.1021/jp412438f](https://doi.org/10.1021/jp412438f)
87. J. R. REIMERS, M. J. FORD, S. M. MARCUCCIO, J. ULSTRUP, *et al.* Competition of van der waals and chemical forces on gold-sulfur surfaces and nanoparticles, *Nat. Rev. Chem.*, **1**: 0017, 2017. DOI: [10.1038/s41570-017-0017](https://doi.org/10.1038/s41570-017-0017)
88. X. YUAN, N. GOSWAMI, I. MATHEWS, Y. YU, *et al.* Enhancing the stability through ligand shell engineering: A case study with Au<sub>25</sub>(SR)<sub>18</sub> nanocluster, *Nano Res.*, **8**: 3488-3495, 2015. DOI: [10.1007/s12274-015-0847-2](https://doi.org/10.1007/s12274-015-0847-2)
89. J. JUNG, S. KANG, AND Y.-K. HAN. Ligand effects on the stability of thiol-stabilized gold nanoclusters: Au<sub>25</sub>(SR)<sub>18</sub><sup>-</sup>, Au<sub>38</sub>(SR)<sub>24</sub><sup>-</sup>, and Au<sub>102</sub>(SR)<sub>44</sub><sup>-</sup>, *Nanoscale*, **4**: 4206-4210, 2012. DOI: [10.1039/c2nr30501a](https://doi.org/10.1039/c2nr30501a)
90. Y.-T. TSENG, Z. YUAN, Y.-Y. YANG, C.-C. HUANG, *et al.* Photoluminescent gold nanodots: Role of the accessing ligands, *RSC Adv.*, **4**: 33629-33635, 2014. DOI: [10.1039/c4ra04774e](https://doi.org/10.1039/c4ra04774e)
91. Z. WU AND R. JIN. On the ligand's role in the fluorescence of gold nanoclusters, *Nano Lett.*, **10**: 2568-2573, 2010. DOI: [10.1021/nl101225f](https://doi.org/10.1021/nl101225f)
92. S. KNOPPE AND T. BÜRGI. Chirality in thiolate-protected gold clusters, *Acc. Chem. Res.*, **47**: 1318-1326, 2014. DOI: [10.1021/ar400295d](https://doi.org/10.1021/ar400295d)
93. M. AGRACHEV, S. ANTONELLO, T. DAINESE, J. A. GASCÓN, *et al.* A magnetic look into the protecting layer of Au<sub>25</sub> clusters, *Chem. Sci.*, **7**: 6910-6918, 2016. DOI: [10.1039/c6sc03691k](https://doi.org/10.1039/c6sc03691k)
94. A. H. HOLM, M. CECCATO, R. L. DONKERS, L. FABRIS, *et al.* Effect of peptide ligand dipole moments on the redox potentials of Au<sub>38</sub> and Au<sub>140</sub> nanoparticles, *Langmuir*, **22**: 10584-10589, 2006. DOI: [10.1021/la061553b](https://doi.org/10.1021/la061553b)
95. I. GURYANOV, F. POLO, E. V. UBYVOVK, E. KORZHIKOVA-VLAKH, *et al.* Polylysine-grafted Au<sub>144</sub> nanoclusters: Birth and growth of a healthy surface-plasmon-resonance-like band, *Chem. Sci.*, **8**: 3228-3238, 2017. DOI: [10.1039/c6sc05187a](https://doi.org/10.1039/c6sc05187a)
96. L. SEMENTA, G. BARCARO, A. DASS, M. STENER, *et al.* Designing ligand-enhanced optical absorption of thiolated gold nanoclusters, *Chem. Commun.*, **51**: 7935-7938, 2015. DOI: [10.1039/c5cc01951f](https://doi.org/10.1039/c5cc01951f)

97. S. H. XU, T. GAO, X. Y. FENG, Y. N. MAO, *et al.* Dual ligand co-functionalized fluorescent gold nanoclusters for the "turn on" sensing of glutathione in tumor cells, *J. Mater. Chem. B*, **4**: 1270-1275, 2016. DOI: [10.1039/c5tb02195b](https://doi.org/10.1039/c5tb02195b)
98. F. SCHULZ, G. T. DAHL, S. BESZTEJAN, M. A. SCHROER, *et al.* Ligand layer engineering to control stability and interfacial properties of nanoparticles, *Langmuir*, **32**: 7897-7907, 2016. DOI: [10.1021/acs.langmuir.6b01704](https://doi.org/10.1021/acs.langmuir.6b01704)
99. D. AILI AND M. M. STEVENS. Bioresponsive peptide-inorganic hybrid nanomaterials, *Chem. Soc. Rev.*, **39**: 3358-3370, 2010. DOI: [10.1039/b919461b](https://doi.org/10.1039/b919461b)
100. Q. YUAN, Y. WANG, L. ZHAO, R. LIU, *et al.* Peptide protected gold clusters: Chemical synthesis and biomedical applications, *Nanoscale*, **8**: 12095-12104, 2016. DOI: [10.1039/c6nr02750d](https://doi.org/10.1039/c6nr02750d)
101. A. YAHIA-AMMAR, D. SIERRA, F. MÉROLA, N. HILDEBRANDT, *et al.* Self-assembled gold nanoclusters for bright fluorescence imaging and enhanced drug delivery, *ACS Nano*, **10**: 2591-2599, 2016. DOI: [10.1021/acsnano.5b07596](https://doi.org/10.1021/acsnano.5b07596)
102. X. M. KANG, X. M. GUO, W. W. AN, X. J. NIU, *et al.* Photothermal therapeutic application of gold nanorods-porphyrin, *Sci. Rep.*, **7**: 42069, 2017. DOI: [10.1038/srep42069](https://doi.org/10.1038/srep42069)
103. B. R. SMITH AND S. S. GAMBHIR. Nanomaterials for *in vivo* imaging, *Chem. Rev.*, **117**: 901-986, 2017. DOI: [10.1021/acs.chemrev.6b00073](https://doi.org/10.1021/acs.chemrev.6b00073)
104. Y. ZHANG, W. CHU, A. FOROUSHANI, H. WANG, *et al.* New gold nanostructures for sensor applications: A review, *Materials*, **7**: 5169-5201, 2014. DOI: [10.3390/ma7075169](https://doi.org/10.3390/ma7075169)
105. L. ZHANG AND E. WANG. Metal nanoclusters: New fluorescent probes for sensors and bioimaging, *Nano Today*, **9**: 132-157, 2014. DOI: [10.1016/j.nantod.2014.02.010](https://doi.org/10.1016/j.nantod.2014.02.010)
106. L. CUI, S. HER, M. DUNNE, G. R. BORST, *et al.* Significant radiation enhancement effects by gold nanoparticles in combination with cisplatin in triple negative breast cancer cells and tumor xenografts, *Radiat. Res.*, **187**: 147-160, 2017. DOI: [10.1667/RR14578.1](https://doi.org/10.1667/RR14578.1)
107. R. VANKAYALA, Y.-K. HUANG, P. KALLURU, C.-S. CHIANG, *et al.* First demonstration of gold nanorods-mediated photodynamic therapeutic destruction of tumors via near infra-red light activation, *Small*, **10**: 1612-1622, 2014. DOI: [10.1002/smll.201302719](https://doi.org/10.1002/smll.201302719)
108. S. BALAKRISHNAN, F. A. BHAT, P. RAJA SINGH, S. MUKHERJEE, *et al.* Gold nanoparticle-conjugated quercetin inhibits epithelial-mesenchymal transition, angiogenesis and invasiveness via egfr/vegfr-2-mediated pathway in breast cancer, *Cell Proliferation*, **49**: 678-697, 2016. DOI: [10.1111/cpr.12296](https://doi.org/10.1111/cpr.12296)
109. Y. TIAN, Y. ZHANG, Z. TENG, W. TIAN, *et al.* pH-dependent transmembrane activity of peptide-functionalized gold nanostars for computed tomography/photoacoustic imaging and photothermal therapy, *ACS Appl. Mater. Interfaces*, **9**: 2114-2122, 2017. DOI: [10.1021/acsami.6b13237](https://doi.org/10.1021/acsami.6b13237)
110. Y. XIA, W. LI, C. M. COBLEY, J. CHEN, *et al.* Gold nanocages: From synthesis to theranostic applications, *Acc. Chem. Res.*, **44**: 914-924, 2011. DOI: [10.1021/ar200061q](https://doi.org/10.1021/ar200061q)
111. C. VILLIERS, "Gold nanoparticles for sensors and drug delivery," in *Gold Nanoparticles for Physics, Chemistry and Biology*, C. Louis and O. Pluchery, Eds., 1 ed. London, U.K.: Imperial College Press, 2012.
112. A. SASIDHARAN AND N. A. MONTEIRO-RIVIERE. Biomedical applications of gold nanomaterials: Opportunities and challenges, *WIREs Nanomed. Nanobiotechnol.*, **7**: 779-796, 2015. DOI: [10.1002/wnan.1341](https://doi.org/10.1002/wnan.1341)
113. C. D. WALKEY, J. B. OLSEN, F. SONG, R. LIU, *et al.* Protein corona fingerprinting predicts the cellular interaction of gold and silver nanoparticles, *ACS Nano*, **8**: 2439-2455, 2014. DOI: [10.1021/nn406018q](https://doi.org/10.1021/nn406018q)
114. A. E. NEL, L. MÄDLER, D. VELEGOL, T. XIA, *et al.* Understanding biophysicochemical interactions at the nano-bio interface, *Nat. Mater.*, **8**: 543-557, 2009. DOI: [10.1038/nmat2442](https://doi.org/10.1038/nmat2442)
115. M. P. MONOPOLI, C. ABERG, A. SALVATI, AND K. A. DAWSON. Biomolecular coronas provide the biological identity of nanosized materials, *Nat. Nanotechnol.*, **7**: 779-786, 2012. DOI: [10.1038/nnano.2012.207](https://doi.org/10.1038/nnano.2012.207)

116. Z. ZHANG, C. WANG, Y. ZHA, W. HU, *et al.* Corona-directed nucleic acid delivery into hepatic stellate cells for liver fibrosis therapy, *ACS Nano*, **9**: 2405-2419, 2015. DOI: [10.1021/nn505166x](https://doi.org/10.1021/nn505166x)
117. M. HADJIDEMETRIOU AND K. KOSTARELOS. Nanomedicine: Evolution of the nanoparticle corona, *Nat. Nanotechnol.*, **12**: 288-290, 2017. DOI: [10.1038/nnano.2017.61](https://doi.org/10.1038/nnano.2017.61)
118. W. SUN, A. FERRETTI, D. VARSANO, G. BRANCOLINI, *et al.* Charge transfer rates at a bio-inorganic interface, *J. Phys. Chem. C*, **118**: 18820-18828, 2014. DOI: [10.1021/jp507346a](https://doi.org/10.1021/jp507346a)
119. T. M. CARDUCCI, R. E. BLACKWELL, AND R. W. MURRAY. Charge-transfer effects in ligand exchange reactions of Au<sub>25</sub> monolayer-protected clusters, *J. Phys. Chem. Lett.*, **6**: 1299-1302, 2015. DOI: [10.1021/acs.jpcllett.5b00506](https://doi.org/10.1021/acs.jpcllett.5b00506)
120. L. SHANG, Y. WANG, J. JIANG, AND S. DONG. pH-dependent protein conformational changes in albumin:Gold nanoparticle bioconjugates: A spectroscopic study, *Langmuir*, **23**: 2714-2721, 2007. DOI: [10.1021/la062064e](https://doi.org/10.1021/la062064e)
121. F. HANKE AND J. BJÖRK. Structure and local reactivity of the Au(111) surface reconstruction, *Phys. Rev. B: Condens. Matter Mater. Phys.*, **87**: 235422, 2013. DOI: [10.1103/PhysRevB.87.235422](https://doi.org/10.1103/PhysRevB.87.235422)
122. H. HEINZ, T.-J. LIN, R. KISHORE MISHRA, AND F. S. EMAMI. Thermodynamically consistent force fields for the assembly of inorganic, organic, and biological nanostructures: The interface force field, *Langmuir*, **29**: 1754-1765, 2013. DOI: [10.1021/la3038846](https://doi.org/10.1021/la3038846)
123. J. YU, M. L. BECKER, AND G. A. CARRI. A molecular dynamics simulation of the stability-limited growth mechanism of peptide-mediated gold-nanoparticle synthesis, *Small*, **6**: 2242-2245, 2010. DOI: [10.1002/sml.201000889](https://doi.org/10.1002/sml.201000889)
124. W. KURASHIGE, Y. NIIHORI, S. SHARMA, AND Y. NEGISHI. Recent progress in the functionalization methods of thiolate-protected gold clusters, *J. Phys. Chem. Lett.*, **5**: 4134-4142, 2014. DOI: [10.1021/jz501941p](https://doi.org/10.1021/jz501941p)
125. D.-E. JIANG. The expanding universe of thiolated gold nanoclusters and beyond, *Nanoscale*, **5**: 7149-7160, 2013. DOI: [10.1039/c3nr34192e](https://doi.org/10.1039/c3nr34192e)
126. Z. MA, P. WANG, L. XIONG, AND Y. PEI. Thiolate-protected gold nanoclusters: Structural prediction and the understandings of electronic stability from first principles simulations, *WIREs Comput. Mol. Sim.*, **7**: e1315, 2017. DOI: [10.1002/wcms.1315](https://doi.org/10.1002/wcms.1315)
127. J. SCHNEIDER AND L. COLOMBI CIACCHI. Specific material recognition by small peptides mediated by the interfacial solvent structure, *J. Am. Chem. Soc.*, **134**: 2407-2413, 2012. DOI: [10.1021/ja210744g](https://doi.org/10.1021/ja210744g)
128. W. HUMPHREY, A. DALKE, AND K. SCHULTEN. Vmd: Visual molecular dynamics, *J. Mol. Graph.*, **14**: 33-38, 1996. DOI: [10.1016/0263-7855\(96\)00018-5](https://doi.org/10.1016/0263-7855(96)00018-5)
129. J. J. W. WILTZIUS, S. A. SIEVERS, M. R. SAWAYA, D. CASCIO, *et al.* Atomic structure of the cross- $\beta$  spine of islet amyloid polypeptide (amylin), *Protein Sci.*, **17**: 1467-1474, 2008. DOI: [10.1110/ps.036509.108](https://doi.org/10.1110/ps.036509.108)
130. C. L. HEINECKE, T. W. NI, S. MALOLA, V. MÄKINEN, *et al.* Structural and theoretical basis for ligand exchange on thiolate monolayer protected gold nanoclusters, *J. Am. Chem. Soc.*, **134**: 13316-13322, 2012. DOI: [10.1021/ja3032339](https://doi.org/10.1021/ja3032339)
131. M. W. HEAVEN, A. DASS, P. S. WHITE, K. M. HOLT, *et al.* Crystal structure of the gold nanoparticle [N(C<sub>8</sub>H<sub>17</sub>)<sub>4</sub>][Au<sub>25</sub>(SCH<sub>2</sub>CH<sub>2</sub>Ph)<sub>18</sub>], *J. Am. Chem. Soc.*, **130**: 3754-3755, 2008. DOI: [10.1021/ja800561b](https://doi.org/10.1021/ja800561b)
132. M. AZUBEL, J. KOIVISTO, S. MALOLA, D. BUSHNELL, *et al.* Electron microscopy of gold nanoparticles at atomic resolution, *Science*, **345**: 909-912, 2014. DOI: [10.1126/science.1251959](https://doi.org/10.1126/science.1251959)
133. J. AKOLA, M. WALTER, R. L. WHETTEN, H. HÄKKINEN, *et al.* On the structure of thiolate-protected Au<sub>25</sub>, *J. Am. Chem. Soc.*, **130**: 3756-3757, 2008. DOI: [10.1021/ja800594p](https://doi.org/10.1021/ja800594p)
134. M. ZHU, C. M. AIKENS, F. J. HOLLANDER, G. C. SCHATZ, *et al.* Correlating the crystal structure of a thiol-protected Au<sub>25</sub> cluster and optical properties, *J. Am. Chem. Soc.*, **130**: 5883-5885, 2008. DOI: [10.1021/ja801173r](https://doi.org/10.1021/ja801173r)

135. O. LOPEZ-ACEVEDO, H. TSUNOYAMA, T. TSUKUDA, H. HÄKKINEN, *et al.* Chirality and electronic structure of the thiolate-protected Au<sub>38</sub> nanocluster, *J. Am. Chem. Soc.*, **132**: 8210-8218, 2010. DOI: [10.1021/ja102934q](https://doi.org/10.1021/ja102934q)
136. H. QIAN, W. T. ECKENHOFF, Y. ZHU, T. PINTAUER, *et al.* Total structure determination of thiolate-protected Au<sub>38</sub> nanoparticles, *J. Am. Chem. Soc.*, **132**: 8280-8281, 2010. DOI: [10.1021/ja103592z](https://doi.org/10.1021/ja103592z)
137. P. D. JADZINSKY, G. CALERO, C. J. ACKERSON, D. A. BUSHNELL, *et al.* Structure of a thiol monolayer-protected gold nanoparticle at 1.1 Å resolution, *Science*, **318**: 430-433, 2007. DOI: [10.1126/science.1148624](https://doi.org/10.1126/science.1148624)
138. Y. PEI, J. TANG, X. TANG, Y. HUANG, *et al.* New structure model of au<sub>22</sub>(SR)<sub>18</sub>: Bitetrahedron golden kernel enclosed by [au<sub>6</sub>(SR)<sub>6</sub>] Au(i) complex, *J. Phys. Chem. Lett.*, **6**: 1390-1395, 2015. DOI: [10.1021/acs.jpcllett.5b00364](https://doi.org/10.1021/acs.jpcllett.5b00364)
139. Y. YU, Z. LUO, D. M. CHEVRIER, D. T. LEONG, *et al.* Identification of a highly luminescent au<sub>22</sub>(SG)<sub>18</sub> nanocluster, *J. Am. Chem. Soc.*, **136**: 1246-1249, 2014. DOI: [10.1021/ja411643u](https://doi.org/10.1021/ja411643u)
140. P. R. NIMMALA, B. YOON, R. L. WHETTEN, U. LANDMAN, *et al.* Au<sub>67</sub>(SR)<sub>35</sub> nanomolecules: Characteristic size-specific optical, electrochemical, structural properties and first-principles theoretical analysis, *J. Phys. Chem. A*, **117**: 504-517, 2013. DOI: [10.1021/jp311491v](https://doi.org/10.1021/jp311491v)
141. D. BAHENA, N. BHATTARAI, U. SANTIAGO, A. TLAHUICE, *et al.* Stem electron diffraction and high-resolution images used in the determination of the crystal structure of the Au<sub>144</sub>(SR)<sub>60</sub> cluster, *J. Phys. Chem. Lett.*, **4**: 975-981, 2013. DOI: [10.1021/jz400111d](https://doi.org/10.1021/jz400111d)
142. D. F. YANCEY, S. T. CHILL, L. ZHANG, A. I. FRENKEL, *et al.* A theoretical and experimental examination of systematic ligand-induced disorder in Au dendrimer-encapsulated nanoparticles, *Chem. Sci.*, **4**: 2912-2921, 2013. DOI: [10.1039/c3sc50614b](https://doi.org/10.1039/c3sc50614b)
143. A. TLAHUICE-FLORES. New insight into the structure of thiolated gold clusters: A structural prediction of the au<sub>187</sub>(SR)<sub>68</sub> cluster, *Phys. Chem. Chem. Phys.*, **17**: 5551-5555, 2015. DOI: [10.1039/c4cp05695g](https://doi.org/10.1039/c4cp05695g)
144. H. QIAN, Y. ZHU, AND R. JIN. Atomically precise gold nanocrystal molecules with surface plasmon resonance, *Proc. Natl. Acad. Sci. U. S. A.*, **109**: 696-700, 2012. DOI: [10.1073/pnas.1115307109](https://doi.org/10.1073/pnas.1115307109)
145. A. COSSARO, R. MAZZARELLO, R. ROUSSEAU, L. CASALIS, *et al.* X-ray diffraction and computation yield the structure of alkanethiols on gold(111), *Science*, **321**: 943-946, 2008. DOI: [10.1126/science.1158532](https://doi.org/10.1126/science.1158532)
146. B. M. BARNGROVER AND C. M. AIKENS. Oxidation of gold clusters by thiols, *J. Phys. Chem. A*, **117**: 5377-5384, 2013. DOI: [10.1021/jp403633a](https://doi.org/10.1021/jp403633a)
147. V. ROJAS-CERVELLERA, E. GIRALT, AND C. ROVIRA. Staple motifs, initial steps in the formation of thiolate-protected gold nanoparticles: How do they form?, *Inorg. Chem.*, **51**: 11422-11429, 2012. DOI: [10.1021/ic301079k](https://doi.org/10.1021/ic301079k)
148. M. ASKERKA, D. PICHUGINA, N. KUZ'MENKO, AND A. SHESTAKOV. Theoretical prediction of S-H bond rupture in methanethiol upon interaction with gold, *J. Phys. Chem. A*, **116**: 7686-7693, 2012. DOI: [10.1021/jp303001x](https://doi.org/10.1021/jp303001x)
149. D. M. P. MINGOS. Structural and bonding patterns in gold clusters, *Dalton Trans.*, **44**: 6680-6695, 2015. DOI: [10.1039/c5dt00253b](https://doi.org/10.1039/c5dt00253b)
150. Y. NEGISHI, N. K. CHAKI, Y. SHICHIBU, R. L. WHETTEN, *et al.* Origin of magic stability of thiolated gold clusters: A case study on Au<sub>25</sub>(sc<sub>6</sub>h<sub>13</sub>)<sub>18</sub>, *J. Am. Chem. Soc.*, **129**: 11322-11323, 2007. DOI: [10.1021/ja073580+](https://doi.org/10.1021/ja073580+)
151. F. MUNIZ-MIRANDA, M. C. MENZIANI, AND A. PEDONE. Assessment of exchange-correlation functionals in reproducing the structure and optical gap of organic-protected gold nanoclusters, *J. Phys. Chem. C*, **118**: 7532-7544, 2014. DOI: [10.1021/jp411483x](https://doi.org/10.1021/jp411483x)
152. Y. PEI, R. PAL, C. LIU, Y. GAO, *et al.* Interlocked catenane-like structure predicted in Au<sub>24</sub>(SR)<sub>20</sub>: Implication to structural evolution of thiolated gold clusters from homoleptic gold(i)

- thiolates to core-stacked nanoparticles, *J. Am. Chem. Soc.*, **134**: 3015-3024, 2012. DOI: [10.1021/ja208559y](https://doi.org/10.1021/ja208559y)
153. A. DAS, T. LI, G. LI, K. NOBUSADA, *et al.* Crystal structure and electronic properties of a thiolate-protected Au<sub>24</sub> nanocluster, *Nanoscale*, **6**: 6458-6462, 2014. DOI: [10.1039/c4nr01350f](https://doi.org/10.1039/c4nr01350f)
154. P. KOSKINEN, H. HÄKKINEN, G. SEIFERT, S. SANNA, *et al.* Density-functional based tight-binding study of small gold clusters, *New J. Phys.*, **8**: 9, 2006. DOI: [10.1088/1367-2630/8/1/009](https://doi.org/10.1088/1367-2630/8/1/009)
155. V. MÄKINEN, P. KOSKINEN, AND H. HÄKKINEN. Modeling thiolate-protected gold clusters with density-functional tight-binding, *Eur. Phys. J. D*, **67**: 38, 2013. DOI: [10.1140/epjd/e2012-30486-4](https://doi.org/10.1140/epjd/e2012-30486-4)
156. L. RINCON, A. HASMY, M. MARQUEZ, AND C. GONZALEZ. A perturbatively corrected tight-binding method with hybridization: Application to gold nanoparticles, *Chem. Phys. Lett.*, **503**: 171-175, 2011. DOI: [10.1016/j.cplett.2010.12.075](https://doi.org/10.1016/j.cplett.2010.12.075)
157. R. OUYANG, Y. XIE, AND D.-E. JIANG. Global minimization of gold clusters by combining neural network potentials and the basin-hopping method, *Nanoscale*, **7**: 14817-14821, 2015. DOI: [10.1039/c5nr03903g](https://doi.org/10.1039/c5nr03903g)
158. A. BRUMA, R. ISMAIL, L. OLIVER PAZ-BORBON, H. ARSLAN, *et al.* DFT study of the structures and energetics of 98-atom aupd clusters, *Nanoscale*, **5**: 646-652, 2013. DOI: [10.1039/c2nr32517a](https://doi.org/10.1039/c2nr32517a)
159. L. A. MANCERA AND D. M. BENOIT. An alternative methodology to assess the quality of empirical potentials for small gold clusters, *Comput. Theor. Chem.*, **1067**: 24-32, 2015. DOI: [10.1016/j.comptc.2015.05.026](https://doi.org/10.1016/j.comptc.2015.05.026)
160. Z. WU, J. LIU, Y. LI, Z. CHENG, *et al.* Self-assembly of nanoclusters into mono-, few-, and multilayered sheets via dipole-induced asymmetric van der waals attraction, *ACS Nano*, **9**: 6315-6323, 2015. DOI: [10.1021/acsnano.5b01823](https://doi.org/10.1021/acsnano.5b01823)
161. X.-N. ZHANG, R. WANG, AND G. XUE. Theoretical insights into the formation of thiolate-protected nanoparticles from gold (iii) chloride, *Chin. Phys. B*, **23**: 098201, 2014. DOI: [10.1088/1674-1056/23/9/098201](https://doi.org/10.1088/1674-1056/23/9/098201)
162. S. M. NEIDHART, B. M. BARNROVER, AND C. M. AIKENS. Theoretical examination of solvent and r group dependence in gold thiolate nanoparticle synthesis, *Phys. Chem. Chem. Phys.*, **17**: 7676-7680, 2015. DOI: [10.1039/c4cp04314f](https://doi.org/10.1039/c4cp04314f)
163. K.-M. XU, T. HUANG, H. WEN, Y.-R. LIU, *et al.* A density functional study of phosphorus-doped gold clusters: Au<sub>n</sub>P<sup>-</sup> (n = 1-8), *RSC Adv.*, **3**: 24492-24502, 2013. DOI: [10.1039/c3ra43938k](https://doi.org/10.1039/c3ra43938k)
164. H. YANG, Y. WANG, J. LEI, L. SHI, *et al.* Ligand-stabilized Au<sub>13</sub>Cu<sub>x</sub> (x = 2, 4, 8) bimetallic nanoclusters: Ligand engineering to control the exposure of metal sites, *J. Am. Chem. Soc.*, **135**: 9568-9571, 2013. DOI: [10.1021/ja402249s](https://doi.org/10.1021/ja402249s)
165. V. G. YARZHEMSKY, M. A. KAZARYAN, N. A. BULYCHEV, E. N. MURAVIEV, *et al.* Structure and properties of substituted gold clusters, *J. Nanotechnol. Diagn. Treat.*, **2**: 27-33, 2014. DOI: [10.12974/2311-8792.2014.02.02.2](https://doi.org/10.12974/2311-8792.2014.02.02.2)
166. A. TRINCHERO, S. KLACAR, L. O. PAZ-BORBÓN, A. HELLMAN, *et al.* Oxidation at the subnanometer scale, *J. Phys. Chem. C*, **119**: 10797-10803, 2015. DOI: [10.1021/jp508302b](https://doi.org/10.1021/jp508302b)
167. A. HADLEY AND C. M. AIKENS. Thiolate ligand exchange mechanisms of au1 and subnanometer gold particle au11, *J. Phys. Chem. C*, **114**: 18134-18138, 2010. DOI: [10.1021/jp911054e](https://doi.org/10.1021/jp911054e)
168. A. FERNANDO AND C. M. AIKENS. Ligand exchange mechanism on thiolate monolayer protected Au<sub>25</sub>(SR)<sub>18</sub> nanoclusters, *J. Phys. Chem. C*, **119**: 20179-20187, 2015. DOI: [10.1021/acs.jpcc.5b06833](https://doi.org/10.1021/acs.jpcc.5b06833)
169. J. ZHONG, X. TANG, J. TANG, J. SU, *et al.* Density functional theory studies on structure, ligand exchange, and optical properties of ligand-protected gold nanoclusters: Thiolate versus selenolate, *J. Phys. Chem. C*, **119**: 9205-9214, 2015. DOI: [10.1021/jp511615r](https://doi.org/10.1021/jp511615r)
170. N. TAKAGI, K. ISHIMURA, M. MATSUI, R. FUKUDA, *et al.* How can we understand au<sub>8</sub> cores and entangled ligands of selenolate- and thiolate-protected gold nanoclusters Au<sub>24</sub>(er)<sub>20</sub> and Au<sub>20</sub>(er)<sub>16</sub> (e = se, S; r = ph, me)? A theoretical study, *J. Am. Chem. Soc.*, **137**: 8593-8602, 2015. DOI: [10.1021/jacs.5b04337](https://doi.org/10.1021/jacs.5b04337)

171. E. FERTITTA, E. VOLOSHINA, AND B. PAULUS. Adsorption of multivalent alkylthiols on Au(111) surface: Insights from DFT, *J. Comput. Chem.*, **35**: 204-213, 2014. DOI: [10.1002/jcc.23484](https://doi.org/10.1002/jcc.23484)
172. D. MOLLENHAUER, N. GASTON, E. VOLOSHINA, AND B. PAULUS. Interaction of pyridine derivatives with a gold (111) surface as a model for adsorption to large nanoparticles, *J. Phys. Chem. C*, **117**: 4470-4479, 2013. DOI: [10.1021/jp309625h](https://doi.org/10.1021/jp309625h)
173. R. OUYANG, J. YAN, P. S. JENSEN, E. ASCIC, *et al.* Intermixed adatom and surface-bound adsorbates in regular self-assembled monolayers of racemic 2-butanethiol on Au(111), *ChemPhysChem*, **16**: 928-932, 2015. DOI: [10.1002/cphc.201402904](https://doi.org/10.1002/cphc.201402904)
174. H. BARRON, L. FERNÁNDEZ-SEIVANE, AND X. LÓPEZ-LOZANO. Systematic study of the adsorption of thiol molecules on a Au<sub>55</sub> nanoparticle, *Phys. Status Solidi B*, **251**: 1239-1247, 2014. DOI: [10.1002/pssb.201350183](https://doi.org/10.1002/pssb.201350183)
175. F. DUFOUR, B. FRESCH, O. DURUPHTY, C. CHANEAC, *et al.* Ligand and solvation effects on the structural and electronic properties of small gold clusters, *J. Phys. Chem. C*, **118**: 4362-4376, 2014. DOI: [10.1021/jp409019z](https://doi.org/10.1021/jp409019z)
176. X.-J. LIU AND I. HAMILTON. Adsorption of small molecules on helical gold nanorods: A relativistic density functional study, *J. Comput. Chem.*, **35**: 1967-1976, 2014. DOI: [10.1002/jcc.23711](https://doi.org/10.1002/jcc.23711)
177. A. S. BARNARD. Modeling the impact of alkanethiol sams on the morphology of gold nanocrystals, *Cryst. Growth Des.*, **13**: 5433-5441, 2013. DOI: [10.1021/cg401397y](https://doi.org/10.1021/cg401397y)
178. A. MATHEW, G. NATARAJAN, L. LEHTOVAARA, H. HÄKKINEN, *et al.* Supramolecular functionalization and concomitant enhancement in properties of Au<sub>25</sub> clusters, *ACS Nano*, **8**: 139-152, 2014. DOI: [10.1021/nn406219x](https://doi.org/10.1021/nn406219x)
179. S. SHARMA, W. KURASHIGE, K. NOBUSADA, AND Y. NEGISHI. Effect of trimetallization in thiolate-protected Au<sub>24-n</sub>Cu<sub>n</sub>Pd clusters, *Nanoscale*, **7**: 10606-10612, 2015. DOI: [10.1039/c5nr01491c](https://doi.org/10.1039/c5nr01491c)
180. I. DOLAMIC, B. VARNHOLT, AND T. BÜRGI. Chirality transfer from gold nanocluster to adsorbate evidenced by vibrational circular dichroism, *Nat. Commun.*, **6**: 7117, 2015. DOI: [10.1038/ncomms8117](https://doi.org/10.1038/ncomms8117)
181. K. FORSTER-TONIGOLD AND A. GROB. A systematic DFT study of substrate reconstruction effects due to thiolate and selenolate adsorption, *Surf. Sci.*, **640**: 18-24, 2015. DOI: [10.1016/j.susc.2015.04.003](https://doi.org/10.1016/j.susc.2015.04.003)
182. J. POLTE. Fundamental growth principles of colloidal metal nanoparticles - a new perspective, *CrystEngComm*, **17**: 6809-6830, 2015. DOI: [10.1039/c5ce01014d](https://doi.org/10.1039/c5ce01014d)
183. C. LIU, Y. PEI, H. SUN, AND J. MA. The nucleation and growth mechanism of thiolate-protected Au nanoclusters, *J. Am. Chem. Soc.*, **137**: 15809-15816, 2015. DOI: [10.1021/jacs.5b09466](https://doi.org/10.1021/jacs.5b09466)
184. C. ADAMO AND D. JACQUEMIN. The calculations of excited-state properties with time-dependent density functional theory, *Chem. Soc. Rev.*, **42**: 845-856, 2013. DOI: [10.1039/c2cs35394f](https://doi.org/10.1039/c2cs35394f)
185. A. TLAHUICE-FLORES, R. L. WHETTEN, AND M. JOSE-YACAMAN. Ligand effects on the structure and the electronic optical properties of anionic Au<sub>25</sub>(SR)<sub>18</sub> clusters, *J. Phys. Chem. C*, **117**: 20867-20875, 2013. DOI: [10.1021/jp407150t](https://doi.org/10.1021/jp407150t)
186. S. ANTONELLO, N. V. PERERA, M. RUZZI, J. A. GASCÓN, *et al.* Interplay of charge state, lability, and magnetism in the molecule-like Au<sub>25</sub>(SR)<sub>18</sub> cluster, *J. Am. Chem. Soc.*, **135**: 15585-15594, 2013. DOI: [10.1021/ja407887d](https://doi.org/10.1021/ja407887d)
187. S. CHEN, S. WANG, J. ZHONG, Y. SONG, *et al.* The structure and optical properties of the [Au<sub>18</sub>(SR)<sub>14</sub>] nanocluster, *Angew. Chem. Int. Ed.*, **54**: 3145-3149, 2015. DOI: [10.1002/anie.201410295](https://doi.org/10.1002/anie.201410295)
188. A. DAS, C. LIU, H. Y. BYUN, K. NOBUSADA, *et al.* Structure determination of [Au<sub>18</sub>(SR)<sub>14</sub>], *Angew. Chem. Int. Ed.*, **54**: 3140-3144, 2015. DOI: [10.1002/anie.201410161](https://doi.org/10.1002/anie.201410161)
189. A. FIHEY, F. MAUREL, AND A. PERRIER. Modeling the absorbance properties of a pyrene chromophore grafted onto a Au<sub>25</sub> nanocluster: A TD-DFT study, *J. Phys. Chem. C*, **118**: 4444-4453, 2014. DOI: [10.1021/jp410695v](https://doi.org/10.1021/jp410695v)

190. A. FIHEY, F. MAUREL, AND A. PERRIER. A DFT study of a new class of gold nanocluster-photochrome multi-functional switches, *Phys. Chem. Chem. Phys.*, **16**: 26240-26251, 2014. DOI: [10.1039/c4cp03287j](https://doi.org/10.1039/c4cp03287j)
191. A. FIHEY, B. LE GUENNIC, AND D. JACQUEMIN. Toward an enhancement of the photoactivity of multiphotochromic dimers using plasmon resonance: A theoretical study, *J. Phys. Chem. Lett.*, **6**: 3067-3073, 2015. DOI: [10.1021/acs.jpcllett.5b01333](https://doi.org/10.1021/acs.jpcllett.5b01333)
192. A. FIHEY, F. MAUREL, AND A. PERRIER. Plasmon-excitation coupling for dithienylethene/gold nanoparticle hybrid systems: A theoretical study, *J. Phys. Chem. C*, **119**: 9995-10006, 2015. DOI: [10.1021/acs.jpcc.5b01118](https://doi.org/10.1021/acs.jpcc.5b01118)
193. A. TLAHUICE-FLORES, R. L. WHETTEN, AND M. JOSE-YACAMAN. Vibrational normal modes of small thiolate-protected gold clusters, *J. Phys. Chem. C*, **117**: 12191-12198, 2013. DOI: [10.1021/jp4033063](https://doi.org/10.1021/jp4033063)
194. A. ANGIONI, S. CORNI, AND B. MENNUCCI. Can we control the electronic energy transfer in molecular dyads through metal nanoparticles? A QM/continuum investigation, *Phys. Chem. Chem. Phys.*, **15**: 3294-3303, 2013. DOI: [10.1039/c2cp44010e](https://doi.org/10.1039/c2cp44010e)
195. P. N. DAY, K. A. NGUYEN, AND R. PACHTER. Calculation of one- and two-photon absorption spectra of thiolated gold nanoclusters using time-dependent density functional theory, *J. Chem. Theory Comput.*, **6**: 2809-2821, 2010. DOI: [10.1021/ct100139t](https://doi.org/10.1021/ct100139t)
196. G. T. BAE AND C. M. AIKENS. Time-dependent density functional theory studies of optical properties of Au nanoparticles: Octahedra, truncated octahedra, and icosahedra, *J. Phys. Chem. C*, **119**: 23127-23137, 2015. DOI: [10.1021/acs.jpcc.5b05978](https://doi.org/10.1021/acs.jpcc.5b05978)
197. E. B. GUIDEZ AND C. M. AIKENS. Time-dependent density functional theory study of the luminescence properties of gold phosphine thiolate complexes, *J. Phys. Chem. A*, **119**: 3337-3347, 2015. DOI: [10.1021/jp5104033](https://doi.org/10.1021/jp5104033)
198. Q. MENG, S. P. MAY, M. T. BERRY, AND D. S. KILIN. Time-resolved electronic and optical properties of a thiolate-protected Au<sub>38</sub> nanocluster, *Mol. Phys.*, **113**: 408-417, 2015. DOI: [10.1080/00268976.2014.999838](https://doi.org/10.1080/00268976.2014.999838)
199. X. LÓPEZ LOZANO, C. MOTTET, AND H.-C. WEISSKER. Effect of alloying on the optical properties of Ag–Au nanoparticles, *J. Phys. Chem. C*, **117**: 3062-3068, 2013. DOI: [10.1021/jp309957y](https://doi.org/10.1021/jp309957y)
200. F. MUNIZ-MIRANDA, M. C. MENZIANI, AND A. PEDONE. Influence of silver doping on the photoluminescence of protected Ag<sub>25</sub>–n nanoclusters: A time-dependent density functional theory investigation, *J. Phys. Chem. C*, **119**: 10766-10775, 2015. DOI: [10.1021/acs.jpcc.5b02655](https://doi.org/10.1021/acs.jpcc.5b02655)
201. E. POHJOLAINEN, H. HÄKKINEN, AND A. CLAYBORNE. The role of the anchor atom in the ligand of the monolayer-protected Au<sub>25</sub>(xr)<sub>18</sub><sup>-</sup> nanocluster, *J. Phys. Chem. C*, **119**: 9587-9594, 2015. DOI: [10.1021/acs.jpcc.5b01068](https://doi.org/10.1021/acs.jpcc.5b01068)
202. G. LUGO, V. SCHWANEN, B. FRESCH, AND F. REMACLE. Charge redistribution effects on the uv-vis spectra of small ligated gold clusters: A computational study, *J. Phys. Chem. C*, **119**: 10969-10980, 2015. DOI: [10.1021/jp511120j](https://doi.org/10.1021/jp511120j)
203. H.-C. WEISSKER, O. LOPEZ-ACEVEDO, R. L. WHETTEN, AND X. LÓPEZ-LOZANO. Optical spectra of the special Au<sub>144</sub> gold-cluster compounds: Sensitivity to structure and symmetry, *J. Phys. Chem. C*, **119**: 11250-11259, 2015. DOI: [10.1021/jp512310x](https://doi.org/10.1021/jp512310x)
204. K. L. D. M. WEERAWARDENE AND C. M. AIKENS. Theoretical insights into origin of photoluminescence of Au<sub>25</sub>(SR)<sub>18</sub><sup>-</sup> nanoparticles, *J. Am. Chem. Soc.*, **138**: 11202-11210, 2016. DOI: [10.1021/jacs.6b05293](https://doi.org/10.1021/jacs.6b05293)
205. X.-K. WAN, W. W. XU, S.-F. YUAN, Y. GAO, *et al.* A near-infrared-emissive alkynyl-protected Au<sub>24</sub> nanocluster, *Angew. Chem. Int. Ed.*, **54**: 9683-9686, 2015. DOI: [10.1002/anie.201503893](https://doi.org/10.1002/anie.201503893)
206. K. MOTH-POULSEN, *Handbook of single-molecule electronics*: Pan Stanford, 2015.
207. J. KLIMEŠ AND A. MICHAELIDES. Perspective: Advances and challenges in treating van der waals dispersion forces in density functional theory, *J. Chem. Phys.*, **137**: 120901, 2012. DOI: [10.1063/1.4754130](https://doi.org/10.1063/1.4754130)



208. P. TERESHCHUK AND J. L. F. DA SILVA. Ethanol and water adsorption on close-packed 3d, 4d, and 5d transition-metal surfaces: A density functional theory investigation with van der waals correction, *J. Phys. Chem. C*, **116**: 24695-24705, 2012. DOI: [10.1021/jp308870d](https://doi.org/10.1021/jp308870d)
209. W. LIU, J. CARRASCO, B. SANTRA, A. MICHAELIDES, *et al.* Benzene adsorbed on metals: Concerted effect of covalency and van der waals bonding, *Phys. Rev. B: Condens. Matter Mater. Phys.*, **86**: 245405, 2012. DOI: [10.1103/PhysRevB.86.245405](https://doi.org/10.1103/PhysRevB.86.245405)
210. T. S. CHWEE AND M. B. SULLIVAN. Adsorption studies of c6h6 on cu (111), Ag (111), and Au (111) within dispersion corrected density functional theory, *J. Chem. Phys.*, **137**: 134703, 2012. DOI: [10.1063/1.4755993](https://doi.org/10.1063/1.4755993)
211. J. L. C. FAJÍN, F. TEIXEIRA, J. R. B. GOMES, AND M. N. D. S. CORDEIRO. Effect of van der waals interactions in the DFT description of self-assembled monolayers of thiols on gold, *Theor. Chem. Acc.*, **134**: 67, 2015. DOI: [10.1007/s00214-015-1666-y](https://doi.org/10.1007/s00214-015-1666-y)
212. R. NADLER AND J. F. SANZ. Effect of dispersion correction on the Au(1 1 1)-h<sub>2</sub>O interface: A first-principles study, *J. Chem. Phys.*, **137**: 114709, 2012. DOI: [10.1063/1.4752235](https://doi.org/10.1063/1.4752235)
213. J. CARRASCO, J. KLIMEŠ, AND A. MICHAELIDES. The role of van der waals forces in water adsorption on metals, *J. Chem. Phys.*, **138**: 024708, 2013. DOI: [10.1063/1.4773901](https://doi.org/10.1063/1.4773901)
214. K. TONIGOLD AND A. GROß. Dispersive interactions in water bilayers at metallic surfaces: A comparison of the pbe and rpbe functional including semiempirical dispersion corrections, *J. Comput. Chem.*, **33**: 695-701, 2012. DOI: [10.1002/jcc.22900](https://doi.org/10.1002/jcc.22900)
215. F. IORI, R. DI FELICE, E. MOLINARI, AND S. CORNI. GoIP: An atomistic force-field to describe the interaction of proteins with Au(111) surfaces in water, *J. Comput. Chem.*, **30**: 1465-1476, 2009. DOI: [10.1002/jcc.21165](https://doi.org/10.1002/jcc.21165)
216. L. B. WRIGHT, P. M. RODGER, S. CORNI, AND T. R. WALSH. GoIP-CHARMM: First-principles based force fields for the interaction of proteins with Au(111) and Au(100), *J. Chem. Theory Comput.*, **9**: 1616-1630, 2013. DOI: [10.1021/ct301018m](https://doi.org/10.1021/ct301018m)
217. M. HOEFLING, F. IORI, S. CORNI, AND K.-E. GOTTSCHALK. The conformations of amino acids on a gold(111) surface, *ChemPhysChem*, **11**: 1763-1767, 2010. DOI: [10.1002/cphc.200900990](https://doi.org/10.1002/cphc.200900990)
218. M. DION, H. RYDBERG, E. SCHRÖDER, D. C. LANGRETH, *et al.* Van der waals density functional for general geometries, *Phys. Rev. Lett.*, **92**: 246401, 2004. DOI: [10.1103/PhysRevLett.92.246401](https://doi.org/10.1103/PhysRevLett.92.246401)
219. T. THONHAUSER, V. R. COOPER, S. LI, A. PUZDER, *et al.* Van der waals density functional: Self-consistent potential and the nature of the van der waals bond, *Phys. Rev. B: Condens. Matter Mater. Phys.*, **76**: 125112, 2007. DOI: [10.1103/PhysRevB.76.125112](https://doi.org/10.1103/PhysRevB.76.125112)
220. B. HAMMER, L. B. HANSEN, AND J. K. NØRSKOV. Improved adsorption energetics within density-functional theory using revised perdew-burke-ernzerhof functionals, *Phys. Rev. B: Condens. Matter Mater. Phys.*, **59**: 7413-7421, 1999. DOI: [10.1103/PhysRevB.59.7413](https://doi.org/10.1103/PhysRevB.59.7413)
221. S. BANERJEE, J. A. MONTGOMERY, JR., AND J. A. GASCÓN. A QM/mm approach for the study of monolayer-protected gold clusters, *J. Mater. Sci.*, **47**: 7686-7692, 2012. DOI: [10.1007/s10853-012-6356-8](https://doi.org/10.1007/s10853-012-6356-8)
222. G. BRANCOLINI, D. TOROZ, AND S. CORNI. Can small hydrophobic gold nanoparticles inhibit  $\beta_2$ -microglobulin fibrillation?, *Nanoscale*, **6**: 7903-7911, 2014. DOI: [10.1039/c4nr01514b](https://doi.org/10.1039/c4nr01514b)
223. Y. ZHAO, F. ZHOU, H. ZHOU, AND H. SU. The structural and bonding evolution in cysteine-gold cluster complexes, *Phys. Chem. Chem. Phys.*, **15**: 1690-1698, 2013. DOI: [10.1039/c2cp42830j](https://doi.org/10.1039/c2cp42830j)
224. H.-J. XIE, Q.-F. LEI, AND W.-J. FANG. Intermolecular interactions between gold clusters and selected amino acids cysteine and glycine: A DFT study, *J. Mol. Model.*, **18**: 645-652, 2012. DOI: [10.1007/s00894-011-1112-6](https://doi.org/10.1007/s00894-011-1112-6)
225. A. H. PAKIARI AND Z. JAMSHIDI. Interaction of amino acids with gold and silver clusters, *J. Phys. Chem. A*, **111**: 4391-4396, 2007. DOI: [10.1021/jp070306t](https://doi.org/10.1021/jp070306t)
226. Z. ALIAKBAR TEHRANI, Z. JAMSHIDI, M. JEBELI JAVAN, AND A. FATTAHI. Interactions of glutathione tripeptide with gold cluster: Influence of intramolecular hydrogen bond on complexation behavior, *J. Phys. Chem. A*, **116**: 4338-4347, 2012. DOI: [10.1021/jp2080226](https://doi.org/10.1021/jp2080226)

227. S. PIANA AND A. BILIC. The nature of the adsorption of nucleobases on the gold [111] surface, *J. Phys. Chem. B*, **110**: 23467-23471, 2006. DOI: [10.1021/jp064438i](https://doi.org/10.1021/jp064438i)
228. L. ZHANG, T. REN, X. YANG, L. ZHOU, *et al.* Intermolecular interactions of a size-expanded guanine analogue with gold nanoclusters, *Int. J. Quantum Chem.*, **113**: 2234-2242, 2013. DOI: [10.1002/qua.24436](https://doi.org/10.1002/qua.24436)
229. A. SARMAH AND R. K. ROY. Interaction between small gold clusters and nucleobases: A density functional reactivity theory based study, *J. Phys. Chem. C*, **119**: 17940-17953, 2015. DOI: [10.1021/acs.jpcc.5b04948](https://doi.org/10.1021/acs.jpcc.5b04948)
230. S. RAI, H. SINGH, AND U. D. PRIYAKUMAR. Binding to gold nanocluster alters the hydrogen bonding interactions and electronic properties of canonical and size expanded DNA base pairs, *RSC Adv.*, **5**: 49408-49419, 2015. DOI: [10.1039/c5ra04668h](https://doi.org/10.1039/c5ra04668h)
231. L. B. WRIGHT, N. A. MERRILL, M. R. KNECHT, AND T. R. WALSH. Structure of arginine overlayers at the aqueous gold interface: Implications for nanoparticle assembly, *ACS Appl. Mater. Interfaces*, **6**: 10524-10533, 2014. DOI: [10.1021/am502119g](https://doi.org/10.1021/am502119g)
232. G. BRANCOLINI, L. Z. POLZI, AND S. CORNI. Computational strategies for protein-surface and protein-nanoparticle interactions, *J. Self-Assem. Mol. Electron.*, **2**: 1-26, 2015. DOI: [10.13052/jsame2245-4551.211](https://doi.org/10.13052/jsame2245-4551.211)
233. M. HOEFLING, F. IORI, S. CORNI, AND K.-E. GOTTSCHALK. Interaction of amino acids with the Au(111) surface: Adsorption free energies from molecular dynamics simulations, *Langmuir*, **26**: 8347-8351, 2010. DOI: [10.1021/la904765u](https://doi.org/10.1021/la904765u)
234. Z. TANG, J. P. PALAFOX-HERNANDEZ, W.-C. LAW, Z. E. HUGHES, *et al.* Biomolecular recognition principles for bionanocombinatorics: An integrated approach to elucidate enthalpic and entropic factors, *ACS Nano*, **7**: 9632-9646, 2013. DOI: [10.1021/nn404427y](https://doi.org/10.1021/nn404427y)
235. H. HEINZ, B. L. FARMER, R. B. PANDEY, J. M. SLOCIK, *et al.* Nature of molecular interactions of peptides with gold, palladium, and pd-Au bimetal surfaces in aqueous solution, *J. Am. Chem. Soc.*, **131**: 9704-9714, 2009. DOI: [10.1021/ja900531f](https://doi.org/10.1021/ja900531f)
236. R. B. PANDEY, H. HEINZ, J. FENG, B. L. FARMER, *et al.* Adsorption of peptides (a3, flg, pd2, pd4) on gold and palladium surfaces by a coarse-grained Monte Carlo simulation, *Phys. Chem. Chem. Phys.*, **11**: 1989-2001, 2009. DOI: [10.1039/b816187a](https://doi.org/10.1039/b816187a)
237. J. FENG, J. M. SLOCIK, M. SARIKAYA, R. R. NAIK, *et al.* Influence of the shape of nanostructured metal surfaces on adsorption of single peptide molecules in aqueous solution, *Small*, **8**: 1049-1059, 2012. DOI: [10.1002/sml.201102066](https://doi.org/10.1002/sml.201102066)
238. A. VILA VERDE, P. J. BELTRAMO, AND J. K. MARANAS. Adsorption of homopolypeptides on gold investigated using atomistic molecular dynamics, *Langmuir*, **27**: 5918-5926, 2011. DOI: [10.1021/la104814z](https://doi.org/10.1021/la104814z)
239. R. BRAUN, M. SARIKAYA, AND K. SCHULTEN. Genetically engineered gold-binding polypeptides: Structure prediction and molecular dynamics, *J. Biomater. Sci. Polym. Ed.*, **13**: 747-757, 2002. DOI: [10.1163/156856202760197384](https://doi.org/10.1163/156856202760197384)
240. L. B. WRIGHT, J. P. PALAFOX-HERNANDEZ, P. M. RODGER, S. CORNI, *et al.* Facet selectivity in gold binding peptides: Exploiting interfacial water structure, *Chem. Sci.*, **6**: 5204-5214, 2015. DOI: [10.1039/c5sc00399g](https://doi.org/10.1039/c5sc00399g)
241. J. FENG, R. B. PANDEY, R. J. BERRY, B. L. FARMER, *et al.* Adsorption mechanism of single amino acid and surfactant molecules to Au {111} surfaces in aqueous solution: Design rules for metal-binding molecules, *Soft Matter*, **7**: 2113-2120, 2011. DOI: [10.1039/c0sm01118e](https://doi.org/10.1039/c0sm01118e)
242. V. P. RAUT, M. A. AGASHE, S. J. STUART, AND R. A. LATOUR. Molecular dynamics simulations of peptide-surface interactions, *Langmuir*, **21**: 1629-1639, 2005. DOI: [10.1021/la047807f](https://doi.org/10.1021/la047807f)
243. S. CORNI, M. HNILOVA, C. TAMERLER, AND M. SARIKAYA. Conformational behavior of genetically-engineered dodecapeptides as a determinant of binding affinity for gold, *J. Phys. Chem. C*, **117**: 16990-17003, 2013. DOI: [10.1021/jp404057h](https://doi.org/10.1021/jp404057h)

244. A. VILA VERDE, J. M. ACRES, AND J. K. MARANAS. Investigating the specificity of peptide adsorption on gold using molecular dynamics simulations, *Biomacromolecules*, **10**: 2118-2128, 2009. DOI: [10.1021/bm9002464](https://doi.org/10.1021/bm9002464)
245. J. ZHAO, X. WANG, N. JIANG, T. YAN, *et al.* Polarization effect and electric potential changes in the stimuli-responsive molecular monolayers under an external electric field, *J. Phys. Chem. C*, **119**: 22866-22881, 2015. DOI: [10.1021/acs.jpcc.5b04805](https://doi.org/10.1021/acs.jpcc.5b04805)
246. H. HEINZ, K. C. JHA, J. LUETTNER-STRAHMANN, B. L. FARMER, *et al.* Polarization at metal-biomolecular interfaces in solution, *J. R. Soc. Interface*, **8**: 220-232, 2011. DOI: [10.1098/rsif.2010.0318](https://doi.org/10.1098/rsif.2010.0318)
247. Z. E. HUGHES, M. A. NGUYEN, Y. LI, M. T. SWIHART, *et al.* Elucidating the influence of materials-binding peptide sequence on Au surface interactions and colloidal stability of Au nanoparticles, *Nanoscale*, **9**: 421-432, 2017. DOI: [10.1039/c6nr07890g](https://doi.org/10.1039/c6nr07890g)
248. Z. E. HUGHES, R. KOCHANDRA, AND T. R. WALSH. Facet-specific adsorption of tripeptides at aqueous Au interfaces: Open questions in reconciling experiment and simulation, *Langmuir*, **33**: 3742-3754, 2017. DOI: [10.1021/acs.langmuir.6b04558](https://doi.org/10.1021/acs.langmuir.6b04558)
249. S. KHAN, A. GUPTA, A. CHAUDHARY, AND C. K. NANDI. Orientational switching of protein conformation as a function of nanoparticle curvature and their geometrical fitting, *J. Chem. Phys.*, **141**: 084707, 2014. DOI: [10.1063/1.4893441](https://doi.org/10.1063/1.4893441)
250. L. B. WRIGHT, P. M. RODGER, AND T. R. WALSH. Aqueous citrate: A first-principles and force-field molecular dynamics study, *RSC Adv.*, **3**: 16399-16409, 2013. DOI: [10.1039/c3ra42437e](https://doi.org/10.1039/c3ra42437e)
251. J.-W. PARK AND J. S. SHUMAKER-PARRY. Structural study of citrate layers on gold nanoparticles: Role of intermolecular interactions in stabilizing nanoparticles, *J. Am. Chem. Soc.*, **136**: 1907-1921, 2014. DOI: [10.1021/ja4097384](https://doi.org/10.1021/ja4097384)
252. L. B. WRIGHT, P. M. RODGER, AND T. R. WALSH. Structure and properties of citrate overlayers adsorbed at the aqueous Au(111) interface, *Langmuir*, **30**: 15171-15180, 2014. DOI: [10.1021/la503690t](https://doi.org/10.1021/la503690t)
253. G. BRANCOLINI, A. CORAZZA, M. VUANO, F. FOGOLARI, *et al.* Probing the influence of citrate-capped gold nanoparticles on an amyloidogenic protein, *ACS Nano*, **9**: 2600-2613, 2015. DOI: [10.1021/nn506161j](https://doi.org/10.1021/nn506161j)
254. S.-T. WANG, Y. LIN, N. TODOROVA, Y. XU, *et al.* Facet-dependent interactions of islet amyloid polypeptide with gold nanoparticles: Implications for fibril formation and peptide-induced lipid membrane disruption, *Chem. Mater.*, **29**: 1550-1560, 2017. DOI: [10.1021/acs.chemmater.6b04144](https://doi.org/10.1021/acs.chemmater.6b04144)
255. W. LIN, T. INSLEY, M. D. TUTTLE, L. ZHU, *et al.* Control of protein orientation on gold nanoparticles, *J. Phys. Chem. C*, **119**: 21035-21043, 2015. DOI: [10.1021/acs.jpcc.5b07701](https://doi.org/10.1021/acs.jpcc.5b07701)
256. A. C. TEMPLETON, M. J. HOSTETLER, C. T. KRAFT, AND R. W. MURRAY. Reactivity of monolayer-protected gold cluster molecules: Steric effects, *J. Am. Chem. Soc.*, **120**: 1906-1911, 1998. DOI: [10.1021/ja973863+](https://doi.org/10.1021/ja973863+)
257. V. ROJAS-CERVELLERA, L. RAICH, J. AKOLA, AND C. ROVIRA. The molecular mechanism of the ligand exchange reaction of an antibody against a glutathione-coated gold cluster, *Nanoscale*, **9**: 3121-3127, 2017. DOI: [10.1039/c6nr08498b](https://doi.org/10.1039/c6nr08498b)
258. D. AN, J. SU, J. K. WEBER, X. GAO, *et al.* A peptide-coated gold nanocluster exhibits unique behavior in protein activity inhibition, *J. Am. Chem. Soc.*, **137**: 8412-8418, 2015. DOI: [10.1021/jacs.5b00888](https://doi.org/10.1021/jacs.5b00888)
259. L. N. ZHAO, J. ZHAI, X. J. ZHANG, X. Y. GAO, *et al.* Computational design of peptide-Au cluster probe for sensitive detection of  $\alpha_{\text{Ib}}\beta_3$  integrin, *Nanoscale*, **8**: 4203-4208, 2016. DOI: [10.1039/c5nr09175f](https://doi.org/10.1039/c5nr09175f)
260. M. LIU, L. GAO, L. ZHAO, J. HE, *et al.* Peptide-Au clusters induced tumor cells apoptosis via targeting glutathione peroxidase-1: The molecular dynamics assisted experimental studies, *Sci. Rep.*, **7**: 131, 2017. DOI: [10.1038/s41598-017-00278-6](https://doi.org/10.1038/s41598-017-00278-6)

261. M. E. SIWKO AND S. CORNI. Cytochrome C on a gold surface: Investigating structural relaxations and their role in protein-surface electron transfer by molecular dynamics simulations, *Phys. Chem. Chem. Phys.*, **15**: 5945-5956, 2013. DOI: [10.1039/c3cp00146f](https://doi.org/10.1039/c3cp00146f)
262. L. ZANETTI-POLZI, I. DAIDONE, C. A. BORTOLOTTI, AND S. CORNI. Surface packing determines the redox potential shift of cytochrome c adsorbed on gold, *J. Am. Chem. Soc.*, **136**: 12929-12937, 2014. DOI: [10.1021/ja505251a](https://doi.org/10.1021/ja505251a)
263. C. PENG, J. LIU, AND J. ZHOU. Molecular simulations of cytochrome c adsorption on a bare gold surface: Insights for the hindrance of electron transfer, *J. Phys. Chem. C*, **119**: 20773-20781, 2015. DOI: [10.1021/acs.jpcc.5b07581](https://doi.org/10.1021/acs.jpcc.5b07581)
264. L. ZANETTI-POLZI AND S. CORNI. A dynamical approach to non-adiabatic electron transfers at the bio-inorganic interface, *Phys. Chem. Chem. Phys.*, **18**: 10538-10549, 2016. DOI: [10.1039/c6cp00044d](https://doi.org/10.1039/c6cp00044d)
265. A. HUNG, S. MWENIFUMBO, M. MAGER, J. J. KUNA, *et al.* Ordering surfaces on the nanoscale: Implications for protein adsorption, *J. Am. Chem. Soc.*, **133**: 1438-1450, 2011. DOI: [10.1021/ja108285u](https://doi.org/10.1021/ja108285u)
266. A. HUNG, M. MAGER, M. HEMBURY, F. STELLACCI, *et al.* Amphiphilic amino acids: A key to adsorbing proteins to nanopatterned surfaces?, *Chem. Sci.*, **4**: 928-937, 2013. DOI: [10.1039/c2sc21639f](https://doi.org/10.1039/c2sc21639f)
267. J. J. KUNA, K. VOITCHOVSKY, C. SINGH, H. JIANG, *et al.* The effect of nanometre-scale structure on interfacial energy, *Nat. Mater.*, **8**: 837-842, 2009. DOI: [10.1038/nmat2534](https://doi.org/10.1038/nmat2534)
268. N. TODOROVA, C. CHIAPPINI, M. MAGER, B. SIMONA, *et al.* Surface presentation of functional peptides in solution determines cell internalization efficiency of TAT conjugated nanoparticles, *Nano Lett.*, **14**: 5229-5237, 2014. DOI: [10.1021/nl5021848](https://doi.org/10.1021/nl5021848)
269. R. C. VAN LEHN AND A. ALEXANDER-KATZ. Pathway for insertion of amphiphilic nanoparticles into defect-free lipid bilayers from atomistic molecular dynamics simulations, *Soft Matter*, **11**: 3165-3175, 2015. DOI: [10.1039/c5sm00287g](https://doi.org/10.1039/c5sm00287g)
270. N. A. BROOKS, D. S. POUNIOTIS, C.-K. TANG, V. APOSTOLOPOULOS, *et al.* Cell-penetrating peptides: Application in vaccine delivery, *Biochim. Biophys. Acta*, **1805**: 25-34, 2010. DOI: [10.1016/j.bbcan.2009.09.004](https://doi.org/10.1016/j.bbcan.2009.09.004)
271. Ž. KRPEČIĆ, S. SALEEMI, I. A. PRIOR, V. SÉE, *et al.* Negotiation of intracellular membrane barriers by TAT-modified gold nanoparticles., *ACS Nano*, **5**: 5195-5201, 2011. DOI: [10.1021/nn201369k](https://doi.org/10.1021/nn201369k)
272. J. M. DE LA FUENTE AND C. C. BERRY. Tat peptide as an efficient molecule to translocate gold nanoparticles into the cell nucleus, *Bioconjugate Chem.*, **16**: 1176-1180, 2005. DOI: [10.1021/bc050033+](https://doi.org/10.1021/bc050033+)
273. B. SONG, H. YUAN, C. J. JAMESON, AND S. MURAD. Role of surface ligands in nanoparticle permeation through a model membrane: A coarse-grained molecular dynamics simulations study, *Mol. Phys.*, **110**: 2181-2195, 2012. DOI: [10.1080/00268976.2012.668964](https://doi.org/10.1080/00268976.2012.668964)
274. R. C. VAN LEHN, P. U. ATUKORALE, R. P. CARNEY, Y.-S. YANG, *et al.* Effect of particle diameter and surface composition on the spontaneous fusion of monolayer-protected gold nanoparticles with lipid bilayers, *Nano Lett.*, **13**: 4060-4067, 2013. DOI: [10.1021/nl401365n](https://doi.org/10.1021/nl401365n)
275. J.-Q. LIN, Y.-G. ZHENG, H.-W. ZHANG, AND Z. CHEN. A simulation study on nanoscale holes generated by gold nanoparticles on negative lipid bilayers, *Langmuir*, **27**: 8323-8332, 2011. DOI: [10.1021/la201086u](https://doi.org/10.1021/la201086u)
276. G. ROSSI AND L. MONTICELLI. Gold nanoparticles in model biological membranes: A computational perspective, *Biochim. Biophys. Acta*, **1858**: 2380-2389, 2016. DOI: [10.1016/j.bbamem.2016.04.001](https://doi.org/10.1016/j.bbamem.2016.04.001)
277. X. QUAN, C. PENG, D. ZHAO, L. LI, *et al.* Molecular understanding of the penetration of functionalized gold nanoparticles into asymmetric membranes, *Langmuir*, **33**: 361-371, 2017. DOI: [10.1021/acs.langmuir.6b02937](https://doi.org/10.1021/acs.langmuir.6b02937)

278. R. C. VAN LEHN AND A. ALEXANDER-KATZ. Penetration of lipid bilayers by nanoparticles with environmentally-responsive surfaces: Simulations and theory, *Soft Matter*, **7**: 11392-11404, 2011. DOI: [10.1039/c1sm06405c](https://doi.org/10.1039/c1sm06405c)
279. R. C. VAN LEHN AND A. ALEXANDER-KATZ. Structure of mixed-monolayer-protected nanoparticles in aqueous salt solution from atomistic molecular dynamics simulations, *J. Phys. Chem. C*, **117**: 20104-20115, 2013. DOI: [10.1021/jp406035e](https://doi.org/10.1021/jp406035e)
280. R. C. VAN LEHN AND A. ALEXANDER-KATZ. Fusion of ligand-coated nanoparticles with lipid bilayers: Effect of ligand flexibility, *J. Phys. Chem. A*, **118**: 5848-5856, 2014. DOI: [10.1021/jp411662c](https://doi.org/10.1021/jp411662c)
281. R. C. VAN LEHN AND A. ALEXANDER-KATZ. Free energy change for insertion of charged, monolayer-protected nanoparticles into lipid bilayers, *Soft Matter*, **10**: 648-658, 2014. DOI: [10.1039/c3sm52329b](https://doi.org/10.1039/c3sm52329b)
282. R. C. VAN LEHN AND A. ALEXANDER-KATZ. Membrane-embedded nanoparticles induce lipid rearrangements similar to those exhibited by biological membrane proteins, *J. Phys. Chem. B*, **118**: 12586-12598, 2014. DOI: [10.1021/jp506239p](https://doi.org/10.1021/jp506239p)
283. R. C. VAN LEHN, M. RICCI, P. H. J. SILVA, P. ANDREOZZI, *et al.* Lipid tail protrusions mediate the insertion of nanoparticles into model cell membranes, *Nat. Commun.*, **5**: 4482, 2014. DOI: [10.1038/ncomms5482](https://doi.org/10.1038/ncomms5482)
284. A. HEUER-JUNGEMANN, P. K. HARIMECH, T. BROWN, AND A. G. KANARAS. Gold nanoparticles and fluorescently-labelled DNA as a platform for biological sensing, *Nanoscale*, **5**: 9503-9510, 2013. DOI: [10.1039/c3nr03707j](https://doi.org/10.1039/c3nr03707j)
285. R. ELGHANIAN, J. J. STORHOFF, R. C. MUCIC, R. L. LETSINGER, *et al.* Selective colorimetric detection of polynucleotides based on the distance-dependent optical properties of gold nanoparticles, *Science*, **277**: 1078-1081, 1997. DOI: [10.1126/science.277.5329.1078](https://doi.org/10.1126/science.277.5329.1078)
286. O. S. LEE, T. R. PRYTKOVA, AND G. C. SCHATZ. Using DNA to link gold nanoparticles, polymers, and molecules: A theoretical perspective, *J. Phys. Chem. Lett.*, **1**: 1781-1788, 2010. DOI: [10.1021/jz100435a](https://doi.org/10.1021/jz100435a)
287. O. S. LEE, V. Y. CHO, AND G. C. SCHATZ. A- to B-form transition in DNA between gold surfaces, *J. Phys. Chem. B*, **116**: 7000-7005, 2012. DOI: [10.1021/jp300877e](https://doi.org/10.1021/jp300877e)
288. V. A. NGO, R. K. KALIA, A. NAKANO, AND P. VASHISHTA. Supercrystals of DNA-functionalized gold nanoparticles: A million-atom molecular dynamics simulation study, *J. Phys. Chem. C*, **116**: 19579-19585, 2012. DOI: [10.1021/jp306133v](https://doi.org/10.1021/jp306133v)
289. A. J. MAKARUCHA, N. TODOROVA, AND I. YAROVSKY. Nanomaterials in biological environment: A review of computer modelling studies, *Eur. Biophys. J.*, **40**: 103-115, 2011. DOI: [10.1007/s00249-010-0651-6](https://doi.org/10.1007/s00249-010-0651-6)
290. C. LIU, J. LIN, Y. SHI, AND G. LI. Efficient synthesis of Au<sub>99</sub>(SR)<sub>42</sub> nanoclusters, *Nanoscale*, **7**: 5987-5990, 2015. DOI: [10.1039/c5nr00543d](https://doi.org/10.1039/c5nr00543d)
291. S. LINSE, C. CABALEIRO-LAGO, W.-F. XUE, I. LYNCH, *et al.* Nucleation of protein fibrillation by nanoparticles, *Proc. Natl. Acad. Sci. U. S. A.*, **104**: 8691-8696, 2007. DOI: [10.1073/pnas.0701250104](https://doi.org/10.1073/pnas.0701250104)
292. T. P. J. KNOWLES, M. VENDRUSCOLO, AND C. M. DOBSON. The amyloid state and its association with protein misfolding diseases, *Nat. Rev. Mol. Cell Biol.*, **15**: 384-396, 2014. DOI: [10.1038/nrm3810](https://doi.org/10.1038/nrm3810)
293. R. VÁCHA, S. LINSE, AND M. LUND. Surface effects on aggregation kinetics of amyloidogenic peptides, *J. Am. Chem. Soc.*, **136**: 11776-11782, 2014. DOI: [10.1021/ja505502e](https://doi.org/10.1021/ja505502e)
294. C. ZHANG, C. LI, Y. LIU, J. ZHANG, *et al.* Gold nanoclusters-based nanoprobes for simultaneous fluorescence imaging and targeted photodynamic therapy with superior penetration and retention behavior in tumors, *Adv. Funct. Mater.*, **25**: 1314-1325, 2015. DOI: [10.1002/adfm.201403095](https://doi.org/10.1002/adfm.201403095)
295. M. HOEFLING, S. MONTI, S. CORNI, AND K. E. GOTTSCHALK. Interaction of  $\beta$ -sheet folds with a gold surface, *PLOS One*, **6**: e20925, 2011. DOI: [10.1371/journal.pone.0020925](https://doi.org/10.1371/journal.pone.0020925)

296. S. MIRSADEGHI, R. DINARVAND, M. H. GHAREMANI, M. R. HORMOZI-NEZHAD, *et al.* Protein corona composition of gold nanoparticles/nanorods affects amyloid beta fibrillation process, *Nanoscale*, **7**: 5004-5013, 2015. DOI: [10.1039/c4nr06009a](https://doi.org/10.1039/c4nr06009a)
297. H. Y. MAO, S. LAURENT, W. CHEN, O. AKHAVAN, *et al.* Graphene: Promises, facts, opportunities, and challenges in nanomedicine, *Chem. Rev.*, **113**: 3407-3424, 2013. DOI: [10.1021/cr300335p](https://doi.org/10.1021/cr300335p)
298. M. MAHMOUDI, M. P. MONOPOLI, M. REZAEI, I. LYNCH, *et al.* The protein corona mediates the impact of nanomaterials and slows amyloid beta fibrillation, *ChemBioChem*, **14**: 568-572, 2013. DOI: [10.1002/cbic.201300007](https://doi.org/10.1002/cbic.201300007)
299. F. RAMEZANI AND H. RAFII-TABAR. An in-depth view of human serum albumin corona on gold nanoparticles, *Mol. BioSyst.*, **11**: 454-462, 2015. DOI: [10.1039/c4mb00591k](https://doi.org/10.1039/c4mb00591k)
300. O. CARRILLO-PARRAMON, G. BRANCOLINI, AND S. CORNI. Simulation of protein-surface interactions by a coarse-grained method, *BioNanoSci.*, **3**: 12-20, 2013. DOI: [10.1007/s12668-012-0073-2](https://doi.org/10.1007/s12668-012-0073-2)
301. F. TAVANTI, A. PEDONE, AND M. C. MENZIANI. Competitive binding of proteins to gold nanoparticles disclosed by molecular dynamics simulations, *J. Phys. Chem. C*, **119**: 22172-22180, 2015. DOI: [10.1021/acs.jpcc.5b05796](https://doi.org/10.1021/acs.jpcc.5b05796)
302. F. TAVANTI, A. PEDONE, AND M. C. MENZIANI. A closer look into the ubiquitin corona on gold nanoparticles by computational studies, *New J. Chem.*, **39**: 2474-2482, 2015. DOI: [10.1039/c4nj01752h](https://doi.org/10.1039/c4nj01752h)
303. J. R. PERILLA, B. C. GOH, C. K. CASSIDY, B. LIU, *et al.* Molecular dynamics simulations of large macromolecular complexes, *Curr. Opin. Struct. Biol.*, **31**: 64-74, 2015. DOI: [10.1016/j.sbi.2015.03.007](https://doi.org/10.1016/j.sbi.2015.03.007)
304. E. H. LEE, J. HSIN, M. SOTOMAYOR, G. COMELLAS, *et al.* Discovery through the computational microscope, *Structure*, **17**: 1295-1306, 2009. DOI: [10.1016/j.str.2009.09.001](https://doi.org/10.1016/j.str.2009.09.001)
305. A. R. LEACH, *Molecular modelling: Principles and applications*, 2nd ed. Harlow, Essex, UK: Prentice Hall, 2001.
306. D. J. GRIFFITHS, *Introduction to quantum mechanics*, 2nd ed. Upper Saddle River, New Jersey, USA: Pearson Prentice Hall, 2005.
307. F. JENSEN, *Introduction to computational chemistry*, 2nd ed. West Sussex, England, UK: John Wiley & Sons Ltd, 2007.
308. E. CANADELL, M.-L. DOUBLET, AND C. LUNG, *Orbital approach to the electronic structure of solids*. Oxford, England, UK: Oxford University Press, 2012.
309. I. N. LEVINE, *Quantum chemistry*, 5th ed. New Jersey, USA: Prentice Hall, 2000.
310. M. BORN AND R. OPPENHEIMER. Zur quantentheorie der molekeln, *Ann. Phys.*, **389**: 457-484, 1927. DOI: [10.1002/andp.19273892002](https://doi.org/10.1002/andp.19273892002)
311. J. C. SLATER. The theory of complex spectra, *Phys. Rev.*, **34**: 1293-1322, 1929. DOI: [10.1103/PhysRev.34.1293](https://doi.org/10.1103/PhysRev.34.1293)
312. V. FOCK. Näherungsmethode zur lösung des quantenmechanischen mehrkörperproblems, *Z. Phys.*, **61**: 126-148, 1930. DOI: [10.1007/BF01340294](https://doi.org/10.1007/BF01340294)
313. D. R. HARTREE. The wave mechanics of an atom with a non-coulomb central field. Part i. Theory and methods, *Mathematical Proceedings of the Cambridge Philosophical Society*, **24**: 89, 2008. DOI: [10.1017/s0305004100011919](https://doi.org/10.1017/s0305004100011919)
314. E. R. DAVIDSON. The iterative calculation of a few of the lowest eigenvalues and corresponding eigenvectors of large real-symmetric matrices, *J. Comput. Phys.*, **17**: 87-94, 1975. DOI: [10.1016/0021-9991\(75\)90065-0](https://doi.org/10.1016/0021-9991(75)90065-0)
315. C. MØLLER AND M. S. PLESSET. Note on an approximation treatment for many-electron systems, *Phys. Rev.*, **46**: 618-622, 1934. DOI: [10.1103/PhysRev.46.618](https://doi.org/10.1103/PhysRev.46.618)
316. R. J. BARTLETT. Coupled-cluster approach to molecular structure and spectra: A step toward predictive quantum chemistry, *J. Phys. Chem.*, **93**: 1697-1708, 1989. DOI: [10.1021/j100342a008](https://doi.org/10.1021/j100342a008)
317. P. HOHENBERG AND W. KOHN. Inhomogeneous electron gas, *Phys. Rev.*, **136**: B864-B871, 1964. DOI: [10.1103/PhysRev.136.B864](https://doi.org/10.1103/PhysRev.136.B864)

318. W. KOHN AND L. J. SHAM. Self-consistent equations including exchange and correlation effects, *Phys. Rev.*, **140**: A1133-A1138, 1965. DOI: [10.1103/PhysRev.140.A1133](https://doi.org/10.1103/PhysRev.140.A1133)
319. P. KOSKINEN AND V. MÄKINEN. Density-functional tight-binding for beginners, *Comput. Mater. Sci.*, **47**: 237-253, 2009. DOI: [10.1016/j.commatsci.2009.07.013](https://doi.org/10.1016/j.commatsci.2009.07.013)
320. J. J. STEWART. Optimization of parameters for semiempirical methods v: Modification of nndo approximations and application to 70 elements, *J. Mol. Model.*, **13**: 1173-1213, 2007. DOI: [10.1007/s00894-007-0233-4](https://doi.org/10.1007/s00894-007-0233-4)
321. W. THIEL. Semiempirical quantum-chemical methods, *WIREs Comput. Mol. Sim.*, **4**: 145-157, 2014. DOI: [10.1002/wcms.1161](https://doi.org/10.1002/wcms.1161)
322. C. K. SKYLARIS, P. D. HAYNES, A. A. MOSTOFI, AND M. C. PAYNE. Using onetep for accurate and efficient O(N) density functional calculations, *J. Phys.: Condens. Matter*, **17**: 5757-5769, 2005. DOI: [10.1088/0953-8984/17/37/012](https://doi.org/10.1088/0953-8984/17/37/012)
323. A. A. MOSTOFI, P. D. HAYNES, C. K. SKYLARIS, AND M. C. PAYNE. Onetep: Linear-scaling density-functional theory with plane-waves, *Mol. Simul.*, **33**: 551-555, 2007. DOI: [10.1080/08927020600932801](https://doi.org/10.1080/08927020600932801)
324. J. M. SOLER, E. ARTACHO, J. D. GALE, A. GARCIA, *et al.* The siesta method for ab initio order-N materials simulation, *J. Phys.: Condens. Matter*, **14**: 2745-2779, 2002. DOI: [10.1088/0953-8984/14/11/302](https://doi.org/10.1088/0953-8984/14/11/302)
325. D. J. COLE AND N. D. M. HINE. Applications of large-scale density functional theory in biology, *J. Phys.: Condens. Matter*, **28**: 393001, 2016. DOI: [10.1088/0953-8984/28/39/393001](https://doi.org/10.1088/0953-8984/28/39/393001)
326. A. RUIZ-SERRANO AND C. K. SKYLARIS. A variational method for density functional theory calculations on metallic systems with thousands of atoms, *J. Chem. Phys.*, **139**: 054107, 2013. DOI: [10.1063/1.4817001](https://doi.org/10.1063/1.4817001)
327. L. LEE, P., D. COLE, J., M. PAYNE, C., AND C.-K. SKYLARIS. Natural bond orbital analysis in the onetep code: Applications to large protein systems, *J. Comput. Chem.*, **34**: 429-444, 2013. DOI: [10.1002/jcc.23150](https://doi.org/10.1002/jcc.23150)
328. N. TODOROVA, A. J. MAKARUCHA, N. D. M. HINE, A. A. MOSTOFI, *et al.* Dimensionality of carbon nanomaterials determines the binding and dynamics of amyloidogenic peptides: Multiscale theoretical simulations, *PLOS Comput. Biol.*, **9**: e1003360, 2013. DOI: [10.1371/journal.pcbi.1003360](https://doi.org/10.1371/journal.pcbi.1003360)
329. H. C. WANG AND Y. S. LENG. Gold/benzenedithiolate/gold molecular junction: A driven dynamics simulation on structural evolution and breaking force under pulling, *J. Phys. Chem. C*, **119**: 15216-15223, 2015. DOI: [10.1021/acs.jpcc.5b02843](https://doi.org/10.1021/acs.jpcc.5b02843)
330. M. L. SUSHKO, P. V. SUSHKO, I. V. ABARENKOV, AND A. L. SHLUGER. QM/mm method for metal-organic interfaces, *J. Comput. Chem.*, **31**: 2955-2966, 2010. DOI: [10.1002/jcc.21591](https://doi.org/10.1002/jcc.21591)
331. V. ROJAS-CERVELLERA, C. ROVIRA, AND J. AKOLA. How do water solvent and glutathione ligands affect the structure and electronic properties of Au<sub>25</sub>(SR)<sub>18</sub><sup>-</sup>?, *J. Phys. Chem. Lett.*, **6**: 3859-3865, 2015. DOI: [10.1021/acs.jpcllett.5b01382](https://doi.org/10.1021/acs.jpcllett.5b01382)
332. W. D. CORNELL, P. CIEPLAK, C. I. BAYLY, I. R. GOULD, *et al.* A second generation force field for the simulation of proteins, nucleic acids, and organic molecules, *J. Am. Chem. Soc.*, **117**: 5179-5197, 1995. DOI: [10.1021/ja00124a002](https://doi.org/10.1021/ja00124a002)
333. A. D. MACKERELL, JR., D. BASHFORD, M. BELLOTT, R. L. DUNBRACK, *et al.* All-atom empirical potential for molecular modeling and dynamics studies of proteins, *J. Phys. Chem. B*, **102**: 3586-3616, 1998. DOI: [10.1021/jp973084f](https://doi.org/10.1021/jp973084f)
334. L. D. SCHULER, X. DAURA, AND W. F. VAN GUNSTEREN. An improved gromos96 force field for aliphatic hydrocarbons in the condensed phase, *J. Comput. Chem.*, **22**: 1205-1218, 2001. DOI: [10.1002/jcc.1078](https://doi.org/10.1002/jcc.1078)
335. W. L. JORGENSEN, D. S. MAXWELL, AND J. TIRADO-RIVES. Development and testing of the opl's all-atom force field on conformational energetics and properties of organic liquids, *J. Am. Chem. Soc.*, **118**: 11225-11236, 1996. DOI: [10.1021/ja9621760](https://doi.org/10.1021/ja9621760)

336. R. A. LATOUR. Perspectives on the simulation of protein-surface interactions using empirical force field methods, *Colloids Surf. B*, **124**: 25-37, 2014. DOI: [10.1016/j.colsurfb.2014.06.050](https://doi.org/10.1016/j.colsurfb.2014.06.050)
337. F. IORI AND S. CORNI. Including image charge effects in the molecular dynamics simulations of molecules on metal surfaces, *J. Comput. Chem.*, **29**: 1656-1666, 2008. DOI: [10.1002/jcc.20928](https://doi.org/10.1002/jcc.20928)
338. X. CHEN, O. V. PREZHDO, Z. MA, T. HOU, *et al.* Ab initio phonon-coupled nonadiabatic relaxation dynamics of  $[\text{Au}_{25}(\text{sh})_{18}]^-$  clusters, *Phys. Status Solidi B*, **253**: 458-462, 2015. DOI: [10.1002/pssb.201552405](https://doi.org/10.1002/pssb.201552405)
339. L. L. JENSEN AND L. JENSEN. Electrostatic interaction model for the calculation of the polarizability of large noble metal nanoclusters, *J. Phys. Chem. C*, **112**: 15697-15703, 2008. DOI: [10.1021/jp804116z](https://doi.org/10.1021/jp804116z)
340. K. C. JHA, H. LIU, M. R. BOCKSTALLER, AND H. HEINZ. Facet recognition and molecular ordering of ionic liquids on metal surfaces, *J. Phys. Chem. C*, **117**: 25969-25981, 2013. DOI: [10.1021/jp4032404](https://doi.org/10.1021/jp4032404)
341. G. HEIMEL AND J.-L. BRÉDAS. Molecular electronics: Reflections on charge transport, *Nat. Nanotechnol.*, **8**: 230-231, 2013. DOI: [10.1038/nnano.2013.42](https://doi.org/10.1038/nnano.2013.42)
342. M. ROSA, S. CORNI, AND R. DI FELICE. Enthalpy-entropy tuning in the adsorption of nucleobases at the Au(111) surface, *J. Chem. Theory Comput.*, **10**: 1707-1716, 2014. DOI: [10.1021/ct401117g](https://doi.org/10.1021/ct401117g)
343. L. B. WRIGHT, P. M. RODGER, T. R. WALSH, AND S. CORNI. First-principles-based force field for the interaction of proteins with Au(100)(5 × 1): An extension of GoIP-CHARMM, *J. Phys. Chem. C*, **117**: 24292-24306, 2013. DOI: [10.1021/jp4061329](https://doi.org/10.1021/jp4061329)
344. Z. E. HUGHES, S. M. TOMASIO, AND T. R. WALSH. Efficient simulations of the aqueous bio-interface of graphitic nanostructures with a polarisable model, *Nanoscale*, **6**: 5438-5448, 2014. DOI: [10.1039/c4nr00468j](https://doi.org/10.1039/c4nr00468j)
345. H. HEINZ AND H. RAMEZANI-DAKHEL. Simulations of inorganic-bioorganic interfaces to discover new materials: Insights, comparisons to experiment, challenges, and opportunities, *Chem. Soc. Rev.*, **45**: 412-448, 2016. DOI: [10.1039/C5CS00890E](https://doi.org/10.1039/C5CS00890E)
346. H. HEINZ, R. A. VAIA, B. L. FARMER, AND R. R. NAIK. Accurate simulation of surfaces and interfaces of face-centered cubic metals using 12-6 and 9-6 lennard-jones potentials, *J. Phys. Chem. C*, **112**: 17281-17290, 2008. DOI: [10.1021/jp801931d](https://doi.org/10.1021/jp801931d)
347. H. SUN. Compass: An ab initio force-field optimized for condensed-phase applications - overview with details on alkane and benzene compounds, *J. Phys. Chem. B*, **102**: 7338-7364, 1998. DOI: [10.1021/jp980939v](https://doi.org/10.1021/jp980939v)
348. P. DAUBER-OSGUTHORPE, V. A. ROBERTS, D. J. OSGUTHORPE, J. WOLFF, *et al.* Structure and energetics of ligand binding to proteins: Escherichia coli dihydrofolate reductase-trimethoprim, a drug-receptor system, *Proteins: Struct. Funct. Genet.*, **4**: 31-47, 1988. DOI: [10.1002/prot.340040106](https://doi.org/10.1002/prot.340040106)
349. K. KUBIAK-OSSOWSKA, P. A. MULHERAN, AND W. NOWAK. Fibronectin module fn(iii)9 adsorption at contrasting solid model surfaces studied by atomistic molecular dynamics, *J. Phys. Chem. B*, **118**: 9900-9908, 2014. DOI: [10.1021/jp5020077](https://doi.org/10.1021/jp5020077)
350. A. KYRYCHENKO. Nanogold decorated by phlip peptide: Comparative force field study, *Phys. Chem. Chem. Phys.*, **17**: 12648-12660, 2015. DOI: [10.1039/c5cp01136a](https://doi.org/10.1039/c5cp01136a)
351. A. R. MHASHAL AND S. ROY. Effect of gold nanoparticle on structure and fluidity of lipid membrane, *PLOS One*, **9**: e0114152, 2014. DOI: [10.1371/journal.pone.0114152](https://doi.org/10.1371/journal.pone.0114152)
352. F. RAMEZANI, M. AMANLOU, AND H. RAFII-TABAR. Gold nanoparticle shape effects on human serum albumin corona interface: A molecular dynamic study, *J. Nanopart. Res.*, **16**: 2512, 2014. DOI: [10.1007/s11051-014-2512-1](https://doi.org/10.1007/s11051-014-2512-1)
353. M. J. GUBERMAN-PFEFFER, J. ULCICKAS, AND J. A. GASCÓN. Connectivity-based biocompatible force field for thiolated gold nanoclusters, *J. Phys. Chem. C*, **119**: 27804-27812, 2015. DOI: [10.1021/acs.jpcc.5b08648](https://doi.org/10.1021/acs.jpcc.5b08648)



354. C. R. L. CHAPMAN, E. C. M. TING, A. KERESZTI, AND I. PACI. Self-assembly of cysteine dimers at the gold surface: A computational study of competing interactions, *J. Phys. Chem. C*, **117**: 19426-19435, 2013. DOI: [10.1021/jp405478n](https://doi.org/10.1021/jp405478n)
355. G. NAWROCKI AND M. CIEPLAK. Aqueous amino acids and proteins near the surface of gold in hydrophilic and hydrophobic force fields, *J. Phys. Chem. C*, **118**: 12929-12943, 2014. DOI: [10.1021/jp5030558](https://doi.org/10.1021/jp5030558)
356. O. D. VILLARREAL, L. Y. CHEN, R. L. WHETTEN, AND M. J. YACAMAN. Ligand-modulated interactions between charged monolayer-protected Au<sub>144</sub>(SR)<sub>60</sub> gold nanoparticles in physiological saline, *Phys. Chem. Chem. Phys.*, **17**: 3680-3688, 2015. DOI: [10.1039/c4cp05137h](https://doi.org/10.1039/c4cp05137h)
357. T. POPA AND I. PACI. Structure and chirality in sulfur-containing amino acids adsorbed on Au(111) surfaces, *J. Phys. Chem. C*, **119**: 9829-9838, 2015. DOI: [10.1021/acs.jpcc.5b00380](https://doi.org/10.1021/acs.jpcc.5b00380)
358. R. GOPALAKRISHNAN, E. R. AZHAGIYA SINGAM, J. VIJAYA SUNDAR, AND V. SUBRAMANIAN. Interaction of collagen like peptides with gold nanosurfaces: A molecular dynamics investigation, *Phys. Chem. Chem. Phys.*, **17**: 5172-5186, 2015. DOI: [10.1039/c4cp04969a](https://doi.org/10.1039/c4cp04969a)
359. T. DJEBAILI, J. RICHARDI, S. ABEL, AND M. MARCHI. Atomistic simulations of self-assembled monolayers on octahedral and cubic gold nanocrystals, *J. Phys. Chem. C*, **119**: 21146-21154, 2015. DOI: [10.1021/acs.jpcc.5b05256](https://doi.org/10.1021/acs.jpcc.5b05256)
360. T. DJEBAILI, J. RICHARDI, S. ABEL, AND M. MARCHI. Atomistic simulations of the surface coverage of large gold nanocrystals, *J. Phys. Chem. C*, **117**: 17791-17800, 2013. DOI: [10.1021/jp403442s](https://doi.org/10.1021/jp403442s)
361. S. L. MAYO, B. D. OLAFSON, AND W. A. GODDARD, III. Dreiding: A generic force field for molecular simulations, *J. Phys. Chem.*, **94**: 8897-8909, 1990. DOI: [10.1021/j100389a010](https://doi.org/10.1021/j100389a010)
362. A. K. RAPPÉ, C. J. CASEWIT, K. S. COLWELL, W. A. GODDARD, III, *et al.* Uff, a full periodic-table force-field for molecular mechanics and molecular-dynamics simulations, *J. Am. Chem. Soc.*, **114**: 10024-10035, 1992. DOI: [10.1021/ja00051a040](https://doi.org/10.1021/ja00051a040)
363. P. M. AGRAWAL, B. M. RICE, AND D. L. THOMPSON. Predicting trends in rate parameters for self-diffusion on fcc metal surfaces, *Surf. Sci.*, **515**: 21-35, 2002. DOI: [10.1016/s0039-6028\(02\)01916-7](https://doi.org/10.1016/s0039-6028(02)01916-7)
364. J. HAUTMAN AND M. L. KLEIN. Simulation of a monolayer of alkyl thiol chains, *J. Chem. Phys.*, **91**: 4994-5001, 1989. DOI: [10.1063/1.457621](https://doi.org/10.1063/1.457621)
365. E. BENASSI, G. GRANUCCI, M. PERSICO, AND S. CORNI. Can azobenzene photoisomerize when chemisorbed on a gold surface? An analysis of steric effects based on nonadiabatic dynamics simulations, *J. Phys. Chem. C*, **119**: 5962-5974, 2015. DOI: [10.1021/jp511269p](https://doi.org/10.1021/jp511269p)
366. S. PIPOLO AND S. CORNI. Wettability of azobenzene self-assembled monolayers, *Langmuir*, **30**: 4415-4421, 2014. DOI: [10.1021/la404922f](https://doi.org/10.1021/la404922f)
367. M. V. IVANOV, M. R. TALIPOV, AND Q. K. TIMERGHAZIN. Genetic algorithm optimization of point charges in force field development: Challenges and insights, *J. Phys. Chem. A*, **119**: 1422-1434, 2015. DOI: [10.1021/acs.jpca.5b00218](https://doi.org/10.1021/acs.jpca.5b00218)
368. O. STUEKER, V. A. ORTEGA, G. G. GOSS, AND M. STEPANOVA. Understanding interactions of functionalized nanoparticles with proteins: A case study on lactate dehydrogenase, *Small*, **10**: 2006-2021, 2014. DOI: [10.1002/smll.201303639](https://doi.org/10.1002/smll.201303639)
369. Z. YANG, Y. LI, G. ZHOU, X. CHEN, *et al.* Molecular dynamics simulations of hydrogen bond dynamics and far-infrared spectra of hydration water molecules around the mixed monolayer-protected Au nanoparticle, *J. Phys. Chem. C*, **119**: 1768-1781, 2015. DOI: [10.1021/jp506875m](https://doi.org/10.1021/jp506875m)
370. D. B. KOKH, S. CORNI, P. J. WINN, M. HOEFLING, *et al.* ProMetCS: An atomistic force field for modeling protein-metal surface interactions in a continuum aqueous solvent, *J. Chem. Theory Comput.*, **6**: 1753-1768, 2010. DOI: [10.1021/ct100086j](https://doi.org/10.1021/ct100086j)
371. Y. SHI, Z. XIA, J. ZHANG, R. BEST, *et al.* Polarizable atomic multipole-based amoeba force field for proteins, *J. Chem. Theory Comput.*, **9**: 4046-4063, 2013. DOI: [10.1021/ct4003702](https://doi.org/10.1021/ct4003702)

372. G. A. KAMINSKI, R. A. FRIESNER, J. TIRADO-RIVES, AND W. L. JORGENSEN. Evaluation and reparametrization of the OPLS-AA force field for proteins via comparison with accurate quantum chemical calculations on peptides, *J. Phys. Chem. B*, **105**: 6474-6487, 2001. DOI: [10.1021/jp003919d](https://doi.org/10.1021/jp003919d)
373. S. PIANA, K. LINDORFF-LARSEN, AND DAVID E. SHAW. How robust are protein folding simulations with respect to force field parameterization?, *Biophys. J.*, **100**: L47-L49, 2011. DOI: [10.1016/j.bpj.2011.03.051](https://doi.org/10.1016/j.bpj.2011.03.051)
374. A. D. MACKERELL, JR., M. FEIG, AND C. L. BROOKS, III. Extending the treatment of backbone energetics in protein force fields: Limitations of gas-phase quantum mechanics in reproducing protein conformational distributions in molecular dynamics simulations, *J. Comput. Chem.*, **25**: 1400-1415, 2004. DOI: [10.1002/jcc.20065](https://doi.org/10.1002/jcc.20065)
375. D. M. KOLB. Reconstruction phenomena at metal-electrolyte interfaces, *Prog. Surf. Sci.*, **51**: 109-173, 1996. DOI: [10.1016/0079-6816\(96\)00002-0](https://doi.org/10.1016/0079-6816(96)00002-0)
376. S. ANTONELLO, G. ARRIGONI, T. DAINESE, M. DE NARDI, *et al.* Electron transfer through 3D monolayers on Au<sub>25</sub> clusters, *ACS Nano*, **8**: 2788-2795, 2014. DOI: [10.1021/nn406504k](https://doi.org/10.1021/nn406504k)
377. R. OUYANG AND D.-E. JIANG. Ligand-conformation energy landscape of thiolate-protected gold nanoclusters, *J. Phys. Chem. C*, **119**: 21555-21560, 2015. DOI: [10.1021/acs.jpcc.5b06994](https://doi.org/10.1021/acs.jpcc.5b06994)
378. N. V. PERERA, W. ISLEY, F. MARAN, AND J. A. GASCÓN. Molecular modeling characterization of a conformationally constrained monolayer-protected gold cluster, *J. Phys. Chem. C*, **114**: 16043-16050, 2010. DOI: [10.1021/jp102585n](https://doi.org/10.1021/jp102585n)
379. E. HEIKKILÄ, A. A. GURTOVENKO, H. MARTINEZ-SEARA, H. HÄKKINEN, *et al.* Atomistic simulations of functional Au<sub>144</sub>(SR)<sub>60</sub> gold nanoparticles in aqueous environment, *J. Phys. Chem. C*, **116**: 9805-9815, 2012. DOI: [10.1021/jp301094m](https://doi.org/10.1021/jp301094m)
380. S. A. ALSHARIF, L. Y. CHEN, A. TLAHUICE-FLORES, R. L. WHETTEN, *et al.* Interaction between functionalized gold nanoparticles in physiological saline, *Phys. Chem. Chem. Phys.*, **16**: 3909-3913, 2014. DOI: [10.1039/c3cp54503b](https://doi.org/10.1039/c3cp54503b)
381. E. POHJOLAINEEN, X. CHEN, S. MALOLA, G. GROENHOF, *et al.* A unified AMBER-compatible molecular mechanics force field for thiolate protected gold nanoclusters, *J. Chem. Theory Comput.*, **12**: 1342-1350, 2016. DOI: [10.1021/acs.jctc.5b01053](https://doi.org/10.1021/acs.jctc.5b01053)
382. P. P. EWALD. Die berechnung optischer und elektrostatischer gitterpotentiale, *Ann. Phys.*, **369**: 253-287, 1921. DOI: [10.1002/andp.19213690304](https://doi.org/10.1002/andp.19213690304)
383. T. DARDEN, D. YORK, AND L. PEDERSEN. Particle mesh ewald: An nlog(N) method for ewald sums in large systems, *J. Chem. Phys.*, **98**: 10089-10092, 1993. DOI: [10.1063/1.464397](https://doi.org/10.1063/1.464397)
384. U. ESSMANN, L. PERERA, M. L. BERKOWITZ, T. DARDEN, *et al.* A smooth particle mesh ewald method, *J. Chem. Phys.*, **103**: 8577-8593, 1995. DOI: [10.1063/1.470117](https://doi.org/10.1063/1.470117)
385. H. WANG, F. DOMMERT, AND C. HOLM. Optimizing working parameters of the smooth particle mesh ewald algorithm in terms of accuracy and efficiency, *J. Chem. Phys.*, **133**: 034117, 2010. DOI: [10.1063/1.3446812](https://doi.org/10.1063/1.3446812)
386. B. J. ALDER AND T. E. WAINWRIGHT. Studies in molecular dynamics. I. General method, *J. Chem. Phys.*, **31**: 459-466, 1959. DOI: [10.1063/1.1730376](https://doi.org/10.1063/1.1730376)
387. B. J. ALDER AND T. E. WAINWRIGHT. Studies in molecular dynamics. II. Behavior of a small number of elastic spheres, *J. Chem. Phys.*, **33**: 1439-1451, 1960. DOI: [10.1063/1.1731425](https://doi.org/10.1063/1.1731425)
388. A. RAHMAN. Correlations in the motion of atoms in liquid argon, *Phys. Rev.*, **136**: A405-A411, 1964. DOI: [10.1103/PhysRev.136.A405](https://doi.org/10.1103/PhysRev.136.A405)
389. L. VERLET. Computer experiments on classical fluids .I. Thermodynamical properties of lennard-jones molecules, *Phys. Rev.*, **159**: 98-103, 1967. DOI: [10.1103/PhysRev.159.98](https://doi.org/10.1103/PhysRev.159.98)
390. R. W. HOCKNEY, R. A. WARRINER, AND M. REISER. Two-dimensional particle models in semiconductor-device analysis, *Electron. Lett.*, **10**: 484, 1974. DOI: [10.1049/el:19740386](https://doi.org/10.1049/el:19740386)
391. D. BEEMAN. Some multistep methods for use in molecular dynamics calculations, *J. Comput. Phys.*, **20**: 130-139, 1976. DOI: [10.1016/0021-9991\(76\)90059-0](https://doi.org/10.1016/0021-9991(76)90059-0)

392. W. C. SWOPE, H. C. ANDERSEN, P. H. BERENS, AND K. R. WILSON. A computer simulation method for the calculation of equilibrium constants for the formation of physical clusters of molecules: Application to small water clusters, *J. Chem. Phys.*, **76**: 637-649, 1982. DOI: [10.1063/1.442716](https://doi.org/10.1063/1.442716)
393. H. J. C. BERENDSEN, J. P. M. POSTMA, W. F. VAN GUNSTEREN, A. DI NOLA, *et al.* Molecular dynamics with coupling to an external bath, *J. Chem. Phys.*, **81**: 3684-3690, 1984. DOI: [10.1063/1.448118](https://doi.org/10.1063/1.448118)
394. S. NOSÉ. A molecular dynamics method for simulations in the canonical ensemble, *Mol. Phys.*, **52**: 255-268, 1984. DOI: [10.1080/00268978400101201](https://doi.org/10.1080/00268978400101201)
395. W. G. HOOVER. Canonical dynamics: Equilibrium phase-space distributions, *Phys. Rev. A: Gen. Phys.*, **31**: 1695-1697, 1985. DOI: [10.1103/PhysRevA.31.1695](https://doi.org/10.1103/PhysRevA.31.1695)
396. H. C. ANDERSEN. Molecular-dynamics simulations at constant pressure and-or temperature, *J. Chem. Phys.*, **72**: 2384-2393, 1980. DOI: [10.1063/1.439486](https://doi.org/10.1063/1.439486)
397. G. BUSSI, D. DONADIO, AND M. PARRINELLO. Canonical sampling through velocity rescaling, *J. Chem. Phys.*, **126**: 014101, 2007. DOI: [10.1063/1.2408420](https://doi.org/10.1063/1.2408420)
398. M. R. SHIRTS. Simple quantitative tests to validate sampling from thermodynamic ensembles, *J. Chem. Theory Comput.*, **9**: 909-926, 2013. DOI: [10.1021/ct300688p](https://doi.org/10.1021/ct300688p)
399. M. PARRINELLO AND A. RAHMAN. Polymorphic transitions in single crystals: A new molecular dynamics method, *J. Appl. Phys.*, **52**: 7182-7190, 1981. DOI: [10.1063/1.328693](https://doi.org/10.1063/1.328693)
400. S. NOSÉ AND M. L. KLEIN. Constant pressure molecular dynamics for molecular systems, *Mol. Phys.*, **50**: 1055-1076, 2006. DOI: [10.1080/00268978300102851](https://doi.org/10.1080/00268978300102851)
401. J.-P. RYCKAERT, G. CICCOTTI, AND H. J. C. BERENDSEN. Numerical integration of the cartesian equations of motion of a system with constraints: Molecular dynamics of n-alkanes, *J. Comput. Phys.*, **23**: 327-341, 1977. DOI: [10.1016/0021-9991\(77\)90098-5](https://doi.org/10.1016/0021-9991(77)90098-5)
402. B. HESS, H. BEKKER, H. J. C. BERENDSEN, AND J. G. E. M. FRAAIJE. Lincs: A linear constraint solver for molecular simulations, *J. Comput. Chem.*, **18**: 1463-1472, 1997. DOI: [10.1002/\(Sici\)1096-987x\(199709\)18:12<1463::Aid-Jcc4>3.0.Co;2-H](https://doi.org/10.1002/(Sici)1096-987x(199709)18:12<1463::Aid-Jcc4>3.0.Co;2-H)
403. S. KUMAR, D. BOUZIDA, R. H. SWENDSEN, P. A. KOLLMAN, *et al.* The weighted histogram analysis method for free-energy calculations on biomolecules. I. The method, *J. Comput. Chem.*, **13**: 1011-1021, 1992. DOI: [10.1002/jcc.540130812](https://doi.org/10.1002/jcc.540130812)
404. A. BARDUCCI, M. BONOMI, AND M. PARRINELLO. Metadynamics, *WIREs Comput. Mol. Sim.*, **1**: 826-843, 2011. DOI: [10.1002/wcms.31](https://doi.org/10.1002/wcms.31)
405. G. BUSSI, F. L. GERVASIO, A. LAIO, AND M. PARRINELLO. Free-energy landscape for  $\beta$  hairpin folding from combined parallel tempering and metadynamics, *J. Am. Chem. Soc.*, **128**: 13435-13441, 2006. DOI: [10.1021/ja062463w](https://doi.org/10.1021/ja062463w)
406. P. LIU, B. KIM, R. A. FRIESNER, AND B. J. BERNE. Replica exchange with solute tempering: A method for sampling biological systems in explicit water, *Proc. Natl. Acad. Sci. U. S. A.*, **102**: 13749-13754, 2005. DOI: [10.1073/pnas.0506346102](https://doi.org/10.1073/pnas.0506346102)
407. D. J. EARL AND M. W. DEEM. Parallel tempering: Theory, applications, and new perspectives, *Phys. Chem. Chem. Phys.*, **7**: 3910-3916, 2005. DOI: [10.1039/B509983H](https://doi.org/10.1039/B509983H)
408. X. LI, J. A. SNYDER, S. J. STUART, AND R. A. LATOUR. Tiger2 with solvent energy averaging (tiger2a): An accelerated sampling method for large molecular systems with explicit representation of solvent, *J. Chem. Phys.*, **143**: 144105, 2015. DOI: [10.1063/1.4932341](https://doi.org/10.1063/1.4932341)
409. A. H. BROWN AND T. R. WALSH. An improved tiger2 implementation for namd suitable for the blue gene architecture, *Comput. Phys. Commun.*, **192**: 278-281, 2015. DOI: [10.1016/j.cpc.2015.02.025](https://doi.org/10.1016/j.cpc.2015.02.025)
410. X. LI, R. A. LATOUR, AND S. J. STUART. Tiger2: An improved algorithm for temperature intervals with global exchange of replicas, *J. Chem. Phys.*, **130**: 174106, 2009. DOI: [10.1063/1.3129342](https://doi.org/10.1063/1.3129342)
411. X. LI, C. P. O'BRIEN, G. COLLIER, N. A. VELLORE, *et al.* An improved replica-exchange sampling method: Temperature intervals with global energy reassignment, *J. Chem. Phys.*, **127**: 164116, 2007. DOI: [10.1063/1.2780152](https://doi.org/10.1063/1.2780152)

412. R. C. BERNARDI, M. C. R. MELO, AND K. SCHULTEN. Enhanced sampling techniques in molecular dynamics simulations of biological systems, *Biochim. Biophys. Acta*, **1850**: 872-877, 2014. DOI: [10.1016/j.bbagen.2014.10.019](https://doi.org/10.1016/j.bbagen.2014.10.019)
413. V. SPIWOK, Z. SUCUR, AND P. HOSEK. Enhanced sampling techniques in biomolecular simulations, *Biotechnol. Adv.*, **33**: 1130-1140, 2015. DOI: [10.1016/j.biotechadv.2014.11.011](https://doi.org/10.1016/j.biotechadv.2014.11.011)
414. M. LUITZ, R. BOMBLIES, K. OSTERMEIR, AND M. ZACHARIAS. Exploring biomolecular dynamics and interactions using advanced sampling methods, *J. Phys.: Condens. Matter*, **27**: 323101, 2015. DOI: [10.1088/0953-8984/27/32/323101](https://doi.org/10.1088/0953-8984/27/32/323101)
415. F. PIETRUCCI. Strategies for the exploration of free energy landscapes: Unity in diversity and challenges ahead, *Rev. Phys.*, **2**: 32-45, 2017. DOI: [10.1016/j.revip.2017.05.001](https://doi.org/10.1016/j.revip.2017.05.001)
416. R. C. NOWINSKI, M. R. TAM, L. C. GOLDSTEIN, L. STONG, *et al.* Monoclonal antibodies for diagnosis of infectious diseases in humans, *Science*, **219**: 637-644, 1983. DOI: [10.1126/science.6297006](https://doi.org/10.1126/science.6297006)
417. N. AMINO, S. R. HAGEN, N. YAMADA, AND S. REFETOFF. Measurement of circulating thyroid microsomal antibodies by tanned red-cell hemagglutination technique: Its usefulness in diagnosis of autoimmune thyroid diseases, *Clin. Endocrinol.*, **5**: 115-125, 1976. DOI: [10.1111/j.1365-2265.1976.tb02822.x](https://doi.org/10.1111/j.1365-2265.1976.tb02822.x)
418. L. WIDE, H. BENNICH, AND S. G. O. JOHANSSO. Diagnosis of allergy by an in-vitro test for allergen antibodies, *Lancet*, **2**: 1105-1107, 1967. DOI: [10.1016/S0140-6736\(67\)90615-0](https://doi.org/10.1016/S0140-6736(67)90615-0)
419. Y. XIANG AND Y. LU. Portable and quantitative detection of protein biomarkers and small molecular toxins using antibodies and ubiquitous personal glucose meters, *Anal. Chem.*, **84**: 4174-4178, 2012. DOI: [10.1021/ac300517n](https://doi.org/10.1021/ac300517n)
420. H. ANDRESEN AND C. GROTZINGER. Deciphering the antibodyome - peptide arrays for serum antibody biomarker diagnostics, *Curr. Proteomics*, **6**: 1-12, 2009. DOI: [10.2174/157016409787847457](https://doi.org/10.2174/157016409787847457)
421. A. BECK, E. WAGNER-ROUSSET, D. AYOUB, A. VAN DORSSELAER, *et al.* Characterization of therapeutic antibodies and related products, *Anal. Chem.*, **85**: 715-736, 2013. DOI: [10.1021/ac3032355](https://doi.org/10.1021/ac3032355)
422. J. P. PALAFOX-HERNANDEZ, C.-K. LIM, Z. TANG, K. L. M. DREW, *et al.* Optical actuation of inorganic/organic interfaces: Comparing peptide-azobenzene ligand reconfiguration on gold and silver nanoparticles, *ACS Appl. Mater. Interfaces*, **8**: 1050-1060, 2016. DOI: [10.1021/acsami.5b11989](https://doi.org/10.1021/acsami.5b11989)
423. L. BELLUCCI, A. ARDEVOL, M. PARRINELLO, H. LUTZ, *et al.* The interaction with gold suppresses fiber-like conformations of the amyloid  $\beta$  (16-22) peptide, *Nanoscale*, **8**: 8737-8748, 2016. DOI: [10.1039/c6nr01539e](https://doi.org/10.1039/c6nr01539e)
424. C. J. MUNRO, Z. E. HUGHES, T. R. WALSH, AND M. R. KNECHT. Peptide sequence effects control the single pot reduction, nucleation, and growth of Au nanoparticles, *J. Phys. Chem. C*, **120**: 18917-18924, 2016. DOI: [10.1021/acs.jpcc.6b06046](https://doi.org/10.1021/acs.jpcc.6b06046)
425. L. DUCHESNE, G. WELLS, D. G. FERNIG, S. A. HARRIS, *et al.* Supramolecular domains in mixed peptide self-assembled monolayers on gold nanoparticles, *ChemBioChem*, **9**: 2127-2134, 2008. DOI: [10.1002/cbic.200800326](https://doi.org/10.1002/cbic.200800326)
426. E. COLANGELO, Q. CHEN, A. M. DAVIDSON, D. PARAMELLE, *et al.* Computational and experimental investigation of the structure of peptide monolayers on gold nanoparticles, *Langmuir*, **33**: 438-449, 2017. DOI: [10.1021/acs.langmuir.6b04383](https://doi.org/10.1021/acs.langmuir.6b04383)
427. S. J. WHITE, S. D. JOHNSON, M. A. SELICK, A. BRONOWSKA, *et al.* The influence of two-dimensional organization on peptide conformation, *Angew. Chem. Int. Ed.*, **54**: 974-978, 2015. DOI: [10.1002/anie.201408971](https://doi.org/10.1002/anie.201408971)
428. L. BERGAMINI, V. VOLIANI, V. CAPPELLO, R. NIFOSI, *et al.* Non-linear optical response by functionalized gold nanospheres: Identifying design principles to maximize the molecular photo-release, *Nanoscale*, **7**: 13345-13357, 2015. DOI: [10.1039/c5nr03037d](https://doi.org/10.1039/c5nr03037d)

429. A. K. NOWINSKI, F. SUN, A. D. WHITE, A. J. KEEFE, *et al.* Sequence, structure, and function of peptide self-assembled monolayers, *J. Am. Chem. Soc.*, **134**: 6000-6005, 2012. DOI: [10.1021/ja3006868](https://doi.org/10.1021/ja3006868)
430. B. HESS, C. KUTZNER, D. VAN DER SPOEL, AND E. LINDAHL. GROMACS 4: Algorithms for highly efficient, load-balanced, and scalable molecular simulation, *J. Chem. Theory Comput.*, **4**: 435-447, 2008. DOI: [10.1021/ct700301q](https://doi.org/10.1021/ct700301q)
431. L. MARTÍNEZ, R. ANDRADE, E. G. BIRGIN, AND J. M. MARTÍNEZ. Packmol: A package for building initial configurations for molecular dynamics simulations, *J. Comput. Chem.*, **30**: 2157-2164, 2009. DOI: [10.1002/jcc.21224](https://doi.org/10.1002/jcc.21224)
432. H. J. C. BERENDSEN, J. P. M. POSTMA, W. F. VAN GUNSTEREN, AND J. HERMANS, "Interaction models for water in relation to protein hydration," in *Intermolecular forces*, B. Pullman, Ed., ed Dordrecht, Netherlands: Springer, 1981, pp. 331-342.
433. N. SINHA, S. MOHAN, C. A. LIPSCHULTZ, AND S. J. SMITH-GILL. Differences in electrostatic properties at antibody-antigen binding sites: Implications for specificity and cross-reactivity, *Biophys. J.*, **83**: 2946-2968, 2002. DOI: [10.1016/s0006-3495\(02\)75302-2](https://doi.org/10.1016/s0006-3495(02)75302-2)
434. T. RAMARAJ, T. ANGEL, E. A. DRATZ, A. J. JESAITIS, *et al.* Antigen-antibody interface properties: Composition, residue interactions, and features of 53 non-redundant structures, *Biochim. Biophys. Acta*, **1824**: 520-532, 2012. DOI: [10.1016/j.bbapap.2011.12.007](https://doi.org/10.1016/j.bbapap.2011.12.007)
435. N. KRAUB, H. WESSNER, K. WELFLE, H. WELFLE, *et al.* The structure of the anti-c-myc antibody 9e 10 fab fragment/epitope peptide complex reveals a novel binding mode dominated by the heavy chain hypervariable loops, *Proteins: Struct. Funct. Bioinf.*, **73**: 552-565, 2008. DOI: [10.1002/prot.22080](https://doi.org/10.1002/prot.22080)
436. K. HILPERT, G. HANSEN, H. WESSNER, G. KUTTNER, *et al.* Anti-c-myc antibody 9e10: Epitope key positions and variability characterized using peptide spot synthesis on cellulose, *Protein Eng.*, **14**: 803-806, 2001. DOI: [10.1093/protein/14.10.803](https://doi.org/10.1093/protein/14.10.803)
437. Y. ZHENG, L. LAI, W. LIU, H. JIANG, *et al.* Recent advances in biomedical applications of fluorescent gold nanoclusters, *Adv. Colloid Interface Sci.*, **242**: 1-16, 2017. DOI: [10.1016/j.cis.2017.02.005](https://doi.org/10.1016/j.cis.2017.02.005)
438. L. SHANG, S. DONG, AND G. U. NIENHAUS. Ultra-small fluorescent metal nanoclusters: Synthesis and biological applications, *Nano Today*, **6**: 401-418, 2011. DOI: [10.1016/j.nantod.2011.06.004](https://doi.org/10.1016/j.nantod.2011.06.004)
439. J. XIE, Y. ZHENG, AND J. Y. YING. Protein-directed synthesis of highly fluorescent gold nanoclusters, *J. Am. Chem. Soc.*, **131**: 888-889, 2009. DOI: [10.1021/ja806804u](https://doi.org/10.1021/ja806804u)
440. Y. YU, S. Y. NEW, J. XIE, X. SU, *et al.* Protein-based fluorescent metal nanoclusters for small molecular drug screening, *Chem. Commun.*, **50**: 13805-13808, 2014. DOI: [10.1039/c4cc06914e](https://doi.org/10.1039/c4cc06914e)
441. H. KAWASAKI, K. HAMAGUCHI, I. OSAKA, AND R. ARAKAWA. Ph-dependent synthesis of pepsin-mediated gold nanoclusters with blue green and red fluorescent emission, *Adv. Funct. Mater.*, **21**: 3508-3515, 2011. DOI: [10.1002/adfm.201100886](https://doi.org/10.1002/adfm.201100886)
442. C.-L. LIU, H.-T. WU, Y.-H. HSIAO, C.-W. LAI, *et al.* Insulin-directed synthesis of fluorescent gold nanoclusters: Preservation of insulin bioactivity and versatility in cell imaging, *Angew. Chem. Int. Ed.*, **50**: 7056-7060, 2011. DOI: [10.1002/anie.201100299](https://doi.org/10.1002/anie.201100299)
443. Y. KONG, J. CHEN, F. GAO, R. BRYDSON, *et al.* Near-infrared fluorescent ribonuclease-a-encapsulated gold nanoclusters: Preparation, characterization, cancer targeting and imaging, *Nanoscale*, **5**: 1009-1017, 2013. DOI: [10.1039/c2nr32760k](https://doi.org/10.1039/c2nr32760k)
444. Y.-H. LIN AND W.-L. TSENG. Ultrasensitive sensing of hg<sup>2+</sup> and ch<sub>3</sub>hg<sup>+</sup> based on the fluorescence quenching of lysozyme type vi-stabilized gold nanoclusters, *Anal. Chem.*, **82**: 9194-9200, 2010. DOI: [10.1021/ac101427y](https://doi.org/10.1021/ac101427y)
445. P. L. XAVIER, K. CHAUDHARI, P. K. VERMA, S. K. PAL, *et al.* Luminescent quantum clusters of gold in transferrin family protein, lactoferrin exhibiting fret, *Nanoscale*, **2**: 2769-2776, 2010. DOI: [10.1039/c0nr00377h](https://doi.org/10.1039/c0nr00377h)

446. X. WU, X. HE, K. WANG, C. XIE, *et al.* Ultrasmall near-infrared gold nanoclusters for tumor fluorescence imaging in vivo, *Nanoscale*, **2**: 2244-2249, 2010. DOI: [10.1039/c0nr00359j](https://doi.org/10.1039/c0nr00359j)
447. S. LINK, A. BEEBY, S. FITZGERALD, M. A. EL-SAYED, *et al.* Visible to infrared luminescence from a 28-atom gold cluster, *J. Phys. Chem. B*, **106**: 3410-3415, 2002. DOI: [10.1021/jp014259v](https://doi.org/10.1021/jp014259v)
448. Y. NEGISHI, K. NOBUSADA, AND T. TSUKUDA. Glutathione-protected gold clusters revisited: Bridging the gap between gold(i)-thiolate complexes and thiolate-protected gold nanocrystals, *J. Am. Chem. Soc.*, **127**: 5261-5270, 2005. DOI: [10.1021/ja042218h](https://doi.org/10.1021/ja042218h)
449. E. S. SHIBU, M. A. H. MUHAMMED, T. TSUKUDA, AND T. PRADEEP. Ligand exchange of  $\text{Au}_{25}\text{Sg}_{18}$  leading to functionalized gold clusters: Spectroscopy, kinetics, and luminescence, *J. Phys. Chem. C*, **112**: 12168-12176, 2008. DOI: [10.1021/jp800508d](https://doi.org/10.1021/jp800508d)
450. M. ZHOU, S. TIAN, C. ZENG, M. Y. SFEIR, *et al.* Ultrafast relaxation dynamics of  $\text{Au}_{38}(\text{SC}_2\text{H}_4\text{Ph})_{24}$  nanoclusters and effects of structural isomerism, *J. Phys. Chem. C*, **121**: 10686-10693, 2017. DOI: [10.1021/acs.jpcc.6b10360](https://doi.org/10.1021/acs.jpcc.6b10360)
451. G. WANG, T. HUANG, R. W. MURRAY, L. MENARD, *et al.* Near-IR luminescence of monolayer-protected metal clusters, *J. Am. Chem. Soc.*, **127**: 812-813, 2005. DOI: [10.1021/ja0452471](https://doi.org/10.1021/ja0452471)
452. K. G. STAMPLECOSKIE AND P. V. KAMAT. Size-dependent excited state behavior of glutathione-capped gold clusters and their light-harvesting capacity, *J. Am. Chem. Soc.*, **136**: 11093-11099, 2014. DOI: [10.1021/ja505361n](https://doi.org/10.1021/ja505361n)
453. C. C. HUANG, Z. YANG, K. H. LEE, AND H. T. CHANG. Synthesis of highly fluorescent gold nanoparticles for sensing mercury(II), *Angew. Chem. Int. Ed.*, **46**: 6824-6828, 2007. DOI: [10.1002/anie.200700803](https://doi.org/10.1002/anie.200700803)
454. S.-H. CHA, J.-U. KIM, K.-H. KIM, AND J.-C. LEE. Preparation and photoluminescent properties of gold(i)-alkanethiolate complexes having highly ordered supramolecular structures, *Chem. Mater.*, **19**: 6297-6303, 2007. DOI: [10.1021/cm7024944](https://doi.org/10.1021/cm7024944)
455. C. JOBBAGY, P. BARANYAI, P. SZABO, T. HOLCZBAUER, *et al.* Unexpected formation of a fused double cycle trinuclear gold(i) complex supported by ortho-phenyl metallated aryl-diphosphine ligands and strong aurophilic interactions, *Dalton Trans.*, **45**: 12569-12575, 2016. DOI: [10.1039/c6dt01528j](https://doi.org/10.1039/c6dt01528j)
456. K. PYO, V. D. THANTHIRIGE, K. KWAK, P. PANDURANGAN, *et al.* Ultrabright luminescence from gold nanoclusters: Rigidifying the Au(i)-thiolate shell, *J. Am. Chem. Soc.*, **137**: 8244-8250, 2015. DOI: [10.1021/jacs.5b04210](https://doi.org/10.1021/jacs.5b04210)
457. G. WANG, R. GUO, G. KALYUZHNY, J.-P. CHOI, *et al.* Nir luminescence intensities increase linearly with proportion of polar thiolate ligands in protecting monolayers of  $\text{Au}_{38}$  and  $\text{Au}_{140}$  quantum dots, *J. Phys. Chem. B*, **110**: 20282-20289, 2006. DOI: [10.1021/jp0640528](https://doi.org/10.1021/jp0640528)
458. C. M. AIKENS. Effects of core distances, solvent, ligand, and level of theory on the tddft optical absorption spectrum of the thiolate-protected  $\text{Au}_{25}$  nanoparticle, *J. Phys. Chem. A*, **113**: 10811-10817, 2009. DOI: [10.1021/jp9051853](https://doi.org/10.1021/jp9051853)
459. R. LIU, Y. WANG, Q. YUAN, D. AN, *et al.* The Au clusters induce tumor cell apoptosis via specifically targeting thioredoxin reductase 1 (trxr1) and suppressing its activity, *Chem. Commun.*, **50**: 10687-10690, 2014. DOI: [10.1039/c4cc03320e](https://doi.org/10.1039/c4cc03320e)
460. A. A. SOUSA, S. A. HASSAN, L. L. KNITTEL, A. BALBO, *et al.* Biointeractions of ultrasmall glutathione-coated gold nanoparticles: Effect of small size variations, *Nanoscale*, **8**: 6577-6588, 2016. DOI: [10.1039/c5nr07642k](https://doi.org/10.1039/c5nr07642k)
461. K. H. LEE AND F. M. YTREBERG. Effect of gold nanoparticle conjugation on peptide dynamics and structure, *Entropy*, **14**: 630-641, 2012. DOI: [10.3390/e14040630](https://doi.org/10.3390/e14040630)
462. Y. CUI, Y. WANG, R. LIU, Z. SUN, *et al.* Serial silver clusters biomineralized by one peptide, *ACS Nano*, **5**: 8684-8689, 2011. DOI: [10.1021/nn202566n](https://doi.org/10.1021/nn202566n)
463. F. W. P. C. VAN OVERVELD, G. R. M. M. HAENEN, J. RHEMREV, J. P. W. VERMEIDEN, *et al.* Tyrosine as important contributor to the antioxidant capacity of seminal plasma, *Chem.-Biol. Interact.*, **127**: 151-161, 2000. DOI: [10.1016/s0009-2797\(00\)00179-4](https://doi.org/10.1016/s0009-2797(00)00179-4)

464. A. R. CLAPP, I. L. MEDINTZ, J. M. MAURO, B. R. FISHER, *et al.* Fluorescence resonance energy transfer between quantum dot donors and dye-labeled protein acceptors, *J. Am. Chem. Soc.*, **126**: 301-310, 2004. DOI: [10.1021/ja037088b](https://doi.org/10.1021/ja037088b)
465. W. C. WIMLEY AND S. H. WHITE. Experimentally determined hydrophobicity scale for proteins at membrane interfaces, *Nat. Struct. Mol. Biol.*, **3**: 842-848, 1996. DOI: [10.1038/nsb1096-842](https://doi.org/10.1038/nsb1096-842)
466. T. DAINESE, S. ANTONELLO, J. A. GASCÓN, F. PAN, *et al.* Au<sub>25</sub>(SET)<sub>18</sub>, a nearly naked thiolate-protected Au<sub>25</sub> cluster: Structural analysis by single crystal x-ray crystallography and electron nuclear double resonance, *ACS Nano*, **8**: 3904-3912, 2014. DOI: [10.1021/nn500805n](https://doi.org/10.1021/nn500805n)
467. K. LINDORFF-LARSEN, S. PIANA, K. PALMO, P. MARAGAKIS, *et al.* Improved side-chain torsion potentials for the amber ff99sb protein force field, *Proteins: Struct. Funct. Bioinf.*, **78**: 1950-1958, 2010. DOI: [10.1002/prot.22711](https://doi.org/10.1002/prot.22711)
468. W. L. JORGENSEN, J. CHANDRASEKHAR, J. D. MADURA, R. W. IMPEY, *et al.* Comparison of simple potential functions for simulating liquid water, *J. Chem. Phys.*, **79**: 926-935, 1983. DOI: [10.1063/1.445869](https://doi.org/10.1063/1.445869)
469. M. J. FRISCH, G. W. TRUCKS, H. B. SCHLEGEL, G. E. SCUSERIA, *et al.*, "Gaussian 09, revision C.01," ed. Wallingford, CT, USA: Gaussian, Inc., 2010.
470. A. E. TORDA, R. M. SCHEEK, AND W. F. VAN GUNSTEREN. Time-dependent distance restraints in molecular dynamics simulations, *Chem. Phys. Lett.*, **157**: 289-294, 1989. DOI: [10.1016/0009-2614\(89\)87249-5](https://doi.org/10.1016/0009-2614(89)87249-5)
471. E.-H. KANG, M. L. MANSFIELD, AND J. F. DOUGLAS. Numerical path integration technique for the calculation of transport properties of proteins, *Phys. Rev. E: Stat. Nonlinear Soft Matter Phys.*, **69**: 031918, 2004. DOI: [10.1103/PhysRevE.69.031918](https://doi.org/10.1103/PhysRevE.69.031918)
472. G. TE VELDE, F. M. BICKELHAUPT, E. J. BAERENDS, C. FONSECA GUERRA, *et al.* Chemistry with adf, *J. Comput. Chem.*, **22**: 931-967, 2001. DOI: [10.1002/jcc.1056](https://doi.org/10.1002/jcc.1056)
473. E. VAN LENTHE, A. EHLERS, AND E.-J. BAERENDS. Geometry optimizations in the zero order regular approximation for relativistic effects, *J. Chem. Phys.*, **110**: 8943-8953, 1999. DOI: [10.1063/1.478813](https://doi.org/10.1063/1.478813)
474. C. C. PYE, T. ZIEGLER, E. VAN LENTHE, AND J. N. LOUWEN. An implementation of the conductor-like screening model of solvation within the amsterdam density functional package — part II. Cosmo for real solvents1, *Can. J. Chem.*, **87**: 790-797, 2009. DOI: [10.1139/v09-008](https://doi.org/10.1139/v09-008)
475. J. P. PERDEW, K. BURKE, AND M. ERNZERHOF. Generalized gradient approximation made simple, *Phys. Rev. Lett.*, **77**: 3865-3868, 1996. DOI: [10.1103/PhysRevLett.77.3865](https://doi.org/10.1103/PhysRevLett.77.3865)
476. J. TOMASI, B. MENNUCCI, AND R. CAMMI. Quantum mechanical continuum solvation models, *Chem. Rev.*, **105**: 2999-3093, 2005. DOI: [10.1021/cr9904009](https://doi.org/10.1021/cr9904009)
477. C.-K. SKYLARIS, P. HAYNES, D., A. MOSTOFI, A., AND M. PAYNE, C. Introducing onetep: Linear-scaling density functional simulations on parallel computers, *J. Chem. Phys.*, **122**: 084119, 2005. DOI: [10.1063/1.1839852](https://doi.org/10.1063/1.1839852)
478. C.-K. SKYLARIS, A. A. MOSTOFI, P. D. HAYNES, O. DIÉGUEZ, *et al.* Nonorthogonal generalized wannier function pseudopotential plane-wave method, *Phys. Rev. B*, **66**: 2002. DOI: [10.1103/PhysRevB.66.035119](https://doi.org/10.1103/PhysRevB.66.035119)
479. A. A. MOSTOFI, P. D. HAYNES, C.-K. SKYLARIS, AND M. C. PAYNE. Preconditioned iterative minimization for linear-scaling electronic structure calculations, *J. Chem. Phys.*, **119**: 8842-8848, 2003. DOI: [10.1063/1.1613633](https://doi.org/10.1063/1.1613633)
480. M. ELSTNER, P. HOBZA, T. FRAUENHEIM, S. SUHAI, *et al.* Hydrogen bonding and stacking interactions of nucleic acid base pairs: A density-functional-theory based treatment, *J. Chem. Phys.*, **114**: 5149-5155, 2001. DOI: [10.1063/1.1329889](https://doi.org/10.1063/1.1329889)
481. R. BORRELLI AND A. PELUSO. Elementary electron transfer reactions: From basic concepts to recent computational advances, *WIREs Comput. Mol. Sim.*, **3**: 542-559, 2013. DOI: [10.1002/wcms.1147](https://doi.org/10.1002/wcms.1147)
482. V. BALZANI, Ed., *Electron transfer in chemistry*. Weinheim, Germany: Wiley-VCH Verlag GmbH, 2001, p.^pp. Pages.

483. J. YANG, H. FANG, AND Y. GAO. Effect of water adsorption on the photoluminescence of silicon quantum dots, *J. Phys. Chem. Lett.*, **7**: 1788-1793, 2016. DOI: [10.1021/acs.jpcllett.6b00574](https://doi.org/10.1021/acs.jpcllett.6b00574)
484. A. P. DE SILVA, T. S. MOODY, AND G. D. WRIGHT. Fluorescent pet (photoinduced electron transfer) sensors as potent analytical tools, *Analyst*, **134**: 2385-2393, 2009. DOI: [10.1039/b912527m](https://doi.org/10.1039/b912527m)
485. Y. YONEZAWA, T. SATO, M. OHNO, AND H. HADA. Photochemical formation of colloidal metals, *J. Chem. Soc. Faraday Trans. 1*, **83**: 1559, 1987. DOI: [10.1039/F19878301559](https://doi.org/10.1039/F19878301559)
486. T. SATO, S. KURODA, A. TAKAMI, Y. YONEZAWA, *et al.* Photochemical formation of silver-gold (Ag–Au) composite colloids in solutions containing sodium alginate, *Appl. Organomet. Chem.*, **5**: 261-268, 1991. DOI: [10.1002/aoc.590050409](https://doi.org/10.1002/aoc.590050409)
487. X.-H. JIN, J.-K. SUN, X.-M. XU, Z.-H. LI, *et al.* Conformational and photosensitive adjustment of the 4,4'-bipyridinium in mn(II) coordination complexes, *Chem. Commun.*, **46**: 4695-4697, 2010. DOI: [10.1039/c0cc00135j](https://doi.org/10.1039/c0cc00135j)
488. C. ZHANG, L. SUN, C. ZHANG, S. WAN, *et al.* Novel photo- and/or thermochromic mofs derived from bipyridinium carboxylate ligands, *Inorg. Chem. Front.*, **3**: 814-820, 2016. DOI: [10.1039/c6qi00013d](https://doi.org/10.1039/c6qi00013d)
489. G. MEHLANA AND S. A. BOURNE. Unravelling chromism in metal–organic frameworks, *CrystEngComm*, **19**: 4238-4259, 2017. DOI: [10.1039/c7ce00710h](https://doi.org/10.1039/c7ce00710h)
490. K. L. D. M. WEERAWARDENE, E. B. GUIDEZ, AND C. M. AIKENS. Photoluminescence origin of Au<sub>38</sub>(SR)<sub>24</sub> and au<sub>22</sub>(SR)<sub>18</sub> nanoparticles: A theoretical perspective, *J. Phys. Chem. C*, **121**: 15416-15423, 2017. DOI: [10.1021/acs.jpcc.7b01958](https://doi.org/10.1021/acs.jpcc.7b01958)
491. G. R. GRIMSLEY, J. M. SCHOLTZ, AND C. N. PACE. A summary of the measured pk values of the ionizable groups in folded proteins, *Protein Sci.*, **18**: 247-251, 2009. DOI: [10.1002/pro.19](https://doi.org/10.1002/pro.19)
492. H. ISOBE, T. TANAKA, W. NAKANISHI, L. LEMIEGRE, *et al.* Regioselective oxygenative tetraamination of [60]fullerene. Fullerene-mediated reduction of molecular oxygen by amine via ground state single electron transfer in dimethyl sulfoxide, *J. Org. Chem.*, **70**: 4826-4832, 2005. DOI: [10.1021/jo050432y](https://doi.org/10.1021/jo050432y)
493. L. A. DYKMAN AND N. G. KHLBTSOV. Biomedical applications of multifunctional gold-based nanocomposites, *Biochemistry (Moscow)*, **81**: 1771-1789, 2016. DOI: [10.1134/S0006297916130125](https://doi.org/10.1134/S0006297916130125)
494. J.-F. LI, Y.-J. ZHANG, S.-Y. DING, R. PANNEERSELVAM, *et al.* Core-shell nanoparticle-enhanced raman spectroscopy, *Chem. Rev.*, 2017. DOI: [10.1021/acs.chemrev.6b00596](https://doi.org/10.1021/acs.chemrev.6b00596)
495. H. BLAS, M. SAVE, P. PASETTO, C. BOISSIÈRE, *et al.* Elaboration of monodisperse spherical hollow particles with ordered mesoporous silica shells via dual latex/surfactant templating: Radial orientation of mesopore channels, *Langmuir*, **24**: 13132-13137, 2008. DOI: [10.1021/la801897k](https://doi.org/10.1021/la801897k)
496. Y. ZHAO, L.-N. LIN, Y. LU, S.-F. CHEN, *et al.* Templating synthesis of preloaded doxorubicin in hollow mesoporous silica nanospheres for biomedical applications, *Adv. Mater.*, **22**: 5255-5259, 2010. DOI: [10.1002/adma.201002395](https://doi.org/10.1002/adma.201002395)
497. B. XIA, B. WANG, W. ZHANG, AND J. SHI. High loading of doxorubicin into styrene-terminated porous silicon nanoparticles via  $\pi$ -stacking for cancer treatments in vitro, *RSC Adv.*, **5**: 44660-44665, 2015. DOI: [10.1039/c5ra04843e](https://doi.org/10.1039/c5ra04843e)
498. S. Y. TAN, C. Y. ANG, P. LI, Q. M. YAP, *et al.* Drug encapsulation and release by mesoporous silica nanoparticles: The effect of surface functional groups, *Chem. Eur. J.*, **20**: 11276-11282, 2014. DOI: [10.1002/chem.201403551](https://doi.org/10.1002/chem.201403551)
499. S. KWON, R. K. SINGH, T.-H. KIM, K. D. PATEL, *et al.* Luminescent mesoporous nanoreservoirs for the effective loading and intracellular delivery of therapeutic drugs, *Acta Biomater.*, **10**: 1431-1442, 2014. DOI: [10.1016/j.actbio.2013.10.028](https://doi.org/10.1016/j.actbio.2013.10.028)
500. X. DU, L. XIONG, S. DAI, AND S. Z. QIAO.  $\Gamma$ -pga-coated mesoporous silica nanoparticles with covalently attached prodrugs for enhanced cellular uptake and intracellular gsh-responsive release, *Adv. Healthc. Mater.*, **4**: 771-781, 2015. DOI: [10.1002/adhm.201400726](https://doi.org/10.1002/adhm.201400726)



501. E. I. RYABCHIKOVA, B. P. CHELOBANOV, R. G. PARKHOMENKO, K. V. KORCHAGINA, *et al.* Degradation of core-shell Au@SiO<sub>2</sub> nanoparticles in biological media, *Microporous Mesoporous Mater.*, **248**: 46-53, 2017. DOI: [10.1016/j.micromeso.2017.04.006](https://doi.org/10.1016/j.micromeso.2017.04.006)
502. T.-T. WANG, F. CHAI, C.-G. WANG, L. LI, *et al.* Fluorescent hollow/rattle-type mesoporous Au@SiO<sub>2</sub> nanocapsules for drug delivery and fluorescence imaging of cancer cells, *J. Colloid Interface Sci.*, **358**: 109-115, 2011. DOI: [10.1016/j.jcis.2011.02.023](https://doi.org/10.1016/j.jcis.2011.02.023)
503. Q. ZHAN, J. QIAN, X. LI, AND S. HE. A study of mesoporous silica-encapsulated gold nanorods as enhanced light scattering probes for cancer cell imaging, *Nanotechnology*, **21**: 055704, 2010. DOI: [10.1088/0957-4484/21/5/055704](https://doi.org/10.1088/0957-4484/21/5/055704)
504. J. L. VIVERO-ESCOTO, SLOWING, II, C. W. WU, AND V. S. LIN. Photoinduced intracellular controlled release drug delivery in human cells by gold-capped mesoporous silica nanosphere, *J. Am. Chem. Soc.*, **131**: 3462-3463, 2009. DOI: [10.1021/ja900025f](https://doi.org/10.1021/ja900025f)
505. D. NIECIECKA AND P. KRYSINSKI. Interactions of doxorubicin with self-assembled monolayer-modified electrodes: Electrochemical, surface plasmon resonance (spr), and gravimetric studies, *Langmuir*, **27**: 1100-1107, 2011. DOI: [10.1021/la103583g](https://doi.org/10.1021/la103583g)
506. A. ULMAN. Formation and structure of self-assembled monolayers, *Chem. Rev.*, **96**: 1533-1554, 1996. DOI: [10.1021/cr9502357](https://doi.org/10.1021/cr9502357)
507. D. BHANDARY, V. VALECHI, M. N. D. S. CORDEIRO, AND J. K. SINGH. Janus gold nanoparticles from nanodroplets of alkyl thiols: A molecular dynamics study, *Langmuir*, **33**: 3056-3067, 2017. DOI: [10.1021/acs.langmuir.6b04680](https://doi.org/10.1021/acs.langmuir.6b04680)
508. Y. Y. YIMER, K. C. JHA, AND M. TSIGE. Epitaxial transfer through end-group coordination modulates the odd-even effect in an alkanethiol monolayer assembly, *Nanoscale*, **6**: 3496-3502, 2014. DOI: [10.1039/c3nr05671f](https://doi.org/10.1039/c3nr05671f)
509. H. KIM, J. K. SAHA, Z. ZHANG, J. JANG, *et al.* Molecular dynamics study on the self-assembled monolayer grown from a droplet of alkanethiol, *J. Phys. Chem. C*, **118**: 11149-11157, 2014. DOI: [10.1021/jp502707d](https://doi.org/10.1021/jp502707d)
510. C.-P. KONG, E. A. J. F. PETERS, G. DE WIT, AND H.-X. ZHANG. Molecular dynamics simulation of a dopa/st monolayer on the Au(111) surface, *Phys. Chem. Chem. Phys.*, **15**: 15426-15433, 2013. DOI: [10.1039/c3cp51973b](https://doi.org/10.1039/c3cp51973b)
511. J. K. SAHA, Y. AHN, H. KIM, G. C. SCHATZ, *et al.* Small size limit to self-assembled monolayer formation on gold(111), *J. Phys. Chem. C*, **115**: 13193-13199, 2011. DOI: [10.1021/jp202564m](https://doi.org/10.1021/jp202564m)
512. Y. AHN, J. K. SAHA, G. C. SCHATZ, AND J. JANG. Molecular dynamics study of the formation of a self-assembled monolayer on gold, *J. Phys. Chem. C*, **115**: 10668-10674, 2011. DOI: [10.1021/jp200447k](https://doi.org/10.1021/jp200447k)
513. J. A. OLMOS-ASAR, M. LUDUENA, AND M. M. MARISCAL. Monolayer protected gold nanoparticles: The effect of the headgroup-Au interaction, *Phys. Chem. Chem. Phys.*, **16**: 15979-15987, 2014. DOI: [10.1039/c4cp01963f](https://doi.org/10.1039/c4cp01963f)
514. Y. LI, Z. YANG, N. HU, R. ZHOU, *et al.* Insights into hydrogen bond dynamics at the interface of the charged monolayer-protected Au nanoparticle from molecular dynamics simulation, *J. Chem. Phys.*, **138**: 184703, 2013. DOI: [10.1063/1.4803504](https://doi.org/10.1063/1.4803504)
515. L. RAMIN AND A. JABBARZADEH. Effect of load on structural and frictional properties of alkanethiol self-assembled monolayers on gold: Some odd-even effects, *Langmuir*, **28**: 4102-4112, 2012. DOI: [10.1021/la204701z](https://doi.org/10.1021/la204701z)
516. F. GOUJON, C. BONAL, B. LIMOGES, AND P. MALFREY. Description of ferrocenylalkylthiol SAMs on gold by molecular dynamics simulations, *Langmuir*, **25**: 9164-9172, 2009. DOI: [10.1021/la9007087](https://doi.org/10.1021/la9007087)
517. P. K. GHORAI AND S. C. GLOTZER. Molecular dynamics simulation study of self-assembled monolayers of alkanethiol surfactants on spherical gold nanoparticles, *J. Phys. Chem. C*, **111**: 15857-15862, 2007. DOI: [10.1021/jp0746289](https://doi.org/10.1021/jp0746289)

518. B. RAI, P. SATHISH, C. P. MALHOTRA, PRADIP, *et al.* Molecular dynamic simulations of self-assembled alkylthiolate monolayers on an Au(111) surface, *Langmuir*, **20**: 3138-3144, 2004. DOI: [10.1021/la0357256](https://doi.org/10.1021/la0357256)
519. E. O. FETISOV AND J. I. SIEPMANN. Structure and phase behavior of mixed self-assembled alkanethiolate monolayers on gold nanoparticles: A Monte Carlo study, *J. Phys. Chem. B*, **120**: 1972-1978, 2016. DOI: [10.1021/acs.jpcc.5b09975](https://doi.org/10.1021/acs.jpcc.5b09975)
520. V. VELACHI, D. BHANDARY, J. K. SINGH, AND M. N. D. S. CORDEIRO. Structure of mixed self-assembled monolayers on gold nanoparticles at three different arrangements, *J. Phys. Chem. C*, **119**: 3199-3209, 2015. DOI: [10.1021/jp512144g](https://doi.org/10.1021/jp512144g)
521. J. REGUERA, E. PONOMAREV, T. GEUE, F. STELLACCI, *et al.* Contact angle and adsorption energies of nanoparticles at the air-liquid interface determined by neutron reflectivity and molecular dynamics, *Nanoscale*, **7**: 5665-5673, 2015. DOI: [10.1039/c5nr00620a](https://doi.org/10.1039/c5nr00620a)
522. P. K. GHORAI AND S. C. GLOTZER. Atomistic simulation study of striped phase separation in mixed-ligand self-assembled monolayer coated nanoparticles, *J. Phys. Chem. C*, **114**: 19182-19187, 2010. DOI: [10.1021/jp105013k](https://doi.org/10.1021/jp105013k)
523. K. M. SALERNO AND G. S. GREST. Temperature effects on nanostructure and mechanical properties of single-nanoparticle thick membranes, *Faraday Discuss.*, **181**: 339-354, 2015. DOI: [10.1039/c4fd00249k](https://doi.org/10.1039/c4fd00249k)
524. J. M. D. LANE AND G. S. GREST. Assembly of responsive-shape coated nanoparticles at water surfaces, *Nanoscale*, **6**: 5132-5137, 2014. DOI: [10.1039/c3nr04658c](https://doi.org/10.1039/c3nr04658c)
525. S. J. KHAN, C. M. SORENSEN, AND A. CHAKRABARTI. Computer simulations of nucleation of nanoparticle superclusters from solution, *Langmuir*, **28**: 5570-5579, 2012. DOI: [10.1021/la2050306](https://doi.org/10.1021/la2050306)
526. B. S. JABES, H. O. S. YADAV, S. K. KUMAR, AND C. CHAKRAVARTY. Fluctuation-driven anisotropy in effective pair interactions between nanoparticles: Thiolated gold nanoparticles in ethane, *J. Chem. Phys.*, **141**: 154904, 2014. DOI: [10.1063/1.4897541](https://doi.org/10.1063/1.4897541)
527. K. M. SALERNO, D. S. BOLINTINEANU, J. M. D. LANE, AND G. S. GREST. High strength, molecularly thin nanoparticle membranes, *Phys. Rev. Lett.*, **113**: 258301, 2014. DOI: [10.1103/PhysRevLett.113.258301](https://doi.org/10.1103/PhysRevLett.113.258301)
528. K. M. SALERNO, D. S. BOLINTINEANU, J. M. D. LANE, AND G. S. GREST. Ligand structure and mechanical properties of single-nanoparticle-thick membranes, *Phys. Rev. E: Stat. Nonlinear Soft Matter Phys.*, **91**: 062403, 2015. DOI: [10.1103/PhysRevE.91.062403](https://doi.org/10.1103/PhysRevE.91.062403)
529. R. C. VAN LEHN AND A. ALEXANDER-KATZ. Ligand-mediated short-range attraction drives aggregation of charged monolayer-protected gold nanoparticles, *Langmuir*, **29**: 8788-8798, 2013. DOI: [10.1021/la400756z](https://doi.org/10.1021/la400756z)
530. M. CUI AND X. YANG. Molecular simulation of gold nanoparticle dispersion and aggregation in supercritical CO<sub>2</sub>, *J. Mater. Sci.*, **48**: 891-899, 2012. DOI: [10.1007/s10853-012-6811-6](https://doi.org/10.1007/s10853-012-6811-6)
531. J.-Q. LIN, H.-W. ZHANG, Z. CHEN, Y.-G. ZHENG, *et al.* Simulation study of aggregations of monolayer-protected gold nanoparticles in solvents, *J. Phys. Chem. C*, **115**: 18991-18998, 2011. DOI: [10.1021/jp204735d](https://doi.org/10.1021/jp204735d)
532. N. BHATTARAI, S. KHANAL, D. BAHENA, J. A. OLMOS-ASAR, *et al.* Structural order in ultrathin films of the monolayer protected clusters based upon 4 nm gold nanocrystals: An experimental and theoretical study, *Phys. Chem. Chem. Phys.*, **16**: 18098-18104, 2014. DOI: [10.1039/c4cp01612b](https://doi.org/10.1039/c4cp01612b)
533. J. MEENA DEVI. Aggregation of thiol coated gold nanoparticles: A simulation study on the effect of polymer coverage density and solvent, *Comput. Mater. Sci.*, **86**: 174-179, 2014. DOI: [10.1016/j.commatsci.2014.01.042](https://doi.org/10.1016/j.commatsci.2014.01.042)
534. E. L. DA ROCHA, G. F. CARAMORI, AND C. R. RAMBO. Nanoparticle translocation through a lipid bilayer tuned by surface chemistry, *Phys. Chem. Chem. Phys.*, **15**: 2282-2290, 2013. DOI: [10.1039/c2cp44035k](https://doi.org/10.1039/c2cp44035k)

535. J. LIN, H. ZHANG, Z. CHEN, AND Y. ZHENG. Penetration of lipid membranes by gold nanoparticles: Insights into cellular uptake, cytotoxicity, and their relationship, *ACS Nano*, **4**: 5421-5429, 2010. DOI: [10.1021/nn1010792](https://doi.org/10.1021/nn1010792)
536. Y. LI, X. ZHANG, AND D. CAO. A spontaneous penetration mechanism of patterned nanoparticles across a biomembrane, *Soft Matter*, **10**: 6844-6856, 2014. DOI: [10.1039/c4sm00236a](https://doi.org/10.1039/c4sm00236a)
537. M. K. BERA, H. CHAN, D. F. MOYANO, H. YU, *et al.* Interfacial localization and voltage-tunable arrays of charged nanoparticles, *Nano Lett.*, **14**: 6816-6822, 2014. DOI: [10.1021/nl502450j](https://doi.org/10.1021/nl502450j)
538. M. E. FERNANDEZ-GARCIA, M. PEREZ-ALVAREZ, D. MENDOZA-ANAYA, AND C. GUTIERREZ-WING. Effect of gamma radiation on alkanethiolate-capped gold nanoparticles: Theoretical studies, *Radiat. Phys. Chem.*, **120**: 81-88, 2016. DOI: [10.1016/j.radphyschem.2015.11.036](https://doi.org/10.1016/j.radphyschem.2015.11.036)
539. X. MA AND P. SHROTRIYA. Molecular dynamics simulation of electrical field induced conformational transition and associated frictional performance of monomolecular films, *J. Phys. D: Appl. Phys.*, **45**: 375306, 2012. DOI: [10.1088/0022-3727/45/37/375306](https://doi.org/10.1088/0022-3727/45/37/375306)
540. M. RAMBUKWELLA, L. SEMENTA, G. BARCARO, A. FORTUNELLI, *et al.* Organosoluble Au<sub>102</sub>(SPh)<sub>44</sub> nanomolecules: Synthesis, isolation, compositional assignment, core conversion, optical spectroscopy, electrochemistry, and theoretical analysis, *J. Phys. Chem. C*, **119**: 25077-25084, 2015. DOI: [10.1021/acs.jpcc.5b07520](https://doi.org/10.1021/acs.jpcc.5b07520)
541. D. ALVAREZ-PAGGI, D. F. MARTIN, P. M. DEBIASE, P. HILDEBRANDT, *et al.* Molecular basis of coupled protein and electron transfer dynamics of cytochrome c in biomimetic complexes, *J. Am. Chem. Soc.*, **132**: 5769-5778, 2010. DOI: [10.1021/ja910707r](https://doi.org/10.1021/ja910707r)
542. K. G. SPRENGER AND J. PFAENDTNER. Strong electrostatic interactions lead to entropically favorable binding of peptides to charged surfaces, *Langmuir*, **32**: 5690-5701, 2016. DOI: [10.1021/acs.langmuir.6b01296](https://doi.org/10.1021/acs.langmuir.6b01296)
543. H.-J. HSU, S.-Y. SHEU, AND R.-Y. TSAY. Preferred orientation of albumin adsorption on a hydrophilic surface from molecular simulation, *Colloids Surf. B*, **67**: 183-191, 2008. DOI: [10.1016/j.colsurfb.2008.08.017](https://doi.org/10.1016/j.colsurfb.2008.08.017)
544. Y. SUN, W. J. WELSH, AND R. A. LATOUR. Prediction of the orientations of adsorbed protein using an empirical energy function with implicit solvation, *Langmuir*, **21**: 5616-5626, 2005. DOI: [10.1021/la046932o](https://doi.org/10.1021/la046932o)
545. T. UTESCH, D. MILLO, M. A. CASTRO, P. HILDEBRANDT, *et al.* Effect of the protonation degree of a self-assembled monolayer on the immobilization dynamics of a [nife] hydrogenase, *Langmuir*, **29**: 673-682, 2013. DOI: [10.1021/la303635q](https://doi.org/10.1021/la303635q)
546. Q. WANG, C. ZHAO, J. ZHAO, J. WANG, *et al.* Comparative molecular dynamics study of  $\alpha\beta$  adsorption on the self-assembled monolayers, *Langmuir*, **26**: 3308-3316, 2010. DOI: [10.1021/la903070y](https://doi.org/10.1021/la903070y)
547. Q. WANG, J. ZHAO, X. YU, C. ZHAO, *et al.* Alzheimer  $\alpha\beta_{1-42}$  monomer adsorbed on the self-assembled monolayers, *Langmuir*, **26**: 12722-12732, 2010. DOI: [10.1021/la1017906](https://doi.org/10.1021/la1017906)
548. A. WEI AND C. DENG. Adsorption of protein on a Au surface studied by all-atom atomistic simulations, *J. Phys. Chem. C*, **120**: 13103-13112, 2016. DOI: [10.1021/acs.jpcc.6b03523](https://doi.org/10.1021/acs.jpcc.6b03523)
549. J. LIU, G. YU, AND J. ZHOU. Ribonuclease a adsorption onto charged self-assembled monolayers: A multiscale simulation study, *Chem. Eng. Sci.*, **121**: 331-339, 2015. DOI: [10.1016/j.ces.2014.07.021](https://doi.org/10.1016/j.ces.2014.07.021)
550. Y. XIE, C. LIAO, AND J. ZHOU. Effects of external electric fields on lysozyme adsorption by molecular dynamics simulations, *Biophys. Chem.*, **179**: 26-34, 2013. DOI: [10.1016/j.bpc.2013.05.002](https://doi.org/10.1016/j.bpc.2013.05.002)
551. H. CHAN AND P. KRÁL. Self-standing nanoparticle membranes and capsules, *Nanoscale*, **3**: 1881-1886, 2011. DOI: [10.1039/c0nr00912a](https://doi.org/10.1039/c0nr00912a)
552. B. VARNHOLT, M. J. GUBERMAN-PFEFFER, P. OULEVEY, S. ANTONELLO, *et al.* Vibrational coupling modulation in *n*-alkanethiolate protected Au<sub>25</sub>(SR)<sub>18</sub><sup>0</sup> clusters, *J. Phys. Chem. C*, **120**: 25378-25386, 2016. DOI: [10.1021/acs.jpcc.6b07592](https://doi.org/10.1021/acs.jpcc.6b07592)

553. J. A. NASH, T. L. TUCKER, W. THERRIault, AND Y. G. YINGLING. Binding of single stranded nucleic acids to cationic ligand functionalized gold nanoparticles, *Biointerphases*, **11**: 04B305, 2016. DOI: [10.1116/1.4966653](https://doi.org/10.1116/1.4966653)
554. V. VASUMATHI AND M. N. D. S. CORDEIRO. How reliable is the ReaxFF potential for describing the structure of alkanethiols on gold? A molecular dynamics study, *J. Phys.: Conf. Ser.*, **490**: 012006, 2014. DOI: [10.1088/1742-6596/490/1/012006](https://doi.org/10.1088/1742-6596/490/1/012006)
555. "Discovery studio modeling environment (release 3.5)," Release 3.5 ed. San Diego: Accelrys Software Inc., 2012.
556. C. CALEMAN, P. J. VAN MAAREN, M. HONG, J. S. HUB, *et al.* Force field benchmark of organic liquids: Density, enthalpy of vaporization, heat capacities, surface tension, isothermal compressibility, volumetric expansion coefficient, and dielectric constant, *J. Chem. Theory Comput.*, **8**: 61-74, 2012. DOI: [10.1021/ct200731v](https://doi.org/10.1021/ct200731v)
557. D. VAN DER SPOEL, P. J. VAN MAAREN, AND C. CALEMAN. GROMACS molecule & liquid database, *Bioinformatics*, **28**: 752-753, 2012. DOI: [10.1093/bioinformatics/bts020](https://doi.org/10.1093/bioinformatics/bts020)
558. J. WANG, R. M. WOLF, J. W. CALDWELL, P. A. KOLLMAN, *et al.* Development and testing of a general amber force field, *J. Comput. Chem.*, **25**: 1157-1174, 2004. DOI: [10.1002/jcc.20035](https://doi.org/10.1002/jcc.20035)
559. L. SUN, J. I. SIEPMANN, AND M. R. SCHURE. Conformation and solvation structure for an isolated n-octadecane chain in water, methanol, and their mixtures, *J. Phys. Chem. B*, **110**: 10519-10525, 2006. DOI: [10.1021/jp0602631](https://doi.org/10.1021/jp0602631)
560. T. R. WALSH. Pathways to structure-property relationships of peptide-materials interfaces: Challenges in predicting molecular structures, *Acc. Chem. Res.*, 2017. DOI: [10.1021/acs.accounts.7b00065](https://doi.org/10.1021/acs.accounts.7b00065)
561. D. A. WINKLER. Recent advances, and unresolved issues, in the application of computational modelling to the prediction of the biological effects of nanomaterials, *Toxicol. Appl. Pharmacol.*, **299**: 96-100, 2016. DOI: [10.1016/j.taap.2015.12.016](https://doi.org/10.1016/j.taap.2015.12.016)
562. Q. TANG AND D.-E. JIANG. Computational insight into the covalent organic-inorganic interface, *Chem. Mater.*, **28**: 5976-5988, 2016. DOI: [10.1021/acs.chemmater.6b01740](https://doi.org/10.1021/acs.chemmater.6b01740)
563. S. KHAN AND C. K. NANDI. Optimizing the underlying parameters for protein-nanoparticle interaction: Advancement in theoretical simulation, *Nanotechnol. Rev.*, **3**: 347-359, 2014. DOI: [10.1515/ntrev-2014-0002](https://doi.org/10.1515/ntrev-2014-0002)
564. S. J. WEINER, P. A. KOLLMAN, D. A. CASE, U. C. SINGH, *et al.* A new force field for molecular mechanical simulation of nucleic acids and proteins, *J. Am. Chem. Soc.*, **106**: 765-784, 1984. DOI: [10.1021/ja00315a051](https://doi.org/10.1021/ja00315a051)
565. C. I. BAYLY, P. CIEPLAK, W. CORNELL, AND P. A. KOLLMAN. A well-behaved electrostatic potential based method using charge restraints for deriving atomic charges: The resp model, *J. Phys. Chem.*, **97**: 10269-10280, 1993. DOI: [10.1021/j100142a004](https://doi.org/10.1021/j100142a004)
566. H. QIAN, M. ZHU, Z. WU, AND R. JIN. Quantum sized gold nanoclusters with atomic precision, *Acc. Chem. Res.*, **45**: 1470-1479, 2012. DOI: [10.1021/ar200331z](https://doi.org/10.1021/ar200331z)
567. M. R. JONES, K. D. OSBERG, R. J. MACFARLANE, M. R. LANGILLE, *et al.* Templated techniques for the synthesis and assembly of plasmonic nanostructures, *Chem. Rev.*, **111**: 3736-3827, 2011. DOI: [10.1021/cr1004452](https://doi.org/10.1021/cr1004452)
568. Y. WANG, Y. CUI, Y. ZHAO, R. LIU, *et al.* Bifunctional peptides that precisely biomineralize Au clusters and specifically stain cell nuclei, *Chem. Commun.*, **48**: 871-873, 2012. DOI: [10.1039/c1cc15926g](https://doi.org/10.1039/c1cc15926g)
569. L. SHANG, N. AZADFAR, F. STOCKMAR, W. SEND, *et al.* One-pot synthesis of near-infrared fluorescent gold clusters for cellular fluorescence lifetime imaging, *Small*, **7**: 2614-2620, 2011. DOI: [10.1002/sml.201100746](https://doi.org/10.1002/sml.201100746)
570. G. BEAUCAGE. Approximations leading to a unified exponential/power-law approach to small-angle scattering, *J. Appl. Crystallogr.*, **28**: 717-728, 1995. DOI: [10.1107/s0021889895005292](https://doi.org/10.1107/s0021889895005292)

# **Appendices**

## Appendix A:

# Force Field Parameterisations

Dr Andrew Christofferson is acknowledged for the parameterisations in Section [A.1](#).

---

## A.1 Parameters for Au-S-C-C Dihedral

In most force fields (FF), the change in energy associated with rotating four atoms A-B-C-D about the dihedral bond B-C is represented by a cosine function of the form:

$$E_{dihedrals} = \frac{V_n}{2(idiv)} [1 + \cos(n\theta - \gamma)] \quad (\text{A.1})$$

The parameters that govern the relationship between energy  $E_{dihedral}$  and angle  $\theta$  are: barrier height (amplitude)  $V_n$ ; phase shift (offset)  $\gamma$ ; and periodicity  $n$ . Additionally, in the AMBER FF<sup>564</sup> there is an extra “*idiv*” term, which can be thought of as the ‘multiplicity’ of the dihedral, i.e. how many times that dihedral appears. This term is typically set to 1 except for generic dihedrals that contain wildcard atoms (e.g. \*-C-C-\*). The typical parameterisation strategy for proper dihedrals is to first perform a potential energy (PE) scan using quantum mechanical (QM) calculations at the MP2/6-31G\* level, and then attempt to replicate the resulting curve using Equation [A.1](#). The missing dihedral for the FF used in Chapters [4](#) and [5](#) is the Au-S-C-C dihedral in [Figure A.1](#). In the FF, gold atom types are defined based on if they are form part of the Au<sub>13</sub> icosahedral core (AuC) or the Au<sub>2</sub>S<sub>3</sub> dimeric staples (AuS), likewise sulphur atoms that are only attached to AuS are termed “staple-sulphur” (SS) and those attached to AuC are termed “core-sulphur” (SC). Therefore, two dihedrals need to be parameterised: AuC-SC-CT-CT and AuS-SS-CT-CT, where CT is any sp<sup>3</sup> carbon.

Since the distance between gold atoms are rigidly maintained during molecular dynamics, gold positions are also kept frozen in the dihedral scan. Apart from the gold atom positions and the Au-S-C-C dihedral itself, all other coordinates are geometry optimised. QM calculations were performed using Gaussian09.<sup>469</sup> The first step was a full optimisation where all coordinates except the gold atom positions were free to move, then a PE scan was performed on the Au-S-C-C dihedral with 36 steps and a step increment of 10°, for a total scan of 360°. This procedure was also done for the AuS-SS-AuS and AuC-SC-AuS configurations. Once the QM scans were obtained, parameters were determined for Equation [A.1](#) to obtain the best fit for the QM data ([Figure A.2](#)).

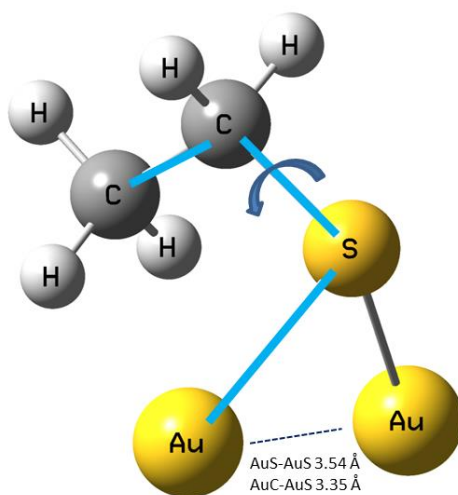


Figure A.1 | Au-S-C-C dihedral examined in dihedral scanning.

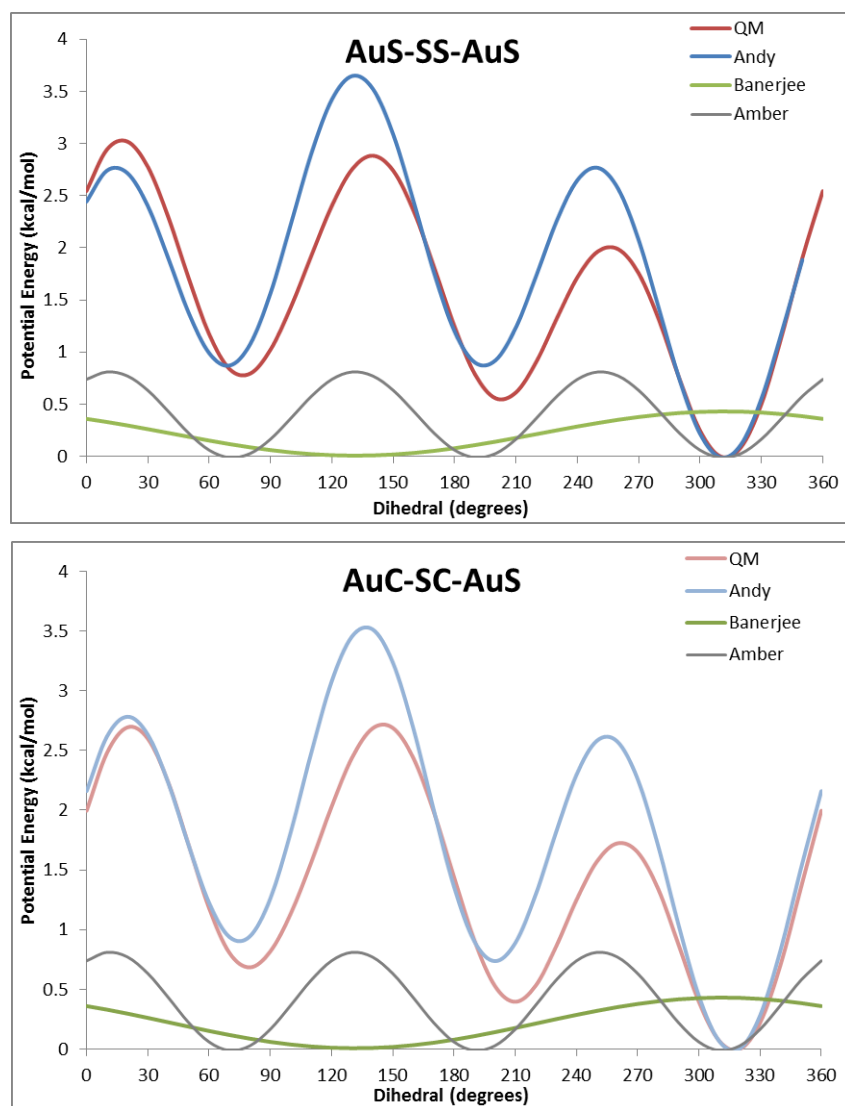


Figure A.2 | Comparison of the quantum mechanical potential energy scan and the derived molecular modelling parameters. Closest existing parameters from Amber and dihedral from Banerjee et al. are shown for comparison.

Each QM PE scan represents two dihedrals; one for each gold type. Therefore, the molecular modelling energy must be a linear combination of these two dihedrals:  $E_{Au_1} + E_{Au_2}$ , where the dihedral angle for  $Au_2$  is offset from  $Au_1$  by a fixed amount;  $97^\circ$  for AuS-SS-AuS and  $90^\circ$  for AuC-SC-AuS (e.g. if  $\theta_1 = 330^\circ$  then  $\theta_2 = 67^\circ$  for AuS-SS-AuS). Final parameters for AuS-SS-AuS and AuC-SC-AuS are given in Table A.1.

**Table A.1 | Final parameters for the Au-S-C-C dihedral.**

AuC-SC-CT-CT	$V_n/2$	$\gamma$	$n$	$idiv$
Andy	0.75	3	0	0
Additional	0.45	1	180	0
Amber	0.75	3	0	3
Banerjee	0.16	1	0	0
AuC-SC-CT-CT	$V_n/2$	$\gamma$	$n$	$idiv$
Andy	0.95	3	0	0
Additional	0.35	1	180	0
Amber	0.75	3	0	3
Banerjee	0.16	1	0	0

To provide a better fit for the QM PE dihedral scan, additional parameters were necessary. Therefore, the total equation for the AuS-SS-AuS dihedral would be

$$E_{\text{AuS-S-AuS}} = E_{\text{AuS\_Andy}} + E_{\text{AuS\_Additional}} + E_{\text{AuS\_Andy}_{(\theta+97)}} + E_{\text{AuS\_Additional}_{(\theta+97)}}$$

The total equation for the AuC-S-AuS dihedral would be

$$E_{\text{AuC-S-AuS}} = E_{\text{AuS\_Andy}} + E_{\text{AuS\_Additional}} + E_{\text{AuC\_Andy}_{(\theta+90)}} + E_{\text{AuC\_Additional}_{(\theta+90)}}$$

Larger fragments were also constructed (Figure A.3) and the same approach as described previously was used for the AuS-S-AuS dihedral. The plot (Figure A.4) indicates a much higher rotational barrier, but a similar global minimum. This greater barrier is most likely due to other interactions (van der Waals, etc) other than the dihedral itself.



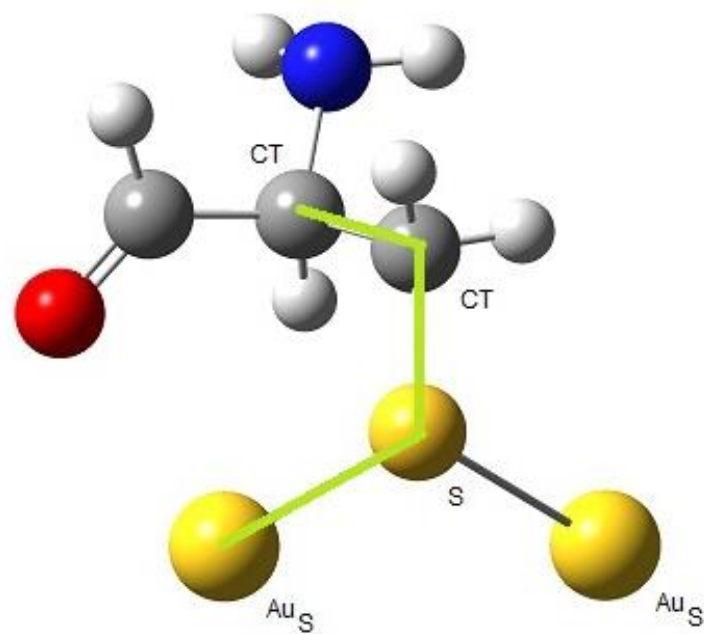


Figure A.3 | Larger fragment for dihedral scan.

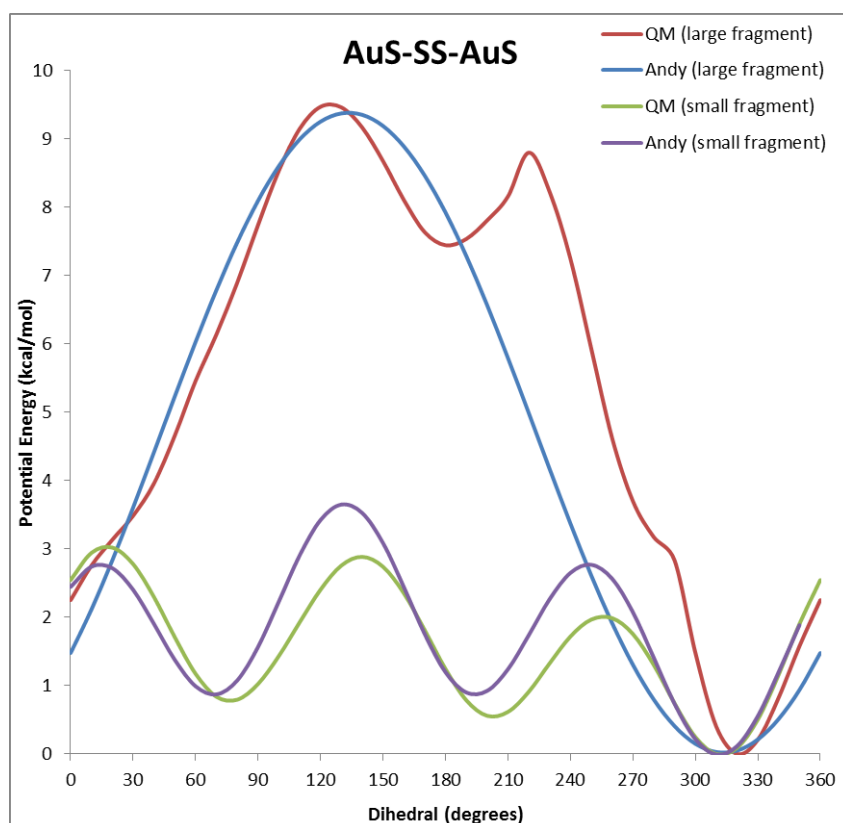


Figure A.4 | Dihedral scan of larger fragment with smaller fragment for comparison.

## A.2 Partial Atomic Charges on $\text{SC}_8\text{H}_{17}$

Two starting structures of  $\text{H}_{17}\text{C}_8\text{S}-\text{SC}_8\text{H}_{17}$  were created, one linear (configuration **I**) and one with a kink (configuration **II**), then Gaussian09<sup>469</sup> with B3LYP/6-31\* was used to produce geometry optimised structures (**I'** and **II'**, see Figure A.5). A single point HF/6-31\* calculation was performed on each configuration to produce an electrostatic potential (ESP) that was then used to determine atomic partial charges with the restrained electrostatic potential energy (RESP), consistent with the parameterisation approach of AMBER.<sup>565</sup> Since the charges generated from the two conformer structures were similar, the final charges used in molecular dynamics were taken from configuration **I** and are displayed in Figure A.6. See Section A.3 for a more comprehensive description of the approach taken to determine atomic charges.

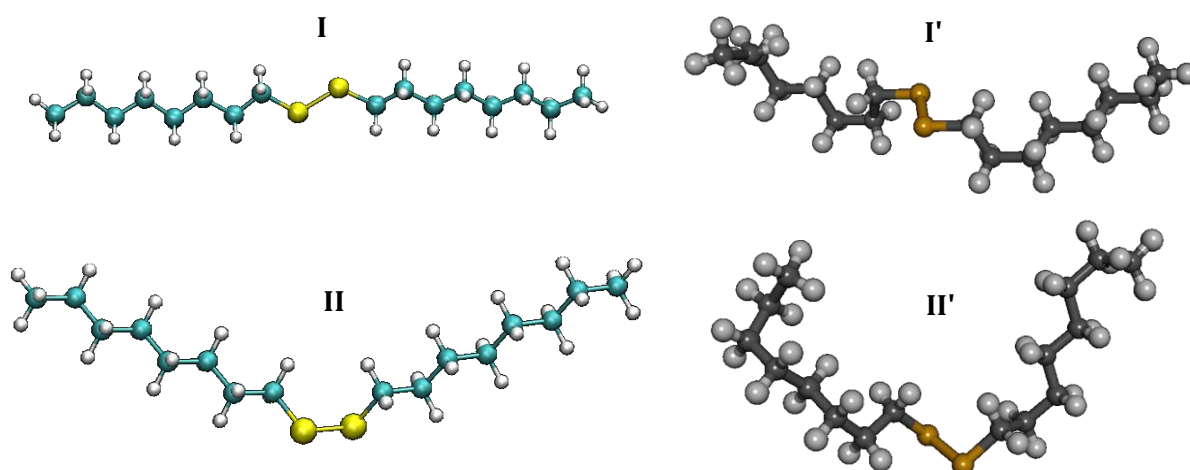


Figure A.5 |  $\text{H}_{17}\text{C}_8\text{S}-\text{SC}_8\text{H}_{17}$  geometries before and after geometry optimisation.

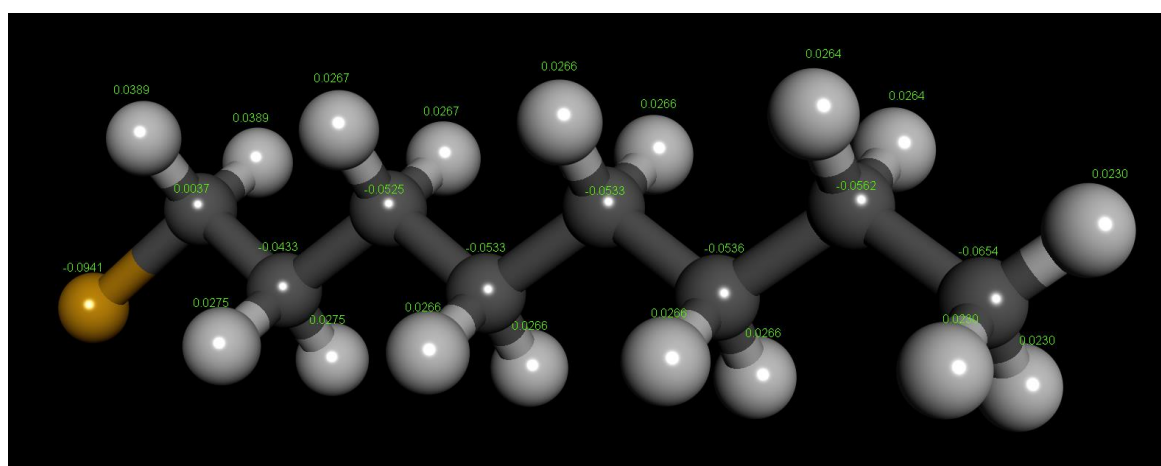


Figure A.6 | Final  $\text{SC}_8\text{H}_{17}$  partial charges used in molecular dynamics simulations.

### A.3 General Amber Force Field Parameterisation of Doxorubicin

1. Doxorubicin (DOX) structure taken from the Protein Data Bank ligand chemical component of 4DX7 (see DOI: [10.1039/c3sm52499j](https://doi.org/10.1039/c3sm52499j) or [10.1039/c5sm01028d](https://doi.org/10.1039/c5sm01028d)).
2. Discovery Studio 3.5 Visualiser<sup>555</sup> software was used to add hydrogen atoms and ensure  $\text{NH}_3^+$  protonation state leaving DOX with a net charge of +1 since amine is protonated at physiological pH (see Figure A.7).

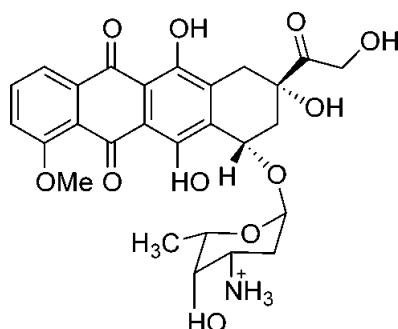


Figure A.7 | Chemical schematic of doxorubicin at physiological pH.

3. GaussView used to add and correct for any missing bonds, and make .gjf file (Figure A.8).

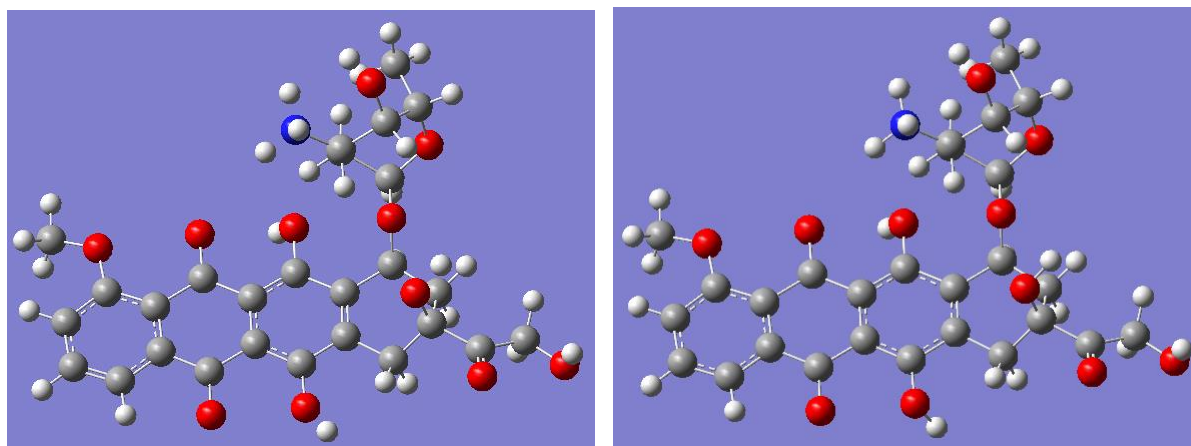


Figure A.8 | Before (left) and after (right) correcting doxorubicin bonds.

4. Gaussian (.gjf) file is edited to have net charge = 1, multiplicity = 1 and correct file header for Gaussian to do geometry optimisation:

```
%chk=dox_GeomOpt_B3LYP.chk
%mem=8000MB
%NprocShared=16
# B3LYP/6-31G* geom=connectivity scfcyc=500 opt(maxcycles=500)
```

5. Geometry optimisation performed.
6. Checkpoint file (.chk) from geometry optimisation used as input for single-point Hartree-Fock (HF) calculation. So, new multiplicity, charge, and file header used for .gjf is:

```
%chk=dox_SPE_HF.chk
%mem=8000MB
```

```
%NprocShared=16
# HF/6-31G* geom=checkpoint scfcyc=500 guess=read Pop=MK IOp(6/50=1)
IOp(6/33=2) IOp(6/42=6)
```

Title Card Required

1 1

7. Single-point energy calculation performed.

8. ESP output from HF calculation used as input to determine RESP charges:

```
antechamber -i dox_AMBERinp.out -fi gout -o dox_GAFF.prep -fo prepi
-c resp
```

9. Converted prep file to mol2 and opened in DiscoveryStudio (Figure A.9) to visualise and check atom types, charges and optimised structure of DOX:

```
antechamber -i dox_GAFF.prep -fi prepi -o dox_GAFF.mol2 -fo mol2 -at
gaff
```

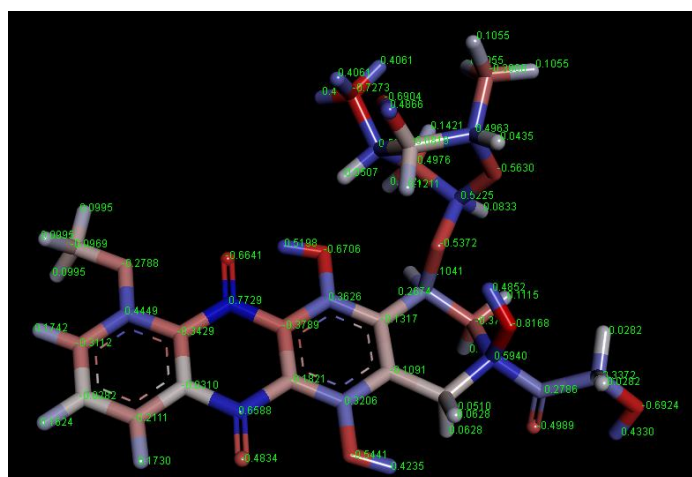


Figure A.9 | Final doxorubicin structure and partial charges.

10. Used **parmchk2** to make sure all bonds are defined assigning anything that may be missing:

```
parmchk2 -i dox_GAFF.mol2 -f mol2 -o dox_GAFF.frcmod -a Y
```

11. Used **tleap** to build an AMBER topology.

```
tleap
source leaprc.gaff
DOX = loadmol2 dox_GAFF.mol2
list
check DOX
loadamberparams dox_GAFF.frcmod
check DOX
set DOX box {30.0 30.0 30.0}
saveoff DOX dox.lib
saveamberparm DOX dox.prmtop dox.inpcrd
quit
```

## Appendix B:

# Non-standard Analysis Techniques

---

### B.1 Moment of inertia to determine AuNC size/shape

The moment of inertia (MOI) is a quantitative measure of a body's resistance to rotational acceleration about an axis and depends on the distribution of mass in the body with respect to that axis. In other words, depending on the axis of rotation defined for a system, the MOI will describe how *hard* it will be to rotate all atoms around that axis. It essentially gives a measure of where mass is distributed in three dimensions in reference to an axis. For spatial movement of a body, the MOI is defined by a  $3 \times 3$  *inertia matrix*, or *inertia tensor* ( $\mathbf{I}$ ):

$$\mathbf{I} = \begin{bmatrix} I_{xx} & I_{xy} & I_{xz} \\ I_{yx} & I_{yy} & I_{yz} \\ I_{zx} & I_{zy} & I_{zz} \end{bmatrix} = \sum_{i=1}^n \begin{bmatrix} m_i(y_i^2 + z_i^2) & -m_i x_i y_i & -m_i x_i z_i \\ -m_i y_i x_i & m_i(x_i^2 + z_i^2) & -m_i y_i z_i \\ -m_i z_i x_i & -m_i z_i y_i & m_i(x_i^2 + y_i^2) \end{bmatrix}$$

where  $m_i$  is the mass of the  $i^{\text{th}}$  particle at position  $(x_i, y_i, z_i)$  from the axis of rotation and  $n$  is all particles in the rigid body.

For all  $\mathbf{I}$  there is a rotation matrix  $[Q]$  that will produce a diagonalised tensor  $\tilde{\mathbf{I}}$ :

$$\mathbf{I} = [Q][\tilde{\mathbf{I}}][Q^T]$$

$$\text{where } \tilde{\mathbf{I}} = \begin{bmatrix} \tilde{I}_1 & 0 & 0 \\ 0 & \tilde{I}_2 & 0 \\ 0 & 0 & \tilde{I}_3 \end{bmatrix}$$

The three columns that make up the rotation matrix  $[Q]$  are the eigenvectors of the  $\mathbf{I}$  and are mutually orthogonal unit vectors that define the directions of the *principal axes* of the body. The important thing about the principal axes is that if the rigid body rotates about any one of them, the angular momentum and angular velocity vectors of the body become parallel and the inertia tensor can be replaced with a single scalar moment of inertia. These are the constants  $\tilde{I}_1$ ,  $\tilde{I}_2$  and  $\tilde{I}_3$  and are the eigenvalues of  $\mathbf{I}$ , called the *principal moments of inertia*. Two of these principal moments are the maximum and minimum moments of inertia of the body about any axis and the third is somewhere between the two.

Consider the inertia tensor for an ellipsoid of uniform density centred at the origin with its axes along the  $x$ -,  $y$ -, and  $z$ -axes shown below:

$$\mathbf{I}_{\text{ellipsoid}} = \frac{M}{5} \begin{bmatrix} (b^2 + c^2) & 0 & 0 \\ 0 & (a^2 + c^2) & 0 \\ 0 & 0 & (a^2 + b^2) \end{bmatrix}$$

where  $M$  is the total mass of the ellipsoid and  $a$ ,  $b$  and  $c$  are the major, intermediate and minor semi-axes lengths of the ellipsoid (see Figure 5.5 or 6.8).

By correlating  $\tilde{\mathbf{I}}$  to  $\mathbf{I}_{\text{ellipsoid}}$  the semi-axes lengths of a representative ellipsoid of the Au-ligand complexes can be determined:

$$\tilde{\mathbf{I}}_{\text{complex}} = \mathbf{I}_{\text{ellipsoid}}$$

$$\begin{bmatrix} \tilde{I}_1 & 0 & 0 \\ 0 & \tilde{I}_2 & 0 \\ 0 & 0 & \tilde{I}_3 \end{bmatrix} = \frac{M}{5} \begin{bmatrix} (b^2 + c^2) & 0 & 0 \\ 0 & (a^2 + c^2) & 0 \\ 0 & 0 & (a^2 + b^2) \end{bmatrix}$$

So,

$$\tilde{I}_1 = \frac{M}{5}(b^2 + c^2), \quad \tilde{I}_2 = \frac{M}{5}(a^2 + c^2), \quad \tilde{I}_3 = \frac{M}{5}(a^2 + b^2)$$

Therefore,

$$a = \sqrt{\frac{5}{2M}(\tilde{I}_2 + \tilde{I}_3 - \tilde{I}_1)}, \quad b = \sqrt{\frac{5}{2M}(\tilde{I}_3 + \tilde{I}_1 - \tilde{I}_2)}, \quad c = \sqrt{\frac{5}{2M}(\tilde{I}_1 + \tilde{I}_2 - \tilde{I}_3)}$$

However, the  $\text{Au}_{25}(\text{SC}_8\text{H}_{17})_{18}$  and  $\text{Au}_{25}(\text{SP})_{18}$  nanoclusters are far from uniform density (heavy gold core surrounded by light organic molecules) and hence the representative uniform density ellipsoids using all atoms underestimates nanocluster size (Figure B.1). Instead the MOI (of the total complex) is deconvoluted into contributions from the gold atoms and the ligand molecules separately, leading to two ellipsoids (blue and green, Figure B.2) of approximately uniform density. The outer (blue) ellipsoid, only containing ligand atoms, is indicative of the apparent AuNC size and comparing against many snapshots from MD suggests that the monolayer-protected nanoclusters' size and shape can be satisfactorily described with ellipsoids.

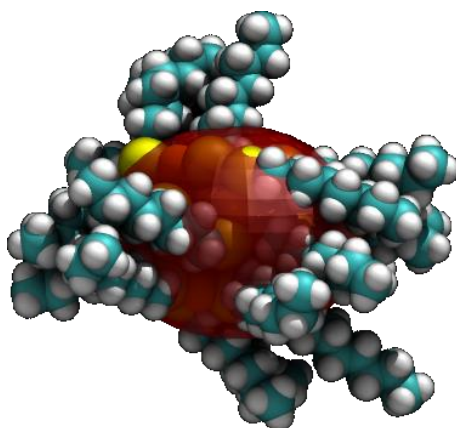


**Figure B.1 | Example ellipsoid of the whole complex.** The ellipsoid surface (red) underrepresents the size of the nanocluster because it assumes the complex is uniformly dense. Gold (orange), sulphur (yellow), carbon (cyan), hydrogen (white) atoms are shown for  $\text{Au}_{25}(\text{SC}_8\text{H}_{17})_{18}$ .

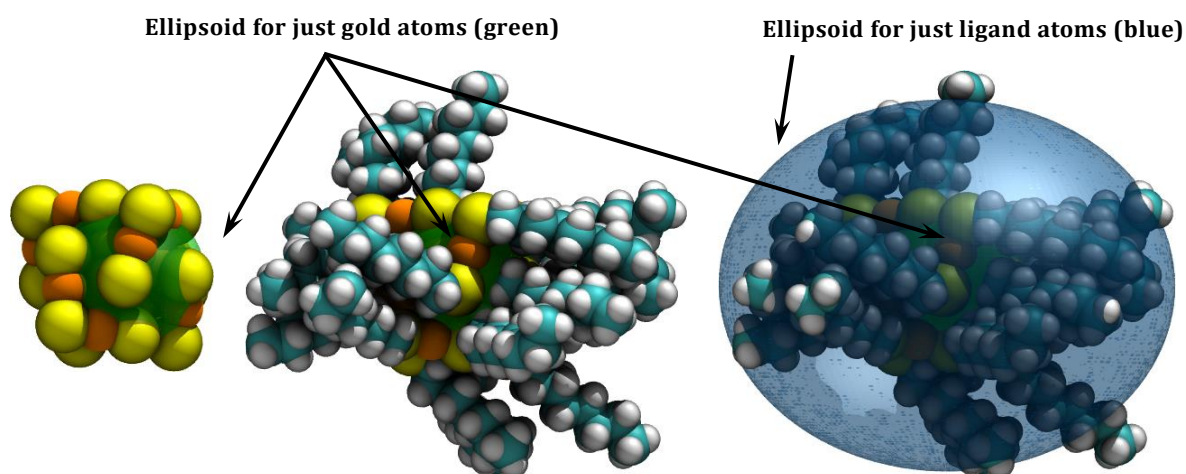


**Figure B.2 | Accurate ellipsoid representation of dynamic nanocluster size. (Left)**  $\text{Au}_{25}\text{S}_{18}$  and ellipsoid<sub>gold</sub> surface (green). **(b)**  $\text{Au}_{25}(\text{SC}_8\text{H}_{17})_{18}$  and ellipsoid<sub>gold</sub>. **(c)**  $\text{Au}_{25}(\text{SC}_8\text{H}_{17})_{18}$ , ellipsoid<sub>gold</sub>, and ellipsoid<sub>ligands</sub> (blue). Atoms are coloured as per Figure B.1.

To deconvolute the MOI, the inertia tensors  $I$ , rotation matrices  $[Q]$ , and diagonalised inertia tensors  $\tilde{I}$  are separately determined for the total gold-ligand complex, just the ligand atoms and just the gold atoms.

$$I_{\text{complex}} = [Q_{\text{complex}}][\tilde{I}_{\text{complex}}][Q_{\text{complex}}^T]$$

$$I_{\text{ligands}} = [Q_{\text{ligands}}][\tilde{I}_{\text{ligands}}][Q_{\text{ligands}}^T]$$

$$I_{\text{gold}} = [Q_{\text{gold}}][\tilde{I}_{\text{gold}}][Q_{\text{gold}}^T]$$

Then it is important to note that while the inertia tensors  $\mathbf{I}$  are in parallel inertial reference frames for each different set of atoms, the diagonalised matrices  $\tilde{\mathbf{I}}$  are not, they've each undergone different rotations  $[Q]$  (Figure B.3).

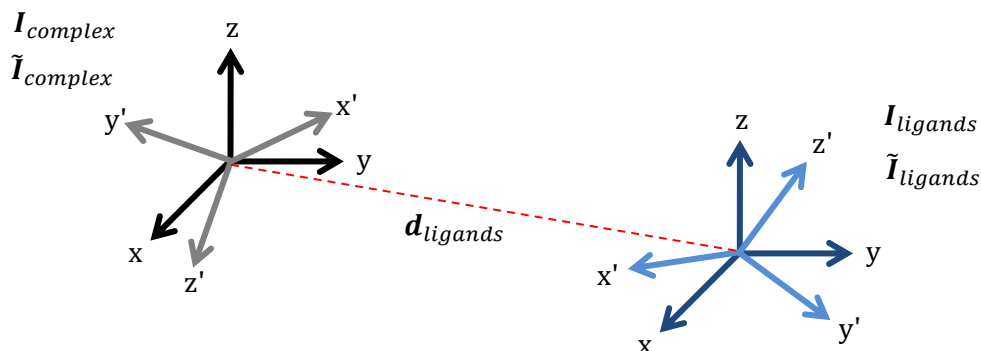


**Figure B.3 | Schematic example of the inertial reference frames for inertia and diagonalised tensors.** Note the difference in both position and rotation.

The parallel axis theorem is then applied to  $\mathbf{I}_{ligands}$  and  $\mathbf{I}_{gold}$  in order to translate them to the same location as the inertial reference for  $\mathbf{I}_{complex}$ . This requires the vectors between the two sets of atoms centre of masses, i.e.  $\mathbf{d}_{ligands}$  and  $\mathbf{d}_{gold}$ .

The parallel axis theorem states that if  $\mathbf{I}$  is the inertia around an object of mass  $m$  and  $\mathbf{I}'$  is the inertia around a parallel axis at distance  $d$  away then:

$$\mathbf{I}' = \mathbf{I} + m\mathbf{d}^2$$

So,

$$\mathbf{I}'_{ligands} = \mathbf{I}_{ligands} + m_{ligands} \cdot \mathbf{d}_{ligands}^2$$

$$\mathbf{I}'_{gold} = \mathbf{I}_{gold} + m_{gold} \cdot \mathbf{d}_{gold}^2$$

Now that the inertia tensors are all in the same inertial reference frame:

$$\mathbf{I}_{complex} = \mathbf{I}'_{ligands} + \mathbf{I}'_{gold}$$

Finally,  $\tilde{\mathbf{I}}'_{ligands}$  and  $\tilde{\mathbf{I}}'_{gold}$  need to be at the same rotation as the original  $\tilde{\mathbf{I}}_{complex}$ , i.e.:

$$\tilde{\mathbf{I}}'_{ligands} = [Q_{complex}^T][\mathbf{I}'_{ligands}][Q_{complex}]$$

$$\tilde{\mathbf{I}}'_{gold} = [Q_{complex}^T][\mathbf{I}'_{gold}][Q_{complex}]$$

Finally, from the diagonal terms  $\tilde{I}'_1$ ,  $\tilde{I}'_2$  and  $\tilde{I}'_3$  of  $\tilde{\mathbf{I}}'_{ligands}$  and  $\tilde{\mathbf{I}}'_{gold}$  the semi-axes lengths  $a$ ,  $b$  and  $c$  can be determined from the representative ellipsoids (just containing ligand atoms)



but aligned along the principal axes of the total complex. From this properties such as ellipsoid volume and sphericity ( $c/a$ ) can be determined.

$$V_{\text{ellipsoid}} = \frac{4}{3}\pi abc$$

## B.2 Electrostatic Potential Acting on Subset of Molecular System

To gain a classical, first-order approximation of the energy needed to remove an electron from an aspartate's carboxylate group, the system's total potential energy is subtracted from an *a posteriori* calculated total potential energy where a single electron charge has been neglected. While configurations are unable to respond to the charge removal in this approach and the electrostatic potential around both oxygen atoms is assumed to be constant, the energy difference obtained is still useful to crudely and simply evaluate how much the potential energy changes upon possible aspartate charge transfer.

For situations where a smaller energetic penalty is paid, it may be more likely for an electron to migrate from aspartate to gold and encourage PL quenching. The aim of this analysis is simply to classically explore if it is electrostatically more feasible for aspartate to lose an electron in different environments (e.g. close to  $\text{Au}_{25}\text{S}_{18}$ ). Below is a description of the approach taken to achieve this. The following nomenclature will be used in this section:

- OLD – input/output files from the original MD run
- NEW – input/output files from `mdrun -rerun`
- MOD – to label input/output files where the charge has been modified

**1. Duplicate the (OLD.top) topology file and remove a total of  $1e^-$  charge equally from the partial charge of the atoms of interest (NEW\_MOD.top).**

In this case, the carbonyl oxygen atoms (OD1, OD2) of a particular ASP residue are perturbed by adding  $0.5e^-$  to each atom.

---

```

OLD.top
...
[ atoms ]
;  nr      type  resnr residue  atom   cgnr      charge      mass  t
...

```

```

; residue 5 ASP rtp ASP q -1.0
934      N      5      ASP      N      934      -0.5163      14.01
935      H      5      ASP      H      935      0.2936      1.008
936      CT     5      ASP      CA     936      0.0381      12.01
937      H1     5      ASP      HA     937      0.088      1.008
938      CT     5      ASP      CB     938      -0.0303     12.01
939      HC     5      ASP      HB1    939      -0.0122     1.008
940      HC     5      ASP      HB2    940      -0.0122     1.008
941      C      5      ASP      CG     941      0.7994      12.01
942      O2     5      ASP      OD1    942      -0.8014      16
943      O2     5      ASP      OD2    943      -0.8014      16
944      C      5      ASP      C      944      0.5366      12.01
945      O      5      ASP      O      945      -0.5819      16
...
NEW_MOD.top
...
[ atoms ]
; nr      type  resnr residue atom  cgnr      charge      mass  t
...
; residue 5 ASP rtp ASP q -1.0
934      N      5      ASP      N      934      -0.5163      14.01
935      H      5      ASP      H      935      0.2936      1.008
936      CT     5      ASP      CA     936      0.0381      12.01
937      H1     5      ASP      HA     937      0.088      1.008
938      CT     5      ASP      CB     938      -0.0303     12.01
939      HC     5      ASP      HB1    939      -0.0122     1.008
940      HC     5      ASP      HB2    940      -0.0122     1.008
941      C      5      ASP      CG     941      0.7994      12.01
942      O2     5      ASP      OD1    942      -0.3014      16
943      O2     5      ASP      OD2    943      -0.3014      16
944      C      5      ASP      C      944      0.5366      12.01
945      O      5      ASP      O      945      -0.5819      16
...

```

**2. Run `grompp` on the (`NEW_MOD.top`) topology file to create a binary (`NEW_MOD.tpr`) topology file using the (`OLD.mdp`) parameter file.**

```
grompp -f OLD.mdp -c OLD.pdb -n OLD.ndx -p NEW_MOD.top -o NEW_MOD.tpr
```

**3. Run `mdrun -rerun` using the previously generated trajectory to produce a new binary (`.edr`) energy file.**

`mdrun -rerun` uses an input trajectory and (re)calculates forces and energies. Neighbor searching will be performed for every frame, unless `nstlist` is zero (see the `.mdp` file).

Do this for both the original unmodified `OLD.tpr` and the newly created `NEW_MOD.tpr`.

```
mdrun -rerun OLD.xtc -s OLD.tpr -e NEW.edr
mdrun -rerun OLD.xtc -s NEW_MOD.tpr -e NEW_MOD.edr
```

Even though `NEW_MOD.tpr` is built using `OLD.mdp`, the energies in `NEW_MOD.edr` can be at a lower accuracy than those of `OLD.edr` because of how they were calculated:

```
; freq to calc energies & pressures (steps)
```

```
nstcalcenergy          = 10
```

whereas, the trajectory (which we are now calculating new energies from) have an accuracy that's limited from:

```
; freq to write coords to output traj (steps)
nstxout                = 1000
; freq to write coords to xtc traj (steps)
nstxtcout              = 1000
```

For this reason, it is best to also recalculate the energies of `OLD.tpr` to ensure that `NEW.edr` and `NEW_MOD.edr` are at the same accuracy.

#### 4. Use `g_energy` to calculate the potential energy of the entire system at each frame.

```
g_energy -f NEW.edr -o NEW.xvg
g_energy -f NEW_MOD.edr -o NEW_MOD.xvg
```

Example outputs:

---

```
NEW.xvg
...
@ title "Gromacs Energies"
@ xaxis label "Time (ps)"
@ yaxis label "(kJ/mol)"
@TYPE xy
@ view 0.15, 0.15, 0.75, 0.85
@ legend on
@ legend box on
@ legend loctype view
@ legend 0.78, 0.8
@ legend length 2
@ s0 legend "Potential"
81000.000000 -772421.750000
81002.000000 -772128.562500
81004.000000 -770502.125000
81006.000000 -771327.250000
81008.000000 -771929.687500
...
```

---

```
NEW_MOD.xvg
...
@ title "Gromacs Energies"
@ xaxis label "Time (ps)"
@ yaxis label "(kJ/mol)"
@TYPE xy
@ view 0.15, 0.15, 0.75, 0.85
@ legend on
@ legend box on
@ legend loctype view
@ legend 0.78, 0.8
@ legend length 2
@ s0 legend "Potential"
81000.000000 -771783.500000
81002.000000 -771463.187500
81004.000000 -769868.875000
81006.000000 -770668.562500
```

81008.000000 -771313.812500

...

**5. (optional) To find the magnitude of the *electrostatic potential* ( $V$ ) at the atoms of interest (not reported in this thesis), the potential energy difference ( $\Delta U$ , before and after electron removal) is divided by the summed partial charges ( $\Sigma q$ ) of the modified groups (and divided again by 96.4869 to convert from  $\text{kJ}\cdot\text{mol}^{-1}$  to eV).**

$$V = \Delta U / \Sigma q \times 1/96.4869 = (U_{\text{after}} - U_{\text{before}}) / -1.6028 \times 1/96.4869$$

Note that the electrostatic potential *energy* is the energy resulting from Coulomb forces between a configuration of point charges in a defined system. Therefore, by taking the difference between the two total potential energies,  $_{\text{NEW}}$  and  $_{\text{NEW\_MOD}}$ , the contribution that a single electron charge (distributed equally on the two ASP oxygen atoms) provides to the total electrostatic potential *energy* can be calculated. Specifically, the magnitude of this difference delivers an indication to how the system's potential energy responds to the removal of  $1e^-$  charge, e.g. if electron transferred. This is a simple first-order classical approximation of the energy required to remove an electron from the system via ASP.

By dividing this by the original partial charges on the atoms of interest, the electrostatic potential, which is a property of the electrostatic field itself, can be obtained. In other words, this approach calculates the *electrostatic potential* acting on a specific group ( $_{\text{OD1}}$ ,  $_{\text{OD2}}$ ) as a result of the cumulative electrostatic influence of all other point charges in the system, which is assumed to be a constant effect around these atoms. The closer the electrostatic potential is to zero, the easier it is for an electron to be donated/removed.

**6. Repeat for the other  $31 \times$  ASP residues in the ligand layer.**

## Supplementary Results (Chapter 4)

---

### C.1 Progressively Loaded Peptides on Au(111)

The bio-functionalisation of the gold nanoparticles (AuNPs) with peptides is envisaged as a progressive self-assembly process. In solution, the peptides' approach to the surface involves no selectivity and is controlled by diffusion,<sup>89</sup> hence contact with the AuNP and subsequent partially formed layer occurs at various random times. Structural rearrangement of the AuNP passivating layer occurs to facilitate further epitope binding until spatial competition for sites is saturated and equilibrium is reached.

To emulate this scenario, successive simulations were performed wherein the epitope density was sequentially increased on the gold surface (Figure C.1). This involved initially packing 6 linear peptides onto Au(111) and equilibrating by molecular dynamics (MD) for 20 ns, which was found to be sufficient time to allow the peptides' conformations to relax. Following this, the final peptide-gold structure was extracted from the trajectory (devoid of water and ions) and an additional 6 linear peptides were placed onto the Au(111) surface where gaps had formed in the layer to expose gold atoms. A further 20 ns of explicit solvent MD was then commenced. This process was repeated for a final time by adding another 4 linear peptides and the system was simulated for 100 ns of MD. This density of 16 peptides per unit cell was determined to be the highest possible number of peptides that can be accommodated per AuNP surface area without causing ejection of peptides due to steric/electrostatic repulsion. Subsequently, this density has been used to set up the initial fully extended systems for equilibration and analysis. While MD was performed for both the progressively loaded and initially sterically-saturated setups, only the latter is reported in Chapter 4 as similar findings were obtained for both approaches.

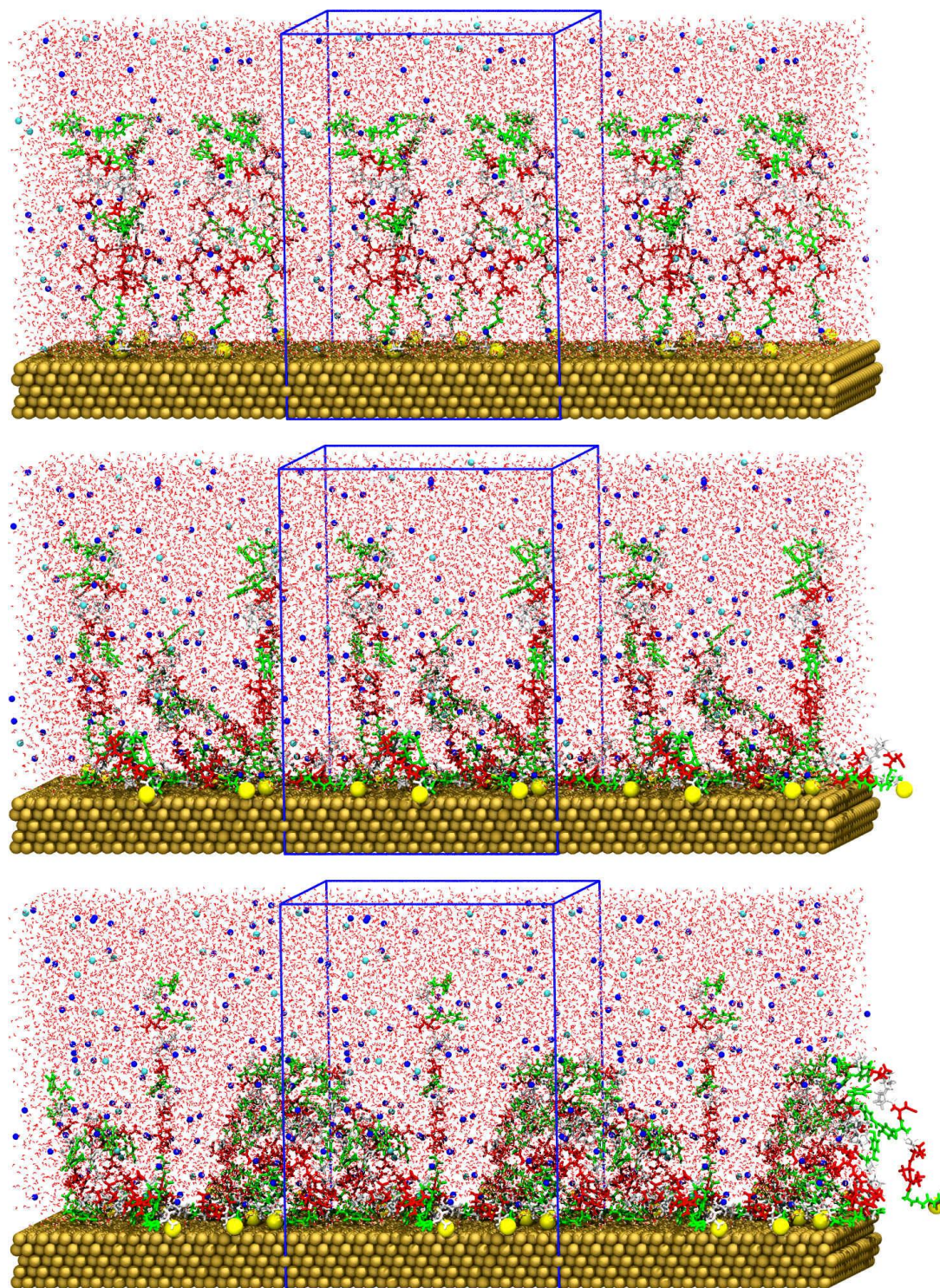


**Figure C.1 | Setup of progressively loaded peptide-gold systems. (a)** Initial fully extended immobilisation (total of 6 peptides). **(b)** Intermediate step with 4 more peptides added (total of 10 peptides). **(c)** Additional peptides added (total of 13 peptides). The epitopes' negatively charged (red), polar (green) and non-polar (white) residues are displayed in liquorice representation with the terminal immobilisation sulphurs presented as yellow spheres. The Au(111) surface (gold), periodic unit cell (blue), water molecules, Na<sup>+</sup> ions (dark blue) and Cl<sup>-</sup> ions (cyan) are shown.

## C.2 Equilibration of Sterically-Saturated Systems

Energy drifts and root-mean-square deviations (RMSD) of atomic positions are monitored in Figure C.2. While the potential energy is very quick to converge ( $< 1$  ns), structural rearrangements in the monolayers' constituent peptide chains continue for quite some time ( $> 100$  ns). To ensure thermal and structural equilibration, statistical analysis is only conducted on the ensemble of structures collected over the final 5 ns of the trajectories.

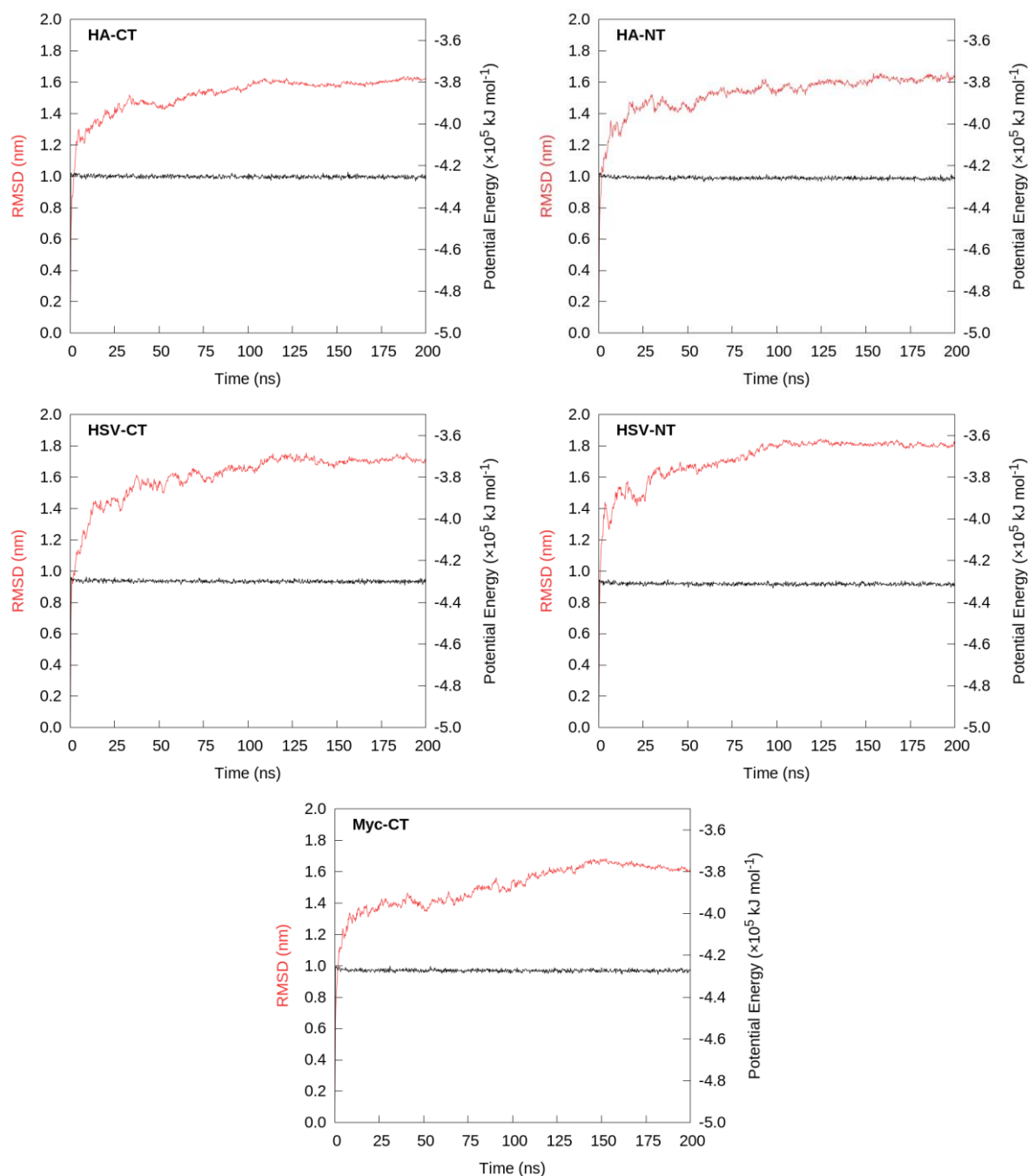


**Figure C.2 | Time evolution of peptide monolayer root-mean-square deviations and system potential energy.** RMSDs (red) of all monolayer atomic coordinates are calculated with reference to the initial linearly extended structures. Black lines in the plots show total potential energy.

### C.3 Peptide Root-Mean-Square Fluctuations

The flexibility of peptides within the epitope–monolayers is assessed by root-mean-square fluctuations (RMSF) of each residue's  $\alpha$ -carbon ( $C\alpha$ ) atoms. The RMSFs presented in Figure C.3 are the standard deviation of atomic positions with respect to a reference structure – the simulations frame at the start of the equilibration period, i.e. after 195 ns of MD.

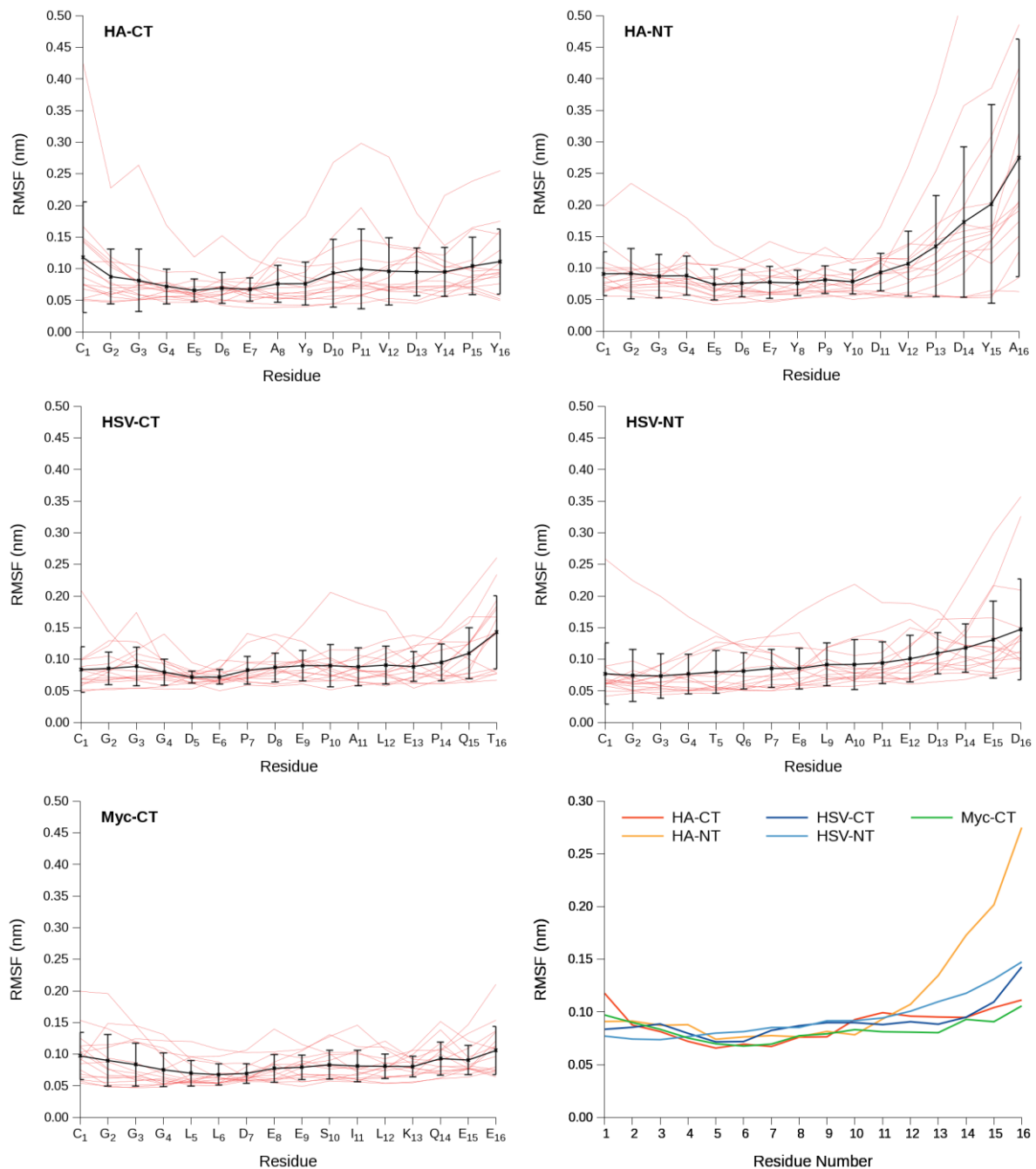


**Figure C.3 | Root-mean-square fluctuations of peptide-monolayer amino acids.** The black lines are ensemble averaged RMSFs (y-axes) with standard deviation error bars, whereas the 16 thin red lines are the RMSFs for single peptides. Numbering of residues (x-axes) is from the gold-attachment point (cysteine). The plot in the bottom right juxtaposes the average peptide RMSFs for each system.



## C.4 Single Immobilised Epitopes on Au (111)

To elucidate how HA and HSV peptide-epitopes interact with Au(111), 50 ns MD simulations of individually immobilised peptides on gold were conducted. During MD, sulphur atoms were constrained to Au(111) to emulate a covalent Au–S bond and limit lateral movement of the peptides. Simulations were independently repeated three times using different initial atomic velocities to improve statistics.

The majority of the MD simulations reveal that the peptides collapse onto Au(111) in a sequential manner starting with the adsorption of linker residues, followed by the middle residues in the primary sequence, and finally the terminal residues anchor to gold. However, in two out of the three HA-CT simulations, tyrosine residues at the untethered N-terminus adsorb to Au(111) almost immediately after the initial linker. This aromatic driven peptide adsorption appears to be epitaxially motivated with the six-membered phenol rings in tyrosine fitting into the hexagonal packing of gold atoms on the Au(111) crystallographic facet<sup>235</sup> (Figure C.4). For both HA immobilisation directions, peptide conformations remain fluid and dynamic as the chains laterally rotate about the sulphur attachment point until aromatic binding to gold, thereafter the peptides remain relatively rigid and stationary.

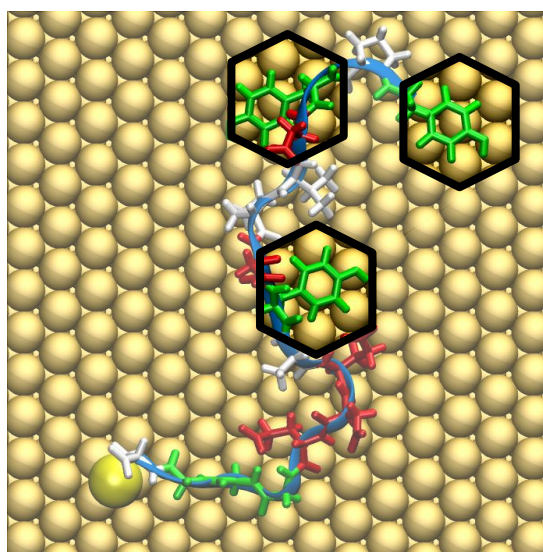


**Figure C.4 | Au(111) adsorbed HA-CT peptide highlighting the epitaxial matching of tyrosine phenol rings and hexagonal packing of gold atoms.** Peptide backbones are shown in ribbon representation with residues shown in liquorice and coloured as per Figure C.1.

In contrast, the HSV epitopes don't contain any aromatic residues and hence appear to be more flexible during the adsorption process and on average take longer to collapse onto the surface (data not included). Interestingly, five-membered imidazole rings in proline residues occasionally (in two out of six simulations) adsorbed onto the gold edge-to-face and prop the negatively charged glutamate and aspartate residues away from the surface

(Figure C.5). While this only infrequently appeared, common in all HA and HSV simulations is that after peptide adsorption to Au(111), negatively charged residues are manoeuvred to be facing away from the surface and as solvent exposed as possible.

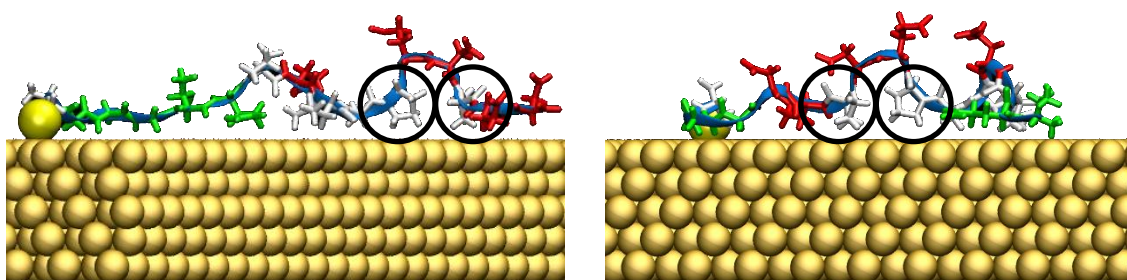


**Figure C.5 | Side views of HSV peptides adsorbed onto Au(111).** Proline residues (circled) bind to gold edge-to-face causing the peptide backbone to protrude from Au(111) in a loop to solvent expose negatively charged residues. The left image is HSV-CT and the right image is HSV-NT. Peptide backbones are shown in ribbon representation with residues shown in liquorice and coloured as per Figure C.1.

## C.5 Density Distribution of Immuno-Dominant HA Residues

Figure C.6 presents the normalised atomic distribution profiles (technique described in Section 4.3.1) for charged and aromatic immuno-dominant residues of the HA-monolayers. The aspartate residues in HA-CT (Figure C.6a) cluster in two regions 1.7 nm and 2.3 nm above Au(111) whereas for HA-NT the distribution is more evenly spread but attenuates further ( $> 3.0$  nm) from the gold surface. Two-times more hydrophobic Tyr residues are Au-bound in HA-CT versus HA-NT (Figure C.6a) owing to the primary sequenced location of the aromatic amino acids in the peptide chains.

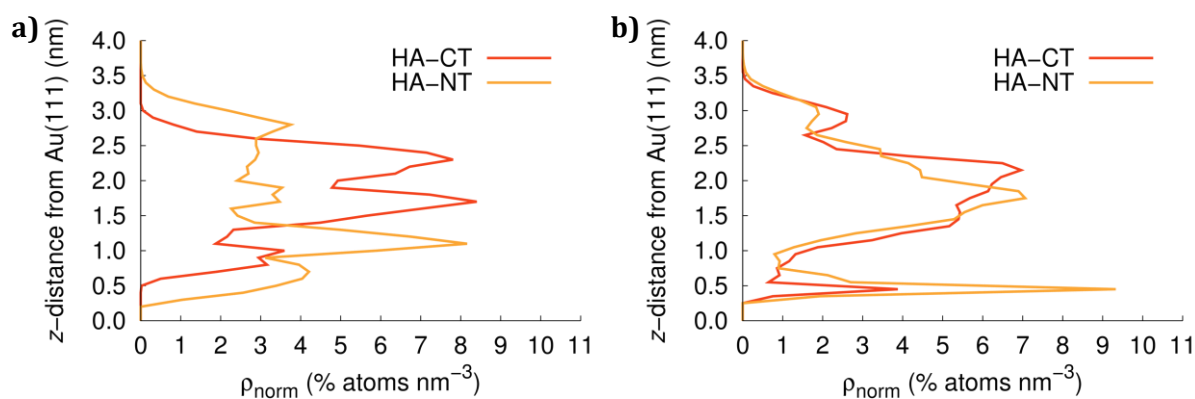


**Figure C.6 | Normalised atomic number density of HA immuno-dominant residues as a function of height above the Au(111) surface.** The distribution of (a) aspartate and (b) tyrosine residues.

## C.6 Radial Distributions of Solvent Atoms

Peptide-solvent intermolecular pair correlation functions,  $g(r)$ , are presented in Figure C.7 and show that water and  $\text{Na}^+$  cations both accumulate around the peptide-epitopes however  $\text{Cl}^-$  anions do not. The  $\text{H}_2\text{O}$  radial distribution functions (RDFs) also reveal that in each system, although water interacts with the immuno-dominant sequences (IDS) of the peptides through both their hydrogen and oxygen atoms, there is a prevalence for water to orient towards the peptides in a specific direction, i.e. either with their oxygen or hydrogen atoms facing the peptide chains. The approximate ratio of the hydrogen to oxygen RDF peak amplitudes at the first hydration shell ( $\sim 0.18$  nm in the  $\text{H}_2\text{O}$  RDFs Figure C.7) is used to estimate the directional orientation of water molecules near the peptides' IDS. The radial distances and amplitudes of both the hydrogen and oxygen peaks are presented in Table C.1 along with the relative H:O ratios. These results show that while in all systems (except HA-CT), there is a higher proportion of hydrogen atoms that are spontaneously and preferentially directed towards the IDS of the peptide chains.

**Table C.1 | Orientation information of  $\text{H}_2\text{O}$  atoms relative to the peptides IDS.**

System	Hydrogen $g(r)$ maxima*	Oxygen $g(r)$ maxima*	H:O Ratio <sup>†</sup>	H--IDS <sup>‡</sup>	O--IDS <sup>‡</sup>
HA-CT	<b>0.258 (0.180 nm)</b>	<b>0.175 (0.180 nm)</b>	2.00:1.36	42%	57%
HA-NT	<b>0.363 (0.174 nm)</b> 0.310 (0.182 nm)	0.088 (0.174 nm) <b>0.109 (0.182 nm)</b>	2.00:0.58	63%	37%
HSV-CT	<b>0.389 (0.172 nm)</b> 0.309 (0.182 nm)	0.107 (0.172 nm) <b>0.129 (0.182 nm)</b>	2.00:0.67	60%	40%
HSV-NT	<b>0.435 (0.169 nm)</b> 0.268 (0.188 nm)	0.036 (0.169 nm) <b>0.097 (0.188 nm)</b>	2.00:0.30	77%	23%
Myc-CT	<b>0.332 (0.171 nm)</b> 0.283 (0.180 nm)	0.105 (0.171 nm) <b>0.129 (0.180 nm)</b>	2.00:0.75	57%	43%

\*The amplitude of the first hydrogen and oxygen peak is bolded and the radial distance this occurs at is in brackets.

<sup>†</sup>The H:O ratio is attained by averaging the ratio of all 1<sup>st</sup> hydration shell amplitudes at different distances. For example, the HA-NT H:O ratio is calculated as:  $(0.363/0.088 + 0.363/0.109 + 0.310/0.088 + 0.310/0.109)/4$

<sup>‡</sup>The percentage of water molecules with either H or O atoms facing the IDS is calculated by weighting the hydrogen atoms as half (since there is two per  $\text{H}_2\text{O}$  molecule). For example, O--IDS in HA-NT is:  $0.58/(2 \times 0.5 + 0.58) \times 100\%$

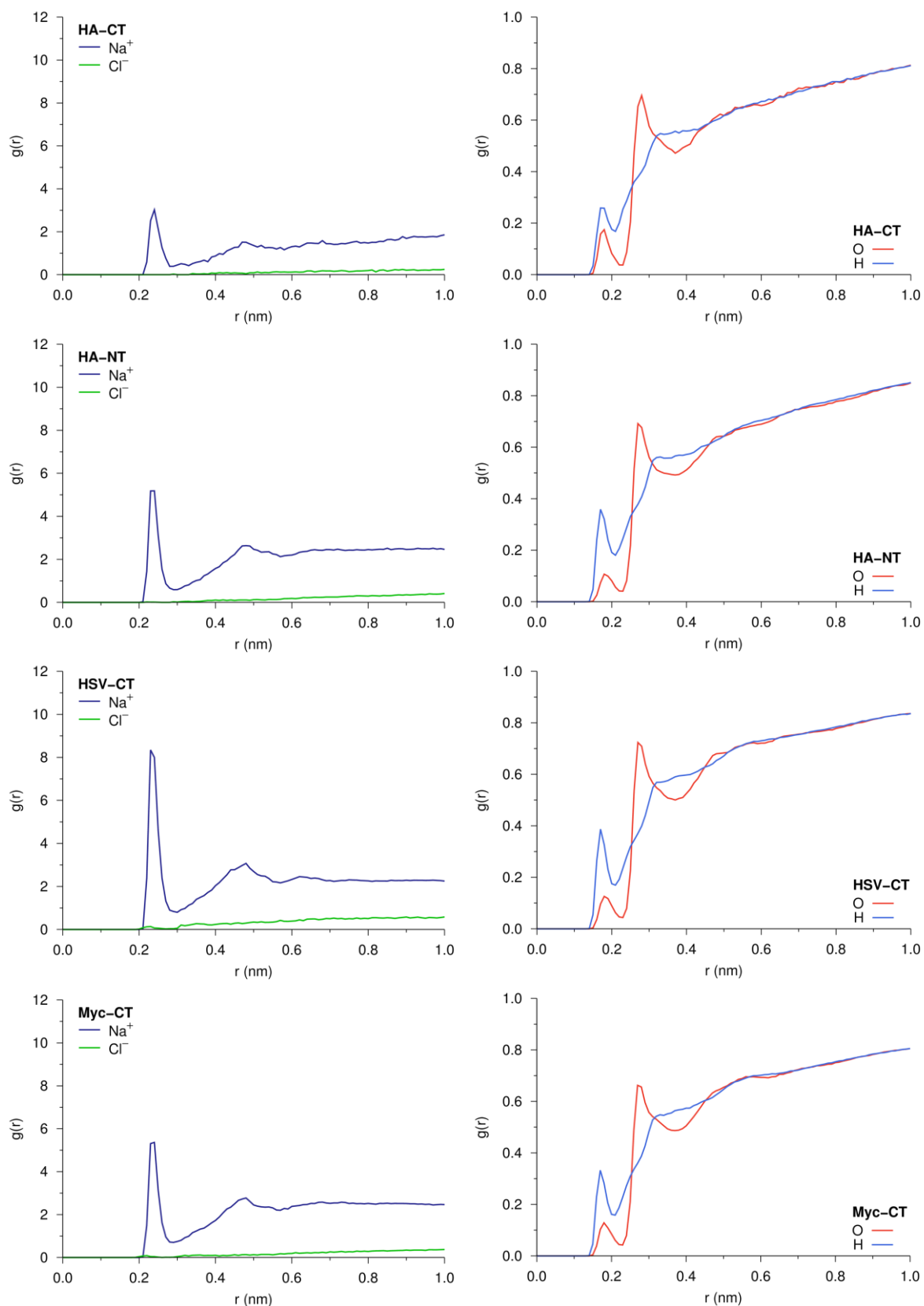


**Figure C.7 | Radial distribution of solvent atoms relative to peptide IDS. (Left)** The radial distribution of Na<sup>+</sup> (blue) and Cl<sup>-</sup> (green) ions relative to the IDS in each peptide monolayer. **(Right)** The RDF of hydrogen (blue) and oxygen (red) atoms of water molecules around the IDS show (at least) two prominent solvation shells.

## Appendix D:

# Supplementary Results (Chapter 5)

Dr Yiyang Lin (Imperial College London) is acknowledged for the experimental synthesis, analysis, and interpretation of results presented in Section D.1.1. Dr Michael Thomas (Imperial College London) and Dr James Douth (ISIS Neutron and Muon Source, U.K.) conducted the work in Section D.1.2. All other results were solely contributed by the author of this thesis, with guidance and recommendations from external parties recognised in the opening outline for Chapter 5.

---

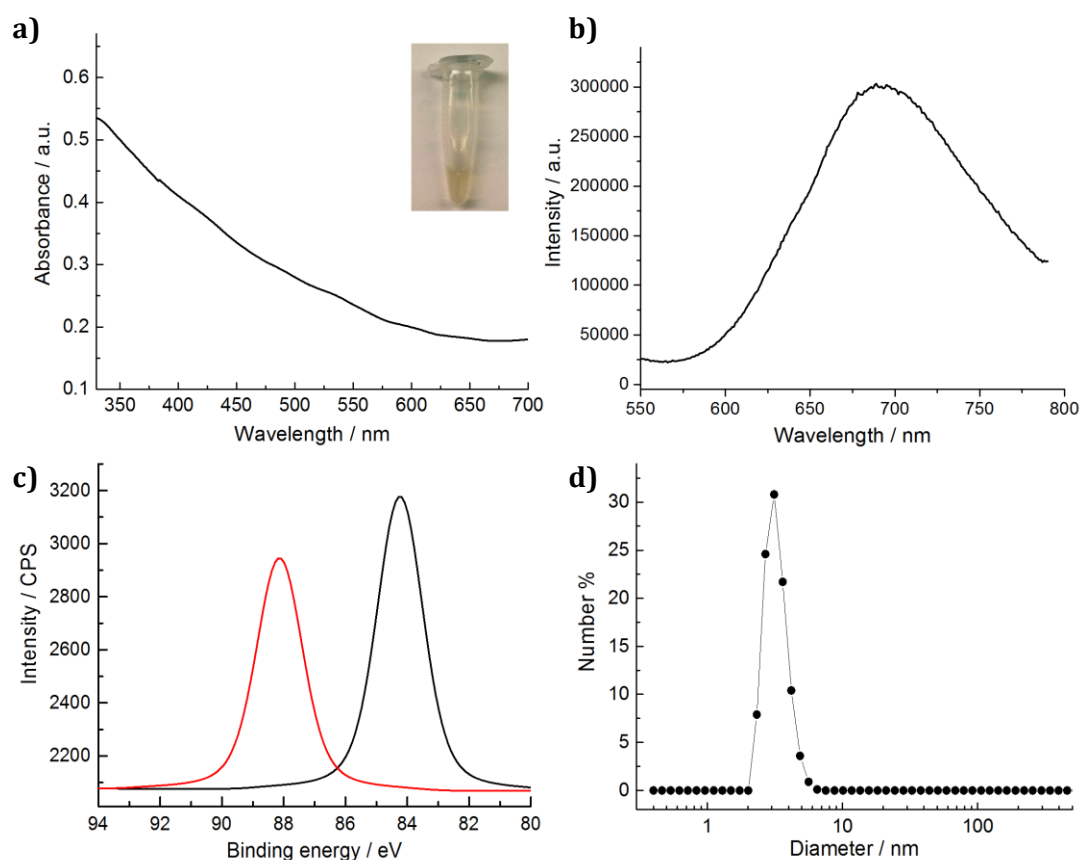
## D.1 Experimental Characterisations for Au<sub>25</sub>(SP)<sub>18</sub>

Figure D.1 shows experimental characterisations performed on an exemplar Au<sub>25</sub>(SP)<sub>18</sub> system (where P = peptide = CHYGDD). The resultant gold nanocluster (AuNC) solution displays a brown appearance (Figure D.1a, inset), which signifies the formation of small metallic NCs.<sup>566</sup> Unlike the UV-Vis absorption spectra of larger Au nanoparticles which display a strong surface plasmon resonance around 520 nm,<sup>567</sup> the as-synthesised AuNCs do not exhibit a strong UV-Vis absorbance peak over the range of 350–700 nm (Figure D.1a). Intense luminescence from the clusters is observable to the naked eye and by exciting with a 400 nm laser, the photoluminescence (PL) spectrum is recorded to display an emission peak located at 680 nm (Figure D.1b), similar to the spectra of peptide-protected Au<sub>25</sub> clusters.<sup>568</sup> X-ray photoelectron spectroscopy (XPS) confirms the binding energy of Au 4f<sub>5/2</sub> and Au 4f<sub>7/2</sub> at 88.1 eV and 84.2 eV, respectively (Figure D.1c). It is noted that the binding energy of Au 4f<sub>7/2</sub> falls between the Au(0) BE (84 eV) of a metallic gold film and the Au(I) BE (86 eV) of gold thiolate, suggesting the coexistence of Au(0) and Au(I) in the clusters as had been previously reported for similar small AuNCs.<sup>569</sup> Dynamic light scattering (DLS) suggests a hydrodynamic diameter (D<sub>h</sub>) of ~3.1 nm (Figure D.1c). Similar characterisations are also obtained for all AuNCs prepared with other peptide sequences (Figure D.2).

Size differences between various Au<sub>25</sub>(SP)<sub>18</sub> nanoclusters are confirmed by small angle X-ray scattering (SAXS), where scattered functions of the clusters are fitted using a generalised global model. This function, as explained by Beaucage,<sup>570</sup> is appropriate for systems with multiple-levels of structurally related features such as polymers that present both a radius of gyration (R<sub>g</sub>) and a polymer persistence length. The R<sub>g</sub> indicates the size of

the system, whilst the power law decay slope can indicate the dimensionality of the structure being probed. Flexibility in conformations of the peptides will act to smear out the features of the scattering function expected from the monodisperse AuNC core. Figure D.3 shows plots of the unified power law function fitted to the scattered intensity data. The AuNC  $R_g$  is found to be larger for Ac-CGGGDD ( $\sim 1.08$  nm) and Ac-CYHGDD ( $\sim 1.18$  nm) versus the uncapped CGGGDD ( $\sim 1.01$  nm), in agreement with molecular dynamics (MD).

### D.1.1 Absorbance, Emission and Light Scattering Properties



**Figure D.1 | Experimental characterisation of an exemplar peptide-protected AuNC (where the coating peptides are CHYGDD).** (a) No specific absorbance peak is observed in the UV-Vis spectrum. Inset shows the formation of a brown solution (in ambient light) indicative of small AuNC synthesis. (b) The photoluminescence emission peak of the AuNCs is found to be located at  $\sim 670$ – $680$  nm. (c) XPS is used to show the binding energy of the Au(4f) band. (d) The hydrodynamic diameter of as-synthesised AuNCs is determined to be  $\sim 3.1$  nm by DLS.

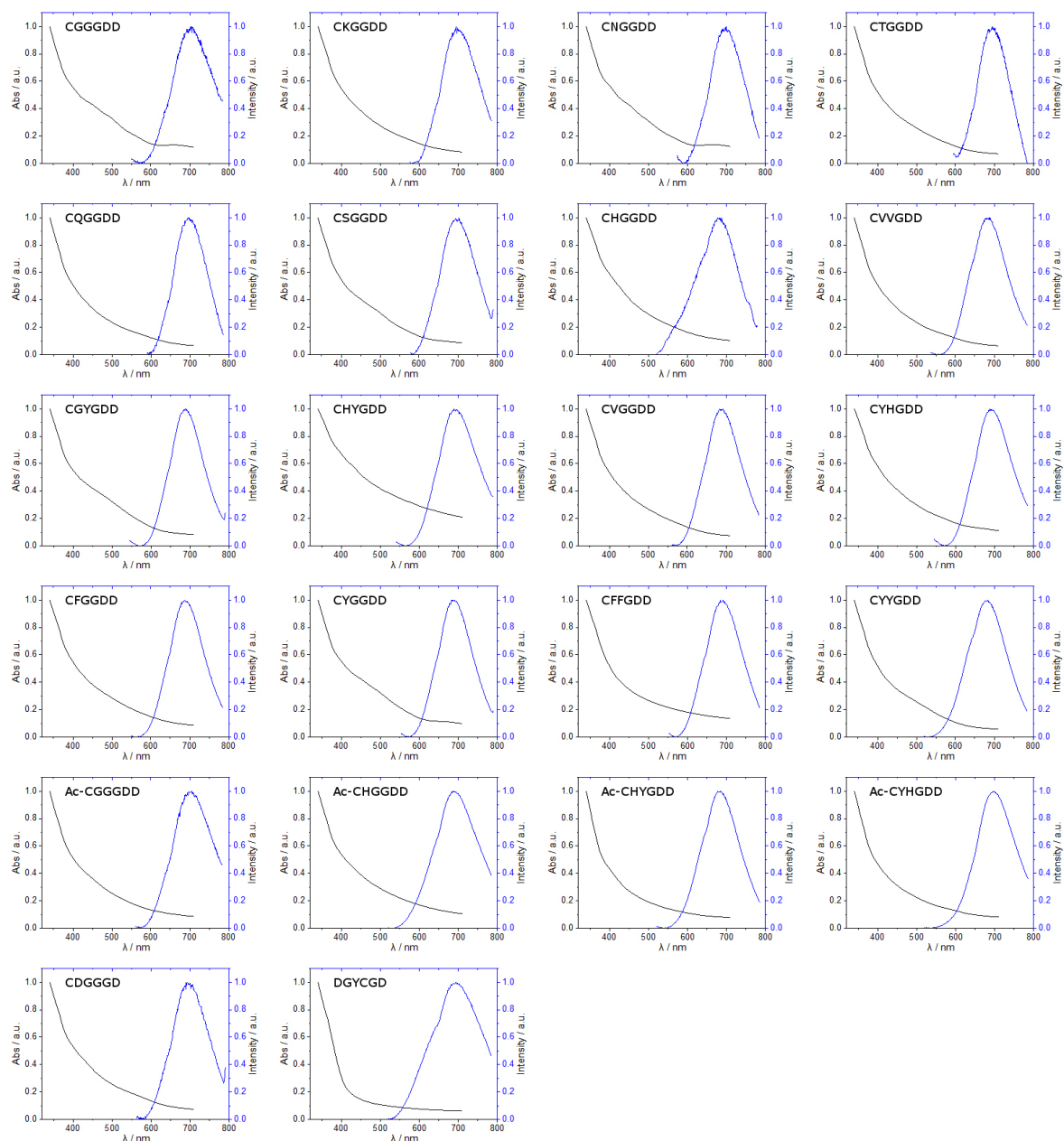


**Figure D.2 | UV-Vis absorbance and photoluminescence spectra of peptide-protected Au clusters.** Both UV-Vis (black) and fluorescence emission (blue,  $E_x = 400$  nm) spectra are normalised, with peak emission occurring between 684 nm – 704 nm. In order of appearance:

CGGGDD (704 nm); CKGGDD (694 nm); CNGGDD (699 nm); CTGGDD (695 nm);  
 CQGGDD (697 nm); CSGGDD (703 nm); CHGGDD (687 nm); CVVGDD (688 nm);  
 CGYGDD (688 nm); CHYGDD (689 nm); CVGGDD (686 nm); CYHGDD (688 nm);  
 CFGGDD (687 nm); CYGGDD (691 nm); CFFGDD (691 nm); CYYGDD (684 nm);  
 Ac-CGGGDD (704 nm); Ac-CHGGDD (689 nm); Ac-CHYGDD (686 nm); Ac-CYHGDD (696 nm);  
 CDGGGD (690 nm); DGYCGD (693 nm).

### D.1.2 Small Angle X-Ray Scattering

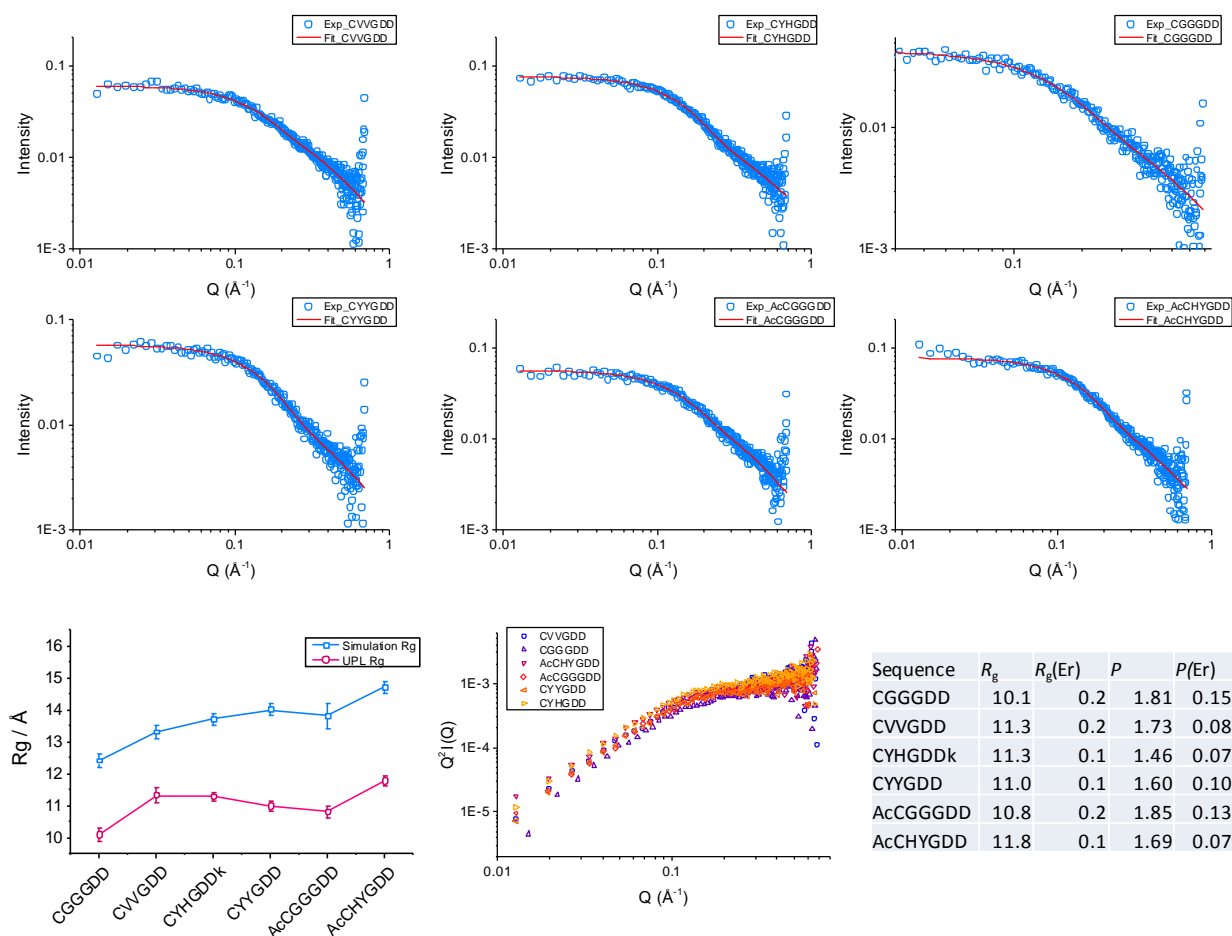


**Figure D.3 | Findings from small angle X-ray scattering.** Plots of scattered X-ray intensity with  $Q$  (blue) as well as unified power law simulation fits (red traces). Plot of the value of  $R_g$  obtained for computational simulations (blue) and from the unified power law fits to the scattering data (pink) as a function of peptide sequence. Kratky plots of scattered intensity highlighting the plateau formation of these systems which indicates flexible, extended peptide configurations.

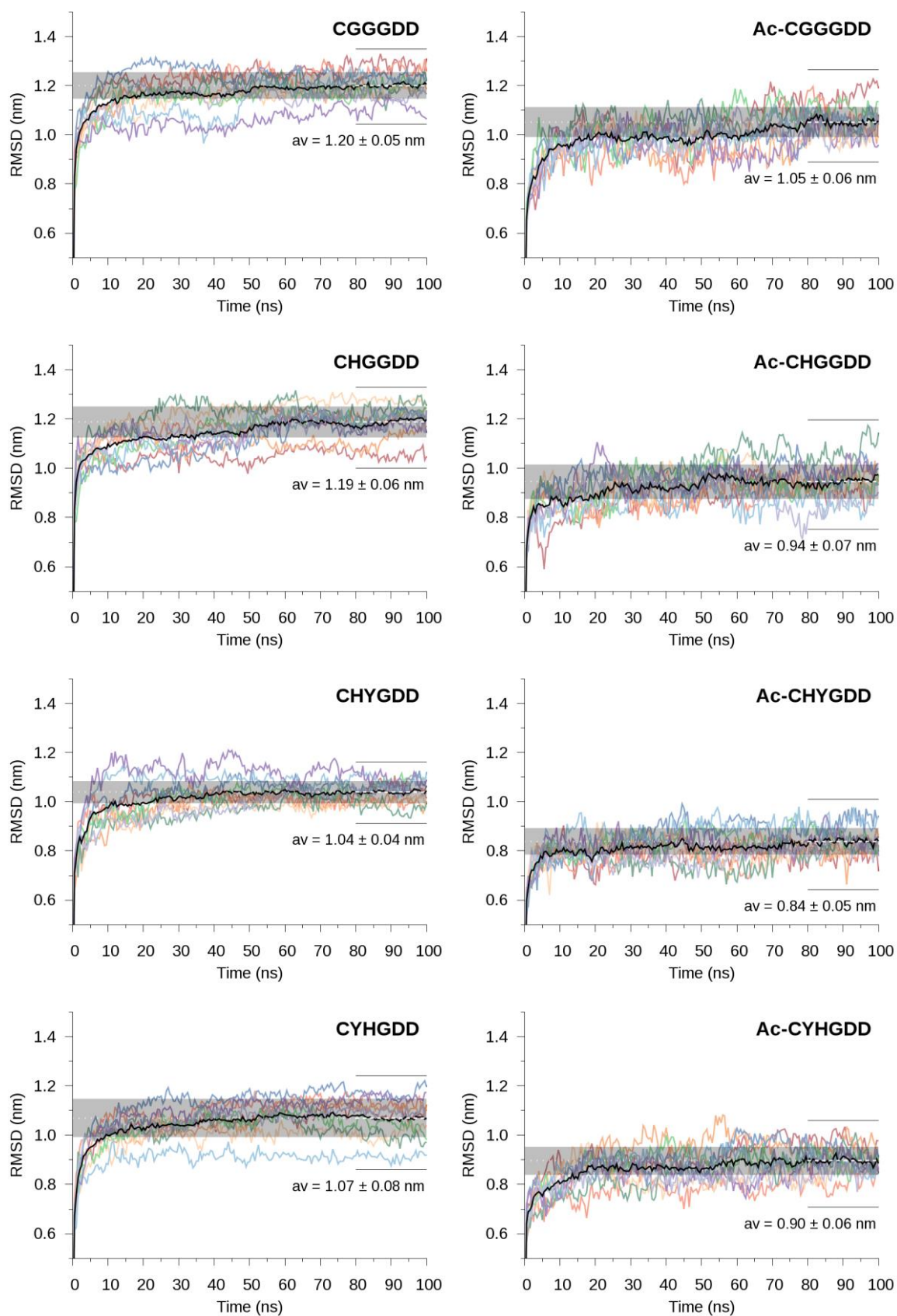
### D.2 Equilibration of MD Models

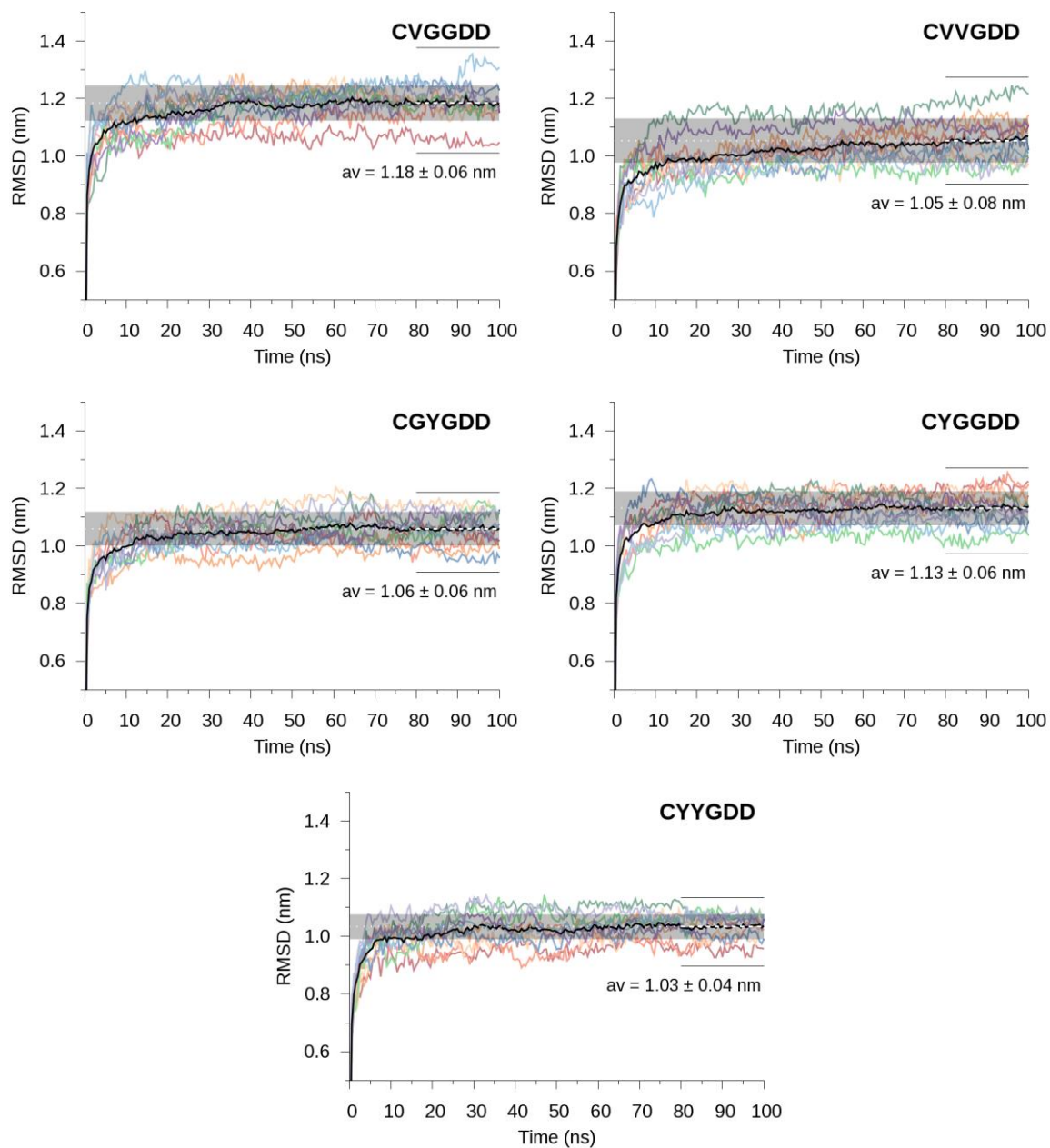
In the initial configurations ( $R_g = 1.5 \text{ nm} - 1.6 \text{ nm}$ ), all peptides are fully extended and uniformly distributed. During the first  $\sim 10 \text{ ns}$  of dynamics, the overall  $R_g$  of the AuNCs quickly decreases while the RMSD concurrently increases (Figures D.4 and D.5). These changes result from initial structural rearrangements and symmetry breaking in the peptide layers. Over the remaining 80 ns, both the RMSD and  $R_g$  of the AuNCs asymptote with minor fluctuations indicative of the small configurational diversity and disorder the peptide layers experience due to their dense packing and short chain lengths (6 amino acids). To allow ample time for the thermodynamic and structural equilibration of the AuNCs, only the final 20 ns of each simulation, unless otherwise stated, has been utilised for further analysis.



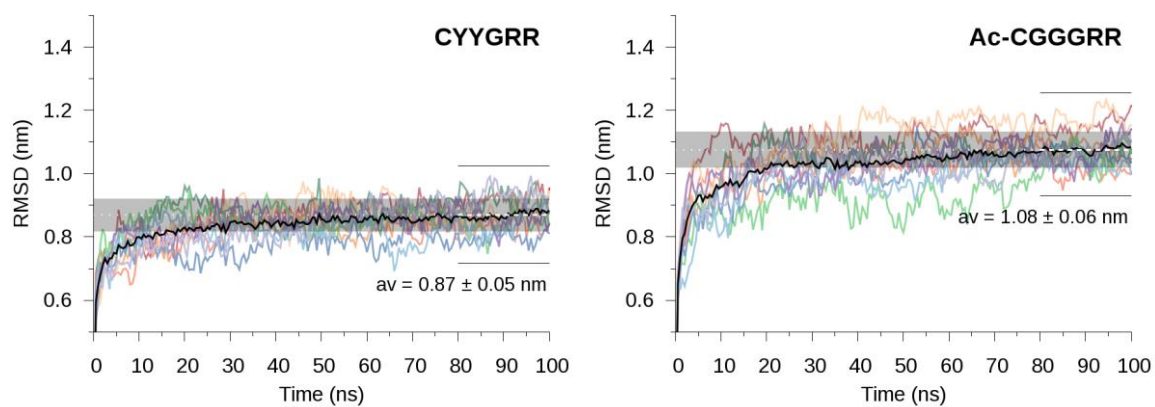
**D.2.1 Root-Mean-Square Deviations (RMSD)**

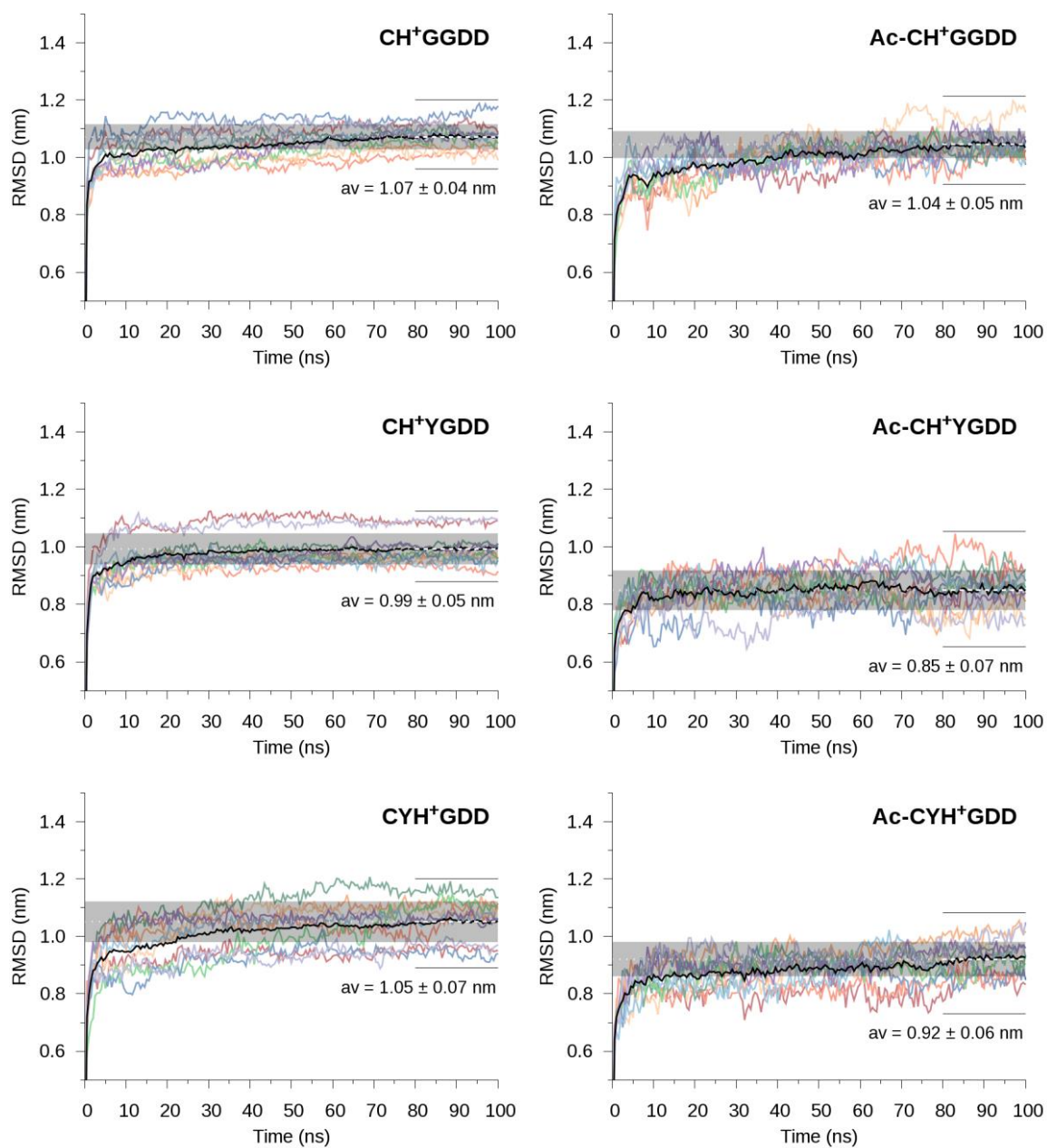
*Varying Sequence: (Ac-)CXXGDD, where X = G, V, H, or Y*





Arginine C-terminus: CYYGRR and Ac-CGGGRR

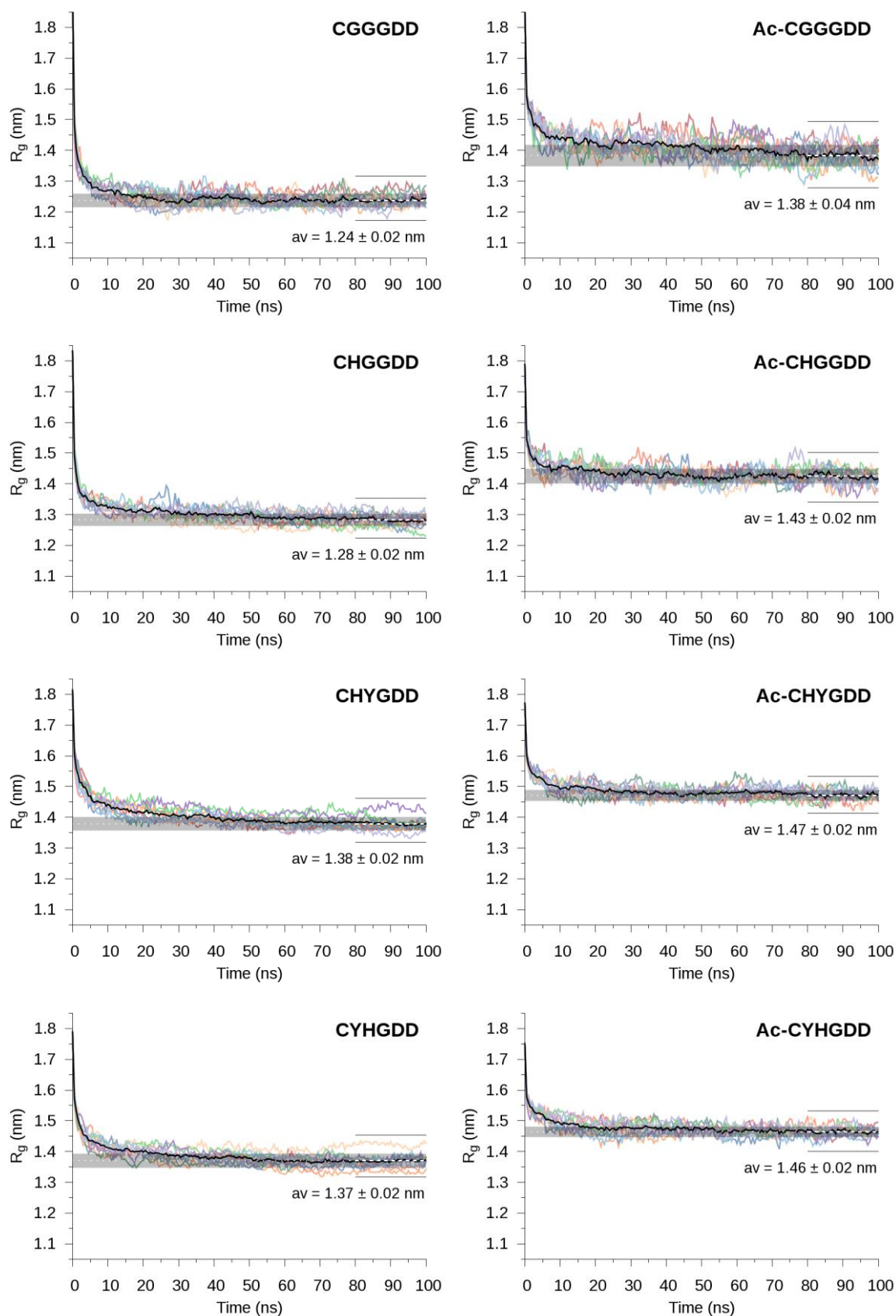


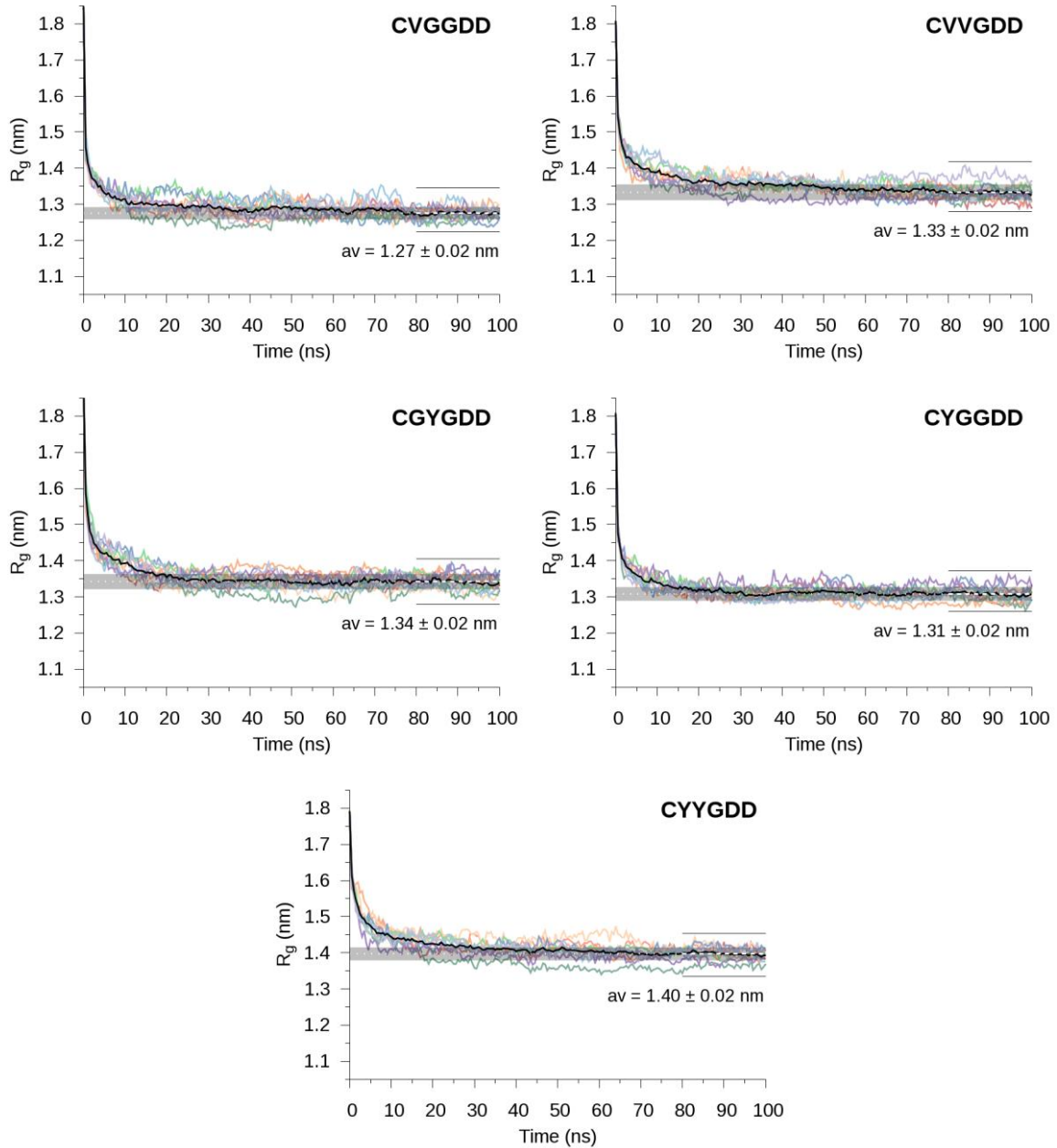
*Protonated Histidine: (Ac-)CXXGDD, where one X = G, or Y and the other X = H<sup>+</sup>*

**Figure D.4 | Time evolved average root-mean-square deviations for each Au<sub>25</sub>(SP)<sub>18</sub>.** RMSD is performed on backbone atoms of the peptide-ligands.

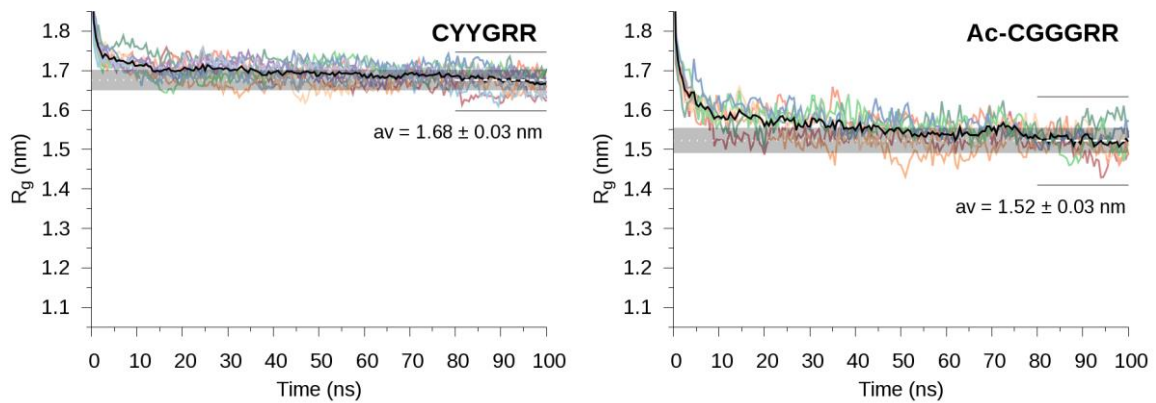
**D.2.2 Radius of Gyration ( $R_g$ )**

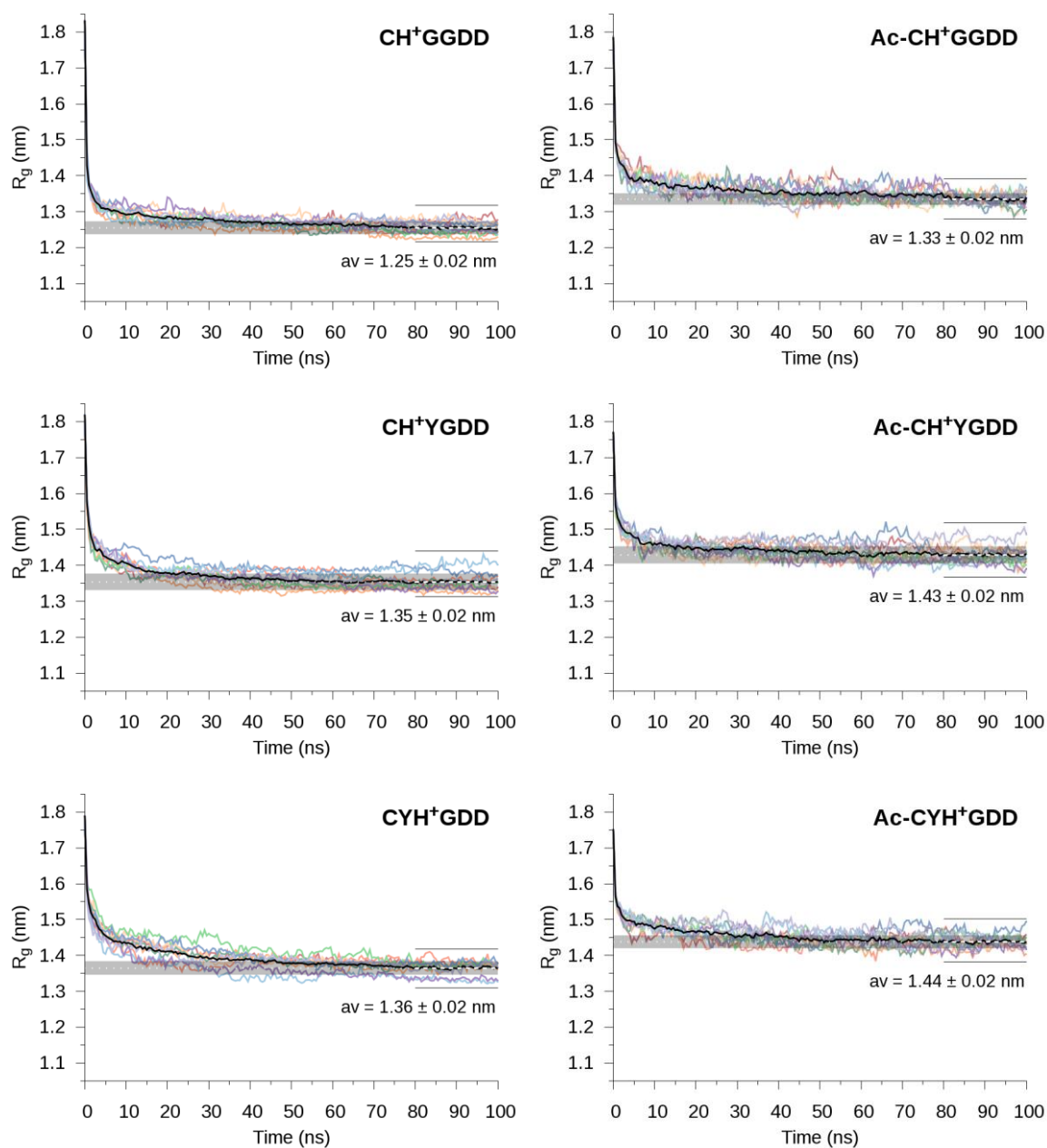
*Varying Sequence: (Ac-)CXXGDD, where X = G, V, H, or Y*





Arginine C-terminus: CYYGRR and Ac-CGGGRR

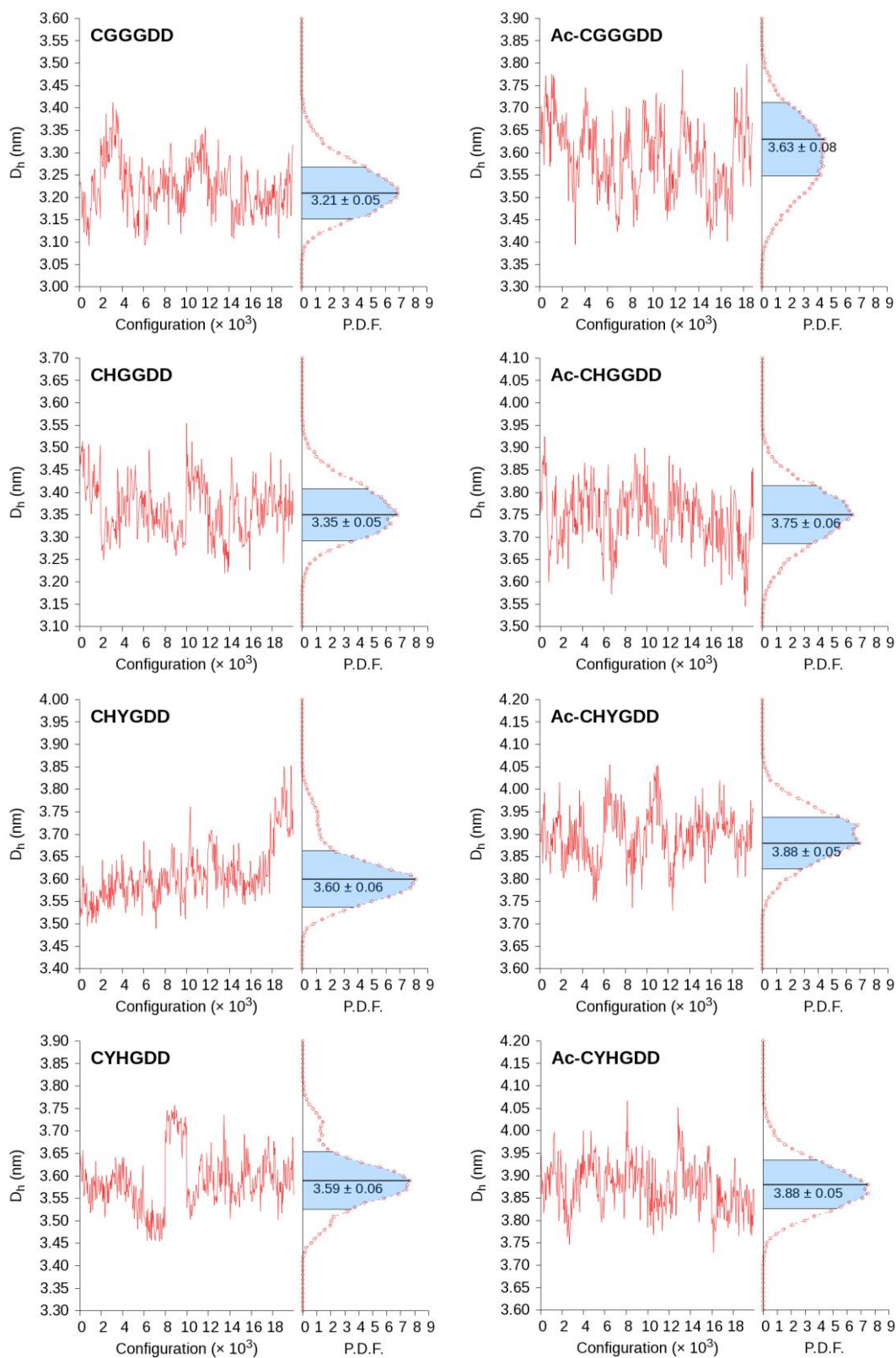


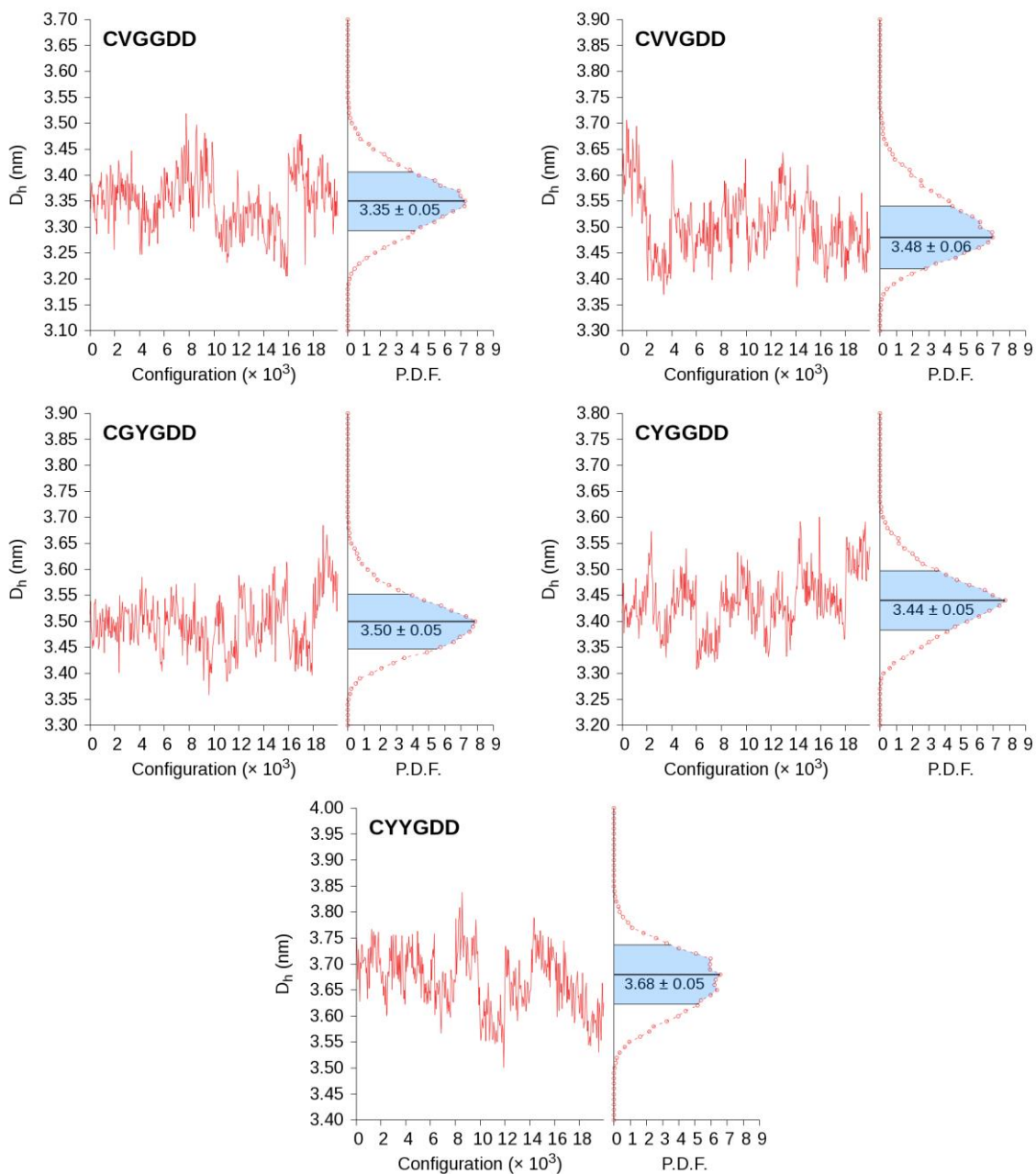
*Protonated Histidine: (Ac-)CXXGDD, where one X = G, or Y and the other X = H<sup>+</sup>***Figure D.5 | Time-evolution of the radius of gyration for each Au<sub>25</sub>(SP)<sub>18</sub>.**

## D.3 Overall Au<sub>25</sub>(SP)<sub>18</sub> Structure and Peptide Flexibility

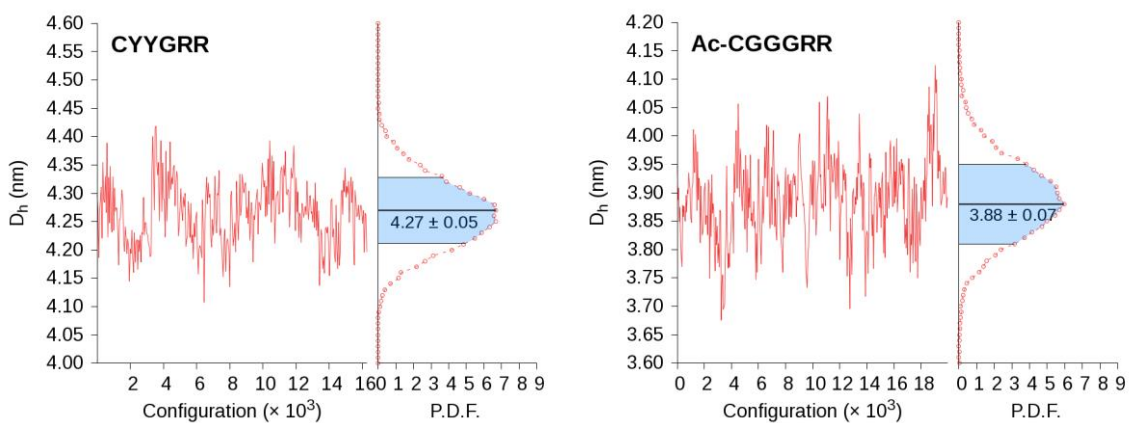
### D.3.1 Hydrodynamic Diameter ( $D_h$ )

*Varying Sequence: (Ac-)CXXGDD, where X = G, V, H, or Y*

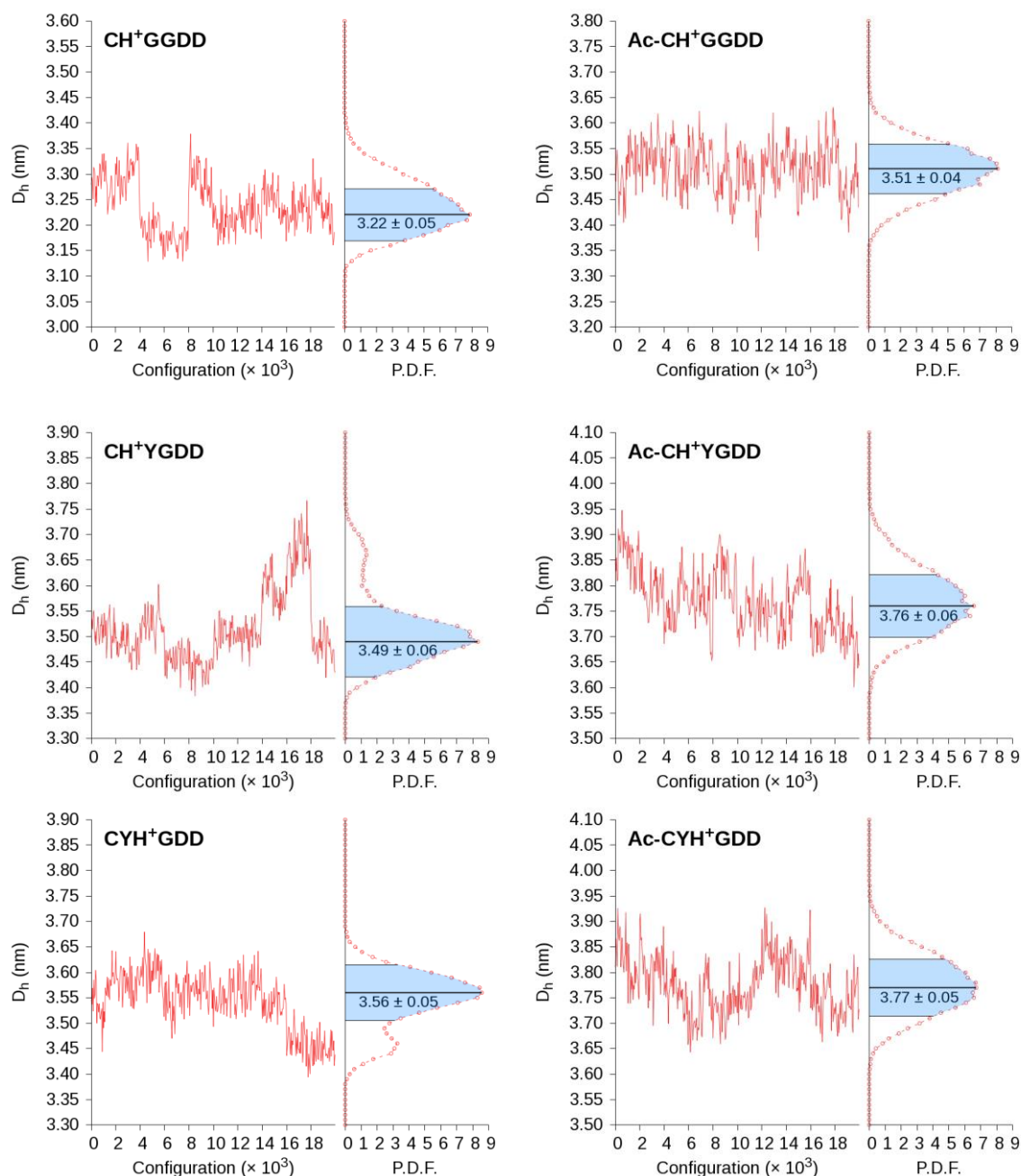




Arginine C-terminus: CYYGRR and Ac-CGGGRR

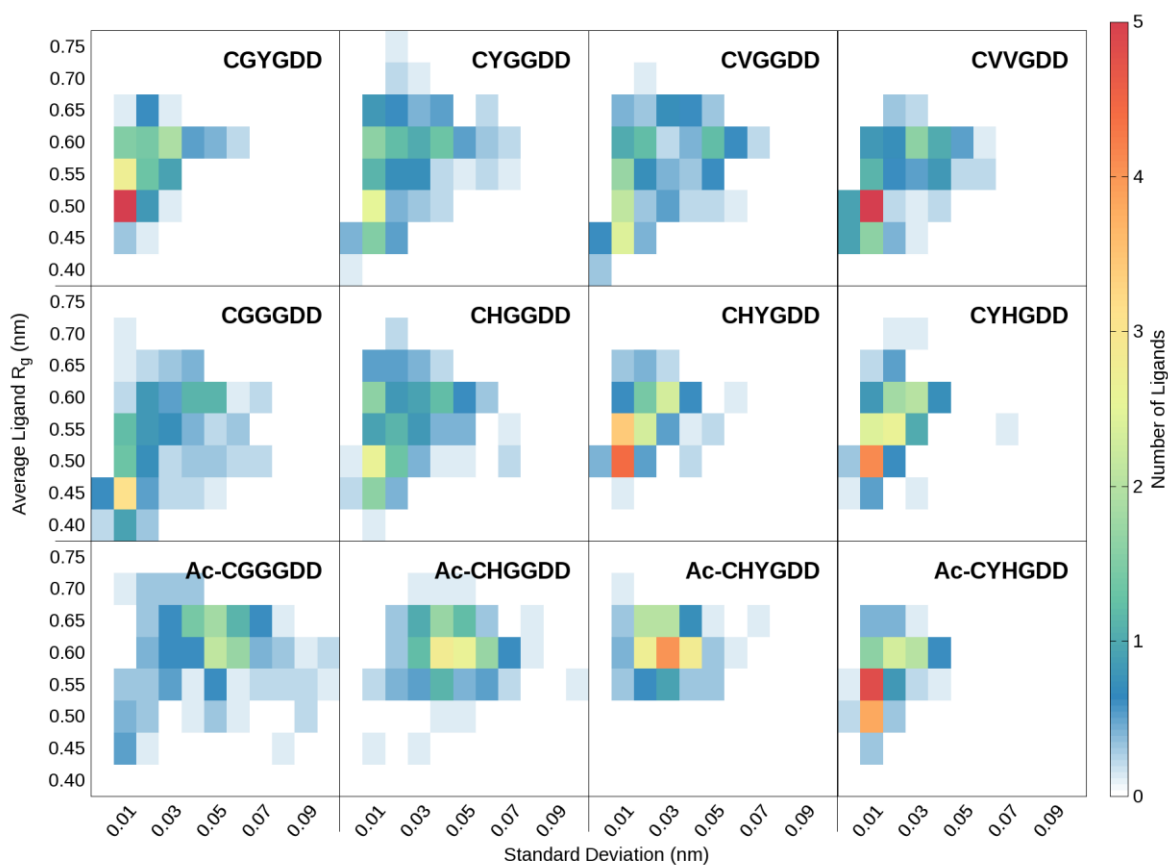




Protonated Histidine: (Ac-)CXXGDD, where one X = G, or Y and the other X = H<sup>+</sup>

**Figure D.6 | Hydrodynamic diameter calculated from the equilibrated trajectories.** (Left panels) Hydrodynamic diameter ( $D_h$ ) computed for  $2 \times 10^4$  configurations using the ZENO<sup>471</sup> path-integration program. It should be noted that configurations within consecutive blocks of  $2 \times 10^3$  are correlated since they are taken from independent equilibrated trajectories and only every 50<sup>th</sup> data point is plotted for clarity. (Right panels) Probability density function (P.D.F.) of the ensemble shown with the modal  $D_h$  and one standard deviation (shaded region).

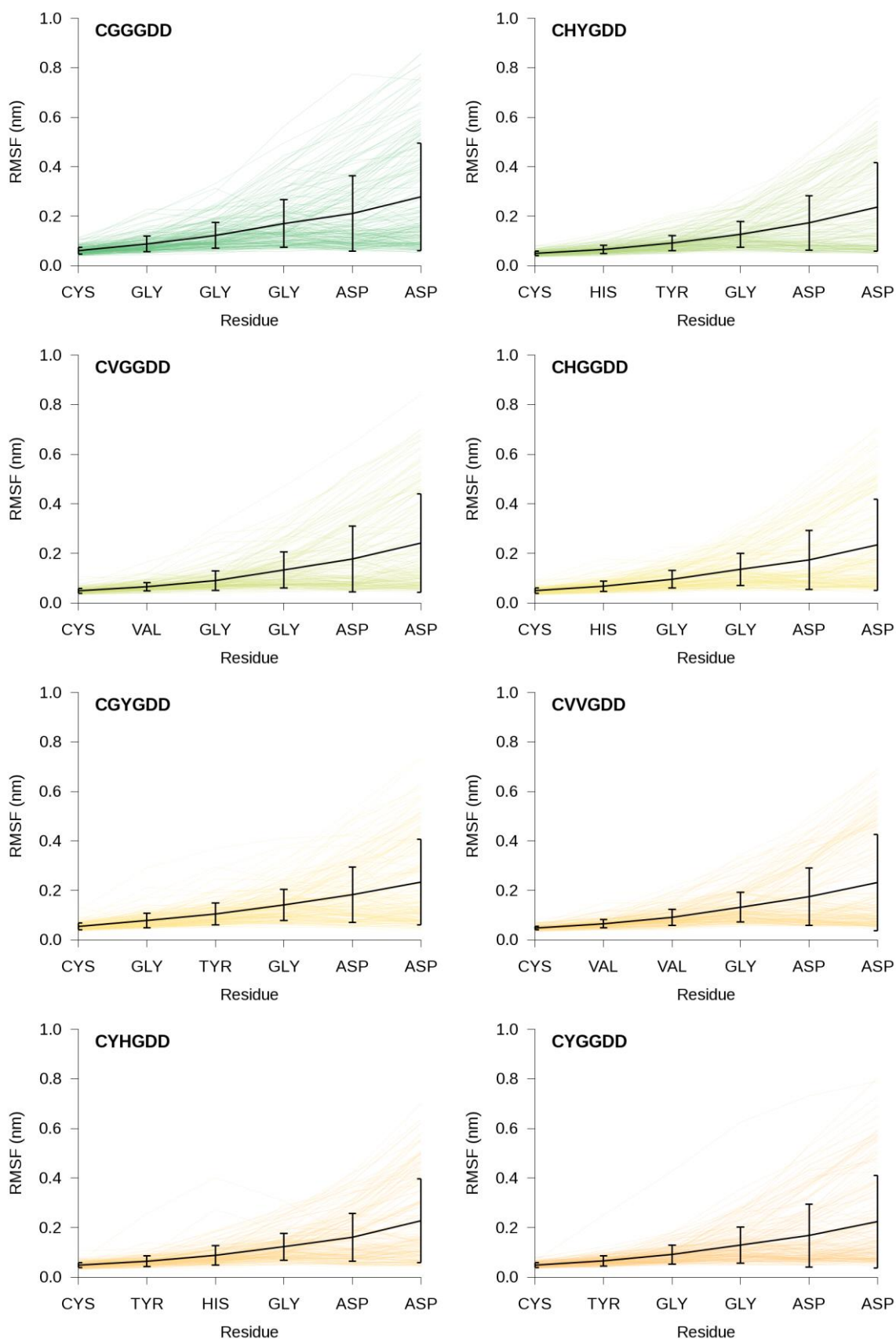
### D.3.2 Ligand Radius of Gyration ( $R_g$ )

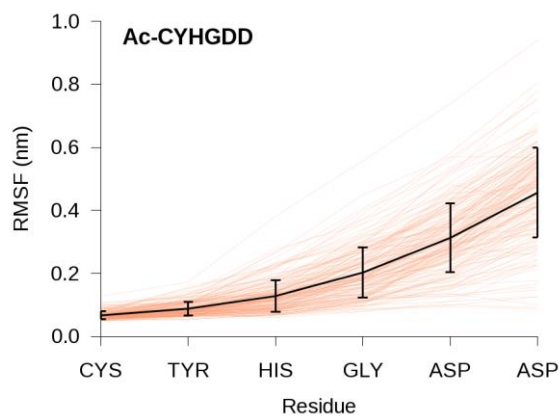
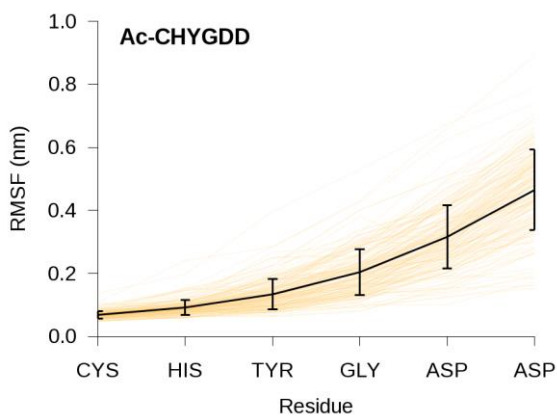
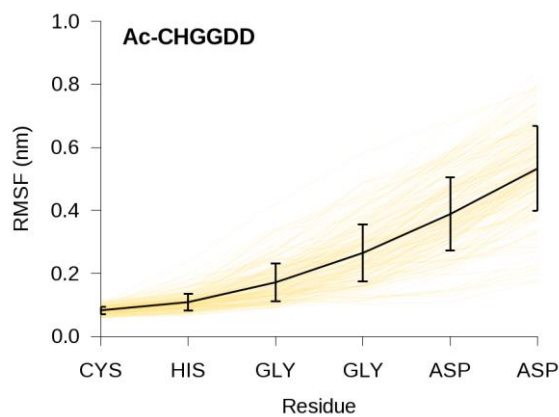
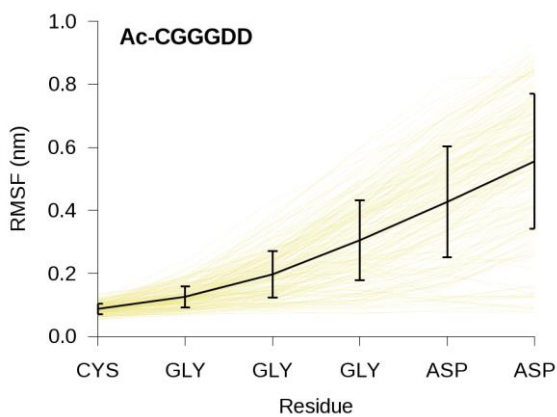
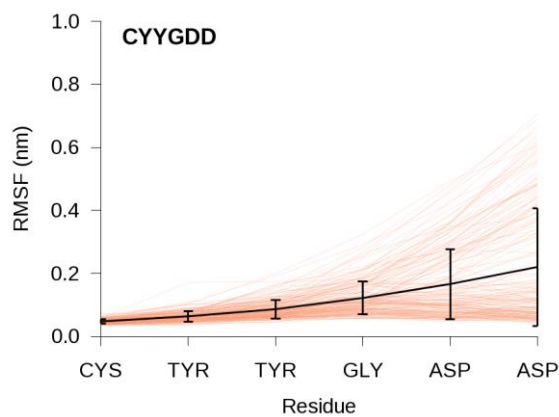


**Figure D.7 | Density map comparing average ligand radius of gyration against standard deviation.** Note that fully extended peptides have a  $R_g$  of 0.67–0.86 nm and that a large standard deviation implies that peptides fluctuate between compact and extended conformations.

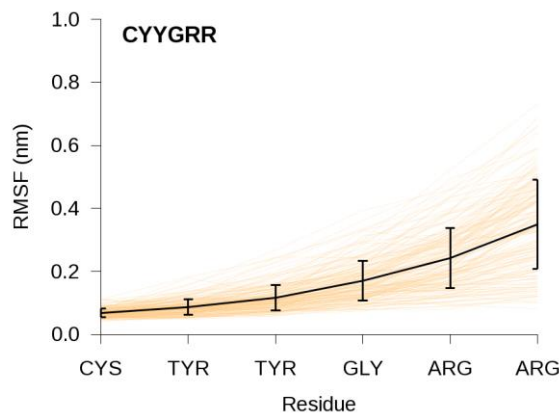
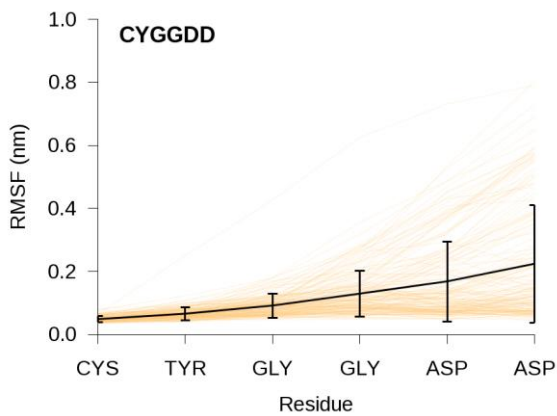
### D.3.3 Atomic Root-Mean-Square Fluctuations (RMSF)

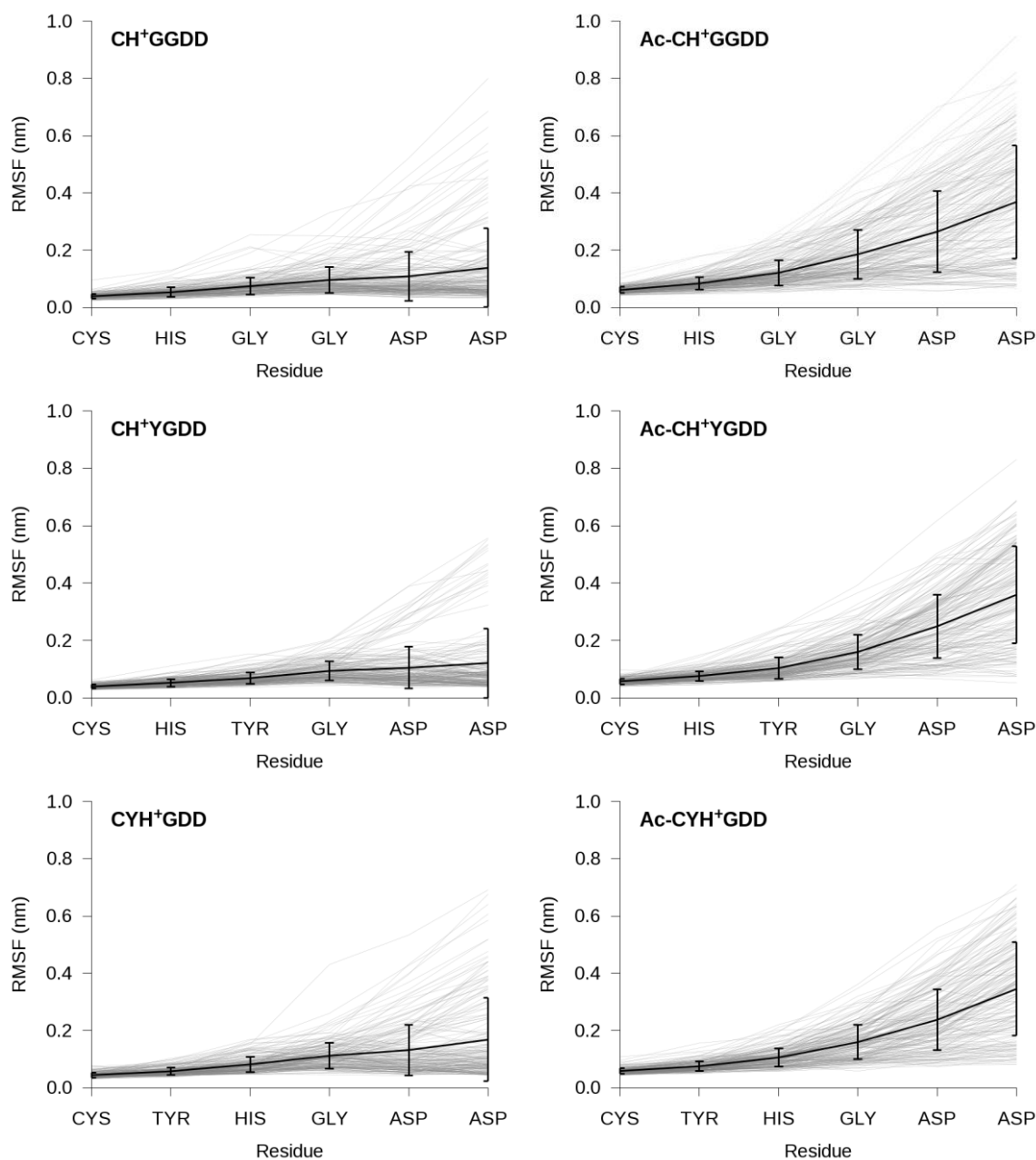
*Varying Sequence: (Ac-)CXXGDD, where X = G, V, H, or Y*





Arginine C-terminus: CYYGRR and Ac-CGGGRR



*Protonated Histidine: (Ac-)CXXGGDD, where one X = G, or Y and the other X = H<sup>+</sup>*

**Figure D.8 | Average C $\alpha$  root-mean-square fluctuations for each residue.** The black line is the ensemble averaged RMSF with standard deviation error bars, whereas coloured lines are the RMSFs for single ligands (18 ligands per system  $\times$  10 simulations) with colours based on Table 4.2. Even though protonated histidine plots are expected to have similar PL as their neutral counterparts, they are coloured grey in the plots because the PL cannot be directly compared from the empirical results.

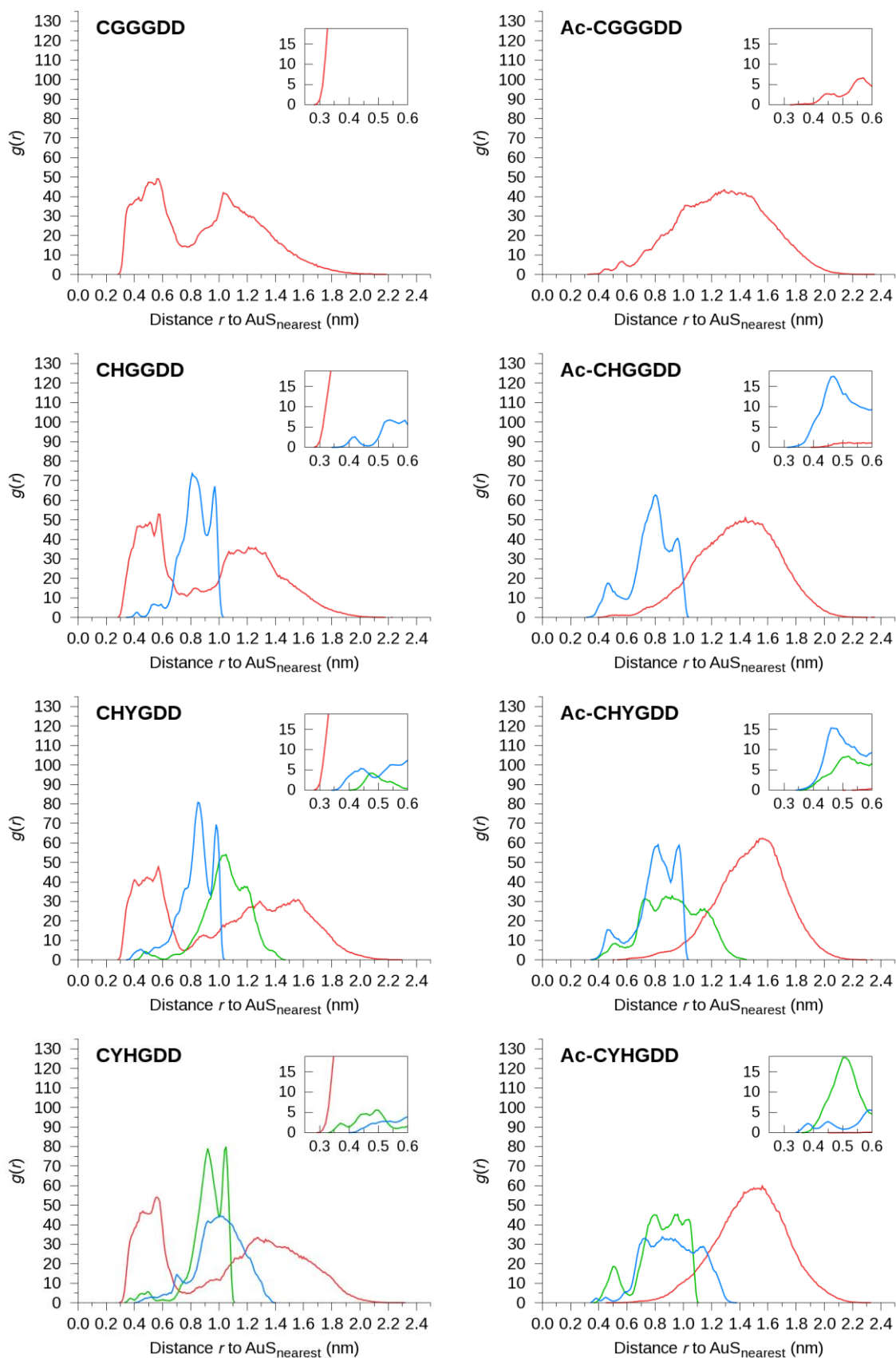
## D.4 Location of Specific Residues and Peptide Configurational Entropy

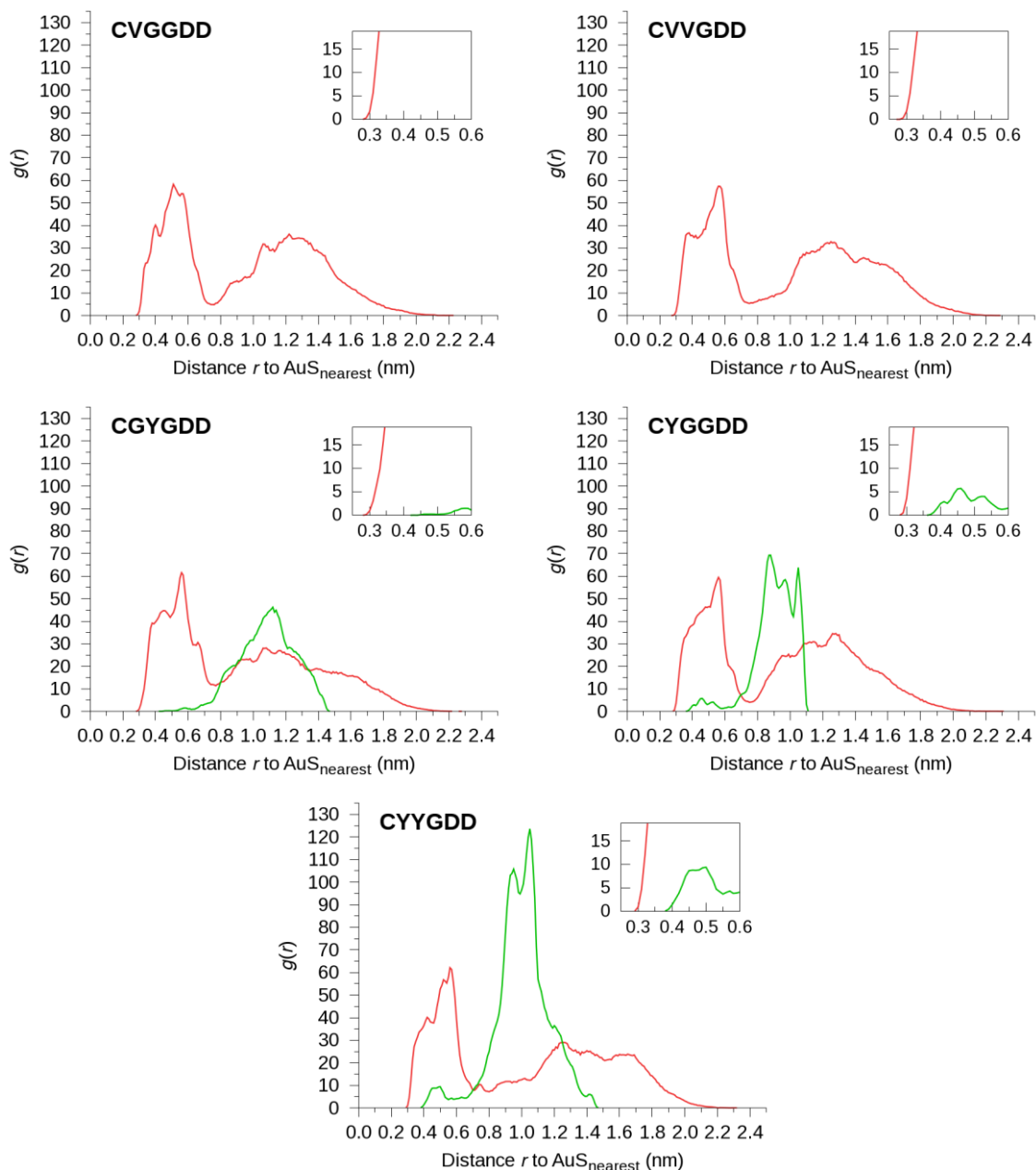
### D.4.1 Residue Minimum Distances to the Gold Core

**Table D.1 | Number of residues within 0.5 nm to any Au<sub>25</sub>S<sub>18</sub> atom.\***

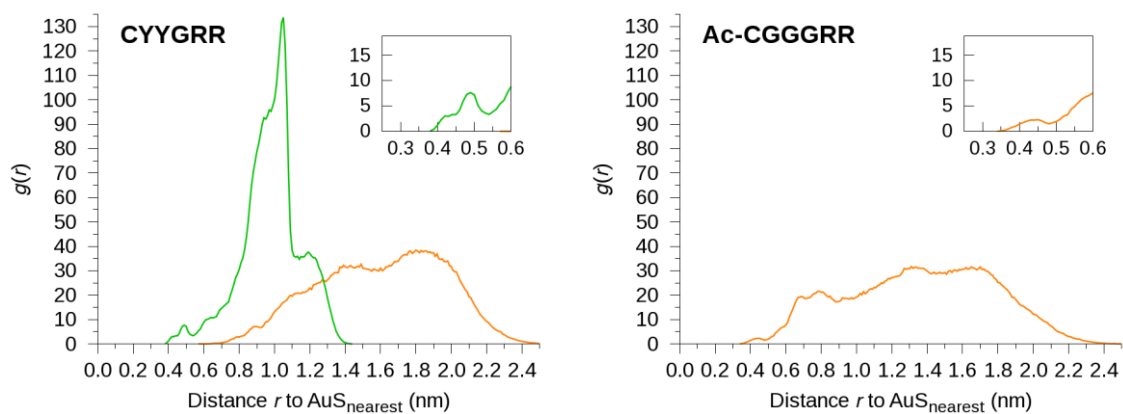
System	ASP	TYR	HIS
CGGGDD	6.74 (0.35 nm)	-	-
CVGGDD	6.65 (0.36 nm)	-	-
CVVGDD	6.26 (0.36 nm)	-	-
CHGGDD	6.85 (0.36 nm)	-	0.15 (0.65 nm)
CHYGDD	6.58 (0.36 nm)	0.21 (0.80 nm)	0.49 (0.59 nm)
CYHGDD	6.31 (0.37 nm)	0.50 (0.72 nm)	0.12 (0.70 nm)
CGYGDD	6.52 (0.37 nm)	0.01 (0.81 nm)	-
CYGGDD	7.14 (0.35 nm)	0.44 (0.70 nm)	-
CYYGDD	6.57 (0.36 nm)	0.71 (0.55 nm)	-
Ac-CGGGDD	0.22 (0.66 nm)	-	-
Ac-CHGGDD	0.05 (0.83 nm)	-	1.44 (0.47 nm)
Ac-CHYGDD	0.00 (0.97 nm)	0.44 (0.58 nm)	1.08 (0.50 nm)
Ac-CYHGDD	0.00 (0.98 nm)	0.91 (0.51 nm)	0.26 (0.65 nm)
CH+GGDD	7.96 (0.37 nm)	-	0.00 (0.71 nm)
CH+YGDD	7.87 (0.36 nm)	0.12 (0.88 nm)	0.00 (0.76 nm)
CYH+GDD	7.04 (0.36 nm)	0.68 (0.56 nm)	0.00 (0.86 nm)
Ac-CH+GGDD	0.19 (0.64 nm)	-	0.24 (0.62 nm)
Ac-CH+YGDD	0.08 (0.72 nm)	0.47 (0.56 nm)	0.10 (0.66 nm)
Ac-CYH+GDD	0.00 (0.79 nm)	1.18 (0.49 nm)	0.00 (0.71 nm)
System	ARG	TYR	-
CYYGRR	0.00 (0.94 nm)	0.45 (0.61 nm)	-
Ac-CGGGRR	0.23 (0.63 nm)	-	-

\*Values in brackets denote the nearest integer residues (ASP, TYR, HIS, and ARG) residues within 0.5 nm to Au<sub>25</sub>S<sub>18</sub>.

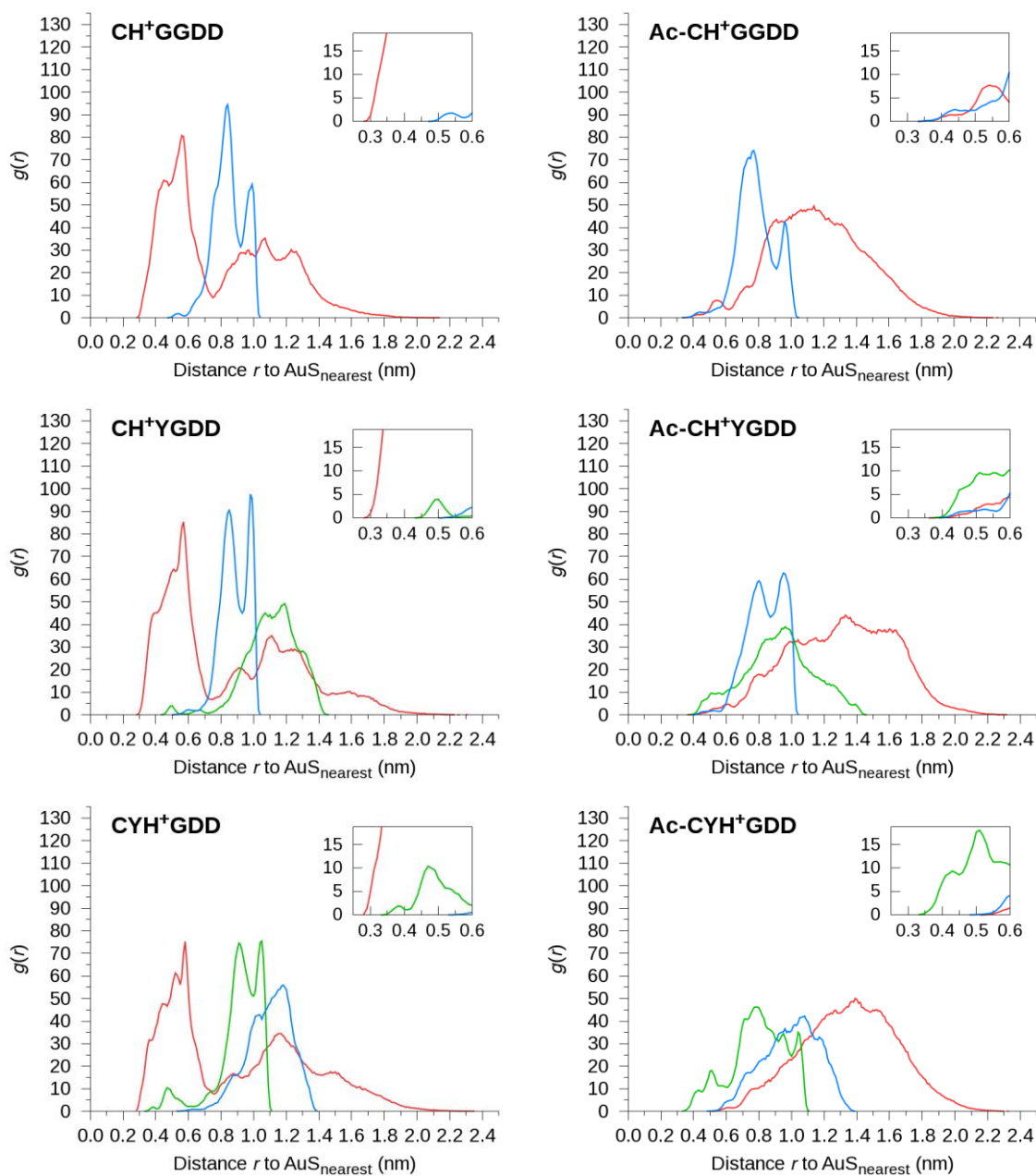
Varying Sequence: (Ac-)CXXGDD, where X = G, V, H, or Y



Arginine C-terminus: CYYGRR and Ac-CGGGRR



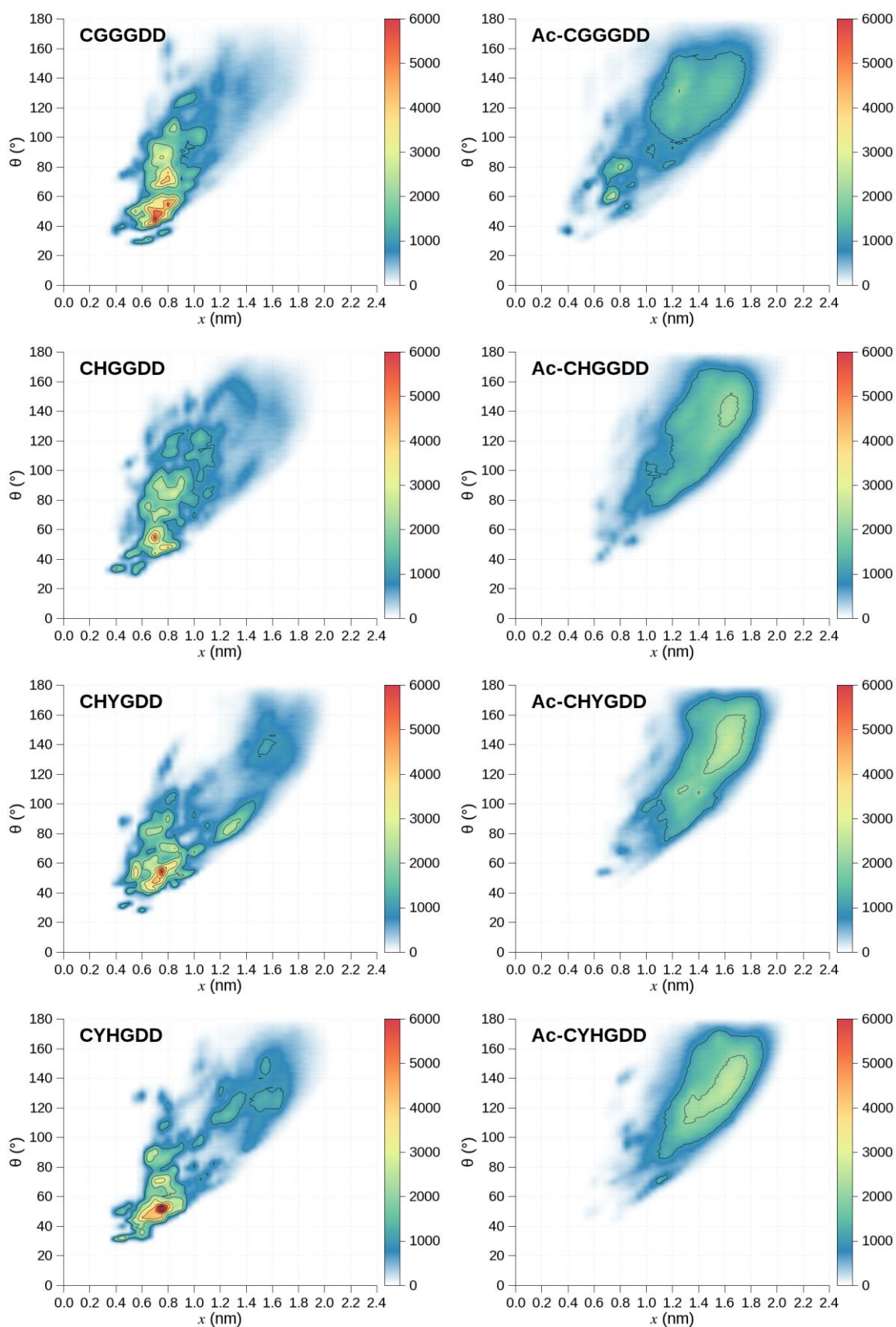


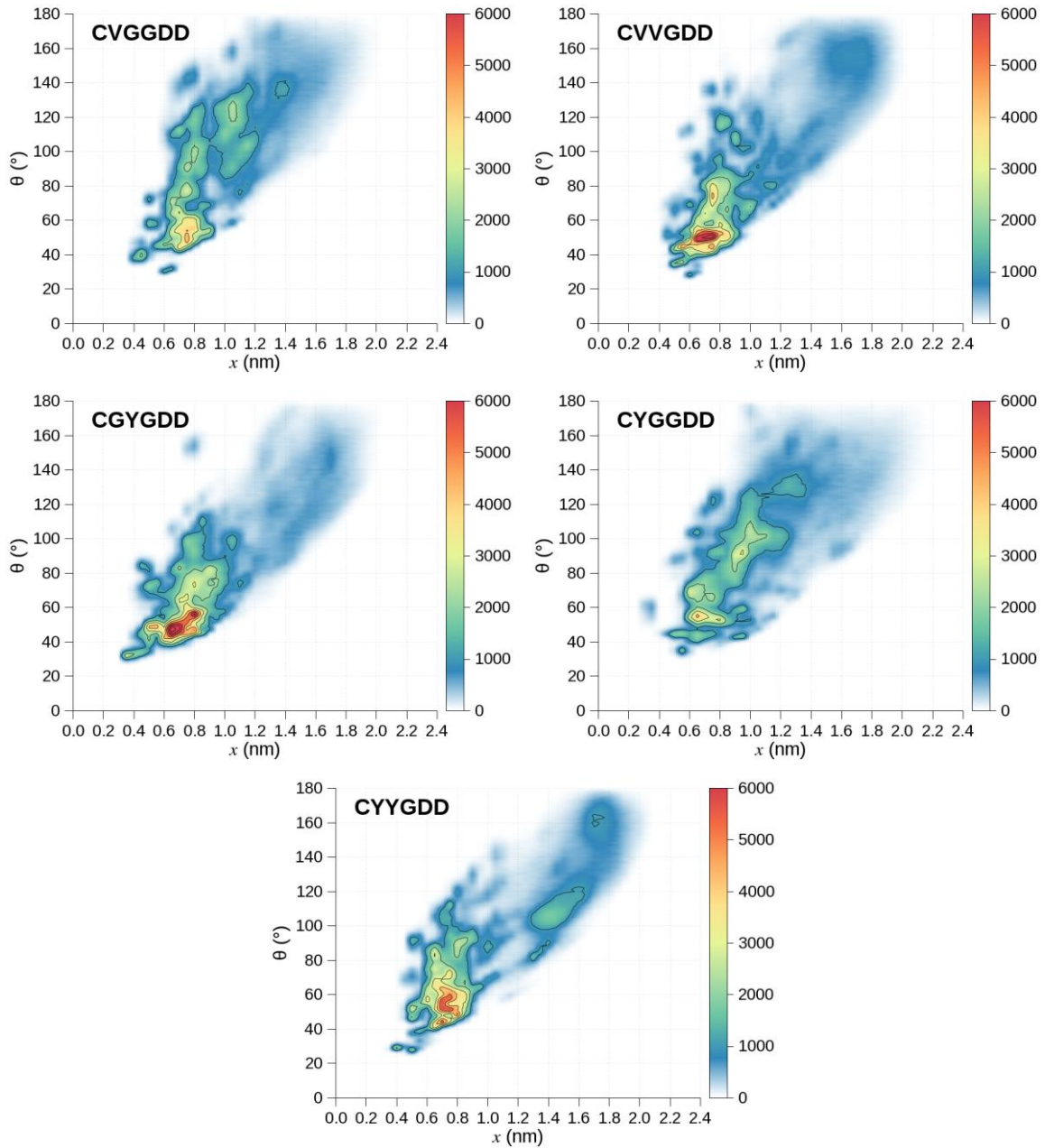
Protonated Histidine: (Ac-)CXXGDD, where one X = G, or Y and the other X = H<sup>+</sup>

**Figure D.9 | Average minimum distance distributions between residues and Au<sub>25</sub>S<sub>18</sub>.** Pairwise distribution functions,  $g(r)$ , for each sequence showing the minimum distances from ASP (red), TYR (green), HIS (blue), and ARG (orange) residues to the closest Au<sub>25</sub>S<sub>18</sub> atom. The insets show enlarged regions to better illustrate the probability of residues being within close proximity to the gold core.

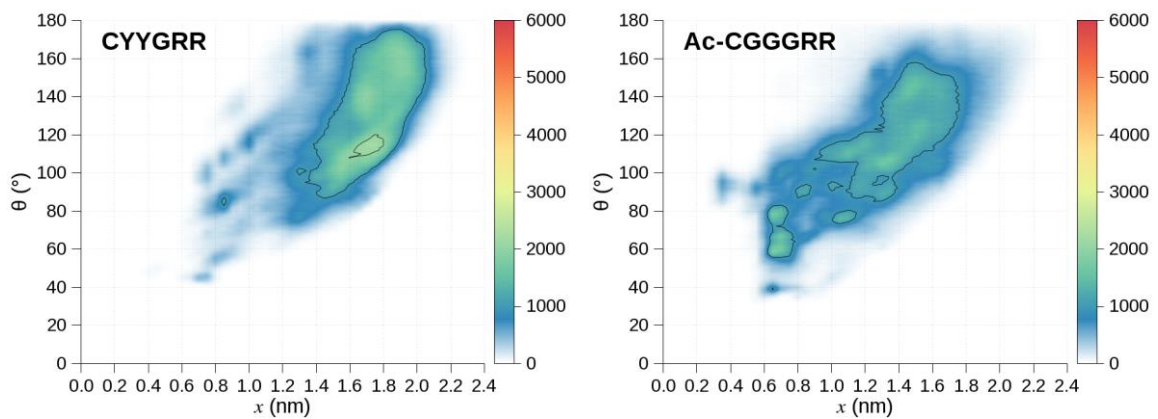
**D.4.2 Peptide Backbone Angle vs. C-terminal-Au<sub>25</sub>S<sub>18</sub> Distances**

*Varying Sequence: (Ac-)CXXGDD, where X = G, V, H, or Y*





Arginine C-terminus: CYYGRR and Ac-CGGGRR



*Protonated Histidine: (Ac-)CXXGGDD, where one X = G, or Y and the other X = H<sup>+</sup>*

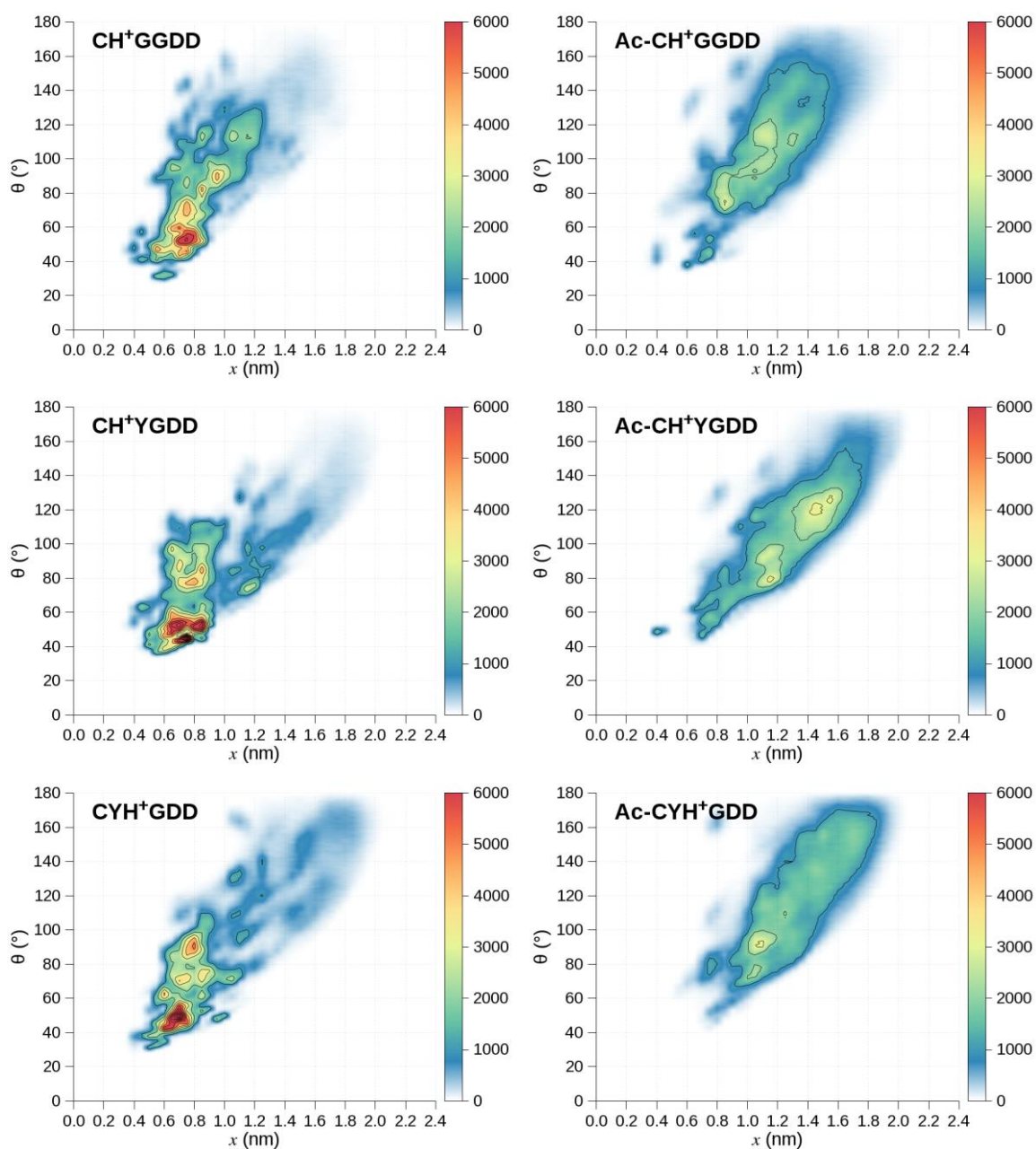
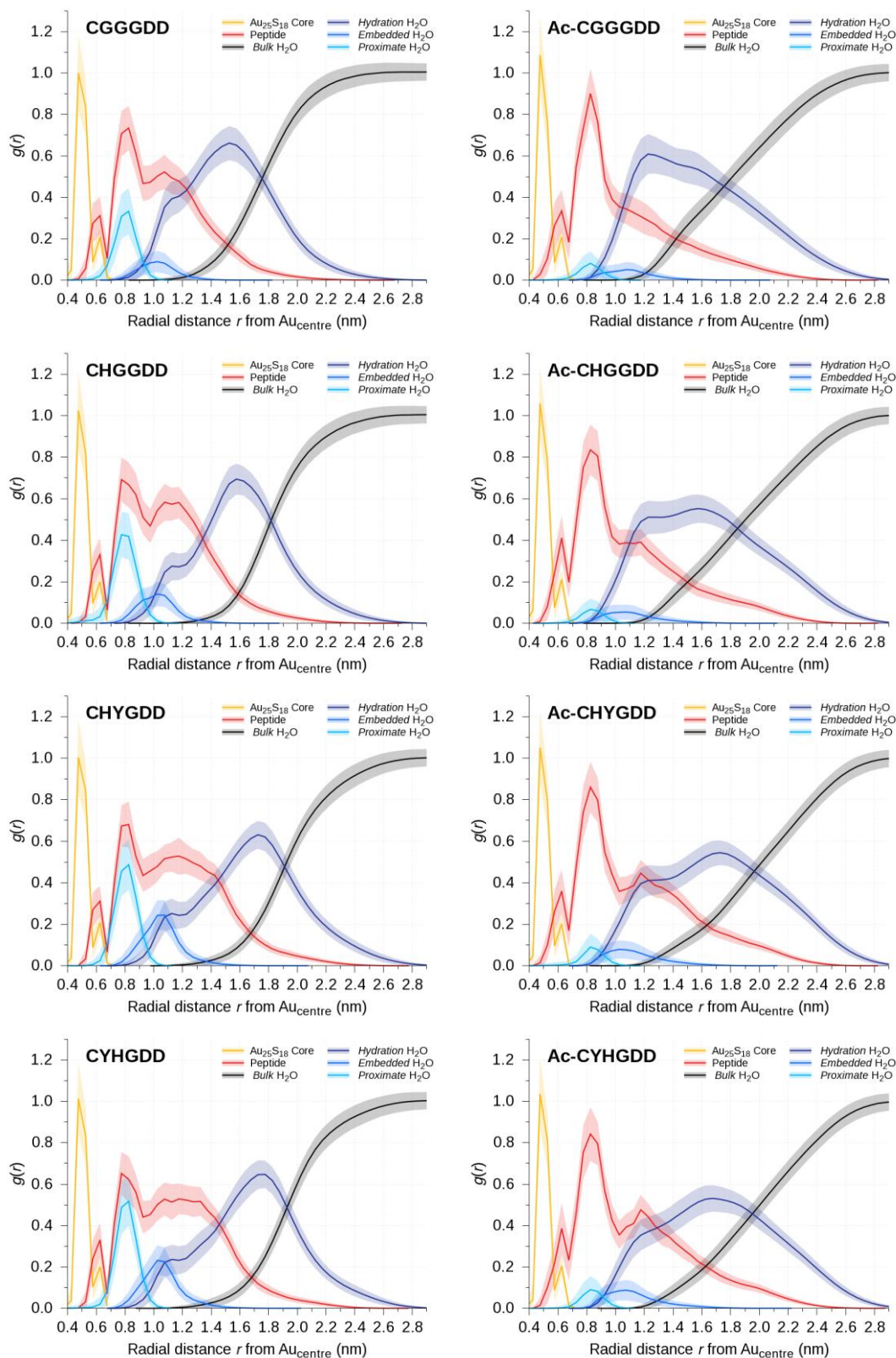


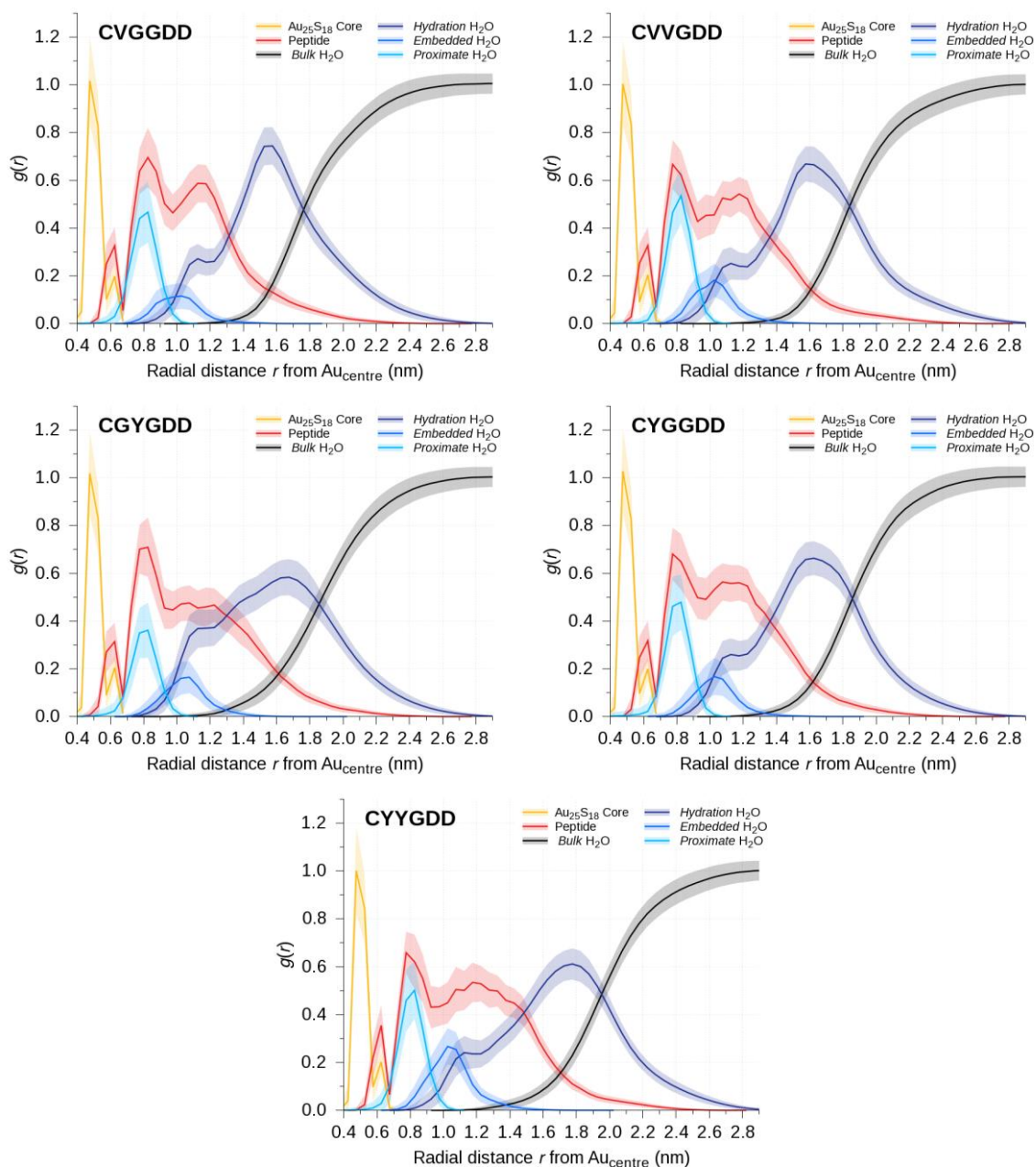
**Figure D.10 | Density maps of peptide backbone angle as a function of C-terminal to  $\text{AuS}_{\text{nearest}}$  distance.** Angle  $\theta$  is measured between backbone alpha carbon atoms 1, 3 and 6 ( $\text{C}\alpha_1\text{-C}\alpha_3\text{-C}\alpha_6$ , where numbering starts from the N-terminus) and peptide C-terminal locations are taken as  $\text{C}\alpha_6$  atom positions. Contour lines are drawn around density regions in increments of 1,000 frequency.

## D.5 Water Structuring

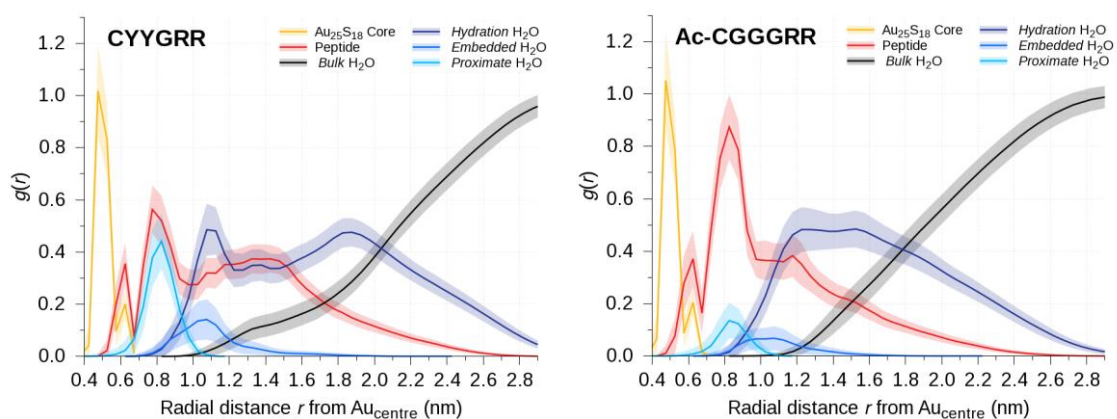
## D.5.1 Radial Distribution Functions

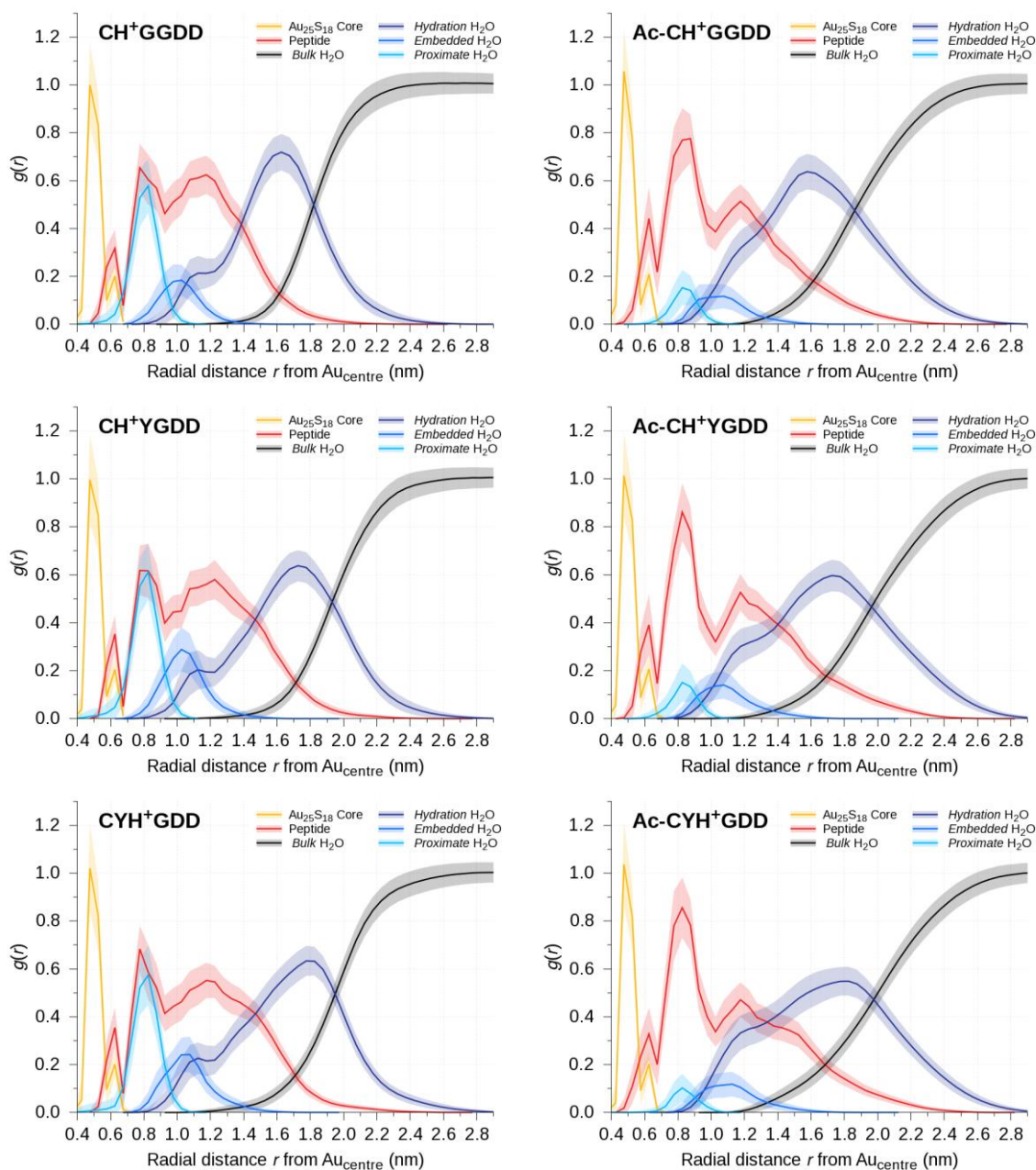
*Varying Sequence: (Ac-)CXXGDD, where X = G, V, H, or Y*





Arginine C-terminus: CYYGRR and Ac-CGGGRR



Protonated Histidine: (Ac-)CXXGDD, where one X = G, or Y and the other X = H<sup>+</sup>

**Figure D.11 | Average radial distributions of selected atomic components relative to the central  $\text{Au}_{25}(\text{SP})_{18}$  gold atom ( $\text{Au}_{\text{centre}}$ ).** The plots highlight differences in the amount of water that internalises (light blue lines) in the various peptide sequences.  $g(r)$  has been normalised by volume in each radial shell ( $dr = 0.05$  nm) by the density of *bulk* water far from the AuNCs ( $\rho_{\text{bulk-water}} = 0.100573$ ). Explicitly,  $g(r) = (N_{\text{atoms in } V_{\text{shell}}} / V_{\text{shell}}) / (\rho_{\text{bulk-water}}) = [N_{(r+dr)} - N_r] / [(4\pi/3) ((r+dr)^3 - r^3) (\rho_{\text{bulk-water}})]$ . Note that standard deviation is shown as the shaded region around each line.

## D.5.2 Hydrogen Bonding

Table D.2 | Hydrogen bonds involving water within 0.4 nm of Au<sub>25</sub>S<sub>18</sub>.

System	Donor	Acceptor	H-bonds*	Occupancy	Weighting†
CGGGDD	CYS <sub>1</sub> (Main_N)	SOL <sub>x</sub> (Side_OW)	12.2 ± 1.7	45.5 ± 18.1	5.6 ± 3.0
	SOL <sub>x</sub> (Side_OW)	CYS <sub>1</sub> (Main_O)	9.2 ± 1.9	46.0 ± 15.8	4.2 ± 2.4
	SOL <sub>x</sub> (Side_OW)	ASP <sub>6</sub> (Side_OD)	11.8 ± 3.2	63.4 ± 33.3	7.5 ± 6.0
	GLY <sub>2</sub> (Main_N)	SOL <sub>x</sub> (Side_OW)	6.2 ± 1.4	36.8 ± 11.0	2.3 ± 1.2
	SOL <sub>x</sub> (Side_OW)	ASP <sub>5</sub> (Side_OD)	8.4 ± 2.7	61.8 ± 32.3	5.2 ± 4.4
	SOL <sub>x</sub> (Side_OW)	GLY <sub>2</sub> (Main_O)	4.0 ± 1.7	44.9 ± 22.5	1.8 ± 1.7
				51.8 ± 8.9	50.6 ± 26.2
CHGGDD	CYS <sub>1</sub> (Main_N)	SOL <sub>x</sub> (Side_OW)	12.9 ± 1.9	48.8 ± 18.3	6.3 ± 3.3
	SOL <sub>x</sub> (Side_OW)	ASP <sub>6</sub> (Side_OD)	13.7 ± 3.9	70.9 ± 35.1	9.7 ± 7.6
	SOL <sub>x</sub> (Side_OW)	SOL <sub>x</sub> (Side_OW)	14.2 ± 3.1	42.3 ± 21.7	6.0 ± 4.4
	SOL <sub>x</sub> (Side_OW)	CYS <sub>1</sub> (Main_O)	8.0 ± 2.3	47.6 ± 14.5	3.8 ± 2.3
	SOL <sub>x</sub> (Side_OW)	ASP <sub>5</sub> (Side_OD)	9.8 ± 3.0	67.0 ± 32.3	6.6 ± 5.2
	HIS <sub>2</sub> (Main_N)	SOL <sub>x</sub> (Side_OW)	7.0 ± 1.9	44.7 ± 13.9	3.1 ± 1.9
	SOL <sub>x</sub> (Side_OW)	HIS <sub>2</sub> (Main_O)	5.6 ± 1.3	47.8 ± 23.5	2.7 ± 1.9
			71.2 ± 6.3	53.8 ± 27.3	38.2 ± 19.8
CHYGDD	CYS <sub>1</sub> (Main_N)	SOL <sub>x</sub> (Side_OW)	14.7 ± 0.9	50.2 ± 20.7	7.4 ± 3.5
	SOL <sub>x</sub> (Side_OW)	ASP <sub>6</sub> (Side_OD)	14.4 ± 3.0	69.7 ± 30.5	10.0 ± 6.5
	SOL <sub>x</sub> (Side_OW)	CYS <sub>1</sub> (Main_O)	8.1 ± 1.6	45.6 ± 16.4	3.7 ± 2.1
	HIS <sub>2</sub> (Main_N)	SOL <sub>x</sub> (Side_OW)	5.5 ± 1.1	41.6 ± 14.4	2.3 ± 1.3
	SOL <sub>x</sub> (Side_OW)	SOL <sub>x</sub> (Side_OW)	16.9 ± 5.3	38.6 ± 21.9	6.5 ± 5.8
	SOL <sub>x</sub> (Side_OW)	HIS <sub>2</sub> (Main_O)	5.3 ± 1.9	47.1 ± 20.2	2.5 ± 2.0
	SOL <sub>x</sub> (Side_OW)	ASP <sub>5</sub> (Side_OD)	7.9 ± 3.5	61.2 ± 30.1	4.8 ± 4.5
			72.8 ± 6.2	51.3 ± 26.1	37.5 ± 19.5
CYHGDD	CYS <sub>1</sub> (Main_N)	SOL <sub>x</sub> (Side_OW)	14.8 ± 1.7	53.7 ± 20.3	8.0 ± 3.9
	SOL <sub>x</sub> (Side_OW)	ASP <sub>6</sub> (Side_OD)	15.7 ± 3.4	64.2 ± 27.5	10.1 ± 6.5
	SOL <sub>x</sub> (Side_OW)	CYS <sub>1</sub> (Main_O)	9.7 ± 1.7	45.9 ± 14.1	4.5 ± 2.1
	SOL <sub>x</sub> (Side_OW)	SOL <sub>x</sub> (Side_OW)	17.8 ± 3.5	40.6 ± 24.3	7.2 ± 5.8
	SOL <sub>x</sub> (Side_OW)	TYR <sub>2</sub> (Main_O)	6.3 ± 1.7	52.3 ± 23.0	3.3 ± 2.4
	TYR <sub>2</sub> (Main_N)	SOL <sub>x</sub> (Side_OW)	6.0 ± 1.8	41.9 ± 14.5	2.5 ± 1.6
			70.3 ± 7.9	50.7 ± 24.0	35.5 ± 17.4
CGYGDD	CYS <sub>1</sub> (Main_N)	SOL <sub>x</sub> (Side_OW)	13.9 ± 1.0	49.7 ± 18.0	6.9 ± 3.0
	SOL <sub>x</sub> (Side_OW)	ASP <sub>6</sub> (Side_OD)	14.7 ± 1.8	61.4 ± 30.7	9.0 ± 5.6
	SOL <sub>x</sub> (Side_OW)	CYS <sub>1</sub> (Main_O)	8.0 ± 2.0	44.9 ± 15.0	3.6 ± 2.1
	GLY <sub>2</sub> (Main_N)	SOL <sub>x</sub> (Side_OW)	5.9 ± 1.6	39.3 ± 12.7	2.3 ± 1.4
	SOL <sub>x</sub> (Side_OW)	SOL <sub>x</sub> (Side_OW)	7.2 ± 2.8	39.1 ± 17.9	2.8 ± 2.4
	SOL <sub>x</sub> (Side_OW)	ASP <sub>6</sub> (Main_O)	2.5 ± 1.1	33.1 ± 10.6	0.8 ± 0.6
	SOL <sub>x</sub> (Side_OW)	ASP <sub>5</sub> (Side_OD)	8.4 ± 4.1	57.2 ± 27.6	4.8 ± 4.7
			60.6 ± 6.2	50.4 ± 24.0	30.3 ± 14.4
CYGGDD	CYS <sub>1</sub> (Main_N)	SOL <sub>x</sub> (Side_OW)	14.0 ± 1.3	50.5 ± 19.8	7.1 ± 3.4
	SOL <sub>x</sub> (Side_OW)	ASP <sub>6</sub> (Side_OD)	13.0 ± 2.9	72.3 ± 34.1	9.4 ± 6.5
	SOL <sub>x</sub> (Side_OW)	CYS <sub>1</sub> (Main_O)	9.5 ± 2.3	51.4 ± 19.4	4.9 ± 3.0
	SOL <sub>x</sub> (Side_OW)	ASP <sub>5</sub> (Side_OD)	9.6 ± 2.1	68.3 ± 38.8	6.6 ± 5.2
	TYR <sub>2</sub> (Main_N)	SOL <sub>x</sub> (Side_OW)	5.7 ± 1.2	43.2 ± 10.0	2.5 ± 1.1
	SOL <sub>x</sub> (Side_OW)	SOL <sub>x</sub> (Side_OW)	12.8 ± 3.6	48.5 ± 26.5	6.2 ± 5.2



## Appendix D: Supplementary Results (Chapter 5)

System	Donor	Acceptor	H-bonds*	Occupancy	Weighting†
	SOL <sub>x</sub> (Side_OW)	TYR <sub>2</sub> (Main_O)	6.1 ± 2.1	47.7 ± 24.2	2.9 ± 2.5
			70.7 ± 6.8	56.0 ± 29.0	39.5 ± 20.7
CYYGDD	SOL <sub>x</sub> (Side_OW)	ASP <sub>6</sub> (Side_OD)	17.3 ± 2.3	69.4 ± 34.5	12.0 ± 7.6
	CYS <sub>1</sub> (Main_N)	SOL <sub>x</sub> (Side_OW)	14.4 ± 2.5	52.0 ± 21.2	7.5 ± 4.4
	SOL <sub>x</sub> (Side_OW)	CYS <sub>1</sub> (Main_O)	10.1 ± 2.0	54.2 ± 17.5	5.5 ± 2.8
	TYR <sub>2</sub> (Main_N)	SOL <sub>x</sub> (Side_OW)	6.3 ± 1.3	41.5 ± 14.4	2.6 ± 1.4
	SOL <sub>x</sub> (Side_OW)	SOL <sub>x</sub> (Side_OW)	18.3 ± 4.4	40.8 ± 24.4	7.5 ± 6.3
	SOL <sub>x</sub> (Side_OW)	TYR <sub>2</sub> (Main_O)	5.6 ± 1.7	50.0 ± 21.8	2.8 ± 2.1
			72.0 ± 7.7	52.6 ± 27.2	37.9 ± 20.2
CVGGDD	CYS <sub>1</sub> (Main_N)	SOL <sub>x</sub> (Side_OW)	14.3 ± 1.1	48.5 ± 18.8	6.9 ± 3.2
	SOL <sub>x</sub> (Side_OW)	CYS <sub>1</sub> (Main_O)	9.4 ± 1.5	53.9 ± 16.2	5.1 ± 2.3
	SOL <sub>x</sub> (Side_OW)	VAL <sub>2</sub> (Main_O)	7.6 ± 1.4	54.5 ± 23.0	4.1 ± 2.5
	SOL <sub>x</sub> (Side_OW)	ASP <sub>6</sub> (Side_OD)	12.4 ± 3.3	69.3 ± 38.6	8.6 ± 7.1
	SOL <sub>x</sub> (Side_OW)	ASP <sub>5</sub> (Side_OD)	12.0 ± 4.0	66.5 ± 32.6	8.0 ± 6.6
	VAL <sub>2</sub> (Main_N)	SOL <sub>x</sub> (Side_OW)	6.0 ± 1.4	44.8 ± 14.6	2.7 ± 1.5
	SOL <sub>x</sub> (Side_OW)	SOL <sub>x</sub> (Side_OW)	13.4 ± 4.5	48.8 ± 28.8	6.5 ± 6.1
			75.1 ± 8.0	55.9 ± 28.5	41.9 ± 22.0
CVVGDD	CYS <sub>1</sub> (Main_N)	SOL <sub>x</sub> (Side_OW)	15.3 ± 1.4	50.8 ± 19.7	7.8 ± 3.7
	SOL <sub>x</sub> (Side_OW)	ASP <sub>6</sub> (Side_OD)	15.9 ± 1.8	67.3 ± 37.1	10.7 ± 7.1
	SOL <sub>x</sub> (Side_OW)	CYS <sub>1</sub> (Main_O)	11.3 ± 2.1	48.5 ± 17.5	5.5 ± 3.0
	SOL <sub>x</sub> (Side_OW)	VAL <sub>2</sub> (Main_O)	8.7 ± 2.0	52.0 ± 21.6	4.5 ± 2.9
	SOL <sub>x</sub> (Side_OW)	SOL <sub>x</sub> (Side_OW)	16.7 ± 4.3	42.2 ± 22.0	7.0 ± 5.5
	SOL <sub>x</sub> (Side_OW)	ASP <sub>5</sub> (Side_OD)	6.5 ± 2.5	70.5 ± 29.4	4.6 ± 3.6
	VAL <sub>2</sub> (Main_N)	SOL <sub>x</sub> (Side_OW)	5.4 ± 1.4	43.7 ± 15.8	2.4 ± 1.5
			79.8 ± 5.3	53.0 ± 27.0	42.5 ± 21.9
Ac-CGGGDD	SOL <sub>x</sub> (Side_OW)	CYS <sub>1</sub> (Main_O)	11.6 ± 3.8	55.0 ± 20.9	6.4 ± 4.5
	SOL <sub>x</sub> (Side_OW)	ACE <sub>0</sub> (Main_O)	10.5 ± 4.4	55.4 ± 24.1	5.8 ± 5.0
	GLY <sub>2</sub> (Main_N)	SOL <sub>x</sub> (Side_OW)	5.5 ± 1.9	41.0 ± 12.3	2.3 ± 1.4
	SOL <sub>x</sub> (Side_OW)	GLY <sub>2</sub> (Main_O)	2.1 ± 0.9	42.4 ± 15.1	0.9 ± 0.7
			29.7 ± 8.0	50.2 ± 21.4	15.3 ± 8.6
Ac-CHGGDD	SOL <sub>x</sub> (Side_OW)	CYS <sub>1</sub> (Main_O)	11.0 ± 4.6	52.1 ± 18.1	5.7 ± 4.4
	SOL <sub>x</sub> (Side_OW)	ACE <sub>0</sub> (Main_O)	10.1 ± 4.4	55.3 ± 22.7	5.6 ± 4.7
	HIS <sub>2</sub> (Main_N)	SOL <sub>x</sub> (Side_OW)	5.9 ± 2.2	44.0 ± 15.3	2.6 ± 1.9
	CYS <sub>1</sub> (Main_N)	SOL <sub>x</sub> (Side_OW)	3.3 ± 1.6	39.8 ± 12.2	1.3 ± 1.1
			30.3 ± 11.4	48.0 ± 19.7	15.2 ± 8.9
Ac-CHYGDD	SOL <sub>x</sub> (Side_OW)	CYS <sub>1</sub> (Main_O)	12.2 ± 3.2	54.1 ± 16.0	6.6 ± 3.7
	SOL <sub>x</sub> (Side_OW)	ACE <sub>0</sub> (Main_O)	11.2 ± 3.9	52.8 ± 21.0	5.9 ± 4.4
	HIS <sub>2</sub> (Main_N)	SOL <sub>x</sub> (Side_OW)	5.7 ± 2.0	44.3 ± 16.9	2.5 ± 1.9
	CYS <sub>1</sub> (Main_N)	SOL <sub>x</sub> (Side_OW)	4.6 ± 2.0	39.7 ± 14.6	1.8 ± 1.5
	SOL <sub>x</sub> (Side_OW)	HIS <sub>2</sub> (Main_O)	2.7 ± 1.2	39.3 ± 11.3	1.1 ± 0.8
			36.4 ± 9.8	48.7 ± 18.4	17.9 ± 8.8
Ac-CYHGDD	SOL <sub>x</sub> (Side_OW)	CYS <sub>1</sub> (Main_O)	14.3 ± 3.7	52.1 ± 17.1	7.5 ± 3.1
	SOL <sub>x</sub> (Side_OW)	ACE <sub>0</sub> (Main_O)	10.7 ± 3.1	54.4 ± 21.7	5.8 ± 1.8
	TYR <sub>2</sub> (Main_N)	SOL <sub>x</sub> (Side_OW)	6.8 ± 1.7	51.0 ± 15.6	3.5 ± 1.6
	CYS <sub>1</sub> (Main_N)	SOL <sub>x</sub> (Side_OW)	3.8 ± 1.2	39.8 ± 12.7	1.5 ± 0.6
	SOL <sub>x</sub> (Side_OW)	TYR <sub>2</sub> (Main_O)	3.8 ± 1.9	47.6 ± 18.1	1.8 ± 0.2

## Appendix D: Supplementary Results (Chapter 5)

System	Donor	Acceptor	H-bonds*	Occupancy	Weighting†
			$39.4 \pm 8.7$	$50.4 \pm 18.5$	$20.1 \pm 8.6$
CH+GGDD	CYS <sub>1</sub> (Main_N)	SOL <sub>x</sub> (Side_OW)	$13.5 \pm 1.3$	$51.1 \pm 20.9$	$6.9 \pm 3.5$
	SOL <sub>x</sub> (Side_OW)	ASP <sub>6</sub> (Side_OD)	$18.9 \pm 3.8$	$68.7 \pm 37.5$	$13.0 \pm 9.7$
	SOL <sub>x</sub> (Side_OW)	ASP <sub>5</sub> (Side_OD)	$10.8 \pm 2.2$	$64.3 \pm 32.3$	$7.0 \pm 4.9$
	SOL <sub>x</sub> (Side_OW)	CYS <sub>1</sub> (Main_O)	$8.6 \pm 2.3$	$50.1 \pm 18.2$	$4.3 \pm 2.7$
	SOL <sub>x</sub> (Side_OW)	SOL <sub>x</sub> (Side_OW)	$16.6 \pm 4.0$	$44.0 \pm 26.1$	$7.3 \pm 6.1$
	SOL <sub>x</sub> (Side_OW)	HIS <sub>2</sub> (Main_O)	$5.3 \pm 1.3$	$49.8 \pm 18.9$	$2.6 \pm 1.6$
	HIS <sub>2</sub> (Main_N)	SOL <sub>x</sub> (Side_OW)	$4.8 \pm 1.4$	$43.7 \pm 15.0$	$2.1 \pm 1.3$
	SOL <sub>x</sub> (Side_OW)	GLY <sub>3</sub> (Main_O)	$3.7 \pm 1.3$	$48.3 \pm 23.1$	$1.8 \pm 1.5$
			$82.2 \pm 8.3$	$54.8 \pm 29.3$	$45.0 \pm 24.6$
CH+YGDD	SOL <sub>x</sub> (Side_OW)	ASP <sub>6</sub> (Side_OD)	$18.7 \pm 3.7$	$71.1 \pm 31.5$	$13.3 \pm 8.5$
	CYS <sub>1</sub> (Main_N)	SOL <sub>x</sub> (Side_OW)	$14.8 \pm 1.5$	$51.6 \pm 20.3$	$7.6 \pm 3.8$
	SOL <sub>x</sub> (Side_OW)	CYS <sub>1</sub> (Main_O)	$11.4 \pm 2.1$	$50.3 \pm 16.8$	$5.7 \pm 3.0$
	SOL <sub>x</sub> (Side_OW)	SOL <sub>x</sub> (Side_OW)	$25.2 \pm 6.3$	$42.2 \pm 23.6$	$10.6 \pm 8.6$
	SOL <sub>x</sub> (Side_OW)	ASP <sub>5</sub> (Side_OD)	$9.4 \pm 3.2$	$66.8 \pm 33.0$	$6.3 \pm 5.2$
	HIS <sub>2</sub> (Main_N)	SOL <sub>x</sub> (Side_OW)	$4.7 \pm 1.6$	$43.4 \pm 15.3$	$2.0 \pm 1.4$
				$84.2 \pm 8.8$	$54.3 \pm 27.7$
CYH+GDD	CYS <sub>1</sub> (Main_N)	SOL <sub>x</sub> (Side_OW)	$15.0 \pm 1.0$	$51.9 \pm 20.8$	$7.8 \pm 3.6$
	SOL <sub>x</sub> (Side_OW)	CYS <sub>1</sub> (Main_O)	$11.3 \pm 1.4$	$55.6 \pm 19.4$	$6.3 \pm 3.0$
	SOL <sub>x</sub> (Side_OW)	ASP <sub>6</sub> (Side_OD)	$15.3 \pm 3.6$	$67.1 \pm 35.0$	$10.3 \pm 7.8$
	SOL <sub>x</sub> (Side_OW)	ASP <sub>5</sub> (Side_OD)	$9.1 \pm 2.1$	$69.3 \pm 32.9$	$6.3 \pm 4.4$
	SOL <sub>x</sub> (Side_OW)	SOL <sub>x</sub> (Side_OW)	$21.4 \pm 6.2$	$42.3 \pm 23.7$	$9.1 \pm 7.7$
	TYR <sub>2</sub> (Main_N)	SOL <sub>x</sub> (Side_OW)	$4.7 \pm 1.2$	$39.6 \pm 15.0$	$1.9 \pm 1.2$
	SOL <sub>x</sub> (Side_OW)	TYR <sub>2</sub> (Main_O)	$3.7 \pm 1.7$	$45.9 \pm 20.1$	$1.7 \pm 1.5$
			$80.5 \pm 7.4$	$53.9 \pm 28.0$	$43.2 \pm 22.8$
Ac-CH+GGDD	SOL <sub>x</sub> (Side_OW)	CYS <sub>1</sub> (Main_O)	$13.2 \pm 1.5$	$48.7 \pm 15.1$	$6.4 \pm 2.7$
	HIS <sub>2</sub> (Main_N)	SOL <sub>x</sub> (Side_OW)	$8.0 \pm 1.3$	$52.8 \pm 15.1$	$4.2 \pm 1.9$
	SOL <sub>x</sub> (Side_OW)	ACE <sub>0</sub> (Main_O)	$9.3 \pm 2.1$	$54.4 \pm 18.0$	$5.1 \pm 2.8$
	SOL <sub>x</sub> (Side_OW)	HIS <sub>2</sub> (Main_O)	$4.2 \pm 2.1$	$45.1 \pm 14.9$	$1.9 \pm 1.6$
	CYS <sub>1</sub> (Main_N)	SOL <sub>x</sub> (Side_OW)	$4.2 \pm 2.4$	$42.2 \pm 14.5$	$1.8 \pm 1.6$
	SOL <sub>x</sub> (Side_OW)	SOL <sub>x</sub> (Side_OW)	$6.0 \pm 2.6$	$40.9 \pm 20.6$	$2.5 \pm 2.3$
			$44.9 \pm 6.4$	$48.6 \pm 17.2$	$21.8 \pm 8.5$
Ac-CH+YGDD	SOL <sub>x</sub> (Side_OW)	CYS <sub>1</sub> (Main_O)	$13.5 \pm 2.1$	$50.4 \pm 16.3$	$6.8 \pm 3.3$
	SOL <sub>x</sub> (Side_OW)	ACE <sub>0</sub> (Main_O)	$9.9 \pm 2.1$	$52.7 \pm 16.9$	$5.2 \pm 2.8$
	HIS <sub>2</sub> (Main_N)	SOL <sub>x</sub> (Side_OW)	$7.9 \pm 0.9$	$48.8 \pm 17.4$	$3.9 \pm 1.8$
	CYS <sub>1</sub> (Main_N)	SOL <sub>x</sub> (Side_OW)	$5.0 \pm 1.6$	$39.7 \pm 14.6$	$2.0 \pm 1.4$
			$36.3 \pm 4.6$	$49.4 \pm 17.0$	$17.9 \pm 6.5$
Ac-CYH+GDD	SOL <sub>x</sub> (Side_OW)	CYS <sub>1</sub> (Main_O)	$12.6 \pm 2.4$	$56.0 \pm 16.7$	$7.1 \pm 3.4$
	SOL <sub>x</sub> (Side_OW)	ACE <sub>0</sub> (Main_O)	$11.8 \pm 3.0$	$55.5 \pm 23.0$	$6.5 \pm 2.2$
	TYR <sub>2</sub> (Main_N)	SOL <sub>x</sub> (Side_OW)	$6.1 \pm 2.4$	$50.3 \pm 14.9$	$3.1 \pm 1.0$
	CYS <sub>1</sub> (Main_N)	SOL <sub>x</sub> (Side_OW)	$4.8 \pm 1.4$	$42.1 \pm 13.6$	$2.0 \pm 0.8$
			$35.3 \pm 6.6$	$52.5 \pm 19.0$	$18.7 \pm 7.7$

## Appendix D: Supplementary Results (Chapter 5)

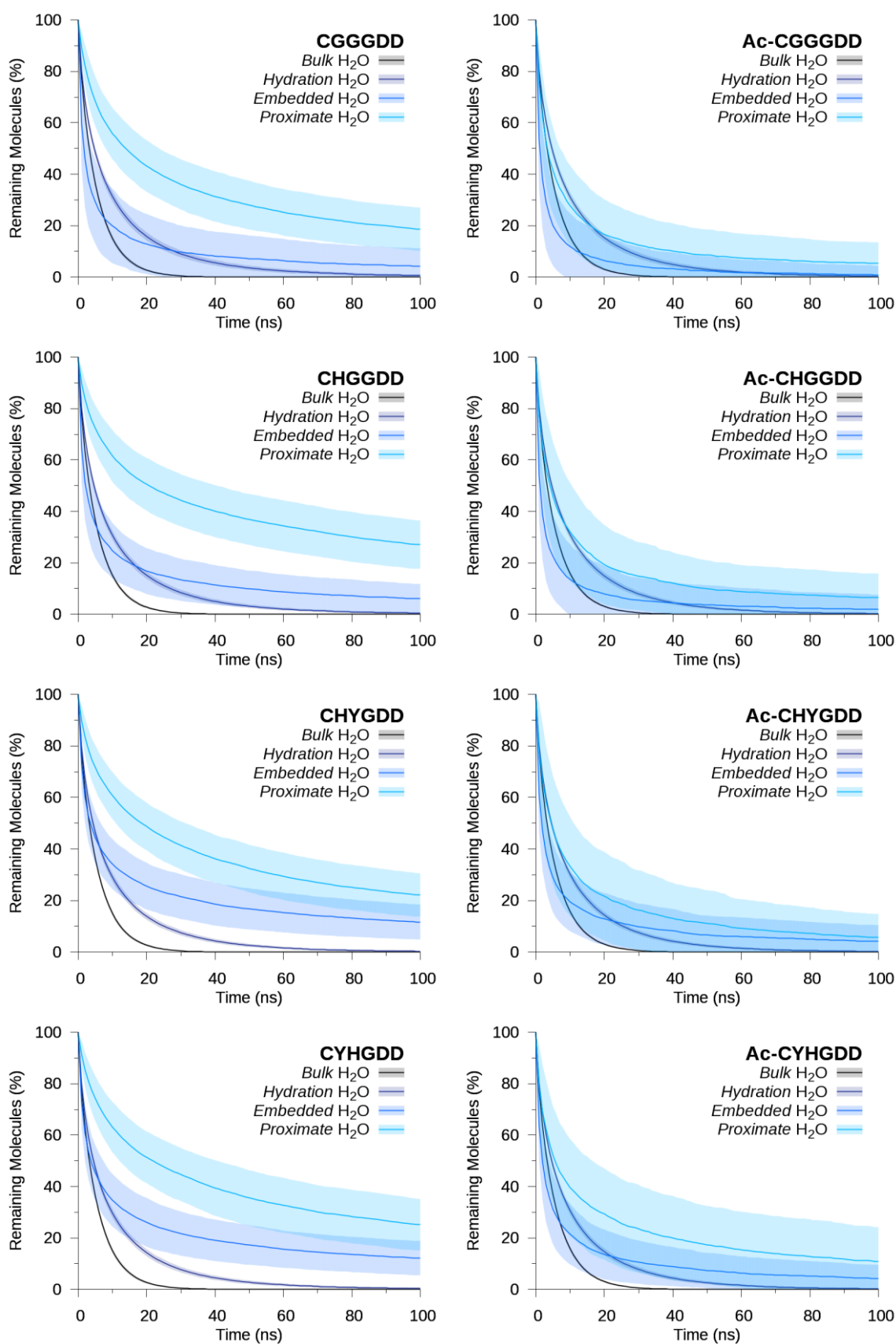
System	Donor	Acceptor	H-bonds*	Occupancy	Weighting†
CYYGRR	CYS <sub>1</sub> (Main_N)	SOL <sub>x</sub> (Side_OW)	15.9 ± 3.6	49.6 ± 16.7	7.9 ± 4.4
	SOL <sub>x</sub> (Side_OW)	CYS <sub>1</sub> (Main_O)	11.6 ± 2.5	46.4 ± 13.9	5.4 ± 2.8
	TYR <sub>2</sub> (Main_N)	SOL <sub>x</sub> (Side_OW)	7.3 ± 3.7	37.1 ± 11.1	2.7 ± 2.2
			34.8 ± 8.7	45.2 ± 15.5	16.0 ± 7.1
Ac-CGGGRR	SOL <sub>x</sub> (Side_OW)	CYS <sub>1</sub> (Main_O)	11.5 ± 4.6	49.7 ± 16.3	5.7 ± 4.2
	SOL <sub>x</sub> (Side_OW)	ACE <sub>0</sub> (Main_O)	10.4 ± 3.4	49.0 ± 19.6	5.1 ± 3.7
	GLY <sub>2</sub> (Main_N)	SOL <sub>x</sub> (Side_OW)	6.7 ± 1.8	45.0 ± 14.3	3.0 ± 1.8
	CYS <sub>1</sub> (Main_N)	SOL <sub>x</sub> (Side_OW)	4.7 ± 1.0	37.0 ± 12.4	1.7 ± 1.0
			33.3 ± 9.2	45.9 ± 17.1	15.6 ± 7.6

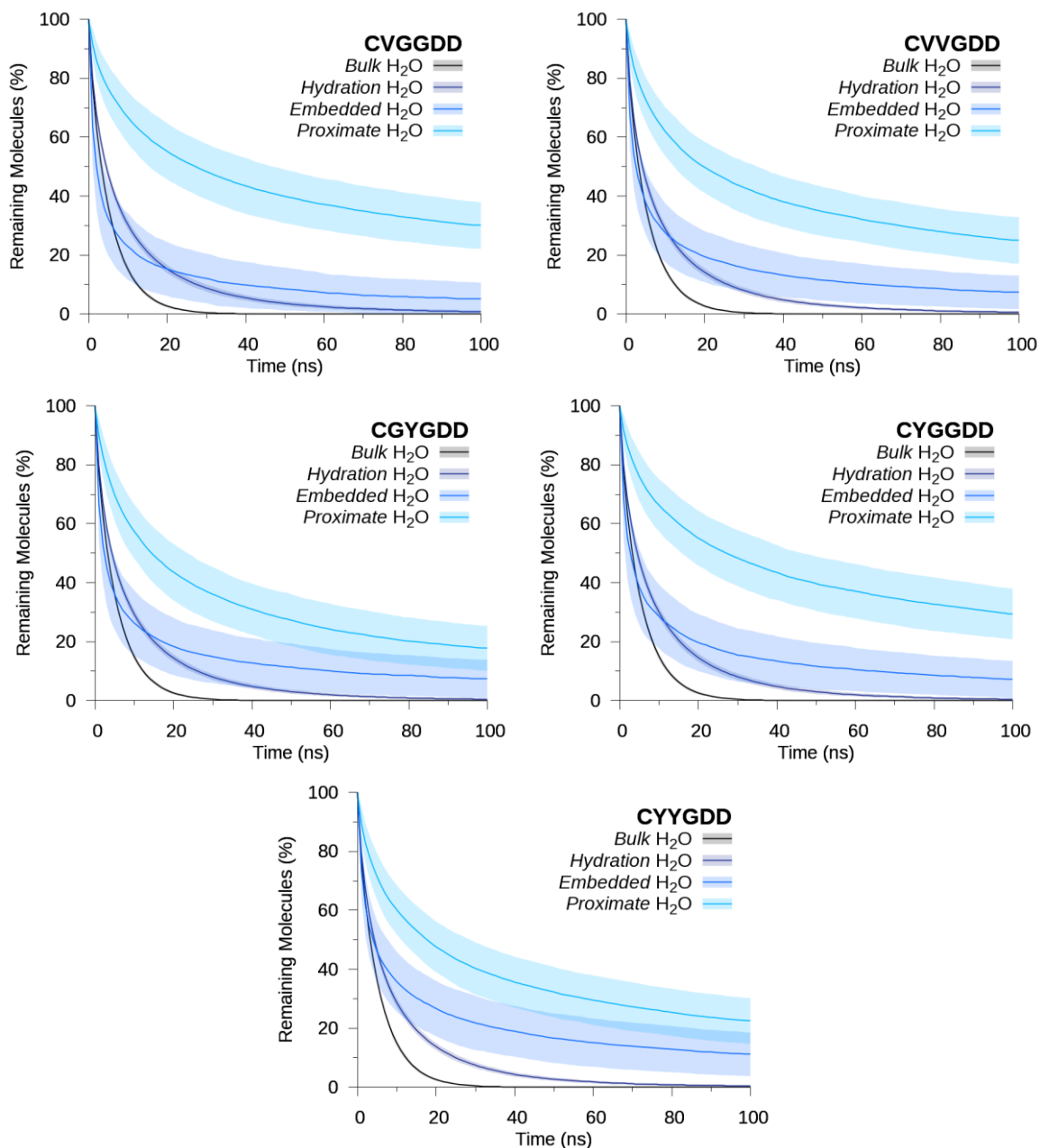
\*Only *proximal* solvent H-bonds with an occupancy > 20 % are reported.

†Weighting = no. H-bonds × Occupancy/100. Only H-bonds with a weighting – standard deviation > 0.1 are reported.

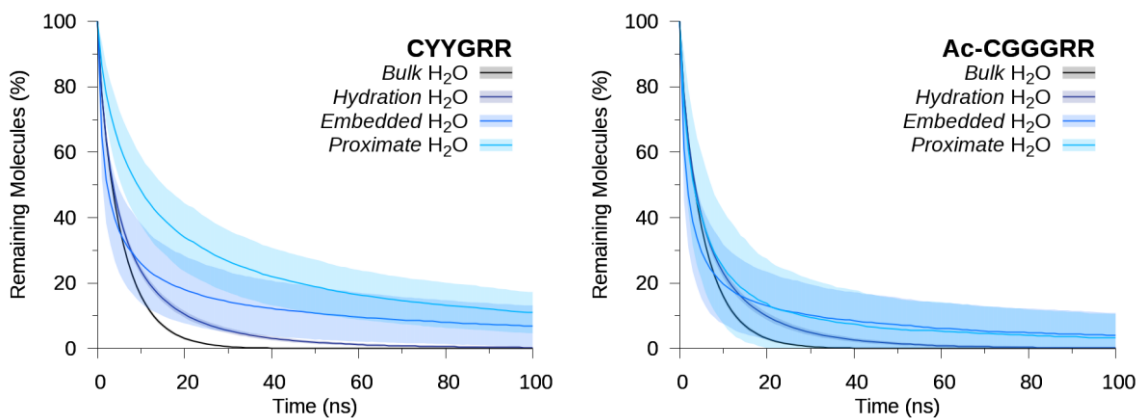
## D.5.3 Water Mobility

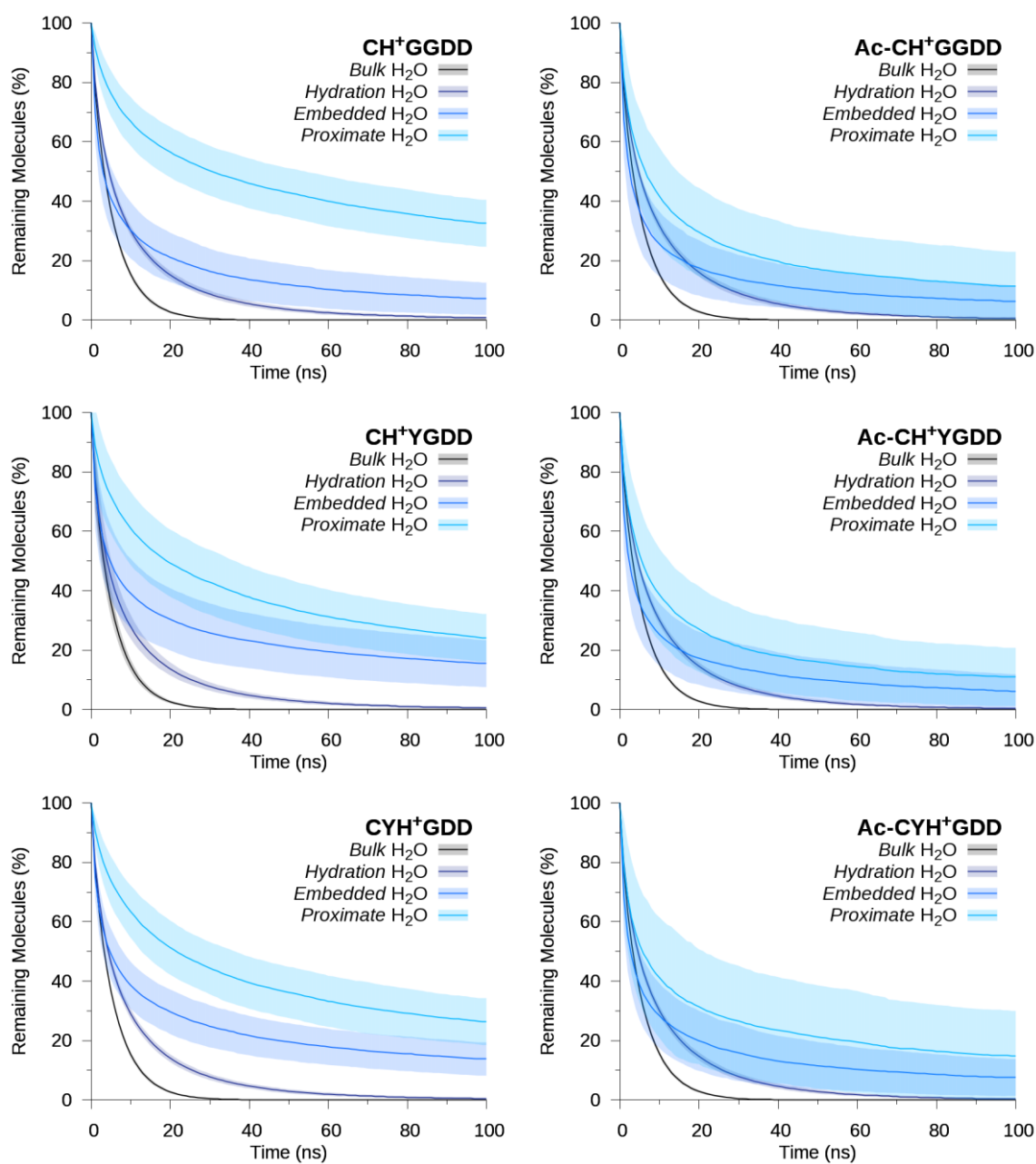
*Varying Sequence: (Ac-)CXXGDD, where X = G, V, H, or Y*





Arginine C-terminus: CYYGRR and Ac-CGGGRR



*Protonated Histidine: (Ac-)CXXGDD, where one X = G, or Y and the other X = H<sup>+</sup>*

**Figure D.12 | Decay of water out of dynamic water selections.** Water atom indices are determined for each selection (e.g. *Bulk*, *Hydration*, etc.) then updated at each frame only maintaining a count of the water atoms whose indices were initially present in the initial selection. Selections are updated for 99 ps, then to avoid correlated data, a break of 99 ps is allowed before the next selection is made. In other words, 1–100 ps data is collected, 101–200 ps no data is collected, 201–300 ps data is collect and so on. At the end of data collection, all decays are averaged and presented with their standard deviation (shaded region). To obtain a decay of *bulk* water, a *shell of bulk water* 0.6 nm out from *hydration* water was used.

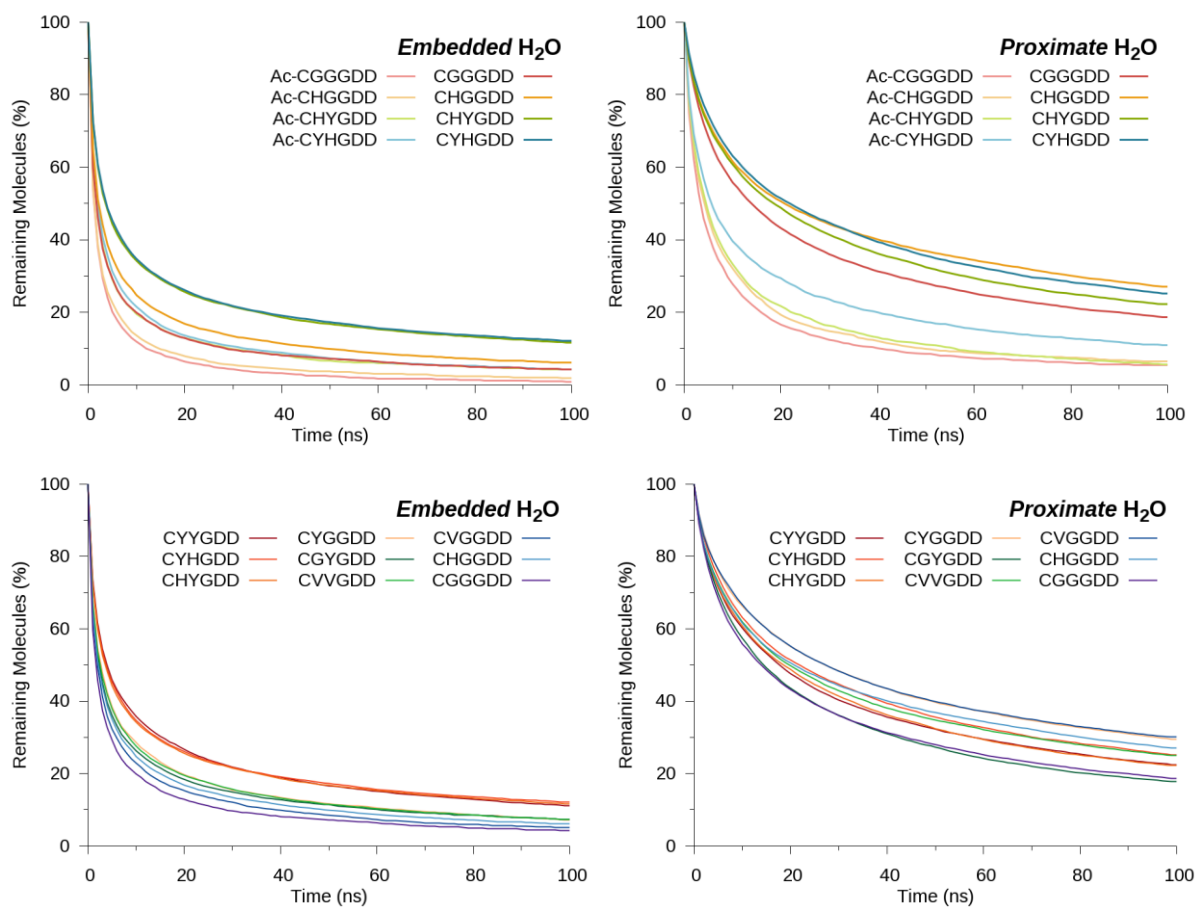
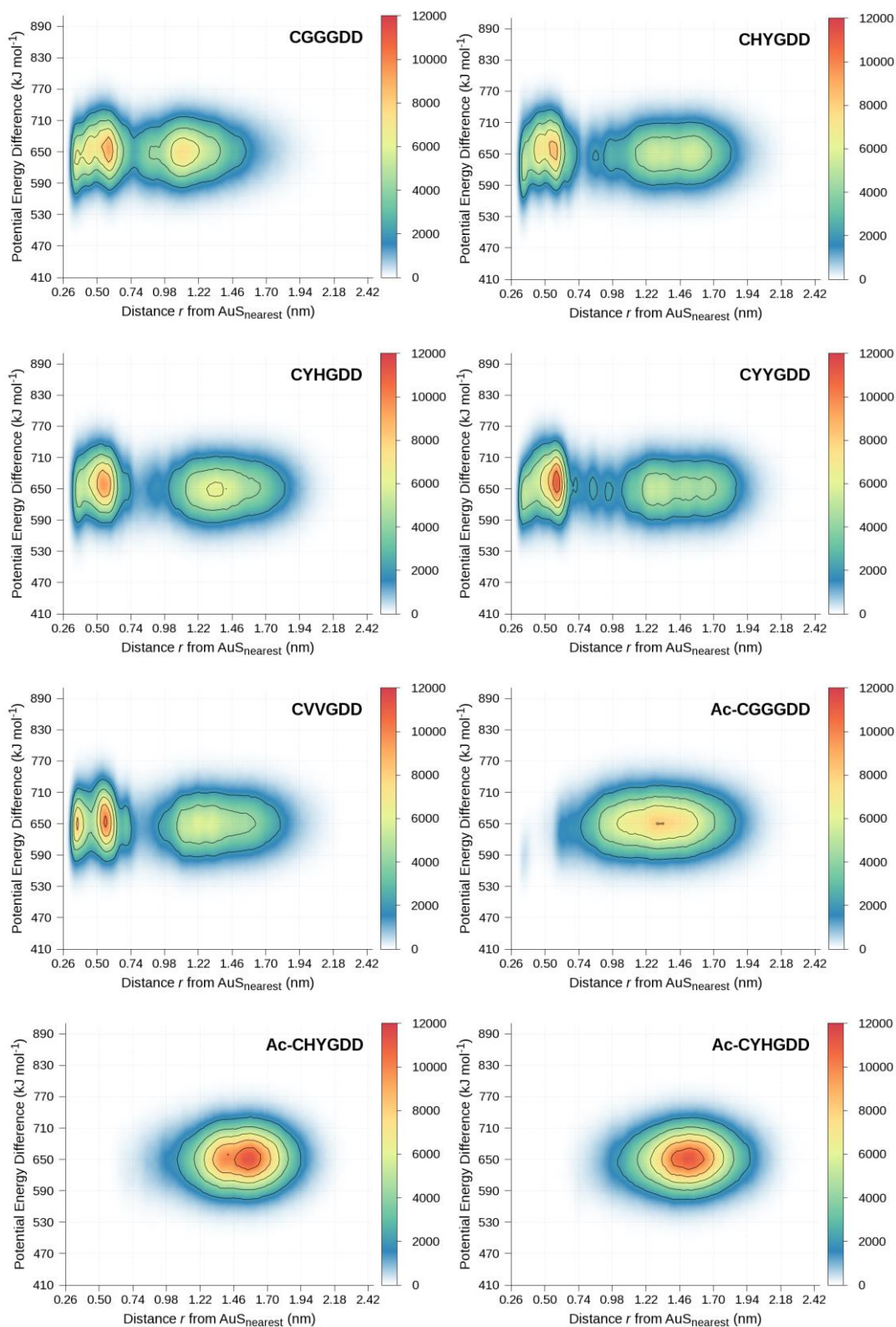


Figure D.13 | Comparison of water decay for acetylated and non-acetylated systems.

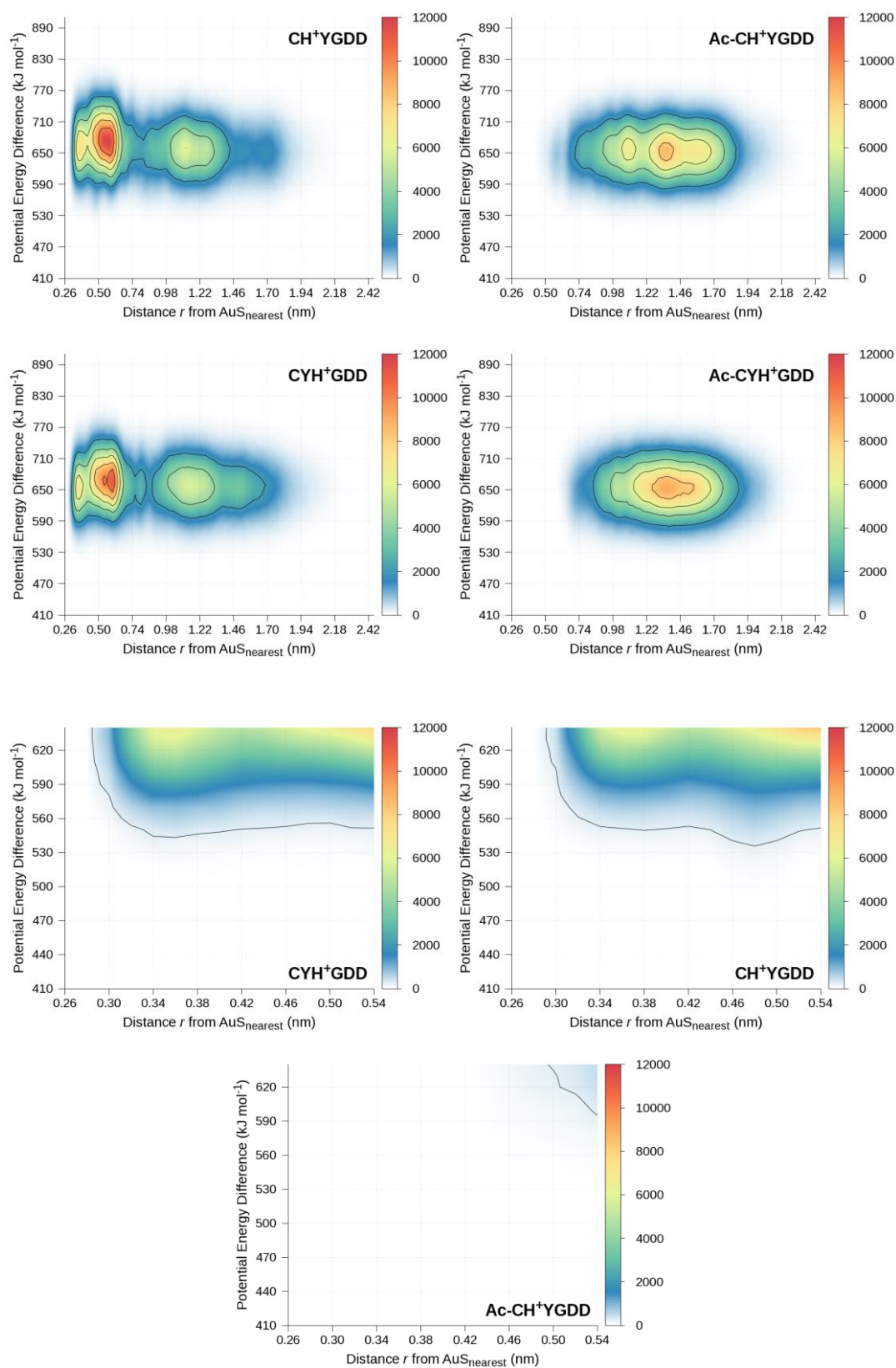
## D.6 Suggestion for Aspartate Electron Transfer to Au and PL Quenching

### D.6.1 Classical Electrostatic Potential Energy

Varying Sequence: (Ac-)CXXGDD, where X = G, V, H, or Y





*Protonated Histidine: (Ac-)CXXGDD, where one X = G, or Y and the other X = H<sup>+</sup>*

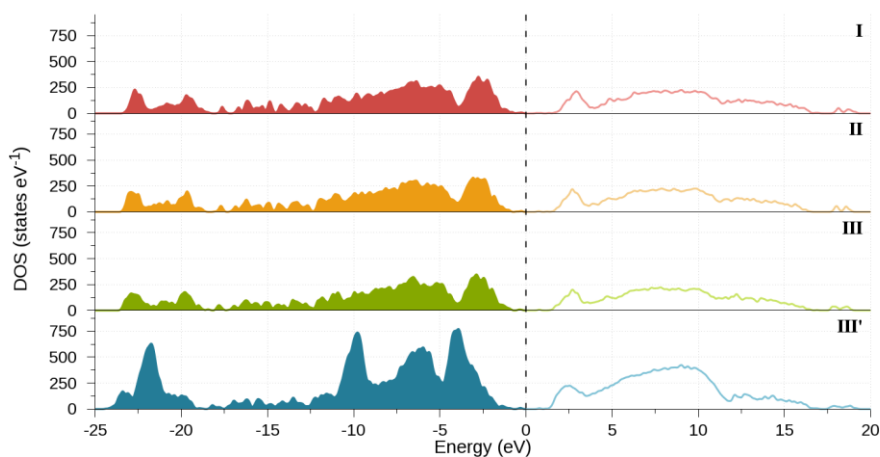
**Figure D.14 | Aspartate classical electrostatic potential energy versus Au<sub>25</sub>S<sub>18</sub> distance. Note the last three plots are close-ups.**

**Table D.3 | Electrostatic energy difference before electron removal and after.**

System	$\Delta U$ (kJ·mol <sup>-1</sup> )	Percentage of states with distance < 0.51 nm and $\Delta U$ < 600 kJ·mol <sup>-1</sup> )
CGGGDD	650.4 ± 42.4	3.1
CHYGDD	651.3 ± 43.0	2.8
CYHGDD	652.6 ± 42.6	2.0
CVVGDD	650.1 ± 42.2	2.5
CYYGDD	652.9 ± 43.1	2.4
Ac-CGGGDD	650.8 ± 42.3	0.3
Ac-CHYGDD	651.4 ± 41.9	0.0
Ac-CYHGDD	651.1 ± 42.0	0.0
CH+YGDD	663.9 ± 44.5	1.7
CYH+GDD	660.9 ± 42.7	1.8
Ac-CH+YGDD	653.6 ± 42.0	0.0
Ac-CYH+GDD	654.2 ± 42.0	0.0

\*Total population = 3,600,000 (36 ASP residues × 10,000 frames × 10 independent trajectories)

## D.6.2 Quantum Mechanical (ONETEP) Results

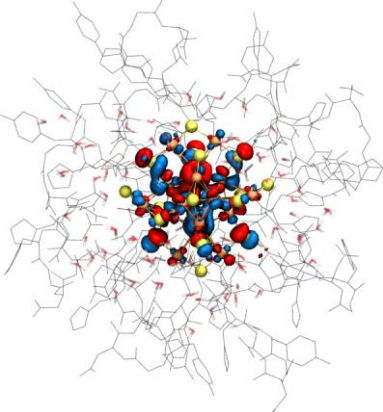
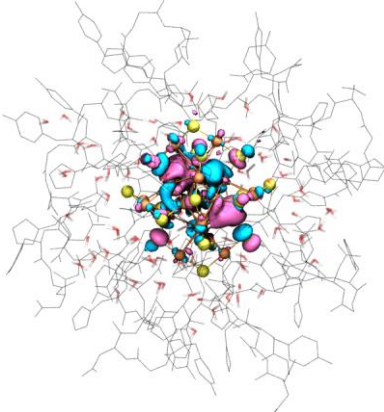
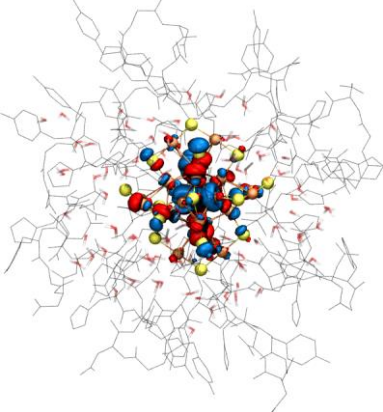
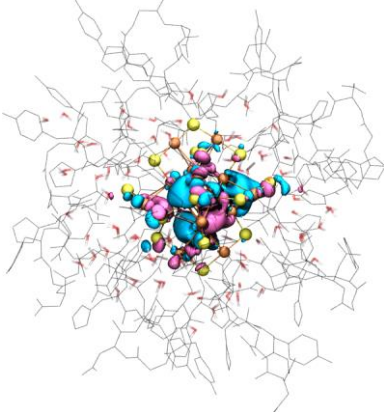
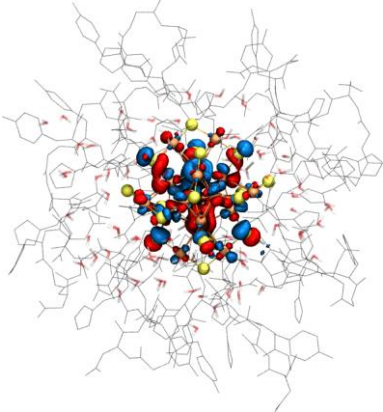
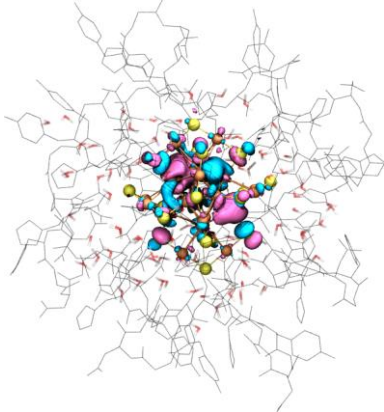


**Figure D.15 | Density of states for Au<sub>25</sub>(SP)<sub>18</sub> conformers, where P = CH+YGDD.** Note the shift in the density of states for conformer III', especially near the HOMO-LUMO gap, implying the importance of including *hydration* water in the single-point calculations.

**Table D.4 | Mulliken atomic partial charges.**

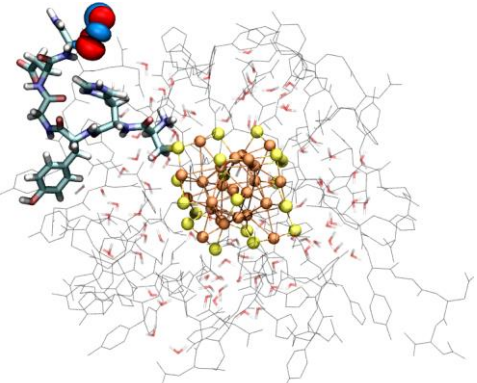
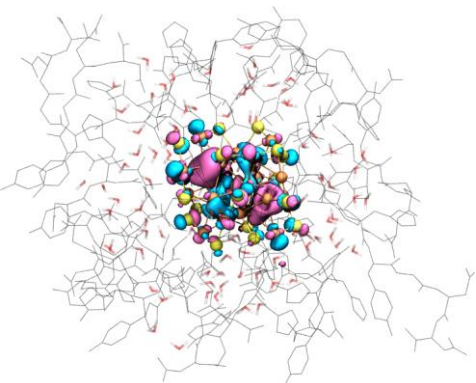
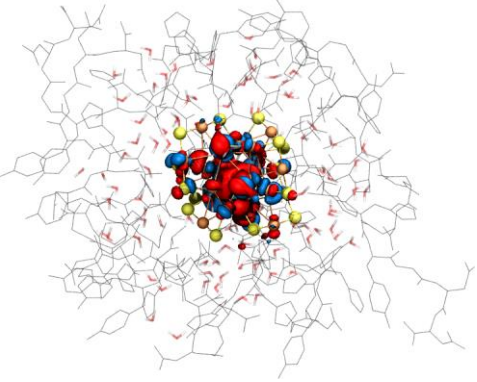
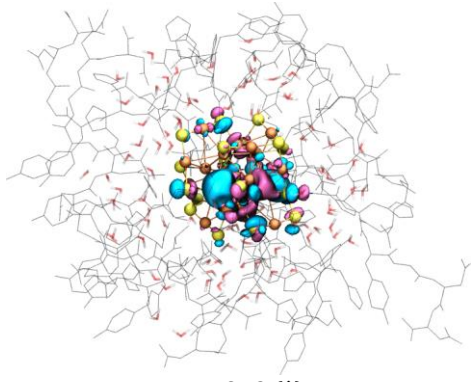
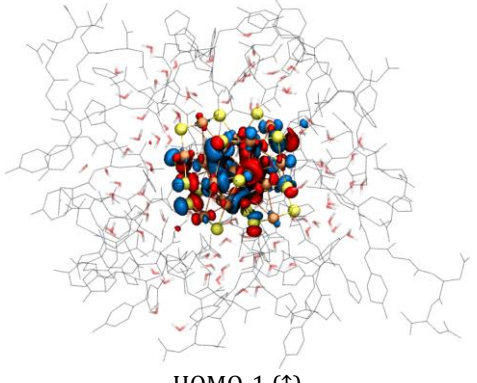
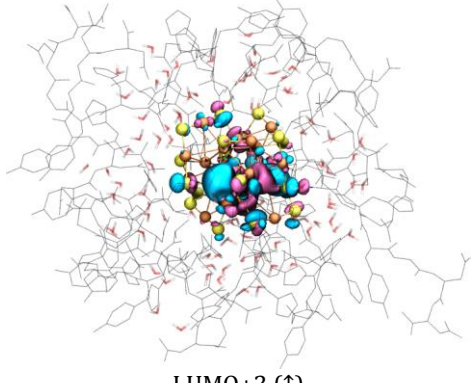
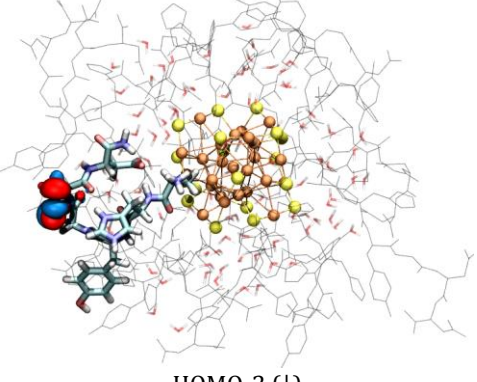
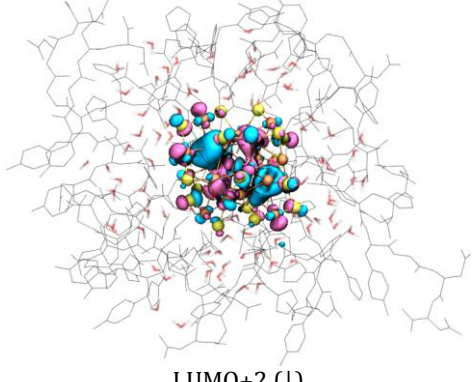
Conformer	Au <sub>25</sub> S <sub>18</sub>	Au <sub>25</sub>	S <sub>18</sub>	Au <sub>13</sub> core	[S-(Au-S) <sub>2</sub> ] <sub>6</sub> staples
I	0.747	1.095	-0.348	0.237	-0.111
II	0.781	1.166	-0.385	0.319	-0.066
III	0.881	1.242	-0.361	0.234	-0.127
III'	0.950	1.268	-0.318	0.205	-0.113

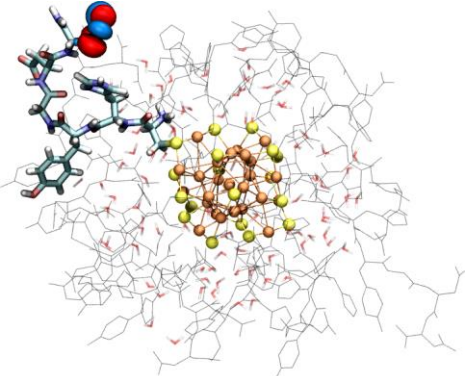
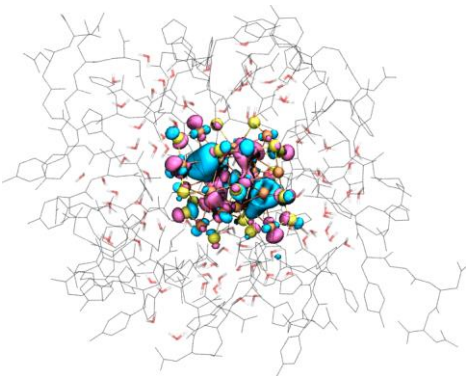
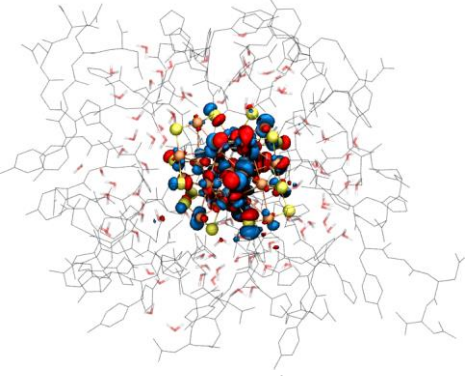
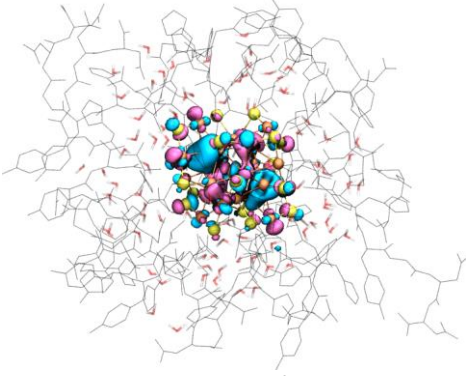
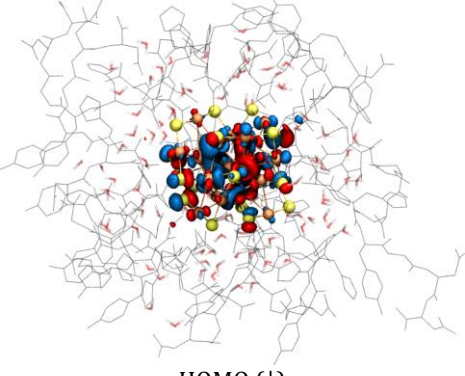
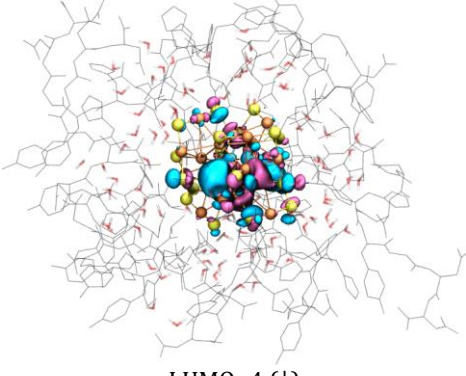
Table D.5 | Kohn–Sham orbitals of Au<sub>25</sub>(SP)<sub>18</sub> (conformer I). \*

		eV (nm)
	HOMO-2 (↑)	1.81127 (684.5)
	LUMO+2 (↑)	
	HOMO (↑)	1.88012 (659.4)
	LUMO+3 (↑)	
	HOMO-1 (↓)	1.80577 (686.6)
	LUMO+3 (↓)	

\*(where P = CH+YGDD) and energy gaps = 655–695 nm.

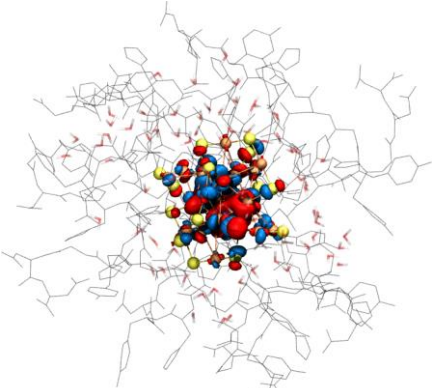
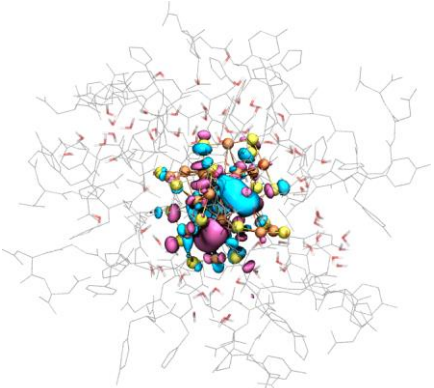
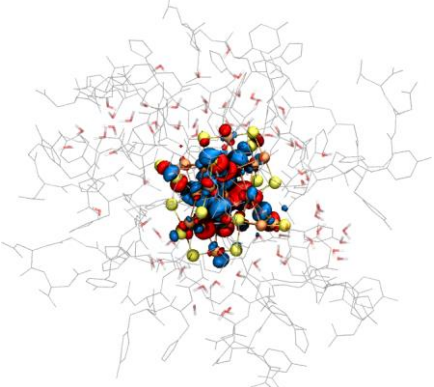
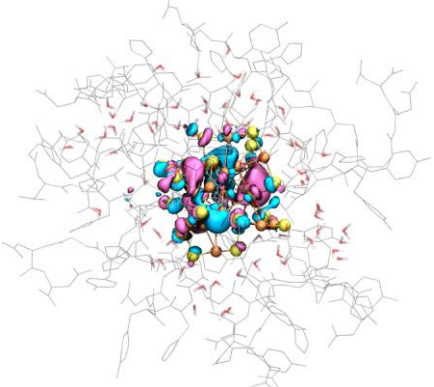
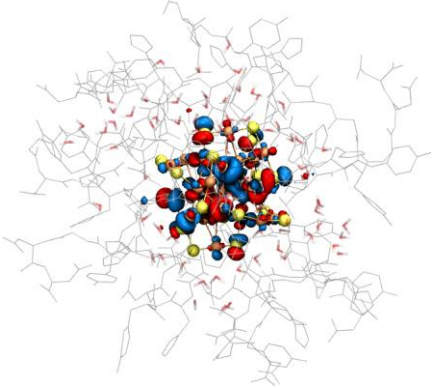
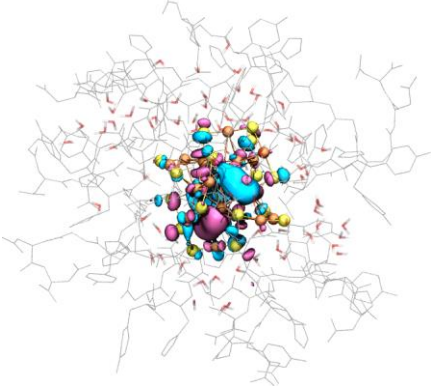
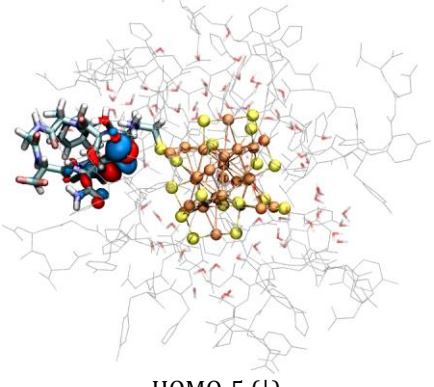
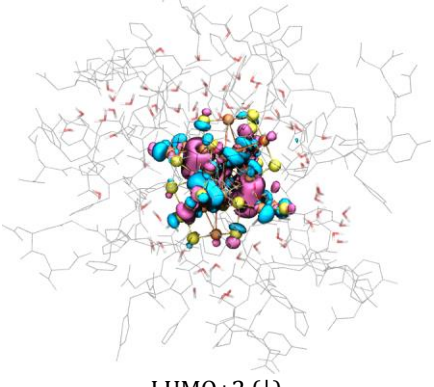
Table D.6 | Kohn–Sham orbitals of Au<sub>25</sub>(SP)<sub>18</sub> (conformer II).\*

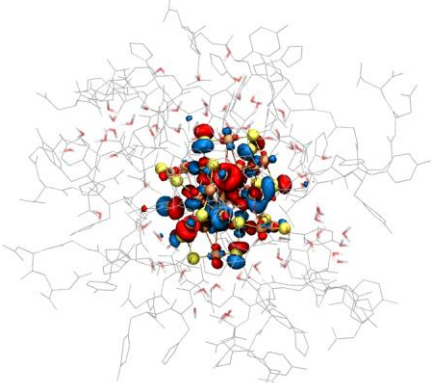
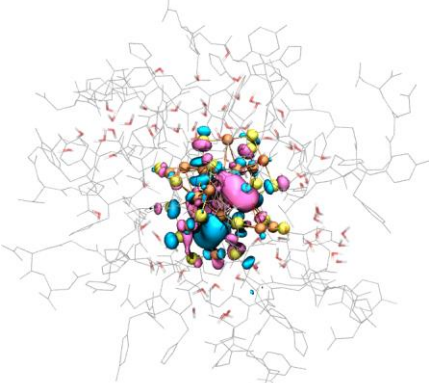
HOMO	LUMO	eV (nm)
 HOMO-5 (↑)	 LUMO+1 (↑)	1.79206 (691.9)
 HOMO (↑)	 LUMO+3 (↑)	1.79476 (690.8)
 HOMO-1 (↑)	 LUMO+3 (↑)	1.83397 (676.0)
 HOMO-3 (↓)	 LUMO+2 (↓)	1.79509 (690.7)

HOMO	LUMO	eV (nm)
 <p>HOMO-4 (↓)</p>	 <p>LUMO+2 (↓)</p>	1.81909 (681.6)
 <p>HOMO-5 (↓)</p>	 <p>LUMO+2 (↓)</p>	1.83249 (676.6)
 <p>HOMO (↓)</p>	 <p>LUMO+4 (↓)</p>	1.82618 (678.9)

\*(where P = CH+YGDD) and energy gaps = 655–695 nm.

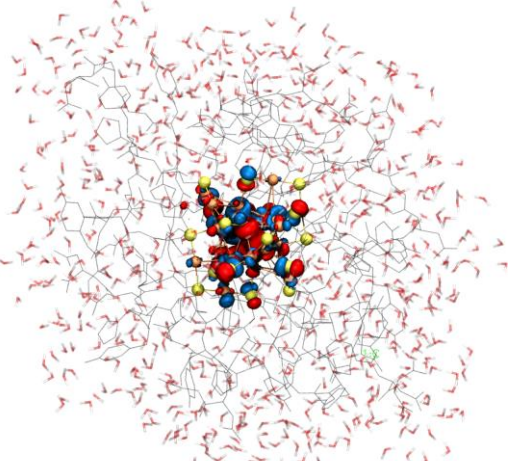
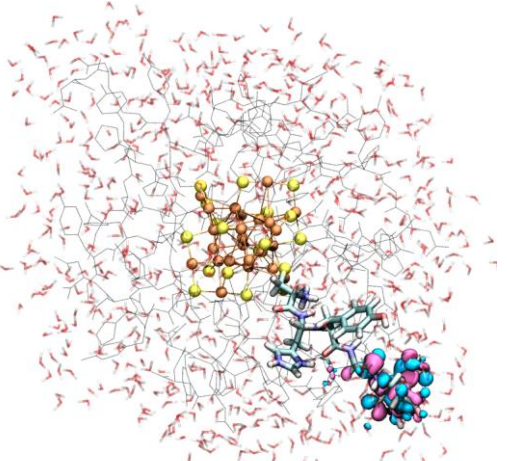
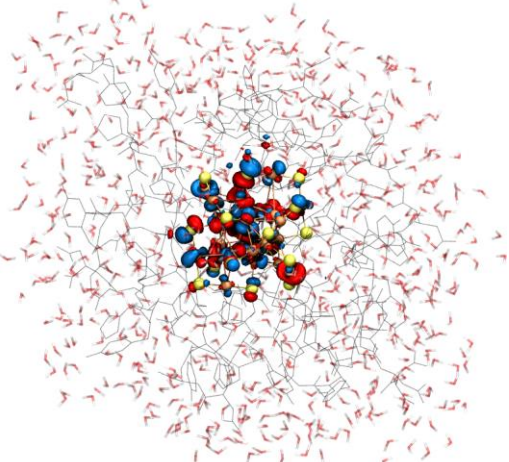
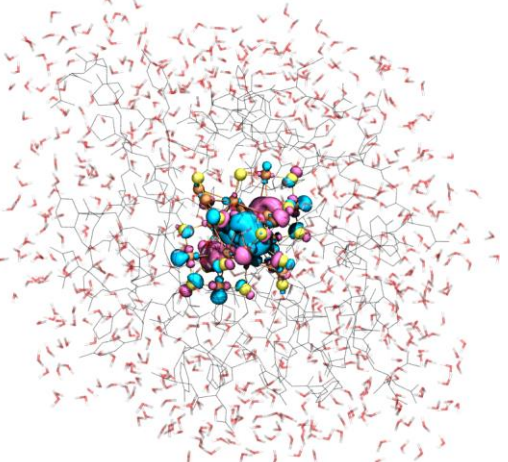
Table D.7 | Kohn–Sham orbitals of Au<sub>25</sub>(SP)<sub>18</sub> (conformer III).\*

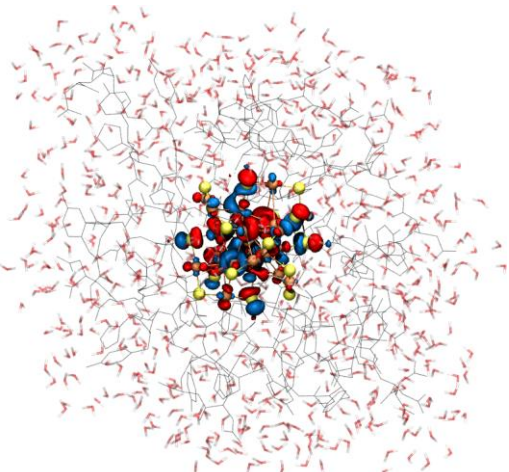
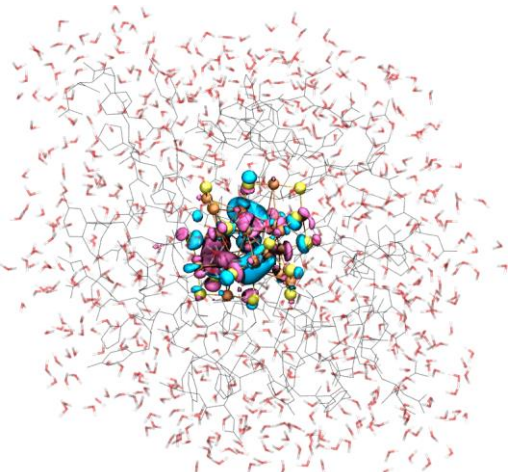
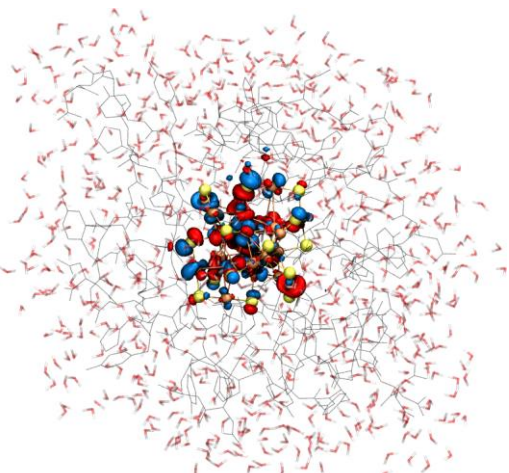
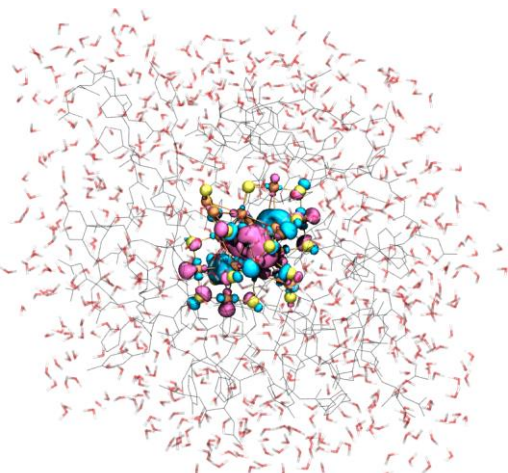
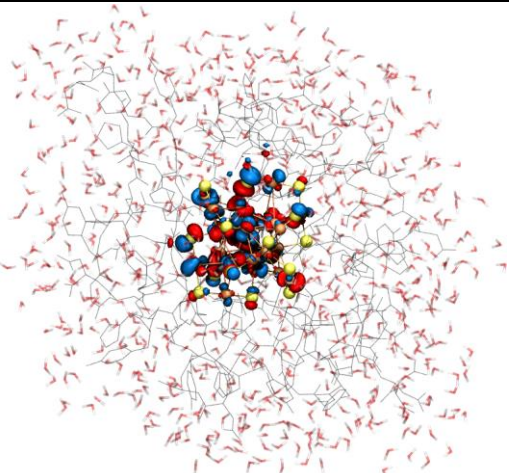
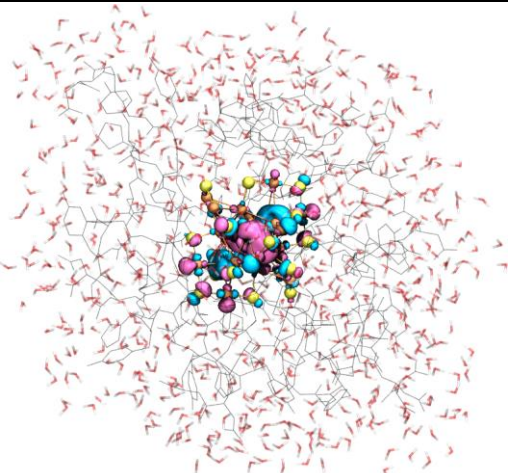
HOMO	LUMO	eV (nm)
 HOMO-1 (↑)	 LUMO+2 (↑)	1.79710 (689.9)
 HOMO (↑)	 LUMO+3 (↑)	1.84388 (672.4)
 HOMO-2 (↑)	 LUMO+2 (↑)	1.87503 (661.2)
 HOMO-5 (↓)	 LUMO+2 (↓)	1.85418 (668.7)

HOMO	LUMO	eV (nm)
		1.87247 (662.1)
HOMO-1 (↓)	LUMO+3 (↓)	

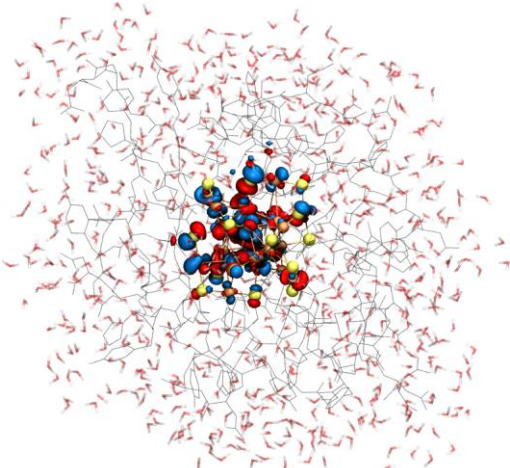
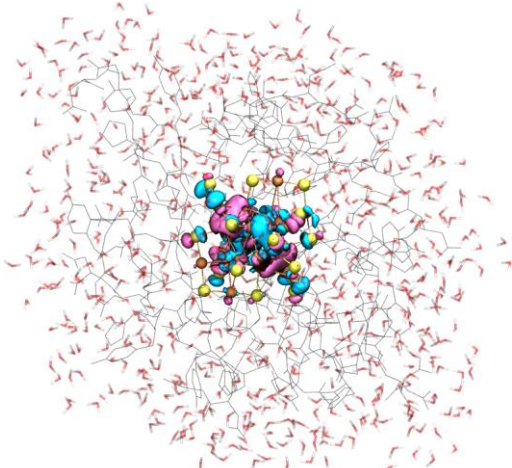
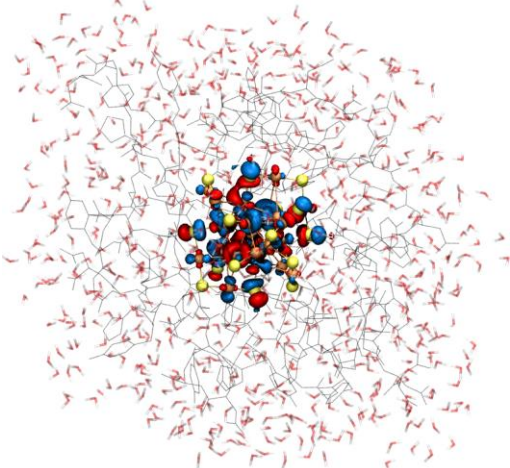
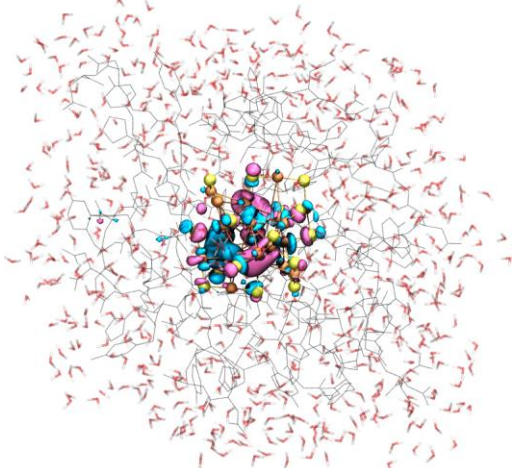
\*(where P = CH+YGDD) and energy gaps = 655–695 nm.

**Table D.8 | Kohn–Sham orbitals of Au<sub>25</sub>(SP)<sub>18</sub> (conformer III').\***

HOMO	LUMO	eV (nm)
		1.80908 (685.3)
HOMO-1 (↑)	LUMO+5 (↑)	
		1.81977 (681.3)
HOMO-5 (↑)	LUMO (↑)	

HOMO	LUMO	eV (nm)
 <p>HOMO-2 (↑)</p>	 <p>LUMO+4 (↑)</p>	1.85461 (668.5)
 <p>HOMO-5 (↑)</p>	 <p>LUMO+1 (↑)</p>	1.88633 (657.3)
 <p>HOMO-4 (↓)</p>	 <p>LUMO+1 (↓)</p>	1.82018 (681.2)



HOMO	LUMO	eV (nm)
		1.87821 (660.1)
HOMO-4 (↓)	LUMO+2 (↓)	
		1.86434 (665.0)
HOMO-1 (↓)	LUMO+5 (↓)	

\*(where P = CH+YGDD) and energy gaps = 655–695 nm.